


ADVERTIMENT. L'accés als continguts d'aquesta tesi queda condicionat a l'acceptació de les condicions d'ús establertes per la següent llicència Creative Commons:  http://cat.creativecommons.org/?page_id=184

ADVERTENCIA. El acceso a los contenidos de esta tesis queda condicionado a la aceptación de las condiciones de uso establecidas por la siguiente licencia Creative Commons:  <http://es.creativecommons.org/blog/licencias/>

WARNING. The access to the contents of this doctoral thesis it is limited to the acceptance of the use conditions set by the following Creative Commons license:  <https://creativecommons.org/licenses/?lang=en>



**Universitat Autònoma
de Barcelona**

**Pyrazole as a framework for ligand design:
synthesis of new ligands and coordination
compounds**

Joan Soldevila Sanmartín

DOCTORAL THESIS

Ph. D. In Chemistry

SUPERVISORS

Dra. Josefina Pons Picart

Dr. José Giner Planas

Departament de Química – Facultat de Ciències (UAB)
Institut de Ciència de Materials de Barcelona (ICMAB-CSIC)

2021

Memòria presentada per aspirar al Grau de Doctor per Joan Soldevila Sanmartín

Joan Soldevila Sanmartín

Vist i Plau:

Dra. Josefina Pons Picart

Dept. de Química

Facultat de Ciències (UAB)

Dr. José Giner Planas

Institut de Ciència dels

Materials de Barcelona

ICMAB-CSIC

Bellaterra, 08 de Juliol del 2021

Agraïments

Com totes les grans tasques, la confecció d'una tesi doctoral no és mai un èxit individual. Aquest document no s'hauria escrit sense la ajuda de les persones anomenades a continuació, i és per aquest motiu que vull aprofitar les primeres ratlles d'aquest treball per agrair-ne la seva contribució.

Primer de tot, vull agrair a la Dra. Josefina Pons i al Dr. José Giner la seva constant ajuda, atenció i dedicació a aquest projecte. Sense el seu lideratge i guia, no hauria estat possible realitzar aquest treball. També vull agrair tant al Dr. Francesc Teixidor com a la Dra. Clara Viñas per la seva bona acollida al grup “Inorganic Materials and Catalysts” de l'ICMAB, a més del seu suport científic i financer. També vull agrair la ajuda rebuda, especialment en temes de fluorescència, a la Dra. Rosario Núñez i, en les mesures termogravimètriques, a la Dra. Teresa Calvet de la UB.

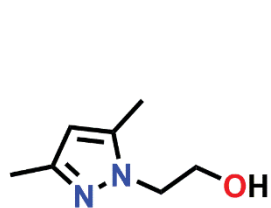
La resolució de les estructures cristallines obtingudes durant aquesta tesi ha estat a càrrec de la Dra. Mercè Font-Bardia, el Dr. Duane Choquesillo-Lazarte i el Dr. Mark E. Light, als qui els hi he de oferir el meu agraïment més sincer. Les dades d'algunes d'aquestes estructures van ser obtingudes al sincrotró ALBA, i és per això que agraeixo a el seu staff la atenció rebuda durant aquest procés. Respecte al Dr. Eliseo Ruiz vull agrair-li que ens permetés la realització de mesures de fluorescència en estat sòlid, així com la realització del càlculs TD-DFT. També vull agrair al Dr. Miguel Guerrero la seva ajuda en la redacció de d'articles d'investigació. En aquesta llista d'agraïments cal mencionar-hi també a Jordi Cortés, pel manteniment del laboratori, la preparació dels dissolvents secs i facilitar-nos enormement la feina en general. Finalment, vull agrair a la ajuda en diverses mesures realitzades al llarg d'aquesta feina als diferents serveis científicotècnics de la UAB, l'ICMAB i el ICN2.

Estar envoltat de bons companys aquests anys ha estat una gran ajuda tant a nivell científic com moral. En aquest aspecte, voldria remarcar la meua alegria en compartir “casa” amb companys tant excel·lents com Fran Sánchez, Dani Ejarque, el Dr. Jordi Borràs, la Dra. Isabel Fuentes, la Dra. Begoña Buades, el Dr. Lei Gan, la Dra. Fangchang Tan, Sohini Sinha, Jewel Ann Xavier, Zhen Li, Miquel Nuez, el Dr. Mahdi Chaari, Isabel Guerrero, la Dra. Silvia Mena i la Sara Santiago. Aquest anys també m'han permès gaudir de la companyia de moltes altres persones que han treballat al departament de Química

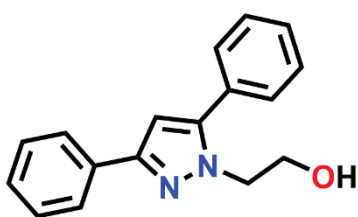
Inorgànica de la UAB. A totes els hi vull agrair les estones d'esbarjo i diversió que hem compartit.

No podia acabar aquest escrit sense agrair el suport incondicional que he rebut a tots els nivells per part de la meva parella i dels meus pares, qui realment no han deixat mai de fer-me costat. Necessitaria unes altres quatre-centes pàgines per expressar el meu agraïment, i tot i així faria molt curt.

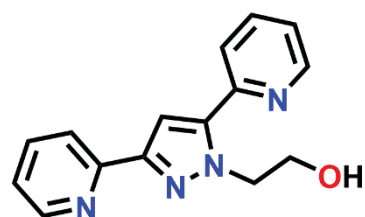
Ligands



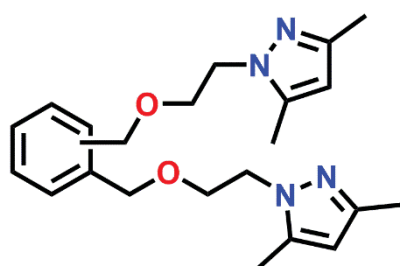
HL1



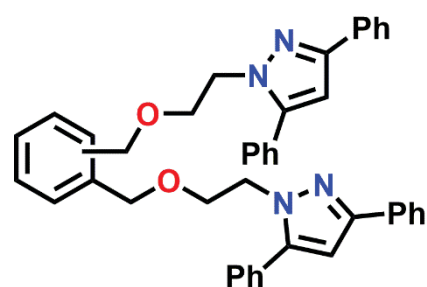
HL2



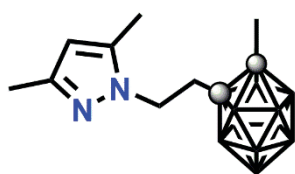
HL3



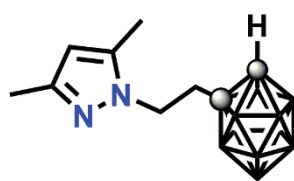
L4 = para-
L5 = ortho-



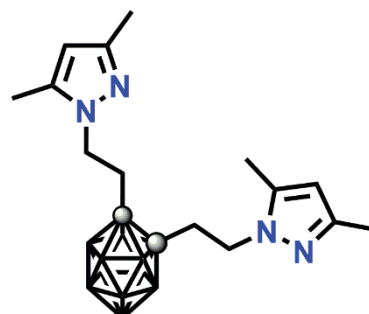
L6 = para-
L7 = meta-
L8 = ortho-



L9

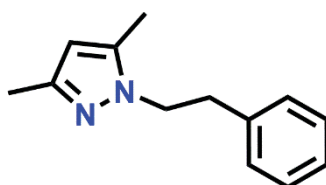


L10



L11

● = C, rest = B-H



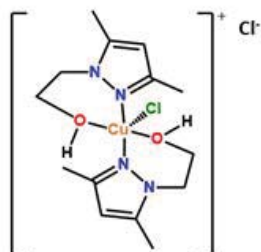
L12

Complexes

Section 3.2



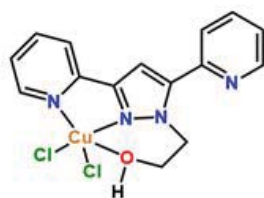
$[\text{CuCl}(\mu\text{-L1})]_2$ (1)



$[\text{CuCl}(\text{HL1})_2]\text{Cl}$ (2)



$\text{R} = \text{C}_6\text{H}_5$
 $[\text{CuCl}(\mu\text{-L2})]_2 \cdot \text{HL2}$
(3·HL2)



$[\text{CuCl}_2(\text{HL3})] \cdot (\text{CH}_2\text{Cl}_2) \cdot (\text{H}_2\text{O})$
(4·(CH₂Cl₂)(H₂O))



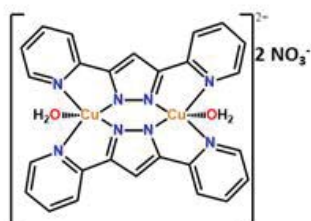
$\{[\text{Cu}(\mu\text{-NO}_3)(\mu\text{-L1})]_2\}_n$ (5)



$[\text{Cu}(\text{NO}_3)(\text{HL1})_2]\text{NO}_3$ (6)



$[\text{Cu}(\text{NO}_3)(3,5\text{-DPP})(\mu\text{-L2})]_2 \cdot 2(\text{CH}_3\text{CN})$
(7·2CH₃CN)

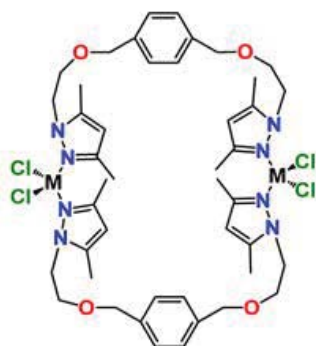


$[\text{Cu}(3,5\text{-DPP})(\text{H}_2\text{O})]_2(\text{NO}_3)_2 \cdot (\text{H}_2\text{O})$
(8·H₂O)

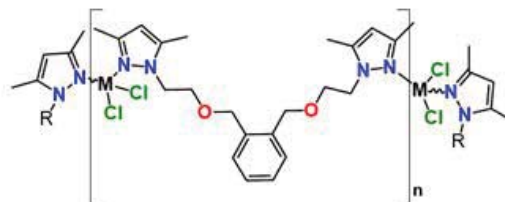


$[\text{Cu}(\text{CH}_3\text{COO})(\mu\text{-L1})]_2 \cdot 6\text{H}_2\text{O}$
(9·6H₂O)

Section 3.3

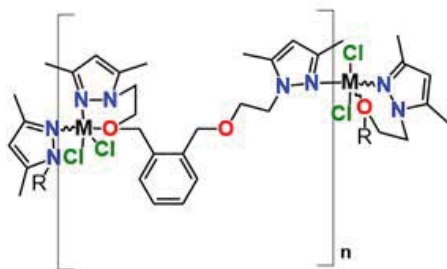


$[MCl_2(L4)]_2$
 $M = Zn(II)$ (10), $Cd(II)$ (11), $[CoCl_2(L4)]_2 \cdot 1/2H_2O$ (13)
 $Hg(II)$ (12)



$\{[MCl_2(L5)] \cdot 1/2H_2O\}_n$
 $M = Zn(II)$ (15), $Co(II)$ (18)

$[CuCl_2(L4)]$
 (14)



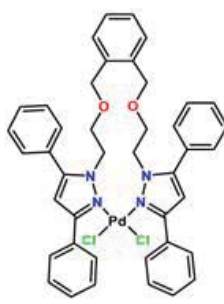
$\{[MCl_2(L5)] \cdot 1/2EtOH\}_n$
 $M = Cd(II)$ (16), $Hg(II)$ (17)



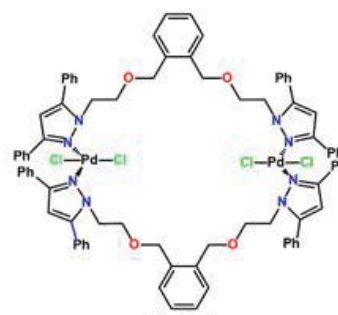
$[Cu_2Cl_4(L5)]$
 (19)



$[PdCl_2(L6)]$ (20)
 $[PdCl_2(L7)]$ (21)

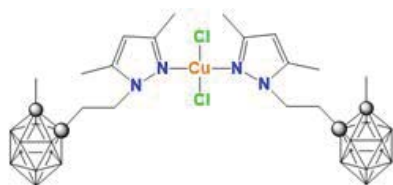


$[PdCl_2(L8)]$ (22)



$Ph = C_6H_5$
 $[PdCl_2(L8)]_2$ (23)

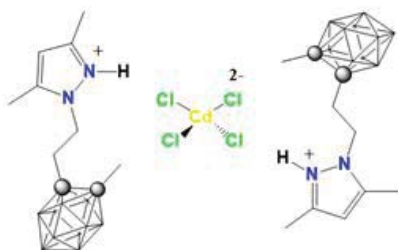
Section 3.4



**[CuCl₂(L9)₂]
(24)**



**[ZnCl₂(L9)₂]
(25)**


$$[\text{CdCl}_4][(\text{HL9})]_2$$

(26)


$$[\text{HgCl}_4][(\text{HL9})]_2$$

(27)



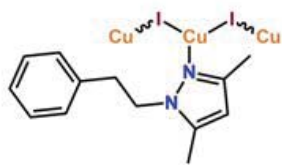
**[PdCl₂(L10)₂]
(28)**



[PdCl₂(L11)]
(29)

● = C, rest of vertexes = B-H

Section 3.5

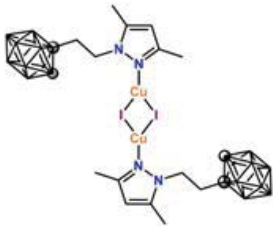


$\{[\text{Cu}(\text{L12})]\}_n$
(30)

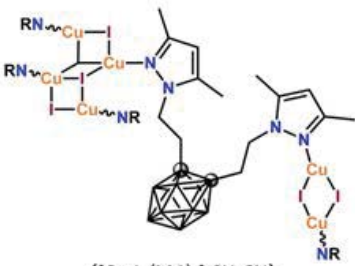


$[\text{Cu}(\text{L9})]_4$
(32)

● = C, rest of vertexes = B-H



$[\text{Cu}(\text{L10})]_2$
(31)



$\{[\text{Cu}_4(\text{L11})_2] \cdot \text{CH}_3\text{CN}\}_n$
(33)

List of Abbreviations

Chemical Compounds			
Ph	Phenyl	Pyr	2-pyridine
Oct	Octyl	Et	Ethyl
ⁱ Pro	Iso-propyl	^t But	Tert-butyl
Eth	Ether	AcOEt	Ethyl Acetate
THF	Tetrahydrofuran	MeOH	Methanol
EtOH	Ethanol	Et ₂ O	Diethyl ether
Pz	Pyrazole	Ts	Tosylate
ACN	Acetonitrile	Carb	Carborane
AcD ₆	Deuterated Acetone	Alk	Alkyl
MeCO ₂	Acetate	Meth	Methyl
DMF	Dimethylformamide	<i>n</i> -BuLi	<i>n</i> -Butyllithium
W	Water	<i>o</i> -, <i>m</i> - or <i>p</i> -	<i>Ortho</i> -, <i>meta</i> - or <i>para</i> -
MCPBA	<i>Meta</i> -chloroperoxybenzoic acid		
PzOTs	3,5-dimethyl-1-(2-toluene- <i>p</i> -sulfonyloxyethyl)pyrrole		
3,5-DPP	3,5-diphenylpyrazole		
3,5-DpyP	3,5-di(2-pyridyl)pyrazole		

Characterization	
EA	Elemental Analyses
M.p.	Melting Point
IR	Infrared
FTIR-ATR	Fourier Transformed Infrared Attenuated Total Reflectance
NMR	Nuclear Magnetic Resonance
HSQC	Heteronuclear Single Quantum Coherence
COSY	Homonuclear Correlation Spectroscopy
DOSY	Diffusion-Ordered Spectroscopy
PXRD	Powder X-ray Diffraction
SCXRD	Single-Crystal X-ray Diffraction
UV-Vis	Ultraviolet-Visible
TGA/TDA	Thermogravimetric Analysis / Thermal Differential Analysis
TDDFT	Time-Dependent Density-Functional Theory
TLC	Thin Layer Chromatography

FTIR-ATR			
ν	Stretching vibration	δ	Deformation vibration
ar	Aromatic	al	Aliphatic
ip	In-plane	oop	Out of plane
as	Asymmetric	s	Symmetric
Intensity s = strong, m = medium, w = weak, br = broad			

NMR	
δ (ppm)	Chemical shift in parts per million
Multiplicity s = singlet, d = doublet, t = triplet, m = multiplet	

Luminescence			
LE HOMO	Low Energy Highest Occupied Molecular Orbital	HE LUMO	High Energy Lowest Unoccupied Molecular Orbital
CT	Charge Transfer		
MLCT	Metal-to-Ligand Charge Transfer		
XLCT	Halide-to-Ligand Charge Transfer		
(X+M)LCT	Halide and Metal-to-Ligand Charge Transfer		
XMCT	Halide-to-metal Charge Transfer		
ILCT	Intra-Ligand Charge Transfer		
CC	Cluster-Centred charge transfer		
PLQY, Φ_F	Photoluminescence Quantum Yield		

Other	
<i>ata</i>	Average Torsion Angle
V_{vdW}	Van der Waals Volume
D	Dipolar Moment
BNCT	Boron Neutron Capture Therapy
CCDC	Cambridge Crystallographical Data Centre
CSD	Cambridge Structural Database
CP	Coordination Polymer
MOF	Metal-Organic Framework
0D/1D/2D/3D	Zero/one/two/three dimensional
RT or r.t.	Room Temperature
LECs	Light-emitting Cells

Abstract

This PhD mainly revolves about the synthesis of pyrazole-derived ligands and their coordination compounds. The particular ligands used in this work are tri-substituted pyrazole rings (positions 1- (*N*-substitution), 3- and 5-), which can be classified in three families: *N*-hydroxyethylpyrazole, bispyrazole ether and *N*-alkylcarborane ligands. In this work, six previously unreported ligands have been synthesized for the first time, and thirty-two metal complexes have been obtained.

Chapter 1 starts by offering an overview of the Design of Metal Organic Materials (DMOM) group past work in the synthesis of pyrazole-derived ligands as well as in the background of the Laboratory of Inorganic Materials and Catalyst's (LMI) group in incorporating *N*-heterocycles to the carborane moiety.

Chapter 2 states the general and specific objectives for this thesis.

Chapter 3, where the results obtained during this work are discussed, is divided in five sections:

Section 3.1 contains the synthesis and characterization of six new pyrazole derived ligands. The first three (**L6-L8**) belong to the bispyrazole ether family, and incorporate phenyl moieties in positions 3- and 5-. The next three (**L9-L11**) are the first examples of *N*-alkylcarborane pyrazole ligands.

Section 3.2 describes the reactivity of a family of three different *N*-hydroxyethylpyrazole ligands bearing methyl, phenyl or 2-pyridyl groups (**HL1-HL3**) against different Cu(II) salts. The crystal structures of the nine resulting compounds have been elucidated, allowing the study of their molecular structures and supramolecular networks. These studies lead to the assessment that the alcohol moiety is the key player in determining the nuclearity of the resulting compounds.

Section 3.3 focuses on bispyrazole ether ligands. In the first part, the reactivity of two positional isomers of a bispyrazole ligand (**L4** and **L5**) against different MCl₂ salts (M = Zn(II), Cd(II), Hg(II), Co(II) and Cu(II)) has been assayed. This afforded ten coordination compounds bearing three clearly different topological motifs: dimeric metallacycles for **L4**, and 1D polymers and dimers for **L5**, demonstrating the effect of the relative position of the pyrazole arms in the topology of the resulting compounds. In the

second part, the reactivity of the novel ligands **L6-L8** against Pd(II) is assayed, and the results compared with those previously obtained with **L4** and **L5**.

In **Section 3.4**, the first coordination complexes containing *N*-alkylcarborane pyrazole ligands are described. In this work, a total of six coordination compound bearing **L9-L11** and different metal centres (Cu(II), Zn(II), Cd(II), Hg(II) and Pd(II)) are described, allowing the observation of the effect of adding the carborane moiety to the pyrazole backbone.

Section 3.5 describes the obtention of four luminescent Cu(I) compounds bearing ligands **L9-L12**. Some of them bear particularly rare motifs, and their obtention during the same work is remarkable. Moreover, the study of their luminescent behaviour has allowed us to investigate the emission processes in some scarcely studied compounds. These studies are backed by TDDFT calculations.

In **Chapter 4** the general conclusions of this work are presented.

Moreover, for the sake of completeness, this work also contains an experimental section (**Chapter 5**) and an annex (**Annex I**) which contains all the spectra and additional information for this work.

Finally, all the related publications for this work can be found in **Annex II**

Table of Contents

1. Introduction	5
1.1 Coordination Chemistry and ligand design	6
1.2 <i>N</i>-donating heterocyclic ligands: pyrazole	7
1.3 Functionalization of pyrazole ligands	8
1.3.1 <i>N</i>-hydroxyalkylpyrazole ligands	12
1.3.2 Flexible <i>N,O</i>-bispyrazole ether ligands	18
1.3.3 Synthetic strategies for the <i>N</i>-functionalization of pyrazole ligands	21
1.4 Carboranes	25
1.4.1 Synthesis and properties	27
1.4.2 Carborane functionalization	30
1.4.3 Carboranes as building blocks for coordination compounds: group antecedents	32
References	38
2. Objectives	53
3. Results and Discussion	56
3.1 Ligands	57
3.1.1 Ligand overview	59
3.1.2 Synthesis and characterization of L6-L8	62
3.1.3 Synthesis and characterization of L9-L11	68
3.1.4 Summary and Conclusions	82
References	83
3.2 Synthesis and characterization of Cu(II) coordination complexes bearing 3,5-disubstituted <i>N</i>-hydroxyethylpyrazole ligands	86
3.2.1 Synthesis and Characterization	90
3.2.2 Crystal and Extended structures	97
3.2.3 Structural discussion	117
3.2.4 Molecular Magnetism for compounds 1, 3, 5 and 9	117
3.2.5 Summary and Conclusions	120
References	121
3.3 Synthesis and characterization of Zn(II), Cd(II), Hg(II), Co(II), Cu(II) and Pd(II) coordination compounds with <i>N</i>-pyrazole, <i>O</i>-ether hybrid ligands	125
3.3.1 Zn(II), Cd(II), Hg(II), Co(II) and Cu(II) compounds with L4 and L5	127
3.3.2 Pd(II) compounds with L6-L8	155
3.3.3 Summary and Conclusions	161

References	162
3.4 Synthesis and characterization of new coordination compounds with <i>N</i>-pyrazole-carborane ligands and divalent metals.....	166
3.4.1 Synthesis and characterization.....	169
3.4.2 Supramolecular structures of 24, 25, 27 and 29	181
3.4.3 Summary and Conclusions	190
References	191
3.5 Synthesis and characterization of new Cu(I) coordination compounds with <i>N</i>-pyrazole-carborane ligands	195
3.5.1 Photoluminescent properties of Cu(I) compounds	197
3.5.2 Cu(I) compounds of L9-L12	199
3.5.3 Photophysical studies for compounds 30-33	216
3.5.4 Summary and Conclusions	226
References	228
4. Conclusions	235
5. Experimental Section	240
5.1 Experimental Section for 3.1	242
5.2 Experimental Section for 3.2	246
5.3 Experimental Section for 3.3	252
5.4 Experimental Section for 3.4	259
5.5 Experimental Section for 3.5	263
5.6 Crystallographic Data.....	267
References	279
ANNEX I: Spectra and Additional Information	A1
Annex for Section 3.1	A2
Annex for Section 3.2	A12
Annex for Section 3.3	A20
Annex for Section 3.4	A50
Annex for Section 3.5	A60
ANNEX II: Publications	A70

1. Introduction

1.1 Coordination Chemistry and ligand design

Coordination chemistry is the study of compounds that have a central atom (often metallic) surrounded by molecules or anions, known as ligands. The ligands are attached to the central atom by dative bonds, also known as coordinate bonds, in which both electrons in the bond are supplied by the same atom on the ligand^{1–3}. It is commonly accepted that the father of modern coordination chemistry is the 1913 Nobel Prize winner Alfred Werner, who identified the principal features of the geometrical structures of metal complexes⁴.

Over the years, enhanced comprehension of the properties of coordination compounds has led to the realization of the intrinsic relationship between their structure and their functionality⁵. This realization has led coordination chemists to investigate the next logical step, that is, to envision new strategies to predict the structure, and thus, the functionality, of new compounds. The natural course of this thought process also leads to the next two logical objectives: i) to optimize said functionalities and ii) to create new ones. Thus, synthesis of coordination compounds bearing desired topological motifs and functionalities has become the driving force of many chemists' research.

The field progressed into a sort of “construction games” competition, ever pursuing new functionalities and architectures. It has been found that the final architecture of the compounds has a strong dependence on the interaction between “building modules” (organic ligands, metal centres and their counter-ions, solvent molecules) as well as reaction conditions (pH, temperature, time and the use of templates or structure-directing anions). Moreover, it has been recognised that non-bonding interactions between molecules are also an integral part of the properties of the resulting coordination compound⁶.

The choice of organic ligand is, perhaps, the “building module” that offers more freedom for the investigator. There are countless possible organic ligands, possessing any number and combination of functional groups. Here, only the imagination of the chemist is the limit. Thus, the concept of “ligand design”, that is, synthesising ligands with the specific aim of obtaining a desired structure, was born.

Perhaps one area where this fact is most obvious is in the synthesis of coordination polymers (CP) and metal-organic frameworks (MOFs). The immense number of possible

compounds afforded by and almost at-will combination of metal centres and organic ligands resulted in the interest for this field skyrocketing, perhaps being one of the most researched topics today^{7–9}. The enormous interest generated by this family of compounds resulted in extensive investigation on ligand design^{10–13}, paving its way into becoming a field of research by itself^{14–17}.

The constant drive for smarter and more efficient materials, as well as new functionalities has led to the emergence of ligands with hetero donating functions, that is, ligands with at least two coordinating atoms of different nature. It is expected that the presence of different atoms on the same scaffold could allow for interesting features such as self-recognition and metal discrimination (based on Pearson's theory of hard and soft acids and bases)^{18–22}.

Among the plethora of strategies available to afford these desired ligands, the Design of Metal Organic Materials (DMOM) group, headed by Dr. Josefina Pons, specializes in the use of *N*-donating heterocycles as scaffolds for the incorporation of new functionalities.

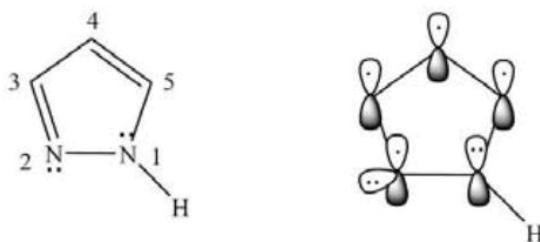
1.2 *N*-donating heterocyclic ligands: pyrazole

Heterocyclic compounds are those that possess a cyclic structure and include at least one atom other than carbon, usually oxygen, nitrogen, or sulphur. Among them *N*-donor heterocycles are of great interest to coordination chemists, owing to their well-known coordination properties to metals.

Pyridines are, arguably, one of the most well-known and used *N*-heterocyclic donors, and for many years the favourite *N*-heterocycle for the synthesis of coordination compounds¹⁸. However, in more recent times, owing to its higher denticity, stronger coordination ability and ease of functionalization, a different family of *N*-heterocycles is gaining attention: azoles^{23–25}.

For almost three decades, the DMOM group has been focusing on a particular member of the family of azole ligands: pyrazole. It consists of a planar five-membered ring comprising two nitrogen atoms on relative positions 1 and 2. It also contains and

uninterrupted π -electronic system consisting of six electrons located on five p orbitals, thus being aromatic (Scheme 1.1).



Scheme 1.1 Schematic representation of pyrazole

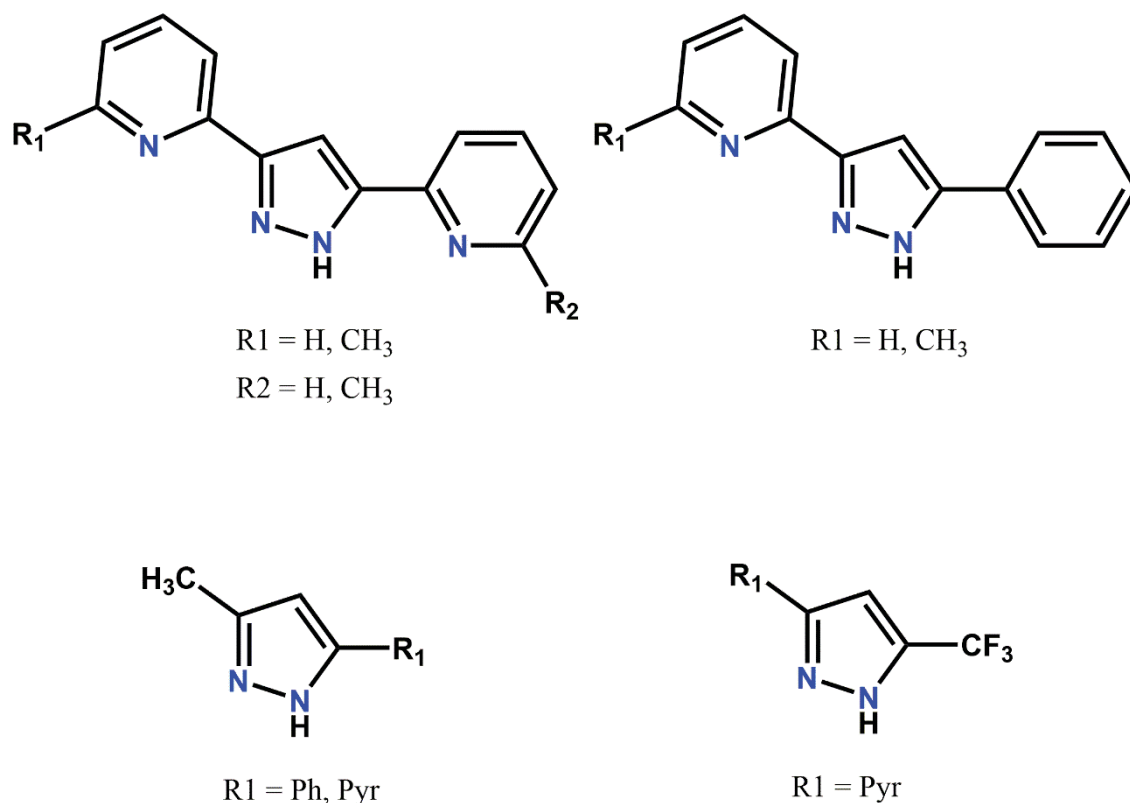
As a ligand, the pyrazole nucleus coordinates *via* its azo nitrogen atom N2. It can also be deprotonated, forming the pyrazolide ion, which acts as an exobidentate ligand coordinating through both nitrogen atoms. Most of the compounds presented in this work are based on neutral pyrazole ligands, and thus they coordinate *via* N2 nitrogen atom.

In the era of ligand design, pyrazoles feature the exciting property of being easily functionalized in positions 1- (*N*-substitution), 3-, 4- and 5-, allowing for the fine tuning of properties such as the acidity of N1 and the nucleophilicity of N2. Thus, this plethora of possibilities has resulted in an increasing interest in the synthesis of pyrazole-derived molecules for multiple applications^{25–32}. Reviews on the subject are not only prolific in number, but also published in a long time scale, as the first one was published in 1972 by Trofimenko³³ and the most recent one was published in 2020 by Mykhailiuk³⁴, attesting the continuous and current relevance of this family of *N*-heterocycles.

1.3 Functionalization of pyrazole ligands

In the early 90s, the DMOM group started working in the functionalization of positions 3- and 5- of pyrazole ligands. These positions were functionalized *via* the incorporation of methyl, phenyl and pyridine groups. Their coordination behaviour against different transition metals such as Mn(II)³⁵, Ru(II) and (III)³⁶, Co(II)^{35,37–39}, Ni(II)^{35,37,39–41}, Pd(II)^{42–44}, Pt(II)⁴³, Cu(II)^{35,39,45–48}, Zn(II)^{35,37} and Cd(II)^{35,37}, was studied, displaying a great structural diversity. Some years later, while continuing with these

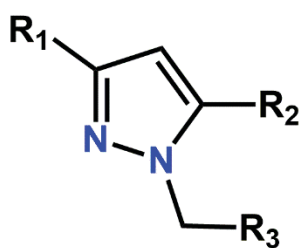
studies, new functional groups were incorporated to the scope of our study, such as trifluoromethyl^{49–51} (Scheme 1.2).



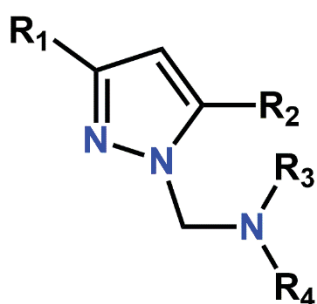
Scheme 1.2 3,5-disubstituted ligands used in the DMOM group. Abbreviation Ph stands for Phenyl, Pyr for pyridine

A new direction was taken when functionalization in position 1- (*N*-functionalization) was incorporated. Thus, the study on the synthesis and coordination of 1,3,5-trisubstituted pyrazole ligands began. The first studies started with the incorporation of alkylic chains, resulting in a family of *N*-alkylpyrazole^{44,49–54} ligands, but soon alkylic chains possessing heteroatoms were employed.

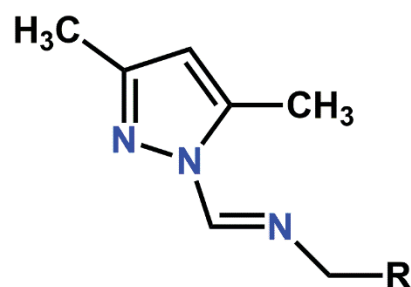
As such, the group developed a library of ligands containing hybrid *N*-pyrazole-*X*-donor groups, such as *N*-amine^{55,56,57–64,65}, *N*-imine⁶⁶, *S*-thiol^{67,68}, *S*-thioether^{55,69}, *S*-sulfoxide/sulfone, *P*-phosphine^{70–74} and *OP*-phosphinite^{75–78} (Scheme 1.3). *N*-pyrazole-*X*-donor ligands containing oxygen atoms in alcohol or ether groups are of special relevance for this PhD work, and will be discussed in detail in sub-sections 1.3.1 and 1.3.2.



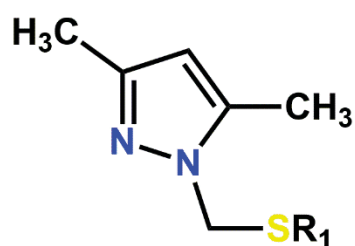
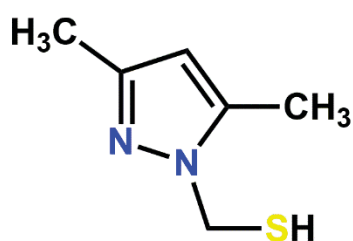
R1 = Pyr, CH₃
 R2 = Ph, Pyr, CF₃
 R3 = Et, Oct



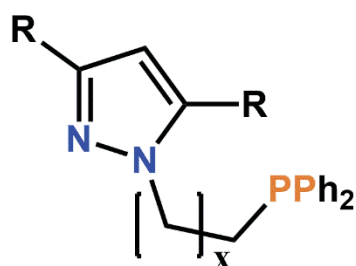
R1 = CH₃, Ph, Pyr,
 R2 = CH₃, Ph
 R3 = H, Et, ^tBut, ⁱPro, Oct
 R4 = H, Et, ⁱPro, Oct



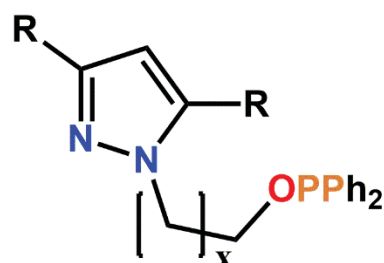
R = CH₃, CH₂CH₃



R1 = CH₂CH₂OH,
 CH₂CH₂CH₂OH, Oct



x = 1,2,3 R = CH₃
 x = 2 R = Ph



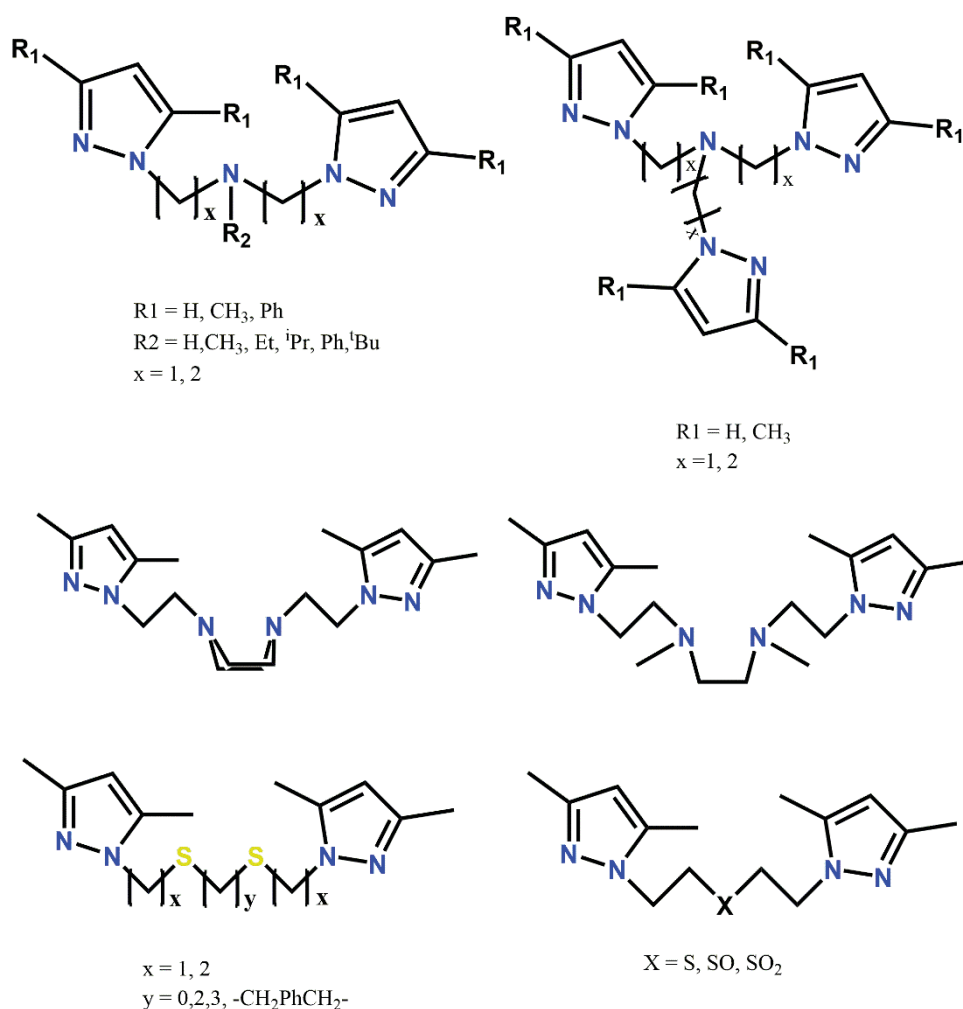
x = 1,2,3 R = CH₃
 x = 2 R = Ph

Scheme 1.3 3,5-disubstituted ligands used in the DMOM group. Abbreviation Ph stands for Phenyl, Pyr for pyridine, Oct for octyl, Et for Ethyl, ⁱPro for iso-propyl and ^tBut for tert-butyl.

Over the years, the coordination behaviour of those ligands against several metals has been studied; mostly using Pd(II)^{44,49,50,52–55,57,58,60,64,65,67–70,75,76} as metal cation, but also other metals such as Fe(II)⁷², Rh(I)^{63,74,77}, Ru(II)^{73,78}, Ni(II)⁶⁹, Pt(II)^{52–54,57,58,61,69}, Cu(I)⁷¹, Ag(I)⁷¹, Au(I)⁷¹, Zn(II)^{62,66} and Cd(II)⁵⁹.

Over the years, it has been demonstrated that conformational freedom of the ligand does have a great impact on the final topology of the coordination polymers. As demonstrated by a plethora of different works, the presence of a flexible moiety between the *N*-pyrazole coordinating sites greatly increases the possibility of obtaining interesting networks and promotes different types of self-assembly. Besides, the inclusion of new functional groups bearing heteroatoms in di-, tri- or tetrapyrazole ligands could also further increase the variability of coordination modes and promote fascinating interactions such as hemilability or selective coordination. Thus, as early as 2001, our group also dedicated great efforts to the synthesis of new polypyrazole ligands linked by chains containing different heteroatoms. This line of work started with the synthesis of bispyrazole ligands linked by amino groups^{59,61–63,79–82}, but soon grew to encompass polypyrazole ligands^{83,84} and bispyrazole ligands^{85,86} linked by diamino groups and bispyrazole ligands linked by thioether^{87–91}, dithioether^{92–98}, thiolate⁹⁹, sulfoxide^{100,101} and sulfone^{100,101} groups (Scheme 1.4). Flexible bispyrazole ligands containing ether groups are of special relevance for this PhD work, and will be discussed in detail in subsection 1.3.2.

Their coordinative properties against several metals such as Rh(I)^{63,79,83,84,98}, Ni(II)⁹⁹, Zn(II)⁶² and Cd(II)⁵⁹ has been studied. However, our main focus has perhaps been Pd(II)^{82,85,86,90,93–95,99,101}, Pt(II)^{61,91,95,99} compounds and the reactivity of the resulting coordination complexes^{80,81,87–89,92,96,97}



Scheme 1.4 Flexible polypyrazole 1,3,5-trisubstituted ligands used in the DMOM group. Abbreviation Ph stands for Phenyl, Et for Ethyl, ⁱPro for iso-propyl and ^tBut for tert-butyl.

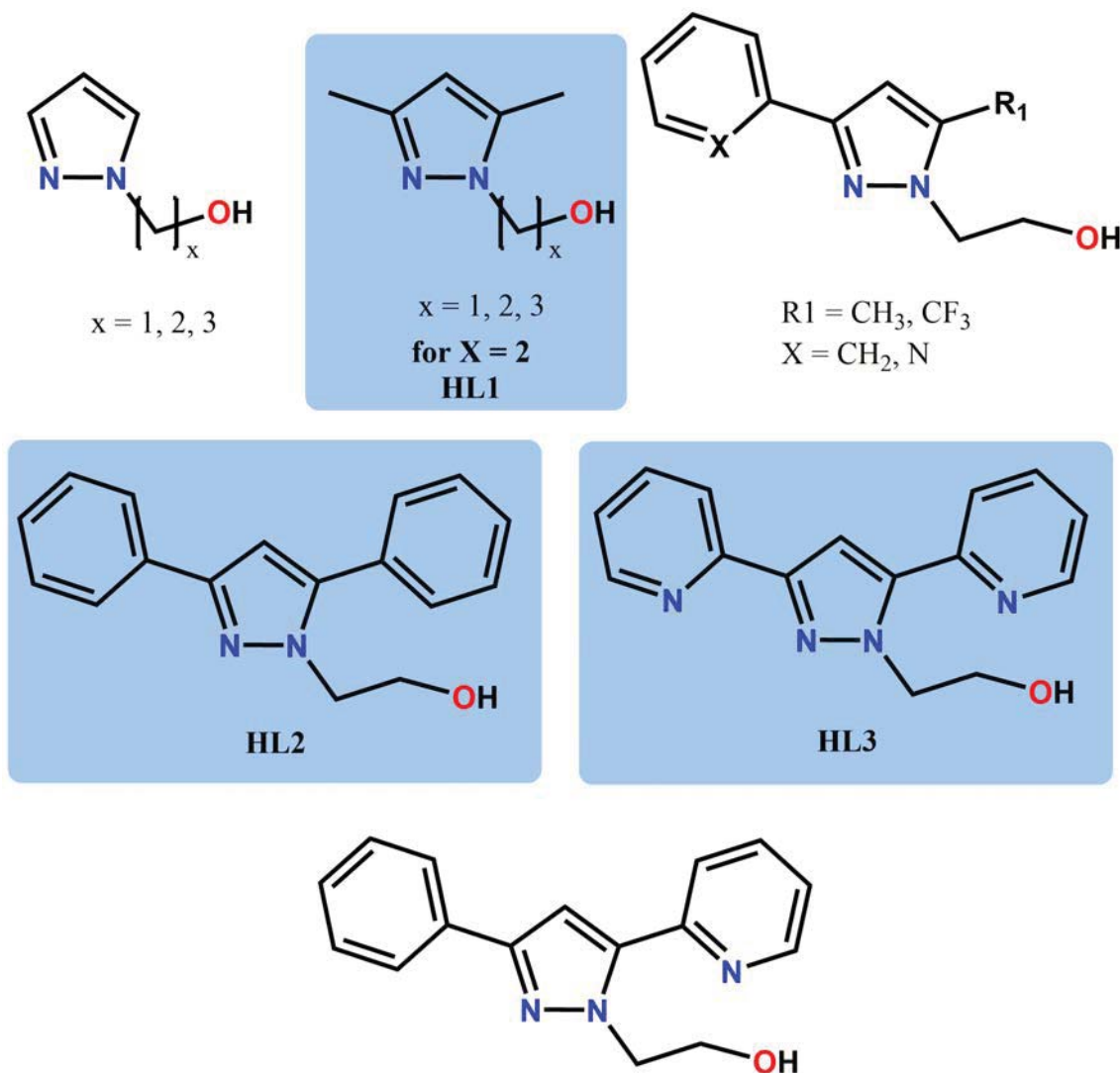
1.3.1 *N*-hydroxyalkylpyrazole ligands

Since 2002, the DMOM group started investigating *N*-pyrazol-*O*-alcohol hybrid ligands. During these years, several reported ligands have been the target of our interest, and several others have been developed, especially those featuring substituted 3,5-positions with methyl, phenyl and pyridyl groups.

For such small and relatively simple molecules, this set of ligands display a rather interesting variability of coordination behaviours. The key player is the alcohol moiety, which can act in variety of manners (*vide infra*).

As such, our group has used and developed several 1-hydroxyalkylpyrazole^{102,103}, 1-hydroxyalkyl-3,5-dimethylpyrazole^{104–107}, ligands bearing aromatic moieties such as

phenyl and pyridines^{108–110} and ligands bearing two heteroleptic substituents in positions 3,5-^{44,111–113}, including groups such as CF₃^{49,50,114} (Scheme 1.5).

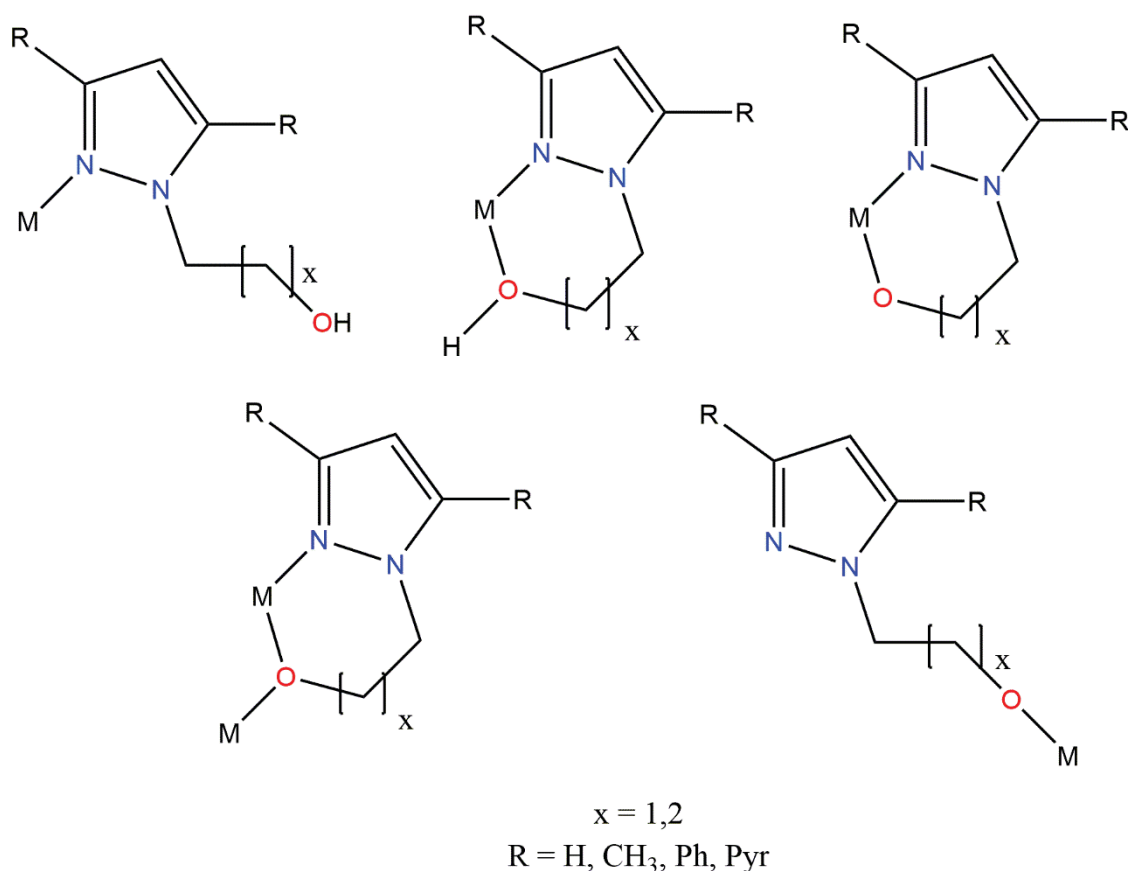


Scheme 1.5 Hybrid *N*-pyrazole-*O*-alcohol ligands used and developed in the DMOM group. Ligands used in this PhD work are highlighted in blue and labelled.

Ligands 2-(3,5-dimethyl-1*H*-pyrazol-1-yl)ethanol (**HL1**), 2-(3,5-diphenyl-1*H*-pyrazol-1-yl)ethanol (**HL2**) and 2-(3,5-pyridyl-1*H*-pyrazol-1-yl)ethanol (**HL3**) will be object of study during this PhD work, and thus will be discussed further below.

As stated before, these molecule offers a great deal of coordination flexibility, resulting in a notable amount of structural variability in the resulting coordination compounds. The flexible alkyl chain allows for easy coordination of the alcohol moiety to the metal centre, or for its participation in intermolecular hydrogen bond or other intermolecular interactions. Moreover, this alcohol moiety can be protonated or

deprotonated, fundamentally changing the nature of the ligand, which becomes an ionic ligand instead of a neutral one (Scheme 1.6).



Scheme 1.6 Reported coordination modes of *N*-hydroxyalkylpyrazole ligands. Abbreviation Ph stands for Phenyl and Pyr for Pyridine.

Our reported investigations on the reactivity of **HL1** against Pd(II) and Pt(II), showed its behaviour as a monodentate ligand, coordinating through the azo-*N* moiety. NMR studies of these compounds displayed a hindered rotation around the *N*-bond, allowing the observation of the *cis*- and *trans*- isomer, although only the crystal structure of the *trans*- Pd(II) and *cis*- Pt(II) isomers were elucidated (Figure 1.1)^{104,107}.

The use of coordinatively flexible metals such as Zn(II), Cd(II) and Hg(II) brought out the diverse coordination possibilities for **HL1**, as well as the result variable topologies. In those metals, **HL1** acted as monodentate and bidentate chelate, often with the same metal, affording monomers, dimers and polymers (Figure 1.2)^{105,106}.

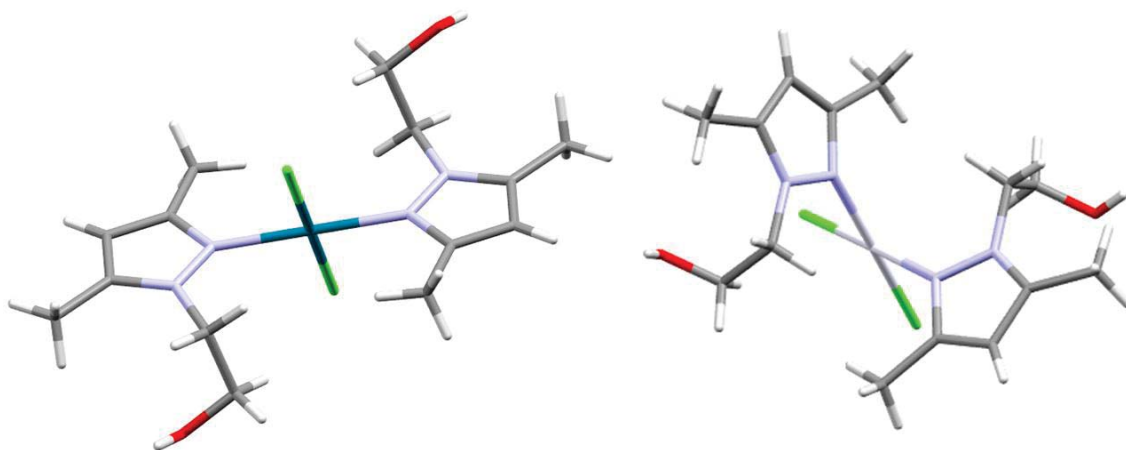


Figure 1.1 Crystal structure of trans-[Pd(HL1)₂Cl₂] (left) and cis-[Pt(HL1)Cl₂]^{104,107}. Colour code: grey (C), light blue (N), light green (Cl), red (O), white (H), dark turquoise (Pd), light-grey (Pt).

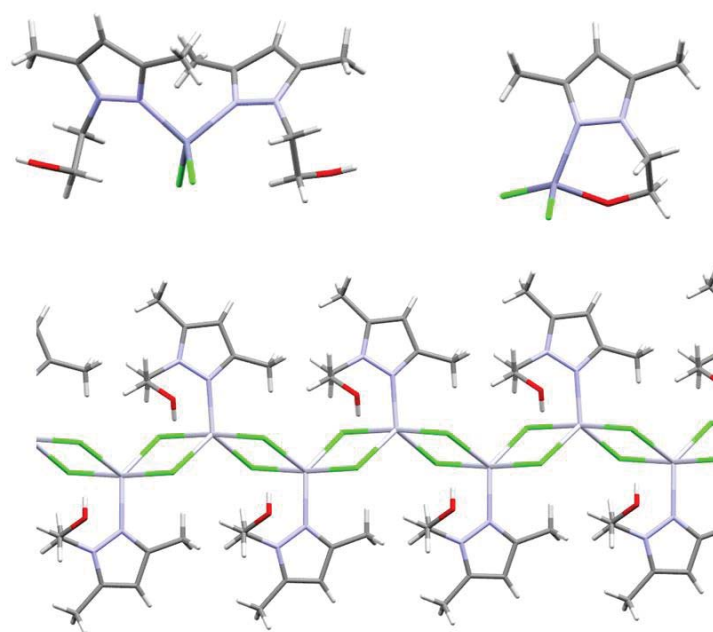


Figure 1.2 Crystal structures of [Zn(HL1)₂Cl₂] (top-left), [Zn(HL1)Cl₂] (top-right) and {[Hg(HL1)Cl₂]}_n (bottom)^{105,106}. Colour code: Grey (C), light blue (N), light green (Cl), red (O), white (H), blue-grey (Zn), light grey (Hg).

Other reported examples including Co(II) and Cu(II) metal centres also reveal the possibility of obtaining new coordinating modes, for instance, in compounds [Cu(L1)Cl]₂¹¹⁵ and [Cu(L1)Br]₂¹¹⁶ where its deprotonation results in the ligand acting as a bidentate chelate and bridging ligand or even combining different coordination modes in the same compound, as in [Cu(L1)(HL1)]₂(ClO₄)¹¹⁷ (Figure 1.3), where a

bidentate chelate and a bidentate chelate and bridging (deprotonated ligand) behaviours are observed.

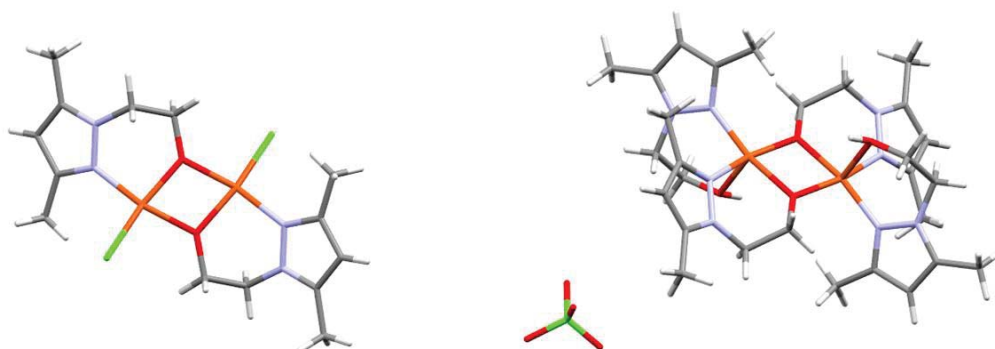


Figure 1.3 Crystal structures of $[\text{Cu}(\text{L1})\text{Cl}]_2$ (left)¹¹⁵, and $\text{Cu}(\text{L1})(\text{HL1})]_2(\text{ClO}_4)$ (right)¹¹⁷. Colour code: grey (C), light blue (N), light green (Cl), red (O), white (H), orange (Cu).

Contrary to **HL1**, coordination behavior of **HL2** and **HL3** has been much less investigated, and only a few reports, most of them published by our group, have been published.

For **HL2**, its coordination behaviour against Pd(II), Zn(II) and Cu(II) has been studied, resulting on the isolation of monomers and dimers¹⁰⁸. In each compound, this ligand displays different coordination behaviours: *N*-monodentate for Pd(II), *N,O*-chelated for Zn(II) (bearing a protonated alcohol group) and *N,O*-chelating and bridging for Cu(II) (bearing a deprotonated alcohol group) (Figure 1.4).

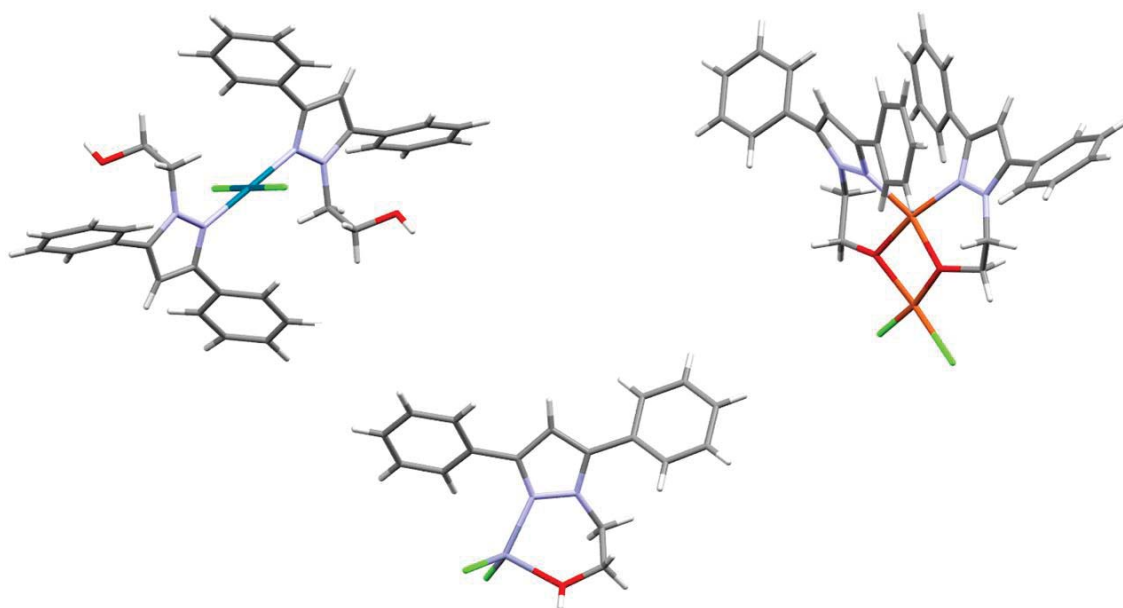


Figure 1.4 Crystal structures of $\text{trans-[Pd(HL2)}_2\text{Cl}_2]$ (left), $[\text{Zn(HL2)Cl}_2]$ (middle) and $[\text{Cu(L2)Cl}]_2$ (right)¹⁰⁸. Note that in each compound the ligand has a different coordination behaviour. Colour code: Grey (C), light blue (N), light green (Cl), red (O), white (H), dark turquoise (Pd), blue grey (Zn), orange (Cu).

Regarding **HL3**, it has been used for the synthesis of coordination compounds bearing Pd(II), Pt(II), Cu(I), Ag(I), and Cu(II) metal centres, resulting in the obtention of monomeric and dimeric compounds¹¹⁰. In all of them, it displayed a *N,N'*-bidentate chelating behaviour, involving one nitrogen atom of the pyrazole ring and one from the pyridine ring. Notably, in all cases the alcohol moiety is protonated, and does not participate in the coordination. As an example, the resulting coordination compound bearing Pd(II) is shown (Figure 1.5).

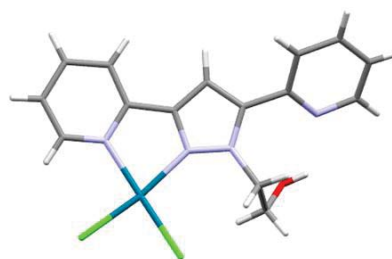


Figure 1.5 Crystal structure of $\text{cis-[Pd(HL3)Cl}_2]$ ¹¹⁰. Colour code: grey (C), light blue (N), light green (Cl), red (O), white (H), dark turquoise (Pd).

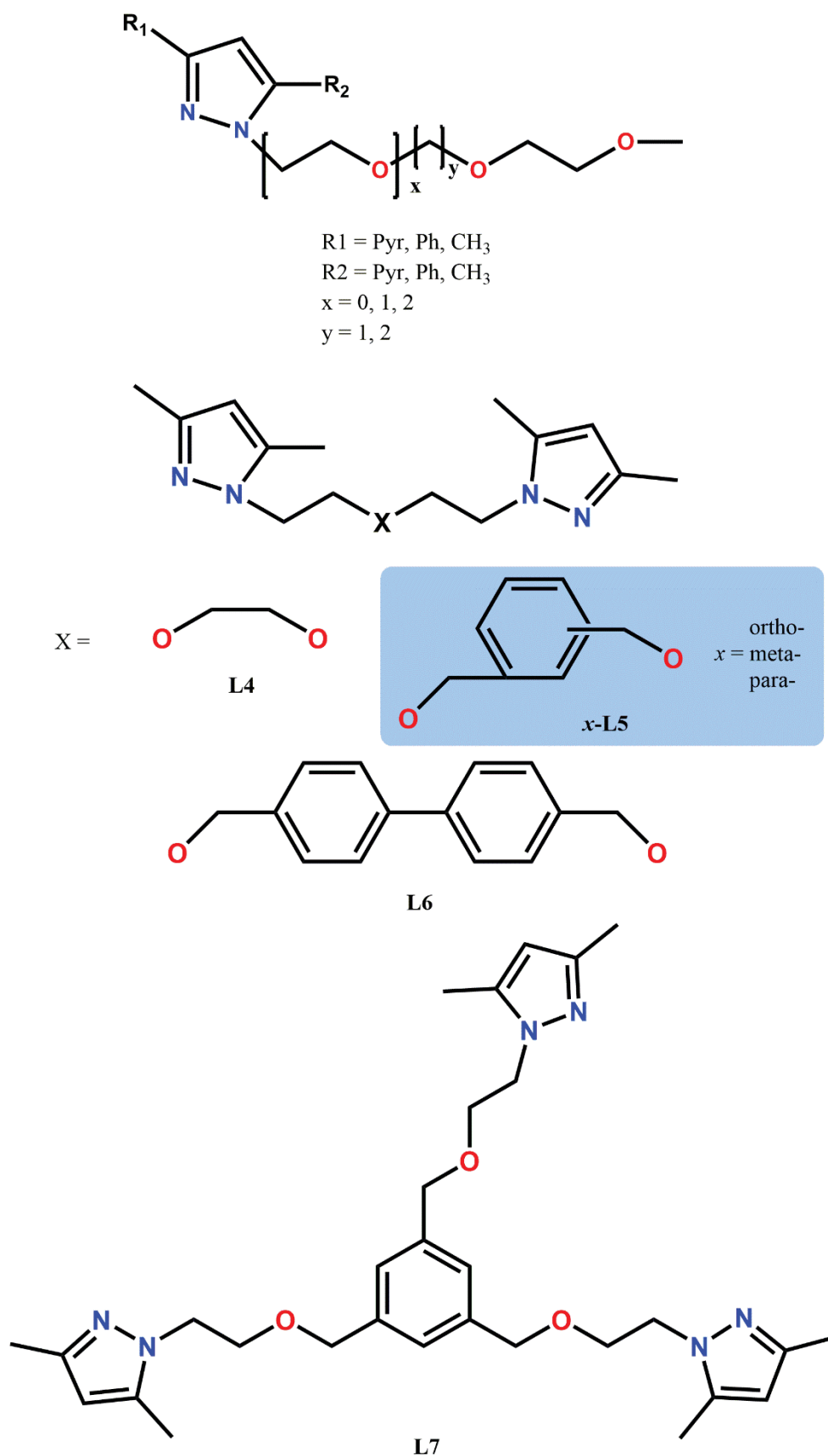
Owing to this lack of reports concerning **HL2** and **HL3**, it was decided to expand the library of coordination compounds bearing these ligands during this PhD work, as well as studying the influence of the use of different metal salts in the resulting coordination compounds for **HL1-HL3**.

1.3.2 Flexible *N,O*-bispyrazole ether ligands

Around the same time as the development of *N,O*-hydroxyalkylpyrazole ligands in our group started, so did the interest in pyrazole ligands containing the ether functionality. First, the research was focused in the addition of polyether chains to the pyrazole moiety, and the reactivity of the resulting ligands was assayed against Rh(I)¹¹⁸, Pd(II)¹¹⁹. On latter years, new polyether pyrazole ligands were synthesized, bearing different substituents in their positions 3- and 5-. Besides its reactivity against Pd(II)¹²⁰ and Pt(II)¹²⁰, the regioselectivity of their synthesis was also studied using theoretical support¹²¹.

However, as already mentioned, our interest grew to encompass flexible polypyrazole ligands containing multiple pyrazole groups bonded to ether or polyether chains *via* their N1 atoms. Examples of such ligands are bis[2-(3,5-dimethyl-1*H*-pyrazolyl)ethyl]ether which is one of the most widely known ligands of this family. Besides our own studies on its reactivity against Rh(I)¹²², Pd(II)¹²³ and Pt(II)¹²³ there are plenty of other reports including metal centres such as Co(II), Cu(I), Zn(II) and Cd(II)¹²⁴⁻¹²⁶.

In this sense, by 2008 the DMOM group started developing a family of new hybrid bispyrazole *N,O*-diether ligands: 1,8-bis(3,5-dimethyl-1*H*-pyrazol-1-yl)3,6-dioxaoctane (**L4**), 1,2-bis[4-(3,5-dimethyl-1*H*-pyrazol-1-yl)2-oxabutyl]benzene (**o-L5**), 1,3-bis[4-(3,5-dimethyl-1*H*-pyrazol-1-yl)2-oxabutyl]benzene (**m-L5**), 1,4-bis[4-(3,5-dimethyl-1*H*-pyrazol-1-yl)2-oxabutyl]benzene (**p-L5**), 4,4'-bis[4-(3,5-dimethyl-1*H*-pyrazol-1-yl)-2-oxabutyl]biphenyl (**L6**), and even a trispyrazole 1,3,5-tris[4-(3,5-dimethyl-1*H*-pyrazol-1-yl)-2-oxabutyl]benzene (**L7**) *N,O*-triether ligand^{127,128} (Scheme 1.7).



Scheme 1.7 Hybrid N,O-ether pyrazole ligands developed by the DMOM group. Ligands used in this PhD work are highlighted in blue. Abbreviation Ph stands for Phenyl and Pyr for Pyridine.

The synthesis of Pd(II) coordination compounds bearing ligands **L4** and all the isomers of **L5** revealed that two distinct types of products were obtained, depending on the reaction solvent. In the first one, the ligand acted in a *NN'*-bidentate chelate fashion, resulting in the isolation of monomers. In the second one, two ligands acted in a *NN'*-bidentate bridged fashion, binding together two Pd(II) atoms in a dimeric macrocycle of thirty members (Figure 1.6). It was also seen that monomeric compounds are the thermodynamically favoured products, as it was possible to convert the dimeric complexes into monomeric ones^{129–131}.

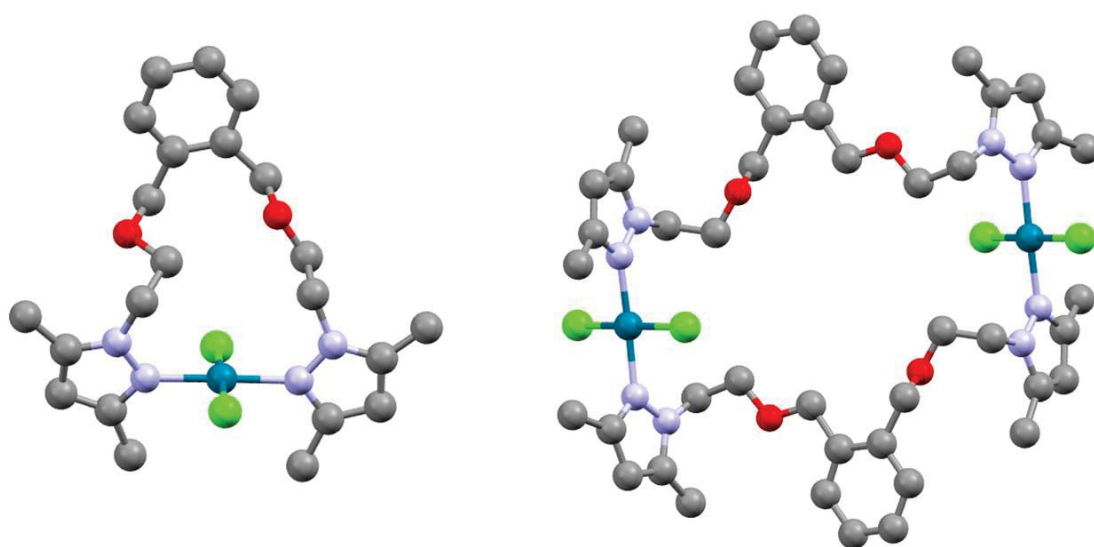


Figure 1.6 Crystal Structure of monomeric $[\text{Pd}(\text{o-L5})\text{Cl}_2]$ (left) and dimeric macrocycle $[\text{Pd}(\text{o-L5})\text{Cl}_2]_2$ (right)¹²⁹. Colour code: grey (C), light blue (N), light green (Cl), red (O), dark turquoise (Pd).

For ligand **L4**, its reactivity against Zn(II), Cd(II), Hg(II), Pt(II) and Ni(II) was also studied^{130,131}. The choice of coordinatively flexible metals proved the versatility of the ligand, as structures with different dimensionalities and coordination behaviours were observed. For instance, its reactivity against ZnCl_2 resulted in the isolation of a polymer where **L4** acts in a *NN'*-bridging fashion, while for CdCl_2 and $\text{NiCl}_2 \cdot 6\text{H}_2\text{O}$ monomers with **L4** acting in a *NOO'N'*-chelate fashion were obtained (Figure 1.7, top). Moreover, it was observed that the use of different metal salts had a great impact in the resulting product, as proven by the product resulting of the reaction of **L4** against $\text{Zn}(\text{ClO}_4)_2$, which resulted in a monomer instead of the previously obtained polymer. (Figure 1.7, bottom)

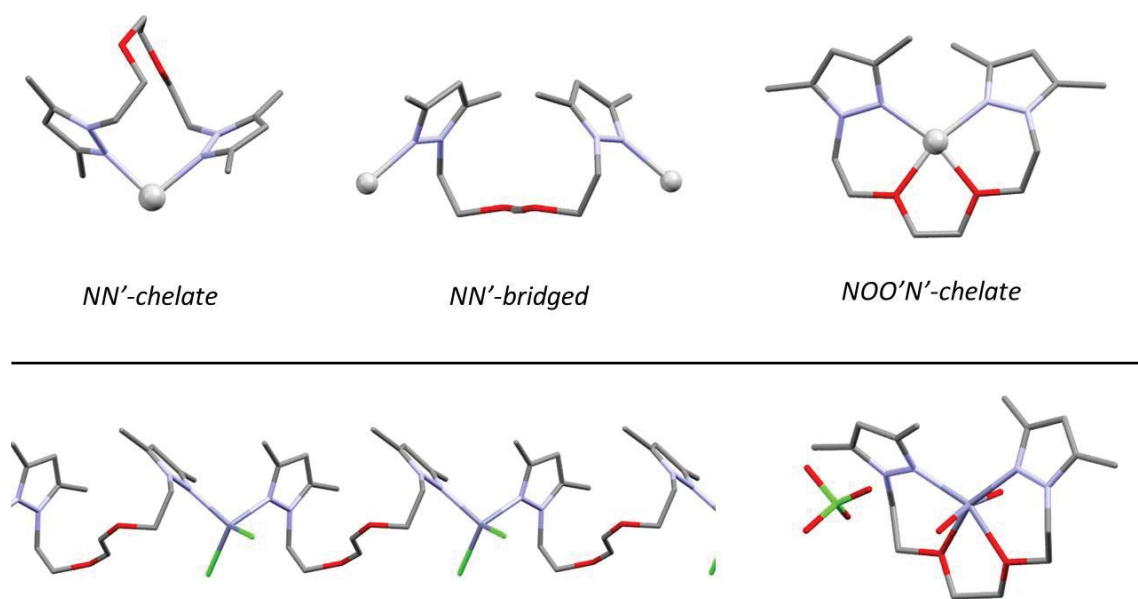


Figure 1.7 Coordination modes of **L4** (top). Crystal structures of polymer $\{[Zn(\mathbf{L4})Cl_2]\}_n$ (bottom left) and ionic monomeric $[Zn(\mathbf{L4})(H_2O)_2](ClO_4)_2$ (bottom right)¹³⁰. Colour code: grey (C), light blue (N), light green (Cl), red (O), blue grey (Zn).

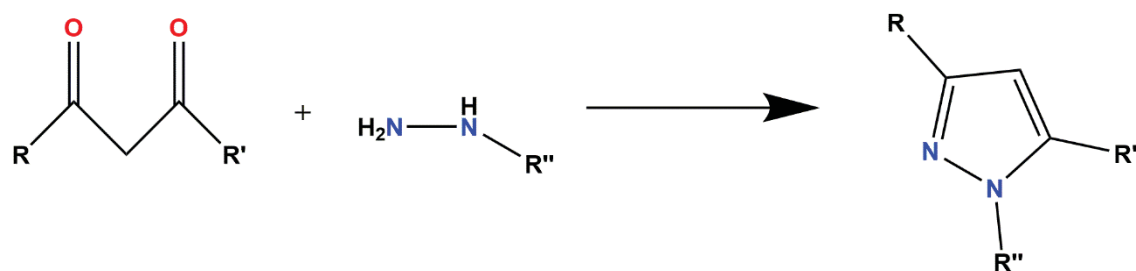
Inspired by those results, it was decided to include the study the behaviour of *o*-**L5**, *m*-**L5** and *p*-**L5** ligands against coordinatively flexible metals such as Co(II), Cu(II), Zn(II), Cd(II) and Hg(II) in the framework of this PhD, as well as developing new hybrid bispyrazole *N,O*-diether ligands.

1.3.3 Synthetic strategies for the *N*-functionalization of pyrazole ligands

Over the years, our group has employed a set of different synthetic strategies for the obtention of new functionalized *N*-pyrazole ligands. They can be broadly classified in three groups. The first one affects the very synthesis of the pyrazole ring, as involving the modification of their parent β -diketones or hydrazine. The second and third groups encompass synthetic strategies involving the modification of already synthesized pyrazole rings, either by adding new functionalities on them or by directly modifying the functional groups present in them. A brief overview of each of this strategy will be offered here.

- Modification of the parent β -diketone

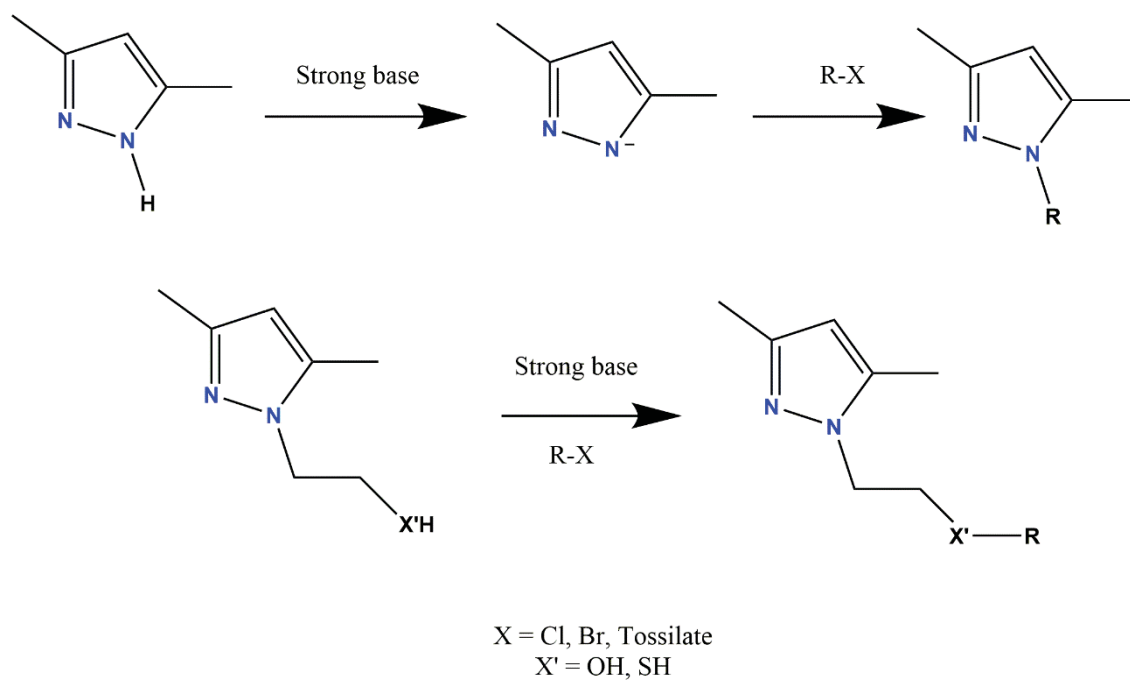
One of the most well-known methods employed by our group for the synthesis of pyrazole ligands involves reacting a suitable β -diketone with hydrazine (Scheme 1.8). Modifying the parent diketone by including different groups in their positions 1- and 5- is an efficient way of obtaining 3,5- substituted pyrazole ligands. Moreover, using different derivatives of hydrazine allows for the control of the substituent in position 1- (*N*-substitution). We have employed successfully this strategy in the synthesis of 3,5-disubstituted^{38,51} pyrazole ligands and 3,5-disubstituted-*N*-hydroxyalkyl pyrazole ligands^{109,114}, both symmetrically and asymmetrically substituted, and even more complex bispyrazole ligands¹³². This strategy will be used in this PhD for the synthesis of 3,5-disubstituted-*N*-hydroxyalkyl pyrazole ligands.



Scheme 1.8 Synthesis of pyrazole ligands using β -diketones. Note that if $R \neq R'$, different regioisomers can be obtained.

- Addition of new functional groups

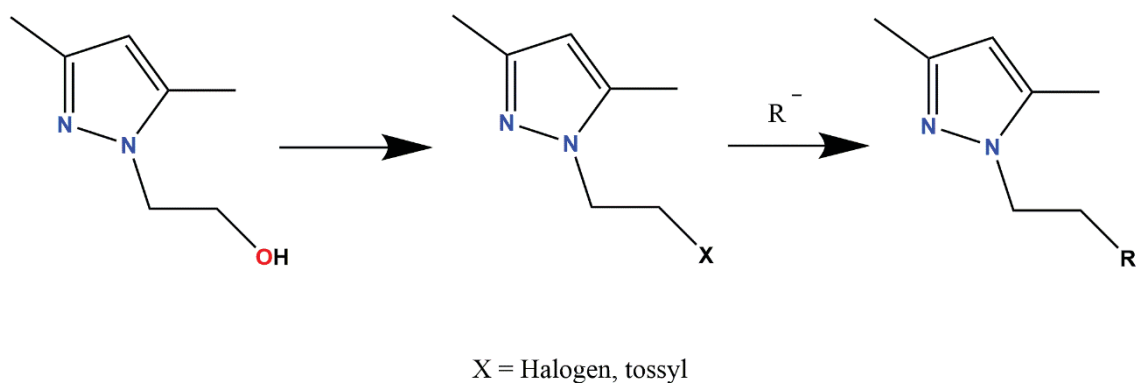
This strategy involves taking advantage of the acidity of proton groups attached to N1 of pyrazole ligands ($pK_a = 14.2$), hydroxyl groups, or even thiol groups. They can easily be deprotonated using strong bases, and the resulting nucleophile can react with classical electrophile groups (Scheme 1.9). This strategy has been employed successfully for the synthesis of hybrid *N,O*-polypyrazole ethers¹²⁷, polyether pyrazole ligands^{119,121}, thioether pyrazole ligands^{69,87} and *N*-alkylpyrazole ligands⁵³.



Scheme 1.9 Synthesis of N-substituted pyrazole ligands using pyrazole precursors as nucleophiles

N-hydroxyalkylpyrazole ligands also allow their use as electrophiles, provided its alcohol functionality is substituted for a suitable leaving group, such as a halogen or a tosyl. Then, the resulting precursor is the subject of a nucleophilic attack, resulting in the desired ligands (Scheme 1.10). This strategy has been especially useful for the synthesis of N-alkylaminopyrazole ligands^{58,81} and thioether pyrazole ligands^{69,87}.

Both variants of this strategy will be used during this PhD work.



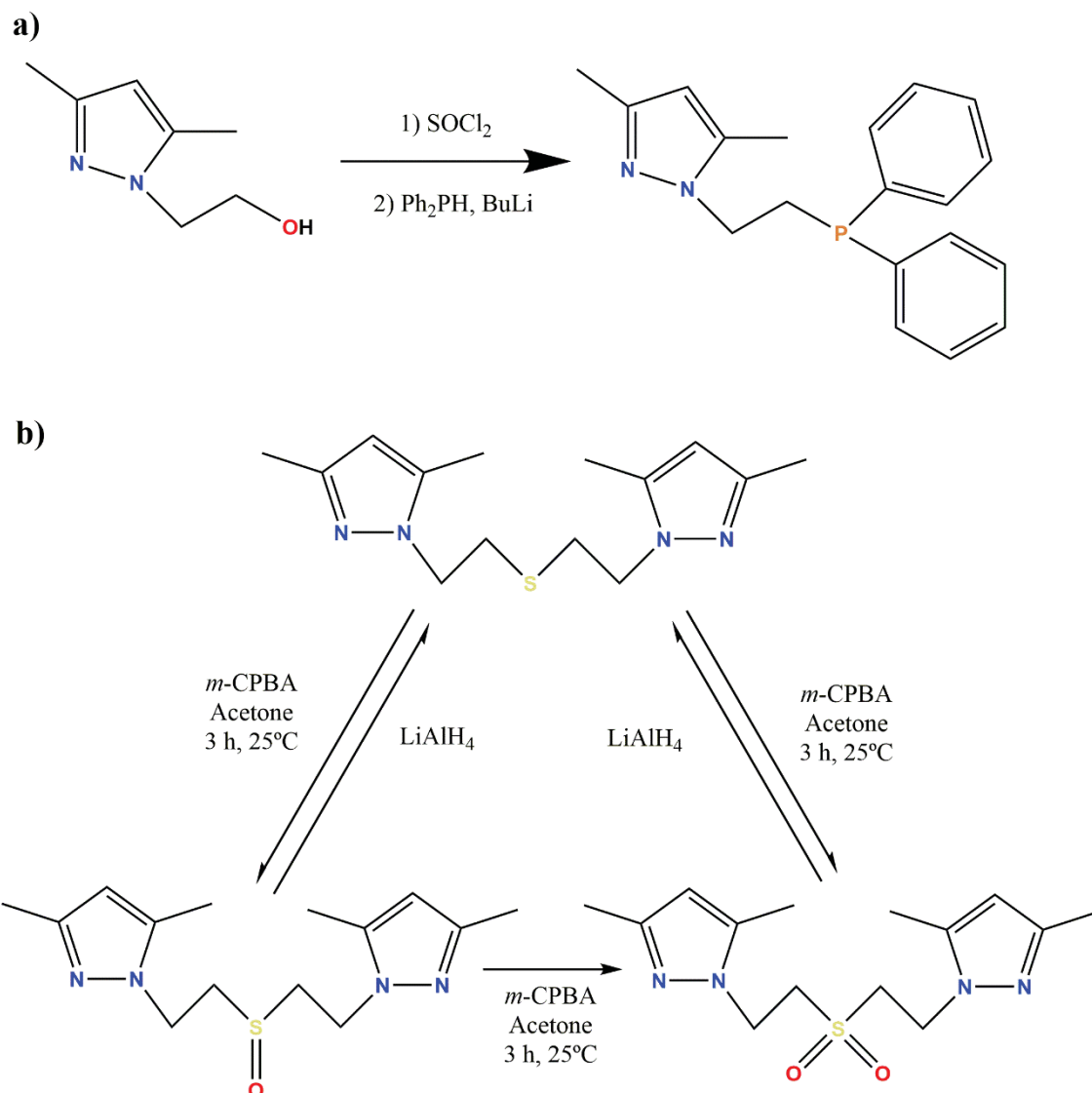
Scheme 1.10 Synthesis of *N*-substituted pyrazole ligands using pyrazole precursors as electrophiles

- Direct modification of the functional group

This strategy consists in the direct substitution of one functional group by a different one. It mainly involves *N*-hydroxyalkylpyrazole ligands, and the substitution of their alcohol groups for chlorine and tosyl groups for the synthesis of pyrazole precursors for further reactions, as well as phosphine (involving two reactions of this type)⁷⁰ and phosphinite^{76,77} groups (Scheme 1.11 a).

Other, perhaps more advanced, examples of this strategy include the synthesis of imine-substituted pyrazole ligands *via* reaction of aldehyde groups with amines⁶⁶ or the oxidation of sulphur groups in thioether-functionalized pyrazole ligands to sulfoxides and sulfones¹⁰⁰ (Scheme 1.11 b). This case is particularly interesting, as the desired result has been achieved *via* classical chemical reactions, using hydrogen peroxide and *m*-chloroperbenzoic acid (MCPBA) as oxidizing agents, as well as using electrochemical methods¹⁰⁰.

This strategy will be used in this PhD work mainly for the synthesis of tosyl-substituted pyrazole precursors.



Scheme 1.11 Synthesis of phosphine and sulfone/sulfoxide containing pyrazole ligands^{70,100}

1.4 Carboranes

Boron is known to form several neutral and anionic cage-like boron-hydrogen clusters. They can have up to twelve members, and fall into three categories: *closo*, *nido* and *arachno*. Compounds with the *closo* structure have a $[\text{B}_n\text{H}_n]^{2-}$ general formula, and anions with $n = 5$ to 12 are known. An example is the iconic $[\text{B}_{12}\text{H}_{12}]^{2-}$ anion. On the other hand, *nido* compounds, with general formula $[\text{B}_n\text{H}_{n+4}]$ can be regarded as a *closo* borane compound which has lost one vertex and displays B-H-B as well as B-B bonds. Lastly, *arachno* boranes, $[\text{B}_n\text{H}_{n+6}]$ can be regarded as *closo* boranes which have lost two vertexes, and are highly reactive and thermally unstable (Figure 1.8)⁴.

The electrons in this kind of clusters are considered to be located in fully delocalized molecular orbitals, contributing to the stability of the entire molecule. Thus, from now on, the lines representing atomic bonds in diagrams, schemes and figures are not to be considered as classical atomic bonds⁴.

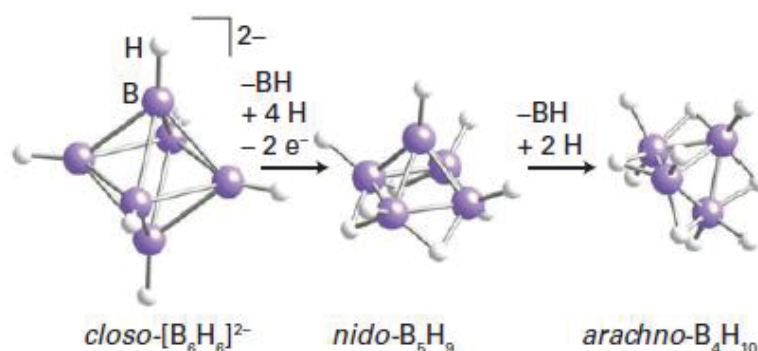


Figure 1.8 Examples of closo, nido and arachno borane-hydrogen compounds⁴. Colour code: violet (B), white (H).

In 1960, Pitochelli and Hawthorne isolated $[B_{12}H_{12}]^{2-}$ salts¹³³, demonstrating the existence of a boron-hydrogen icosahedral cage, which were in fact theorized in 1955 by Longuet-Higgins and Roberts¹³⁴. Soon, theoretical chemists such as W. Lipscomb and R. Hoffman realized that the substitution of two boron atoms for two carbon atoms would result in a neutral molecule, and proposed the existence of icosahedral dicarba-*closo*-dodecaborane cages¹³⁵. In fact, members of the $C_xB_yH_z$ carborane family had been allegedly obtained as by-products in boron hydride experiments performed in 1923 by A. Stock and E. Kuss¹³⁶. Finally, in 1963 the synthesis of 1,2- $C_2B_{10}H_{12}$ were reported in a series of journal articles by D. Grafstein *et al.*^{137,138} and R.P. Alexander and H.A. Schroeder *et al.*¹³⁹

In this PhD work, dicarba-*closo*-dodecaborane cages are of special relevance, and from now on will simply be referred as carboranes for ease. Atoms of the carborane cage are numbered starting at the apex atom with the lowest number of bonds and proceeding clockwise, in such a manner that carbon atoms are given the lowest possible number. As a result of this convention, its three existing well-known and commercial *ortho*-, *meta*- and *para*- isomers are identified as 1,2-; 1,7- and 1,12- $C_2B_{10}H_{12}$ respectively, differing in the relative positions of the carbon atoms (Figure 1.9).

Since their discovery in 1963, they have been employed as ligands in coordination^{140,141} and organic chemistry^{142–144} and in medicine as a source of boron for imaging techniques and boron neutron capture treatment (BNCT)^{145,146}, and as pharmacophores^{147,148}. Besides, they are also making inroads in their application in the material science field, where reports in their use as luminescent materials^{149–151}, catalysts^{152,153}, metal-organic frameworks¹⁵⁴ and other fields of nanoscience¹⁵⁵ are surfacing.

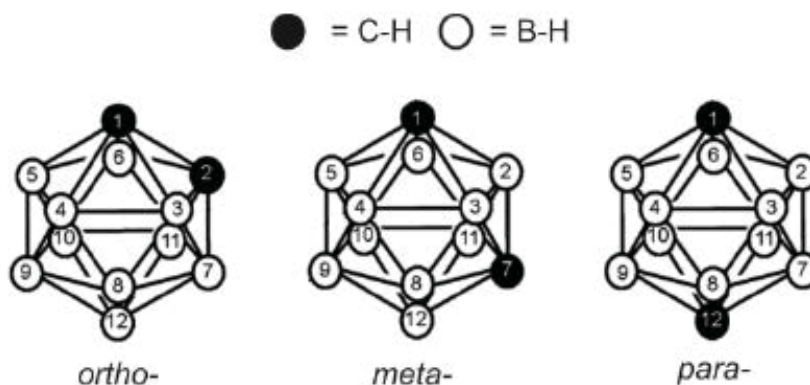


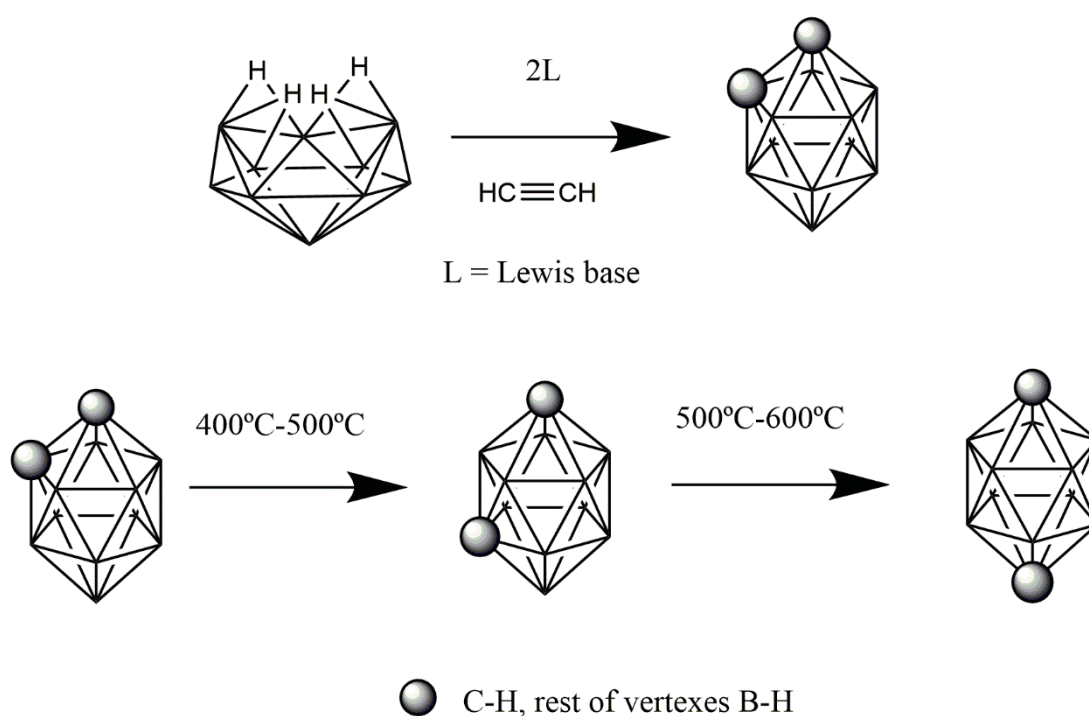
Figure 1.9 Graphical representation of *ortho*-, *meta*- and *para*- isomers of carborane, with vertex numbering.

1.4.1 Synthesis and properties

The first method to synthesize *ortho*-carborane, described in 1963, consists in the reaction of $B_{10}H_{14}$ with acetylenes in the presence of a Lewis base^{137,156}, while the *meta*- and *para*- isomers can be obtained *via* thermal isomerization at 400–500°C and 600–700°C, respectively, under inert conditions (Scheme 1.12)^{157–159}. However, the isomerization of *m*-carborane to *p*-carborane has low yields, and also results in the obtention of intractable products¹⁵⁷. As further purification is required, the price of the *para*- isomer is notably higher when compared to the other isomers (ca. 895 \$/g vs. 150 \$/g for the *meta* and 75 \$/g for the *ortho*- isomer). Regardless of their price, carborane cages feature a series of fascinating properties, both at a geometrical and electronic level.

The atoms of the cluster are hexacoordinated, five bonds linking the cluster together and one exohedral bond. In those, the C-H distances are slightly shorter (1.09 Å) than B-H distances (1.17 Å), while B-B distances range from 1.76 to 1.81 Å^{160,161}. Both the symmetry (C_{2v} for *ortho*- and *meta*- isomers and D_{5d} for the *para*- isomer) and the C-C

distance (1.61 Å for *ortho*-, 2.61 Å for *meta*- and 3.06 Å for *para*-) are obviously dependant on the isomer^{160,161}. These different C-C distances and relative positions result in these molecules being especially interesting in the field of ligand design. As such, in *ortho*- carborane derivatives, two different substituents attached to the carbon atoms lie at a rough angle of 60° (unsubstituted H-C-C-H angle is 52°), while for the *meta*- isomer this value is 120° (unsubstituted H-C-C-H angle is 115°) and 180° for *para*- isomer (unsubstituted H-C-C-H angle is 180° as well)¹⁶². All these parameters are summarized in Table 1.1.



Scheme 1.12 Schematic representation of the synthesis of carboranes

In a simple analogy, carborane cages have been compared to a rotating benzene rings, owing both to its shape and electronic properties (*vide infra*). However, it has been determined from crystal structures that the Van der Waals volume (V_{vdw}) of the different isomers ranges between 141 to 148 Å³ (Table 1.1)¹⁴⁸, much bigger than that of a rotating benzene ring (102 Å³, 79 Å³ without rotation) and more akin to that of adamantane (136 Å³)¹⁴⁸. This fact must be taken in consideration when accounting for possible steric hindrances caused by the cluster.

Regarding its bonding structure, they feature a $4n + 2$ number of electrons, that is 26 skeletal electrons for 12 vertices. They reveal nonclassical bonding interactions, giving rise to a complex electronic structure¹⁴⁸. As the cluster electrons are delocalized inside the cluster, they are labelled as three-dimensional aromatic compounds^{163,164}. Coupled with its characteristic shape, it has prompted its comparison with the volume generated by a spinning benzene ring. Further, the fact that two different atoms (that is, boron and carbon) form this aromatic cluster, give rise to some of its most characteristic properties. Thus, carbon atoms are slightly more electronegative than boron atoms ($\Delta_\chi(C, B) = 0.51$)¹⁶⁵, and B-C bond are stronger than C-C bonds¹⁴⁸, explaining why carbon atoms prefer non-adjacent positions and why the *para*- isomer is the most stable of the three isomers. Moreover, electronegativity values also explain why hydrogen atoms bonded to carbon atoms are acidic ($\Delta_\chi(C, H) = 0.35$) while those bonded to boron atoms have an hydride-like nature ($\Delta_\chi(B, H) = -0.16$). This fact has a huge importance when it comes to carborane-cluster functionalization. The pK_a values for the acidic protons decrease in the *ortho*-, *meta*- and *para*-carborane order (Table 1.1)¹⁶⁶. However, the presence of other substituents in the cluster can greatly affect these values and can be tuned for desired purposes¹⁴⁸. In the same spirit, attaching carborane clusters to other functional groups can also alter their acidity¹⁴⁸.

Their icosahedral shape results in a spherical presentation, which coupled with the presence of 10 hydride-like protons in the surface of this sphere, makes carboranes extremely hydrophobic¹⁴⁸. Hydrophobicity increases in the *ortho*-, *meta*- and *para*-carborane order, which is mirrored by the decrease of the dipolar moment (D): 4.53 for *ortho*-, 2.85 for *meta*- and 0 for *para*-carborane (Table 1.1)^{148,167}.

Besides the already discussed characteristics, carboranes also display high thermal and chemical stability, rigidity and tunability make them an interesting choice for their use in the design of new ligands and coordination compounds^{148,168}.

Table 1.1 Properties and geometric parameters of carborane isomers

	<i>Ortho</i> -C ₂ B ₁₀ H ₁₂	<i>Meta</i> -C ₂ B ₁₀ H ₁₂	<i>Para</i> -C ₂ B ₁₀ H ₁₂
Symmetry	C _{2v}	C _{2v}	D _{5d}
V_{dw} Volume (Å³)	148	143	141
pKa values			
- Streitweiser's scale	23	28	30
- Polarographic scale	19	24	26
Dipolar moment (D)	4.53	2.85	0
H-C-C-H angle (°)	~52	~115	180

1.4.2 Carborane functionalization

Over the years, scientist have created an enormous collection of different synthetic strategies for carborane functionalization. As carborane chemistry is an ever-expanding topic, only the main synthetic methodologies will be mentioned, focusing on those used in this work.

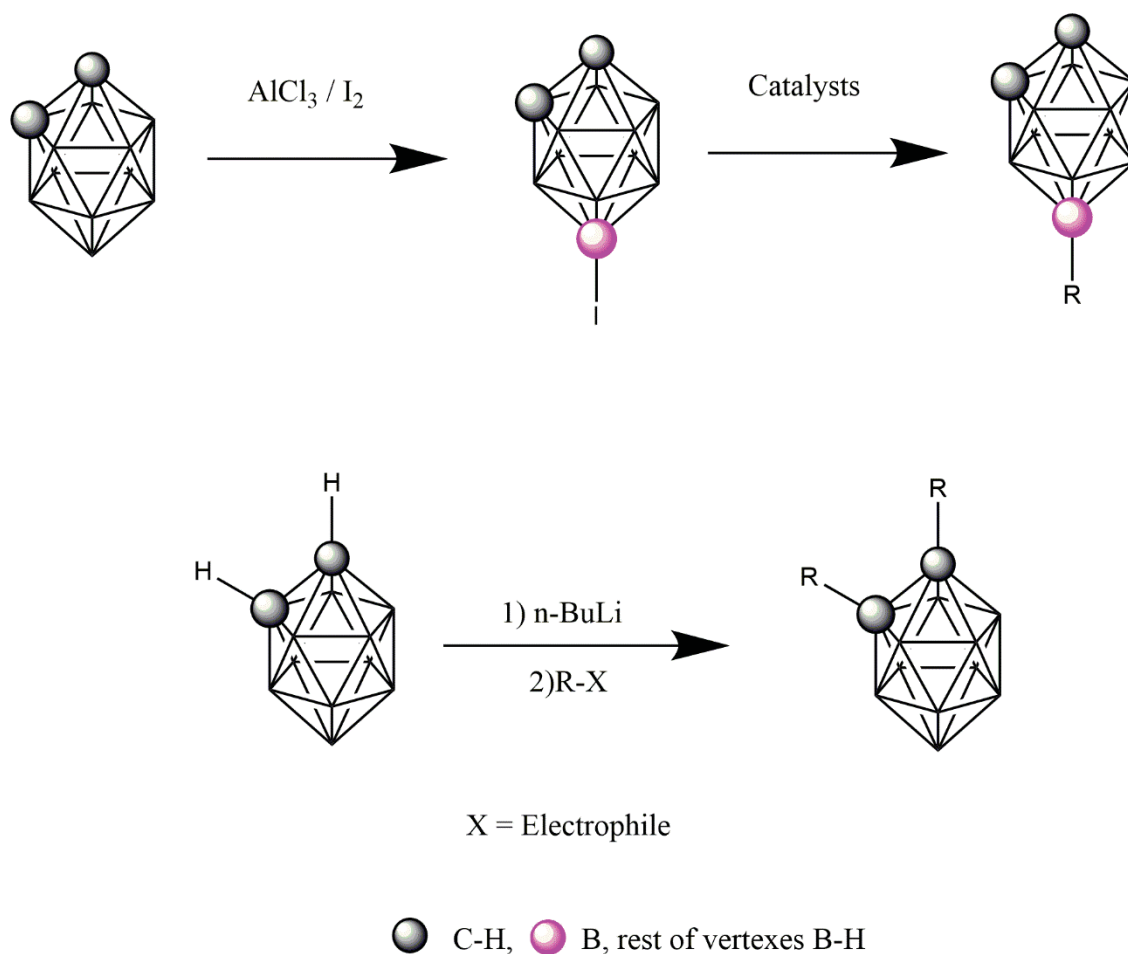
Owing to the different nature of the vertexes, carborane cages can be functionalized at carbon or boron positions without the need to use protecting/deprotecting methods. However, when designing new ligands containing carborane moieties, it is important to note that the mentioned differences in the electron density of the carborane cluster give rise to a series of different inductive and resonance effect on the substituents, with the inductive effects dominating¹⁴⁴. As such, substituents attached to carbon atoms experience an electron-withdrawing effect¹⁴⁸. Regarding substituents attached to boron atoms, substitution in different positions results in different behaviours. Those attached to boron atoms 3 and 6 (adjacent to two carbon atoms) might experience slight electron-withdrawing effects^{148,169}, whereas those attached to boron atoms 9 and 12 (antipodal to carbon atoms) experience electron-donating effects^{148,170}. Meanwhile, boron atoms adjacent to only one carbon (4, 5, 7, 8, 10 and 11) exert almost no inductive effect¹⁴⁸.

Substitution on the boron atoms is carried out based on electrophilic substitution, owing to their hydride-like nature. As there are ten different vertexes, their selective substitution is challenging, and strongly depend on the selected isomer. For instance, for *ortho*- and *meta*-carboranes, B9 and B12 can be substituted rather selectively, while B3

and B6 are much less reactive. The main strategy is the halogenation of the boron atoms using halides and AlCl_3 , followed by cross-coupling reactions with different groups (Scheme 1.13). A comprehensive review by Teixidor *et al.* summarizes different strategies for the formation of different B-C, B-P, B-N or B-S bonds¹⁷¹.

Carbon substitution can be achieved *via* different routes. One of such tactics is to use substituted acetylene derivatives in their reaction with $\text{B}_{10}\text{H}_{14}$ for the synthesis of carboranes (see Scheme 1.12) and is favoured when sterically crowded *ortho*-carboranes are desired. However, perhaps the most popular method for functionalizing carboranes, and the one used in this work, involves taking advantage of the acidic nature of the C-H protons. Those can be easily removed using bases like butyl-lithium or Grignard reagents, and then used as nucleophiles in substitution reactions (Scheme 1.13). The lithiation of the carboranes is essentially quantitative, so the yield of the reactions is basically dependant on the nature of the electrophile¹⁴⁸.

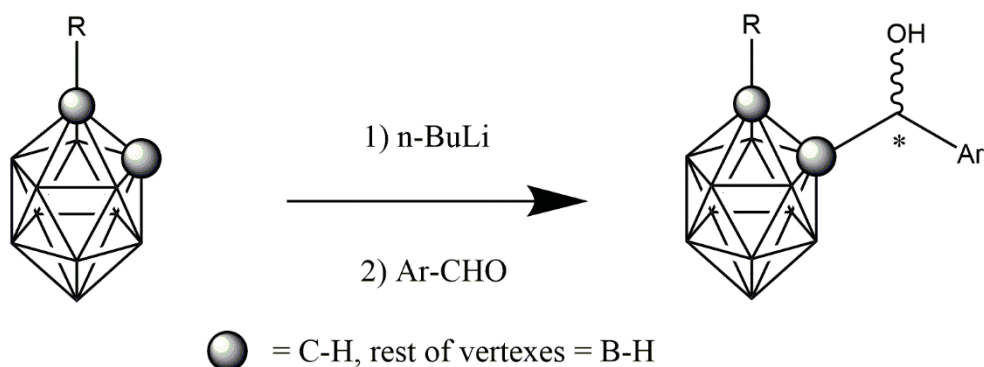
This strategy has been used successfully to carry out all types of nucleophilic substitutions, using alkyl halides, tosylates and triflates as electrophiles, as well as carborane nucleophiles being used in ring-opening reactions and cycloadditions¹⁴⁸. In recent years, the Laboratory of Inorganic Material and Catalysts (LMI) group has employed this strategy using pyridylaldehydes as electrophiles, resulting in the obtention of hybrid *N,O*-pyridylalcohol ligands (*vide infra*)¹⁶⁸.



Scheme 1.13 General strategies for carborane functionalization

1.4.3 Carboranes as building blocks for coordination compounds: group antecedents

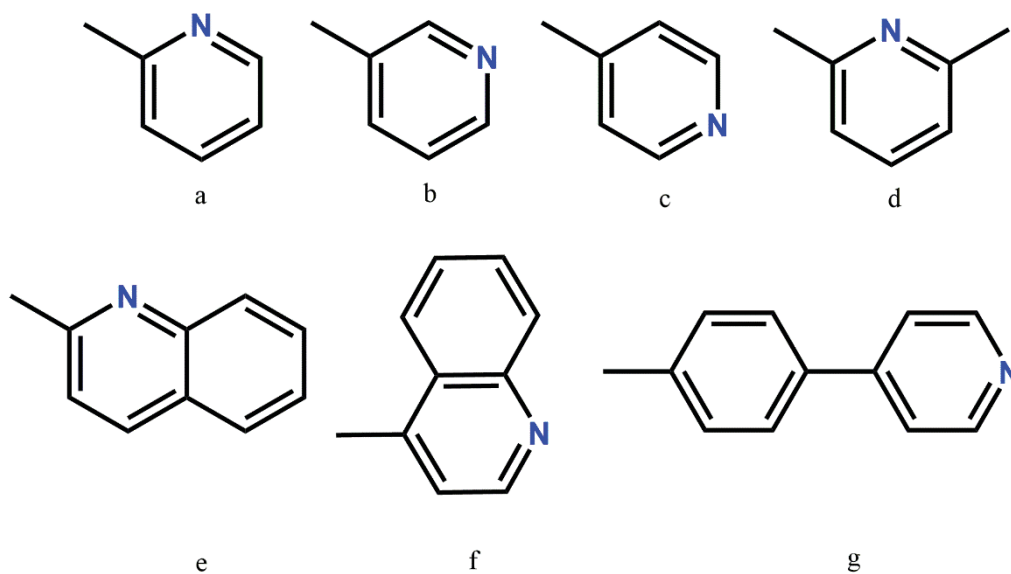
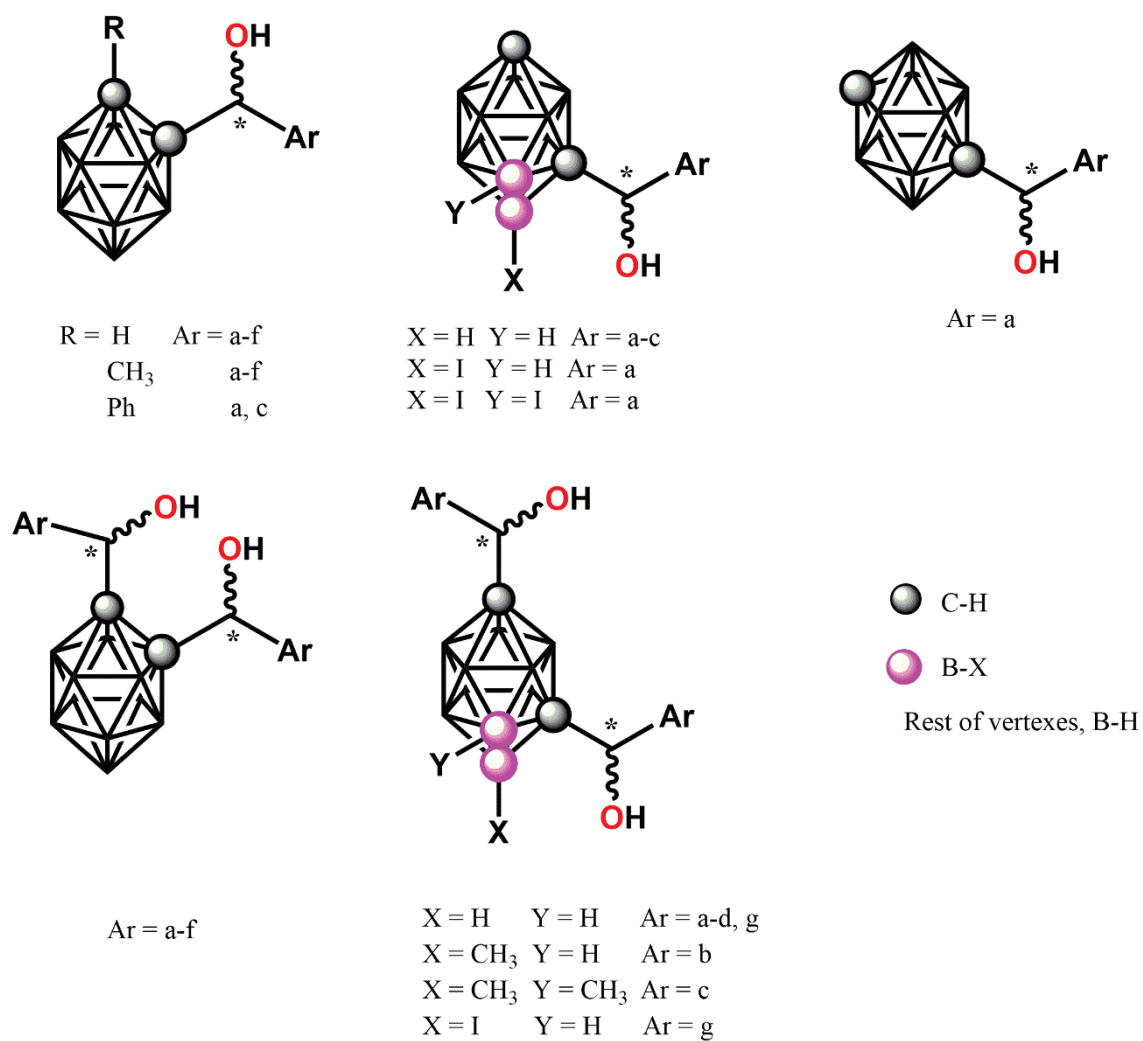
The LMI group has developed a keen interest in the synthesis of new carborane ligands and their use as building blocks in the synthesis of organometallic and coordination compounds as well as coordination polymers and metal organic frameworks. One of the main lines of work focuses on carboranyl alcohol-based ligands, which, as stated before, are synthesized by the addition of lithiocarboranes to the corresponding pyridylaldehydes (Scheme 1.14). Owing to the nature of the substrates, the resulting ligands possess one, or more chiral centers.



Scheme 1.14 General Synthetic strategy for the synthesis of carboranyl alcohols

Among this family of ligands, we are particularly interested in those possessing a nitrogen heteroatom. Considering the well-known reported properties of other hybrid *N,O*-donor ligands, particularly those containing pyridines, but also those containing other groups, such as pyrazole, the inclusion of a carborane moiety in their skeleton would strongly influence its coordination behavior, but also hopefully infuse the resulting compounds with some of the properties associated to this groups: higher stability, hydrophobicity and desirable properties in (bio)medicine. Although other groups have demonstrated the possibility of incorporating groups such as pyrrole¹⁷², imine¹⁷³ or oxazoliny¹⁷⁴, to the carboranyl alcohol framework, the LMI group has focused in the incorporation of pyridine groups.

The first ligands developed in our group consisted of a series of heterosubstituted *o*-carboranes, one of the substituents being a pyridylalcohol group, and the other being a methyl or a phenyl group^{175,176}. Soon, this small group of ligands grew to encompass new pyridylalcohol groups¹⁷⁷ and *meta*- and *para*- carboranes, some of them halogen-substituted^{168,178,179}. Moreover, homo-substituted carboranes bearing two pyridyl alcohol moieties, hence bearing two chiral centers, were also developed^{168,179–181} (Scheme 1.15).



Scheme 1.15 Hybrid *N*-pyridine, *O*-alcohol carborane ligands used in the LMI group

Those ligands opened the door towards the synthesis of relatively unexplored carboranes-based coordination complexes. Their resulting Fe(III)^{182,183}, Pd(II)^{184,185} and Co(II)¹⁸⁶ molecular compounds afforded a host of coordination behaviors, such as *N*-monodentate, *N,O*-chelate (both with protonated and deprotonated alcohol moieties), *N,O*-chelate and bridged (deprotonated alcohol moiety) for monosubstituted compounds and *NN'*-bridged, *NOO'N'*-chelated and bridged (deprotonated alcohol moieties) and *NBN'*-pincer chelate for disubstituted compounds (Figure 1.10).

Moreover, those compounds showed interesting structure-properties relationships. For instance, Co(II) compounds display homochiral supramolecular interactions (owing to the nature of the ligand) and porosity¹⁸⁶, while Fe(III) compounds^{182,183} displayed chiroptical and magnetic properties and *NBN'*-pincer Pd(II) compounds revealed themselves as great catalysts for the Suzuki reaction¹⁸⁵ and highly efficient host-guest interactions¹⁸⁴.

The disubstituted ligands in Scheme 1.15 have also been used as building blocks for the synthesis of Metal-Organic Frameworks (MOF)^{187–190}. Those ligands provide flexibility and water stability to the new MOFs. A more rigid dicarboxylate carborane ligand has recently provided the most water stable MOF in the literature¹⁹¹. The high hydrolytic stability is the result of the highly hydrophobic carborane fragments, and the new MOF can efficiently separate biobutanol from a mixture where water content is > 80%.

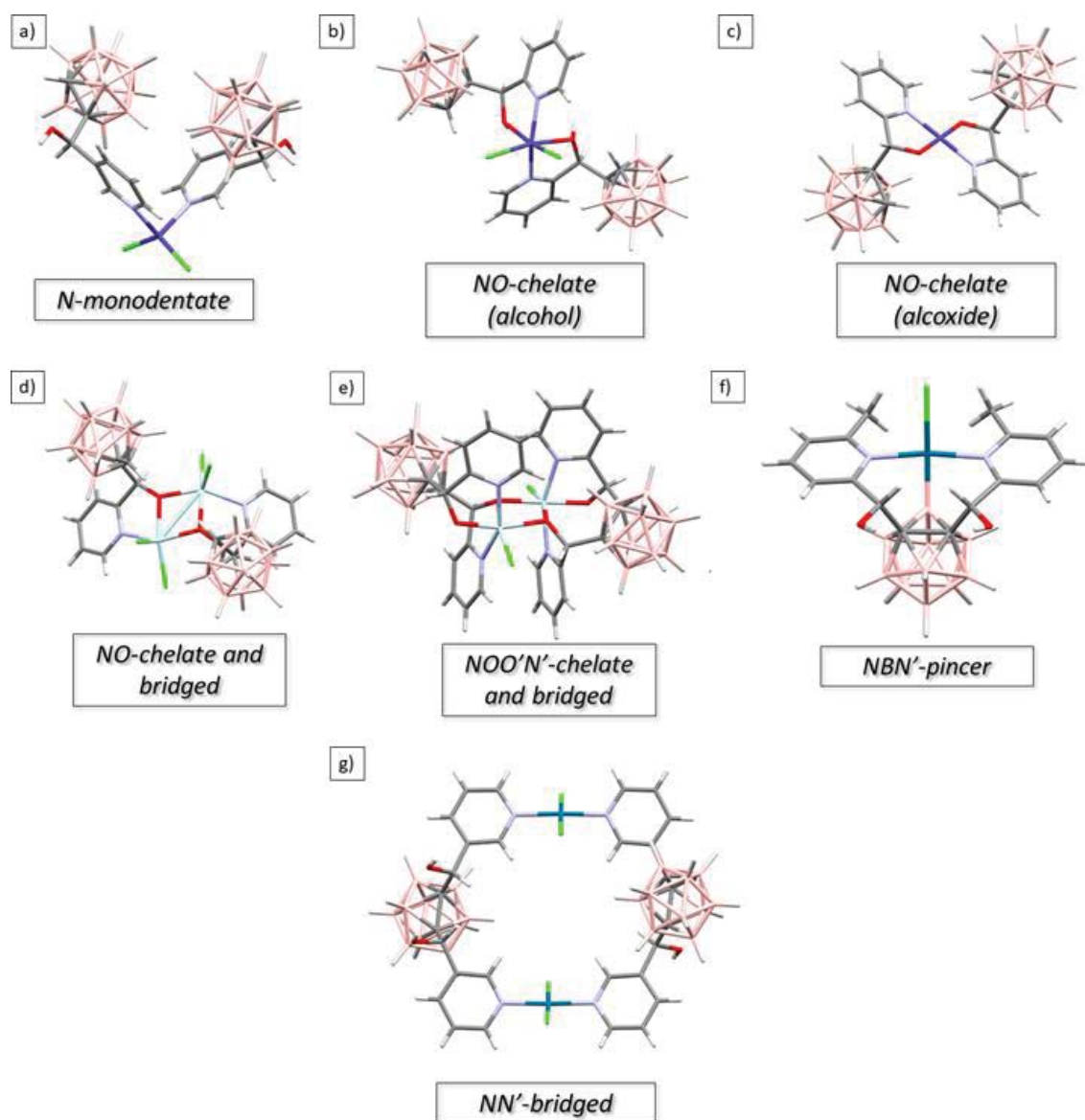


Figure 1.10 Different coordination modes of *N,O*-hybrid carborane ligands against Co(II) (a-c), Fe(III) (d, e) and Pd(II) (f,g). Colour code: grey (C), pink (B), white (H), red (O), light green (Cl), light blue (N), dark blue (Co), light turquoise (Fe), dark turquoise (Pd).

Based on those precedents, we decided to expand our knowledge in functionalized carborane ligands with *N*-containing motifs. It is, in fact, one of the burgeoning research fields in carborane chemistry, owing to their use as pharmacophores or in BNCT for cancer^{147,148,192}. Among them, there is a thriving research in the functionalization of carboranes with *N*-heterocyclic rings¹⁹³, with functional groups such as pyridines^{168,194}, pyrroles¹⁴² and indoles^{142,195} featuring prominently. As one of such *N*-heterocyclic rings, pyrazoles display some interesting properties. Besides their already well-known medical

applications^{29,196}, they are also easily functionalized *via* modification of the parent pyrazole^{26,30,31}, allowing fine tuning of the desired properties.

In this sense, early works can be traced back to the late 60s and early 70s reports by Zakharkhin *et al.*, which synthesized a whole family of new carborane pyrazole-containing ligands^{197–199}. More recent works focus on the synthesis of drug analogues, as full advantage of the interesting biomedical properties of both functional groups can be taken. For instance, work carried out by Vázquez *et al.*²⁰⁰ features the synthesis of Rimonabant²⁰¹ analogues, a drug useful for obesity treatment²⁰², while recently published work by Buzharevsky *et al.*²⁰³ report a 5-carborane substituted pyrazole as an analogue of a non-steroidal anti-inflammatory drug. Pyrazole containing carboranes also feature as part of investigations in new strategies for functionalization of carboranes with *N*-containing heterocycles^{204–206} or azo-groups²⁰⁷.

Despite the reported bibliography, examples of *N*-alkylcarbaborane pyrazole derivative ligands are scarce, and coordination compounds bearing said ligands even more rare. Consequently, combining the extensive expertise in the design of *N*-substituted pyrazole ligands in the DMOM group^{66,70,103} and in the functionalization of carboranes with *N*-containing heterocycles by the LMI group^{175,178,187}, the synthesis of *N*-alkylcarbaborane pyrazole derivative ligands and synthesis of coordination compounds was proposed for this PhD thesis.

References

- 1 Nature Portfolio: Coordination Chemistry, <https://www.nature.com/subjects/coordination-chemistry>, (accessed 19 April 2021).
- 2 G. A. Lawrance, *Introduction to Coordination Chemistry*, John Wiley & Sons, Ltd, Chichester, UK, 2010.
- 3 V. Gold, Ed., *The IUPAC Compendium of Chemical Terminology*, International Union of Pure and Applied Chemistry (IUPAC), Research Triangle Park, NC, 2019.
- 4 P. Atkins, T. Overton, J. Rourke, M. Weller and F. Armstrong, *Shriver and Atkins' Inorganic Chemistry*, Oxford University Press, Fifth Edit., 2009.
- 5 W. Lu, Z. Wei, Z. Y. Gu, T. F. Liu, J. Park, J. Park, J. Tian, M. Zhang, Q. Zhang, T. Gentle, M. Bosch and H. C. Zhou, *Chem. Soc. Rev.*, 2014, **43**, 5561–5593.
- 6 L. Brammer, *Chem. Soc. Rev.*, 2004, **33**, 476–489.
- 7 C. Sanchez, K. J. Shea and S. Kitagawa, *Chem. Soc. Rev.*, 2011, **40**, 471.
- 8 M. E. Davis, *Nature*, 2002, **417**, 813–821.
- 9 G. Maurin, C. Serre, A. Cooper and G. Férey, *Chem. Soc. Rev.*, 2017, **46**, 3104–3107.
- 10 P. J. Steel, *Acc. Chem. Res.*, 2005, **38**, 243–250.
- 11 F. A. Almeida Paz, J. Klinowski, S. M. F. Vilela, J. P. C. Tomé, J. A. S. Cavaleiro and J. Rocha, *Chem. Soc. Rev.*, 2012, **41**, 1088–1110.
- 12 M. Eddaoudi, D. B. Moler, H. Li, B. Chen, T. M. Reineke, M. O'Keeffe and O. M. Yaghi, *Acc. Chem. Res.*, 2001, **34**, 319–330.
- 13 M. Stradiotto and R. J. Lundgren, Eds., *Ligand Design in Metal Chemistry*, John Wiley & Sons, Ltd, Chichester, UK, 2016.
- 14 E. C. Constable, *Coord. Chem. Rev.*, 2008, **252**, 842–855.
- 15 A. L. Gavrilova and B. Bosnich, *Chem. Rev.*, 2004, **104**, 349–384.

- 16 M. D. Fryzuk, *Inorg. Chem.*, 2015, **54**, 9671–9674.
- 17 T. R. Cook, Y.-R. Zheng and P. J. Stang, *Chem. Rev.*, 2013, **113**, 734–777.
- 18 A. Y. Robin and K. M. Fromm, *Coord. Chem. Rev.*, 2006, **250**, 2127–2157.
- 19 P. Teo and T. S. A. Hor, *Coord. Chem. Rev.*, 2011, **255**, 273–289.
- 20 R. E. Morris and L. Brammer, *Chem. Soc. Rev.*, 2017, **46**, 5444–5462.
- 21 S. Maggini, *Coord. Chem. Rev.*, 2009, **253**, 1793–1832.
- 22 A. M. Masdeu-Bultó, M. Diéguez, E. Martin and M. Gómez, *Chiral thioether ligands: Coordination chemistry and asymmetric catalysis*, 2003, vol. 242.
- 23 S.-S. Chen, *CrystEngComm*, 2016, **18**, 6543–6565.
- 24 G. Aromí, L. A. Barrios, O. Roubeau and P. Gamez, *Coord. Chem. Rev.*, 2011, **255**, 485–546.
- 25 J.-P. Zhang, Y. Zhang, J. Lin and X. Chen, *Chem. Rev.*, 2012, **112**, 1001–1033.
- 26 F. Mani, *Coord. Chem. Rev.*, 1992, **120**, 325–359.
- 27 J. Klingele, S. Dechert and F. Meyer, *Coord. Chem. Rev.*, 2009, **253**, 2698–2741.
- 28 R. Mukherjee, *Coord. Chem. Rev.*, 2000, **203**, 151–218.
- 29 J. V. Faria, P. F. Vegi, A. G. C. Miguita, M. S. dos Santos, N. Boechat and A. M. R. Bernardino, *Bioorganic Med. Chem.*, 2017, **25**, 5891–5903.
- 30 A. Adach, *J. Coord. Chem.*, 2017, **70**, 757–779.
- 31 I. Alkorta, R. M. Claramunt, E. Díez-Barra, J. Elguero, A. de la Hoz and C. López, *Coord. Chem. Rev.*, 2017, **339**, 153–182.
- 32 A. Otero, J. Fernández-Baeza, A. Lara-Sánchez and L. F. Sánchez-Barba, *Coord. Chem. Rev.*, 2013, **257**, 1806–1868.
- 33 S. Trofimenko, *Chem. Rev.*, 1972, **72**, 497–509.
- 34 P. K. Mykhailiuk, *Chem. Rev.*, , DOI:10.1021/acs.chemrev.0c01015.
- 35 J. Casabó, J. Pons, K. S. Siddiqi, F. Teixidor, E. Molins and C. Miravittles, *J. Chem. Soc. Dalt. Trans.*, 1989, **6**, 1401–1403.

- 36 S. Roeser, S. Maji, J. Benet-Buchholz, J. Pons and A. Llobet, *Eur. J. Inorg. Chem.*, 2013, **2013**, 232–240.
- 37 J. Pons, X. López, E. Benet, J. Casabó, F. Teixidor and F. J. Sánchez, *Polyhedron*, 1990, **9**, 2839–2845.
- 38 A. Chadghan, J. Pons, A. Caubet, J. Casabó, J. Ros, A. Alvarez-Larena and J. Francesc Piniella, *Polyhedron*, 2000, **19**, 855–862.
- 39 J. Pons, A. Chadghan, A. Alvarez-Larena, J. F. Piniella and J. Ros, *Inorganica Chim. Acta*, 2001, **324**, 342–346.
- 40 J. Pons, A. Chadghan, J. Casabó, A. Alvarez-Larena, J. F. Piniella, X. Solans, M. Font-Bardia and J. Ros, *Polyhedron*, 2001, **20**, 1029–1035.
- 41 M. Guerrero, J. Pons, M. Font-Bardia, T. Calvet and J. Ros, *Polyhedron*, 2010, **29**, 1083–1087.
- 42 J. Pons, A. Chadghan, J. Casabo, A. Alvarez-Larena, J. Francesc Piniella and J. Ros, *Inorg. Chem. Commun.*, 2000, **3**, 296–299.
- 43 J. A. Perez, J. Pons, X. Solans, M. Font-Bardia and J. Ros, *Inorganica Chim. Acta*, 2005, **358**, 617–622.
- 44 V. Montoya, J. Pons, J. García-Antón, X. Solans, M. Font-Bardía and J. Ros, *Organometallics*, 2007, **26**, 3183–3190.
- 45 J. Pons, F. J. Sánchez, A. Labarta, J. Casabó, F. Teixidor and A. Caubet, *Inorganica Chim. Acta*, 1993, **208**, 167–171.
- 46 J. Pons, A. Chadghan, A. Alvarez-Larena, J. Francesc Piniella and J. Ros, *Inorg. Chem. Commun.*, 2001, **4**, 610–612.
- 47 J. Pons, F. J. Sanchez, J. Casabó, A. Alvarez-Larena, J. F. Piniella and J. Ros, *Inorg. Chem. Commun.*, 2003, **6**, 833–836.
- 48 J. Pons, X. López, J. Casabó, F. Teixidor, A. Caubet, J. Rius and C. Miravittles, *Inorganica Chim. Acta*, 1992, **195**, 61–66.
- 49 V. Montoya, J. Pons, V. Branchadell, J. Garcia-Antón, X. Solans, M. Font-Bardía and J. Ros, *Organometallics*, 2008, **27**, 1084–1091.

- 50 V. Montoya, J. Pons, J. Garcia-Antón, X. Solans, M. Font-Bardia and J. Ros, *Inorganica Chim. Acta*, 2007, **360**, 625–637.
- 51 V. Montoya, J. Pons, V. Branchadell and J. Ros, *Tetrahedron*, 2005, **61**, 12377–12385.
- 52 V. Montoya, J. Pons, X. Solans, M. Font-Bardia and J. Ros, *Inorganica Chim. Acta*, 2006, **359**, 25–34.
- 53 V. Montoya, J. Pons, X. Solans, M. Font-Bardia and J. Ros, *Inorganica Chim. Acta*, 2005, **358**, 2763–2769.
- 54 V. Montoya, J. Pons, X. Solans, M. Font-bardia and J. Ros, *Inorganica Chim. Acta*, 2005, **358**, 2312–2318.
- 55 D. Peral, F. Gómez-Villarraga, X. Sala, J. Pons, J. Carles Bayón, J. Ros, M. Guerrero, L. Vendier, P. Lecante, J. García-Antón and K. Philippot, *Catal. Sci. Technol.*, 2013, **3**, 475–489.
- 56 G. Aragay, J. Pons, J. Ros and A. Merkoçi, *Langmuir*, 2010, **26**, 10165–10170.
- 57 J. Pons, G. Aragay, J. García-Antón, T. Calvet, M. Font-Bardia and J. Ros, *Inorganica Chim. Acta*, 2010, **363**, 911–917.
- 58 G. Aragay, J. Pons, V. Branchadell, J. García-Antón, X. Solans, M. Font-Bardía and J. Ros, *Aust. J. Chem.*, 2010, **63**, 257.
- 59 J. Pons, J. García-Antón, M. Font-Bardia, T. Calvet and J. Ros, *Inorganica Chim. Acta*, 2009, **362**, 2698–2703.
- 60 G. Aragay, J. Pons, J. García-Antón, X. Solans, M. Font-Bardia and J. Ros, *J. Organomet. Chem.*, 2008, **693**, 3396–3404.
- 61 M. del Carme Castellano, J. Pons, J. García-Antón, X. Solans, M. Font-Bardia and J. Ros, *Inorganica Chim. Acta*, 2008, **361**, 2491–2498.
- 62 M. del C. Castellano, J. Pons, J. García-Antón, X. Solans, M. Font-Bardía and J. Ros, *Inorganica Chim. Acta*, 2008, **361**, 2923–2928.
- 63 G. Esquiús, J. Pons, R. Yáñez and J. Ros, *J. Organomet. Chem.*, 2001, **619**, 14–23.

- 64 A. Pañella, J. Pons, J. García-Antón, X. Solans, M. Font-Bardia and J. Ros, *Inorganica Chim. Acta*, 2006, **359**, 2343–2349.
- 65 A. Pañella, J. Pons, J. Garcia-Anton, X. Solans, M. Font-Bardia and J. Ros, *Inorganica Chim. Acta*, 2006, **359**, 2226–2231.
- 66 M. Guerrero, L. Rivas, T. Calvet, M. Font-Bardia and J. Pons, *Aust. J. Chem.*, 2015, **68**, 749.
- 67 A. de León, J. Pons, J. García-Antón, X. Solans, M. Font-Bardia and J. Ros, *Inorganica Chim. Acta*, 2009, **362**, 1528–1534.
- 68 J. García-Antón, J. Pons, X. Solans, M. Font-Bardia and J. Ros, *Inorganica Chim. Acta*, 2004, **357**, 571–580.
- 69 J. García-Antón, J. Pons, X. Solans, M. Font-Bardia and J. Ros, *Eur. J. Inorg. Chem.*, 2003, **2003**, 2992–3000.
- 70 M. Guerrero, S. Muñoz, J. Ros, T. Calvet, M. Font-Bardía and J. Pons, *J. Organomet. Chem.*, 2015, **799–800**, 257–264.
- 71 S. Muñoz, J. Pons, J. Ros, C. A. Kilner and M. A. Halcrow, *J. Organomet. Chem.*, 2011, **696**, 2736–2741.
- 72 R.-M. Tribó, J. Ros, J. Pons, R. Yáñez, A. Álvarez-Larena and J.-F. Piniella, *J. Organomet. Chem.*, 2003, **676**, 38–42.
- 73 G. Esquiús, J. Pons, R. Yáñez, J. Ros, R. Mathieu, N. Lugan and B. Donnadieu, *J. Organomet. Chem.*, 2003, **667**, 126–134.
- 74 G. Esquiús, J. Pons, R. Yáñez, J. Ros, R. Mathieu, B. Donnadieu and N. Lugan, *Eur. J. Inorg. Chem.*, 2002, **2002**, 2999–3006.
- 75 S. Muñoz, M. Guerrero, J. Ros, T. Parella, M. Font-Bardia and J. Pons, *Cryst. Growth Des.*, 2012, **12**, 6234–6242.
- 76 S. Muñoz, J. Pons, J. García-Antón, X. Solans, M. Font-Bardia and J. Ros, *J. Coord. Chem.*, 2009, **62**, 3940–3950.
- 77 S. Muñoz, J. Pons, X. Solans, M. Font-Bardía and J. Ros, *J. Organomet. Chem.*, 2008, **693**, 2132–2138.

- 78 R. Tribó, S. Muñoz, J. Pons, R. Yáñez, Á. Álvarez-Larena, J. F. Piniella and J. Ros, *J. Organomet. Chem.*, 2005, **690**, 4072–4079.
- 79 R. Mathieu, G. Esquiús, N. Lugan, J. Pons and J. Ros, *Eur. J. Inorg. Chem.*, 2001, **2001**, 2683–2688.
- 80 A. Pañella, J. Pons, J. García-Antón, X. Solans, M. Font-Bardia and J. Ros, *Inorganica Chim. Acta*, 2006, **359**, 4477–4482.
- 81 A. Pañella, J. Pons, J. García-Antón, X. Solans, M. Font-Bardia and J. Ros, *Eur. J. Inorg. Chem.*, 2006, **2006**, 1678–1685.
- 82 G. Aragay, J. Pons, J. García-Antón, Á. Mendoza, G. Mendoza-Díaz, T. Calvet, M. Font-Bardia and J. Ros, *Aust. J. Chem.*, 2009, **62**, 475.
- 83 G. Zamora, J. Pons and J. Ros, *Inorganica Chim. Acta*, 2004, **357**, 2899–2904.
- 84 G. Zamora, J. Pons, X. Solans, M. Font-Bardia and J. Ros, *J. Organomet. Chem.*, 2004, **689**, 980–986.
- 85 M. Espinal, J. Pons, J. García-Antón, X. Solans, M. Font-Bardia and J. Ros, *Inorganica Chim. Acta*, 2008, **361**, 2648–2658.
- 86 M. Espinal, J. Pons, J. García-Antón, X. Solans, M. Font-Bardia and J. Ros, *Inorg. Chem. Commun.*, 2009, **12**, 368–370.
- 87 J. García-Antón, J. Pons, X. Solans, M. Font-Bardia and J. Ros, *Eur. J. Inorg. Chem.*, 2003, **2003**, 3952–3957.
- 88 A. de León, J. Pons, J. García-Antón, X. Solans, M. Font-Bardia and J. Ros, *Inorganica Chim. Acta*, 2009, **362**, 3801–3806.
- 89 A. De León, J. Pons, J. García-Antón and J. Ros, *Polyhedron*, 2010, **29**, 2318–2323.
- 90 A. de León, J. Antonio Ayllón and J. Pons, *J. Organomet. Chem.*, 2012, **696**, 4275–4280.
- 91 A. de León, J. Pons, J. García-Antón, X. Solans, M. Font-Bardia and J. Ros, *Polyhedron*, 2007, **26**, 2498–2506.
- 92 J. García-Antón, J. Pons, X. Solans, M. Font-Bardia and J. Ros, *Eur. J. Inorg.*

- Chem.*, 2002, **2002**, 3319–3327.
- 93 J. García-Antón, J. Pons, J. Ros, X. Solans and M. Font-Bardía, *Acta Crystallogr. Sect. E Struct. Reports Online*, 2004, **60**, m1087–m1089.
- 94 A. de Leon, J. Pons, J. García-Antón, X. Solans, M. Font-Bardía and J. Ros, *J. Chem. Crystallogr.*, 2007, **37**, 801–805.
- 95 A. de León, J. Pons, J. García-Antón, X. Solans, M. Font-Bardía and J. Ros, *Polyhedron*, 2007, **26**, 2921–2928.
- 96 A. de Leon, J. Pons, J. García-Antón, X. Solans, M. Font-Bardía and J. Ros, *Inorganica Chim. Acta*, 2007, **360**, 2071–2082.
- 97 A. de León, J. Pons, J. García-Antón, X. Solans, M. Font-Bardía and J. Ros, *Polyhedron*, 2009, **28**, 2165–2170.
- 98 J. García-Antón, R. Mathieu, N. Lugan, J. Pons Picart and J. Ros, *J. Organomet. Chem.*, 2004, **689**, 1599–1608.
- 99 J. García-Antón, J. Pons, X. Solans, M. Font-Bardía and J. Ros, *Inorganica Chim. Acta*, 2003, **355**, 87–94.
- 100 A. de León, J. García-Antón, J. Ros, G. Guirado, I. Gallardo and J. Pons, *New J. Chem.*, 2013, **37**, 1889.
- 101 A. De León, M. Guerrero, J. García-Antón, J. Ros, M. Font-Bardía and J. Pons, *CrystEngComm*, 2013, **15**, 1762–1771.
- 102 A. Boixassa, J. Pons, X. Solans, M. Font-Bardía and J. Ros, *Inorganica Chim. Acta*, 2004, **357**, 733–738.
- 103 A. M. López Marzo, M. Guerrero, T. Calvet, M. Font-Bardía, E. Pellicer, M. D. Baró, J. Pons and J. Sort, *RSC Adv.*, 2015, **5**, 32369–32375.
- 104 A. Boixassa, J. Pons, A. Virgili, X. Solans, M. Font-Bardía and J. Ros, *Inorganica Chim. Acta*, 2002, **340**, 49–55.
- 105 M. Guerrero, J. Pons, M. Font-Bardía, T. Calvet and J. Ros, *Aust. J. Chem.*, 2010, **63**, 958.
- 106 M. Guerrero, J. Pons, J. Ros, M. Font-Bardía, O. Vallcorba, J. Rius, V.

- Branchadell and A. Merkoçi, *CrystEngComm*, 2011, **13**, 6457.
- 107 A. Boixassa, J. Pons, X. Solans, M. Font-Bardia and J. Ros, *Inorganica Chim. Acta*, 2003, **355**, 254–263.
 - 108 S. Muñoz, J. Pons, J. Ros, M. Font-Bardia, C. A. Kilner and M. A. Halcrow, *Inorganica Chim. Acta*, 2011, **373**, 211–218.
 - 109 C. Luque, J. Pons, T. Calvet, M. Font-Bardia, J. García-Antón and J. Ros, *Inorganica Chim. Acta*, 2011, **367**, 35–43.
 - 110 M. Guerrero, T. Calvet, M. Font-Bardia and J. Pons, *Polyhedron*, 2016, **119**, 555–562.
 - 111 J. A. Perez, V. Montoya, J. A. Ayllon, M. Font-Bardia, T. Calvet and J. Pons, *Inorganica Chim. Acta*, 2013, **394**, 21–30.
 - 112 M. Guerrero, J. A. Pérez, M. Font-Bardia and J. Pons, *J. Coord. Chem.*, 2013, **66**, 3314–3325.
 - 113 M. Guerrero, J. A. Perez, J. Ros and J. Pons, *Inorg. Chem. Commun.*, 2014, **46**, 234–236.
 - 114 V. Montoya, J. Pons, J. García-Antón, X. Solans, M. Font-Bardia and J. Ros, *J. Fluor. Chem.*, 2007, **128**, 1007–1011.
 - 115 W.-B. Shi, A.-L. Cui and H.-Z. Kou, *CrystEngComm*, 2014, **16**, 8027.
 - 116 W. L. Driessen, S. Gorter, W. G. Haanstra, L. J. J. Laarhoven, J. Reedijk, K. Goubitz and F. R. Seljée, *Recl. des Trav. Chim. des Pays-Bas*, 2010, **112**, 309–313.
 - 117 W. L. Driessen, B. Maase, J. Reedijk, H. Kooijman, M. T. Lakin and A. L. Spek, *Inorganica Chim. Acta*, 2000, **300–302**, 1099–1103.
 - 118 A. Boixassa, R. Mathieu, N. Lugan, J. Pons and J. Ros, *Acta Crystallogr. Sect. E Struct. Reports Online*, 2003, **59**, m658–m660.
 - 119 A. Boixassa, J. Pons, X. Solans, M. Font-Bardia and J. Ros, *Inorganica Chim. Acta*, 2003, **346**, 151–157.
 - 120 M. Guerrero, J. A. Pérez, T. Calvet, M. Font-Bardía and J. Pons, *Aust. J. Chem.*,

- 2013, **66**, 685.
- 121 M. Guerrero, J. Pérez, J. Ros, V. Branchadell, E. Pellicer, J. Sort and J. Pons, *Curr. Org. Synth.*, 2014, **11**, 149–155.
- 122 A. Boixassa, J. Pons, J. Ros, R. Mathieu and N. Lugan, *J. Organomet. Chem.*, 2003, **682**, 233–239.
- 123 A. Boixassa, J. Pons, X. Solans, M. Font-bardia and J. Ros, *Inorganica Chim. Acta*, 2004, **357**, 827–833.
- 124 C. Dowling, V. J. Murphy and G. Parkin, *Inorg. Chem.*, 1996, **35**, 2415–2420.
- 125 E. A. H. Griffith, N. G. Charles, K. Lewinski, E. L. Amma and P. F. Rodesiler, *Inorg. Chem.*, 1987, **26**, 3983–3989.
- 126 T. N. Sorrell and M. R. Malachowski, *Inorg. Chem.*, 1983, **22**, 1883–1887.
- 127 M. Guerrero, J. García-Antón, M. Tristany, J. Pons, J. Ros, K. Philippot, P. Lecante and B. Chaudret, *Langmuir*, 2010, **26**, 15532–15540.
- 128 M. Guerrero, J. Pons, M. Font-Bardia, T. Calvet and J. Ros, *J. Chem. Crystallogr.*, 2011, **41**, 721–726.
- 129 M. Guerrero, J. Pons, V. Branchadell, T. Parella, X. Solans, M. Font-Bardia and J. Ros, *Inorg. Chem.*, 2008, **47**, 11084–11094.
- 130 M. Guerrero, J. Pons, T. Parella, M. Font-Bardia, T. Calvet and J. Ros, *Inorg. Chem.*, 2009, **48**, 8736–8750.
- 131 M. Guerrero, J. Pons, J. Ros, M. Font-Bardia and V. Branchadell, *Cryst. Growth Des.*, 2012, **12**, 3700–3708.
- 132 J. Pons, A. Chadghan, J. Garcia-Anton and J. Ros, *Lett. Org. Chem.*, 2010, **7**, 178–181.
- 133 A. R. Pitochelli and F. M. Hawthorne, *J. Am. Chem. Soc.*, 1960, **82**, 3228–3229.
- 134 H. C. Longuet-Higgins and M. D. V Roberts, *Proc. R. Soc. London. Ser. A. Math. Phys. Sci.*, 1955, **230**, 110–119.
- 135 R. Hoffmann and W. N. Lipscomb, *J. Chem. Phys.*, 1962, **36**, 3489–3493.

- 136 A. Stock and E. Kuss, *Berichte der Dtsch. Chem. Gesellschaft (A B Ser.)*, 1923, **56**, 789–808.
- 137 M. M. Fein, D. Grafstein, J. E. Paustian, J. Bobinski, B. M. Lichstein, N. Mayes, N. N. Schwartz and M. S. Cohen, *Inorg. Chem.*, 1963, **2**, 1115–1119.
- 138 D. Grafstein and J. Dvorak, *Inorg. Chem.*, 1963, **2**, 1128–1133.
- 139 R. P. Alexander and H. Schroeder, *Inorg. Chem.*, 1963, **2**, 1107–1110.
- 140 A. K. Saxena and N. S. Hosmane, *Chem. Rev.*, 1993, **93**, 1081–1124.
- 141 C. E. Housecroft, *J. Organomet. Chem.*, 2015, **798**, 218–228.
- 142 T. L. Chan and Z. Xie, *Chem. Sci.*, 2018, **9**, 2284–2289.
- 143 Y. Quan and Z. Xie, *Chem. Soc. Rev.*, 2019, **48**, 3660–3673.
- 144 V. I. Bregadze, *Chem. Rev.*, 1992, **92**, 209–223.
- 145 M. Frederick Hawthorne, A. Varadarajan, C. B. Knobler, S. Chakrabarti, R. J. Paxton, B. G. Beatty and F. L. Curtis, *J. Am. Chem. Soc.*, 1990, **112**, 5365–5366.
- 146 G. Calabrese, A. Daou, E. Barbu and J. Tsibouklis, *Drug Discov. Today*, 2018, **23**, 63–75.
- 147 F. Issa, M. Kassiou and L. M. Rendina, *Chem. Rev.*, 2011, **111**, 5701–5722.
- 148 M. Scholz and E. Hey-Hawkins, *Chem. Rev.*, 2011, **111**, 7035–7062.
- 149 D. Tu, P. Leong, S. Guo, H. Yan, C. Lu and Q. Zhao, *Angew. Chemie Int. Ed.*, 2017, **56**, 11370–11374.
- 150 M. Chaari, Z. Kelemen, J. G. Planas, F. Teixidor, D. Choquesillo-Lazarte, A. Ben Salah, C. Viñas and R. Núñez, *J. Mater. Chem. C*, 2018, **6**, 11336–11347.
- 151 L. Parejo, M. Chaari, S. Santiago, G. Guirado, F. Teixidor, R. Núñez and J. Hernando, *Chem. – A Eur. J.*, 2021, **27**, 270–280.
- 152 S. P. Fisher, A. W. Tomich, S. O. Lovera, J. F. Kleinsasser, J. Guo, M. J. Asay, H. M. Nelson and V. Lavallo, *Chem. Rev.*, 2019, **119**, 8262–8290.
- 153 Y. Chen, Y. Quan and Z. Xie, *Chem. Commun.*, 2020, **56**, 7001–7004.
- 154 Q. Xia, J. Zhang, X. Chen, C. Cheng, D. Chu, X. Tang, H. Li and Y. Cui, *Coord.*

- Chem. Rev.*, 2021, 435, 213783.
- 155 R. N. Grimes, *Dalt. Trans.*, 2015, **44**, 5939–5956.
- 156 M. M. Fein, J. Bobinski, N. Mayes, N. Schwartz and M. S. Cohen, *Inorg. Chem.*, 1963, **2**, 1111–1115.
- 157 P. I. Dron, W. E. Klein and J. Michl, *Zeitschrift für Naturforsch. A*, 2014, **69**, 326–330.
- 158 D. S. Wilbur, D. K. Hamlin, G. E. Laramore and T. W. Griffin, in *Advances in Neutron Capture Therapy*, Springer US, Boston, MA, 1993, pp. 319–323.
- 159 S. Papetti, C. Obenland and T. L. Heying, *Ind. Eng. Chem. Prod. Res. Dev.*, 1966, **5**, 334–337.
- 160 R. K. Bohn and M. D. Bohn, *Inorg. Chem.*, 1971, **10**, 350–355.
- 161 A. R. Turner, H. E. Robertson, K. B. Borisenko, D. W. H. Rankin and M. A. Fox, *Dalt. Trans.*, 2005, 1310.
- 162 M. G. Davidson, T. G. Hibbert, J. A. K. Howard, A. Mackinnon and K. Wade, *Chem. Commun.*, 1996, **130**, 2285–2286.
- 163 J. Poater, M. Solà, C. Viñas and F. Teixidor, *Angew. Chemie - Int. Ed.*, 2014, **53**, 12191–12195.
- 164 J. Poater, C. Viñas, I. Bennour, S. Escayola, M. Solà and F. Teixidor, *J. Am. Chem. Soc.*, 2020, **142**, 9396–9407.
- 165 L. Pauling, *The Nature of the Chemical Bond*, Cornell University Press, Ithaca, NY, 3rd edn., 1960.
- 166 K. Hermansson, M. Wójcik and S. Sjöberg, *Inorg. Chem.*, 1999, **38**, 6039–6048.
- 167 T. E. Clark, M. Makha, C. L. Raston and A. N. Sobolev, *Dalt. Trans.*, 2006, 5449.
- 168 J. Planas, F. Teixidor and C. Viñas, *Crystals*, 2016, **6**, 50.
- 169 F. Teixidor, G. Barberà, A. Vaca, R. Kivekäs, R. Sillanpää, J. Oliva and C. Viñas, *J. Am. Chem. Soc.*, 2005, **127**, 10158–10159.

- 170 A. M. Spokoyny, C. W. MacHan, D. J. Clingerman, M. S. Rosen, M. J. Wiester, R. D. Kennedy, C. L. Stern, A. A. Sarjeant and C. A. Mirkin, *Nat. Chem.*, 2011, **3**, 590–596.
- 171 D. Olid, R. Núñez, C. Viñas and F. Teixidor, *Chem. Soc. Rev.*, 2013, **42**, 3318.
- 172 R. Satapathy, B. P. Dash, C. Zheng, J. A. Maguire and N. S. Hosmane, *J. Org. Chem.*, 2011, **76**, 3562–3565.
- 173 Z. Yinghuai, X. Shiwei, V. R. Vangala, S. C. Chia, A. Cheong, O. N. Qin and N. S. Hosmane, *J. Organomet. Chem.*, 2012, **721–722**, 119–123.
- 174 M. E. El-Zaria, H. Aarii and H. Nakamura, *Inorg. Chem.*, 2011, **50**, 4149–4161.
- 175 V. Terrasson, Y. García, P. Farràs, F. Teixidor, C. Viñas, J. G. Planas, D. Prim, M. E. Light and M. B. Hursthouse, *CrystEngComm*, 2010, **12**, 4109–4123.
- 176 V. Terrasson, J. G. Planas, D. Prim, C. Viñas, F. Teixidor, M. E. Light and M. B. Hursthouse, *J. Org. Chem.*, 2008, **73**, 9140–9143.
- 177 F. Di Salvo, B. Camargo, Y. García, F. Teixidor, C. Viñas, J. G. Planas, M. E. Light and M. B. Hursthouse, *CrystEngComm*, 2011, **13**, 5788–5806.
- 178 M. Y. Tsang, F. Di Salvo, F. Teixidor, C. Viñas, J. G. Planas, D. Choquesillo-Lazarte and N. Vanthuyne, *Cryst. Growth Des.*, 2015, **15**, 935–945.
- 179 M. Y. Tsang, J. Giner Planas, A. (Lledós i F. Lledós and Universitat Autònoma de Barcelona. Departament de Química., 2015.
- 180 F. Di Salvo, C. Paterakis, M. Y. Tsang, Y. García, C. Viñas, F. Teixidor, J. Giner Planas, M. E. Light, M. B. Hursthouse and D. Choquesillo-Lazarte, *Cryst. Growth Des.*, 2013, **13**, 1473–1484.
- 181 F. Tan, 2019. *Carborane bis-pyridyl alcohols as Globular and Flexible Linkers for Coordination Polymers: From Bulk Crystals to 2D Ultrathin Nanosheets* [Doctoral dissertations, Universitat Autònoma de Barcelona]. Retrieved from TDX.
- 182 F. Di Salvo, M. Y. Tsang, F. Teixidor, C. Viñas, J. G. Planas, J. Crassous, N. Vanthuyne, N. Aliaga-Alcalde, E. Ruiz, G. Coquerel, S. Clevers, V. Dupray, D. Choquesillo-Lazarte, M. E. Light and M. B. Hursthouse, *Chem. Eur. J.*, 2014, **20**,

1081–1090.

- 183 M. Y. Tsang, F. Teixidor, C. Viñas, D. Choquesillo-Lazarte, N. Aliaga-Alcalde and J. G. Planas, *Inorganica Chim. Acta*, 2016, **448**, 97–103.
- 184 M. Y. Tsang, C. Viñas, F. Teixidor, D. Choquesillo-Lazarte and J. Giner Planas, *Eur. J. Inorg. Chem.*, 2017, **2017**, 4589–4598.
- 185 M. Y. Tsang, C. Viñas, F. Teixidor, J. G. Planas, N. Conde, R. SanMartin, M. T. Herrero, E. Dominguez, A. Lledos, P. Vidossich and D. Choquesillo-Lazarte, *Inorg. Chem.*, 2014, **53**, 9284–9295.
- 186 F. Di Salvo, F. Teixidor, C. Viñas, J. G. Planas, M. E. Light, M. B. Hursthouse and N. Aliaga-Alcalde, *Cryst. Growth Des.*, 2012, **12**, 5720–5736.
- 187 M. Y. Tsang, S. Rodríguez-Hermida, K. C. Stylianou, F. Tan, D. Negi, F. Teixidor, C. Viñas, D. Choquesillo-Lazarte, C. Verdugo-Escamilla, M. Guerrero, J. Sort, J. Juanhuix, D. MasPOCH and J. G. Planas, *Cryst. Growth Des.*, 2017, **17**, 846–857.
- 188 F. Tan, A. López-Periago, M. E. Light, J. Cirera, E. Ruiz, A. Borrás, F. Teixidor, C. Viñas, C. Domingo and J. G. Planas, *Adv. Mater.*, 2018, **30**, 1800726.
- 189 S. Rodríguez-Hermida, M. Y. Tsang, C. Vignatti, K. C. Stylianou, V. Guillerme, J. Pérez-Carvajal, F. Teixidor, C. Viñas, D. Choquesillo-Lazarte, C. Verdugo-Escamilla, I. Peral, J. Juanhuix, A. Verdaguer, I. Imaz, D. MasPOCH and J. Giner Planas, *Angew. Chemie - Int. Ed.*, 2016, **55**, 16049–16053.
- 190 Z. Li, J. Fraile, C. Viñas, F. Teixidor and J. G. Planas, *Chem. Commun.*, 2021, **57**, 2523–2526.
- 191 L. Gan, A. Chidambaram, P. G. Fonquernie, M. E. Light, D. Choquesillo-Lazarte, H. Huang, E. Solano, J. Fraile, C. Viñas, F. Teixidor, J. A. R. Navarro, K. C. Stylianou and J. G. Planas, *J. Am. Chem. Soc.*, 2020, **142**, 8299–8311.
- 192 Y. Yin, N. Ochi, T. W. Craven, D. Baker, N. Takigawa and H. Suga, *J. Am. Chem. Soc.*, 2019, **141**, 19193–19197.
- 193 M. Asay, C. E. Kefalidis, J. Estrada, D. S. Weinberger, J. Wright, C. E. Moore, A. L. Rheingold, L. Maron and V. Lavallo, *Angew. Chemie Int. Ed.*, 2013, **52**,

- 11560–11563.
- 194 Z. Yang, W. Zhao, W. Liu, X. Wei, M. Chen, X. Zhang, X. Zhang, Y. Liang, C. Lu and H. Yan, *Angew. Chemie Int. Ed.*, 2019, **58**, 11886–11892.
 - 195 D. Zhao, *Functionalization of Carborane via Carbonyne intermediates*, Springer Theses, Springer Singapore, Singapore, 2016, pp. 47–72.
 - 196 F. K. Keter and J. Darkwa, *BioMetals*, 2012, **25**, 9–21.
 - 197 L. I. Zakharkin, A. V. Grebennikov and L. A. Savina, *Izv. Akad. Nauk SSSR, Seriya Khimicheskaya*, 1968, 1130–1132.
 - 198 L. I. Zakharkin and A. V. Grebennikov, *Zhurnal Obs. Khimii*, 1969, **39**, 575–579.
 - 199 L. I. Zakharkin, A. V. Grebennikov and A. I. L'vov, *Izv. Akad. Nauk SSSR, Seriya Khimicheskaya*, 1970, 106–112.
 - 200 N. Vázquez, V. Gómez-Vallejo and J. Llop, *Tetrahedron Lett.*, 2012, **53**, 4743–4746.
 - 201 M. Rinaldi-Carmona, F. Barth, M. Héaulme, D. Shire, B. Calandra, C. Congy, S. Martinez, J. Maruani, G. Néliat, D. Caput, P. Ferrara, P. Soubrié, J. C. Brelière and G. Le Fur, *FEBS Lett.*, 1994, **350**, 240–244.
 - 202 R. S. Padwal and S. R. Majumdar, *Lancet*, 2007, 369, 71–77.
 - 203 A. Buzharevski, S. Paskas, M. Sárosi, M. Laube, P. Lönnecke, W. Neumann, S. Mijatovic, D. Maksimovic-Ivanic, J. Pietzsch and E. Hey-Hawkins, *ChemMedChem*, 2019, **14**, 315–321.
 - 204 S. M. Ivanov and I. B. Sivaev, *J. Heterocycl. Chem.*, 2020, **57**, 1428–1434.
 - 205 G. L. Rusinov, R. I. Ishmetova, S. G. Tolshchina, N. K. Ignatenko, I. N. Ganebnykh, P. A. Slepukhin, V. A. Ol'shevskaya, V. N. Kalinin and V. N. Charushin, *Russ. Chem. Bull.*, 2010, **59**, 116–121.
 - 206 S. G. Tolshchina, R. I. Ishmetova, N. K. Ignatenko, A. V. Korotina, I. N. Ganebnykh, V. A. Ol'shevskaya, V. N. Kalinin and G. L. Rusinov, *Russ. Chem. Bull.*, 2011, **60**, 985–991.
 - 207 H. Li, F. Bai, H. Yan and C. Lu, *Org. Lett.*, 2017, **19**, 862–865.

2. Objectives

2. Objectives

On the basis of the antecedents illustrated in Chapter 1, the main objectives for this PhD thesis can be summarized as follows:

- Synthesis and characterization of new Cu(II) coordination compounds with ligands **HL1-HL3**, aiming to study the effects of the different substituents in positions 3- and 5-. Moreover, three representative Cu(II) salts (chloride, nitrate and acetate) were used as reactants in order to assess the influence of their counter-anions on the resulting coordination compounds.

- Synthesis and characterization of new coordination compounds with ligands **L4** and **L5**, aiming to prove the coordination versatility of the ligands. On this basis, atoms capable of displaying different coordination numbers and geometries such as Co(II), Cu(II), Zn(II), Cd(II) and Hg(II) have been selected as metal centres.

- Design and obtention of new bispyrazole ether ligands, bearing phenyl substituents in positions 3- and 5-. Synthesis of their coordination compounds with Pd(II) for comparison purposes with those of **L4** and **L5**.

- Development of a new family of pyrazole-carborane derived ligands. Since reports of metal complexes bearing similar ligands are almost non-existent, the synthesis and characterization of their coordination compounds with the resulting ligands was also proposed as one of the main tasks in this work.

- Study of the structural-property correlations in the resulting metal complexes.

3. Results and Discussion

3.1 Ligands

This chapter consists of four sections. The first one offers an overview of the twelve ligands used for the synthesis of coordination compounds in this work.

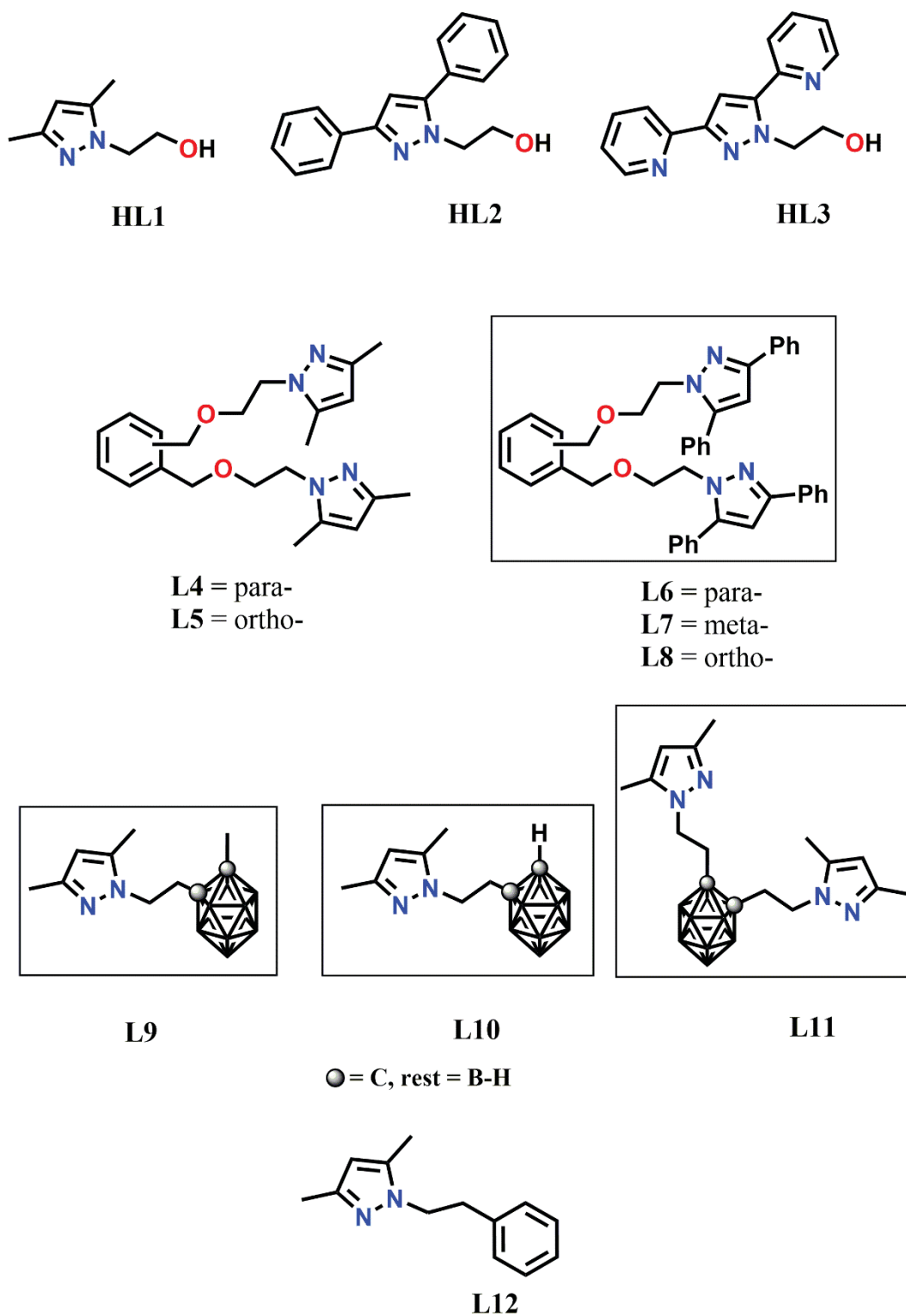
In the second section, the synthesis and characterization of three new *N,O*-ether hybrid bispyrazole ligands is discussed.

The third section contains an in-detail discussion of the synthesis of three new *N*-alkylcarbaboranyl pyrazole derivatives. It also contains a detailed characterization section and the description of the crystal structure of one of the ligands.

The fourth section summarizes the work carried out in this chapter.

3.1.1 Ligand overview

Twelve pyrazole-derived ligands have been used in this work (Scheme 3.1.1).

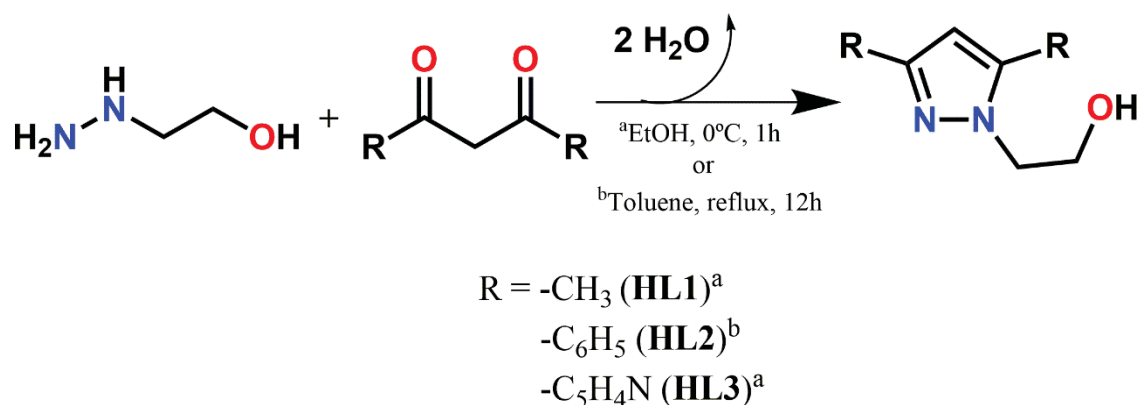


Scheme 3.1.1 Schematic representation of the ligands used in this work. Ligands synthesized for the first time are enclosed in a square.

All ligands feature trisubstituted (1-(*N*-substitution), 3-, 5-substitution) pyrazole ligands. However, the functional groups attached to the *N*-position are the most relevant ones for the purpose of this work (see Chapter 1: Introduction and Chapter 2: Objectives). As such, the following ligands can be classified into four groups: hybrid *N,O*-hydroxyethylpyrazole ligands (**HL1-HL3**), hybrid *N,O*-ether bispyrazole ligands (**L4-L8**), *N*-alkylcarborane pyrazole ligands (**L9-L11**) and one *N*-alkylphenyl substituted pyrazole ligand (**L12**).

The first family, comprising hybrid *N,O*-hydroxyethylpyrazole ligands, consists of 2-(3,5-dimethyl-1*H*-pyrazol-1-yl)ethanol (**HL1**), 2-(3,5-diphenyl-1*H*-pyrazol-1-yl)ethanol (**HL2**) and 2-(3,5-dipyridyl-1*H*-pyrazol-1-yl)ethanol (**HL3**) ligands. Their positions 3- and 5- are substituted by methyl (**HL1**), phenyl (**HL2**) or 2-pyridyl (**HL3**) groups. They are synthesized by condensation of hydroxyethylhydrazine with the corresponding 1,3-diketone (Scheme 3.1.2), a procedure first described by Haanstra *et al.*¹ for **HL1**. This procedure has undergone several iterations in our group, until reaching its current method². Adaptations of this process have been successfully employed in our group for the synthesis of ligands such as **HL2** and **HL3**, which have already been used as ligands for the synthesis of coordination complexes³⁻⁶. Moreover, ligands **HL1-HL3** have been used as starting reactants for the synthesis of new ligands, both in already published reports⁷⁻⁹ and during the course of this work.

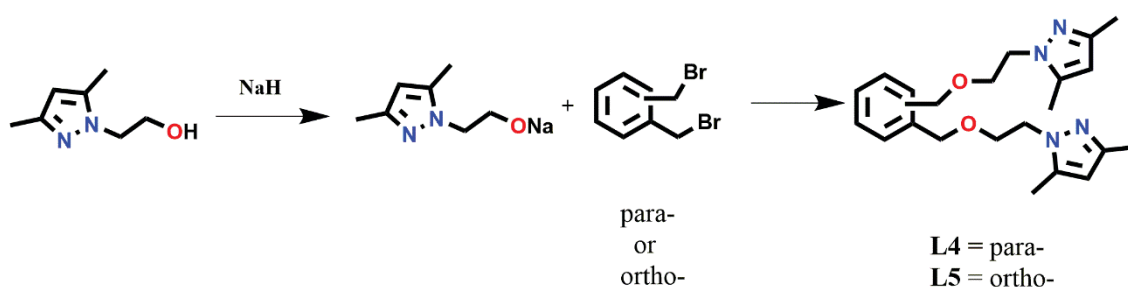
All these reactions are straightforward, and only the synthesis of **HL2** requires the use of temperature and a Dean-Stark apparatus. In all cases, the desired ligands were obtained with high yields and high quantities (ca. 5-10 g, 81-93% yield). Moreover, products are easily purified by recrystallization in diethyl ether (Et₂O).



Scheme 3.1.2 General scheme for the synthetic pathway for **HL1-HL3**.

Regarding hybrid *N,O*-ether bispyrazole ligands, two of them, namely 1,4-bis[4-(3,5-dimethyl-1*H*-pyrazol-2-yl)-2-oxabutyl]benzene (*para*- substitution, **L4**) and its positional isomer 1,2-bis[4-(3,5-dimethyl-1*H*-pyrazol-2-yl)-2-oxabutyl]benzene (*ortho*-substitution, **L5**) were also previously synthesized in our group⁹. In this thesis, three additional new ligands have been synthesized: 1,4-bis[4-(3,5-diphenyl-1*H*-pyrazol-2-yl)-2-oxabutyl]benzene (*para*- substitution, **L6**) and their positional isomers 1,3-bis[4-(3,5-diphenyl-1*H*-pyrazol-2-yl)-2-oxabutyl]benzene (*meta*- substituted phenyl derivative, **L7**) and 1,2-bis[4-(3,5-diphenyl-1*H*-pyrazol-2-yl)-2-oxabutyl]benzene (*ortho*- substituted phenyl derivative, **L8**). It is worth remarking that the *meta*- isomer of **L4** and **L5** (1,3-bis[4-(3,5-diphenyl-1*H*-pyrazol-2-yl)-2-oxabutyl]benzene) has been also synthesized in our group¹⁰, but sadly single crystals of compounds bearing this ligand have not been obtained during this PhD work. Pyrazole positions 3- and 5- are substituted by either methyl (**L4-L5**) or phenyl (**L6-L8**) groups in these compounds.

As mentioned above, the synthetic strategy for **L4** and **L5** was previously reported and consists of a two-step process (Scheme 3.1.3)^{9,11}. In the first step, the sodium salt of **HL1** is prepared by refluxing it with NaH in dry THF for two hours. Next, the corresponding α,α -dibromo-*x*-xylene derivative (*x* = *para*- (**L4**), or *ortho*- (**L5**)) is added, resulting in a nucleophilic substitution that provides the desired ligands. This reaction is straightforward and after extraction with CHCl₃ the products are obtained in pure forms. Both ligands are obtained in high yields and quantities (ca. 2 g, 93-99% yields). A similar synthetic strategy was adapted for **L6-L8** and will be discussed in detail in section 3.1.2.



Scheme 3.1.3 Synthetic scheme for the synthesis of **L4** and **L5**

All ligands comprising the third family of *N*-alkylcarborane pyrazole ligands consists of three ligands that have been synthesized for the first time during this PhD: 1-[4-(3,5-dimethyl-1*H*-pyrazol-1-yl)ethyl]-2-methyl-1,2-dicarba-*closo*-dodecaborane (**L9**), 1-[4-(3,5-dimethyl-1*H*-pyrazol-1-yl)ethyl]-1,2-dicarba-*closo*-dodecaborane (**L10**)

and 1,2-bis[4-(3,5-dimethyl-1*H*-pyrazol-1-yl)ethyl]-1,2-dicarba-*closo*-dodecaborane (**L11**). Their synthesis and characterization will be discussed in detail in section 3.1.3.

Finally, ligand 3,5-dimethyl-1-(2-phenylethyl)-1*H*-pyrazole (**L12**), is commercially available and has been used without further purification.

3.1.2 Synthesis and characterization of L6-L8

3.1.2.1 Synthesis of L6-L8

All the syntheses were carried out under nitrogen atmosphere, using standard Schlenk techniques, unless otherwise noted. Ligands **L6-L8** have been prepared using a similar synthetic route to that used for **L4-L5** (Scheme 3.1.3) but using **HL2** as a reactant instead of **HL1**. As such, the first step of the synthesis consists of the formation of **HL2** sodium salt, **NaL2**, which was obtained by refluxing a mixture of **HL2** and NaH in dry THF for two hours. Next, the corresponding α,α -dibromo-*x*-xylene derivative ($x = para$ - (**L6**), *meta*- (**L7**) or *ortho*- (**L8**)) was added, and the mixture refluxed for twenty-four hours. After that period, H₂O was added to destroy the excess of NaH and then the solvents were evaporated until dryness. The residue was taken up in H₂O and extracted three times using CHCl₃. After drying the organic layers with anhydrous MgSO₄, they were concentrated and purified *via* column chromatography, using a CHCl₃/AcOEt 9:1 mixture as eluent. After evaporation of the organic layers, the resulting compounds were obtained as oils. However, the overall yields for these procedures were poor.

To increase the yields, longer reflux times (from two hours to four in the first step and from twenty-four to ninety-six hours in the second step) and higher temperatures (using dry toluene as solvent instead of dry THF) were employed. This increased their overall yield up to (46-56%). In any case, they are much lower than their **L4** and **L5** counterparts (81-93%), which use **HL1** as a starting reactant. This fact can be attributed to the nature of the phenyl substituents of **HL2**. They may hinder the nucleophilic attack on the electrophile due to steric reasons owing to its increased bulkiness when compared to **HL1**, as well as weakening the nucleophilicity of the alkoxide *via* inductive effects.

3.1.2.2 Characterization of **L6-L8**

Ligands **L6-L8** have been characterized *via* elemental analyses (EA), melting point determination (M.p.), FTIR-ATR, ^1H , $^{13}\text{C}\{^1\text{H}\}$ and Heteronuclear Single Quantum Coherence (HSQC) NMR spectroscopies. EA results agree with the expected values calculated from their empirical formula.

- FTIR-ATR Spectroscopy for **L6-L8**

The FTIR-ATR spectra of pyrazole-containing ligands display a number of easily identifiable signals, such as $[\nu(\text{C-H})_{\text{ar}}]$, $[\nu(\text{C-H})_{\text{al}}]$, $[\nu(\text{C}=\text{C}/\text{C}=\text{N})_{\text{ar}}]$, $[\delta(\text{C}=\text{C}/\text{C}=\text{N})_{\text{ar}}]$, $[\delta(\text{C-H})_{\text{ip}}]$ and $[\delta(\text{C-H})_{\text{oop}}]$ ¹². This set of fingerprint signals will be useful throughout the whole work for the identification of the presence of pyrazole moieties. Thus, these signals are easily observed on the FTIR-ATR spectra of **L6-L8** (Figures 3.1.1, S3.1.1 and S3.1.2). Moreover, the signal corresponding to $[\delta(\text{C-H})_{\text{ip}}]$ is noticeable stronger and broader than in the original **HL2** reactant. This is attributed to the overlapping of $[\delta(\text{C-H})_{\text{ip}}]$ and the $[\nu(\text{C-O-C})]$ signal, which suggests the obtention of **L6-L8** ligands. Lastly, the disappearance of sharp signals attributable to $[\nu(\text{O-H})]$ from the **HL2** precursor, confirm the formation of the new ligands. As an example, FTIR-ATR spectrum of **L6** is shown (Figure 3.1.1), highlighting relevant signals, while those of **L7** and **L9** can be found in Annex I (Figures S3.1.1-S3.1.2).

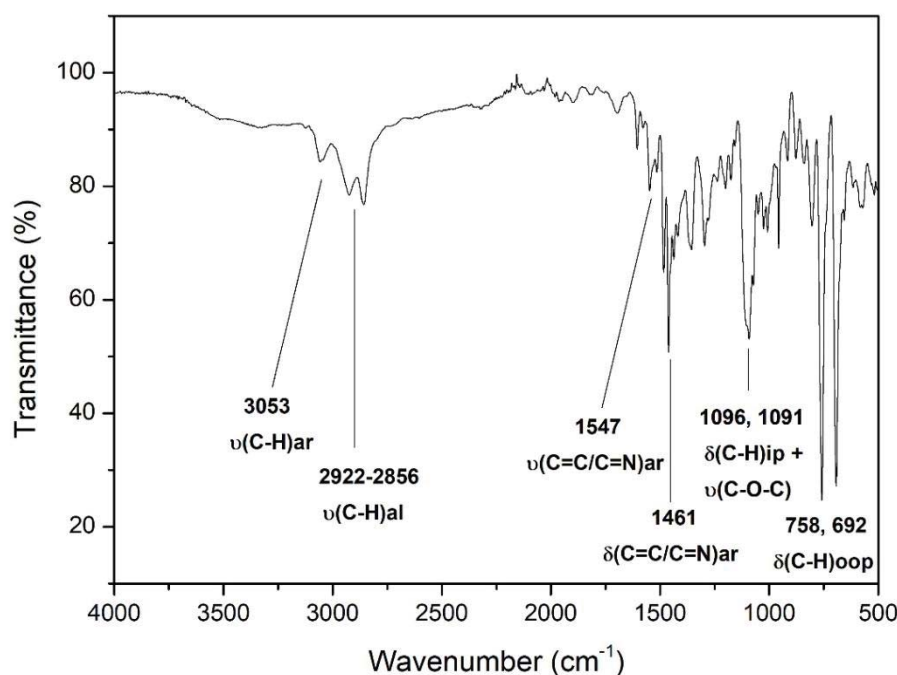


Figure 3.1.8 FTIR-ATR spectrum of **L6**

- NMR Spectroscopy for **L6-L8**

The ^1H , $^{13}\text{C}\{^1\text{H}\}$ and HSQC NMR spectra of **L6-L8** have been recorded in CDCl_3 . First, we will discuss ligand **L6**, as owing to its symmetrical nature, its NMR spectra are simpler than those of **L7** and **L8**. Then, ligands **L7** and **L8** will be discussed. Signal assignment was performed *via* comparison with the reported **HL2** precursor⁵.

In the ^1H NMR spectrum of **L6** three distinct regions can be identified. The region between 8.0-7.0 ppm shows the signals corresponding to phenyl aromatic protons, which display a rather complex pattern. This is due to the non-symmetrical nature of the pyrazole moiety, and thus signals corresponding to substituents in positions 3- and 5- are split. For instance, the protons in *ortho* position of phenyl rings appear as two sets of doublets for **L6** (7.84 ppm and 7.53 ppm, Fig. 3.1.2). However, this splitting also results in a complex pattern, as several different signals overlap (see the multiplet at 7.43 ppm, Fig. 3.1.2). On the other hand, signals attributable to the phenyl ring not attached to the pyrazole group are easier to identify, as they appear slightly downfield and as a singlet (7.10 ppm, Fig. 3.1.2). The next region consists of a single signal at 6.59 ppm, attributable to the pyrazole proton signal. Lastly, the signals corresponding to the ether group linking the pyrazole and the phenyl moiety appear significantly downfield. The $\text{Ph-CH}_2\text{-O}$ signals appears a

singlet (4.40ppm), while signals for O-CH₂-CH₂-Pz appear as triplets (4.34 ppm for CH₂-Pz and 3.95 ppm for O-CH₂).

The signals in the ¹³C{¹H} NMR spectra of **L6** (Figure 3.1.3) mirror the three-region distribution pattern found in the ¹H NMR spectra. As such, significantly upfield (151.0-125.8 ppm) lie those signals corresponding to aromatic carbons, signals belonging to tertiary aromatic carbons lying between 151.0-133.6 ppm, while signals corresponding to secondary aromatic protons lie between 130.8-125.7 ppm in a crowded area. Next, a lone signal in the region of 103.5 ppm is easily identifiable as a pyrazolic carbon. Finally, in the third region, signals belonging to secondary carbons bonded to oxygen atoms appear more upfield (73.0-69.0 ppm) than signals of those bonded to nitrogen atoms (49.4 ppm).

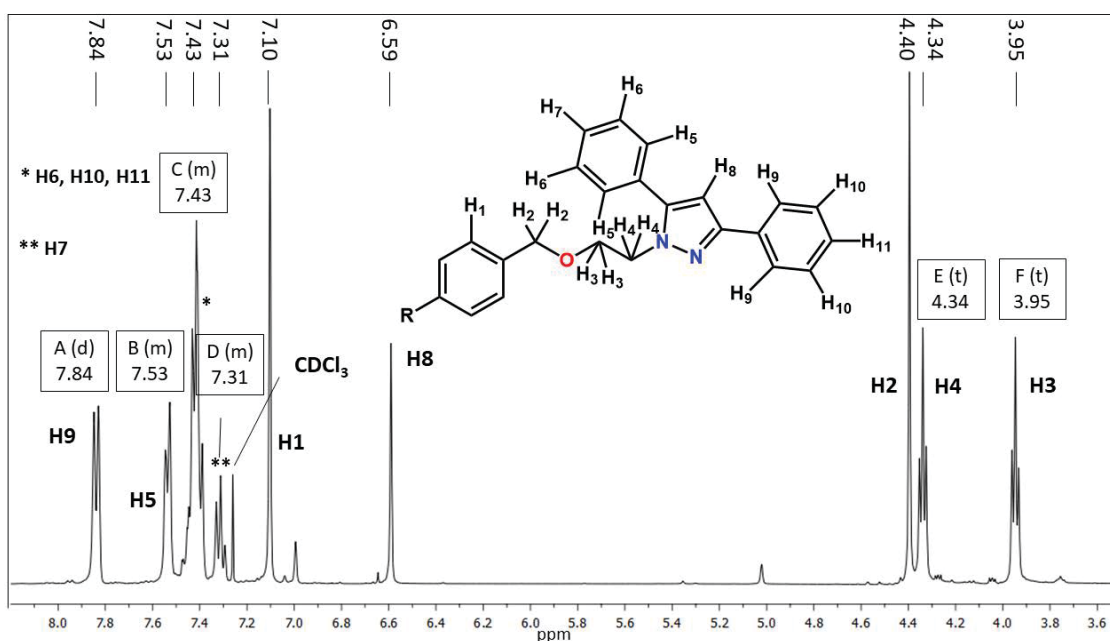


Figure 3.1.9 ¹H NMR spectrum of **L6** (CDCl₃, 400.0 MHz)

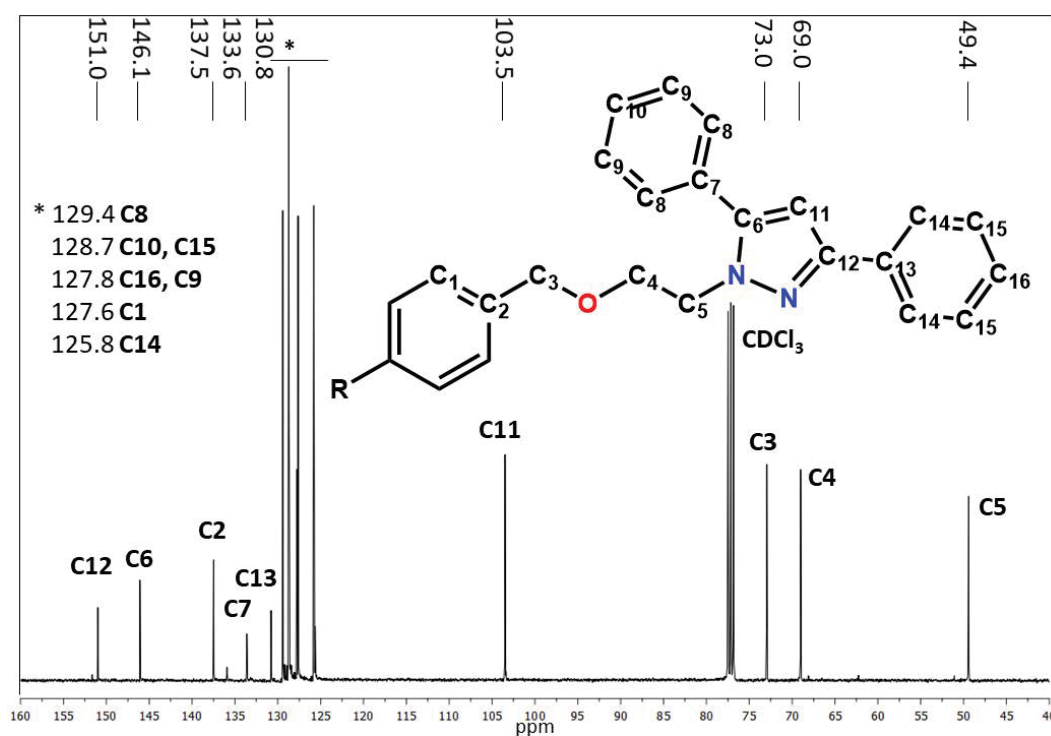


Figure 3.1.10 $^{13}\text{C}\{^1\text{H}\}$ NMR spectrum of **L6** (CDCl_3 , 100.6 MHz)

For the less symmetrical ligands **L7** and **L8**, the region between 8.0-7.0 ppm in their ^1H NMR spectrum (Fig. S3.1.3 and S3.1.4) becomes increasingly complex. To begin with, the signals corresponding to phenyl protons attached to pyrazole rings (7.85-7.31 ppm) are much more overlapped, especially in **L8**. Moreover, whereas the signal corresponding to the phenyl protons not attached to pyrazole still appears as a singlet in **L8** (Figure S3.1.4), the *m*-substitution of the phenyl ring in **L7** results in the observation of three proton signals: a multiplet, a doublet and a singlet (Fig. S3.1.3). Finally, in their $^{13}\text{C}\{^1\text{H}\}$ NMR spectra, the number of signals observed in the region between 129.5-125.7 ppm increases (Fig. S3.1.5 and S3.1.6).

Owing to the complex nature of the upfield regions in both ^1H and $^{13}\text{C}\{^1\text{H}\}$ NMR spectra, further characterization was performed. As the ^1H NMR signals of aromatic protons are much more distinguishable than their corresponding $^{13}\text{C}\{^1\text{H}\}$ NMR signals, it was thought that bidimensional HSQC NMR of **L6-L8** (Figures S3.1.7-S3.1.9) would ease their identification. This is especially relevant for ligands **L7** and **L8**, which feature more complex patterns in the ^1H NMR spectra and more signals in their $^{13}\text{C}\{^1\text{H}\}$ NMR spectra.

On this basis, the proposed signal assignments for ^1H and $^{13}\text{C}\{^1\text{H}\}$ are summarized in Tables 3.1.1 and 3.1.2. For further details, please refer to experimental section 5.1 and Annex I section for this chapter.

Table 3.1.1 ^1H NMR spectra signals for **L6-L8**

	L6	L7	L8
$\text{CH}_{\text{Ph-Pz}}$	7.84(d) / $^3J_{\text{HH}} = 7.4$, 7.53(m) 7.43(m), 7.31(m)	7.85(m), 7.52(m) 7.42(m), 7.32(m)	7.85(m), 7.47(m), 7.39(m), 7.31(m)
CH_{Ph}	7.10 (s)	7.19(m), 7.03(s) 7.08(d) / $^3J_{\text{HH}} =$ 7.51	7.19(s)
CH_{Pz}	6.59 (s)	6.58(s)	6.58(s)
$\text{Ph-CH}_2\text{-O}$	4.40(s)	4.38(s)	4.36(s)
O-CH_2	3.95(t) / $^3J_{\text{HH}} = 5.61$	3.92(t) / $^3J_{\text{HH}} = 5.70$	3.85(t) / $^3J_{\text{HH}} =$ 5.53
$\text{CH}_2\text{-N}$	4.34(t) / $^3J_{\text{HH}} = 5.61$	4.32(t) / $^3J_{\text{HH}} = 5.70$	4.27(t) / $^3J_{\text{HH}} = 5.53$

δ (ppm) / multiplicity s = singlet, d= doublet, t = triplet, m= multiplet/ $^3J_{\text{HH}}$ (Hz)

Table 3.1.2 $^{13}\text{C}\{^1\text{H}\}$ NMR spectra signals for **L6-L8**

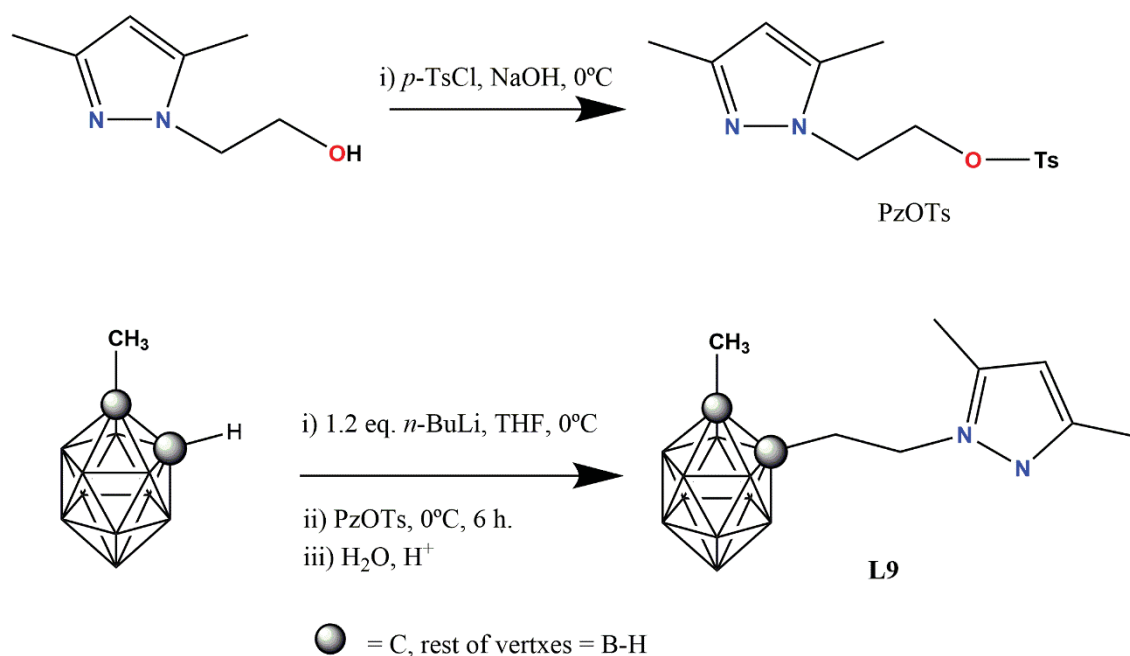
	L6	L7	L8
C_{Pz}	151.0, 146.1	151.0, 146.1	150.9, 146.0
C_{Ph}	137.5, 133.6, 130.8	138.3, 133.7, 130.8	136.2, 133.7, 130.8
$\text{CH}_{\text{Ph-Pz}}$	129.4-125.8	129.7-125.8	129.4-125.7
C_{Ph}	127.6	128.5, 126.8, 126.7	128.5, 128.6
CH_{Pz}	103.5	103.5	103.5
$\text{Ph-CH}_2\text{-O}$	73.0	73.1	70.7
O-CH_2	69.0	69.1	69.0
$\text{CH}_2\text{-N}$	49.4	49.4	49.3

δ (ppm)

3.1.3 Synthesis and characterization of L9-L11

3.1.3.1 Synthesis and characterization of L9, S1 and S2

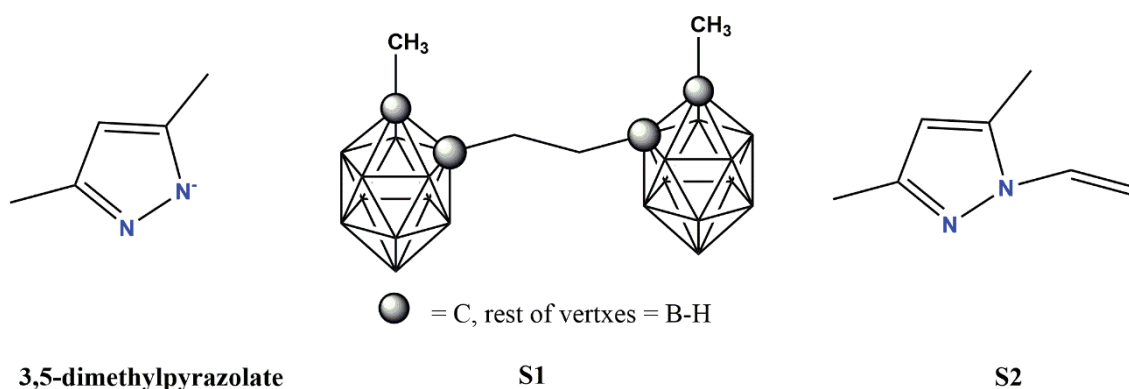
The synthetic procedure for the synthesis of *o*-carborane derived ligands has been extensively established in the Laboratory of Inorganic Materials and Catalysis (LMI) group in the previous years^{13–15}. As mentioned in the introduction of this thesis, the monosubstitution reaction of *o*-carborane at one of the cluster carbons is initiated by the lithiation on the carbon, followed by the nucleophilic addition to an electrophile. However, the monosubstitution of the carborane is not trivial, as monolithitated *o*-carbaboranes tend to disproportionate to the dianion and the *o*-carborane¹⁴. Usually, low temperatures (-70°C) and ethereal solvents are needed in order to avoid mixtures of mono- and disubstituted products and achieve high yields¹⁶. This strategy has been employed successfully in the synthesis of several pyridylalcohol monosubstituted carbaboranes^{13–15}. Another strategy to avoid di-substitution is to use a C-substituted starting *o*-carborane compound such as 1-methyl-*o*-carborane (Scheme 3.1.4).



Scheme 3.1.4 Synthetic scheme for the synthesis of L9

Thus, for simplicity we first introduced 1-methyl-*o*-carborane into a new pyrazole ligand by the nucleophilic addition of the monolithitated 1-methyl-*o*-carborane onto 3,5-dimethyl-1-(2-toluene-*p*-sulfonyloxyethyl)pyrazole (PzOTs), that acts as an electrophile (Scheme 3.1.4). The latter has already been successfully used a number of times as a substrate for nucleophilic substitutions reactions in our group^{7,17}. This synthetic procedure has provided the first example of a carboranylpyrazole compound (**L9**) in the literature.

Pure **L9** was obtained as a white powder from the reaction mixture in nearly 40 % yield after purification. Analysis of the reaction mixture by NMR showed that other carborane and pyrazole species were present, which explains the moderate yield for **L9**. Purification with preparative TLC using AcOEt/Hexane (2:3) allowed for the obtention of **L9** and for the isolation and characterization of the other by-products of the reaction (Scheme 3.1.5). All compounds have been characterized by standard spectroscopic techniques. Thus, **L9** has been characterized by EA, m.p., FTIR-ATR, ^1H , ^{11}B , $^{11}\text{B}\{^1\text{H}\}$, $^{13}\text{C}\{^1\text{H}\}$ NMR spectroscopies and Single-Crystal X-ray diffraction (SCXRD). Compound **S1** has been characterized by ^1H , ^{11}B and $^{11}\text{B}\{^1\text{H}\}$ NMR spectroscopies as well as by SCXRD, while **S2** and 3,5-dimethylpyrazol have been identified by comparison of their ^1H NMR spectra with that of a previously reported¹⁸ or commercially available sample, respectively. Elemental Analyses of **L9** agree with the with the results obtained by NMR spectroscopies and the molecular formulae obtained from its crystal structure.



Scheme 3.1.5 By-products obtained in the synthetic procedure for **L9**

• FTIR-ATR Spectroscopy for **L9**

Infrared spectroscopy (IR) is an especially useful technique for the identification of B-H containing boron species, as $[\nu(\text{B-H})]$ appears in the region of $2600\text{--}2400\text{ cm}^{-1}$. Coupled with the presence of the distinctive pyrazole bands, it allows easy identification of the resulting ligands. Thus, FTIR-ATR spectrum of **L9** (Figure 3.1.4) displays the characteristic bands of the pyrazole group such as $[\nu(\text{C}=\text{C}/\text{C}=\text{N})_{\text{ar}}]$ (1554 cm^{-1}), $[\delta(\text{C}=\text{C}/\text{C}=\text{N})_{\text{ar}}]$ (1452 cm^{-1}), $[\delta(\text{C-H})_{\text{ip}}]$ (1024 cm^{-1}) and $[\delta(\text{C-H})_{\text{oop}}]$ (779 and 726 cm^{-1}), while $[\nu(\text{B-H})]$ signals appears as a broad band centred at 2571 cm^{-1} ¹⁹. A $[\nu(\text{B-B})]$ vibration is also expected²⁰, but it is probably overlaid by $[\delta(\text{C-H})_{\text{oop}}]$ signals. Moreover, signals attributable to $[\nu(\text{C-H})_{\text{ar}}]$ (3134 cm^{-1}) and $[\nu(\text{C-H})_{\text{al}}]$ (bands between 2978 and 2858 cm^{-1}) are also observed.

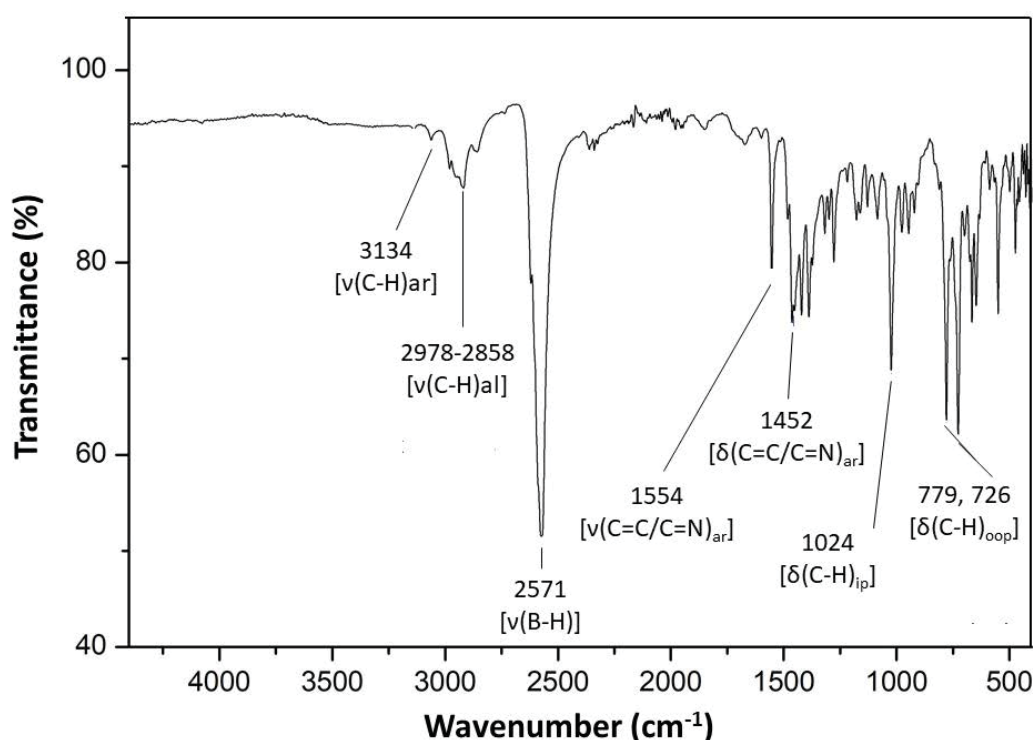


Figure 3.1.11 FTIR-ATR spectrum of **L9**

• NMR Spectroscopy for **L9**

The ^1H NMR spectrum of **L9** (Figure 3.1.5) is relatively straightforward, as only a few signals are observed. First, the pyrazolic hydrogen signal at $\delta = 5.77\text{ ppm}$ is easily identified. Second, the protons of the aliphatic chain ($\delta = 4.07\text{ ppm}$ and 2.72 ppm) appear as complex AA'-BB' type multiplets. Thus, each proton is coupled to its vicinal one and

to two diastereotopic ones, resulting in the observed multiplet. Simulation of the latter using MestReNova provided the detailed coupling constants for the two signals, that include six ^1H - ^1H coupling constants ($^2J_{AA'} = -6.0$ Hz, $^3J_{AB} = 12.7$ Hz, $^3J_{AB'} = 3.4$ Hz, $^3J_{A'B} = 8.8$ Hz, $^3J_{A'B'} = 11.7$ Hz and $^2J_{BB'} = -5.4$ Hz (Figure S3.1.10)). This feature is attributed to a hindered rotation due to the bulkiness of the substituents on both ends of the alkyl chain. Lastly, the signals attributable to the methyl attached to carborane or pyrazole are identified at 2.19 ppm or 2.08 and 2.07 ppm, respectively.

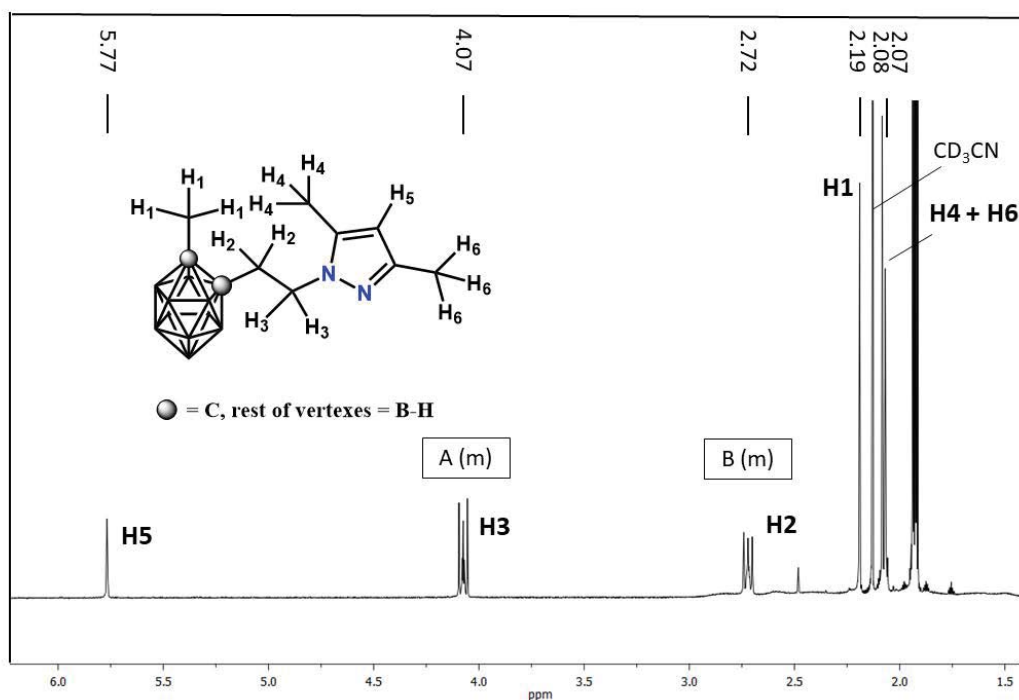


Figure 3.1.12 ^1H NMR spectrum of **L9** (CD_3CN , 400.0 MHz)

Regarding the $^{13}\text{C}\{^1\text{H}\}$ NMR spectrum for **L9** (Fig. 3.1.6), several signals are worth mentioning. First, in upfield regions, signals corresponding to pyrazolyl ring ($\delta = 148.2$, 140.1 and 106.9 ppm) are identified. In the middle region, signals corresponding to the carbons of the carborane group and the alkylic chain ($\delta = 47.7$ and 36.1 ppm) appear. In the low chemical shift region, signals corresponding to the methyl groups attached to carborane ($\delta = 23.6$ ppm) and pyrazole ($\delta = 13.6$ and 11.0 ppm) are identified.

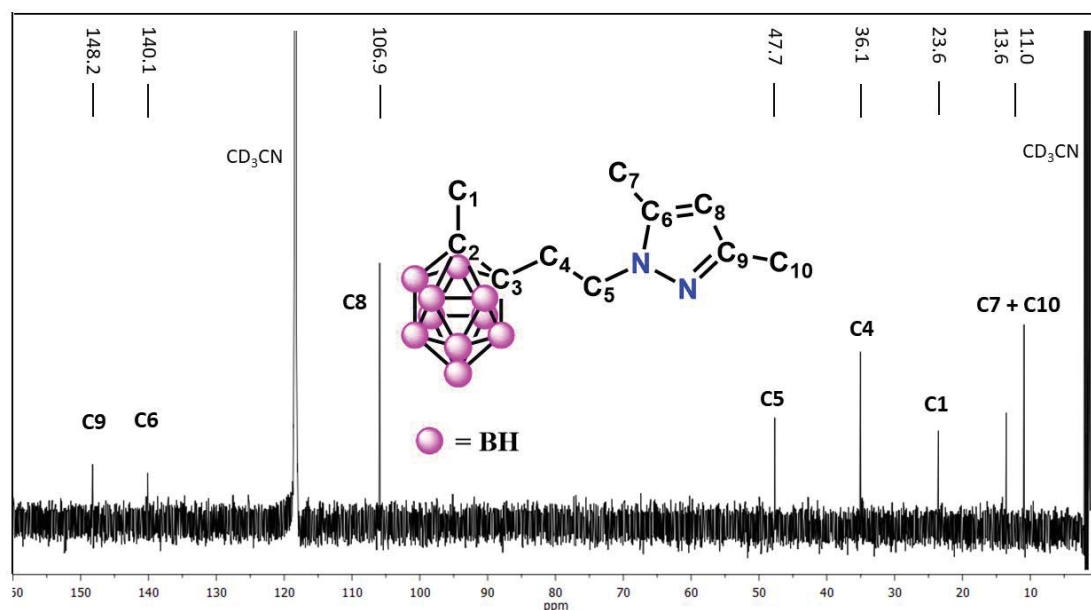


Figure 3.1.13 $^{13}\text{C}\{^1\text{H}\}$ NMR spectrum of **L9** (CD_3CN , 100.6 MHz).

The ^{11}B NMR chemical shifts of boron skeletons in their NMR spectra do not correspond generally to the electron densities of individual vertexes, but rather to various effects (e.g. antipodal or neighbour effect)²⁰. For instance, the boron atoms closest to carbon atoms are the most shielded and exert an antipodal effect on the other vertexes which are more deshielded²⁰. For **L9**, two sets of doublets appear at -4.4 and -6.2 ppm, while several resonances overlap between -8.23 to -11.14 ppm (Figure 3.1.7, left). Thus, we can tentatively assign the downfield-most resonance to the signals of the eight boron nuclei closest to the carbon atoms, whereas the most upfield ones to the boron nuclei furthest away from the carbon atoms²⁰. For the complete characterization of boron skeletons such as carborane, it is also useful to employ $^{11}\text{B}\{^1\text{H}\}$ NMR experiments in tandem with ^{11}B NMR experiments. The resulting resonance patterns are very indicative of the substitution in carborane cages. For instance, for **L9** spectra three resonances can be identified in a 1:1:8 ratio in its $^{11}\text{B}\{^1\text{H}\}$ NMR spectra (Figure 3.1.7, right). This 1:1:8 pattern is typical for asymmetrically *ortho*-substituted carboranes. Complete assignment of B-H signals was done by comparison with related carborane derivative ligands¹⁵.

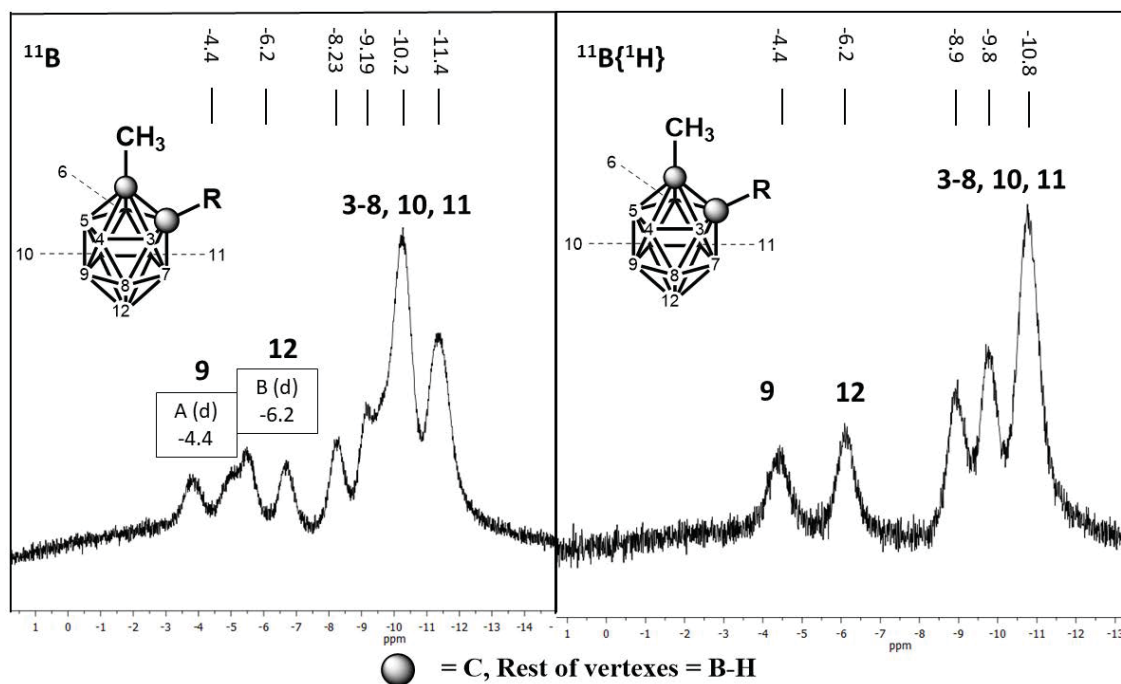


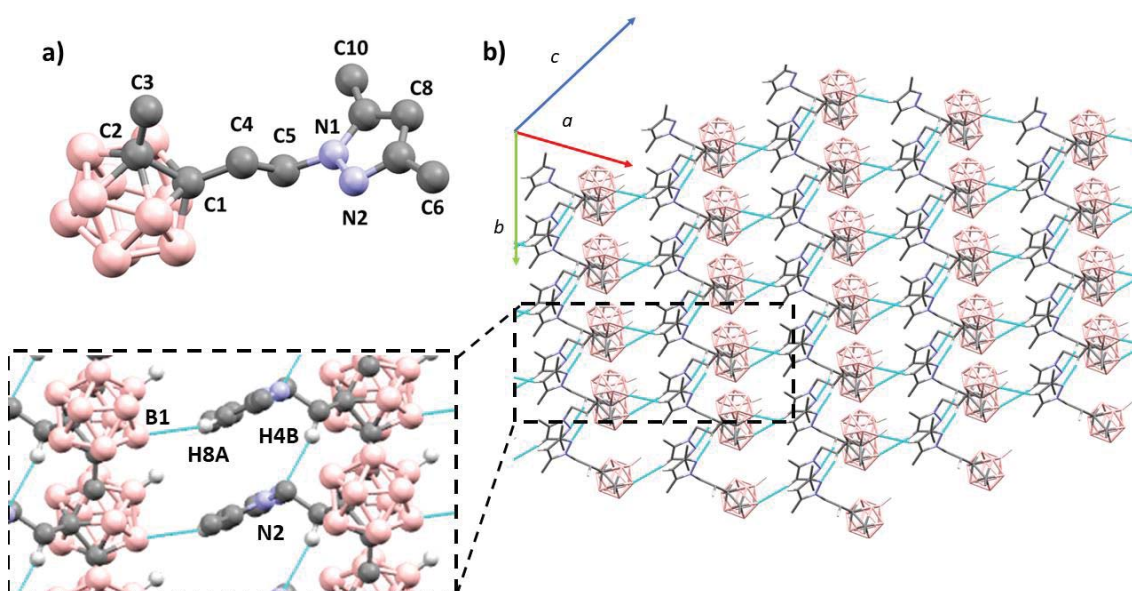
Figure 3.1.14 ^{11}B (left) and $^{11}\text{B}\{^1\text{H}\}$ (right) NMR spectra for **L9** (CD_3CN , 128.6 MHz)

- X-ray Crystal Structure for **L9**

Crystals suitable for X-ray diffraction of **L9** have been obtained by recrystallization in THF. The compound crystallizes in a monoclinic system and a $P2_1/c$ group, each unit cell comprising four **L9** molecules (Fig. 3.1.8). The compound shows a 1-methyl-*o*-carborane unit linked to a 3,5-dimethylpyrazole unit by a $-\text{CH}_2\text{CH}_2-$ alkylic chain. Selected interatomic bond distances and angles are summarized on Table 3.1.3. The elucidated crystal structure univocally confirms the obtention of the ligand, which agrees with the spectroscopic data. A detailed examination of the crystal packing shows that each molecule is linked to four others through hydrogen interactions. The pyrazolyl group plays a key role in the supramolecular structure of **L9**, as it promotes hydrogen bonds with the carboranyl moiety ($\text{C8-H8A}\cdots\text{H1-B1}$) and the aliphatic chain ($\text{C4-H4B}\cdots\text{N2}$), resulting in a 2D supramolecular layer along the *ac* plane (Fig. 3.1.8). Selected bond lengths, angles and supramolecular interactions are summarized on Table 3.1.3.

Table 3.1.3 Selected bond lengths (Å), angles (°) and non-bonding interactions for **L9**.

Bond lengths (Å)				
C1-C2	1.6649(16)	C1-C4	1.5267(15)	
C4-C5	1.5317(17)	C5-N1	1.4509(15)	
Bond angles (°)				
C1-C4-C5	113.42(10)	C4-C5-N1	108.98(10)	
Non-bonding interactions				
	D-H...A (Å)	D-H (Å)	H-D...A (Å)	> D-H...A (°)
L9				
C8-H8A...B1-H8	3.028	0.950	3.949	163.77
C4-H4B...N2	2.535	0.990	3.501	165.21

**Figure 3.1.8** Ligand **L9** showing relevant atoms and their numbering scheme (a). Supramolecular structure of **L9**. Only hydrogen atoms participating in intermolecular interactions are shown (b). Colour code: grey (C), white (H), pink (B), light blue (N). Intermolecular interactions are represented as dashed light-blue lines.

• Characterization of **S1** and **S2**

As mentioned above, the synthesis of **L9** also results in the formation of undesired by-products (Scheme 3.1.5). All by-products have been characterized by NMR and the structure of **S1** has been determined by SCXRD.

The ^1H NMR spectrum of **S1** (Fig. 3.1.9, left) shows few signals, consistent with the high symmetry of the molecule. Thus, signals corresponding to the alkylic chain appear at 2.67 ppm, whereas those belonging to the methyl group appear at 2.22 ppm. Both ^{11}B and $^{11}\text{B}\{^1\text{H}\}$ NMR spectra display the characteristic 1:1:8 pattern of asymmetrically substituted carborane cages (Fig. S3.1.11).

Regarding **S2** (Scheme 3.1.5), its ^1H NMR spectrum (Fig. 3.1.9, right) displays three multiplets at $\delta = 6.85$, 5.57 and 4.73 ppm, consistent with the presence of a vinyl group. Their ^1H - ^1H coupling constants ($^3J_{\text{H1-H3}} = 15.35$ Hz, $^3J_{\text{H2-H3}} = 8.91$ Hz) are also consistent with the presence of a *trans* and *cis* coupling constant. Finally, a signal belonging to the pyrazole group ($\delta = 5.84$) is also identified. Overall, the whole spectra is identical to the reported ones for *N*-vinyl-3,5-dimethylpyrazole¹⁸, a commercial molecule used in the synthesis of polymeric materials^{29,30}.

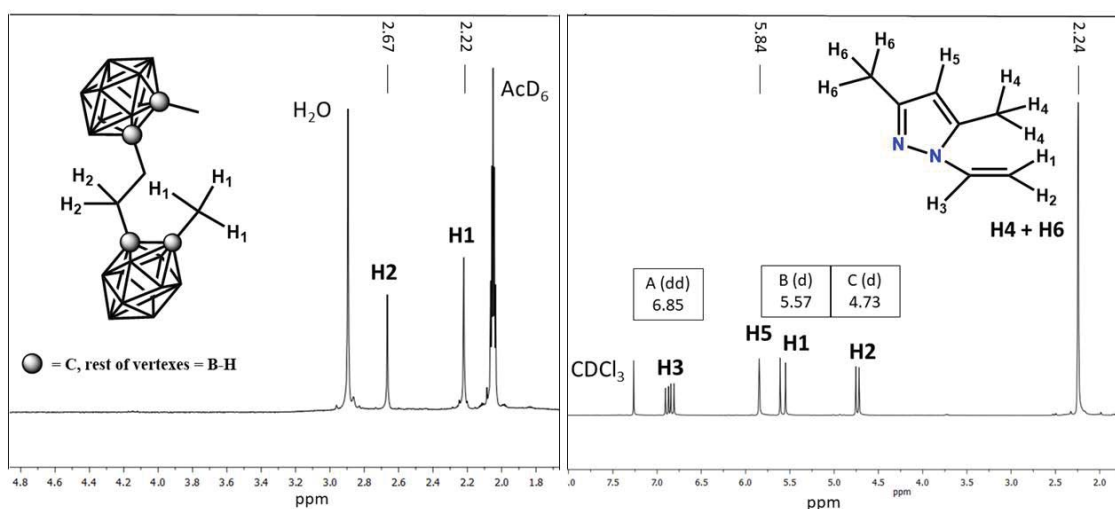


Figure 3.1.9 ^1H NMR spectra of **S1** (left, AcD_6 , 400.0 MHz) and **S2** (right, CDCl_3 , 400.0 MHz)

By-product **S1** crystallizes in an orthorhombic system and *Pbca* space group, each unit cell comprising four molecules, revealing that it consists of two carborane clusters linked by an alkylic chain (Fig. 3.1.10). Similar bis(carborane) compounds have been synthesized as precursors for the synthesis of carborane containing macrocycles^{21,22}, medicinal applications^{23,24} or as by-products of other reactions²⁵. In fact, the *o*-carborane analogue of **S1** has been known since the early 70s^{26,27} and synthesized in our group²⁸. Despite that, product **S1** has not been reported in the literature and is hereby described for the first time.

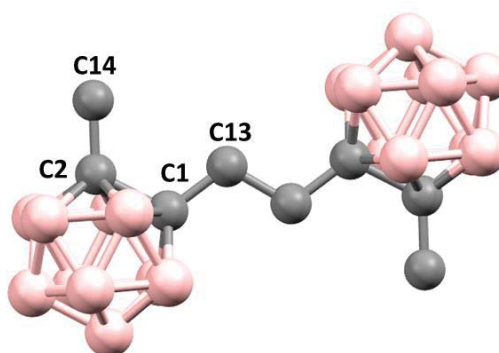


Figure 3.1.10 Compound **S1** showing relevant atoms and their numbering scheme. Colour code: grey (C), pink (B).

- Optimization of the synthesis of **L9**

In the light of these results, several attempts to optimize the yields of the desired **L9** ligand were carried out. First, it was assayed if the order of stepwise addition, that is, adding the electrophile over the nucleophile or the other way around had any effect. The order of the addition showed no obvious effect on the reaction products, therefore, for ease, the PzOTs was added onto the monolithiated carborane. Second, the nucleophilic substitution step of the reaction was tried out at different temperatures. Cooling of the reaction mixture (-78°C and -22°C) up to the quenching step resulted in very low yields. Using reflux conditions, on the other hand, did not improve the results significantly, as although a higher conversion of the reactants was achieved, it also increased the formation of **S1** significantly. Ruling out temperature as a decisive factor, several reactions with different carborane to PzOTs ratio were assayed. The results can be seen on Table 3.1.4.

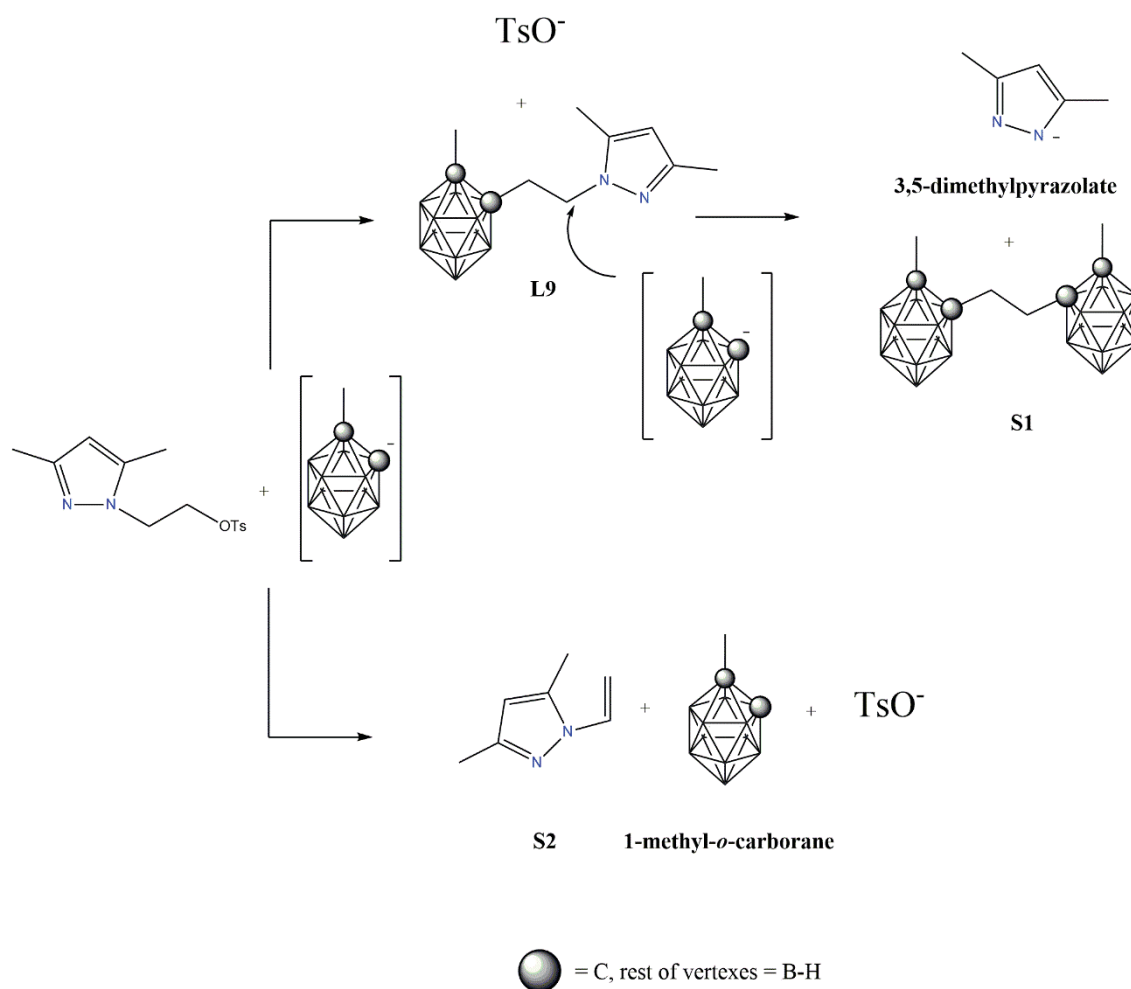
Table 3.1.4 Products percentage* vs. reactants ratio for the synthesis of **L9**

	PzOTs : 1-methyl- <i>o</i> -carborane ratio		
	1:1	1:1.5	1:2
L9	67.8 %	58.7 %	31.4 %
S1	19.8 %	31.8 %	59.7 %
S2	12.4 %	9.5 %	8.9 %

* Data taken from ^1H NMR spectra. Note that percentages indicate only % of obtained products with respect to themselves, not final yields.

The use of a 50 % excess 1-*m-o*-carborane leads to an increase in the quantity of **S1** obtained. However, it is worth taking into consideration that using this reaction ratio results in a higher conversion of the reactants, thus the overall yield for **L9** is somewhat higher. When this excess is increased up to 100 %, the formation of **S1** dominates. Meanwhile, the formation of **S2** seems to be independent of the reactants' ratio.

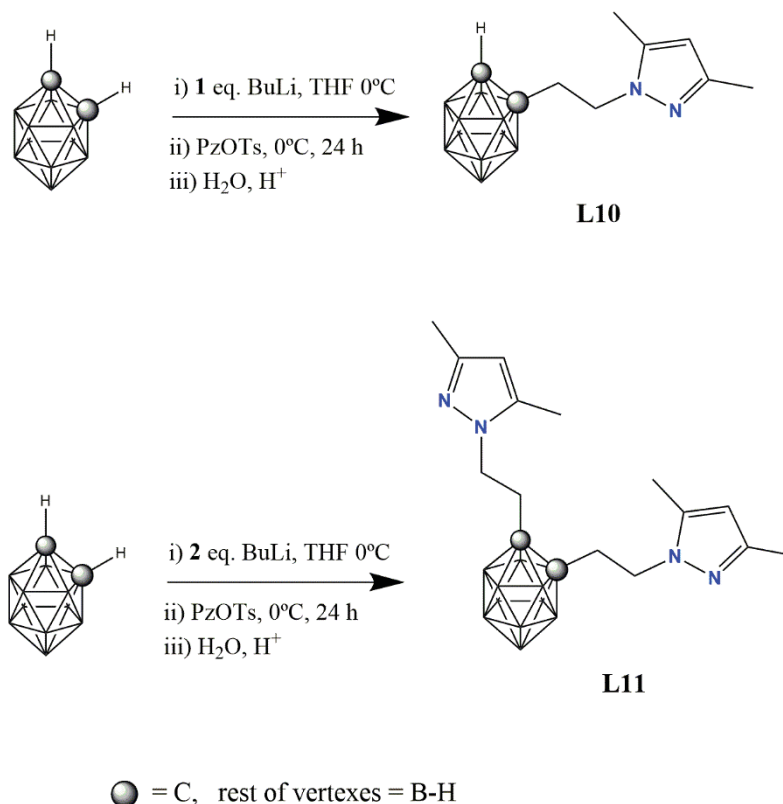
Based on this data, we tentatively propose that **S1** is the result of a nucleophilic substitution of the pyrazole moiety in **L9** by unreacted monolithiated 1-*m-o*-carborane (Scheme 3.1.6, top). Although not common, nucleophile substitutions over *N*-substituted pyrazole groups have been reported^{31–34}. On the other hand, for the formation of **S2** we propose an elimination process as a competitive reaction in the nucleophilic substitution of PzOTs (Scheme 3.1.6, bottom). In this case, the monolithiated 1-*m-o*-carborane could be acting as a base that promotes the elimination reaction.



Scheme 3.1.6 Possible reaction pathways for the formation of **S1** and **S2**

3.1.3.2 Synthesis and characterization of **L10** and **L11**

The knowledge gained in the synthesis of **L9** allowed us to proceed more confidently towards the synthesis of pyrazole mono and disubstituted carborane ligands employing unsubstituted *o*-carborane (Scheme 3.1.7).



Scheme 3.1.7 Synthetic scheme for the synthesis of **L10** and **L11**

First, our efforts were directed towards the monosubstitution, employing a similar synthetic strategy to that of the synthesis of **L9**, but using *o*-carborane as a starting reactant instead of 1-methyl-*o*-carborane. Based on the previously obtained results for **L9**, it was expected that the crude reaction mixture would contain **L10** and **S2**. Moreover, mixtures of **S1** type products possessing different numbers of carborane clusters linked by alkylic chains in polymeric or macrocyclic fashion were also expected. NMR analyses of crude reaction mixtures confirmed our suspicions, as all the expected products are identified, as well as the pyrazole-disubstituted carborane ligand (**L11**).

Therefore, we decided to proceed directly to the synthesis of the disubstituted pyrazole-carborane ligand. Thus, the same synthetic strategy as that of **L10** was employed, using an *o*-carborane to PzOTs ratio of 1:2. A similar mixture to that of the synthesis of **L10** was obtained (Table 3.1.5). In all cases, **S2** can be identified as the majoritarian product (~ 30 %), followed by **L11** (~ 25 %) and then by **L10** and **S1** (~ 10-15 % each). Thus, it can be inferred that the presence of more carboranyl nucleophiles leads to a stronger competition of the elimination reaction over PzOTs, although the substitution reaction is still dominating (sum of **L10**, **L11** and **S1** products yields is ~ 45-55 % respect to ~ 30 % for **S2**).

Table 3.1.5 Product yields* for the synthesis of **L11**

L10	L11	S1	S2
11.8 %	24.2 %	11.1 %	30.2 %
* Data taken from ¹ H NMR spectra			

The increased number of products leads to a more complex purification process. It has been found that it was possible to isolate either pure **L10** (eluent = AcOEt / Chloroform 1:4) or pure **L11** (eluent = AcOEt / Hexane 9:1), but not both products during the same column chromatography. Thus, isolation of the two products required a different purification process for each.

Ligands **L10** and **L11** have been fully characterized by EA, m.p., FTIR-ATR, ¹H, ¹¹B, ¹¹B{¹H} and ¹³C{¹H} NMR spectroscopies. Elemental Analyses of **L10** and **L11** agree with the NMR spectroscopies results.

- FTIR-ATR spectroscopy for **L10-11**

The FTIR-ATR spectra of **L10** and **L11**, much in the same manner to that of **L9**, display the characteristic bands of the pyrazole group such as [$\nu(\text{C}=\text{C}/\text{C}=\text{N})_{\text{ar}}$] (1557-1552 cm⁻¹), [$\delta(\text{C}=\text{C}/\text{C}=\text{N})_{\text{ip}}$] (1452-1416 cm⁻¹), [$\delta(\text{C}-\text{H})_{\text{ip}}$] (1025-1020 cm⁻¹) and [$\delta(\text{C}-\text{H})_{\text{oop}}$] (812-670 cm⁻¹), while [$\nu(\text{B}-\text{H})$] signals appear between 2571 and 2551 cm⁻¹¹⁹. A [$\nu(\text{B}-\text{B})$] vibration is also expected²⁰, but it is probably overlaid by [$\delta(\text{C}-\text{H})_{\text{oop}}$] signals. FTIR-ATR spectra of **L10** and **L11** can be found in Annex I (Fig. S3.1.12 and S3.1.13).

- NMR Spectroscopy for **L10-11**

The ^1H , ^{11}B , $^{11}\text{B}\{^1\text{H}\}$ and $^{13}\text{C}\{^1\text{H}\}$ NMR spectra of **L10** and **L11** were recorded in CD_3CN . Their ^1H NMR spectra are very similar to that of **L9**. Thus, the pyrazolic hydrogen signals ($\delta = 5.84$ and 5.78 ppm, respectively), the protons of the aliphatic chain ($\delta = 4.06$ and 2.75 ppm and 4.09 and 2.79 ppm, respectively) appearing once again as complex AA'-BB' type multiplets, and the signals attributable to the methyl groups (2.19 , 2.10 ppm and 2.21 ppm, respectively) are easily identified. There are, however, a few differences between the spectra of each ligand. For **L10** the signal corresponding to the hydrogen of the unsubstituted -CH vertex of the carborane ($\text{C}_{\text{Carb}}\text{-H}$) appears as a broad band at 4.43 ppm (Figure S3.1.14), whereas no such signal is observed in **L11** due to the disubstitution of the carbon atoms of the cluster (Figure S3.1.15).

In the ^{11}B NMR spectrum of **L10** three doublets are identified at -2.8 , -5.7 and -9.7 ppm, as well as a set of overlapping signals from -10.2 to -13.6 ppm, whereas for **L11** only one doublet at -4.07 ppm and a series of overlapping signals from -9.3 to -11.6 ppm are observed (both spectra can be found in Annex I, Figures S3.1.16 and S3.1.17). Thus, although for both compounds the signals for boron atoms 9 and 12 (those antipodal to carbon atoms) are identified, the signals corresponding to the rest of boron atoms appear in a crowded region of the spectra and are difficult to identify and integrate. As such, it is useful to perform $^{11}\text{B}\{^1\text{H}\}$ NMR experiments, which results in the obtention of simpler spectra. For the $^{11}\text{B}\{^1\text{H}\}$ NMR spectrum of **L10** a 1:1:2:6 pattern is obtained (Figure 3.1.11, left), which is a slight variation of the 1:1:8 expected pattern, confirming its asymmetric substitution. In contrast, for the $^{11}\text{B}\{^1\text{H}\}$ NMR spectrum of **L11** (Figure 3.1.11, right) a 2:8 pattern is observed, expected for symmetric *ortho*-substituted carboranes²⁰. Complete assignment of B-H signals was done by comparison with related carborane derivative ligands¹⁵.

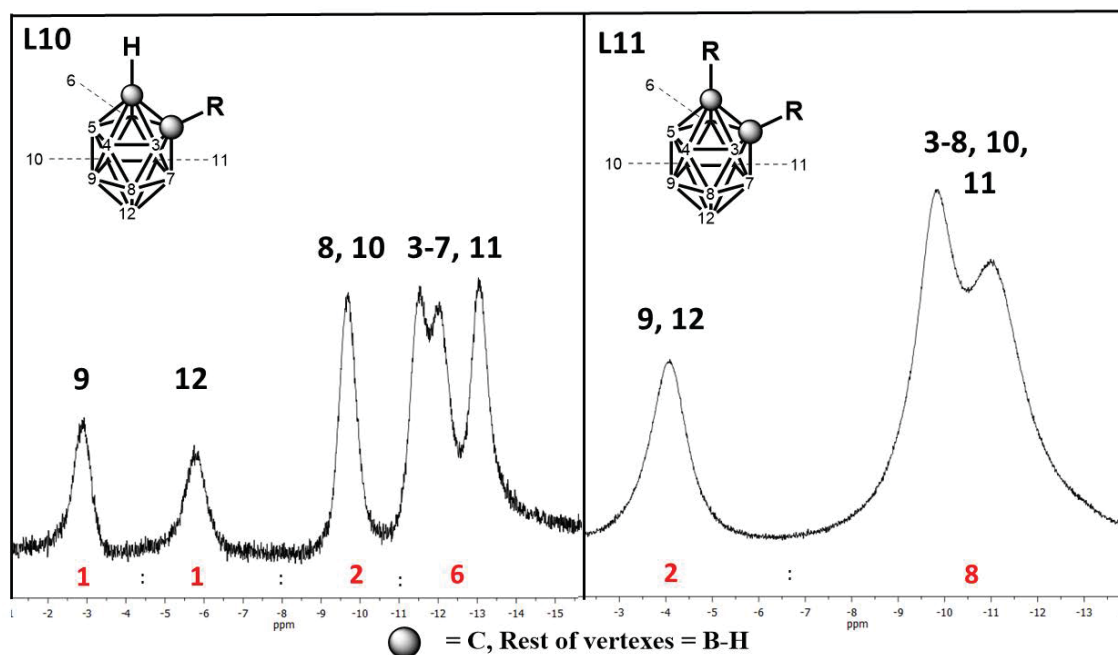


Figure 3.1.11 $^{11}\text{B}\{^1\text{H}\}$ NMR spectra for **L10** (left) and **L11** (right) ligands (CD_3CN , 128.6 MHz). Note the distinct resonance patterns which are indicative of the substitution of the carborane cage. R = $\text{CH}_2\text{-CH}_2\text{-3,5-dimethylpyrazole}$.

Regarding the $^{13}\text{C}\{^1\text{H}\}$ NMR spectrum of **L10** and **L11** (Figures S3.1.18 and S3.1.19), several signals are worth mentioning. Besides the similar resonances to those of **L9**, that is, those belonging to pyrazolyl ring ($\delta = 147.6$, 145.5 and 108.1 ppm for **L10**; 147.7, 139.3 and 106.0 ppm for **L11**), to the alkylic chain ($\delta = 47.3$ and 36.5 ppm for **L10**; 46.6 and 33.9 ppm for **L11**) and to the methyl groups ($\delta = 11.8$ and 11.2 ppm for **L10**; 12.5 and 10.0 ppm for **L11**) only a few other are worth mentioning. Thus, regarding the carbons of the carborane group, for **L10**, which is asymmetrically substituted, two signals appear, much like **L9**. However, contrary to **L9**, in **L10** their chemical shifts are different due to one carbon being bonded to a carbon atom and the other one to a hydrogen atom ($\delta = 73.0$ and 63.7 ppm). For **L11** only one signal appears, as expected ($\delta = 78.0$ ppm).

3.1.4 Summary and Conclusions

- ✓ A total of eleven ligands have been synthesized for this work, six of them (**L6-L11**) described for the first time in this PhD.
- ✓ Three new *N*-pyrazole, *O*-ether type ligands (**L6-L8**) have been successfully synthesized.
- ✓ A family of new *N*-substituted pyrazole carborane derivative ligands (**L9-L11**) has been successfully synthesized. However, the resulting yields are relatively low, as the reaction occurs among several competing processes. It has been possible to isolate and identify the resulting by-products of the formation reaction of **L9-L11**, allowing for the proposition of a mechanism explaining their formation.
- ✓ All new ligands have been characterized by Elemental Analyses, Melting point determinations, FTIR-ATR and NMR spectroscopies. Moreover, the crystal structures of **L9** and **S1** have been elucidated and their molecular and supramolecular structures discussed.

References

- 1 W. G. Haanstra, W. L. Driessen, J. Reedijk, U. Turpeinen and R. Hämäläinen, *J. Chem. Soc. Dalt. Trans.*, 1989, 2309–2314.
- 2 M. Guerrero Hernández, 2010. *Síntesis y caracterización de compuestos de coordinación con ligandos híbridos N,O-pirazol, Aplicaciones en Catálisis y síntesis de Nanopartículas* [Doctoral dissertation, Universitat Autònoma de Barcelona]. Retrieved from TDX.
- 3 A. Boixassa, J. Pons, X. Solans, M. Font-Bardia and J. Ros, *Inorg. Chem. Commun.*, 2003, **6**, 922–925.
- 4 M. Guerrero, J. Pons, J. Ros, M. Font-Bardia, O. Vallcorba, J. Rius, V. Branchadell and A. Merkoçi, *CrystEngComm*, 2011, **13**, 6457.
- 5 S. Muñoz, J. Pons, J. Ros, M. Font-Bardia, C. A. Kilner and M. A. Halcrow, *Inorganica Chim. Acta*, 2011, **373**, 211–218.
- 6 M. Guerrero, T. Calvet, M. Font-Bardia and J. Pons, *Polyhedron*, 2016, **119**, 555–562.
- 7 J. García-Antón, J. Pons, X. Solans, M. Font-Bardia and J. Ros, *Eur. J. Inorg. Chem.*, 2003, **2003**, 2992–3000.
- 8 S. Muñoz, M. Guerrero, J. Ros, T. Parella, M. Font-Bardia and J. Pons, *Cryst. Growth Des.*, 2012, **12**, 6234–6242.
- 9 M. Guerrero, J. Pons, V. Branchadell, T. Parella, X. Solans, M. Font-Bardia and J. Ros, *Inorg. Chem.*, 2008, **47**, 11084–11094.
- 10 M. Guerrero, J. Pons, V. Branchadell, T. Parella, X. Solans, M. Font-Bardia and J. Ros, *Inorg. Chem.*, 2008, **47**, 11084–11094.
- 11 M. Guerrero, J. García-Antón, M. Tristany, J. Pons, J. Ros, K. Philippot, P. Lecante and B. Chaudret, *Langmuir*, 2010, **26**, 15532–15540.
- 12 K. Nakamoto, *Handb. Vib. Spectrosc.*, 2006, 1872–1892.
- 13 V. Terrasson, Y. García, P. Farràs, F. Teixidor, C. Viñas, J. G. Planas, D. Prim, M. E. Light and M. B. Hursthouse, *CrystEngComm*, 2010, **12**, 4109–4123.

- 14 F. Di Salvo, B. Camargo, Y. García, F. Teixidor, C. Viñas, J. G. Planas, M. E. Light and M. B. Hursthouse, *CrystEngComm*, 2011, **13**, 5788.
- 15 M. Y. Tsang, S. Rodríguez-Hermida, K. C. Stylianou, F. Tan, D. Negi, F. Teixidor, C. Viñas, D. Choquesillo-Lazarte, C. Verdugo-Escamilla, M. Guerrero, J. Sort, J. Juanhuix, D. MasPOCH and J. G. Planas, *Cryst. Growth Des.*, 2017, **17**, 846–857.
- 16 A.-R. Popescu, A. D. Musteti, A. Ferrer-Ugalde, C. Viñas, R. Núñez and F. Teixidor, *Chem. - A Eur. J.*, 2012, **18**, 3174–3184.
- 17 J. García-Antón, J. Pons, X. Solans, M. Font-Bardia and J. Ros, *Eur. J. Inorg. Chem.*, 2003, **2003**, 3952–3957.
- 18 H. Ochi, T. Miyasaka and K. Arakawa, *Yakugaku Zasshi*, 1978, **98**, 165–171.
- 19 D. Seyferth, *J. Organomet. Chem.*, 1978, **156**, C47–C48.
- 20 M. Scholz and E. Hey-Hawkins, *Chem. Rev.*, 2011, **111**, 7035–7062.
- 21 I. T. Chizhevsky, S. E. Johnson, C. B. Knobler, F. A. Gomez and M. F. Hawthorne, *J. Am. Chem. Soc.*, 1993, **115**, 6981–6982.
- 22 M. J. Bayer, A. Herzog, M. Diaz, G. A. Harakas, H. Lee, C. B. Knobler and M. F. Hawthorne, *Chem. - A Eur. J.*, 2003, **9**, 2732–2744.
- 23 T. Totani, K. Aono, K. Yamamoto and K. Tawara, *J. Med. Chem.*, 1981, **24**, 1492–1499.
- 24 S. Raddatz, M. Marcello, H.-C. Kliem, H. Tröster, M. F. Trendelenburg, T. Oeser, C. Granzow and M. Wiessler, *ChemBioChem*, 2004, **5**, 474–482.
- 25 S. R. Wang and Z. Xie, *Organometallics*, 2012, **31**, 3316–3323.
- 26 L. I. Zakharkin and A. I. Kovredov, *Bull. Acad. Sci. USSR Div. Chem. Sci.*, 1973, **22**, 1396.
- 27 L. I. Zakharkin, V. N. Kalinin and V. V. Gedymin, *Bull. Acad. Sci. USSR Div. Chem. Sci.*, 1976, **25**, 1583–1584.
- 28 F. Teixidor, A. M. Romerosa, J. Rius, C. Miravittles, J. Casabó, C. Viñas and E. Sanchez, *J. Chem. Soc. Dalt. Trans.*, 1990, **75**, 525–529.

- 29 V. A. Kuznetsov, M. S. Lavlinskaya, I. V. Ostankova, G. V. Shatalov, K. S. Shikhaliev and E. A. Ryzhkova, *Polym. Bull.*, 2018, **75**, 1237–1251.
- 30 G. V. Shatalov, M. S. Lavlinskaya, O. A. Pakhomova, N. Y. Mokshina and V. A. Kuznetsov, *Russ. J. Appl. Chem.*, 2016, **89**, 140–146.
- 31 M. S. Bernatowicz, Y. Wu and G. R. Matsueda, *J. Org. Chem.*, 1992, **57**, 2497–2502.
- 32 N. I. Latosh, G. L. Rusinov, I. N. Ganebnykh and O. N. Chupakhin, *Russ. J. Org. Chem.*, 1999, **35**, 1363–1371.
- 33 M. Bakavoli, M. Pordel, M. Rahimizadeh and P. Jahandari, *J. Chem. Res.*, 2008, **2008**, 432–433.
- 34 G. F. Rudakov, Y. A. Moiseenko and N. Spesivtseva, *Chem. Heterocycl. Compd.*, 2017, **53**, 802–810.

3.2 Synthesis and characterization of Cu(II) coordination complexes bearing 3,5-disubstituted *N*-hydroxyethylpyrazole ligands

This chapter describes the reactivity of **HL1-HL3** ligands against different Cu(II) salts. All the resulting coordination compounds have been characterized by analytical and spectroscopic methods and their crystal structures have been elucidated. Next, the magnetic properties of four of the resulting compounds have been investigated and are discussed. Finally, a comparison between the obtained crystal structures and those found in the literature for similar ligands has allowed us to propose structural trends for *N*-hydroxyethyl pyrazole coordination compounds.

The last section provides a summary of the work, as well as the obtained conclusions.

Part of this work has been published in **Article 1**.

Article 1: “3,5-disubstituted-*N*-hydroxyalkylpyrazole Cu(II) compounds: Anion effect on dimensionality, supramolecular structure and magnetic properties”.

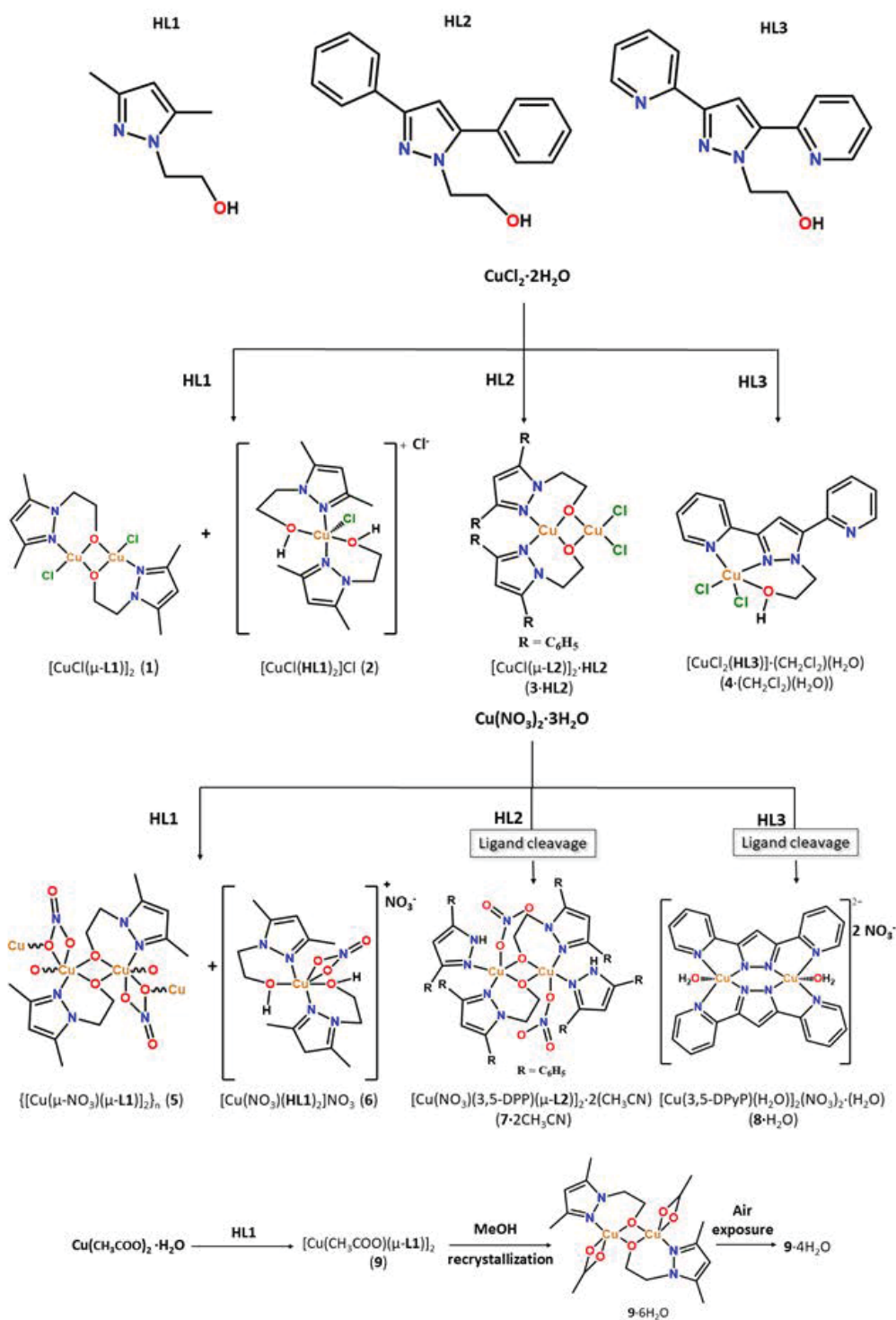
Joan Soldevila-Sanmartín, Xavier Montaner, Teresa Calvet, Mercè Font-Bardia, Josefina Pons.

Polyhedron 188 (2020) 114686

Our group has been interested in the synthesis of new *N*-hydroxyalkylpyrazole ligands for many years. As such, several new ligands have been developed and their reactivity against different metal salts, mainly Pd(II)^{1–6}, but also Pt(II)^{5,6} and Cu(II)⁷, were studied.

Among those studies, several of them were carried out using **HL1**, and its coordination compounds bearing Pd(II)^{8,9}, Pt(II)⁹, and, more recently, Zn(II), Cd(II) and Hg(II)^{10,11} as metal centers. On the other hand, reports of coordination compounds bearing **HL2** and **HL3** are much scarcer. In spite of **HL2** ligand being reported since 1998¹², the first coordination compounds were reported by our group in 2011, using Pd(II), Zn(II) and Cd(II)¹³ as metal centres. More recently, in 2016, the **HL3** ligand was developed in our group, and its reactivity against Pd(II), Pt(II), Cu(I), Ag(I) and Cu(II) was assayed¹⁴.

As a continuation of the ongoing research in the synthesis of new coordination compounds bearing *N*-hydroxyethylpyrazole ligands, the reactivity of **HL1**, **HL2** and **HL3** against different Cu(II) salts (CuCl₂·2H₂O, Cu(NO₃)₂·3H₂O or Cu(CH₃COO)₂·H₂O) was assayed, resulting in the isolation of: [CuCl(μ-**L1**)₂] (1), [CuCl(**HL1**)₂]Cl (2), [CuCl(μ-**L2**)₂]·**HL2** (3·**HL2**), [CuCl₂(**HL3**)]·(CH₂Cl₂)(H₂O) (4·(CH₂Cl₂)(H₂O)), {[Cu(μ-NO₃)(μ-**L1**)₂]_n} (5), [Cu(NO₃)(**HL1**)₂]NO₃ (6), [Cu(NO₃)(3,5-DPP)(μ-**L2**)₂]·2(CH₃CN) (3,5-DPP = 3,5-diphenylpyrazole) (7·2CH₃CN), [Cu(3,5-DPyP)(H₂O)]₂(NO₃)₂·(H₂O) (3,5-DPyP = 3,5-di(2-pyridyl)pyrazolate) (8·H₂O), [Cu(CH₃COO)(μ-**L1**)₂] (9) and its hydrated phases 9·4H₂O and 9·6H₂O (Scheme 3.2.1). Note that for compounds 7·2CH₃CN and 8·H₂O, the ligands suffer a N_{Pz}-CH₂CH₂OH bond cleavage, resulting in the presence of 3,5-DPP and 3,5-DPyP in the resulting compounds. All products have been fully characterized *via* spectroscopic and analytical methods, and their crystal structures have been fully elucidated, allowing for a detailed analysis of their molecular and supramolecular structures.



Scheme 3.2.1 Schematic representation of the synthetic procedure for the obtention of coordination compounds 1-9. Solvent occluded molecules for 3, 4 and 9 have been excluded for clarity. 3,5-DPP = 3,5-diphenylpyrazole, 3,5-DPyP = 3,5-di(2-pyridyl)pyrazolate.

3.2.1 Synthesis and Characterization

For the synthesis of compounds **1-9**, a methanolic solution of the corresponding Cu(II) salt ($\text{CuCl}_2 \cdot 2\text{H}_2\text{O}$, $\text{Cu}(\text{NO}_3)_2 \cdot 3\text{H}_2\text{O}$ or $(\text{Cu}(\text{CH}_3\text{COO})_2 \cdot \text{H}_2\text{O})$ was added dropwise to a methanolic solution of the corresponding ligand (**HL1-HL3**) in a 1:1 metal to ligand ratio (Scheme 3.2.1). The resulting solutions were stirred at room temperature (RT) for 48-96 hours, except for that of **HL1** with $\text{Cu}(\text{NO}_3)_2 \cdot 3\text{H}_2\text{O}$, which was kept for 12 hours under reflux conditions.

After that period, for compounds **3**·**HL2**, **7**· $2\text{CH}_3\text{CN}$ and **8**· H_2O (Scheme 3.2.1), the reaction mixtures were concentrated up to 5 mL and left overnight in the fridge until green precipitates were obtained (yields 27.9 %, 89.6 % and 71.9 %, respectively). For compounds **4**· $(\text{CH}_2\text{Cl}_2)(\text{H}_2\text{O})$ and **9** (Scheme 3.2.1), a green (**4**· $(\text{CH}_2\text{Cl}_2)(\text{H}_2\text{O})$, yield 72.2 %) or blue (**9**, yield 44.7 %) precipitate appeared immediately. Note that for the reaction of **9**, it was found that the addition of a small amount of ammonia was required to obtain a product. Otherwise, upon concentration, unreacted $\text{Cu}(\text{CH}_3\text{COO})_2 \cdot \text{H}_2\text{O}$ precipitated. Lastly, reactions between **HL1** and $\text{CuCl}_2 \cdot 2\text{H}_2\text{O}$ (**1** and **2**) or $\text{Cu}(\text{NO}_3)_2 \cdot 3\text{H}_2\text{O}$ (**5** and **6**, Scheme 3.2.1), showed a distinct behaviour. In both cases, a blue precipitate was obtained immediately (**1** and **5**, yields 7.4 % and 71.4 %, respectively) the remaining mother liquors were concentrated until a dark green oil was obtained, which after treatment with Et_2O resulted in the formation of a green precipitate (**2** and **6** yields 76.8 % and 4.2 %, respectively). All precipitates were filtered off, washed with cold Et_2O and dried under vacuum.

Crystals suitable for X-ray diffraction for compounds **1-9** were obtained *via* recrystallization in an acetone/hexane mixture for **1**, in MeOH for **3**·**HL3**, **6** and **9**, in CH_2Cl_2 for **4**· $(\text{CH}_2\text{Cl}_2)(\text{H}_2\text{O})$, in CH_3CN for **5** and **7**· $2\text{CH}_3\text{CN}$, in a $\text{CH}_3\text{CN}:\text{CHCl}_3$ mixture (3:1 ratio) for **8**· H_2O and *via* diffusion of hexane into a CHCl_3 solution for **2**. For the compounds containing chloride moieties, the elucidation of their crystal structures revealed them as $[\text{CuCl}(\mu\text{-L1})]_2$ (**1**), $[\text{CuCl}(\text{HL1})_2]\text{Cl}$ (**2**), $[\text{CuCl}(\mu\text{-L2})]_2 \cdot \text{HL2}$ (**3**·**HL2**) and $[\text{CuCl}_2(\text{HL3})] \cdot (\text{CH}_2\text{Cl}_2)(\text{H}_2\text{O})$ (**4**· $(\text{CH}_2\text{Cl}_2)(\text{H}_2\text{O})$).

For compounds **5**· H_2O , containing nitrate ligands, SCXRD revealed them as $\{[\text{Cu}(\mu\text{-NO}_3)(\mu\text{-L1})]_2\}_n$ for **5** and $[\text{Cu}(\text{NO}_3)(\text{HL1})_2]\text{NO}_3$ for **6**. For compounds **7**· $2\text{CH}_3\text{CN}$ and **8**· H_2O , on the other hand, the results were rather unexpected. Their crystal structures were revealed as $[\text{Cu}(\text{NO}_3)(3,5\text{-DPP})(\mu\text{-L2})]_2 \cdot 2(\text{CH}_3\text{CN})$ (3,5-DPP = 3,5-

diphenylpyrazole) ($7 \cdot 2\text{CH}_3\text{CN}$) and $[\text{Cu}(3,5\text{-DPyP})(\text{H}_2\text{O})]_2(\text{NO}_3)_2$ (3,5-DPyP = 3,5-di(2-pyridyl)pyrazolate) ($8 \cdot \text{H}_2\text{O}$). Thus, during their synthesis, an unexpected cleavage of the $\text{N}_{\text{Pz}}\text{-C}$ bond happens, resulting in the formation of the pyrazole/pyrazolate ligands without substituent in position 1-. This behaviour is in stark contrast for that of the same ligands in their reaction with Cu(II) chloride, as for the resulting compounds ($3 \cdot \text{HL2}$ and $4 \cdot (\text{CH}_2\text{Cl}_2)(\text{H}_2\text{O})$) the ligands are intact. It is also remarkable that the **HL1** ligand also remains intact in its reaction with Cu(II) nitrate (compounds **5** and **6**). The cleavage of 1-hydroxymethyl pyrazole ligands has been observed in our group, but this is the first time that we report this behaviour for 2-hydroxyethyl ligands^{9,15}. In a report by Baruah *et al.*¹⁶, a similar behaviour was observed for *N*-benzoyl-3,5-dimethylpyrazole and *N*-benzoylimidizaole, which upon reaction with $\text{Cu}(\text{NO}_3) \cdot 3\text{H}_2\text{O}$ cleaved along the $\text{N}_{\text{Pz}}\text{-C}$ bond. This reaction is enhanced in acidic conditions. A similar process could take place in our case.

Lastly, for the reaction of **HL1** with Cu(II) acetate, the crystal structure elucidation for **9** revealed that occluded water molecules were present in the single crystal, thus possessing a $[\text{Cu}(\text{CH}_3\text{COO})(\mu\text{-L1})]_2 \cdot 6\text{H}_2\text{O}$ ($9 \cdot 6\text{H}_2\text{O}$) formulae. However, this crystal structure was not in agreement with the FTIR-ATR spectral data of the bulk powder, which possessed no water molecules in its structure (*vide infra*, Scheme 3.2.1).

The compounds were characterized *via* elemental analyses (EA), conductivity measurements, FTIR-ATR and UV-Vis spectroscopies. Whenever possible, single crystals were used for characterization measurements.

- Elemental analyses (EA)

For $1 \cdot 3 \cdot \text{HL2}$ and $5 \cdot 8 \cdot \text{H}_2\text{O}$ its EA agree with the proposed formulae. Other compounds showed discrepancies owing to the loss of occluded solvent molecules in their structure. For instance, in compound for $4 \cdot (\text{CH}_2\text{Cl}_2)(\text{H}_2\text{O})$ its EA shows that its occluded CH_2Cl_2 molecules are unavoidably lost during sample preparation, and thus the results have been adjusted to a $4 \cdot (\text{H}_2\text{O})$ molecular formulae, even for single-crystal samples. For compound **9**, both a sample of the bulk powder and a sample of the solid recrystallized in MeOH were used for the EA, hoping to identify both **9** and $9 \cdot 6\text{H}_2\text{O}$. However, the preparation of the latter for EA unavoidably leads to the loss of two occluded solvent molecules. Thus, the results were adjusted considering a $9 \cdot 4\text{H}_2\text{O}$ molecular relation.

- Conductivity

Conductivity values were registered in MeOH (**1-5**, **6** and **9**), in DMF (**5**, owing to its insolubility) or CH₃CN (**7**·2CH₃CN and **8**·H₂O) in concentrations around $1 \cdot 10^{-3}$ M. The results agree with the presence of a non-electrolyte for **1**, **3**·**HL2**, **4**·H₂O, **9** (MeOH, $14\text{--}57 \text{ } \Omega^{-1}\text{cm}^2\text{mol}^{-1}$), **5** (DMF, $28 \text{ } \Omega^{-1}\text{cm}^2\text{mol}^{-1}$) and **7**·2CH₃CN (CH₃CN, $44 \text{ } \Omega^{-1}\text{cm}^2\text{mol}^{-1}$), a 1:1 electrolyte for **2** and **6** (MeOH, $94\text{--}111 \text{ } \Omega^{-1}\text{cm}^2\text{mol}^{-1}$) and a 1:2 electrolyte for **8**·H₂O (CH₃CN, $219 \text{ } \Omega^{-1}\text{cm}^2\text{mol}^{-1}$)¹⁷.

- FTIR-ATR Spectroscopy

Regarding their FTIR-ATR spectra, for **1-9** the most characteristic bands are those attributable to the pyrazole groups of the ligands: $[\nu(\text{C}=\text{C}/\text{C}=\text{N})_{\text{ar}}]$ ($1585\text{--}1547 \text{ cm}^{-1}$), $[\delta(\text{C}=\text{C}/\text{C}=\text{N})_{\text{ar}}]$ ($1464\text{--}1389 \text{ cm}^{-1}$), $[\delta(\text{C}-\text{H})_{\text{ip}}]$ ($1073\text{--}1003 \text{ cm}^{-1}$) and $[\delta(\text{C}-\text{H})_{\text{oop}}]$ ($895\text{--}628 \text{ cm}^{-1}$)¹⁸. For compound **3**·**HL2**, since both a deprotonated coordinated and a protonated non-coordinated ligand (**HL2**) are present in the molecule, multiple bands can be identified in these regions. For compounds bearing **HL3** (**4**·H₂O and **8**·H₂O), many of the characteristic signals attributed to the pyrazolyl moiety are also present pyridine rings such as $[\nu(\text{C}=\text{C}/\text{C}=\text{N})_{\text{ar}}]$ ($1613\text{--}1567 \text{ cm}^{-1}$), $[\delta(\text{C}=\text{C}/\text{C}=\text{N})_{\text{ar}}]$ ($1461\text{--}1438 \text{ cm}^{-1}$), $[\delta(\text{C}-\text{H})_{\text{ip}}]$ ($1086\text{--}1043 \text{ cm}^{-1}$) and $[\delta(\text{C}-\text{H})_{\text{oop}}]$ ($781\text{--}679 \text{ cm}^{-1}$)¹⁸. As an example, FTIR-ATR spectrum of **4**·H₂O is shown (Figure 3.2.1), while those of **1-3**·**HL2** and **5-9** can be found in Annex I (Figure S3.2.1-S3.2.8).

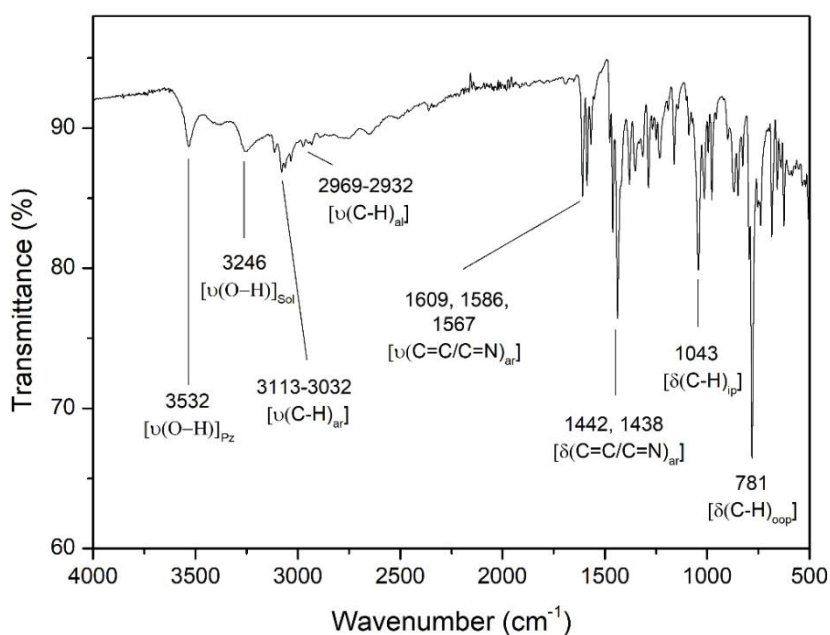


Figure 3.2.1 FTIR-ATR Spectrum of **4**·H₂O

The region between 3600-3100 cm^{-1} is also relevant for the characterization of these compounds, since it hosts signals attributed to $[\nu(\text{O-H})]^{18}$. For compounds **1** and **5**, no signals appear in this region, suggesting the deprotonation of the **HL** ligands and the lack of occluded solvent molecules. For compound **7**·2CH₃CN, a small band is observed at 3122 cm^{-1} , but owing to its shape and neighbouring flat region is attributed to $[\nu(\text{N-H})]^{18}$. For compounds **2**·4·H₂O and **8**·H₂O however, broad signals can be observed in this region. In them, broad bands centred at 3532-3121 cm^{-1} are identified, attributed to the alcohol moieties of **HL** ligands or occluded solvents. For compound **4**·H₂O, this region is specially remarkable, as two distinct $[\nu(\text{O-H})]^{18}$ signals are identified, one corresponding to coordinated **HL3** at 3532 cm^{-1} and one corresponding to occluded water molecules at 3246 cm^{-1} . For compound **9**, this region also merits a little discussion. We were able to measure crystals of compound **9**·6H₂O (Figure 3.2.2 and S3.2.8), and three overlapping bands (3473 cm^{-1} , 3368 cm^{-1} and 3269 cm^{-1}) attributed to $[\nu(\text{O-H})]^{18}$ are identified. This suggests the presence of different types of occluded water molecules, which is consistent with its crystal structure. On the other hand, the FTIR-ATR spectra of the bulk powder of **9** shows no signals in the region between 3600-3000 cm^{-1} , suggesting that no water molecules are present (Figure 3.2.2).

These discrepancies were further investigated using PXRD analyses (Figure 3.2.2). The resulting patterns confirmed that upon removal from the crystallization solvent, compound **9**·6H₂O readily lost two water molecules, as it was not possible to obtain any matching PXRD pattern with that calculated from the crystal structure. However, this loss does not cause the collapse of the crystal structure, as seen by the crystalline PXRD pattern of **9**·4H₂O. Thus, upon loss of those waters, the crystal structure is rearranged. Lastly, the PXRD pattern of the “dry” phase (**9**) was also measured. Surprisingly, it matches the one of the “4-hydrated” phase, suggesting the preservation of the crystal structure between the two phases (Figure 3.2.2).

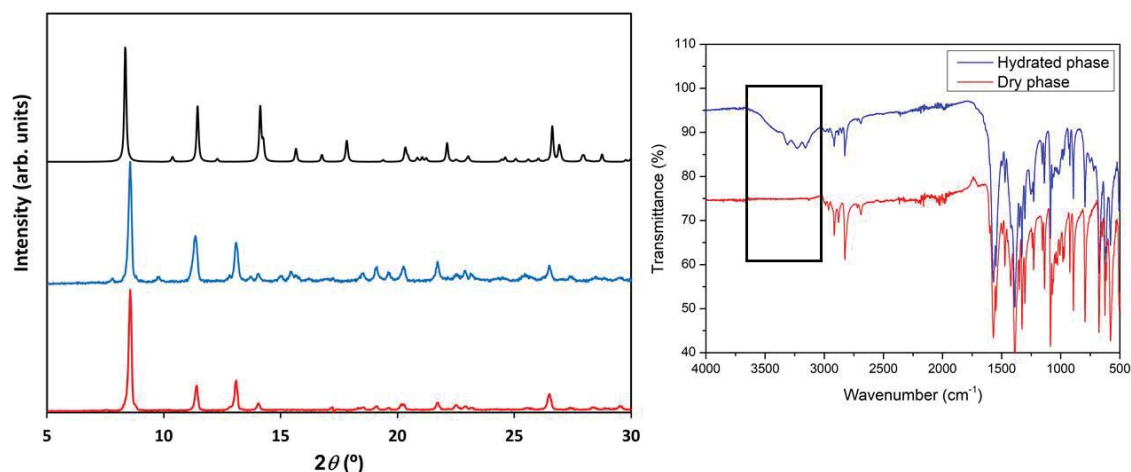
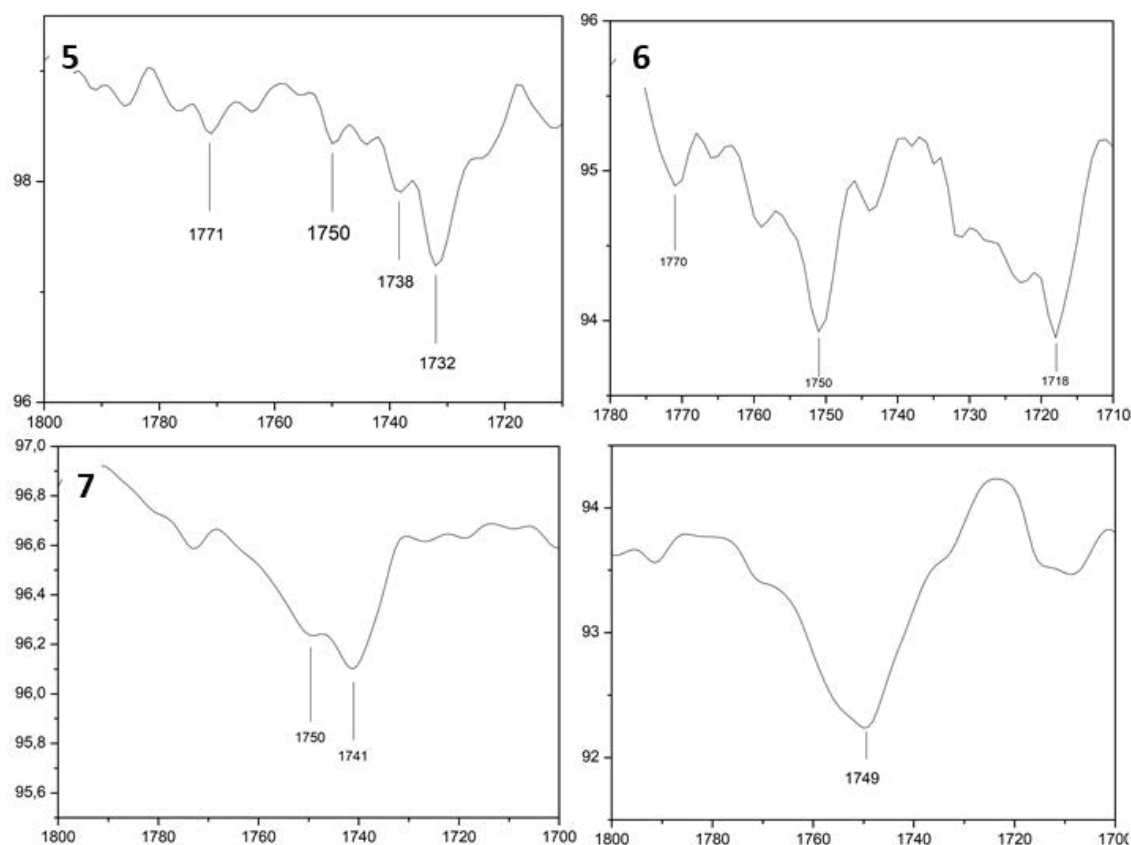


Figure 3.2.2 PXRD patterns for $9 \cdot 4\text{H}_2\text{O}$ (blue) and dry **9** (red). Calculated PXRD pattern from resolved crystal structure ($9 \cdot 6\text{H}_2\text{O}$) is also included (top) as a reference, from monocrystal measured at 150 K (left). FTIR-ATR spectra of $9 \cdot 6\text{H}_2\text{O}$ (blue) and dry **9** (red), pinpointing the $[\nu(\text{O-H})]$ signal region (right).

For compounds $5\text{-}8 \cdot \text{H}_2\text{O}$, signals attributed to $[\nu(\text{NO}_3)]^{18}$ appear at $1453\text{-}1389\text{ cm}^{-1}$ and $1300\text{-}1268\text{ cm}^{-1}$. Regarding those same groups, the region between $1800\text{-}1700\text{ cm}^{-1}$ hosts signals attributed to $\nu_1 + \nu_4$ vibrations¹⁹, which are distinctive of their coordination behaviour. In compounds **5** the region is crowded, although two signals are identified at 1771 and 1750 cm^{-1} , as well as a double overlapping band at 1738 and 1732 cm^{-1} (Figure 3.2.3). This particular pattern agrees with the simultaneous presence of bidentate and monodentate coordination modes in the same nitrate ligand¹⁹. For **6**, three bands are identified. The most intense one at 1750 cm^{-1} is characteristic of ionic nitrates, whereas the other two bands at 1770 and 1712 cm^{-1} suggest a bidentate coordination behaviour¹⁹ (Figure 3.2.3). For compound $7 \cdot 2\text{CH}_3\text{CN}$, two signals at 1750 and 1741 cm^{-1} are identified, which agrees with a monodentate coordination mode. Lastly, for $8 \cdot \text{H}_2\text{O}$, only one band at 1749 cm^{-1} is observed, indicative of the presence of ionic nitrates¹⁹. FTIR-ATR spectra of compounds $5\text{-}8 \cdot \text{H}_2\text{O}$ can be found in Annex I (Figures S3.2.4-S3.2.7).

Finally, for compound $9 \cdot 6\text{H}_2\text{O}$, characteristic $[\nu_{\text{as}}(\text{COO})]$ (1547 cm^{-1}) and $[\nu_{\text{s}}(\text{COO})]$ (1417 cm^{-1}) signals are identified (Figure S3.2.8). The difference between these bands ($\Delta = [\nu_{\text{as}}(\text{COO})] - [\nu_{\text{s}}(\text{COO})] = 130\text{ cm}^{-1}$) suggests a bidentate chelate coordination mode^{18,20}, which is in agreement with the elucidated crystal structure.



Coordination modes (from Crystal structure)

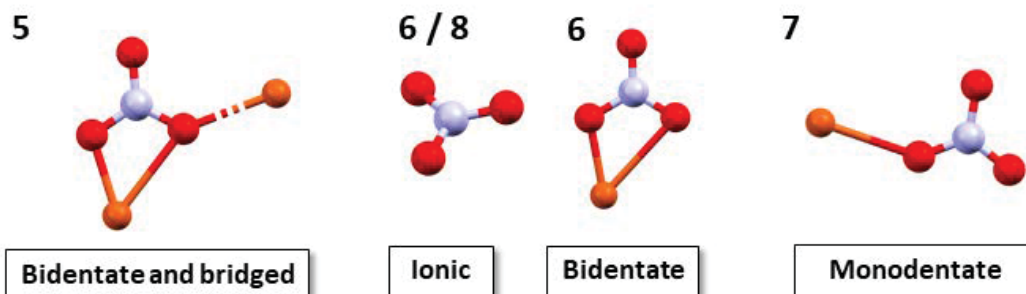


Figure 3.2.3 Detail of the Lever bands in the FTIR-ATR spectrum of compounds **5-8**·H₂O (x axis = wavenumber (cm⁻¹), y axis = transmittance (%)). Coordination modes of the nitrate ligand in compounds **5** and **6**. Colour code: red (O), orange (Cu), light blue (N).

• UV-Vis Spectroscopy

Finally, the UV-Vis spectra have been recorded in MeOH for **1-4**·H₂O, **6** and **9**, in DMF for **5** and in CH₃CN for **7**·2CH₃CN and **8**·H₂O ($\approx 1 \cdot 10^{-3}$ M) (Figure S3.2.9-S3.2.11). For compounds **1**, **3**·HL**2**, **4**·H₂O and **5-9**, their spectra show one band in the visible region between 670 and 769 nm. All ϵ values range between 52 to 154 M⁻¹cm⁻¹. These bands are typical of Cu(II) metal centers in square planar or square pyramidal

coordination geometries, and are assigned to a ${}^2B_{1g}$ to ${}^2A_{1g}$ transition^{21–23}. For compound **2**, on the other hand, the spectrum shows one band at 840 nm and $\epsilon = 46 \text{ M}^{-1}\text{cm}^{-1}$. These absorption bands at higher wavelengths suggest a heavily distorted square pyramidal stereochemistry or even a trigonal bipyramidal one, and thus can be attributed to a ${}^2A_{1g}$ to 2E_g transition^{22,24}. All ϵ values are consistent with Laporte-forbidden transitions²². This spectral data agrees with the elucidated crystal structures (*vide infra*).

- TGA-ATD determination for compounds **9** and **9·4H₂O**

The findings related to occluded water molecules in **9**, **9·6H₂O** and **9·4H₂O** prompted our interest for their desorption processes. Therefore, simultaneous TGA-DTA determinations were carried out to evaluate the thermal stability of the two available phases **9** and **9·4H₂O**. The “dry” phase shows no thermal events except for its thermal decomposition, starting at 167°C and ending at 450°C (Figure S3.2.12). The “hydrated” phase, however, shows the loss of water in a two-step process. The first one occurs between 38°C and 121°C, resulting in the loss of one water molecule, while the second one occurs between 121°C and 189°C, resulting in the loss of the remaining water molecules. From this temperature, a decomposition process is undertaken, ending at 450°C (Figure 3.2.4).

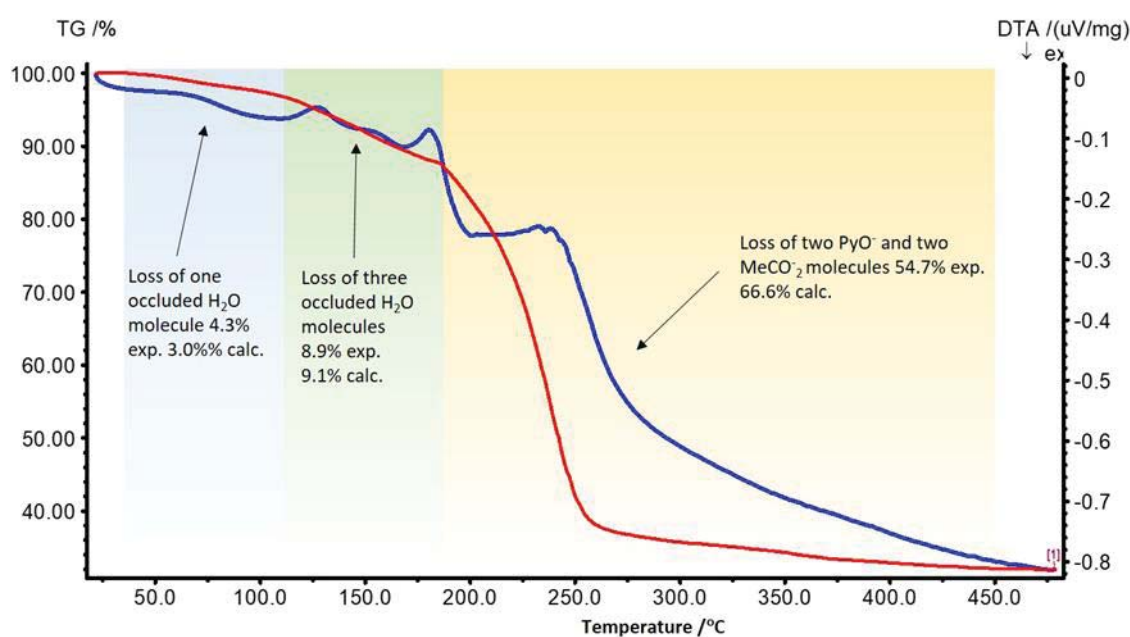


Figure 3.2.4 TGA/DTA Analysis of compound **9·4H₂O** (bulk)

3.2.2 Crystal and Extended structures

For compounds **1-9**·6H₂O four different types of structures were obtained: ionic (**2**, **6** and **8**·H₂O), monomeric (**4**·(CH₂Cl₂)(H₂O)), dimeric (**1**, **3**·**HL2**, **7**·2CH₃CN and **9**·6H₂O) and polymeric (**5**). As several characteristics of each type of structure are shared, they will be described together.

- *Ionic compounds 2, 6 and 8*·H₂O

Compounds **2** and **6** possess a monomeric cation and an either a chlorine or a nitrate anion. The cation possesses a Cu:**HL1**:X (X = Cl[−] (**2**) or NO₃[−] (**6**)) 1:2:1 ratio (Figure 3.2.5). However, they adopt different *cores*: a heavily distorted square pyramidal ($\tau_5 = 0.40^{25}$) [CuO₂N₂Cl] for **2**, or distorted octahedral ($\tau_6 = 47.28^{26,27}$) [CuO₄N₂] for **6**. This different *core* coordination geometry stems from the chelating behaviour of the nitrate moiety. The apical position of compound's **2** *core* is occupied by one oxygen atom of one **HL1** ligand, while for **6** it involves an oxygen atom from the nitrate moiety as well as the oxygen atom from the **HL1** ligand. The rest of the atoms occupy the basal positions.

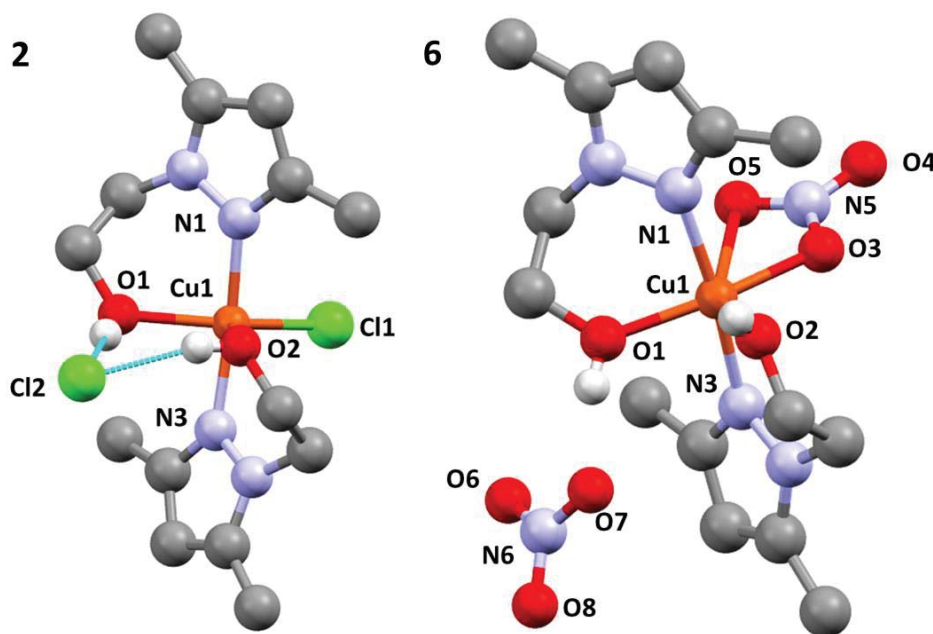


Figure 3.2.5 Ionic monomeric compounds **2** (left) and **6** (right), showing relevant atoms and numbering scheme. Colour code: grey (C), white (H), light blue (N), red (O), light green (Cl), orange (Cu).

In both compounds, **HL1** acts as a bidentate chelate ligand with a boat conformation, bite angles ranging between $85.61(4)^\circ$ to $90.83(6)^\circ$. The spatial constraints induced by this chelating coordination can be clearly seen in their heavily distorted *cores* for both compounds. As such, **2** displays basal angles ranging from $86.88(4)^\circ$ to $93.18(4)^\circ$ and from $149.12(3)^\circ$ to $173.20(5)^\circ$ (instead of 90° and 180° for a regular square pyramid), whereas for **6**, basal angles range from $52.75(5)^\circ$ to $114.21(5)^\circ$ and from $166.58(7)^\circ$ to $173.12(7)^\circ$ (instead of 90° and 180° for a regular octahedra) and apical angles range from $78.05(6)^\circ$ to $100.27(6)^\circ$ and $149.18(5)^\circ$ (instead of regular 90° and 180°). The chelate coordination of the nitrate moiety in **6** also contributes to this deviation of the ideal. It is worth remarking that these chelate behaviour could be considered weak, as the Cu(1)-O(3) / Cu(1)-O(5) distances ($2.0102(13) \text{ \AA}$ / $2.700(2) \text{ \AA}$, $d_1-d_2 = 0.69 \text{ \AA}$) and Cu(1)-O(3)-N(5) / Cu(1)-O(5)-N(5) angles ($109.90(10)^\circ$ / $78.54(10)^\circ$, $\theta_1-\theta_2 = 31.36^\circ$) are on the verge of the anisobidentate ($d_1-d_2 < 0.6 \text{ \AA}$, $\theta_1-\theta_2 < 28^\circ$) and unidentate ($d_1-d_2 > 0.6 \text{ \AA}$, $\theta_1-\theta_2 > 28^\circ$) coordination modes²⁸. Selected bond lengths and angles are reported in Table 3.2.2. They are in agreement with related Cu(II) pyrazole compounds^{29–32}, as well as with the Co(II) analogue of **6**³³.

As mentioned before, during the synthesis of compound **8**, ligand **HL3** is cleaved, resulting in the obtention of an ionic compound bearing a dimeric cation and two nitrate ions. Moreover, three water molecules are also present in its crystal structure, as each of the two Cu(II) metal centres is coordinated to one and a further water molecule is occluded in its crystal structure. Thus, the cation possesses a Cu:**3,5-DPyP**:H₂O 1:1:1 ratio (Figure 3.2.6). Its Cu(II) atoms display an almost perfect square pyramidal ($\tau_5 = 3 \cdot 10^{-3}$)²⁵ [Cu₂N₄O] *core*, with the nitrogen atoms of the pyrazolate ligands forming the basal plane and the oxygen atom of the water molecules in the apical position. It is also worth noting that is deprotonated, thus acting as a pyrazolate ligand. Pyrazolate ligands with no substituents in positions 3- and 5- are known to coordinate by both of their nitrogen groups, forming trimeric or polymeric structures^{34,35}. However, the addition of bulky substituents on these positions prevents the formation of these motifs due to steric constraints, resulting in the formation of dimers, as reported in different publications by our group^{36–40} and others^{41–44}. In fact, the dihydrate analogue of **8**·H₂O (**8**·2H₂O)⁴⁵ has already been synthesized in our group. Moreover, the presence of a coordinating nitrogen atom in the position 2- of the pyridine substituent promotes a chelate behaviour of the ligand, which can result in the formation of monomers in asymmetrically substituted

pyrazoles^{46–50}. Thus, based on these precedents, the chelating and bridging behaviour of the **3,5-DPyP** ligand is clearly rationalized. Relevant bond lengths and angles for compound **8**·H₂O are summarized in Table 3.2.3. They are in agreement with similar compounds reported in the literature^{42–45}.

Table 3.2.2 Selected bond lengths (Å) and angles (°) for compounds **2** and **6**

2		6	
Bond lengths (Å)			
Cu(1)-N(3)	1.9636(12)	Cu(1)-N(3)	1.9801(17)
Cu(1)-N(1)	1.9675(12)	Cu(1)-N(1)	1.9712(15)
Cu(1)-O(2)	2.0760(10)	Cu(1)-O(2)	2.1685(15)
Cu(1)-Cl(1)	2.2584(4)	Cu(1)-O(1)	1.9944(13)
Cu(1)-O(1)	2.2962(10)	Cu(1)-O(3)	2.0102(13)
		Cu(1)-O(5)	2.700(2)
Bond angles (°)			
N(3)-Cu(1)-N(1)	173.20(5)	N(1)-Cu(1)-N(3)	173.12(7)
N(3)-Cu(1)-O(2)	88.57(4)	N(1)-Cu(1)-O(1)	88.06(6)
N(1)-Cu(1)-O(2)	86.88(4)	N(3)-Cu(1)-O(1)	86.57(6)
N(3)-Cu(1)-Cl(1)	93.32(3)	N(1)-Cu(1)-O(3)	91.59(6)
O(2)-Cu(1)-Cl(1)	149.12(3)	N(3)-Cu(1)-O(3)	92.64(6)
N(3)-Cu(1)-O(1)	89.27(4)	N(3)-Cu(1)-O(5)	100.27(6)
N(1)-Cu(1)-O(1)	85.60(4)	O(2)-Cu(1)-O(5)	149.18(5)
O(2)-Cu(1)-O(1)	89.08(4)	O(5)-Cu(1)-O(3)	52.75(5)
Cl(1)-Cu(1)-O(1)	121.74(3)	O(1)-Cu(1)-O(3)	166.58(7)
N(1)-Cu(1)-Cl(1)	93.18(4)	N(1)-Cu(1)-O(2)	93.91(6)
		N(3)-Cu(1)-O(2)	90.83(6)
		O(1)-Cu(1)-O(2)	94.94(6)
		O(1)-Cu(1)-O(3)	98.46(6)
		N(1)-Cu(1)-O(5)	78.05(6)
		O(1)-Cu(1)-O(5)	114.21(5)

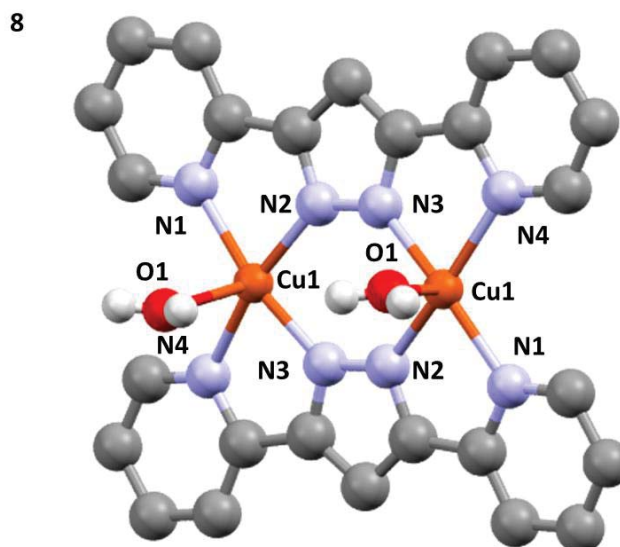


Figure 3.2.6 Dimeric cation of compound **8**·H₂O, showing relevant atoms and numbering scheme. Colour code: grey (C), white (H), light blue (N), red (O), orange (Cu).

Table 3.2.3 Selected bond lengths (Å) and angles (°) for **8**·H₂O

8 ·H ₂ O			
Bond lengths (Å)			
Cu(1)-N(3)	1.955(4)	Cu(1)-N(4)	2.097(5)
Cu(1)-N(2)	1.960(5)	Cu(1)-O(1)	2.207(4)
Cu(1)-N(1)	2.077(5)	Cu(1)···Cu(1)	4.0448(9)
Bond angles (°)			
N(3)-Cu(1)-N(2)	91.43(17)	N(2)-Cu(1)-N(1)	79.81(18)
N(3)-Cu(1)-N(1)	168.8(2)	N(3)-Cu(1)-N(4)	79.70(18)
N(2)-Cu(1)-N(4)	166.74(18)	N(1)-Cu(1)-N(4)	107.63(19)
N(3)-Cu(1)-O(1)	96.43(17)	N(2)-Cu(1)-O(1)	104.99(19)
N(1)-Cu(1)-O(1)	92.55(19)	N(4)-Cu(1)-O(1)	85.93(19)

The supramolecular structure of **2** is dominated by the presence of hydrogen bonds between the anionic chlorine atoms and both protonated alcohol groups and the hydrogen in position 4- of the of the pyrazole ligands. This interaction results in the formation of zig-zag chains along the *c* axis. Moreover, these chains are linked *via* a supramolecular interaction involving the coordinated chlorine atoms and the methyl groups of the pyrazole moieties, resulting in the formation of supramolecular 2D planes along the *bc* plane (Figure 3.2.7, left). For compound **6**, a double interaction between nitrate moieties and protonated alcohol groups results in a zig-zag chain along the *c* axis (Figure 3.2.7,

right). Owing to the presence of some disorder in nitrate anions and occluded water molecules in compound **8**·H₂O, its supramolecular scaffold cannot be studied precisely. However, it is clearly dominated by the formation of strong classical O-H···O hydrogen bonds between both types of water molecules (occluded and coordinated) and nitrate anions. Thus, the overall supramolecular packing could be described as alternating layers of nitrate anions and dimeric cations, with the occluded water molecules embedded in the cationic layer. (Figure 3.2.8). Moreover, some π - π stacking interactions between pyridyl rings of the cations are identified, as pyridyl rings lie completely parallel to each other at 3.487 and 3.862 Å (Figure 3.2.8). In this arrangement, water molecules occupy isolated cavities which account for 1.0 % of its unit cell volume (113.34 Å³, measured with a probe radius of 1.2 Å, Figure 3.2.8). Relevant non-bonding interactions are summarized in Table 3.2.4.

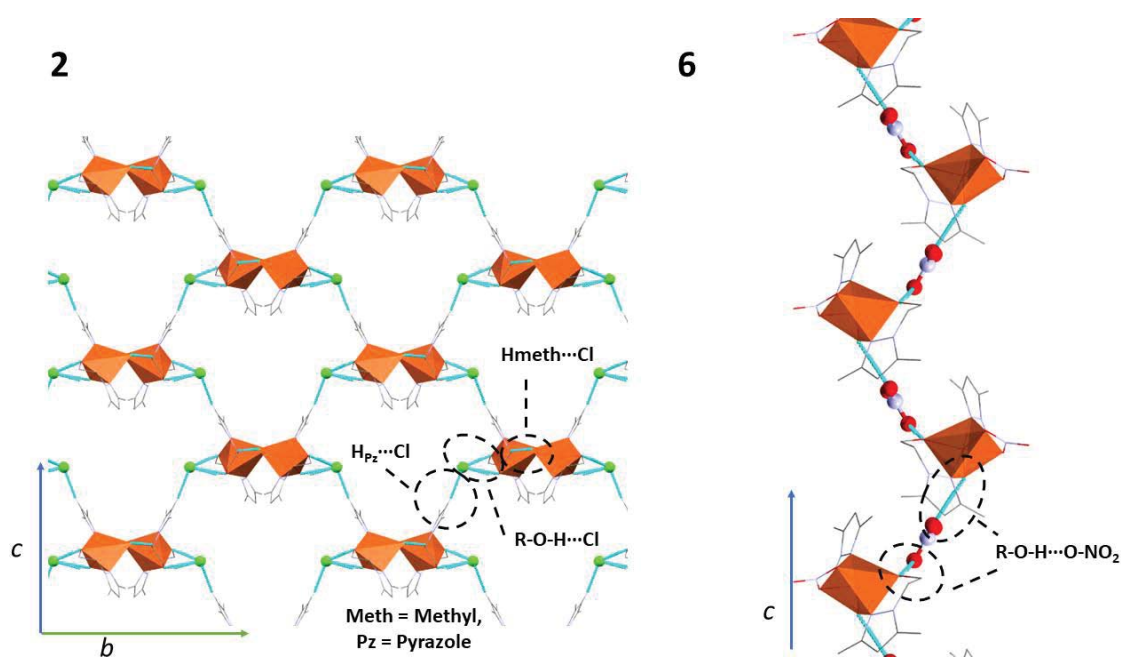


Figure 3.2.7 Supramolecular 2D plane in **2** (left) and 1D chain in **6** (right). Only hydrogen atoms involved in close interactions are shown. Anions are depicted in ball and stick mode. Note the role of chlorine and nitrate anions in forming the supramolecular scaffold. Colour code: grey (C), white (H), light blue (N), red (O), light green (Cl), orange (Cu). Cu(II) atoms are also represented as orange polyhedra.

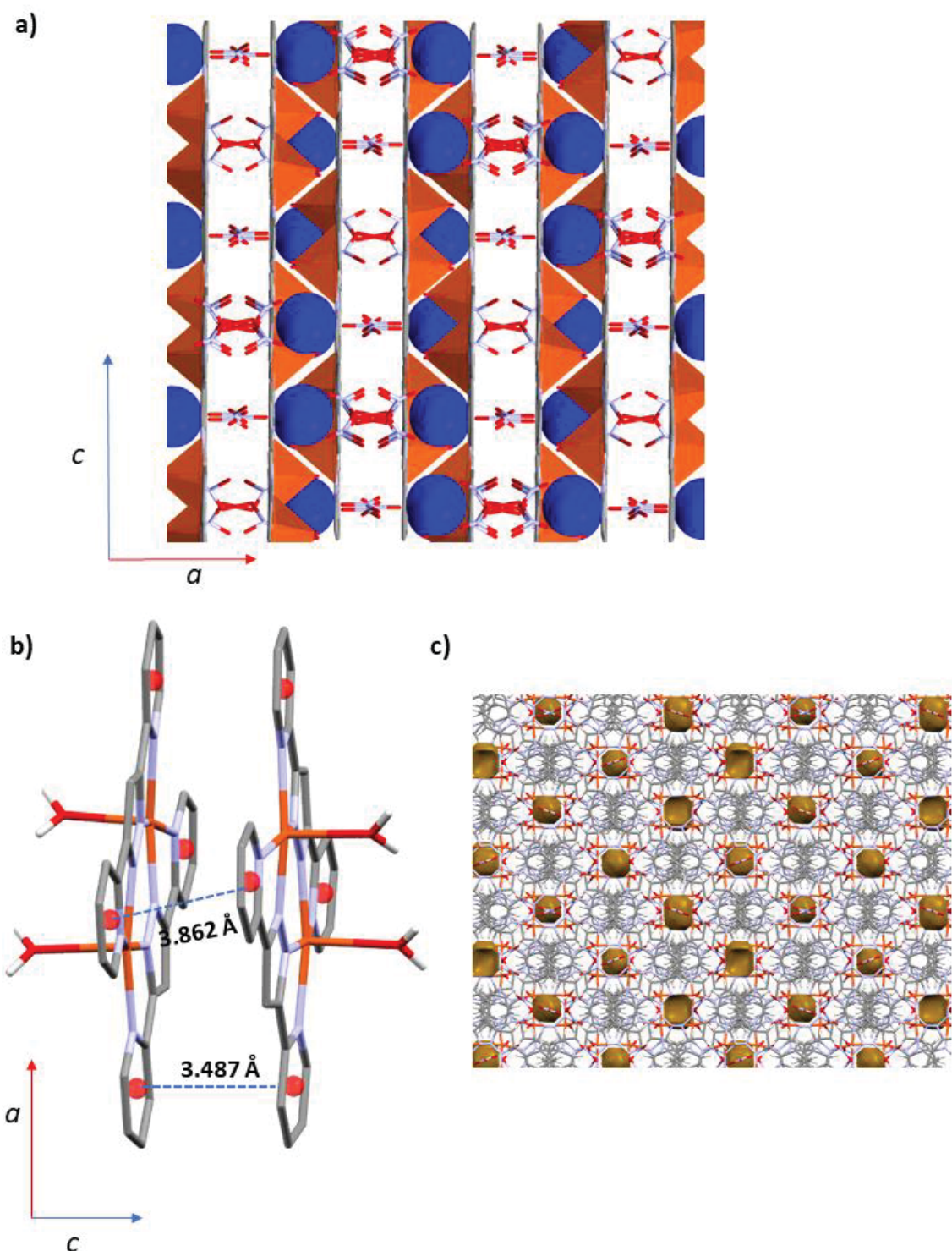


Figure 3.2.8 a. Supramolecular packing of compound **8**·H₂O, showing all non-hydrogen atoms. Water molecules are highlighted in blue and spacefill mode. b. Detail of the π - π stacking interactions in **8**. c. Voids representation in **8**·H₂O (113.34 Å³, 1.0 % of its unit cell). Colour code: grey (C), white (H), light blue (N), red (O), light green (Cl), orange (Cu). Cu(II) atoms are also represented as orange polyhedra.

Table 3.2.4 Non-bonding interactions for **2**, **6** and **8**·H₂O

	D-H...A (Å)	H-D...A (Å)	D-H (Å)	>D-H...A (°)
2				
O1_{al}-H1_{al}...Cl2	2.204	3.016	0.839	162.70
O2_{al}-H2_{al}...Cl2	2.122	2.958	0.840	173.32
C3_{Pz}-H3_{Pz}...Cl2	2.827	3.669	0.930	151.20
C6_{meth}-H6_{Bmeth}...Cl1	2.873	3.745	0.970	150.06
6				
O1_{al}-H1_{Oal}...O7_N	1.796	2.622	0.840	167.81
O2_{al}-H2_{Oal}...O6_N	1.919	2.743	0.840	166.74
8·H₂O				
O_{Wc}-H_{Wc}...O_{NO3}	2.061	2.756	0.797	145.70
O_{Wc}-H_{Wc}...O_{NO3}	1.917	2.724	0.815	170.88
O_{Wo}-H_{Wo}...O_{NO3}	2.080	2.566	0.811	118.33

al = alcohol, meth = methyl, Pz = pyrazole, Wc = coordinated water, Wo = occluded water, Pyr = 2-pyridyl

• *Monomeric compound 4·(CH₂Cl₂)(H₂O)*

Compound **4**·(CH₂Cl₂)(H₂O) crystallizes in a monomeric structure having a Cu:**HL3**:X (X = chlorine) 1:1:2 ratio (Figure 3.2.9). Moreover, it contains one H₂O and one CH₂Cl₂ molecules as occluded solvents in its crystal structure. Its [CuON₂Cl₂] *core* has a slightly distorted square pyramidal geometry ($\tau_5 = 0.22^{25}$). This slight distortion is reflected in the bond angles, with range between 79.50(3)° to 105.162(11)° and from 153.75(3)° to 166.79(3)° (instead of the ideal 90° and 180°).

The basal plane is formed by a chlorine atom and two nitrogen atoms and one oxygen atom provided by the **HL3** ligand, while the apical position is occupied by the last chlorine atom. Thus, **HL3** acts as a tridentate chelate ligand, coordinating *via* its pyrazol, pyridine and protonated alcohol moieties. Its N_{Pz}-Cu-N_{Pyr} and N_{Pz}-Cu-O_{al} bite angles are 79.50(3)° and 87.45(3)° respectively. Selected bond distances and angles are reported in Table 3.2.5. They are in agreement with similar Cu(II) nitrate pyrazole compounds^{30,32}.

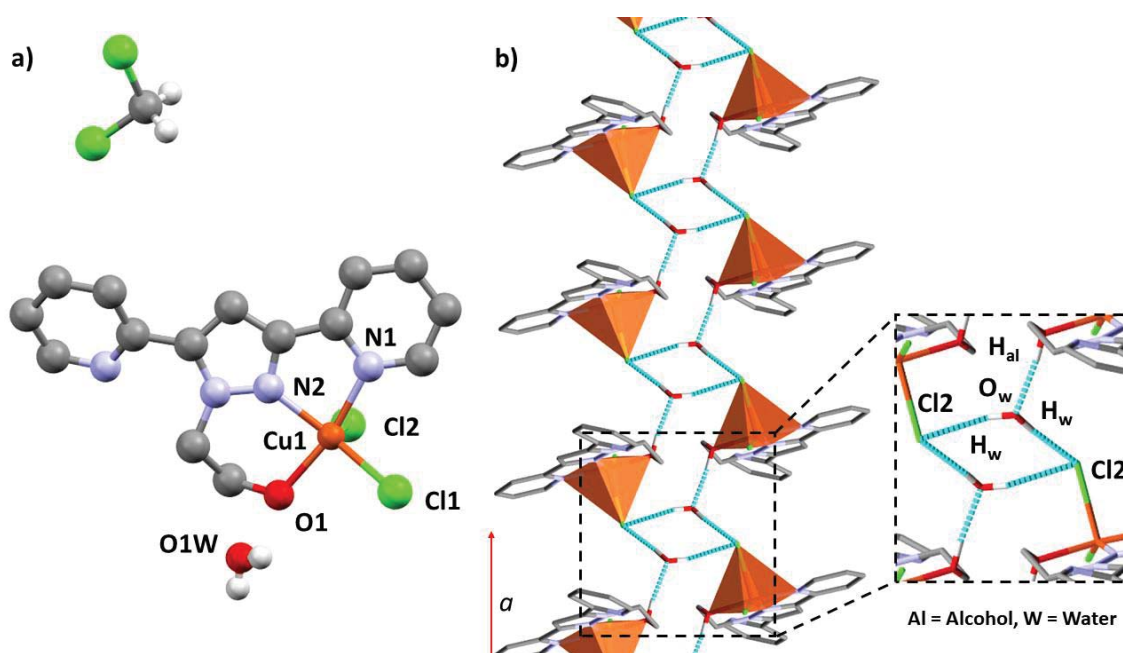


Figure 3.2.9 a. Compound 4·(CH₂Cl₂)(H₂O), showing all its relevant atoms and numbering scheme. b. Supramolecular chains in compound 4·(CH₂Cl₂)(H₂O). View along c axis. Colour code: grey (C), white (H), light blue (N), red (O), light green (Cl), orange (Cu). Cu(II) atoms are also represented as orange polyhedra. Intermolecular interactions are represented as light blue dashed lines.

Table 3.2.5 Selected bond distances (Å), angles (°) and non-bonding interactions for compound 4·(CH₂Cl₂)(H₂O)

4·(CH ₂ Cl ₂)(H ₂ O)				
Bond lengths (Å)				
Cu(1)-N(2)	1.9805(8)	Cu(1)-Cl(1)	2.2322(3)	
Cu(1)-O(1)	1.9985(8)	Cu(1)-Cl(2)	2.4818(4)	
Cu(1)-N(1)	2.0261(9)			
Bond angles (°)				
N(2)-Cu(1)-O(1)	87.45(3)	N(1)-Cu(1)-Cl(1)	97.06(3)	
N(2)-Cu(1)-N(1)	79.50(3)	N(2)-Cu(1)-Cl(2)	101.03(3)	
N(1)-Cu(1)-O(1)	166.79(3)	Cl(2)-Cu(1)-O(1)	90.88(2)	
N(2)-Cu(1)-Cl(1)	153.75(3)	N(1)-Cu(1)-Cl(2)	93.60(3)	
O(1)-Cu(1)-Cl(1)	93.74(2)	Cl(1)-Cu(1)-Cl(2)	105.162(11)	
N(3)-Cu(1)-O(1)	89.27(4)	N(3)-Cu(1)-O(5)	100.27(6)	
Intermolecular interactions				
	D-H···A (Å)	D-H (Å)	H-D···A (Å)	>D-H···A (°)
O1 _{al} -H1O _{al} ···O1W	1.801	0.840	2.624	166.08
O1W-H1WA···Cl2	2.435	0.796	3.215	166.39
O1W-H1WB···Cl2	2.309	0.804	3.111	175.82
Al = alcohol, W = water				

The presence of occluded solvent molecules dictates the supramolecular architecture in $4 \cdot (\text{CH}_2\text{Cl}_2)(\text{H}_2\text{O})$. Thus, sets of two water molecules link four monomers forming a double linear chain along a axis. Chlorine atoms and the hydrogen of protonated alcohol moieties are heavily involved in this scaffold (Figure 3.2.9, Table 3.2.5). Nestled among those chains, lie the CH_2Cl_2 molecules, forming a clathrate-like structure (Figure 3.2.10). Overall, these CH_2Cl_2 molecules occupy isolated cavities representing 13.0 % of its unit cell volume (128.87 \AA^3 , measured with a probe radius of 1.2 \AA). Taking water molecules into consideration, the cavities nestling the solvents account for 15.9 % of its unit cell volume (157.39 \AA^3 , measured with a probe radius of 1.2 \AA , Figure 3.2.10).

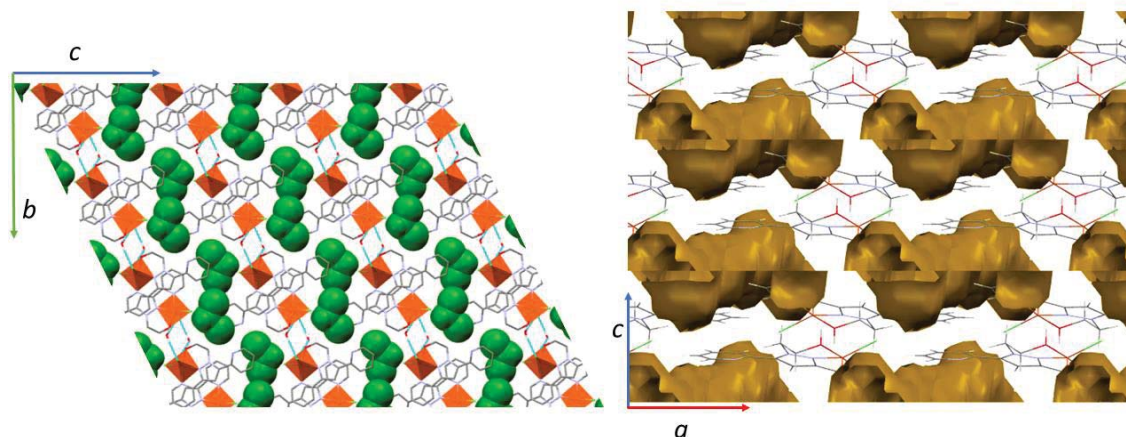


Figure 3.2.9 a. Clathrate-like structure in $4 \cdot (\text{CH}_2\text{Cl}_2)(\text{H}_2\text{O})$, view along a axis (left). CH_2Cl_2 molecules are highlighted in green in the spacefill mode. b. Voids representation in $4 \cdot (\text{CH}_2\text{Cl}_2)(\text{H}_2\text{O})$ (157.3 \AA^3 , 15.9% unit cell volume), view along b axis (right). Colour code: grey (C), white (H), light blue (N), red (O), light green (Cl), orange (Cu). Cu(II) atoms are also represented as orange polyhedra. Intermolecular interactions are represented as light blue dashed lines.

• *Dimeric compounds 1, 3·HL2, 7·2CH₃CN and 9·6H₂O*

Compounds **1**, **3·HL2** and **9·6H₂O** crystallize in a dimeric structure with a Cu:L:X (L = L1 (**1**, **9**), L2 (**3**); X = chlorine (**1**, **3**) or acetate (**9**)) 1:1:1 ratio. For compound **7·2CH₃CN**, on the other hand, an unexpected cleavage of a $\text{N}_{\text{Pz}}\text{-C}$ bond in **HL2** ligand happened during the synthesis, resulting in the formation of 3-5-diphenylpyrazole (3,5-DPP). Thus, its crystal structure has a Cu:L3:3,5-DPP:NO₃ 1:1:1:1 ratio (Figure 3.2.11). Some of those compounds contain occluded molecules in their crystal structures. For instance, compound **3·HL2** contains one occluded **HL2** molecule, compound **7·2CH₃CN** two CH_3CN molecules and compound **9·6H₂O** contains six occluded water molecules.

Lastly, it can be seen that while **1**, $7 \cdot 2\text{CH}_3\text{CN}$ and $9 \cdot 6\text{H}_2\text{O}$ are symmetric dimers, with both Cu(II) atoms displaying the same *core*, **3**·**HL2** is an asymmetric dimer, each Cu(II) metal centre displaying a different *core*. Owing to their similarities, compounds **1** and $9 \cdot 6\text{H}_2\text{O}$ will be described together, whereas **3**·**HL2** and $7 \cdot \text{CH}_3\text{CN}$ will be described separately.

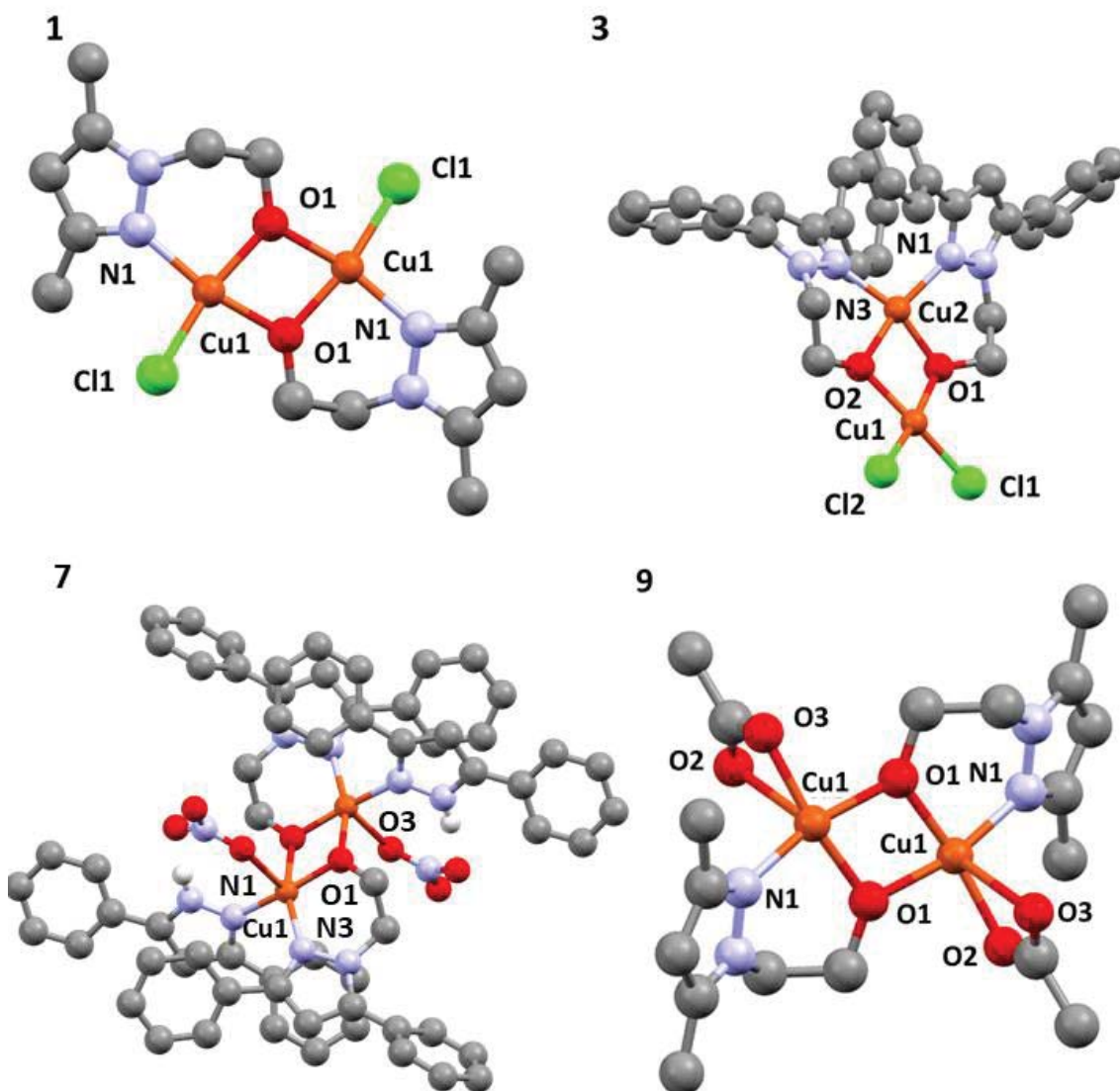


Figure 3.2.11 Dimeric compounds **1**, **3**, **7** and **9**, showing relevant atoms and their numbering scheme. Compound's **3**, **7** and **9** occluded solvent molecules have been excluded for clarity. Colour code: grey (C), white (H), light blue (N), red (O), light green (Cl), orange (Cu).

Despite sharing the same symmetric dimer topology, compound **1** possesses a distorted square planar ($\tau_4 = 0.27$)⁵¹ $[\text{CuO}_2\text{NCl}]$ *core*, while compound $9 \cdot 6\text{H}_2\text{O}$ adopts a square pyramidal ($\tau_5 = 0.03$)²⁵ $[\text{CuO}_3\text{NCl}]$ one, due to the chelating behaviour of the acetate ligand. The distortion in **1** is promoted by the rigidity of the chelating **L1**, as

reflected in their bond angles, ranging from $75.79(4)^\circ$ to $99.76(3)^\circ$ and from $159.68(4)^\circ$ to 162.39° (instead of the ideal 90° and 180°). For compound $\mathbf{9} \cdot 6\text{H}_2\text{O}$, one oxygen atom of the chelated acetate ligand is in the apical position, while the rest of the atoms are on the basal plane. Despite the chelating nature heavily distorting the angles related to the apical position (in the range of $57.71(3)^\circ$ to $114.38(4)^\circ$ instead of ideal 90°), it does not affect its clear square pyramidal nature. In both cases, the alcohol group of **L1** is deprotonated, acting as a bidentate bridging and chelate ligand. Relevant distances and angles are summarized in Table 3.2.6. They are in agreement with related Cu(II) pyrazole compounds^{52,53}.

Table 3.2.6 Selected bond distances (Å) and angles ($^\circ$) for compounds **1** and $\mathbf{9} \cdot 6\text{H}_2\text{O}$

1			
Bond lengths (Å)			
Cu(1)-O(1)	1.9289(8)	Cu(1)-Cl(1)	2.2098(3)
Cu(1)-O(1)#1	1.9142(8)	Cu(1)···Cu(1)#1	3.0328(3)
Cu(1)-N(1)	1.9674(9)		
Bond angles ($^\circ$)			
O(1)#1-Cu(1)-O(1)	75.79(4)	O(1)#1-Cu(1)-Cl(1)	96.96(2)
O(1)#1-Cu(1)-N(1)	159.68(4)	O(1)-Cu(1)-Cl(1)	162.39(3)
O(1)-Cu(1)-N(1)	91.09(3)	N(1)-Cu(1)-Cl(1)	99.76(3)
#1: -x+1, -y+2, -z+1			
$\mathbf{9} \cdot 6\text{H}_2\text{O}$			
Bond lengths (Å)			
Cu(1)-O(1)#1	1.9163(8)	Cu(1)-O(2)	1.9663(8)
Cu(1)-O(1)	1.9276(8)	Cu(1)-N(1)	1.9636(10)
Cu(1)-O(3)	2.494(1)	Cu(1)···Cu(1)#1	3.0176(3)
Bond Angles ($^\circ$)			
O(1)#1-Cu(1)-O(1)	76.55(4)	O(3)-Cu(1)-O(2)	57.71(3)
O(1)#1-Cu(1)-N(1)	164.88(4)	N(1)-Cu(1)-O(2)	98.53(4)
O(1)-Cu(1)-N(1)	92.90(4)	O(2)-Cu(1)- Cu(1)#1	131.23(3)
O(1)#1-Cu(1)-O(2)	93.34(4)	O(3)-Cu(1)- O(1)#1	96.19(4)
O(1)-Cu(1)-O(2)	166.86(4)	O(3)-Cu(1)-N(1)	98.06(4)
O(1)-Cu(1)-O(3)	114.38(4)		
#1: -x+1, -y+1, -z+1			

Compound **3·HL2**, on the other hand, displays two different square planar *cores*, one [CuO₂Cl₂] ($\tau_4 = 0.05^{51}$) and one [CuO₂N₂] ($\tau_4 = 0.06^{51}$). In it, **L2** ligands are deprotonated, acting as bidentate bridging and chelate ligands. A similar compound has already been described by our group¹³ possessing one nitromethane occluded solvent molecule, thus differing a lot in their supramolecular network. Selected bond distances and angles for **3·HL2** are summarized on Table 3.2.7. They are in agreement with reported Cu(II) pyrazole compounds^{33,13}.

Table 3.2.7 Selected bond lengths (Å) and angles (°) for compound **3·HL2**

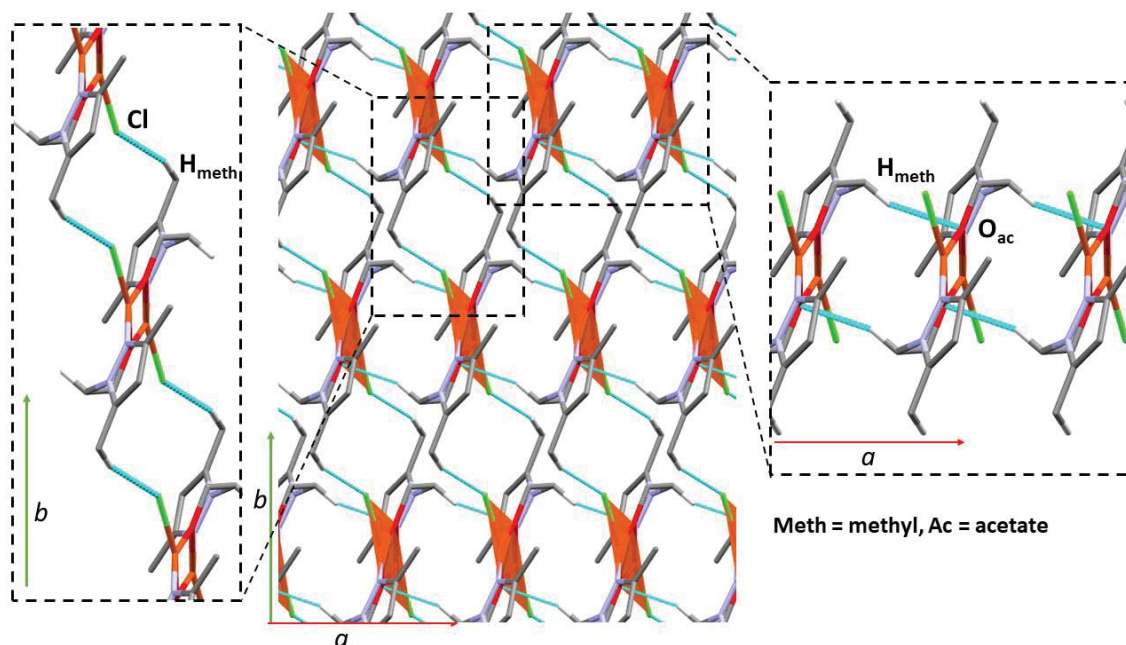
Bond lengths (Å)			
Cu(1)-O(1)	1.9391(17)	Cu(2)-O(1)	1.8958(16)
Cu(1)-O(2)	1.9686(17)	Cu(2)-O(2)	1.9062(17)
Cu(1)-Cl(2)	2.2230(8)	Cu(1)-N(3)	1.945(2)
Cu(1)-Cl(1)	2.2397(7)	Cu(1)-N(1)	1.961(1)
	Cu(1)···Cu(2)	2.9630(5)	
Bond angles (°)			
O(1)-Cu(1)-O(2)	76.09(7)	O(1)-Cu(2)-O(2)	78.61(7)
O(1)-Cu(1)-Cl(2)	168.11(5)	O(1)-Cu(2)-N(3)	156.68(9)
O(2)-Cu(1)-Cl(2)	94.77(5)	O(2)-Cu(2)-N(3)	91.23(8)
O(1)-Cu(1)-Cl(1)	92.80(5)	O(1)-Cu(2)-N(1)	94.23(8)
O(2)-Cu(1)-Cl(1)	161.49(6)	O(2)-Cu(2)-N(1)	165.39(8)
Cl(2)-Cu(1)-Cl(1)	97.93(3)	N(3)-Cu(2)-N(1)	99.84(9)

For compound **7·2CH₃CN**, its [CuO₃N₂] *core* displays a slightly distorted square pyramidal ($\tau_5 = 0.14$)²⁵ coordination geometry. The apical position is occupied by the oxygen atom of the nitrate group, while the rest of the atoms (two oxygens and one nitrogen provided by **L2** and one nitrogen provided by 3,5-DPP) are in the basal plane. Once again, the alcohol moieties are deprotonated, the **L2** acting as chelated and bridged, while the nitrate moiety coordinates in a monodentate fashion. Selected bond lengths and angles are summarized in Table 3.2.8. As stated before, the presence of the 3,5-DPP ligand in this compound owes to the cleavage of the **HL2** ligand. Note that, in compound **7·2CH₃CN** the **3,5-DPP** ligand is neutral, whereas in compound **8·H₂O** the **3,5-DPyP** ligand was deprotonated, thus being ionic.

Table 3.2.8 Selected bond lengths (Å) and angles (°) for compound **7**·2CH₃CN

Bond lengths (Å)			
Cu(1)-O(1)	1.9008(10)	Cu(1)-N(3)	2.0251(11)
Cu(1)-O(1)#1	1.9501(10)	Cu(1)-N(1)	1.9505(11)
Cu(1)-O(3)	2.474(1)	Cu(1)···Cu(1)#1	3.0408(4)
Bond angles (°)			
O(1)-Cu(1)-O(1)#1	75.70(5)	O(1)-Cu(1)-N(1)	169.46(5)
O(1)#1-Cu(1)-N(1)	94.38(4)	O(1)-Cu(1)-N(3)	93.27(4)
O(1)#1-Cu(1)-N(3)	160.89(5)	N(1)-Cu(1)-N(3)	95.27(5)
O(1)-Cu(1)-O(3)	87.74(4)	O(1)#1-Cu(1)-O(3)	94.40(4)
N(1)-Cu(1)-O(3)	96.65(5)	N(3)-Cu(1)-O(3)	100.81(5)

Compound **1** displays a relatively simple supramolecular structure, promoted by two head-to-tail hydrogen bond interactions. The first one, involving chlorine atoms and methyl moieties is responsible for the formation of chains, while the second one, involving coordinated oxygen atoms and the methyl moieties links those chains, forming a plane perpendicular to the *c* axis. (Figure 3.2.12). Relevant non-bonding interactions are summarized in Table 3.2.9.

**Figure 3.2.12** Supramolecular structure of compound **1**. Colour code: grey (C), white (H), light blue (N), red (O), light green (Cl), orange (Cu). Cu(II) atoms are also represented as orange polyhedra. Intermolecular interactions are represented as light blue dashed lines.

For compound **3**·**HL2**, the disorder present in the occluded **HL2** ligand molecule prevents an in-depth study of its supramolecular scaffold. Despite this hindrance, it can be observed that pairs of dimeric units are associated *via* $\text{H}\cdots\text{Cl}$ interactions involving hydrogen groups of the phenyl ring. Then, those pairs of dimers units are linked together thanks to interactions involving the occluded **HL2** solvents through non-bonding associations between the oxygen atoms and hydrogen atoms of the phenyl rings. Overall, the pairs of dimers and the occluded solvents are disposed in alternate AB layers. The occluded solvent molecules occupy isolated cavities accounting for a remarkable 20.2 % of its unit cell volume (1543.68 \AA^3) (Figure 3.2.13). Relevant non-bonding interactions are summarized in Table 3.2.9.

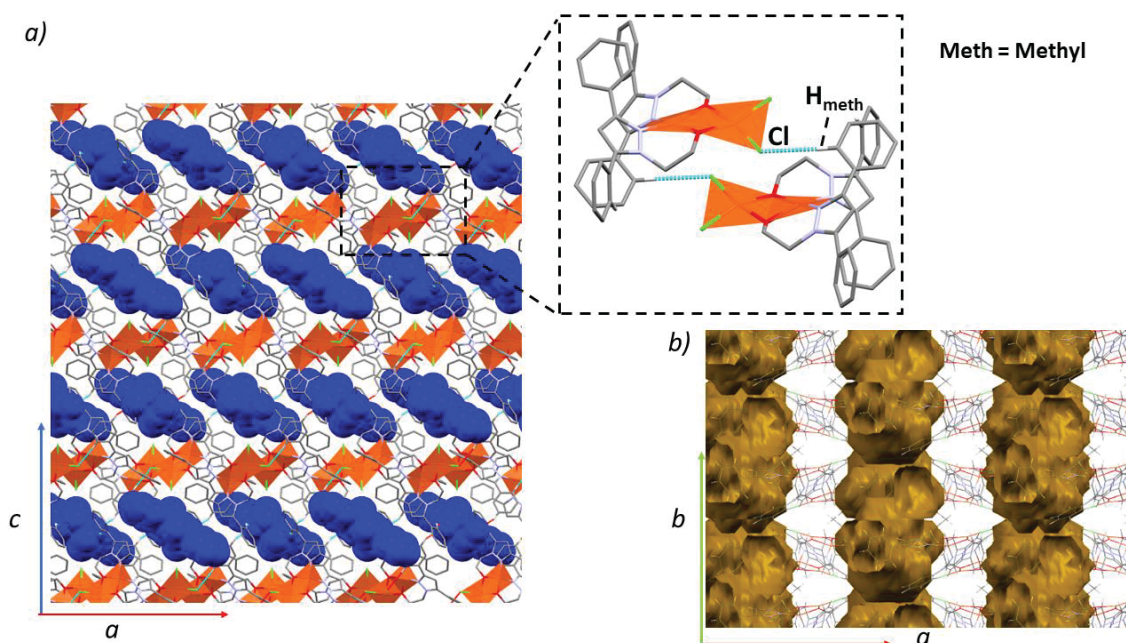


Figure 3.2.13 a. Supramolecular structure of **3**·**HL2**, view along *b* axis. Occluded **HL2** molecules are highlighted in blue. Detail of the association between dimeric units. b. Voids representation (1543.8 \AA^3 , 20.2 % of unit cell volume) in **3**, view along *c* axis. Colour code: grey (C), white (H), light blue (N), red (O), light green (Cl), orange (Cu). Cu(II) atoms are also represented as orange polyhedra. Intermolecular interactions are represented as light blue dashed lines.

The supramolecular scaffold of **7**·2CH₃CN is dominated by the interaction between uncoordinated oxygens of the nitrate group and the hydrogen of the pyrazole ligand. This results in the formation of supramolecular 1D-chains parallel to the *a* axis. Moreover, the occluded molecules also play a role in holding the supramolecular structure, binding together these supramolecular chains in 2D planes. Finally, it is

remarkable to note that the presence of multiple phenyl groups in positions 3- and 5- result in the formation of C-H $\cdots\pi$ interactions, which bind the planes completing the 3D structure (Figure 3.2.14). The occluded solvents occupy isolated cavities, accounting for 6.3% (96.15 Å³) of its unit cell volume (Figure 3.2.14). Relevant interactions are summarized in Table 3.2.9.

The supramolecular structure of compound **9**·6H₂O, on the other hand, is dominated by the presence of water molecules. They do not only form strong hydrogen bond between themselves, but also with the alkylic chain of **L1** and oxygen atoms of the acetate moiety. Thus, **9**·6H₂O has a distinct clathrate like structure, with a solvent accessible surface equal to 21.1 % of its unit cell volume. The detailed examination of these interactions shows that there are three sets of distinct pairs of water molecules. Water molecule II (H2WA-O2W-H2WB) is the lynchpin of the whole architecture, as it binds together H₂O molecules I and III (H1WA-O1W-H1WB, H3WA-O3W-H3WB). Meanwhile, H₂O molecule I and III interact with dimeric molecules *via* different H-bonds, but their interactions with molecule II are the ones which allow the formation of a 3D supramolecular network (Figure 3.2.15). The existence of these three sets of pairs ties in nicely with the fact that three distinct [ν (O-H)] vibrations are identified in **9**·6H₂O FTIR-ATR spectra. Relevant non-bonding interactions are summarized in Table 3.2.9.

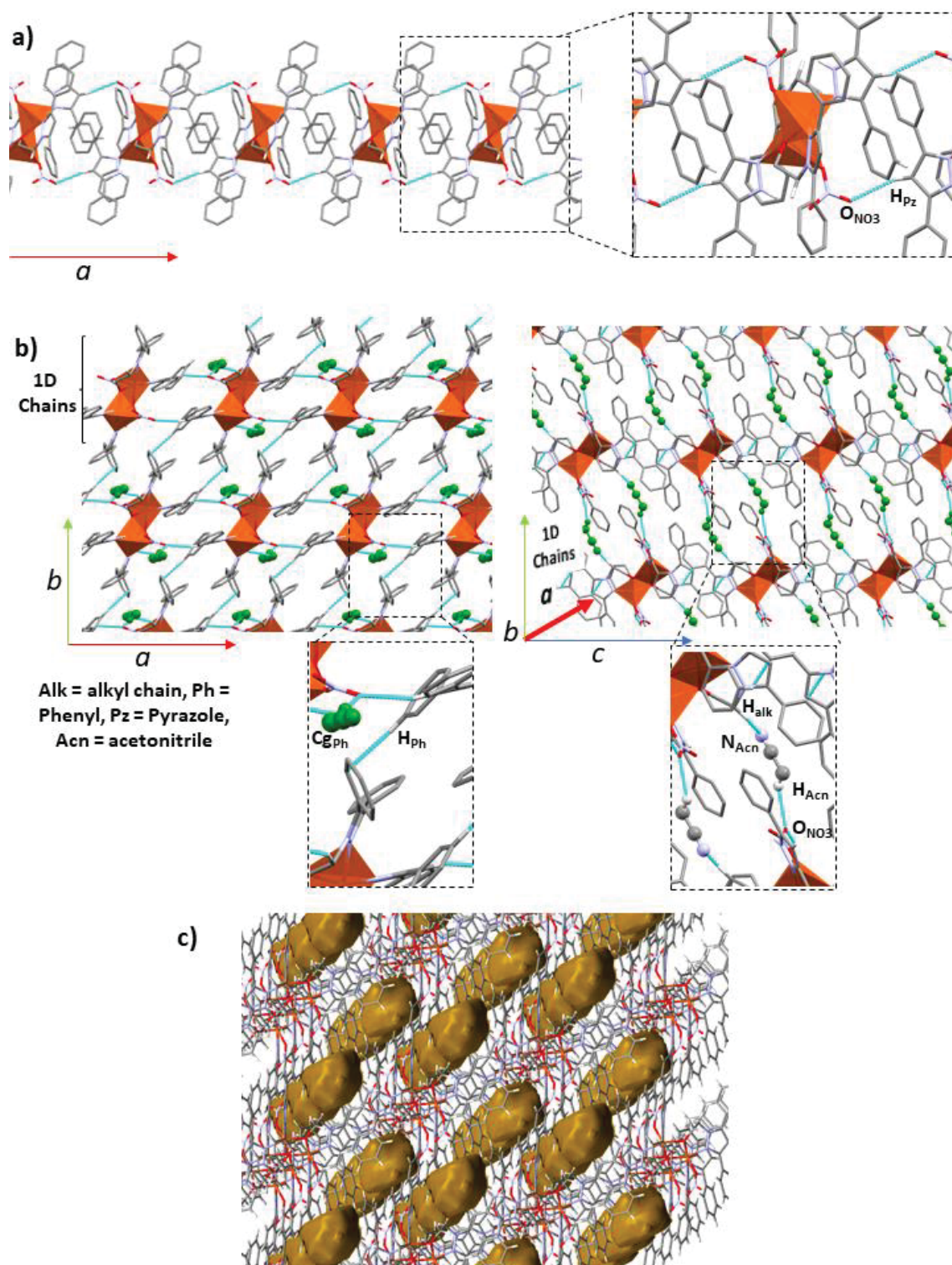
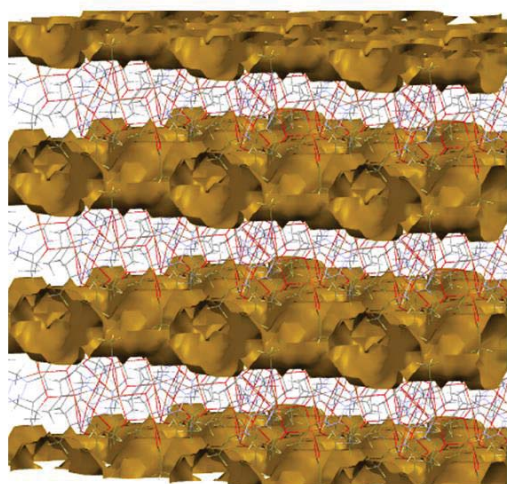


Figure 3.2.14 a. Supramolecular chains in $7 \cdot 2CH_3CN$, view along b axis. b. Interactions between chains along c axis (left) and a axis (right). Occluded CH_3CN molecules are highlighted in green. Only relevant hydrogen atoms are shown. c. Voids representation in $7 \cdot 2CH_3CN$ (96.15 \AA^3 , 6.3 % of unit cell). Colour code: grey (C), white (H), light blue (N), red (O), light green (Cl), orange (Cu). Cu(II) atoms are also represented as orange polyhedra. Intermolecular interactions are represented as light blue dashed lines.

Table 3.2.9 Non-bonding interactions for **1**, **3·HL2**, **7·2CH₃CN** and **9·6H₂O**

	D-H···A (Å)	H-D···A (Å)	D-H (Å)	>D-H···A (°)
1				
C5_{meth}-H5_{meth}···C11	2.680	3.627	0.980	162.69
C6_{meth}-H6_{meth}···O_{ac}	2.550	3.448	0.990	150.82
3·HL2				
C5_{Ph}-H5_{Ph}···C12	2.688	3.636	0.950	175.47
C8_{Ph}-H8_{Ph}···O5_{al}	2.416	3.276	0.950	150.52
C32_{Ph}-H32_{Ph}···O5_{al}	2.527	3.168	0.950	124.94
7·2CH₃CN				
C8_{Pz}-H8_{Pz}···O2_{NO3}	2.531	3.420	0.950	155.83
C31_{alk}-H31_{alk}···N_{Acn}	2.622	3.413	0.990	136.92
C33_{Acn}-H33_{Acn}···O2_{NO3}	2.599	3.464	0.980	147.17
C12_{Ph}-H12_{Ph}···Cg_{Ph}	3.535	4.153	0.950	124.99
9·6H₂O				
O1_W-H1_{WA}···O2_Wⁱ	2.136	2.931	0.799	172.82
O1_W-H1_{WB}···O3_{ac}	1.906	2.702	0.800	173.67
O2_W-H2_{WA}···O3_Wⁱ	2.015	2.808	0.797	173.27
O2_W-H2_{WB}···O1_Wⁱⁱ	1.974	2.753	0.799	164.14
O3_W-H3_{WA}···O2_W	2.052	2.843	0.794	173.85
O3_W-H3_{WB}···O2_{ac}ⁱ	2.037	2.813	0.790	167.14
C6-H6_B···O1_W	2.332	3.161	0.990	140.74
Ph = Phenyl, al = alcohol, alk = Alkyl chain, meth = methyl, ac = acetate, W = water, Acn = acetonitrile Cg1 _{Ph} = C10-C15				
ⁱ [x, 1/2-y, -1/2+z], ⁱⁱ [-x, -1/2+y, 1/2-z]				

a)



b)

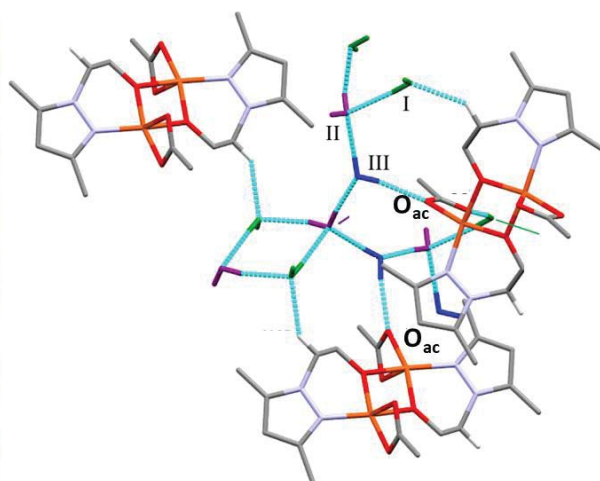


Figure 3.2.15 a. Voids representation (293.14 Å³, 21.1 % of unit cell volume) in **9·6H₂O**. b. Supramolecular structure of **9·6H₂O**. Crystallographically equivalent water molecules in **9·6H₂O** are highlighted in the following colours: I – green, II – blue, III – purple. Colour code: grey (C), white (H), light blue (N), red (O), orange (Cu). Intermolecular interactions are represented as light blue dashed lines

This interesting architecture prompted us to analyse the role of the water moieties in detail. Thus, Hirshfeld surface analyses were performed with Crystal Explorer 17.5⁵⁴ on each crystallographically independent molecule in the unit cell. Hirshfeld surface analysis explores interactions in the crystal structure based on electron densities. Color codes are used to predict the strength of the interactions by mapping the d_{norm} functions onto the Hirshfeld surface. The 3D d_{norm} functions can be resolved into 2D fingerprint plots which show the contributions of the molecular interactions. Individual plots of occluded H₂O molecules allow to ascertain their differences (Figure 3.2.16), as each one displays a distinct plot showing their unique roles in supramolecular structure. In all of them two sharp peaks appear, related to the reciprocal O-H \cdots O hydrogen bonds. For the dimer, its main supramolecular interactions are highlighted in the d_{norm} representation. (Figure 3.2.16). Its analysis once again confirms its interaction with only water molecules I and III, as red spots highlight these interactions.

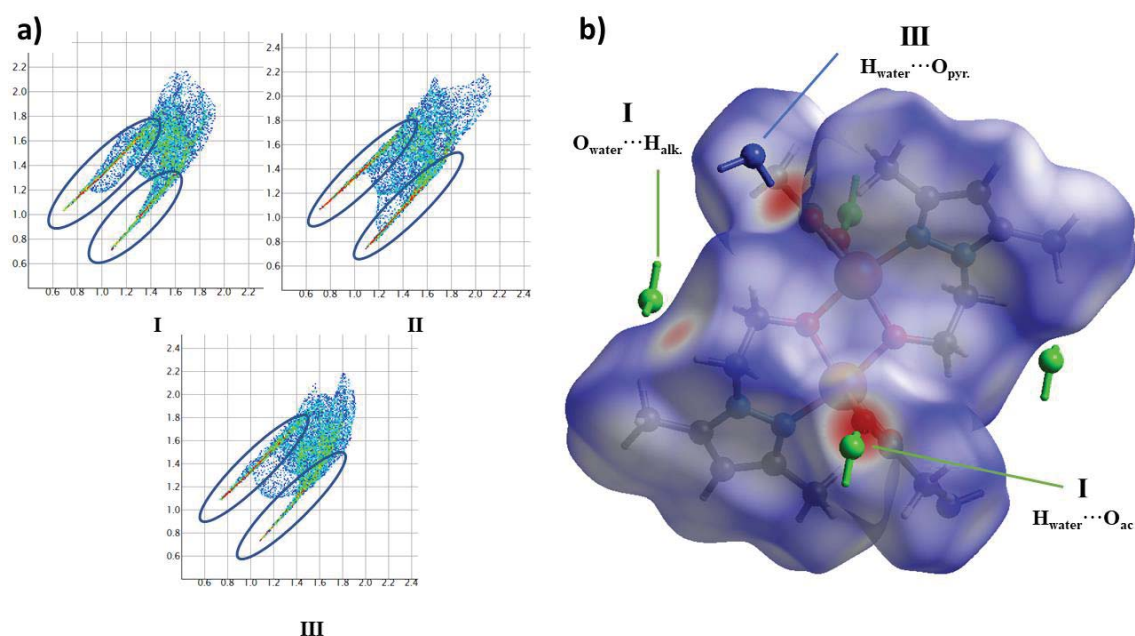


Figure 3.2.16. a. Fingerprint plots of water molecules I, II, III. Circles pinpoint regions belonging to O \cdots H hydrogen bond interactions. b. D_{norm} representation of dimer **9** (b). Colour code: grey (C), white (H), light blue (N), red (O), light green (Cl), orange (Cu).

- *Polymeric compound 5*

Compound **5** displays a polymeric structure formed by centrosymmetric dimeric centres (like compounds **1** and **9**) bridged by nitrate moieties. Those dimeric units display

a Cu:L1:NO₃ 1:1:1 ratio with a distorted octahedral ($\text{ata} = 46.92^\circ$)^{26,27} core. In them, the basal plane comprises two bridging oxygen atoms of deprotonated L1 ligands, one nitrogen atom of a L1 ligand and one oxygen atom of the nitrate moieties. The apical positions are occupied by the bridging oxygen atoms of the nitrate ligand. The spatial constraints of this chelated nitrogen ligand induce a distortion of the octahedral geometry in the apical position, as the apical atom deviates from linearity (O1#1-Cu1-O3, $113.09(9)^\circ$ instead of ca. 90°). For ligand L1, the alcohol moiety is deprotonated, and the ligand acts in a bidentate bridging and chelate fashion, much in the same manner as **1**, **3** and **9**. The nitrate ligand does not only chelate in an anisobidentate fashion²⁸ (Cu(1)-O(2) and Cu(1)-O(3) distances ($2.004(2)$ Å and $2.594(2)$ Å, $d_1-d_2 < 0.6$ Å) and Cu(1)-O(2)-N(3) and Cu(1)-O(3)-N(3) angles ($107.18(2)^\circ$ and $79.94(2)^\circ$, $\theta_1-\theta_2 < 28^\circ$), but also in a bridging one, being responsible in linking those centrosymmetric dimers in edge-sharing dioctahedral polymeric chains (Figure 3.2.17). Relevant bond distances and angles are summarized on Table 3.2.10.

The nitrate ligand also plays a key role in its supramolecular scaffold, as it forms a double-hydrogen bond linking consecutive chains. Not only does its non-coordinated oxygen atom participates in strong H-bonds with hydrogens from the alkylic chain, but also the chelate and bridging oxygen is involved in interactions with hydrogens from the methyl groups. These two interactions result in the formation of 2D planes along the *bc* crystallographic axis. (Fig. 3.2.18). Selected non-bonding interactions are summarized in Table 3.2.10.

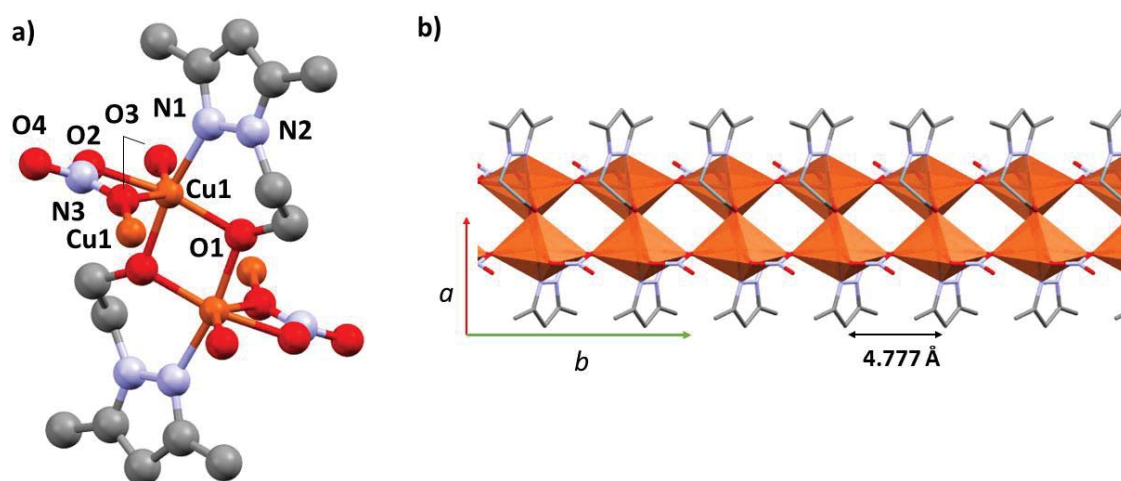


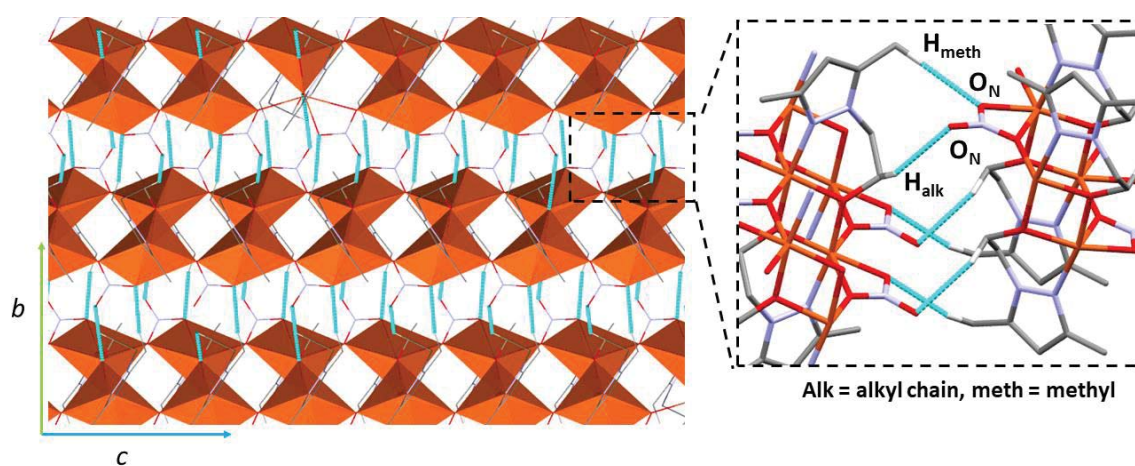
Figure 3.2.17 a. Compound **5**, depicting relevant atoms and its numbering scheme. b. Biocahedral polymeric chain in **5**. Colour code: grey (C), white (H), light blue (N), red (O), light green (Cl), orange (Cu). Cu(II) atoms are also represented as orange polyhedra.

Table 3.2.10 Selected bond distances (Å), angles (°) and non-bonding interactions for compound **5**

5				
Bond lengths (Å)				
Cu(1)-O(1)	1.929(2)	Cu(1)-O(2)	2.004(2)	
Cu(1)-O(1)#1	1.929(2)	Cu(1)-O(3)#2	2.369(3)	
Cu(1)-N(1)#1	1.970(2)	Cu(1)-O(3)	2.594(2)	
Cu(1)⋯Cu(1)	2.9847(9)			
Bond angles (°)				
O(1)-Cu(1)-O(1)#1	78.67(9)	N(1)#1-Cu(1)-O(2)	95.47(10)	
O(1)-Cu(1)-N(1)#1	169.06(9)	O(1)-Cu(1)-O(3)#2	89.54(9)	
O(1)#1-Cu(1)-N(1)#1	91.31(9)	O(1)#1-Cu(1)-O(3)#2	98.39(9)	
O(1)-Cu(1)-O(2)	93.35(9)	N(1)#1-Cu(1)-O(3)#2	96.31(10)	
O(1)#1-Cu(1)-O(2)	165.39(10)	O(2)-Cu(1)-O(3)#2	93.72(9)	
O(1)-Cu(1)-O(1)#1	78.67(9)	N(1)#1-Cu(1)-O(2)	95.47(10)	
Intermolecular interactions				
	D-H⋯A (Å)	D-H (Å)	H-D⋯A (Å)	>D-H⋯A (°)
C5 _{meth} -H5A _{meth} ⋯O2 _N	2.436	3.387	0.980	163.34
C7 _{alk} -H7A _{alk} ⋯O4 _N	2.536	3.329	0.990	136.93

Meth = methyl, alk = alkyl chain, N = nitrate

#1: -x+1, -y+1, -z+1, #2: x, y-1, z

**Figure 3.2.18** Supramolecular structure of **5**, view along *a* axis. Colour code: grey (C), white (H), light blue (N), red (O), orange (Cu). Cu(II) atoms are also represented as orange polyhedra. Intermolecular interactions are represented as light blue dashed lines

3.2.3 Structural discussion

The reactivity of **HL1-HL3** against the selected Cu(II) salts yielded nine compounds showing a great structural diversity. Sadly, crystal structures for compounds **7** and **8** have not been elucidated. However, from the herein gathered data, as well as from bibliographical sources, some proposals if their molecular structure can be done.

First, a bibliographical research in the CCDC⁵⁵ database for coordination compounds bearing similar *N*-hydroxyethylpyrazole was carried out. A total of twenty-five different reported crystal structures of coordination compounds bearing the **HL1** ligand, three bearing **HL2** ligand and one bearing **HL3** ligand were found. Their analysis shows that in all monomeric reported crystal structures (46% of the total) the alcohol is protonated. Moreover, the ligand shows two different coordination modes in monomeric compounds: monodentate or bidentate chelate, the last one being somewhat more favoured (40% and 60% of the reported monomers respectively). Regarding dimeric compounds (43% of the total), two different coordination behaviours are observed: bidentate chelate (36.4%) or bidentate bridge (72.1%), bearing in mind that compound [Cu(μ -**L1**)(**HL1**)]₂·(ClO₄)₂³³ shows both coordination modes. In all dimeric compounds bearing the bidentate bridge coordination mode the pyrazole is deprotonated. This behaviour is mimicked in compounds **1-6** and **9**, with protonated pyrazole ligands resulting in monomers (**2**, **4** and **6**) and deprotonated pyrazole ligands resulting in dimers (**1**, **3**, **5** and **9**). It becomes clear that the behaviour of the alcohol moiety of the *N*-hydroxyethylpyrazole ligands has a key role in the molecular structure of the resulting compounds.

3.2.4 Molecular Magnetism for compounds **1**, **3**, **5** and **9**

In order to study the magneto-structural relationships for compounds **5** and **9**, their phase purity was confirmed by powder x-ray diffraction (PXRD, Figures S3.2.13 and S3.2.14). For **5** and **9** magnetic susceptibility data was collected in the solid state in the range of 5-300 K (Figures 3.2.19 and S3.2.15). The $\chi_M T$ values for **5** and **9** at 300 K are 0.187 and 0.161 cm³mol⁻¹ respectively, substantially lower than the expected for two uncoupled $S = 1/2$ spins assuming $g = 2.00$ (0.75 cm³mol⁻¹). Upon decreasing temperature,

these values decrease almost linearly to 0.0343 and 0.0230 cm³mol⁻¹ for **5** and **9**, respectively, at 5 K, suggesting a strong antiferromagnetic interaction. The experimental data was fitted using Bleany-Bowers equation for binuclear Cu(II) complexes with a $H = -JS_1S_2$ Hamiltonian⁵⁶. Best results are reported on Table 3.2.11. The previously reported magnetic susceptibility values of **1**⁵² and **3**¹³ are also reproduced, owing to the notable structure similarities with **5** and **9**. All values are in agreement with Haase's magneto-structural correlations⁵⁷.

The general consensus is that the magnetic interaction of alkoxo-bridged Cu(II) dimers are heavily dependent on the following topological features: (i) Cu···Cu distance, (ii) Cu-O-Cu angle (θ), (iii) Cu-O distance, (iv) angle between the carbon atom bonded to the bridging oxygen atom and the Cu₂O₂ plane (torsional angle, τ), (v) planarity of the bonds around the bridging oxygen and (vi) hinge distortion⁵⁷⁻⁶¹. However, parameters (i), (ii) and (iii) show some intrinsic relationship, and therefore, it is considered that Cu-O-Cu angle is the main parameter for predicting $-2J$ values^{59,58,61}.

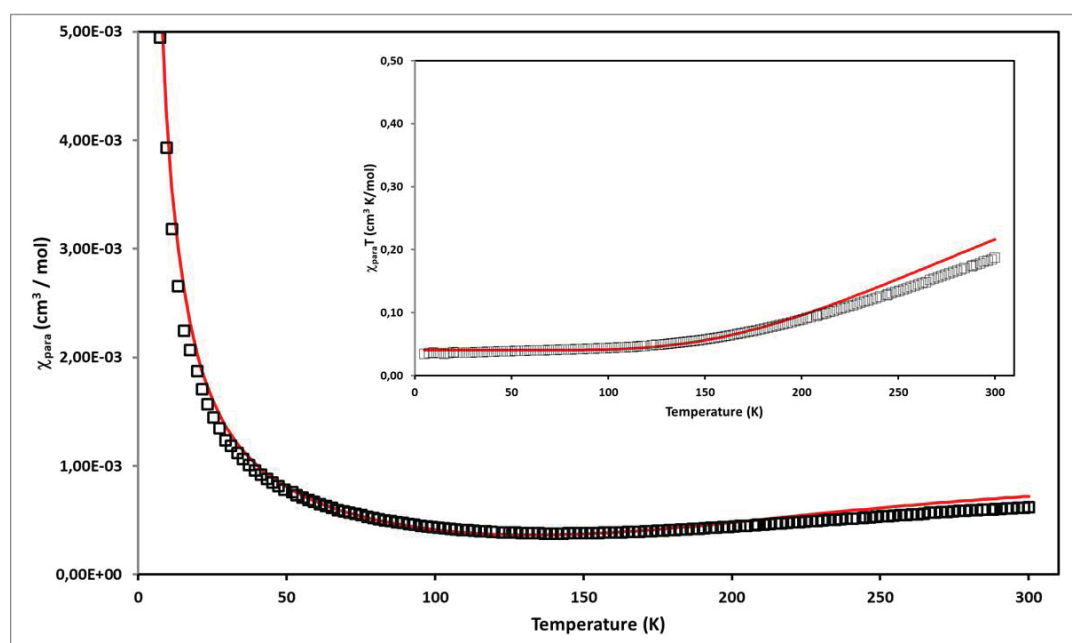


Figure 3.2.19 Thermal variation of χ_ρ and $\chi_\rho T$ (inset) for **5**. Solid line represents the best fit for the proposed model (see text).

All three compounds show almost coplanarity for the bonds around the bridging oxygen. Compounds **1** and **9** possess identical τ values, no hinge distortion, and similar Cu-O-Cu angles. As expected, their $-2J$ values are similar, with **1** having a slightly smaller $-2J$ owing to its slightly higher θ . For **5**, τ values are higher and θ values are smaller,

resulting in a weaker antiferromagnetic interaction, agreeing with the expected results. For **3**, despite having the smallest θ of all four compounds, its $-2J$ value is similar to **1** and **9**, owing to its small τ value. (Table 3.2.11).

Table 3.2.11. Magneto-structural parameters for compounds **1**, **3**, **5** and **9**

	$-2J$ (cm ⁻¹)	g	ρ (%)	$\theta_{Cu-O-Cu}$ (°)	τ (°)
1 ⁵²	-587	2.16	-	104.3	11.2
3 ¹³	-572	2.10	8	100.5	9.2
5	-535	2.01	5.35	101.3	26.5
9	-571	2.14	3.95	103.5	11.2

3.2.5 Summary and Conclusions

- ✓ The reactivity of **HL1-HL3** against different Cu(II) salts ($\text{CuCl}_2 \cdot 2\text{H}_2\text{O}$, $\text{Cu}(\text{NO}_3)_2 \cdot 3\text{H}_2\text{O}$ or $\text{Cu}(\text{CH}_3\text{COO})_2 \cdot \text{H}_2\text{O}$) was successfully assayed, yielding nine coordination compounds.
- ✓ All compounds have been fully characterized *via* spectroscopical and analytical techniques. Their crystal structures have been elucidated, allowing for the detailed study of its molecular and supramolecular architecture.
- ✓ The resulting compounds displayed a notable structural diversity, as ionic, monomeric, two different kinds of dimeric (symmetrical and asymmetrical) and polymeric compounds have been isolated.
- ✓ It has been observed that ligands **HL2** and **HL3** are cleaved along the $\text{N}_{\text{Pz}}\text{-C}$ bond in reaction with $\text{Cu}(\text{NO}_3)_2$, resulting in the presence of 3,5-DPP and 3,5-DPyP in compounds **7**·2CH₃CN and **8**·H₂O, respectively.
- ✓ Structural analyses of the obtained structures and previously reported ones suggests that the protonation or deprotonation of the alcohol moiety in *N*-hydroxyethylpyrazole ligands plays a key role in the nuclearity of the resulting compounds.
- ✓ The water desorption process in compounds **9** and **9**·4H₂O has been studied.
- ✓ The magneto-structural correlations for compounds **1**, **3**, **5** and **9** have been investigated

References

- 1 M. Guerrero, J. A. Perez, J. Ros and J. Pons, *Inorg. Chem. Commun.*, 2014, **46**, 234–236.
- 2 M. Guerrero, J. A. Pérez, M. Font-Bardia and J. Pons, *J. Coord. Chem.*, 2013, **66**, 3314–3325.
- 3 C. Luque, J. Pons, T. Calvet, M. Font-Bardia, J. García-Antón and J. Ros, *Inorganica Chim. Acta*, 2011, **367**, 35–43.
- 4 A. Boixassa, J. Pons, X. Solans, M. Font-Bardia and J. Ros, *Inorganica Chim. Acta*, 2004, **357**, 733–738.
- 5 J. A. Perez, V. Montoya, J. A. Ayllon, M. Font-Bardia, T. Calvet and J. Pons, *Inorganica Chim. Acta*, 2013, **394**, 21–30.
- 6 V. Montoya, J. Pons, X. Solans, M. Font-bardia and J. Ros, *Inorganica Chim. Acta*, 2005, **358**, 2312–2318.
- 7 A. M. López Marzo, M. Guerrero, T. Calvet, M. Font-Bardia, E. Pellicer, M. D. Baró, J. Pons and J. Sort, *RSC Adv.*, 2015, **5**, 32369–32375.
- 8 A. Boixassa, J. Pons, A. Virgili, X. Solans, M. Font-Bardia and J. Ros, *Inorganica Chim. Acta*, 2002, **340**, 49–55.
- 9 A. Boixassa, J. Pons, X. Solans, M. Font-Bardia and J. Ros, *Inorganica Chim. Acta*, 2003, **355**, 254–263.
- 10 M. Guerrero, J. Pons, M. Font-Bardia, T. Calvet and J. Ros, *Aust. J. Chem.*, 2010, **63**, 958.
- 11 M. Guerrero, J. Pons, J. Ros, M. Font-Bardia, O. Vallcorba, J. Rius, V. Branchadell and A. Merkoçi, *CrystEngComm*, 2011, **13**, 6457.
- 12 F. Bondavalli, O. Bruno, A. Ranise, P. Schenone, P. Addonizio, V. De Novellis, A. Loffreda and E. Marmo, *Farm. Ed. Sci.*, 1988, **43**, 725–743.
- 13 S. Muñoz, J. Pons, J. Ros, M. Font-Bardia, C. A. Kilner and M. A. Halcrow, *Inorganica Chim. Acta*, 2011, **373**, 211–218.
- 14 M. Guerrero, T. Calvet, M. Font-Bardia and J. Pons, *Polyhedron*, 2016, **119**, 555–562.
- 15 S. Muñoz, J. Pons, J. García-Antón, X. Solans, M. Font-Bardia and J. Ros, *J. Coord. Chem.*, 2009, **62**, 3940–3950.

- 16 K. Deka, M. Laskar and J. B. Baruah, *Polyhedron*, 2006, **25**, 2525–2529.
- 17 W. J. Geary, *Coord. Chem. Rev.*, 1971, **7**, 81–122.
- 18 K. Nakamoto, *Handb. Vib. Spectrosc.*, 2006, 1872–1892.
- 19 A. B. P. Lever, E. Mantovani and B. S. Ramaswamy, *Can. Journal Chem.*, 1971, **49**, 1957–1963.
- 20 G. Deacon, *Coord. Chem. Rev.*, 1980, **33**, 227–250.
- 21 S. Kumar, R. Pal Sharma, P. Venugopalan, V. Singh Gondil, S. Chhibber, T. Aree, M. Witwicki and V. Ferretti, *Inorganica Chim. Acta*, 2018, **469**, 288–297.
- 22 D. Sutton, *Electronic Spectra of Transition Metal Complexes*, McGraw Hill Publishing Company Ltd., Maidenhead, Berkshire, England, First., 1975.
- 23 F. Sánchez-Férez, M. Guerrero, J. A. Ayllón, T. Calvet, M. Font-Bardia, J. G. Planas and J. Pons, *Inorganica Chim. Acta*, 2019, **487**, 295–306.
- 24 S. S. Massoud, L. Le Quan, K. Gatterer, J. H. Albering, R. C. Fischer and F. A. Mautner, *Polyhedron*, 2012, **31**, 601–606.
- 25 A. W. Addison, T. N. Rao, J. Reedijk, J. van Rijn and G. C. Verschoor, *J. Chem. Soc., Dalt. Trans.*, 1984, 1349–1356.
- 26 J. C. Friese, A. Krol, C. Puke, K. Kirschbaum and D. M. Giolando, *Inorg. Chem.*, 2000, **39**, 1496–1500.
- 27 P. M. Morse and G. S. Girolami, *J. Am. Chem. Soc.*, 1989, **111**, 4114–4116.
- 28 G. J. Kleywegt, W. G. R. Wiesmeijer, G. J. Van Driel, W. L. Driessen, J. Reedijk and J. H. Noordik, *J. Chem. Soc., Dalt. Trans.*, 1985, **53**, 2177–2184.
- 29 J. R. Cubanski, S. A. Cameron, J. D. Crowley and A. G. Blackman, *Dalt. Trans.*, 2013, **42**, 2174–2185.
- 30 R. Pothiraja, M. Sathiyendiran, A. Steiner and R. Murugavel, *Inorganica Chim. Acta*, 2011, **372**, 347–352.
- 31 W. L. Driessen, S. Gorter, W. G. Haanstra, L. J. J. Laarhoven, J. Reedijk, K. Goubitz and F. R. Seljée, *Recl. des Trav. Chim. des Pays-Bas*, 2010, **112**, 309–313.
- 32 A. S. Potapov, E. A. Nudnova, G. A. Domina, L. N. Kirpotina, M. T. Quinn, A. I. Khlebnikov and I. A. Schepetkin, *Dalt. Trans.*, 2009, 4488.
- 33 W. L. Driessen, B. Maase, J. Reedijk, H. Kooijman, M. T. Lakin and A. L. Spek,

- Inorganica Chim. Acta*, 2000, **300–302**, 1099–1103.
- 34 C. Di Nicola, A. Tombesi, M. Moroni, R. Vismara, F. Marchetti, R. Pettinari, L. Nardo, G. Vesco, S. Galli, S. Casassa, L. Pandolfo and C. Pettinari, *CrystEngComm*, 2020, **22**, 3294–3308.
- 35 J.-P. Zhang, Y. Zhang, J. Lin and X. Chen, *Chem. Rev.*, 2012, **112**, 1001–1033.
- 36 G. Esquiús, J. Pons, R. Yáñez, J. Ros, X. Solans and M. Font-Bardía, *Acta Crystallogr. Sect. C Cryst. Struct. Commun.*, 2002, **58**, m133–m134.
- 37 J. Pons, A. Chadghan, A. Alvarez-Larena, J. Francesc Piniella and J. Ros, *Inorg. Chem. Commun.*, 2001, **4**, 610–612.
- 38 J. Pons, A. Chadghan, J. Casabó, A. Alvarez-Larena, J. Francesc Piniella and J. Ros, *Inorg. Chem. Commun.*, 2000, **3**, 296–299.
- 39 J. Pons, X. López, E. Benet, J. Casabó, F. Teixidor and F. J. Sánchez, *Polyhedron*, 1990, **9**, 2839–2845.
- 40 J. Casabó, J. Pons, K. S. Siddiqi, F. Teixidor, E. Molins and C. Miravittles, *J. Chem. Soc. Dalt. Trans.*, 1989, **6**, 1401–1403.
- 41 A. K. Das, A. De, P. Yadav, F. Lloret and R. Mukherjee, *Polyhedron*, 2019, **171**, 365–373.
- 42 T. L. Hu, J. R. Li, C. Sen Liu, X. S. Shi, J. N. Zhou, X. H. Bu and J. Ribas, *Inorg. Chem.*, 2006, **45**, 162–173.
- 43 X. B. Liu, D. H. Huan, G. H. Cui and L. H. Han, *J. Struct. Chem.*, 2015, **56**, 1124–1129.
- 44 M. J. Hallam, C. A. Kilner and M. A. Halcrow, *Acta Crystallogr. Sect. C Cryst. Struct. Commun.*, 2002, **58**, 445–446.
- 45 J. Pons, X. López, J. Casabó, F. Teixidor, A. Caubet, J. Rius and C. Miravittles, *Inorganica Chim. Acta*, 1992, **195**, 61–66.
- 46 S. Roeser, S. Maji, J. Benet-Buchholz, J. Pons and A. Llobet, *Eur. J. Inorg. Chem.*, 2013, **2013**, 232–240.
- 47 J. A. Perez, J. Pons, X. Solans, M. Font-Bardía and J. Ros, *Inorganica Chim. Acta*, 2005, **358**, 617–622.
- 48 J. Pons, A. Chadghan, J. Casabó, A. Alvarez-Larena, J. F. Piniella, X. Solans, M. Font-Bardía and J. Ros, *Polyhedron*, 2001, **20**, 1029–1035.

- 49 J. Pons, A. Chadghan, A. Alvarez-Larena, J. F. Piniella and J. Ros, *Inorganica Chim. Acta*, 2001, **324**, 342–346.
- 50 A. Chadghan, J. Pons, A. Caubet, J. Casabó, J. Ros, A. Alvarez-Larena and J. Francesc Piniella, *Polyhedron*, 2000, **19**, 855–862.
- 51 L. Yang, D. R. Powell and R. P. Houser, *J. Chem. Soc. Dalt. Trans.*, 2007, 955–964.
- 52 W.-B. Shi, A.-L. Cui and H.-Z. Kou, *CrystEngComm*, 2014, **16**, 8027.
- 53 S. Tanase, E. Bouwman, G. J. Long, A. M. Shahin, R. De Gelder, A. M. Mills, A. L. Spek and J. Reedijk, *Polyhedron*, 2005, **24**, 41–48.
- 54 M. A. Spackman and D. Jayatilaka, *CrystEngComm*, 2009, **11**, 19–32.
- 55 F. H. Allen, *Acta Crystallogr. Sect. B Struct. Sci.*, 2002, **58**, 380–388.
- 56 B. Bleaney and K. D. Bowers, *Proc. R. Soc. London. Ser. A. Math. Phys. Sci.*, 1952, **214**, 451–465.
- 57 L. Merz and W. Haase, *J. Chem. Soc. Dalt. Trans.*, 1980, **74**, 875.
- 58 E. Ruiz, P. Alemany, S. Alvarez and J. Cano, *J. Am. Chem. Soc.*, 1997, **119**, 1297–1303.
- 59 E. Ruiz, P. Alemany, S. Alvarez and J. Cano, *Inorg. Chem.*, 1997, **36**, 3683–3688.
- 60 V. H. Crawford, H. W. Richardson, J. R. Wasson, D. J. Hodgson and W. E. Hatfield, *Inorg. Chem.*, 1976, **15**, 2107–2110.
- 61 H. Hu, D. Zhang, Z. Chen and C. Liu, *Chem. Phys. Lett.*, 2000, **329**, 255–260.

3.3 Synthesis and characterization of Zn(II), Cd(II), Hg(II), Co(II), Cu(II) and Pd(II) coordination compounds with *N*-pyrazole, *O*-ether hybrid ligands

This chapter consists of three sections. The first section describes the reactivity of **L4** and **L5** against several $MCl_2 \cdot X(H_2O)$ salts ($M = Zn(II), Cd(II), Hg(II), Cu(II), X = 0$; $M = Co(II), X = 6$), which resulted in the isolation of ten new coordination compounds. All compounds have been fully characterized *via* analytical and spectroscopic techniques. The crystal structure of nine compounds has been elucidated, allowing the detailed study of its molecular and supramolecular network. Finally, the coordination behaviour of **L4** and **L5** has been parametrized, aiming to export the gained knowledge to the future fine-tuning of coordination compounds bearing new architectures. Part of this work has been published in **article 2** (*vide infra*).

In the second section, preliminary results concerning the reactivity of **L6-L8** against $[Pd(CH_3CN)_2Cl_2]$, which yielded four new coordination compounds, are described.

The last section summarizes the work carried out in this chapter

Article 2: “*Dimeric Metallacycles and coordination polymers: Zn(II), Cd(II) and Hg(II) complexes of two positional isomers of a flexible N,O-hybrid bispyrazole derived ligand*”.

Joan Soldevila-Sanmartín, Miguel Guerrero, Duane Choquesillo-Lazarte, José Giner Planas, Josefina Pons.

Inorganica Chimica Acta 506 (2020) 119549

3.3.1 Zn(II), Cd(II), Hg(II), Co(II) and Cu(II) compounds with L4 and L5

Our group has been interested in the synthesis of coordination compounds bearing flexible *N,X*-hybrid bispyrazole ligands for several years. In fact, ligands bearing different functional groups such as amines^{1,2}, sulfones/sulfoxides³, thioethers^{4,5} or ethers^{6,7,8} have been synthesized, and their reactivity against different metal salts studied.

One of these studies was carried out on the coordination behavior of a family of bispyrazole-ether ligands (including 1,4-bis([4-3,5-dimethyl-1*H*-pyrazol-2-yl)-2-oxabutyl]benzene (**L4**) and its positional isomer 1,2-bis([4-3,5-dimethyl-1*H*-pyrazol-2-yl)-2-oxabutyl]benzene (**L5**)) against Pd(II)⁹. The resulting complexes had either a dimeric metallacyclic or a monomeric structure. Moreover, despite the ligand ability to adopt *syn*- or *anti*- conformations, only the first one was observed (Fig. 3.3.1).

In the light of these results, we assayed the reactivity of **L4** and **L5** ligands against coordinatively flexible metal centres such as Zn(II), Cd(II), Hg(II), Co(II) and Cu(II), hoping to obtain new structural motifs for the resulting complexes and to observe new coordination behaviours in the aforementioned ligands.

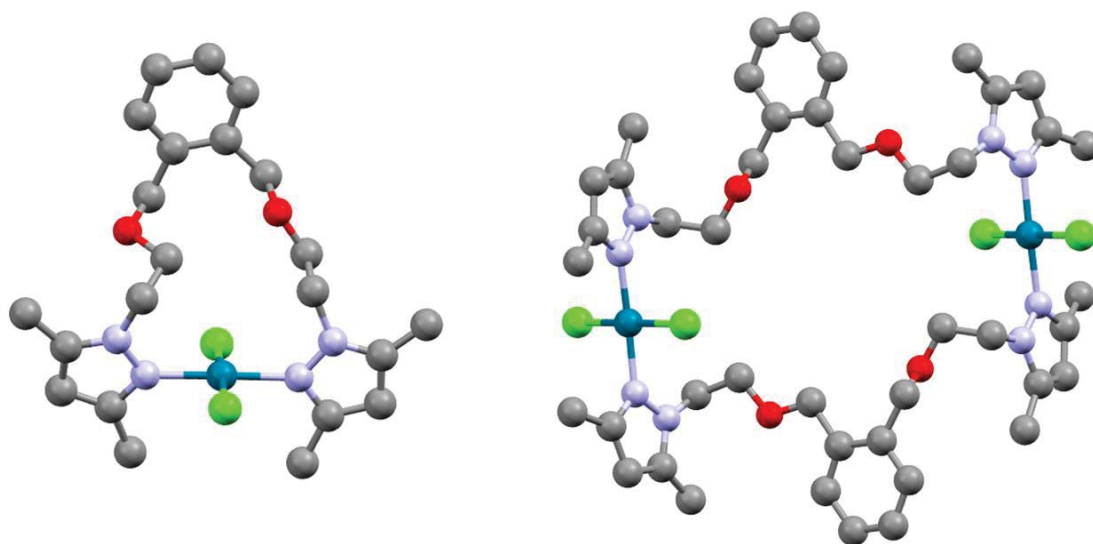
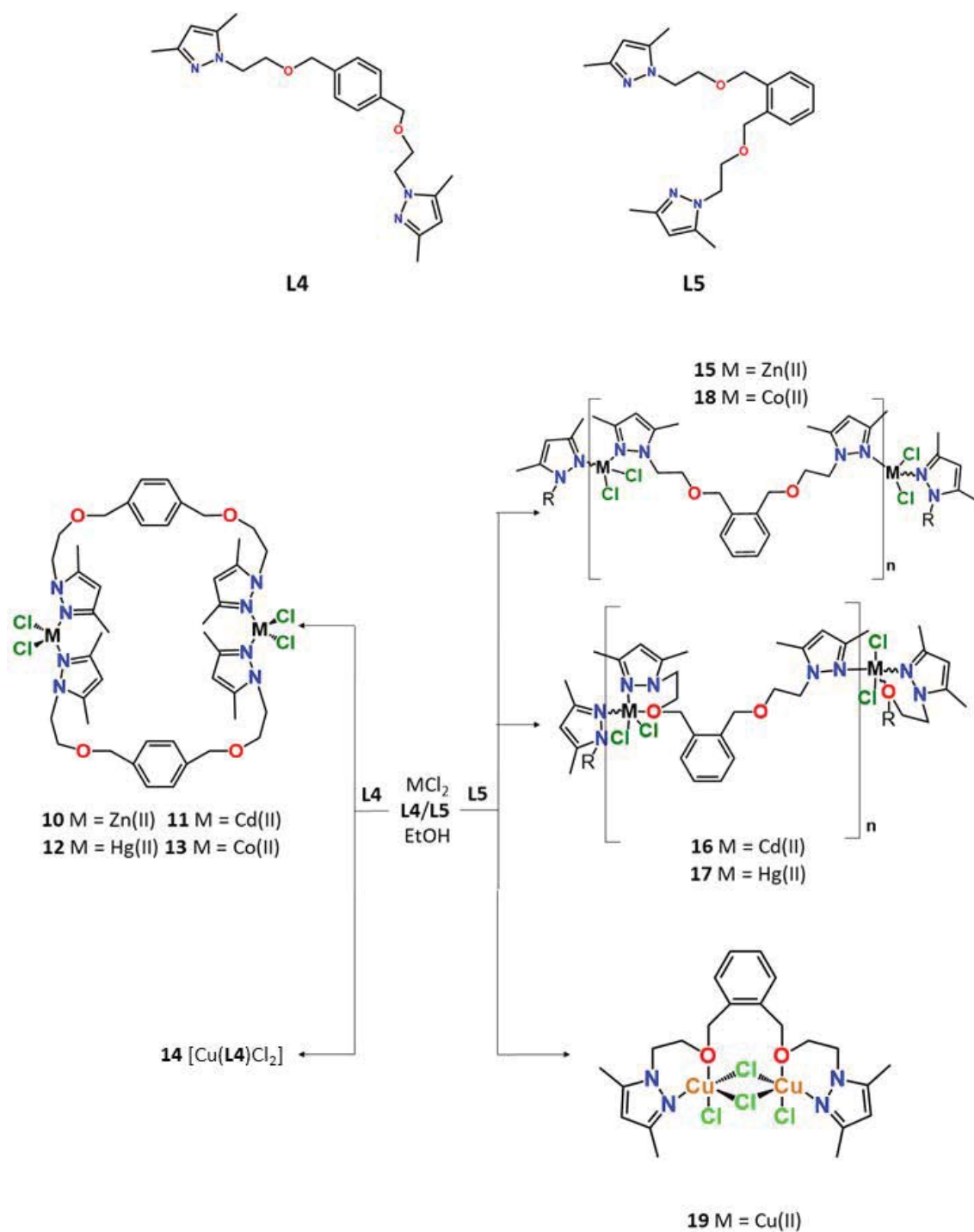


Figure 3.3.1 Previously reported Pd(II) compounds bearing **L5**⁹.

3.3.1.1 Synthesis

The assay of the reactivity of **L4** and **L5** against $MCl_2 \cdot X(H_2O)$ salts ($M = Zn(II)$, $Cd(II)$, $Hg(II)$, $Cu(II)$, $X = 0$; $M = Co(II)$, $X = 6$) resulted in the isolation of ten new coordination compounds (Scheme 3.3.1).



Scheme 3.3.1. Synthetic reactions carried out in this section. Compounds are shown with their numbering scheme. Compounds' **13** and **15-17** occluded solvents have been removed for clarity.

For the synthesis of these complexes, an ethanolic solution of the corresponding $MCl_2 \cdot X(H_2O)$ salt ($M = Zn(II), Cd(II), Hg(II), Cu(II), X = 0$; $M = Co(II), X = 6$) is added dropwise to an ethanolic solution of the corresponding ligand (**L4** or **L5**) in a 1:1 metal to ligand ratio (Scheme. 3.3.1). The solutions were stirred for 48 h. at room temperature (RT), except for the reactions involving $Co(II)$, which required reflux conditions. Next, the solutions were concentrated and left to evaporate, resulting in the precipitation of small microcrystals, which were filtered off, washed with cold Et_2O and dried under vacuum. The solutions involving $CuCl_2$ displayed a differential behaviour, as a green precipitate appeared immediately, which was filtered off, cleaned with Et_2O and dried under vacuum.

Single crystal suitable for X-ray diffraction for **L4** and **L5** compounds with $Zn(II)$, $Cd(II)$, $Hg(II)$ or $Cu(II)$ metal centres were obtained *via* recrystallization in $EtOH$. Compounds containing $Co(II)$ required more sophisticated crystallization techniques, such as recrystallizing in solvent mixtures ($CHCl_3:MeOH:acetone$ for **13**) or layering (hexane over CH_2Cl_2 for **18**). The elucidation of their crystal structure revealed that compounds containing **L4** are isostructural dimeric metallacycles of general formula $[M(L4)Cl_2]_2$ ($M = Zn(II)$ (**10**), $Cd(II)$ (**11**) and $Hg(II)$ (**12**)) which can sometimes contain occluded solvent molecules as in **13** (whose formula is then $[M(L4)Cl_2]_2 \cdot 1/2H_2O$, $M = Co(II)$). On the other hand, those containing **L5** are mostly coordination polymers of general formula $\{[M(L5)Cl_2] \cdot 1/2Solvent\}_n$ ($M = Zn(II)$ (**15**) or $Co(II)$ (**18**), Solvent = H_2O ; $M = Cd(II)$ (**16**) or $Hg(II)$ (**17**), Solvent = $EtOH$). Surprisingly, compound **19**, containing $Cu(II)$, is a dimer of formula $[Cu_2(L5)Cl_4]$. Unfortunately, single crystals suitable for SCXRD for **14** have not been obtained. All compounds were obtained in moderate to good yields (61.7-92.9 %), except for **18** (41.8 %) and **17** (24.5 %).

3.3.1.2 Characterization

Phase purity of compounds **10-19** has been confirmed *via* Powder X-ray diffraction (Fig. S3.3.1-S3.3.10). They have also been characterized *via* Elemental analyses (EA), FTIR-ATR spectroscopy, 1H and $^{13}C\{^1H\}$ NMR spectroscopy when possible and UV-Vis spectroscopy. For compounds **10** and **15-17** DOSY NMR spectra were also recorded. EA for compounds **10-13** and **15-19** agree with the proposed

molecular formulae, whereas for compound **14** agrees with a $[\text{Cu}(\text{L4})\text{Cl}_2]$ molecular formulae.

- FTIR-ATR Spectroscopy

For compounds **10-19**, recorded FTIR-ATR spectra show characteristic pyrazole-derived ligand bands. The most intense are those attributable to $[\nu(\text{C}=\text{C}/\text{C}=\text{N})_{\text{ar}}]$, $[\delta(\text{C}=\text{C}/\text{C}=\text{N})_{\text{ar}}]$, $[\delta(\text{C}-\text{H})_{\text{ip}}]$ and $[\delta(\text{C}-\text{H})_{\text{oop}}]$ of the pyrazolyl group¹⁰. Moreover, the $[\nu(\text{C}-\text{O}-\text{C})]$ band of the ether groups is also identifiable¹⁰. For those compounds possessing occluded solvents in their crystal structure (**13**, **15-18**) signals attributable to $[\nu(\text{O}-\text{H})]$ are noticeable. In FTIR-ATR spectrum of **13**, **15** and **18**, it appears as a broad band between $3600\text{-}3200\text{ cm}^{-1}$, attributable to H_2O molecules¹⁰, whereas for **16** and **17** those bands are much narrower and appear at 3496 and 3515 cm^{-1} respectively, attributed to occluded EtOH molecules¹⁰. As an example, FTIR-ATR spectrum of compound **16** is shown, with relevant bands listed (Fig. 3.3.2), while the spectra of the rest of compounds can be found in Annex I (Fig. S3.3.11-S3.3.19).

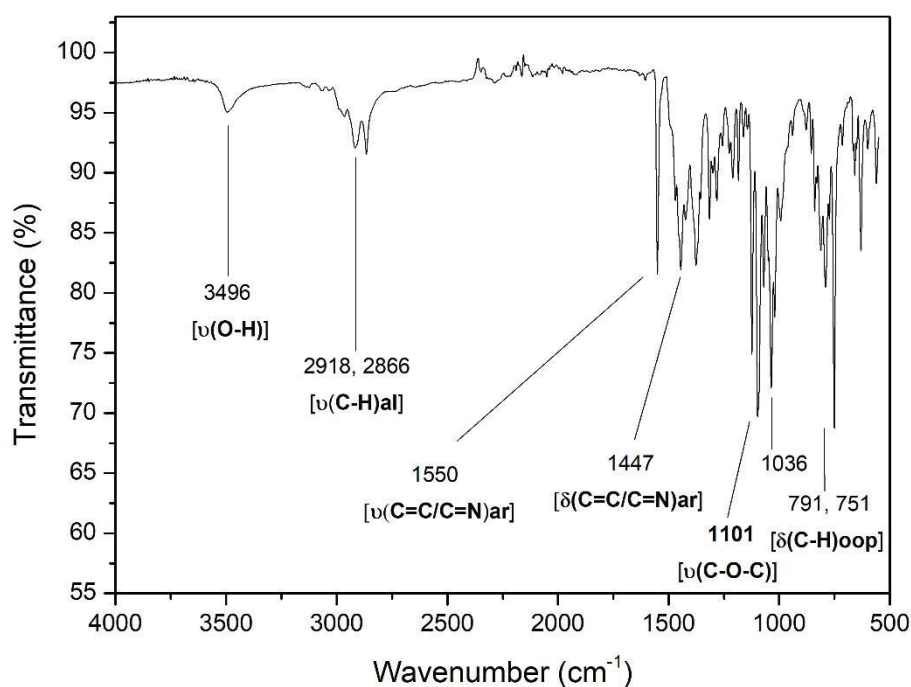


Figure 3.3.2 FTIR-ATR spectra of compound **16**

- NMR Spectroscopy

All ^1H and $^{13}\text{C}\{^1\text{H}\}$ NMR spectra have been recorded in CDCl_3 for compounds **10-12** and **15-17**. For pyrazolyl derived ligands, coordination to metal centre is easily

detected in ^1H NMR spectra as an upfield displacement of the 1-*H* pyrazolyl proton ligand (5.79-5.97 ppm for **10-12** and **15-17** vs. 5.77 (**L4**) and 5.74 (**L5**) ppm for the free ligands⁹). The upfield displacement of the signal corresponding to the $-\text{CH}_2-\text{N}_{\text{pz}}$ fragment at 4.17-4.67 ppm for the compounds vs. 4.14 and 4.12 ppm for **L4** and **L5**⁹, respectively, is also telling of the coordination to the metal centre. Regarding the phenyl proton signals, they appear mostly as a singlet for **10-12** or as a multiplet for **15-17** (7.15-7.26 ppm). The protons of the $-\text{OCH}_2\text{CH}_2\text{Pz}-$ fragment appear as triplets (4.17-4.67 ppm and 3.71-3.84 ppm) with $J = 5.2\text{-}5.7$ Hz, except for Zn(II) complexes (**10** and **15**) where they appear as broad bands. The ^1H NMR spectra of **11** is provided as an example, showing proton assignment (Fig. 3.3.3), while the rest of the spectra can be found in Annex I (Fig. S3.3.20-S3.3.24).

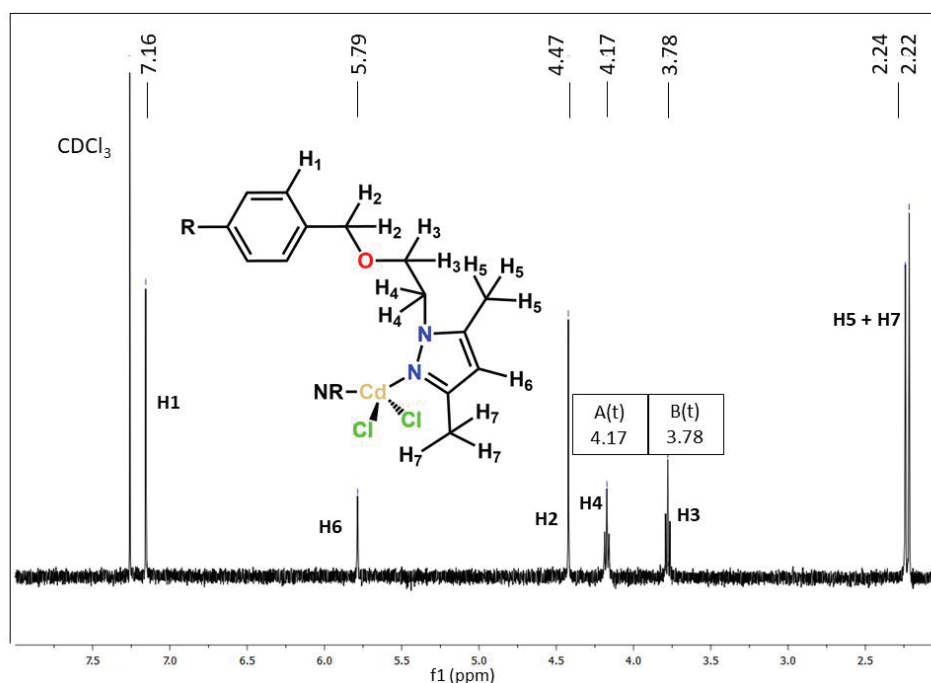


Figure 3.3.3 ^1H NMR spectrum of **11** (CDCl_3 , 400.0 MHz)

For the $^{13}\text{C}\{^1\text{H}\}$ NMR spectra, the coordinated ligands show an upfield displacement of the pyrazolyl carbon (105.6-107.4 ppm vs. 104.9-105.2 ppm in the free ligands) as well as the signals corresponding to the $-\text{O}-\text{CH}_2-\text{Ph}$ fragment in compounds **10-12** (73.1-73.8 ppm vs. 70.7 in **L4**⁹). However, for compounds **15-17**, the same carbon signal shows a downfield displacement (69.9-71.8 ppm vs. 73.2 ppm in **L5**⁹). The $^{13}\text{C}\{^1\text{H}\}$ NMR spectra of **11** is provided as an example, showing carbon assignment (Fig. 3.3.4), while the rest of the spectra can be found in Annex I (Fig. S3.3.25-S3.3.29).

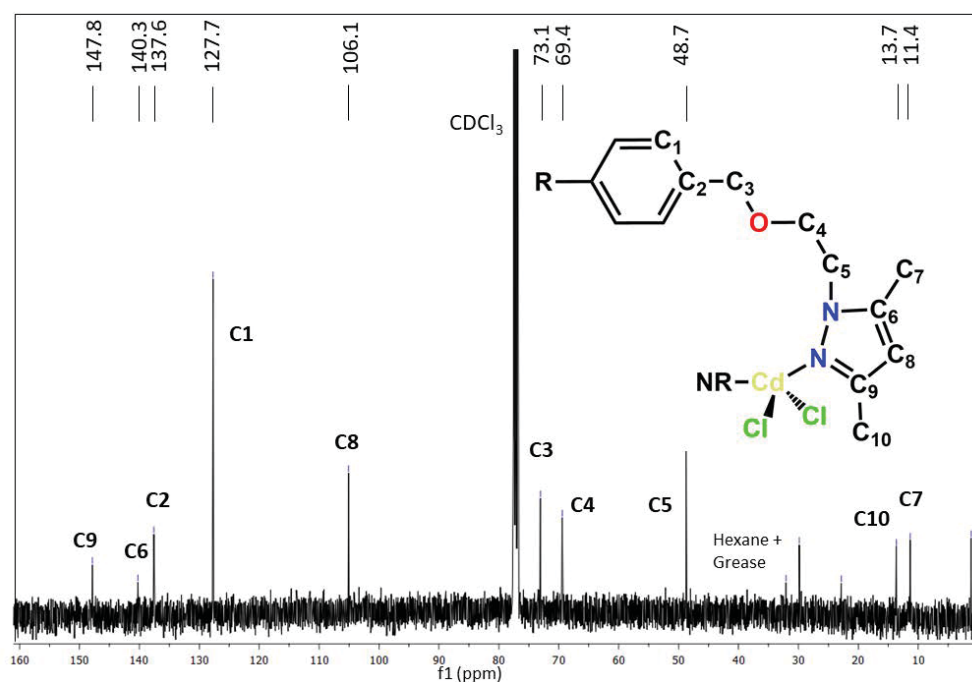


Figure 3.3.4 $^{13}\text{C}\{^1\text{H}\}$ NMR spectra of compound **11** (CDCl_3 , 100.6 MHz)

In order to elucidate if compounds **15–17** remain as polymers in solution, DOSY NMR experiments were carried out in CDCl_3 at RT, which is a powerful tool for studying the behaviour of coordination compounds in solution^{11,12}. Moreover, DOSY NMR spectrum of **10** was carried out for comparison purposes.

It was found that the diffusion coefficient for polymers **15** and **17** were much higher than for the dimeric species in **10** ($D = 16.3 \cdot 10^{-10} \text{ m}^2\text{s}^{-1}$ (**15**) and $D = 8.95 \cdot 10^{-10} \text{ m}^2\text{s}^{-1}$ (**17**) vs. $D = 6.83 \cdot 10^{-10} \text{ m}^2\text{s}^{-1}$ (**10**)). This data suggests that the hydrodynamic radii of **15** and **17** in solution are smaller than **10**. If compound **10** maintains a dimeric structure in solution, those smaller species in **15** and **17** could be attributed to monomers. Compound **16**, on the other hand, displays a more sophisticated spectrum with severe line broadening, where two diffusion peaks were identified. The first one at higher value than **10** ($14.1 \cdot 10^{-10} \text{ m}^2\text{s}^{-1}$) and the second one at a lower value ($6.59 \cdot 10^{-10} \text{ m}^2\text{s}^{-1}$). Integration of those peaks, however, reveals that the one at $14.1 \cdot 10^{-10} \text{ m}^2\text{s}^{-1}$ is fifty-two times more intense than the one at $6.59 \cdot 10^{-10} \text{ m}^2\text{s}^{-1}$. This data suggests that **16** undergoes a monomeric-dimeric species equilibrium in solution, although it is heavily tilted towards the monomeric species.

The obtained diffusion peaks and the MW estimated using the model proposed by Evans *et al.* (Eq. 1¹³). In this equation, MW and MW_S stand for the solute and solvent

MW respectively, η for the viscosity parameter, K_B for the Boltzmann constant and N_A for the Avogadro number. The parameter α is defined as the cubic root of the molecular weight of the solvent divided by the molecular weight of the solute. Lastly, ρ_{eff} is an empirical parameter whose value has been optimized for CDCl_3 at 647 Kg m^{-3} ¹³. Further optimization is required for calculations in CDCl_3 , establishing an effective MW_s value of 83 g mol^{-1} ¹³. Results are reported on Table 3.3.1. The resulting spectra can be found Annex I (Fig. S3.3.30-S3.3.33)

$$D = \frac{K_B T \left(\frac{3\alpha}{2} + \frac{1}{1+\alpha} \right)}{6\pi\eta \sqrt[3]{\frac{3MW}{4\pi\rho_{\text{eff}}N_A}}}, \quad \text{where } \alpha = \sqrt[3]{\frac{MW_s}{MW}}$$

Equation 1¹³Table 3.3.1 DOSY NMR results for compounds **10** and **15-17**

	$D \text{ (m}^2\text{s}^{-1}\text{)}$	MW (g mol ⁻¹)	
		Estimated	Theoretical
10	$6.83 \cdot 10^{-10}$	917	1037.54
15	$16.3 \cdot 10^{-10}$	Severely underestimated	527.78 ⁱ
16	$14.1 \cdot 10^{-10}$	Severely underestimated	588.9 ⁱ
	$6.59 \cdot 10^{-10}$	995	1177.7 ⁱ
17	$8.95 \cdot 10^{-10}$	510	677.02 ⁱ

ⁱ Theoretical values are calculated accounting for a hypothetical monomeric structure in **15** and **17**, and both a monomeric and a dimeric one in **16**.

For compound **10** an estimated MW of 917 g mol^{-1} is obtained ($1037.54 \text{ g mol}^{-1}$), which suggests the conservation of its dimeric structure in solution. For **16**, the diffusion peak at $D = 6.59 \cdot 10^{-10} \text{ m}^2\text{s}^{-1}$ results in an estimated MW of 995 g mol^{-1} ($1177.7 \text{ g mol}^{-1}$ for dimeric **16**), suggesting a dimeric species, whereas for **17** its only diffusion peak results in an estimated MW of 510 g mol^{-1} , suggesting a monomeric species ($677.02 \text{ g mol}^{-1}$ for monomeric **17**). This model, however, severely underestimated the MW of lighter, monomeric species of **15** and **16**. In any case, this data qualitatively supports the reversion of polymeric compounds to monomeric and dimeric species in solution. Note

that the model used for MW estimates severely underestimates the MW of lighter species^{13,14} as seen in **15** and **16** and is not optimized for calculation involving heavy atoms¹⁴.

- UV-Vis Spectroscopy and photoluminescent properties

UV-Vis electronic spectra of the complexes bearing Zn(II), Cd(II) and Hg(II) (**10-12** and **15-17**) metal centres and ligands **L4** and **L5** were recorded on CH₃CN ($\sim 1.1 \cdot 10^{-6}$ M for **10-12** and $\sim 3 \cdot 10^{-6}$ M for **15-17**) at RT. (Fig S3.3.34 and S3.3.35). The d^{10} configuration in Zn(II), Cd(II), and Hg(II) metal centres only allows Charge Transfer (CT) transitions either between the metal and the ligand or by the ligand itself¹⁵. Compounds **10-12** and **15-17** display said CT between 200 nm and 280 nm, featuring small shoulders around 220, 250 and 275 nm.

For compounds bearing Co(II) metal centres, UV-Vis electronic spectra have been recorded in acetone (**13**) or CH₂Cl₂ (**18**) at $\sim 1.1 \cdot 10^{-3}$ M concentrations at RT. (Fig. S3.3.36). The spectra of **13** and **18** are similar, both showing one band at 664/651 nm and a shoulder at 585/587 nm. These bands can be attributed to $^4A_{2g}$ to $^4T_{1g}$ transitions for Co(II) atoms in a distorted tetrahedral geometry¹⁶⁻¹⁸, which is in agreement with its elucidated crystal structure.

UV-Vis electronic spectrum of compounds bearing Cu(II) metal centres (**14** and **19**) has been recorded in MeOH at $\sim 1.1 \cdot 10^{-3}$ M concentrations at RT (Fig. S3.3.37). For compound **19**, two distinct bands at 678 and 867 nm can be identified. For square pyramidal Cu(II) compounds their visible spectra may show occasionally a low energy shoulder ($\lambda > 800$ nm) associated to the main broad band between 550-700 nm^{18,19}. Thus, the signal at 660 nm can be attributed to 2E_g to 2T_g transitions in a square pyramidal Cu(II)^{16,20} which is in agreement with its elucidated crystal structure. On the other hand, the spectrum recorded for **14** shows only a single band centred at 875 nm. The presence of a single band at $\lambda > 800$ nm, is clearly indicative of a Cu(II) compound with a trigonal bipyramidal geometry²⁰. All ϵ values are consistent with Laporte-forbidden transitions²⁰.

The fluorescent emission spectra for **L4**, **L5**, **10-12** and **15-17** were recorded between 270 nm and an excitation wavelength of 260 nm in spectroscopic grade CH₃CN at RT. All compounds show emission bands in the range of 282-286 nm. However, only Hg(II) compounds show a slight fluorescence enhancement effect, which is stronger in compound **17** (Fig. S3.3.38).

3.3.1.3 Crystal and Extended structures

The reaction of **L4** and **L5** with MCl_2 ($M = Zn(II)$, $Cd(II)$, $Hg(II)$ and $Cu(II)$) and $CoCl_2 \cdot 6H_2O$ yielded ten new coordination compounds of general formula $[M(L4)Cl_2]_2$ ($M = Zn(II)$ (**10**), $Cd(II)$ (**11**) and $Hg(II)$ (**12**) or $[Co(L4)Cl_2]_2 \cdot 1/2(H_2O)$ (**13**)) or $\{[M(L5)Cl_2] \cdot 1/2Solvent\}_n$ ($M = Zn(II)$ (**15**) or $Co(II)$ (**18**), Solvent = H_2O ; $M = Cd(II)$ (**16**) or $Hg(II)$ (**16**), Solvent = $EtOH$) and $[Cu_2(L5)Cl_4]$. Suitable crystals for X-ray diffraction were obtained *via* recrystallization in $EtOH$ for twelve days to one month (**10-12**, **15-16** and **19**) or eleven days in the fridge (**17**). For compounds containing $Co(II)$ metal centers, more complex crystallization techniques were required, such as using mixtures ($CHCl_3:MeOH:acetone$ (1:1:1 ratio, **13**) or layering a CH_2Cl_2 solution with hexane (**18**).

Crystal and Extended Structures of compounds 10-13

Compounds **10-13** share the same $[M(L4)Cl_2]_2$ ($M = Zn(II)$ (**10**), $Cd(II)$ (**11**), $Hg(II)$ (**12**) and $Co(II)$ (**13**)) general formula, except for the presence of one occluded water molecule per two dimers in **13**. They are isostructural compounds, two **L4** moieties coordinating as *NN'*-bridged ligands with a *syn* configuration, resulting in a M_2L_2 dimeric metalacyclic motif of thirty-four members (Fig. 3.3.6). The metal centres have a distorted tetrahedral coordination environment ($\tau_4 = 0.88$ to 0.94 ; 1.00 being perfect tetrahedral geometry and 0.00 perfect square planar geometry)²¹ comprising two chlorine atoms and two nitrogen atoms. A search in the CSD²² reveals that while there are sixty-one reported structures bearing a $[Zn(N_{pz})_2Cl_2]$ core and fifty-one bearing a $[Co(N_{pz})_2Cl_2]$, there are only four bearing a $[Hg(N_{pz})_2Cl_2]$ core and none bearing a $[Cd(N_{pz})_2Cl_2]$ one. Moreover, only one $Zn(II)$ structure (1.64%)²³ and one $Co(II)$ structures (1.96%)²⁴ possess the dimeric metallacycle motif, while none of the $Cd(II)$ or $Hg(II)$ structures bear this motif. Selected bond lengths and angles for **10-13** are reported on Table 3.3.2. All bond lengths and angles agree with similar compounds reported in the literature^{7,8,23-26}.

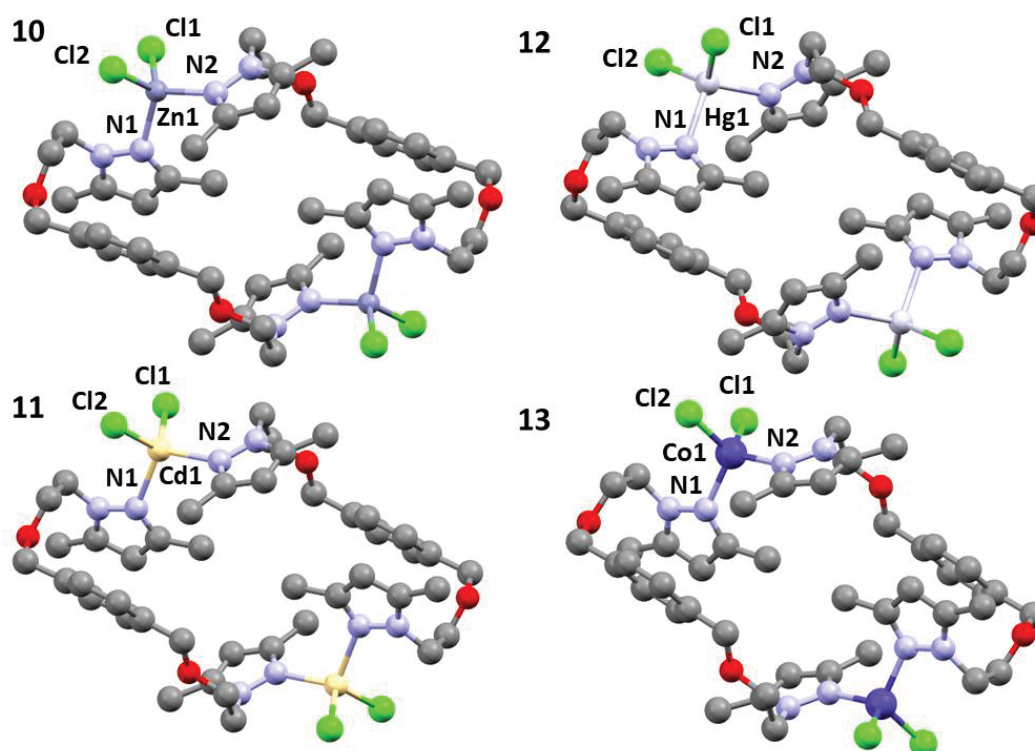


Figure 3.3.5 Dimeric metalacyclic motif in compounds **10-13**, showing all their non-hydrogen atoms and numbering scheme. Compound's **13** occluded water molecules have been removed for clarity. Colour code: grey (C), white (H), light blue (N), red (O), light green (Cl), blue-grey (Zn), bone (Cd), light-grey (Hg), blue (Co).

Table 3.3.2 Selected bond distances (Å) and angles (°) for compounds **10-13**

	10	11	12	13
Bond lengths (Å)				
M(1)-N(1)	2.062(2)	2.258(4)	2.270(6)	2.0345(9)
M(1)-N(2)#1	2.035(2)	2.234(4)	2.331(6)	2.0418(9)
M(1)-Cl(1)	2.2485(7)	2.4277(12)	2.4216(16)	2.2534(3)
M(1)-Cl(2)	2.2563(7)	2.4236(12)	2.4403(16)	2.2613(3)
M(1)···M(1)#1	9.3697(6)	9.5206(7)	9.6635(6)	9.3262(6)
Bond angles (°)				
Cl(1)-M(1)-Cl(2)	113.09(2)	116.75(4)	122.45(6)	112.615(12)
N(2)#1-M(1)-Cl(1)	115.23(7)	112.48(11)	114.16(16)	100.21(3)
N(2)#1-M(1)-Cl(2)	104.59(6)	100.31(11)	102.93(15)	115.75(3)
N(1)-M(1)-Cl(2)	114.57(6)	109.88(15)	107.8(2)	114.88(3)
N(1)-M(1)-Cl(1)	100.45(6)	104.50(10)	98.52 (15)	103.65(3)
N(1)-M(1)-N(2)#1	109.23(8)	113.04(12)	110.47(15)	110.21(4)
#1: -x+1, -y+1, -z+1				

Those metalacyclic compounds are highly reminiscent of the previously reported $[\text{Pd}(\text{L5})\text{Cl}_2]^9$. However, while $[\text{Pd}(\text{L5})\text{Cl}_2]$ has an “open” ring-like structure, allowing for it to be nanoporous⁹, compounds **10–13** are “folded”, which is evinced by the angle between the mean planes of pyrazolyl moieties belonging to the same ligand (87.11° – 89.13° in **10–13**, 10.58° in $[\text{Pd}(\text{L5})\text{Cl}_2]$). These “open” or “folded” conformations owe to the coordination geometry around the metal center, as the tetrahedral geometry in **10–13** promotes a twisting of the pyrazolyl rings, which is prevented in the *trans*- square planar coordination geometry of the Pd(II) compounds⁹.

Although the molecular structures of **10–13** are alike, the presence of occluded water molecules in **13** greatly influence their supramolecular structure. As such, they will be described separately. For **10–12**, their extended structure can be described as a close packing of M_2L_2 rings. Each ring is connected to six other rings *via* intermolecular interactions, forming a three-dimensional lattice (Fig. 3.3.7 and S3.3.39). This supramolecular arrangement is held together by $\text{C-H}\cdots\pi$ interactions between pyrazolyl moieties and both phenyl rings and ether chains. Furthermore, interactions involving chlorine atoms and pyrazolyl methyl moieties are also key in sustaining the supramolecular network. Relevant non-bonding interactions are summarized in Table 3.3.3.

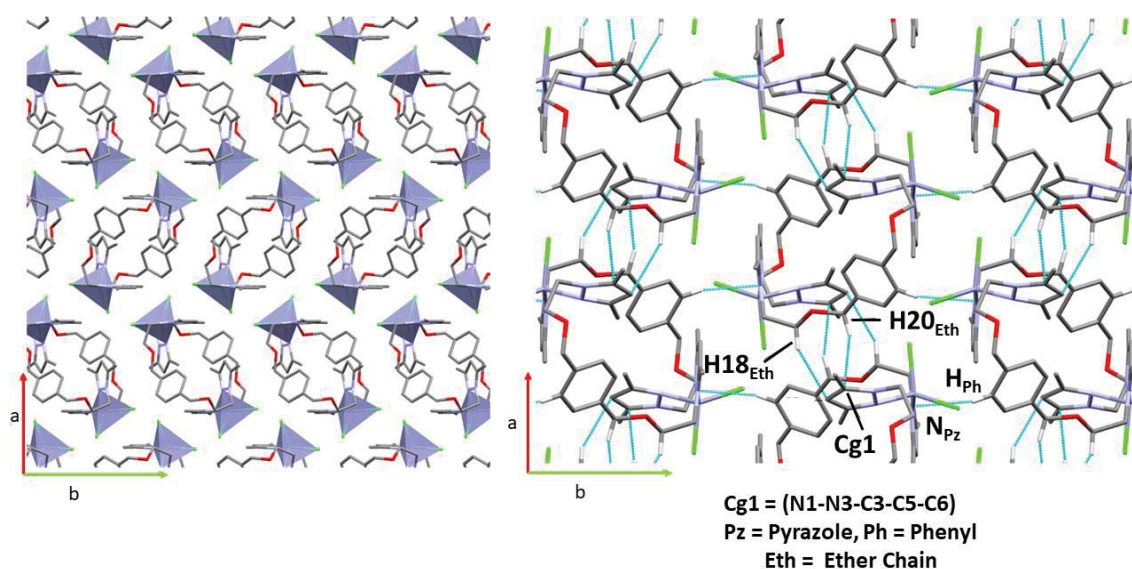


Figure 3.3.6 Supramolecular structure of **10**, view along *c* axis (right). Detail of the non-bonding interactions in **10**, view along *c* axis (left). Colour code: grey (C), white (H), light blue (N), light green (Cl), blue-grey (Zn). Zn(II) atoms are also represented as blue-grey polyhedra. Intermolecular interactions are represented as dashed light-blue lines. Only hydrogen atoms participating in intermolecular interactions are shown.

Table 3.3.3 Non-bonding interactions for **10-13**

	D-H...A (Å)	D-H (Å)	H-D...A (Å)	>D-H...A (°)
10				
C _{Ph} -H _{Ph} ...N _{Pz}	2.691	0.950	3.519	145.91
C18 _{eth} -H18 _{eth} ...Cg1 _{Pz}	2.868	0.990	3.839	167.08
C20 _{eth} -H20 _{Beth} ...Cg1 _{Pz}	3.532	0.990	4.297	135.71
C _{Pz} -H _{Pz} ...Cl2	2.961	0.950	3.861	158.72
C _{meth} -H _{meth} ...Cl2	3.048	0.980	4.011	167.61
11				
C5 _{Meth} -H5 _{A_{Meth}} ...Cg2 _{Ph}	2.797	0.979	3.662	147.56
C _{Ph} -H _{Ph} ...N _{Pz}	2.717	0.949	3.549	146.72
C15 _{eth} -H15 _{Beth} ...Cg3 _{Pz}	2.865	0.991	3.824	163.28
C16 _{eth} -H16 _{Aeth} ...Cg3 _{Pz}	3.430	0.990	4.205	136.64
C _{Pz} -H _{Pz} ...Cl1	2.809	0.950	3.716	159.91
C22 _{meth} -H22 _{Bmeth} ...Cl2	2.849	0.980	3.823	172.48
12				
C _{Pz} -H _{Pz} ...Cl1	2.841	0.980	3.818	179.63
C _{Pz} -H _{Pz} ...Cl2	2.789	0.951	3.692	159.11
C8 _{eth} -H8 _{Aeth} ...Cg4 _{Pz}	2.883	0.991	3.843	163.54
C7 _{eth} -H7 _{Beth} ...Cg4 _{Pz}	3.487	0.990	4.251	135.64
13				
O1 _W -H1 _{WB} ...Cl2	2.495	0.810	3.305	177.34
O1 _W -H1 _{WA} ...O _{eth}	2.460	0.798	3.208	156.65
C _{meth} -H2 _{meth} ...O1 _W	2.424	0.980	3.154	130.87
Cg1 = N1-N3-C3-C5-C6; Cg2 = C9-C10-C11-C12-C13-C14; Cg3 = N1-N3-C1-C3-C4; Cg4 = N2-N4-C18-C20-C21				
Ph = phenyl, eth = ether chains, meth = methyl, Pz = pyrazole, W= water				

Ligands **L4** and **L5** do not possess any hydrogen bond synthons. Thus, whenever a solvent occluded molecule capable of forming strong hydrogen bonds is present, it dominates the supramolecular structure. As such, for compound **13**, the occluded water molecules are the keystones behind the supramolecular scaffold, classical O-H...Cl and H-O...H hydrogen bond interactions being the main non-bonding forces. Each dimer symmetrically interacts with six water molecules through its chlorine, ether, and methyl moieties (Fig. 3.3.8 top-left, Table 3.3.3). Those water molecules link each dimer to ten others (four on each side along the *b* axis and one on each side along the *a* axis) forming a 3D network (Fig. 3.3.8, top right). In them, the rings are arrayed in alternated parallel planes in a ABAB fashion (Fig 3.3.8). These H₂O molecules occupy isolated cavities, which comprise a volume of 36.68 Å³ (1.5 % of unit cell), calculated defining a probe radius of 1.2 Å (Annex I, Fig. S3.3.40).

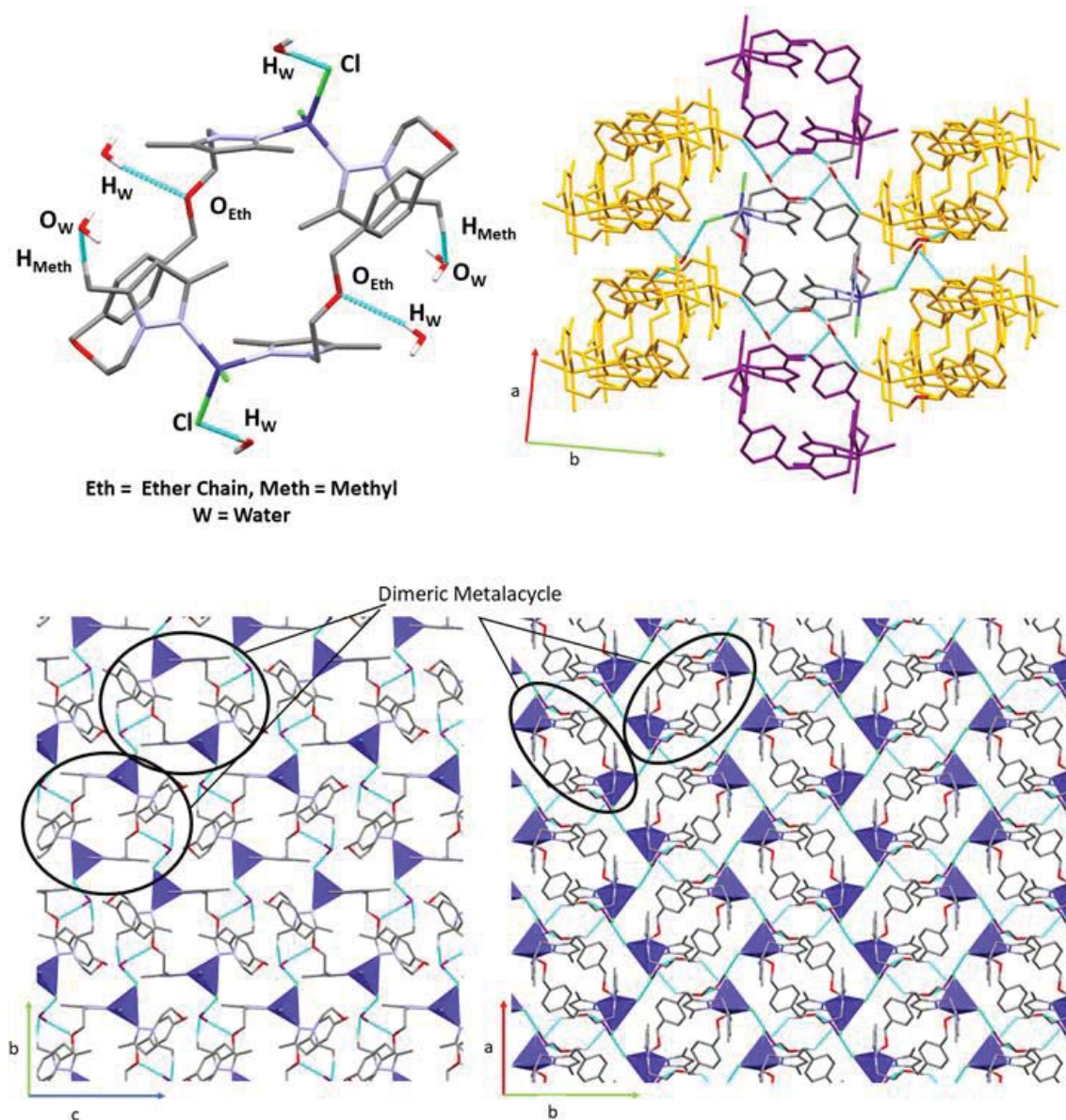


Figure 3.3.7 Detail of the supramolecular interactions of the metalacyclic ring in **13** with occluded H₂O molecules (top-left). Supramolecular environment of each dimeric metallacycle, showing its interactions with other metallacycles along the b axis (highlighted in orange) and a axis (highlighted in violet). Supramolecular packing of compound **13**, view along a axis (bottom-left) and b axis (bottom-right). Water molecules are highlighted in violet. Colour code: grey (C), white (H), light blue (N), light green (Cl), blue (Co). Co(II) atoms are also represented as blue polyhedra. Intermolecular interactions are represented as dashed light-blue lines. Only hydrogen atoms participating in intermolecular interactions are shown.

The networks for **10-13** have also been further investigated using Hirshfeld surface analyses²⁷, which allow for several visual representations of the intermolecular interactions. Surfaces have been calculated using an isovalue of 0.5 e au⁻³. For **13**, being a multi-component crystal, Hirshfeld surface analysis was performed in both the separate components and for the asymmetric unit.

The normalized contact distance (d_{norm}) surface mapping shows red spots where relevant intramolecular interactions occur. For **10**, in the d_{norm} surface mapping red spots can be seen over hydrogen atoms of the ether chains and phenyl rings, as well as over both pyrazolyl moieties, confirming their role in its supramolecular structure (Fig. 3.3.9). It is worth remarking that for **11** and **12** the biggest red spots (and thus the strongest intermolecular interactions) appear over interactions involving chlorine atoms. Interactions involving phenyl, methyl and pyrazolyl moieties are also identified (Fig. S3.3.41). For compound **13**, the d_{norm} representation shows easily identifiable red spots over the atoms involved in classical hydrogen bonding with water molecules: oxygen of the ether chain, chlorine, hydrogens of the methyl group and water molecules themselves for both the metalacyclic component and the asymmetric unit (Fig. 3.3.9 and Fig S3.3.41).

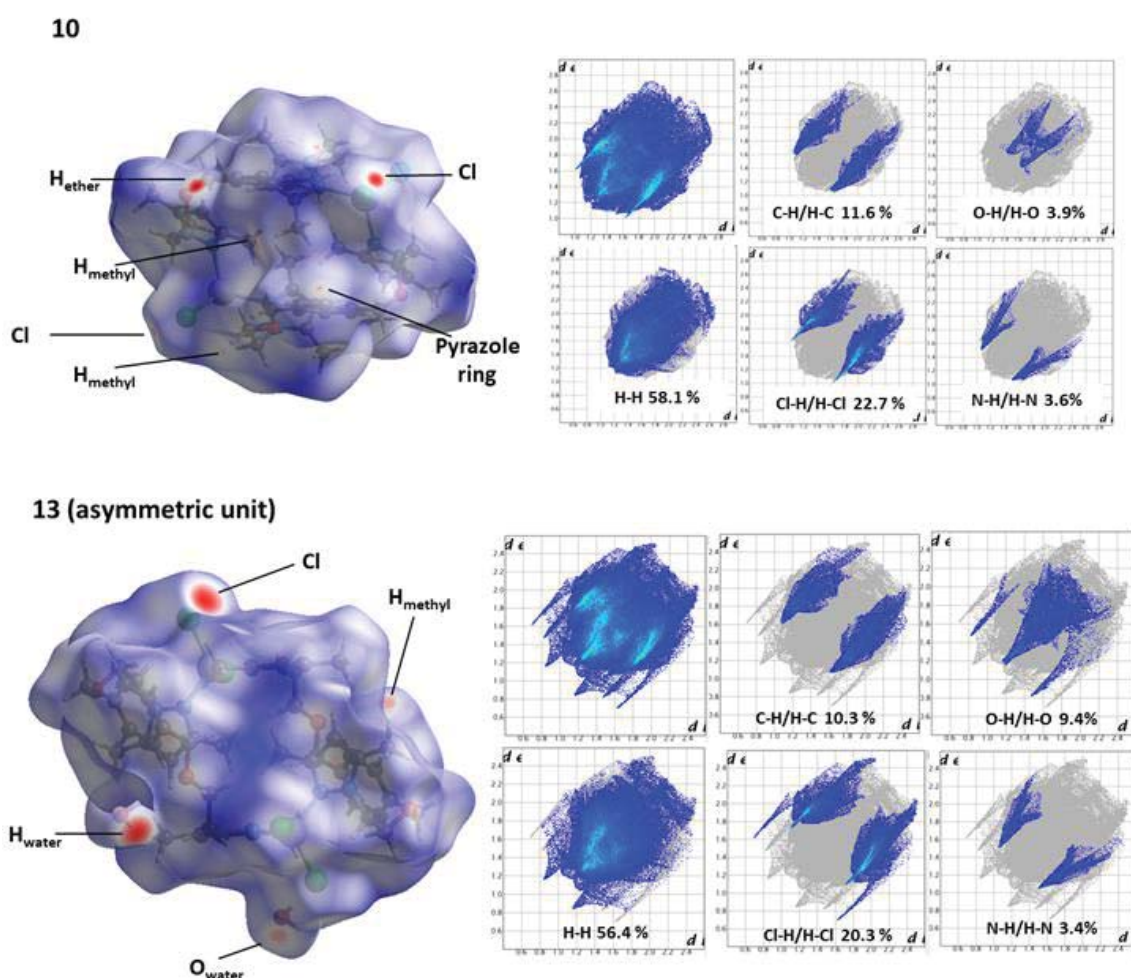


Figure 3.3.8. d_{norm} representation of compound **10** (top-left) and asymmetric unit of compound **13** (bottom-left), with functional groups participating in the supramolecular network listed. Fingerprint plot for compound **10** (top-right) and asymmetric unit of **13** (bottom-right)

Another visual representation, the fingerprint plot, allows for quantification of said interactions. Moreover, each molecule possesses a unique fingerprint depending on their supramolecular interactions. While fingerprints for compounds **10-12** are similar, the one for compound **13** stands out, owing to the different nature of their nonbonding interactions. For **10-12**, fingerprint plots show an overall rounded shape, lacking defined spikes, which suggests that there is not a dominant intermolecular interaction. Analysis of their fingerprint plot show that most intermolecular forces (55.5-58.6 %) are H \cdots H interactions attributed to London dispersive forces²⁸. However, C-H \cdots Cl interactions also have a great role (22.7-24.5 %). On the other hand, C-H \cdots C interactions have a minor contribution to the overall network (11.0-11.6 %). Moreover, their “winged” shape in the fingerprint plot shows their C-H \cdots π character²⁹ (Fig. 3.3.9). For **13**, on the other hand, both patterns possess several clearly defined spikes. Those belong to O-H \cdots O and O-H \cdots Cl (and reciprocal) interactions, as seen in the fingerprint plots. Moreover, the percentage of surface area implied in O-H \cdots O (and reciprocal) interactions is notably increased with respect to **10-12** (9.4 % vs. average 3.7 %). The percentage of surface area involved in other interactions is similar than in **10-12**. Note, however, the shape of the H \cdots Cl fingerprint plot is notably different, as it involved in a classical hydrogen bonding in **13** (O_{Water}-H_{Water} \cdots Cl), whereas in **10-12** indicates C-H \cdots Cl interactions.

Crystal and Extended Structures of compounds 15 and 18

As opposed to **L4**, which bears the same coordination behavior regardless of the metal centre, **L5** shows several different coordination behaviours. For isomeric compounds **15** and **18**, the ligand adopts a *NN'*-bridged coordination mode, with an *anti*-conformation. Moreover, they bear the polymeric chain motif, as opposed to a metalacyclic one (Fig. 3.3.10 and Fig. S3.3.3.42).

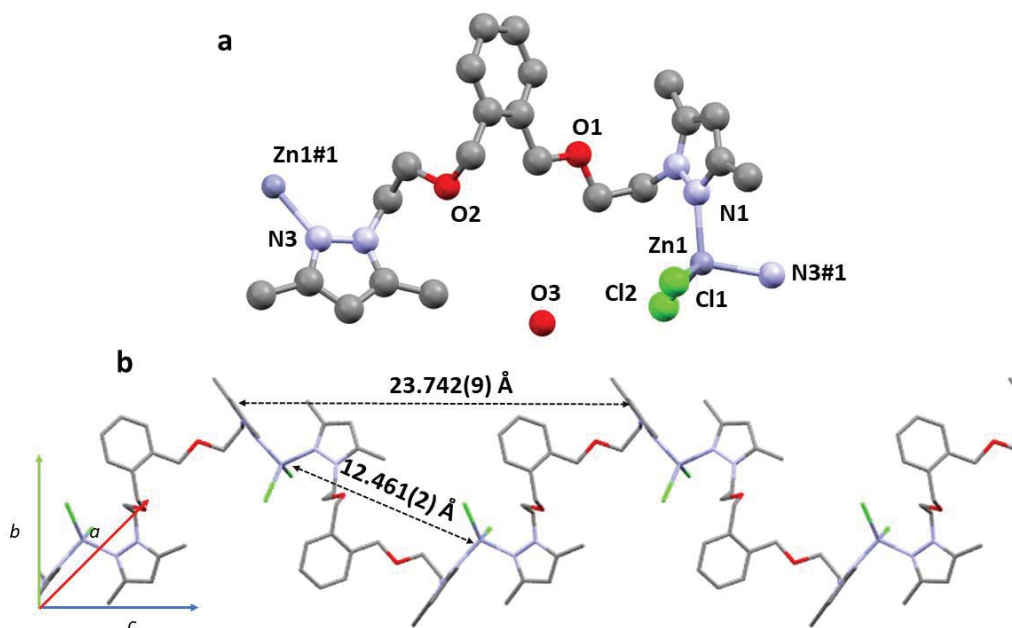


Figure 3.3.9 a. Compound **15**, showing all its non-hydrogen atoms and numbering scheme. b. Representation of the infinite polymeric chain, showing relevant intrachain distances. Colour code: grey (C), white (H), light blue (N), light green (Cl), blue-grey (Zn).

The *core* of isostructural compounds **15** and **18** comprises two chlorine atoms and two different pyrazolyl nitrogen atoms provided by **L5**. Thus, compound **15** bears a $[\text{Zn}(\text{N}_{\text{pz}})_2\text{Cl}_2]$ slightly distorted tetrahedral ($\tau_4 = 0.90$)²¹ *core*. This polymeric structure is reported in eight (13 %) of the sixty-one crystal structures with the same *core*²². In the resulting helical chain polymer, adjacent Zn(II) atoms lie at 12.461(2) Å, which is larger than distances found in similar related compounds^{7,30}. On the other hand, **18** bears a similar tetrahedral ($\tau_4 = 0.89$)³¹ $[\text{Co}(\text{N}_{\text{pz}})_2\text{Cl}_2]$ *core* which is present in up to fifty-one reported crystal structures. Most of them are monomers (forty, 78.4 %)²², while reports of compounds with a similar *core* with a polypyrazole acting as a bridging ligand are much scarce, with only a handful of dimers^{24,25,32,33} and one polymer³⁴ (1.96 %) reported.

In these polymers, adjacent M(II) atoms are connected by **L5** via a *NN*-bidentate bridging mode in an *anti*- conformation, resulting in an infinite helical chain along the *c* axis. The distance between repeating units in the helical chain is ~ 23.7 Å, while adjacent M(II) atoms lie at 12.461/12.490 Å (**15/18**). This M···M distance is larger than the ones found in related bispyrazole polymers (9.523 Å⁷ and 7.976 Å³⁰ for Zn(II) compounds and 9.734 Å³⁴ for Co(II) compounds). The dihedral angle between the mean planes of the pyrazolyl rings in the centrosymmetric **L5** ligands is 68.82°/68.71° (**15/18**), which show its twisting around the benzene rings. However, alternating pyrazolyl rings, belonging to

two different **L5** ligands, are almost parallel (dihedral angles of their mean planes being 15.4°/14.5° (**15/18**)). Selected distances and angles are shown on Table 3.3.4. They are in agreement with similar compounds reported in the literature^{25,32–34}.

Table 3.3.4 Selected bond lengths (Å) and angles (°) for **15** and **18**

	15	18
Bond Lengths (Å)		
M(1)-Cl(1)	2.2313(11)	2.2710(6)
M(1)-Cl(2)	2.2623(11)	2.2388(6)
M(1)-N(1)	2.036(3)	2.0410(16)
M(1)-N(3)#1	2.050(3)	2.0406(17)
M···M#1	12.461(2)	12.490(9)
Bond Angles (°)		
Cl(1)-M(1)-Cl(2)	108.41(4)	106.79(2)
N(3)#1-M(1)-Cl(2)	105.89(9)	105.53(5)
N(3)#1-M(1)-Cl(1)	116.28(9)	117.54(5)
N(1)-M(1)-Cl(2)	117.18(9)	116.91(5)
N(1)-M(1)-Cl(1)	106.45(10)	106.73(5)
N(1)-M(1)-N(3)#1	102.9(13)	103.86(7)
#1 : x, y+1, z + 1/2		

As in **13**, the extended structure of **15** and **18** is dominated by the presence of occluded H₂O molecules. These molecules bind together a left-handed and right-handed chains forming a supramolecular thread in the crystallographic *c* direction, thanks to a double symmetrical O-H···Cl₂ H-bond interaction, forming a supramolecular chain parallel to the *c* axis (Fig. 3.3.11 top and Fig. S3.3.43 top). These chains are stacked together thanks to a C-H···C interaction between the methyl and phenyl rings. Relevant H-bond interactions are summarized on Table 3.3.5.

The distance between the water molecules encapsulated in parallel double chains is 13.536 Å. Therefore, this H₂O molecules, occupy cavities defined by this sets of double helical chains. These non-connected cavities have a volume of 91.22 and 86.91 Å³ (1.9 or 1.8 % of unit cell for **15** and **18**, respectively), calculated defining a probe radius of 1.2 Å (Annex I, Fig. S3.3.44).

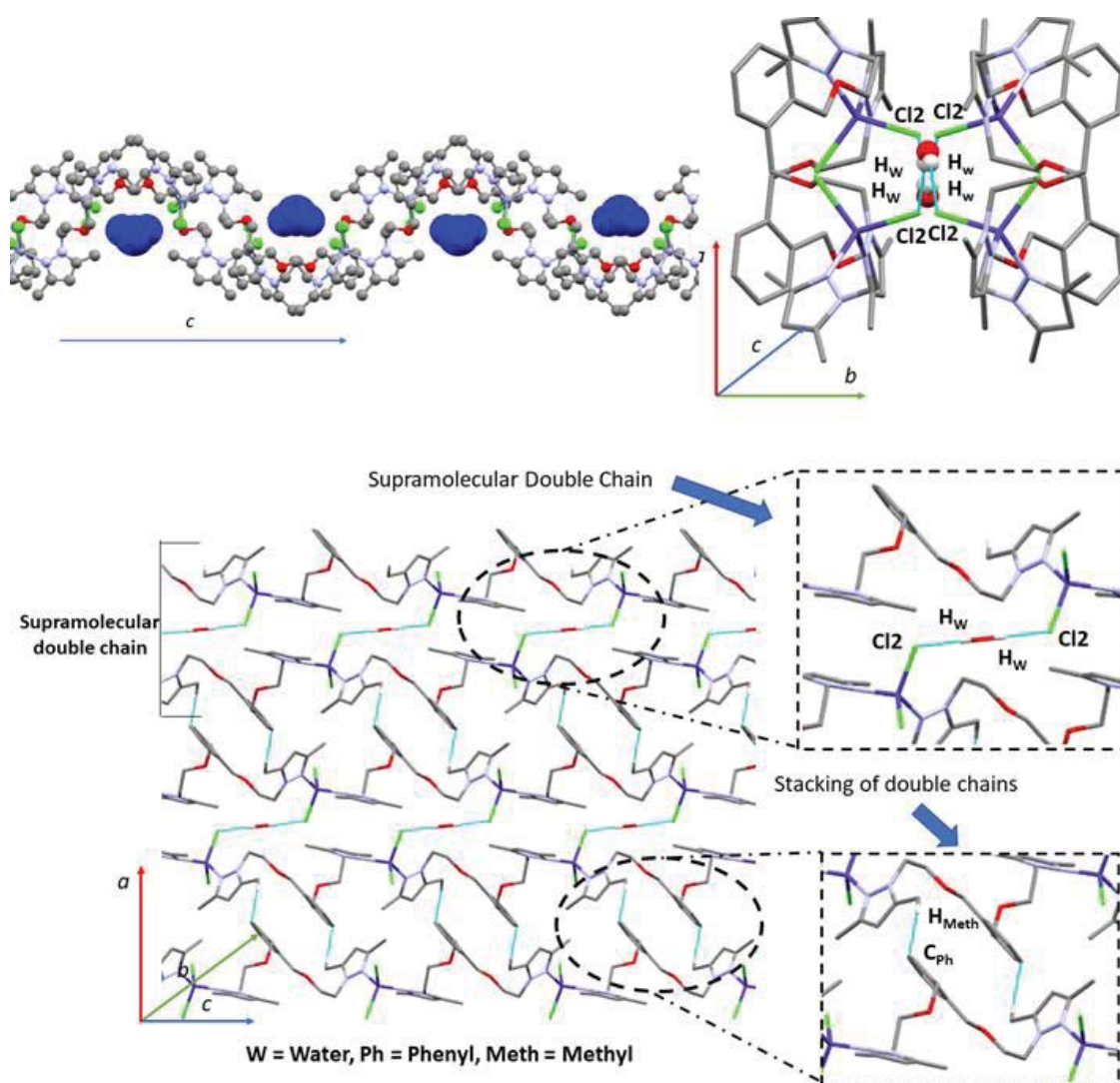


Figure 3.3.10. Detail of the role of H₂O molecules in binding two polymeric chains in **15**. H₂O molecules are represented in blue and spacefill mode (top). Detail of the intermolecular interactions in **15** (bottom), view along b and c axis. Colour code: grey (C), white (H), light blue (N), light green (Cl), blue (Co). Intermolecular interactions are represented as dashed light-blue lines. Only hydrogen atoms participating in intermolecular interactions are shown.

Table 3.3.5 Selected hydrogen bonding distances (Å) and angles (°) for **15** and **18**.

	D-H...A (Å)	D-H (Å)	H-D...A (Å)	> D-H...A (°)
15				
O _W -H _W ...Cl ₂	2.587	0.983	3.531	161.08
C _{meth} -H _{meth} ...C _{Ph}	2.755	0.980	3.727	171.85
18				
O _W -H _W ...Cl ₂	2.572	0.983	3.531	161.41
C _{meth} -H _{meth} ...C _{Ph}	2.755	0.980	3.517	171.18
W = water, meth = methyl, Ph = phenyl				

Crystal and Extended Structures of compounds 16 and 17

In isostructural compounds **16** and **17**, an oxygen atom of **L5** ether group coordinates to the metal centre. This results in a different coordination behaviour of **L5**, while compounds **16** and **17** still bear the polymeric structural motif. Thus, **L5** displays a *NON'*-chelated and bridged coordination behaviour in a distorted *anti*- conformation. Hence, they have a distorted trigonal bipyramidal ($\tau_5 = 0.73$ (**16**), 0.56 (**17**))³⁵ $[M(N_{Pz})_2OCl_2]$ core. In them, the basal plane comprises two chlorine atoms and the nitrogen of the pyrazolyl closest to the coordinating oxygen, forming a six-membered ring. The apical positions are occupied by an oxygen atom and the nitrogen of the other pyrazolyl group (Figure 3.3.12).

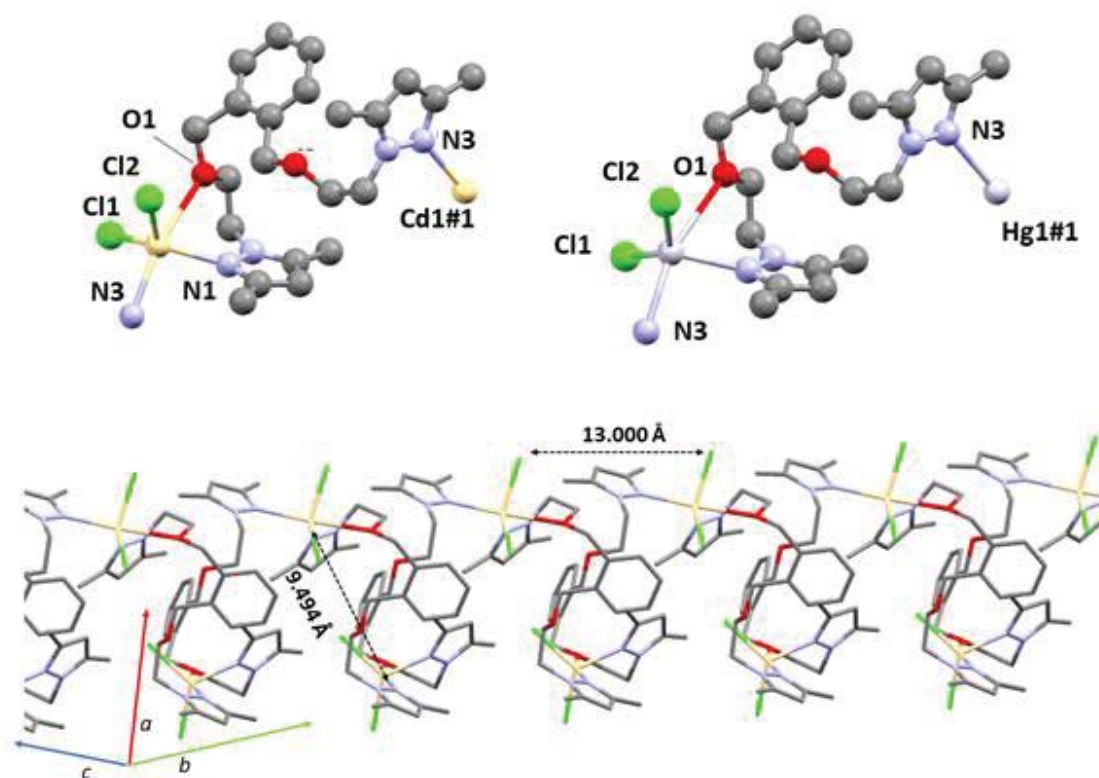


Figure 3.3.11 Compounds **16** and **17**, showing all its non-hydrogen atoms and numbering scheme. Occluded solvents have been removed for clarity (top). Representation of the infinite polymeric chain, showing relevant intrachain distances. Colour code: grey (C), white (H), light blue (N), light green (Cl), bone (Cd), light-grey (Hg).

Bispyrazolyl compound with a similar *core* have not been reported yet²². This can be attributed to the fact that reported bispyrazolyl Cd(II) compounds tend to form dimers or polymers via chlorine bridges^{36,37}, whereas for Hg(II) compounds a great topological variety is observed^{26,38,39}. However, a similar coordination behavior has been observed for a related Cd(II) monomer bearing a similar bispyrazole ligand synthesized in our group⁷, where both oxygen atoms of the two ether groups are bonded to the metal center, resulting in a *NOON'*-chelated coordination mode. It is important to note that for the aforementioned ligand⁷, the group connecting the two ether groups is an alkyl chains instead of a pyrazole ring. Probably, the steric hindrance of the phenyl group in **L5** prevents both the coordination of the second ether group and the chelation of the ligand, resulting in the formation of a polymer. Selected relevant distances and angles are reported in Table 3.3.6. They agree with those reported for similar compounds^{7,8,40,41}.

Due to the coordination of the oxygen atom, the resulting polymeric chains are wrapped, resulting in shorter distances between repeating units (12.999(6) (**16**)/13.094(9) (**17**) Å) and M \cdots M distances (9.4935 Å (**16**), 9.610 Å (**17**)) than those for **15** or **18** (~23.7 Å for repeating units and 12.461 (**15**) or 12.490 Å (**18**) for M \cdots M). This wrapping is also reflected in the fact that pyrazole rings of the same **L5** ligand are almost perpendicular in this conformation, the dihedral angles between their mean planes being 83.49° (**16**)/83.76° (**17**), compared to 68.82°/68.71° in **15/18**.

Due to the presence of disorder in the occluded EtOH molecules, the supramolecular structure of **16** and **17** cannot be studied in detail. However, occluded solvent molecules presumably play a role like H₂O molecules in **15** and **18**, binding together left and right-handed helical chains (Fig. S3.3.45). Moreover, in **16** and **17** those occluded solvents occupy a notably bigger cavities than in **15** or **18** (8.6-8.5 % of the unit cell, 227.28-229.75 Å³, compared to 1.9 % and 91.22 Å³ or 1.8 % and 86.9 Å³, Fig. S3.3.46).

Table 3.3.6 Selected bond lengths (Å) and angles (°) for **16** and **17**

	16	17
Bond Lengths (Å)		
M(1)-Cl(1)	2.4286(11)	2.399(2)
M(1)-Cl(2)	2.4312(9)	2.391(2)
M(1)-N(1)	2.248(3)	2.313(5)
M(1)-N(3)#1	2.361(3)	2.498(5)
M(1)-O(1)	2.743(3)	2.987(4)
M···M#1	9.4935(4)	9.610(1)
Bond Angles (°)		
Cl(1)-M(1)-Cl(2)	120.81(4)	131.16(9)
N(3)#1-M(1)-Cl(2)	117.00(9)	109.22(15)
N(3)#1-M(1)-Cl(1)	113.67(9)	112.12(16)
N(1)-M(1)-Cl(2)	96.51(11)	96.75(18)
N(1)-M(1)-Cl(1)	95.02(9)	107.25(14)
N(1)-M(1)-N(3)#1	107.74(8)	92.68(15)
Cl(1)-M(1)-O(1)	84.63(7)	84.35(9)
Cl(2)-M(1)-O(1)	85.29(7)	89.2(1)
N(1)-M(1)-O(1)	70.3(1)	66.4(2)
#1 -x+1/2, y-1/2, -z+3/2		

Crystal and Extended Structure of compound 19

Compound **19** crystallizes in the orthorhombic $Cmc2_1$ space group, showing a dimeric structure (Fig. 3.3.13). In it, **L5** displays a third different coordination behaviour, and a rather unusual one. Moreover, it does not feature a polymeric motif, but a dimeric one. In it, the **L5** ligand chelates *via* one nitrogen and one oxygen of each side to a Cu(II) atom, resulting in a *NOO'N'*-chelated and bridged coordination mode in a *syn*-conformation.

In this dimer, Cu(II) atoms adopt a $[CuNOCl_3]$ *core* in a slightly distorted square pyramidal ($\tau_5 = 0.11$)³⁵ geometry. The basal plane comprises the two bridging chlorine atoms, the terminal chlorine atom and one nitrogen atom of the **L5** ligand. An oxygen

belonging to **L5** occupies the apical position, which lies at a longer distance due to Jahn-Teller effect⁴². Two chlorine atoms act as bridging ligands, linking two Cu(II) atoms in the same plane, resulting in an overall coplanar bridge geometry for **19**. A final chlorine atom in a terminal position ends the coordination sphere.

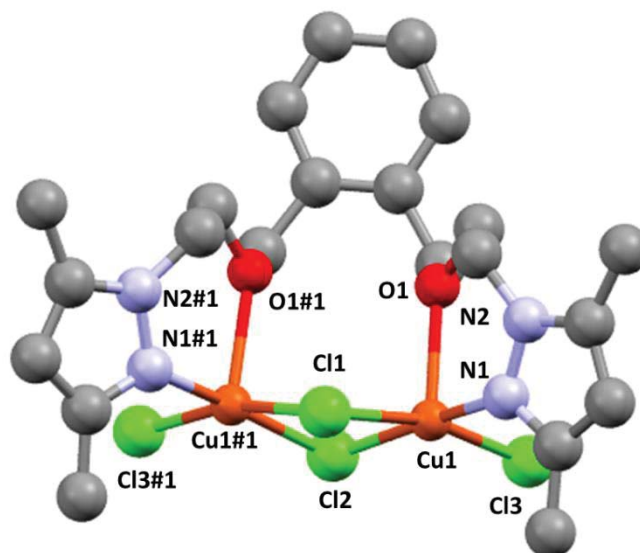


Figure 3.3.12. Compound **19**, showing all its non-hydrogen atoms and their numbering scheme. Colour code: grey (C), light blue (N), light green (Cl), orange (Cu).

A search in the CCDC database²² reveals a total of thirty-one crystal structures bearing a chlorine-bridged dimeric $[\text{CuNOCl}_3]$ *core*, but for the immense majority (twenty-nine crystal structures, 93.5 %) the apical position is occupied by the bridging chlorine atoms, and only in one case⁴³ (3.2 %) by the oxygen atom. Moreover, of the related thirty-one structures with similar *core*, none of them bears a tetradentate ligand. Due to the spatial constraints induced by the coordination of oxygen atoms, **19** has a peculiar throne shape. In it, the phenyl ring acts as the backrest of the throne, being almost perpendicular (85.7°) to the plane containing the Cu(II) and bridging chlorine atoms. The alkylic chain and the pyrazole groups, which resemble the armrests, bind to the Cu(II) atoms in a *syn-syn* mode, defining planes which intersect at an angle of 70.9° between themselves and at 72.7° with the plane containing the Cu(II) and bridging chlorine atoms. Relevant bond lengths and angles for **19** have been summarized in Table 3.3.12. All values agree with related chlorine-bridged dimers⁴³.

The supramolecular structure of **19** is dominated by interaction between the terminal chlorine atoms and hydrogen atoms of the alkylic chain. This symmetrical

double $\text{Cl3}\cdots\text{H}_{\text{al}}$ (al = alkylic chain) interaction results in the formation of supramolecular chains along the c axis (Fig. 3.3.14, Table 3.3.7). These chains form a dense network parallel threads arranged in a zig-zag pattern along the crystallographic (110) direction (Fig. 3.3.14).

Table 3.3.7 Bond lengths (Å), angles (°) and intermolecular interactions for **19**

19				
Bond lengths (Å)				
Cu(1)-N(1)	1.977(8)	Cu(1)-Cl(1)	2.321(2)	
Cu(1)-Cl(3)	2.245(3)	Cu(1)-O(1)	2.340(6)	
Cu(1)-Cl(2)	2.292(3)	Cu(1)⋯Cu(1)	3.348(3)	
Bond Angles (°)				
N(1)-Cu(1)-Cl(3)	93.1(3)	Cl(3)-Cu(1)-Cl(2)	92.27(11)	
N(1)-Cu(1)-Cl(2)	172.4(3)	N(1)-Cu(1)-O(1)	90.0(3)	
Cl(3)-Cu(1)-Cl(2)	92.27(11)	Cl(3)-Cu(1)-O(1)	94.28(18)	
N(1)-Cu(1)-Cl(1)	89.5(3)	Cl(2)-Cu(1)-O(1)	94.9(2)	
Cl(3)-Cu(1)-Cl(1)	165.56(12)	Cl(1)-Cu(1)-O(1)	99.93(19)	
Cl(2)-Cu(1)-Cl(1)	83.98(11)	Cu(1)-Cl(1)-Cu(1)#1	92.32(14)	
N(1)-Cu(1)-Cl(3)	93.1(3)	Cu(1)#1-Cl(2)-Cu(1)	93.81(14)	
N(1)-Cu(1)-Cl(2)	172.4(3)			
Intermolecular interactions				
	D-H⋯A (Å)	D-H (Å)	H-D⋯A (Å)	> D-H⋯A (°)
C _{eth} -H _{eth} ⋯Cl3	2.728	0.970	3.616	152.44

#1: -x, y, z

Eth = Ether chain

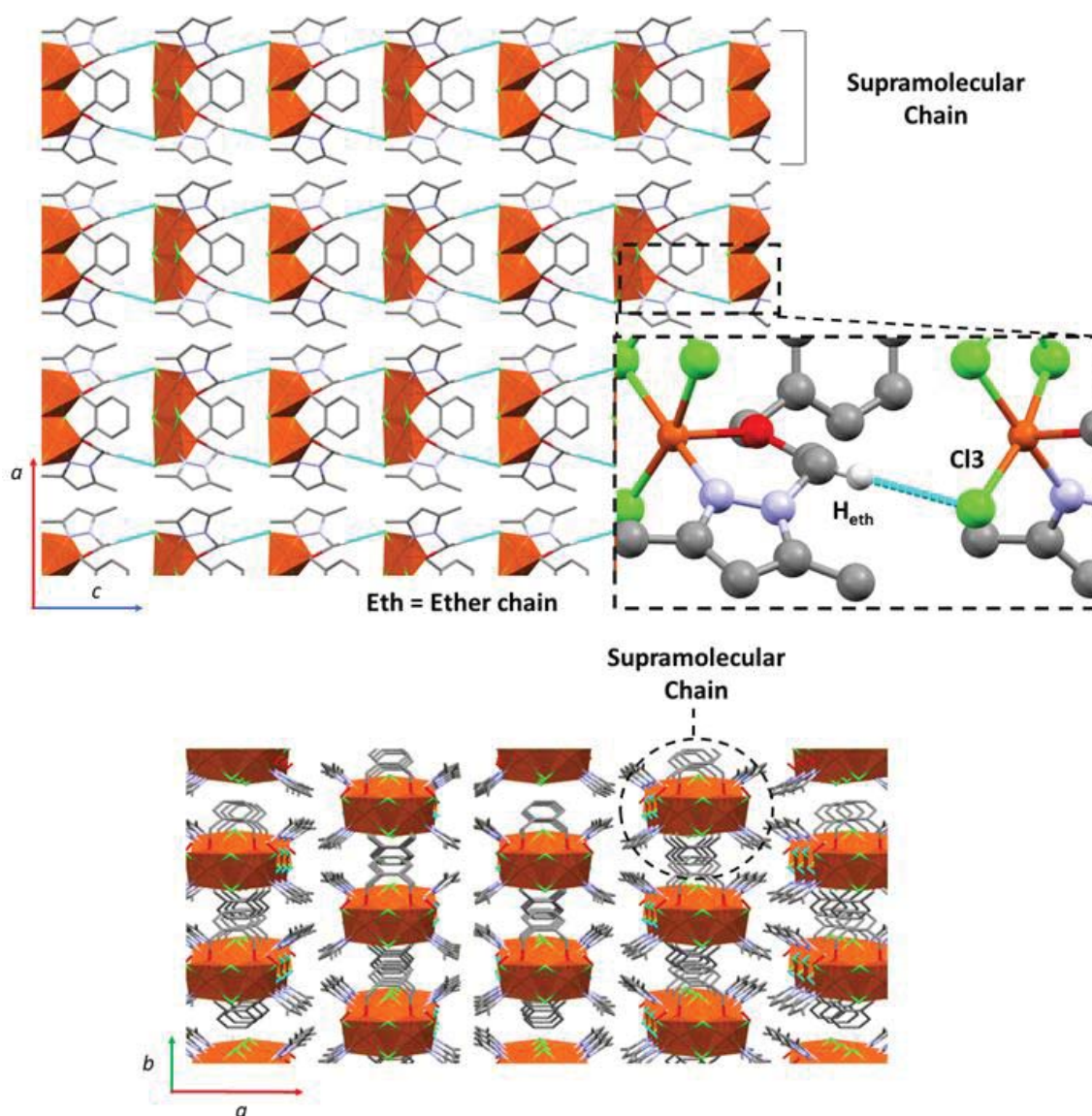


Figure 3.3.13 Intermolecular interactions for compound **15**, view along b axis (top), view along c axis (bottom). Colour code: grey (C), white (H), light blue (N), light green (Cl), orange (Cu). Cu(II) atoms are also represented as orange polyhedra. Intermolecular interactions are represented as dashed light-blue lines. Only hydrogen atoms participating in intermolecular interactions are shown.

3.3.1.4 Structural discussion

For the engineering of crystal structures bearing new architectures, a deep understanding of the coordination behaviour of used ligands is needed. This understanding can be translated in a series of structural parameters which govern the formation of molecular and supramolecular networks of the resulting crystal structures. Thus, the coordination behaviour of **L4** and **L5** has been summarized according to three parameters: θ (angular tilt between the coordinating pyrazolic nitrogen and the centroid

of the phenyl ring), ϕ (dihedral angle between pyrazolyl rings of the same ligand) and d ($M \cdots M$ distance) (Fig. 3.3.15). The results are shown in Table 3.3.8, where also the conformation of the ligands and their coordination mode is reported.

The resulting data suggests that θ values lower than 80° result in *syn*-conformation, and values higher than 80° in an *anti*- conformation. As stated in the Crystal and Extended Structures section, the conformation completely dictates the obtention of dimeric metallacycles or coordination polymers. Detailed examination of parameters' values for compounds **16** and **17** show that they are in the transition between a pure *anti*- and a pure *syn*- conformation, as their θ and ϕ values are closer to compounds **10-13** than to compound **15**. Mondal and co-workers also observed a similar for methylenebis(3,5-dimethylpyrazole) ligand (ligand I, Chart 3.3.1)²³, with higher θ values resulting in *anti*- conformations and lower values in *syn*-, the turning value being around 115° .

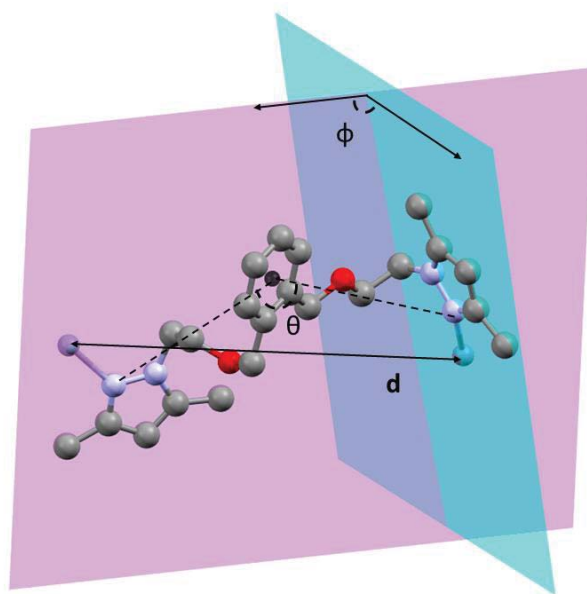


Figure 3.3.14. Geometrical parameters for compound **15** (complete structure not shown). Colour code: grey (C), light blue (N), red (O), blue-grey (Zn).

Table 3.3.8 Coordination behaviour of **L4** and **L5** for **10-19**.

	θ (°)	ϕ (°)	d (Å)	Conformation	Coordination Mode
10	76.58	89.13	9.3697(6)	syn	NN'-bridged
11	76.67	87.78	9.5206(7)		
12	77.03	87.11	9.6636(5)		
13	76.64	88.42	9.3262(6)		
15	105.10	68.82	12.461(2)	anti	NON'-chelated and bridged
16	82.50	83.48	9.4935(4)	Distorted anti	
17	82.94	83.49	9.610(1)		
18	105.26	53.15	12.4898(9)	anti	NN'-bridged
19	53.0	70.92	3.348(3)	syn	NOO'N'-chelated and bridged
θ : Angle between coordinating nitrogen atoms and the phenyl rings' centroid.					
ϕ : Dihedral angles between pyrazolyl planes.					
d: Metal····Metal distance.					

The aforementioned results obtained by Mondal and co-workers²³, however, demonstrated the flexibility of the same ligand. On the contrary, in our work, the *para*-substituted ligand shows a clear preference for a *syn*- conformation, whereas the *ortho*-substituted ligand shows a clear preference for the *anti*- conformation. Reger and co-workers, who have extensive experience in the synthesis of Ag(I) metallacycles, demonstrated that while for alkyl-linked bis(dipyrazole) (ligands II-IV, Chart 3.3.1) ligands the metalacyclic motif was dominant^{44,45}, the introduction of different substituted (*meta*- and *para*-, ligands V-VIII, Chart 3.3.1) arene linkers challenged this domination, as *para*- substituted ligands preferred polymeric or lineal dimeric motifs^{46,47}. They used this knowledge to purposely synthesize a wide array of metalacyclic structures containing different block-*d* metals^{25,48-55}.

In fact, Reger's group synthesized similar bis(dipyrazole) ethers (ligands X-XII, Chart 3.3.1) and tested their reactivity against different block-*d* metals^{56,57}. In their studies, *para*- and *meta*- substituted ligands adopted the mononuclear metalacyclic motif and *ortho*- substituted ligands adopted the polymeric motif⁵⁶⁻⁵⁸. These results have been attributed to the fact that the close proximity of the side arms in *ortho*-substitution prevent the adoption of the *syn*- conformation, preventing the formation of metallacycles⁵⁸. Thus,

the relative position of the pyrazole arms respect to the arene linker is shown to be key in determining the topology of the resulting compounds.

In this work, for ligands **L4** and **L5**, the *para*- substitution results in the formation of dimeric metallacycles whereas *ortho*- substitution results in the polymeric or lineal dimeric motif. For **L5**, the previously reported obtention of macrocycles for Pd(II) bearing compounds⁹, is justified by the steric constraints forced by the square planar geometry of Pd(II) metal ions, which force a *syn*- conformation. On this basis, the coordination behaviour of ligand **L5** in **19** is even more surprising. The chelate effect in combination with the formation of the double chlorine bridge between Cu(II) atoms may overcome the energetic barrier of the *syn*- conformation.

Finally, a closer look to Table 3.3.8 also allows to ascertain that **L5** has a greater flexibility than **L4**, as it can adopt *anti*, distorted *anti* or *syn*⁹ conformations as well as *NN'*-bridged, *NON'*-chelated and bridged and *NN'*-chelated⁹ coordination modes, Moreover, the coordination behaviour of **L5** in **17** is especially remarkable, as it shows an unprecedented tetradentate *NOO'N'*-chelate and bridge coordination mode.

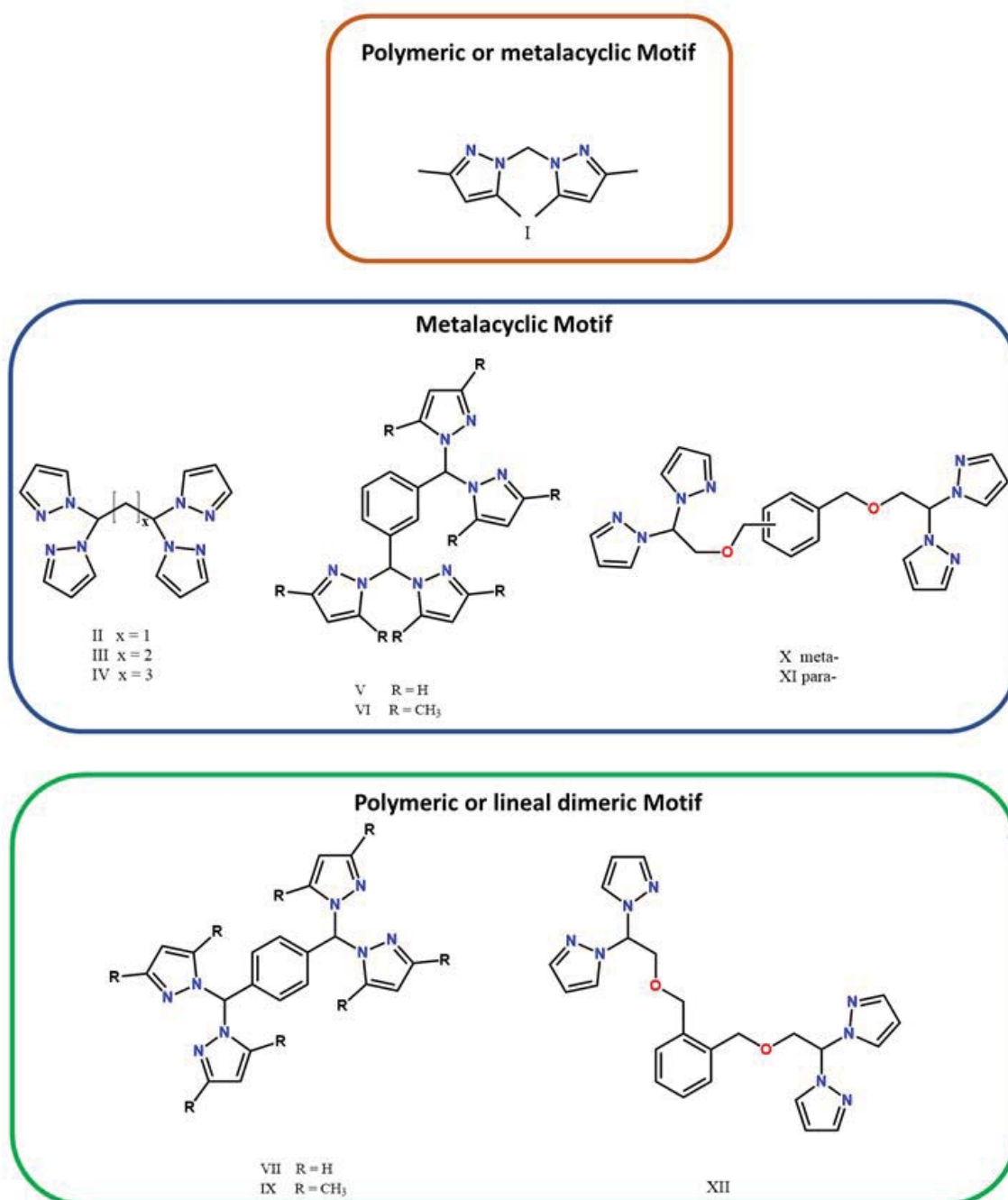


Chart 3.3.1 Selected examples of pyrazolyl ligands promoting coordination compounds with the metalacyclic or polymeric motif

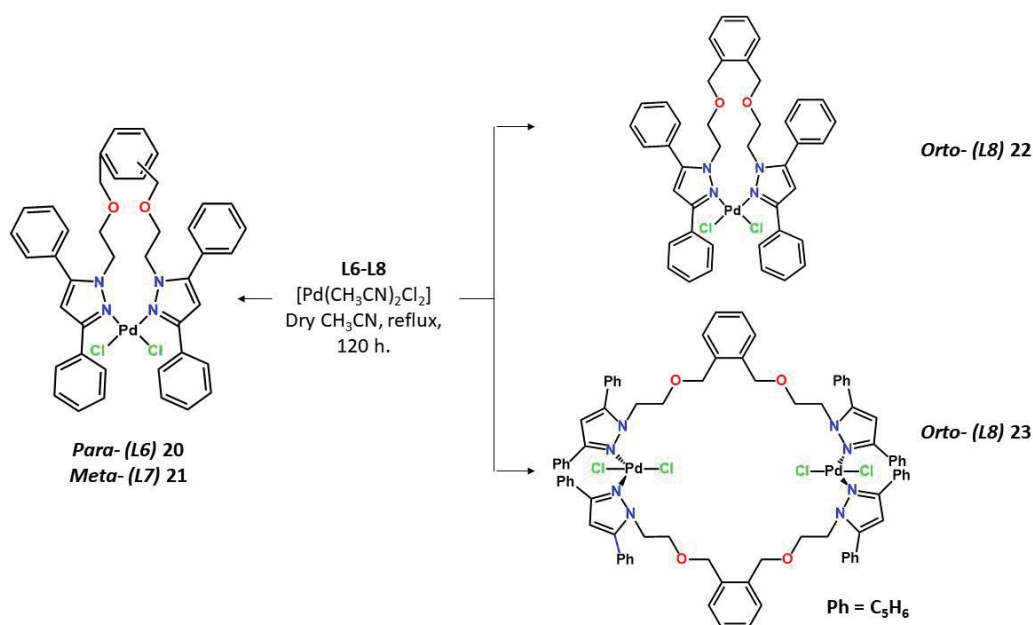
3.3.2 Pd(II) compounds with L6-L8

Continuing our efforts in the synthesis of coordination compounds bearing bispyrazole ligands, the reactivity of **L6-L8** was tested in this work. These new ligands are based on **L4** and **L5** but adding phenyl moieties in positions 3- and 5- of the pyrazole. The reactivity of **L4** and **L5** against Pd(II) has been assayed in our group, yielding monomers and dimers depending on the reaction solvent⁹, a trend followed by related ligands bearing the sulfone/sulfoxide functionality³. Thus, we decided to examine if this behaviour was also present in this family of Pd(II) compounds, as well as expanding our knowledge in the synthesis of coordination compounds bearing flexible *N,O*-hybrid bispyrazole ligands.

3.3.2.1 Synthesis

For the synthesis of these compounds a mixture of $[\text{PdCl}_2(\text{CH}_3\text{CN})_2]$ and the corresponding **L6-L8** ligand in a 1:1 M:L ratio in dry CH_3CN is refluxed for 120 hours (Scheme 3.3.2). According to the results previously obtained for **L4** and **L5**, the use of CH_3CN as solvent yielded exclusively monomers⁹, hence its selection as reaction solvent. After that period, the solution is concentrated up to 1/5 of the original volume and left in the fridge until a yellow precipitate appears. The solid is filtered off and dried under vacuum.

The ^1H NMR spectra (*vide infra*) of the resulting compounds shows that while only one product is obtained for **L6** and **L7**, a mixture of compounds is obtained for **L8**. By analogy with the previous results obtained with **L4** and **L5**⁹, we tentatively guess that for **L6** and **L7** monomers $[\text{PdCl}_2(\text{L6})]$ (**20**, 75.8 % yield) and $[\text{PdCl}_2(\text{L7})]$ (**21**, 58.2 % yield) are obtained, while for **L8**, a mixture of products, containing mainly a monomer $[\text{PdCl}_2(\text{L8})]$ (**22**) and a dimer $[\text{PdCl}_2(\text{L8})]_2$ (**23**) are obtained. It is important to note that compounds **22** and **23** have not been isolated individually, but rather as mixtures of both (Scheme 3.2.2).



Scheme 3.3.2 Synthetic reactions carried out in this section. Compounds are labelled with their numbering scheme.

3.3.2.2 Characterization

Compounds **20-23** have been characterized *via* FTIR-ATR and ^1H and $^{13}\text{C}\{^1\text{H}\}$ NMR spectroscopies.

- FTIR-ATR Spectroscopy

The FTIR-ATR spectra of compounds **20-23** shows the distinctive signals of pyrazole rings, such as $[\nu(\text{C}=\text{C}/\text{C}=\text{N})]$, $[\delta(\text{C}=\text{C}/\text{C}=\text{N})]$, $[\delta(\text{C}-\text{H})_{\text{ip}}]$ and $[\delta(\text{C}-\text{H})_{\text{oop}}]$, those last ones being most intense bands in all spectra. For the $[\delta(\text{C}-\text{H})_{\text{ip}}]$ signals, their strength also comes from their overlapping with $[\nu(\text{C}-\text{O}-\text{C})]$ vibrations related to the ether group, and for compounds **21-22** even two peaks can be identified. The $[\nu(\text{C}-\text{H})_{\text{al}}]$ and $[\nu(\text{C}-\text{H})_{\text{ar}}]$ are also notably intense owing to the presence of phenyl and pyrazole groups. As an example, the FTIR-ATR spectra of compound **20** is shown (Figure 3.3.16), while those of **21-22** are reported in the SI (Figure S3.3.46 and S3.3.47)

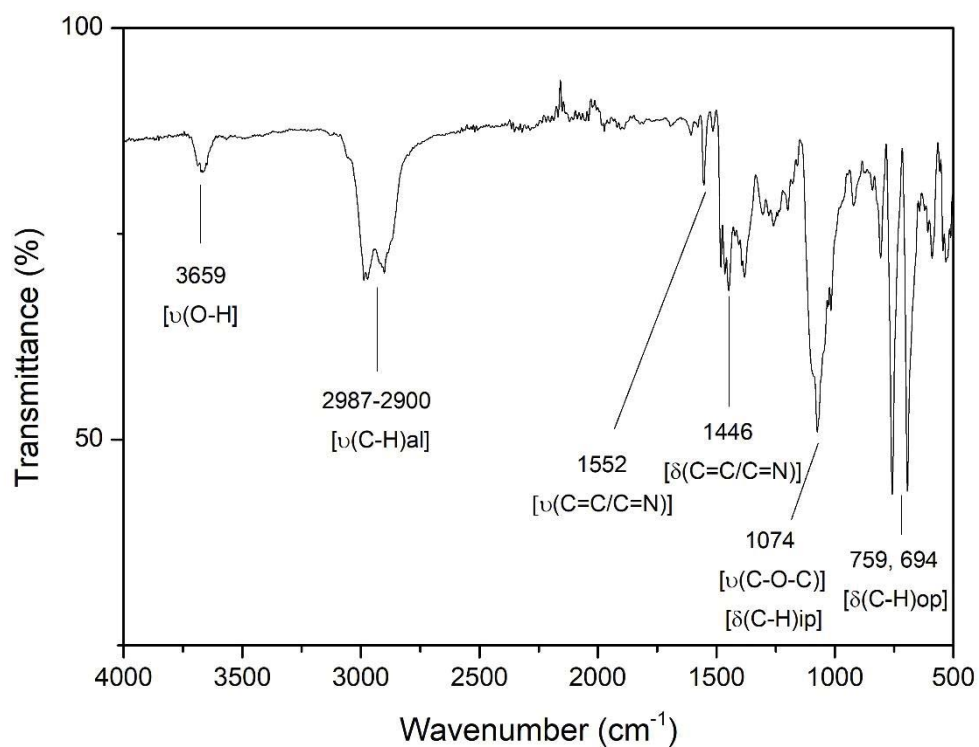


Figure 3.3.15 FTIR-ATR spectrum of compound **20**

- NMR Spectroscopy

The ^1H NMR spectra of compounds **20** and **21** (Figure 3.3.17 and S3.3.48) display the overall same features.

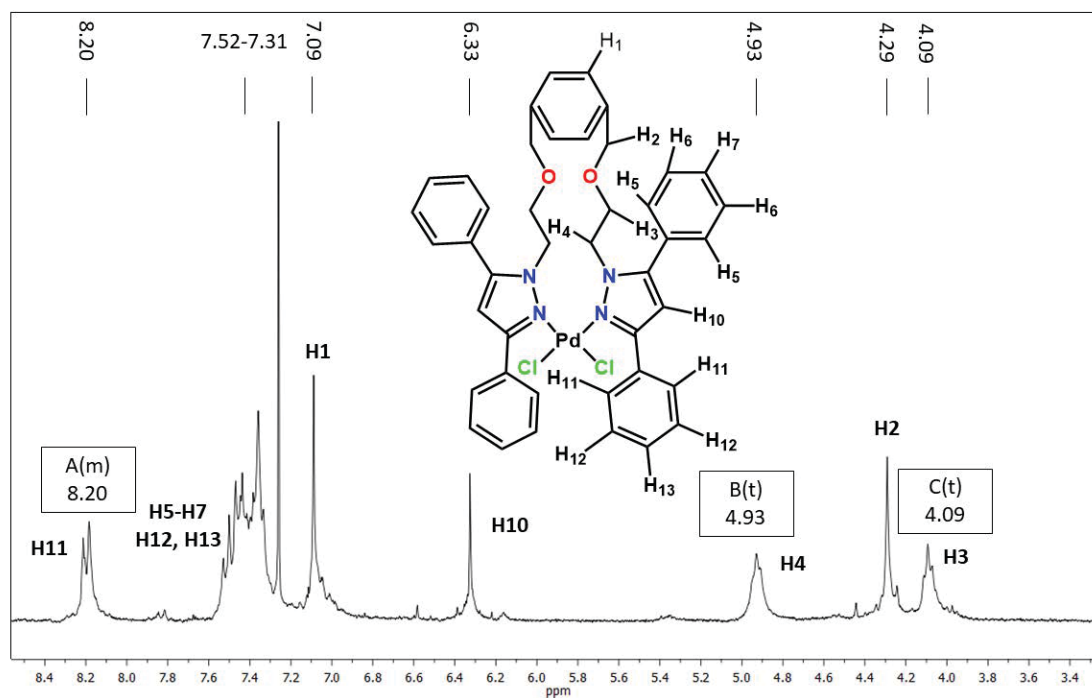


Figure 3.3.16 ^1H NMR spectrum of **20** (CDCl_3 , 400.0 MHz)

The aromatic protons region (8.20 – 6.97 ppm) displays a complicated pattern. A first multiplet is identified at around 8.19 ppm, corresponding to the protons in *ortho*-position of the outer phenyl ring. They are significantly shifted upfield when compared to the free ligands (7.84 - 7.85 ppm). Next, a cluster of overlapping signals is identified. This comprises the rest of the protons belonging to phenyl substituents in 3- and 5-positions. The signals are clustered together at around 7.43 ppm (**20**) and 7.40 ppm (**21**). Next, the signals corresponding to the disubstituted phenyl group acting as the linker between the two pyrazole groups appear. For **20**, they appear as a singlet at 7.09 ppm, whereas for **21**, where three signals are expected, owing to its *meta*-substitution, they appear as a doublet at 7.05 ppm and a singlet at 6.97 ppm, while a last signal at around 7.25 ppm is overlapped with that of the deuterated solvent and cannot be identified clearly.

Following on, signals attributed to the 1*H*-pyrazole appear, being significantly shifted downfield when compared to the free ligands (6.33 and 6.32 ppm, when compared to 6.59 and 6.58 ppm in the free ligand). Signals corresponding to the -O-CH₂-CH₂-N appear shifted upfield, especially the one belonging to -CH₂-N (4.93 and 4.92 ppm in **20** and **21** vs. 4.34 and 4.32 ppm in the free ligands), while in the ones belonging to O-CH₂ fragment this shift is more subtle (4.09 ppm in **20** and **21** vs. 3.95 and 3.92 ppm in the free ligand). Lastly, the signals corresponding to the Ph-CH₂-O fragment are identified at 4.29 and 4.28 ppm for **20** and **21** respectively, slightly downfield when compared to the free ligands (4.40 and 4.28 ppm).

Regarding the ¹³C{¹H} NMR spectra for **20** and **21** there are some significant changes that confirm the coordination of the ligand to the metal centre. First, the signals corresponding to C_{Pz} are shifted slightly upfield (154.9 and 150.0 ppm vs 151.0 ppm and 146.1 ppm for the free ligands). Secondly, signals corresponding to CH_{Ph} are clustered together and more overlapped than in the spectra for the free ligands (130.0 – 127.0 ppm in **20** and **21** vs. 129.7 – 125.8 ppm for the free ligands). Finally, the signal corresponding to CH_{Pz} is also significantly shifted upfield (108.6 ppm in **20** and **21** vs. 103.5 ppm in the free ligand). As an example, ¹³C{¹H} NMR spectrum of **20** is displayed (Fig. 3.3.18) while that of **21** can be found in Annex I (Fig. S.3.3.49).

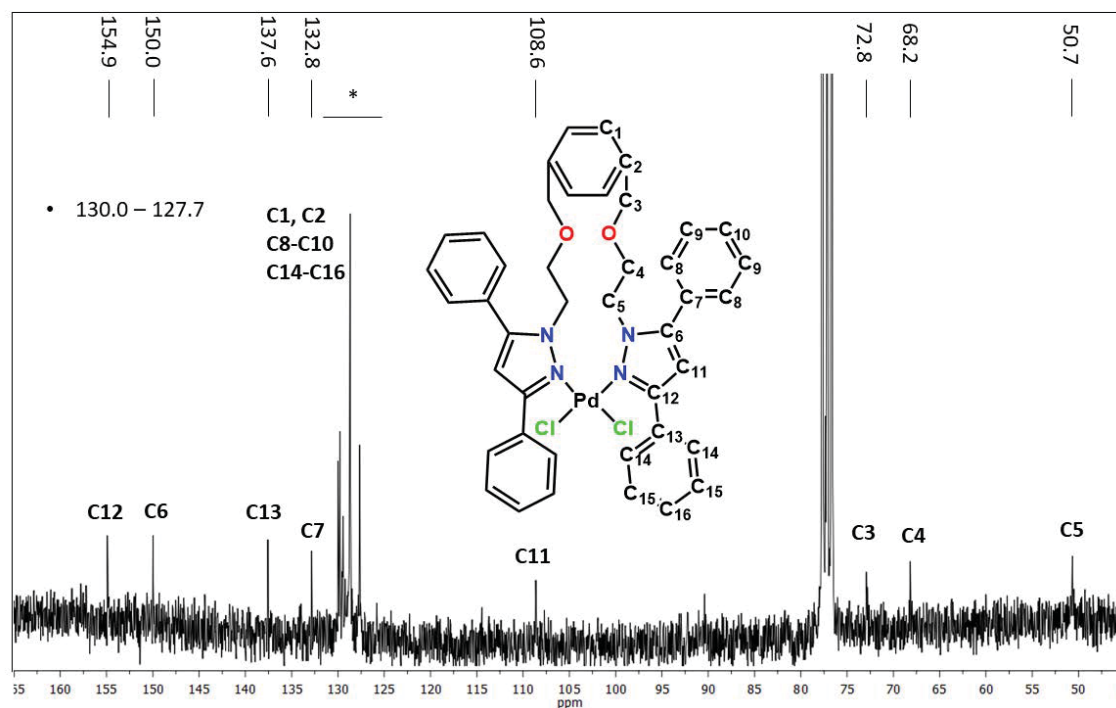


Figure 3.3.17 $^{13}\text{C}\{^1\text{H}\}$ NMR spectrum of compound **20** (CDCl_3 , 100.6 MHz)

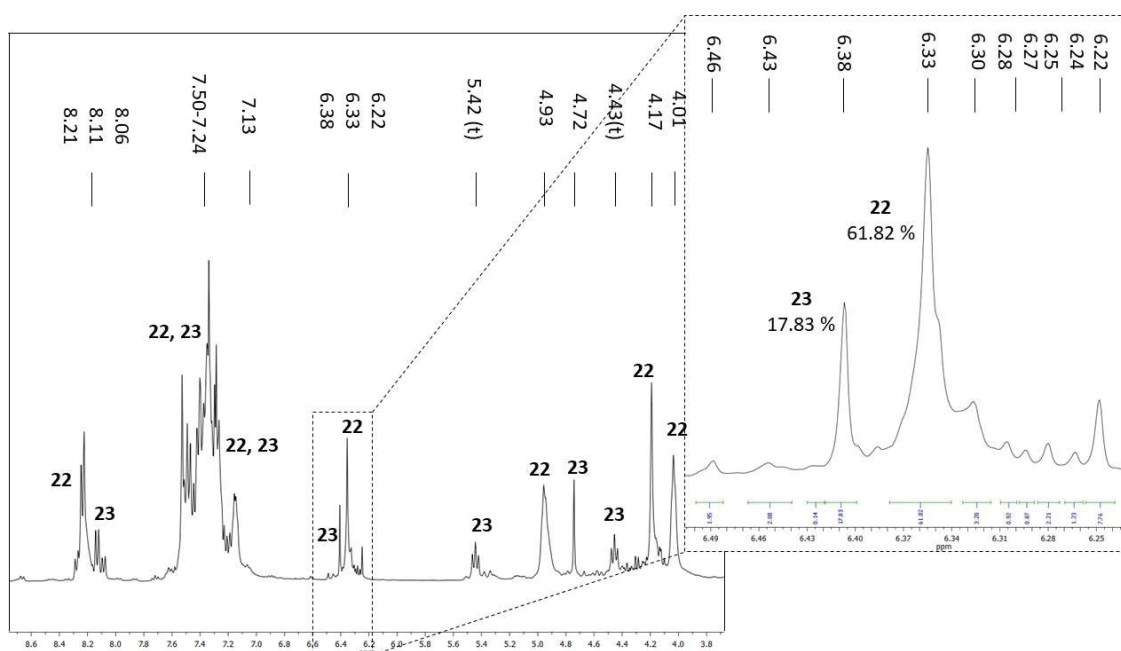
Regarding the reaction of **L8** and $[\text{Pd}(\text{CH}_3\text{CN})_2\text{Cl}_2]$, both its ^1H and $^{13}\text{C}\{^1\text{H}\}$ NMR spectra (Figure 3.3.19 and S3.3.50) immediately reveal the presence of a mixture of compounds. This fact is easily identifiable as multiple peaks appear between 6.46 and 6.22 ppm (attributable to H_{Pz} , all shifted downfield of the free ligand at 6.58 ppm) in its ^1H NMR spectra. Of them, two stand out, at 6.35 ppm (**22**) and 6.41 ppm (**23**). They roughly account for 80 % of the obtained products (60 % for **22** and 20 % for **23**), while the remaining 20 % corresponding to the remaining products mixture. Moreover, multiple signals, attributable to the $\text{Ph-CH}_2\text{-O-CH}_2\text{-CH}_2\text{-Pz}$ fragment, also appear in the region between 5.9 to 3.9 ppm, further evincing this multiplicity of products.

The NMR signals attributed to compound **22** are like those of **20** and **21**, while those attributed to **23** are quite different (Table 3.3.9). Thus, a mixture of a monomer (similar to **20** and **21**) and other products is expected. According to the reported results, reactivity of **L4** and **L5** against $[\text{Pd}(\text{CH}_3\text{CN})_2\text{Cl}_2]$ resulted in mixtures of monomeric and dimeric species (these last ones with multiple conformers coexisting in solution at RT) giving rise to similar sophisticated NMR spectra⁹. We can tentatively assume that a similar result is obtained for the reaction of **L8** and $[\text{Pd}(\text{CH}_3\text{CN})_2\text{Cl}_2]$.

Table 3.3.9 ^1H NMR spectra signals for **20**, **22** and **23**

	20	22	23
$\text{CH}_{\text{Ph-Pz}}$	8.20(m), 7.52-7.31 (overlapping signals)	8.21(m), 7.50- 7.24(overlapping signals)	8.11(m), 7.50-7.24 (overlapping signals)
CH_{Ph}	7.09(s)	7.13 (overlapping signals)	7.13 (overlapping signals)
CH_{Pz}	6.33(s)	6.33(s)	6.38(s)
$\text{CH}_2\text{-N}$	4.93(br)	4.93(br)	5.42(t) / 7.79
Ph- $\text{CH}_2\text{-O}$	4.29(s)	4.17(s)	4.72(s)
O- CH_2	4.09(t)	4.01(br)	4.43(t) / 7.79

δ (ppm) / multiplicity s = singlet, d= doublet, t = triplet, m= multiplet, br = broad /
 $^3J_{\text{HH}}$ (Hz)

**Figure 3.3.18** ^1H NMR spectrum of mixture of compounds **22** and **23** (400 MHz, CDCl_3)

3.3.3 Summary and Conclusions

✓ The reactivity of **L4** and **L5** against MCl_2 ($M = Zn(II), Cd(II), Hg(II)$ and $Cu(II)$) and $CoCl_2 \cdot 6H_2O$ has been assayed.

✓ Ten new coordination compounds have been isolated. They have been characterized *via* EA, FTIR-ATR and UV-Vis spectroscopy. Moreover, for compounds bearing paramagnetic nuclei 1H and $^{13}C\{^1H\}$ NMR spectra have been recorded. Last, crystal structures of nine compounds have been elucidated, and their phase purity determined *via* PXRD.

✓ The crystal structures of compounds **10-13** and **15-19** have been elucidated, allowing detailed study of their molecular and supramolecular architecture.

✓ The use of coordinatively flexible metal cations has evinced the versatility of **L4** and **L5**, as they display new conformations and coordination modes. It has been determined that the substituent position (*para*- (**L4**), *ortho*- (**L5**)) is key for the obtention of different topological motifs and the coordination behaviour of **L4** and **L5** has been rationalised according to a set of new parameters.

✓ The reactivity of **L6-L8** against $[Pd(CH_3CN)_2Cl_2]$ has been assayed. Preliminary results show that while for **L6** and **L7** single products are obtained (most likely monomers), for **L8** a mixture of several compounds is obtained, with two majoritarian products identified (most likely a monomer and a dimer).

References

- 1 A. Pañella, J. Pons, J. García-Antón, X. Solans, M. Font-Bardía and J. Ros, *Eur. J. Inorg. Chem.*, 2006, **2006**, 1678–1685.
- 2 M. del C. Castellano, J. Pons, J. García-Antón, X. Solans, M. Font-Bardía and J. Ros, *Inorganica Chim. Acta*, 2008, **361**, 2923–2928.
- 3 A. De León, M. Guerrero, J. García-Antón, J. Ros, M. Font-Bardía and J. Pons, *CrystEngComm*, 2013, **15**, 1762–1771.
- 4 J. García-Antón, J. Pons, X. Solans, M. Font-Bardía and J. Ros, *Eur. J. Inorg. Chem.*, 2002, **2002**, 3319–3327.
- 5 A. de Leon, J. Pons, J. García-Antón, X. Solans, M. Font-Bardía and J. Ros, *Inorganica Chim. Acta*, 2007, **360**, 2071–2082.
- 6 M. Guerrero, J. García-Antón, M. Tristany, J. Pons, J. Ros, K. Philippot, P. Lecante and B. Chaudret, *Langmuir*, 2010, **26**, 15532–15540.
- 7 M. Guerrero, J. Pons, T. Parella, M. Font-Bardía, T. Calvet and J. Ros, *Inorg. Chem.*, 2009, **48**, 8736–8750.
- 8 M. Guerrero, J. Pons, J. Ros, M. Font-Bardía and V. Branchadell, *Cryst. Growth Des.*, 2012, **12**, 3700–3708.
- 9 M. Guerrero, J. Pons, V. Branchadell, T. Parella, X. Solans, M. Font-Bardía and J. Ros, *Inorg. Chem.*, 2008, **47**, 11084–11094.
- 10 K. Nakamoto, *Handb. Vib. Spectrosc.*, 2006, 1872–1892.
- 11 A. Gasnier, J. M. Barbe, C. Bucher, F. Denat, J. C. Moutet, E. Saint-Aman, P. Terech and G. Royal, *Inorg. Chem.*, 2008, **47**, 1862–1864.
- 12 J. M. J. Paulusse and R. P. Sijbesma, *Chem. Commun.*, 2003, **9**, 1494–1495.
- 13 R. Evans, Z. Deng, A. K. Rogerson, A. S. McLachlan, J. J. Richards, M. Nilsson and G. A. Morris, *Angew. Chemie - Int. Ed.*, 2013, **52**, 3199–3202.
- 14 A. W. J. Poh, J. A. Aguilar, A. M. Kenwright, K. Mason and D. Parker, *Chem. - A Eur. J.*, 2018, **24**, 16170–16175.

- 15 J. E. Huheey, E. A. Keiter and R. L. Keiter, *Inorganic chemistry: Principles of structure and reactivity*, HarperCollins College Publishers, Fourth Edit., 1993.
- 16 S. S. Massoud, L. Le Quan, K. Gatterer, J. H. Albering, R. C. Fischer and F. A. Mautner, *Polyhedron*, 2012, **31**, 601–606.
- 17 S. S. Kandil, G. B. El-Hefnawy and E. A. Baker, *Thermochim. Acta*, 2004, **414**, 105–113.
- 18 S. S. Massoud, F. R. Louka, Y. K. Obaid, R. Vicente, J. Ribas, R. C. Fischer and F. A. Mautner, *Dalt. Trans.*, 2013, **42**, 3968.
- 19 S. S. Massoud, M. Spell, C. C. Ledet, T. Junk, R. Herchel, R. C. Fischer, Z. Trávníček and F. A. Mautner, *Dalt. Trans.*, 2015, **44**, 2110–2121.
- 20 B. J. Hathaway, *Coord. Chem. Rev.*, 1981, **35**, 211–252.
- 21 L. Yang, D. R. Powell and R. P. Houser, *Dalt. Trans.*, 2007, 955–964.
- 22 F. H. Allen, *Acta Crystallogr. Sect. B Struct. Sci.*, 2002, **58**, 380–388.
- 23 R. Mondal, T. Basu, D. Sadhukhan, T. Chattopadhyay and M. kumar Bhunia, *Cryst. Growth Des.*, 2009, **9**, 1095–1105.
- 24 C. Foces-Foces, F. H. Cano and S. García-Blanco, *Acta Crystallogr. Sect. C Cryst. Struct. Commun.*, 1983, **39**, 977–980.
- 25 D. L. Reger, A. E. Pascui, E. A. Foley, M. D. Smith, J. Jezierska, A. Wojciechowska, S. A. Stoian and A. Ozarowski, *Inorg. Chem.*, 2017, **56**, 2884–2901.
- 26 A. Beheshti, A. Lalegani, F. Behvandi, F. Safaeiyan, A. Sarkarzadeh, G. Bruno and H. Amiri Rudbari, *J. Mol. Struct.*, 2015, **1082**, 143–150.
- 27 M. A. Spackman and D. Jayatilaka, *CrystEngComm*, 2009, **11**, 19–32.
- 28 O. Coughlin, N. De Bruyn, D. P. A. Kilgour and S. L. Benjamin, *J. Chem. Crystallogr.*, 2019, 1–7.
- 29 S. K. Seth, G. C. Maity and T. Kar, *J. Mol. Struct.*, 2011, **1000**, 120–126.
- 30 V. Balamurugan and R. Mukherjee, *CrystEngComm*, 2005, **7**, 337.

- 31 L. Yang, D. R. Powell and R. P. Houser, *J. Chem. Soc. Dalt. Trans.*, 2007, 955–964.
- 32 J. Lim, Y. Son, G. Gu, S. Ryu, D. Yoshioka and M. Mikuriya, *X-ray Struct. Anal. Online*, 2015, **31**, 25–26.
- 33 A. Beheshti, F. Safaeiyan, F. Hashemi, H. Motamedi, P. Mayer, G. Bruno and H. A. Rudbari, *J. Mol. Struct.*, 2016, **1123**, 225–237.
- 34 K. V. Domasevitch, *Acta Crystallogr. Sect. C Struct. Chem.*, 2014, **70**, 272–276.
- 35 A. W. Addison, T. N. Rao, J. Reedijk, J. van Rijn and G. C. Verschoor, *J. Chem. Soc., Dalt. Trans.*, 1984, 1349–1356.
- 36 A. Santra, G. Mondal, M. Acharjya, P. Bera, A. Panja, T. K. Mandal, P. Mitra and P. Bera, *Polyhedron*, 2016, **113**, 5–15.
- 37 H.-L. Wu, X.-K. Ma, W.-B. Lv, P. Liu and J.-G. Liu, *Acta Crystallogr. Sect. E Struct. Reports Online*, 2007, **63**, m783–m784.
- 38 I. del Hierro, I. Sierra, D. Pérez-Quintanilla, F. Carrillo-Hermosilla, I. López-Solera and M. Fajardo, *Inorganica Chim. Acta*, 2003, **355**, 347–353.
- 39 S. P. Argent, H. Adams, T. Riis-Johannessen, J. C. Jeffery, L. P. Harding, W. Clegg, R. W. Harrington and M. D. Ward, *Dalt. Trans.*, 2006, 4996.
- 40 A. Santra, G. Mondal, M. Acharjya, P. P. Bera, A. Panja, T. K. Mandal, P. Mitra and P. P. Bera, *Polyhedron*, 2016, **113**, 5–15.
- 41 A. Lalegani, M. Khaledi Sardashti, H. Salavati, A. Asadi, R. Gajda and K. Woźniak, *J. Mol. Struct.*, 2016, **1108**, 288–293.
- 42 L. R. Falvello, *J. Chem. Soc. - Dalt. Trans.*, 1997, 4463–4475.
- 43 P. Kapoor, A. P. S. Pannu, M. Sharma, M. S. Hundal, R. Kapoor, M. Corbella and N. Aliaga-Alcalde, *J. Mol. Struct.*, 2010, **981**, 40–45.
- 44 D. L. Reger, R. P. Watson, J. R. Gardinier and M. D. Smith, *Inorg. Chem.*, 2004, **43**, 6609–6619.
- 45 D. L. Reger, R. P. Watson, M. D. Smith and P. J. Pellechia, *Cryst. Growth Des.*, 2007, **7**, 1163–1170.

- 46 D. L. Reger, R. P. Watson and M. D. Smith, *Inorg. Chem.*, 2006, **45**, 10077–10087.
- 47 D. L. Reger, A. E. Pascui and M. D. Smith, *Eur. J. Inorg. Chem.*, 2012, **2012**, 4593–4604.
- 48 D. L. Reger, A. E. Pascui, P. J. Pellechia and M. D. Smith, *Inorg. Chem.*, 2013, **52**, 11638–11649.
- 49 D. L. Reger, A. E. Pascui, E. A. Foley, M. D. Smith, J. Jezierska and A. Ozarowski, *Inorg. Chem.*, 2014, **53**, 1975–1988.
- 50 D. L. Reger, A. E. Pascui, M. D. Smith, J. Jezierska and A. Ozarowski, *Inorg. Chem.*, 2015, **54**, 1487–1500.
- 51 D. L. Reger, A. E. Pascui, P. J. Pellechia and A. Ozarowski, *Inorg. Chem.*, 2013, **52**, 12741–12748.
- 52 D. L. Reger, A. E. Pascui, M. D. Smith, J. Jezierska and A. Ozarowski, *Inorg. Chem.*, 2012, **51**, 11820–11836.
- 53 D. L. Reger, A. E. Pascui, M. D. Smith, J. Jezierska and A. Ozarowski, *Inorg. Chem.*, 2012, **51**, 7966–7968.
- 54 D. L. Reger, E. A. Foley, R. P. Watson, P. J. Pellechia, M. D. Smith, F. Grandjean and G. J. Long, *Inorg. Chem.*, 2009, **48**, 10658–10669.
- 55 D. L. Reger, R. P. Watson, J. R. Gardinier, M. D. Smith and P. J. Pellechia, *Inorg. Chem.*, 2006, **45**, 10088–10097.
- 56 D. L. Reger, E. A. Foley and M. D. Smith, *Inorg. Chem.*, 2009, **48**, 936–945.
- 57 D. L. Reger, E. A. Foley, R. F. Semeniuc and M. D. Smith, *Inorg. Chem.*, 2007, **46**, 11345–11355.
- 58 R. F. Semeniuc and D. L. Reger, *Eur. J. Inorg. Chem.*, 2016, **2016**, 2253–2271.

3.4 Synthesis and characterization of new coordination compounds with *N*-pyrazole-carborane ligands and divalent metals.

This chapter consists of two sections. The first section of this chapter focuses on the synthesis of coordination compounds bearing the divalent *d*-block metals Cu(II), Zn(II), Cd(II) and Hg(II) with ligand **L9** and the reactivity of ligands **L10** and **L11** against [Pd(CH₃CN)₂Cl₂]. All compounds have been fully characterized *via* analytical and spectroscopic techniques. Moreover, when possible, their crystal structures have been fully elucidated, allowing for a detailed analysis of their molecular structures.

The second section focuses on the study of the supramolecular assembly of the elucidated crystal structures.

The third section provides a summary of the work carried out in this chapter as well as the resulting conclusions.

3.4 Cu(II), Zn(II), Cd(II) and Hg(II) compounds of L9 and Pd(II) compounds of L10 and L11

Cage carbon-functionalization of carboranes with pyrazole groups can be traced back to the late 60s and early 70s reports by Zakharkhin *et al.*, which synthesized a whole family of ligands containing both groups^{1–3}. More recent works focus on the synthesis of drug analogues, as full advantage of the interesting biomedical properties of both functional groups can be taken. For instance, work carried out by Vázquez *et al.*⁴ features the synthesis of Rimonabant⁵ analogues, a drug useful for obesity treatment⁶, while recently published work by Buzharevsky *et al.*⁷ report a pyrazole compound substituted at position 5 by a carborane as an analogue of a non-steroidal anti-inflammatory drug. Pyrazole groups also feature as part of investigations in new strategies for functionalization of carboranes with *N*-heterocycles^{8–10} or azoles¹¹.

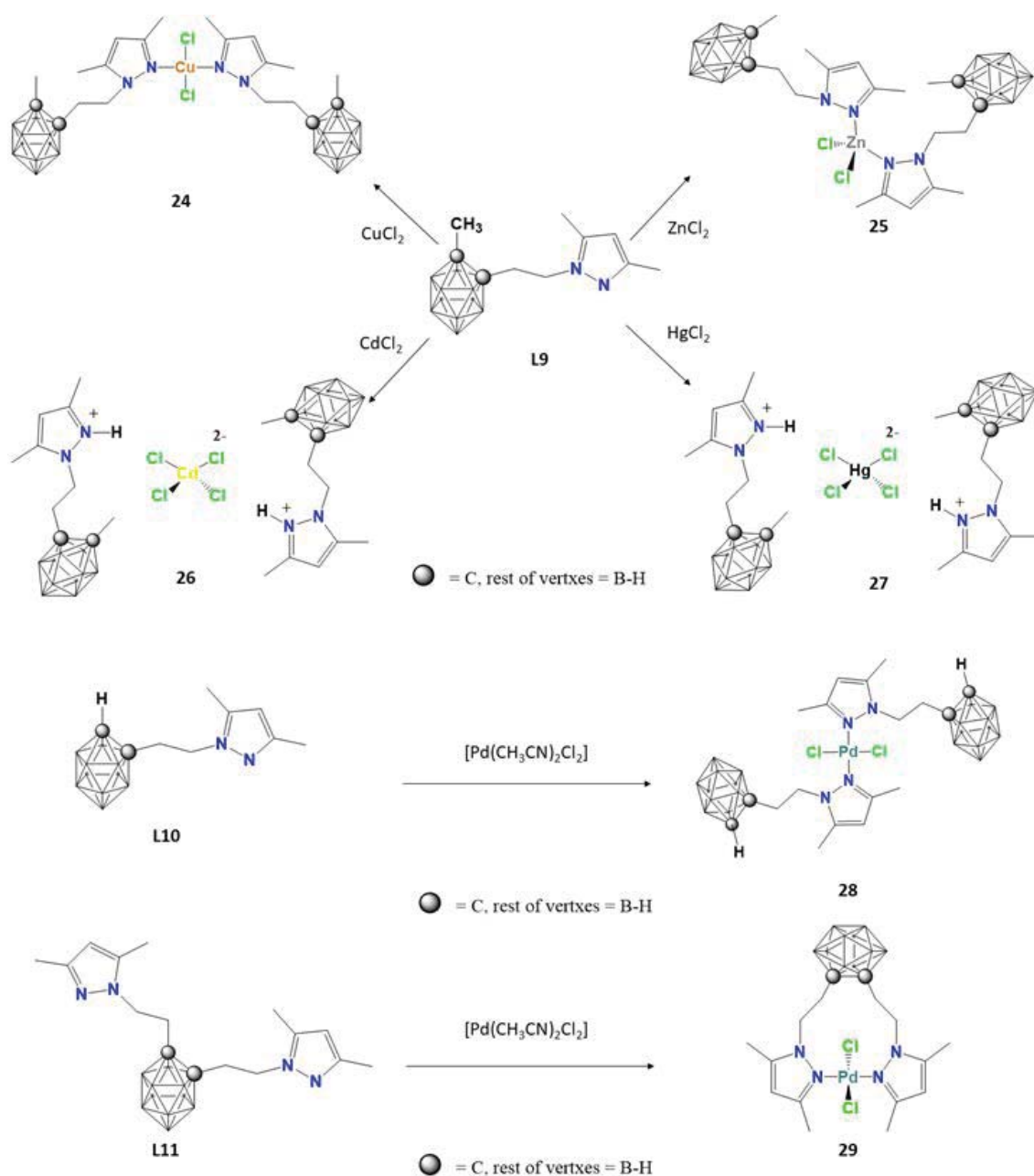
Despite the reported bibliography, examples of *N*-alkylcarbaborane pyrazole derivative ligands are scarce, and coordination compounds bearing those ligands are much scarcer. In this sense, pioneer works of Varadarajan, Hawthorne *et al.*^{12–14}, reported on a series of papers published between 1990-1992, describes a series of *B-N* bonded pyrazole-bridged metalla-bis(dicarbollide) derivatives and its reactivity against different metal salts such as CoCl₂, NiCl₂·6H₂O, FeCl₂·4H₂O and CuSO₄·6H₂O.

Thus, we decided to investigate the coordination behaviour of the carborane-pyrazole derived ligands **L9-L11** with several *d*-block metals. In particular, this chapter describes their reactivity with Cu(II), Zn(II), Cd(II), Hg(II) and Pd(II). Besides the full characterization for the obtained compounds *via* spectroscopic and analytical methods, the crystal structures of four of them have been fully elucidated, allowing for a detailed analysis of their molecular and supramolecular structures.

3.4.1 Synthesis and characterization

3.4.1.1 Synthesis

In this section, a total of six new coordination compounds bearing **L9** (**24-27**), **L10** (**27**) and **L11** (**28**) have been synthesized (Scheme 3.4.1).



Scheme 3.4.1 Synthetic reactions carried out in this section. Compounds are shown with their numbering Scheme.

Reactions for **L9** were carried out by mixing ethanolic solutions of the ligand and the corresponding metal chloride salt (MCl_2 , $M = Cu(II)$, $Zn(II)$, $Cd(II)$ and $Hg(II)$) in a 2:1 ligand to metal ratio. After stirring for certain time (6h-48h), the solutions were concentrated under vacuum and left to stand overnight in the fridge, resulting in the obtention of crystalline solids. However, for the reactions with $Cd(II)$ and $Hg(II)$, the 1H NMR spectra of the resulting products showed no significant shifts when compared to the free ligand, suggesting the non-coordination of **L9**. This fact was also confirmed by FTIR-ATR spectroscopy, and, as the crystal structure of **L9** was elucidated (Chapter 3.1), by comparison of the powder X-ray diffraction (PXRD) patterns. Assaying the same reaction with different solvents (methanol, acetonitrile) and the use of reflux conditions, even for a week, did not result in the coordination of the ligand to the metal center. Finally, it was found that the product obtained when using chloroform as solvent under reflux conditions showed significant shifts in its 1H NMR when compared to the free ligand, suggesting the coordination of the ligand to the metal center. However, the resulting products had low yields (26.4-27.8 %), compared to the moderate to good yields (ca. 80 %) for the rest of compounds.

Single crystals suitable for X-ray diffraction (SCXRD) were obtained for compounds **24**, **25** and **27**, allowing the elucidation of their crystal structures (*vide infra*). Their crystal structure revealed that **24** and **25** were monomers of general formula $[M(L9)_2Cl_2]$ ($M = Cu(II)$ (**24**), $Zn(II)$ (**25**)). Surprisingly, compound **27** is an ionic monomer of formula $[HL9]_2[HgCl_4]$. Although, it has not been possible to obtain crystals suitable for SCXRD for **26**, its synthesis, conductivity values, FTIR-ATR and 1H NMR spectra, as well as its PXRD pattern (Figure S3.4.1) showed notable similarities with those of compound **27**, thus a similar ionic structure is proposed (Scheme 3.4.1).

The protonation of **L9** in products **26** and **27** is attributed to the presence of traces of hydrochloric acid in chloroform, which is also consistent with the low yields obtained. In the light of these results, the reaction of **L9** against $Cd(II)$ and $Hg(II)$ using EtOH as solvent and adding few drops of concentrated HCl was assayed, resulting in the isolation of **26** and **27** in higher yields (ca. 60 %). This suggests that the addition of the carborane moiety to the pyrazole ring results in a decrease of its coordinative ability towards metal atoms, as, for instance, in this same PhD work, $Cd(II)$ and $Hg(II)$ coordination compounds with pyrazole-containing ligands **L4** and **L5** (compounds **11**, **12**, **16** and **17**, see Chapter 3.3) have been easily obtained¹⁵ while $Cd(II)$ and $Hg(II)$ compounds bearing **HL1** have

also been reported by our group^{16,17}. There are, in fact, reports on how the addition of carborane moieties to the backbone of ligands resulted in a decrease of their basicity^{18–20}.

Regarding the reactions involving ligands **L10** and **L11**, solutions of the corresponding ligands were mixed with $[\text{Pd}(\text{CH}_3\text{CN})_2\text{Cl}_2]$ solutions using dry CH_3CN as solvent in a ligand to metal ratio of 2:1 for **L10** and 1:1 for **L11**. After stirring overnight, the solutions were concentrated under vacuum and left to stand on the fridge for sixteen hours, resulting in the obtention of crystalline powders in moderate yields (49.3–68.1 %). Single crystals of **29** suitable for SCXRD were obtained after recrystallization in CHCl_3 , revealing the obtention of a monomer of formula $[\text{Pd}(\text{L11})\text{Cl}_2]$ (**29**). Unfortunately, it has not been possible to obtain crystals suitable for SCXRD for **28**, although a crystal structure is proposed (*vide infra*) (Scheme 3.4.1).

3.4.1.2 Characterization

Compounds **24–29** have been characterized via Elemental analyses (EA), FTIR-ATR spectroscopy, as well as ^1H , ^{11}B , $^{11}\text{B}\{^1\text{H}\}$ and $^{13}\text{C}\{^1\text{H}\}$ NMR spectroscopies when possible. For compounds **24**, **25**, **27** and **29**, their EA agree with the molecular formulae obtained from the crystal structures. For **26**, its EA agrees with a $[\text{Cd}(\text{HL9})_2\text{Cl}_4]$ empirical formula, whereas for **28** agrees with a $[\text{Pd}(\text{L10})_2\text{Cl}_2]$ empirical formula.

- Conductivity

Conductivity values were registered for compounds **24–27** in methanol (MeOH) and **28** and **29** in acetonitrile (CH_3CN). For compounds **24**, **25**, **28** and **29** the measured values ($12\text{--}66\ \Omega^{-1}\text{cm}^2\text{mol}^{-1}$, see Chapter 5: experimental section) agree with the presence of non-electrolytes, while those obtained for **26** and **27** (174 and $184\ \Omega^{-1}\text{cm}^2\text{mol}^{-1}$, respectively) suggest the presence of a 2:1 electrolyte²¹.

- FTIR-ATR Spectroscopy

For compounds **24–29**, FTIR-ATR spectra show characteristic bands for both pyrazole and carborane groups. For carborane, broad $[\nu(\text{B-H})]$ bands centred at $2580\text{--}2569\ \text{cm}^{-1}$ are identified²². Regarding pyrazole groups, the most intense bands attributed to them are $[\nu(\text{C}=\text{C}/\text{C}=\text{N})_{\text{ar}}]$ ($1595\text{--}1553\ \text{cm}^{-1}$), $[\delta(\text{C}=\text{C}/\text{C}=\text{N})_{\text{ar}}]$ ($1464\text{--}1391\ \text{cm}^{-1}$), $[\delta(\text{C-H})_{\text{ip}}]$ ($1046\text{--}1021\ \text{cm}^{-1}$) and $[\delta(\text{C-H})_{\text{oop}}]$ ($813\text{--}780\ \text{cm}^{-1}$ and $730\text{--}658\ \text{cm}^{-1}$)²². Moreover,

signals attributable to the pyrazole rings also appear as $[\nu(\text{C-H})_{\text{ar}}]$ ($3191\text{--}3088\text{ cm}^{-1}$) and $[\nu(\text{C-H})_{\text{al}}]$ ($2980\text{--}2848\text{ cm}^{-1}$). It is worth nothing that the FTIR-ATR spectra of compounds **26** and **27** stand out from all the rest, owing to the presence of a broad band in the region of $2984\text{--}2868\text{ cm}^{-1}$, overlapping with signals attributable to $[\nu(\text{C-H})_{\text{ar}}]$ ²². The presence of this signal could be attributed to $[\nu(\text{N-H}^+)]$, which is consistent with the crystal structure of **27**. Thus, it suggests that compound **26** also contains a protonated **L9**. As an example, FTIR-ATR spectrum of compound **27** is shown (Figure 3.4.1), while those of **24**–**26**, **28** and **29** can be found in Annex I (Figures S3.4.2–3.4.6)

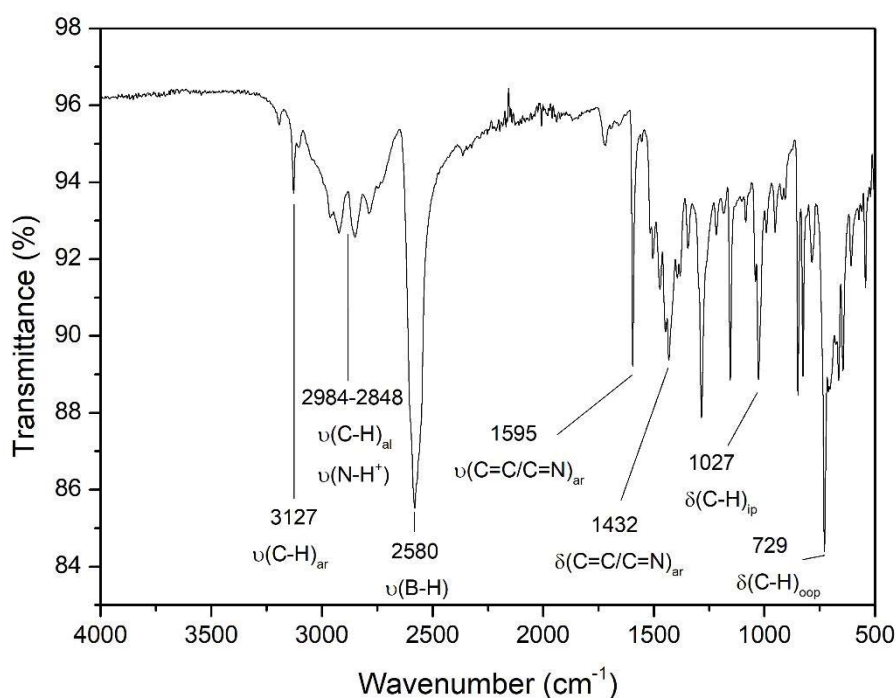


Figure 3.4.1 FTIR-ATR spectrum of compound **27**

- NMR Spectroscopy

All ^1H , ^{11}B , $^{11}\text{B}\{^1\text{H}\}$ and $^{13}\text{C}\{^1\text{H}\}$ NMR spectra have been recorded for compounds **25**–**29** in CDCl_3 . For compound **24**, containing a paramagnetic $\text{Cu}(\text{II})$ metal centre, NMR spectra have not been recorded. The ^1H NMR spectrum of **25** is shown as an example (Figure 3.4.2), while those of **26**–**29** (Figures S3.4.7–S3.4.10) can be found in Annex I. The ^1H NMR spectra of **25** shows significant upfield displacements for signals associated to 1-*H*-pyrazolyl (5.93 ppm for **25** vs. 5.80 for **L9**) as well as for $-\text{CH}_2\text{CH}_2\text{N}_{\text{Pz}}-$ fragments (4.66 ppm for **25** vs. 4.11 for **L9**). The observed upfield shift of the ligands' signals in the ^1H NMR spectra is a clear indication of metal coordination. For compounds

26 and **27** (Figures S3.4.7 and S3.4.8), the signals associated to 1-*H*-pyrazolyl display an even higher upfield displacement than **25** (6.13 and 6.03 ppm), although the displacement for -CH₂CH₂N_{Pz}- fragment is somewhat smaller (4.51 and 4.40 ppm). Contrary to **25**, they also show an upfield displacement for the signals associated to -CH₂CH₂N_{Pz}- (3.00 and 2.87 ppm in **26** and **27** vs 2.69 ppm in free **L9**) as well as for signals associated to CH₃ groups of the pyrazole moiety (2.30-2.49 ppm in **26** and **27** vs. 2.23 and 2.19 in free **L9**). These similarities between **26** and **27** in the ¹H NMR, as well as those previously seen in the FTIR-ATR seem to suggest that both compounds share similar traits.

The ¹H NMR spectra of **28** and **29** (Figures S3.4.9 and 3.4.10), on the other hand, shows significant upfield displacements to signals attributed to 1-*H*-pyrazolyl (5.98 and 5.90 ppm for **28** and **29** vs. 5.79 and 5.78 for **L10** and **L11**, respectively) and -CH₂CH₂N_{Pz}- fragments (5.04 and 4.98 ppm for **28** and **29** vs. 4.03 and 4.11 for **L10** and **L11**, respectively), but also in the -CH₂CH₂N_{Pz}- fragment (3.00 and 3.72 ppm for **28** and **29** vs. 2.75 and 2.73 for **L10** and **L11**, respectively). In fact, this last shift is especially remarkable for compound **29**, which can be attributed to the chelate coordination mode of **L11**, while its much more subtle for compound **28**, which, having only one donor atom, can only have a monodentate coordination mode. For all of them, the alkylic chain signals appear as multiplets or broad bands in the regions of 5.00-4.40 and 3.72-2.70 ppm. As previously discussed for **L9** (Chapter 3.1), their particular shapes owe to an AA'BB' spin system, caused by rigid conformation of the resulting compounds in solution. Data for the ¹H NMR of **25-29** is summarized in Table 3.4.1.

Table 3.4.1 ¹H NMR spectra signals for **25-29**

	25	26	27	28	29
CH _{Pz}	5.96(s)	6.13(s)	6.03 (s)	5.98(s)	5.90(s)
CH ₂ -N	4.66(br)	4.51(m)	4.40(m)	5.00(m)	4.98(m)
C _{carb} -H	-	-	-	3.91(br)	-
C _{carb} -CH ₂	2.70(m)	3.00(m)	2.87(m)	3.00(m)	3.72(m)
C _{carb} -CH ₃	2.31(s)	2.28(s)	2.16(s)	-	-
Pz-CH ₃	2.17(s)	2.49(s)	2.40(s)	2.85(s)	2.73(s)
	2.06(s)	2.40(s)	2.35(s)	2.29(s)	2.30(s)

δ (ppm) / multiplicity s = singlet, m = multiplet, br = broad

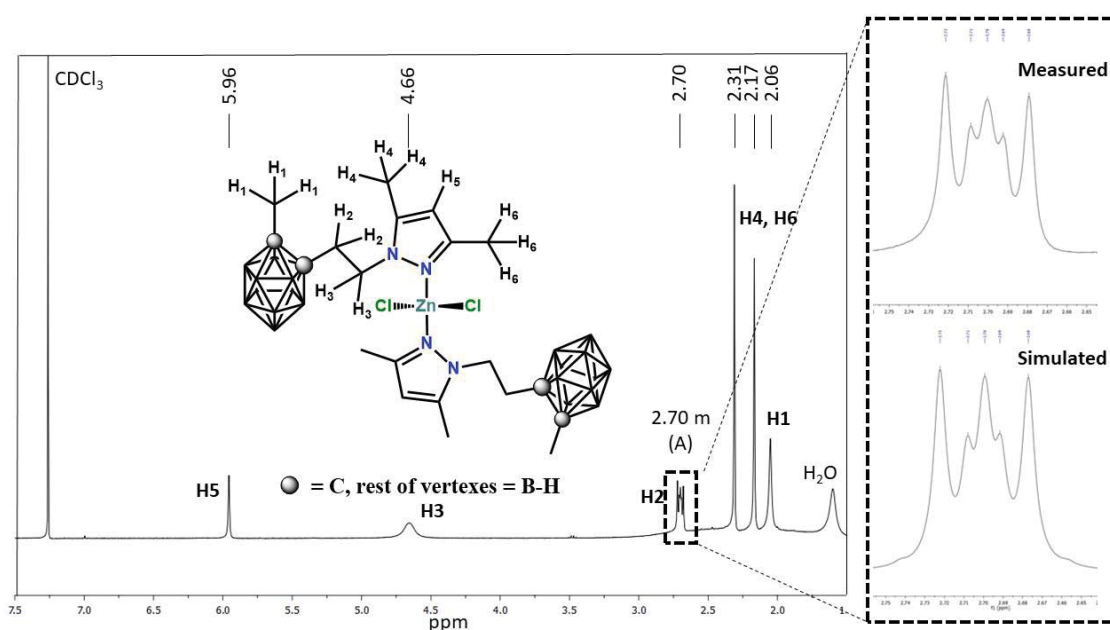


Figure 3.4.2 ^1H NMR spectrum of compound **25** (CDCl_3 , 400.0 MHz). Detail of the simulated and measured multiplets.

^{11}B and $^{11}\text{B}\{^1\text{H}\}$ NMR spectra are consistent with a *closo*-icosahedral geometry for boron cages, as discussed for **L9-L11** in Chapter 3.1. The ^{11}B and $^{11}\text{B}\{^1\text{H}\}$ NMR spectra of **25** is shown as an example (Figure 3.4.3), while those of **26-29** can be found in Annex I (Figures S3.4.11-S3.4.14). In the $^{11}\text{B}\{^1\text{H}\}$ NMR spectra for compounds **25-27** (Figures 3.4.3, S3.4.11 and S3.4.12) three resonances can be identified in a 1:1:8 ratio, a pattern typical for asymmetrically *ortho*-substituted carboranes²³. Compound **28**, on the other hand, displays a 1:1:2:6 pattern (Figure S3.4.13), a slight variation of the previous 1:1:8 pattern, and typical for asymmetrically *ortho*-substituted carbaboranes²³, while **29** (Figures S3.4.14) displays two resonances in a 2:8 ratio, typical of homodi-substituted *o*-carboranes²³.

Lastly, all $^{13}\text{C}\{^1\text{H}\}$ NMR spectra are consistent with the presence of the expected functional groups. It is remarkable that signals do not show any significant displacement, appearing in similar positions to those of the free ligands. The $^{13}\text{C}\{^1\text{H}\}$ NMR spectrum of **25** is shown as an example (Figure 3.4.4), while those of **26-29** can be found in Annex I (Figures S3.4.15-S3.4.18).

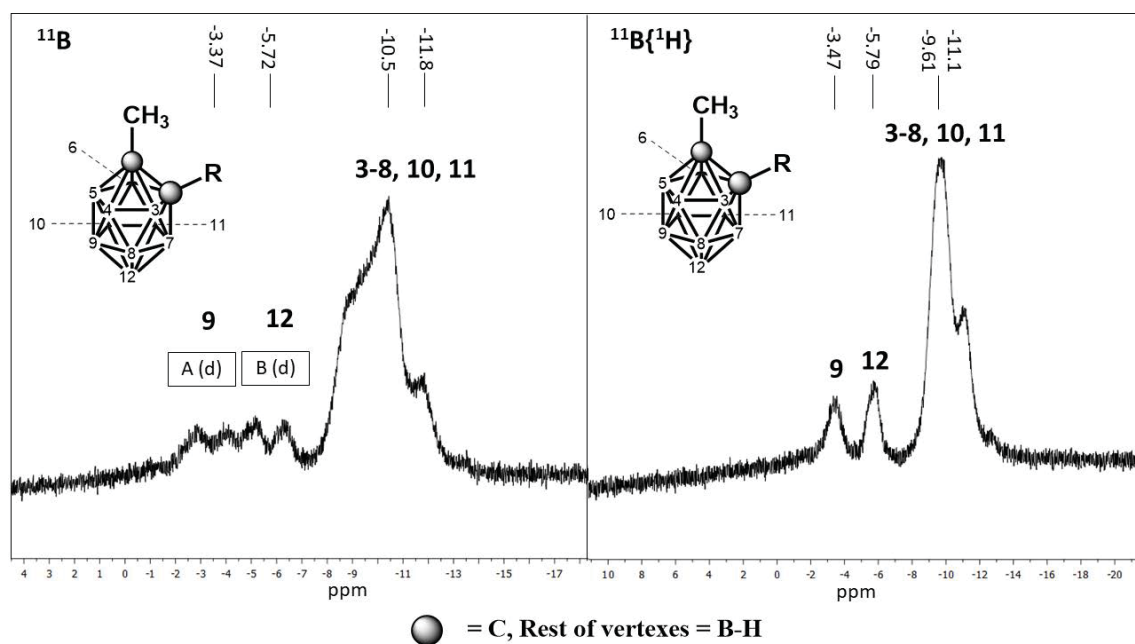


Figure 3.4.3 ^{11}B (left) and $^{11}\text{B}\{^1\text{H}\}$ NMR spectra for **26** (CDCl_3 , 128.6 MHz).

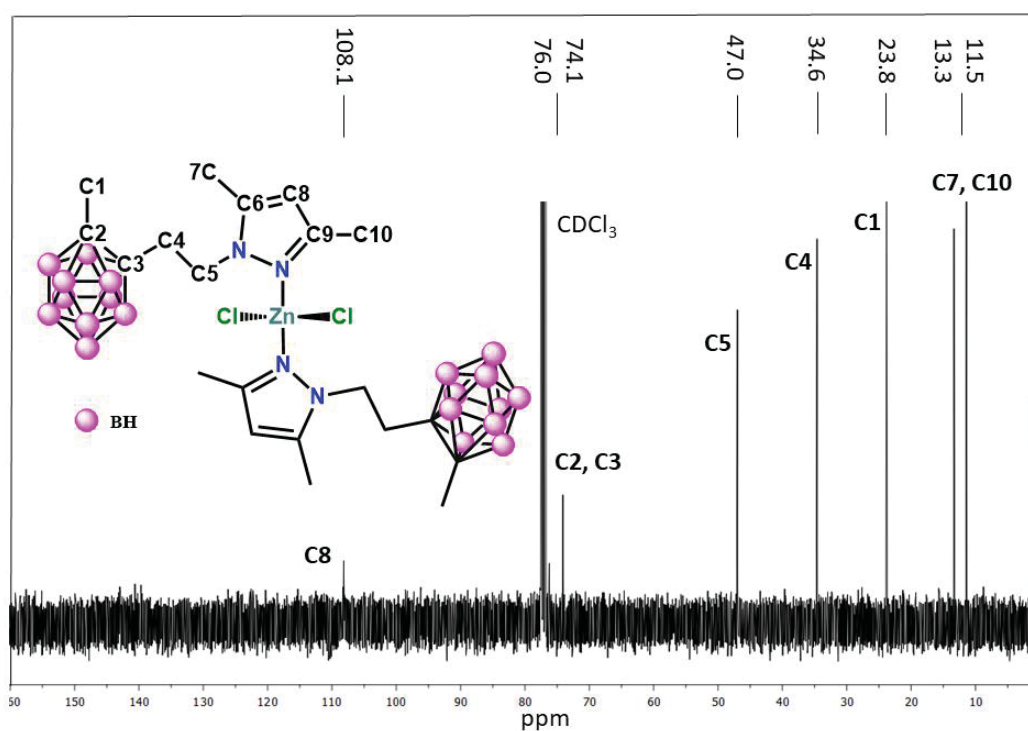


Figure 3.4.4 $^{13}\text{C}\{^1\text{H}\}$ NMR spectrum of compound **25** (CDCl_3 , 100.6 MHz)

- X-Ray Crystal Structures

Molecular structures of [Cu(L9)₂Cl₂] (24) and [Zn(L9)₂Cl₂] (25)

For complexes **24** and **25** (Figure 3.4.5) it was possible to obtain crystals suitable for SCXRD from the reaction mixture and *via* recrystallization in Et₂O, respectively. Both compounds crystallize in the monoclinic system, but in different space groups: C2/c (**24**) and P2₁/c (**25**), showing a monomeric structure with a M:L9:Cl 1:2:2 ratio. Both compounds possess a [M(N_{pz})₂Cl₂] *core*. Thus, the local environment of each metal consists of two nitrogen atoms provided by two different pyrazole ligands subunits (M-N 1.9966(19) Å to 2.081(3) Å), and two chlorine atoms (M-Cl 2.2311(17) Å to 2.2413(19)Å). Even though both compounds possess a similar *core*, their molecular structures are different. The Cu(II) (**24**) metal centre shows a distorted square planar geometry with a *trans* disposition ($\tau_4 = 0.26^{24}$), whereas for Zn(II) (**25**) it shows a tetrahedral geometry ($\tau_4 = 0.93^{24}$). Considering that both compounds display the same coordination environment, we decided to further discuss the factors leading to these geometries. A search in the CSD database²⁵ reveals that the vast majority of Cu(II) compounds containing at least two N and two Cl atoms are five or six-coordinated (2083 out of 2823 reported crystal structures, 73.8 %), whereas four-coordinate Cu(II) compounds only account for 26.2 % of the reported structures (740 out of 2823). For Zn(II) compounds, a higher percentage of them are four-coordinate (1200 out of 1677, 71.6 %). In the case of **24** and **25**, the metal coordination sphere is sterically crowded, as the methyl and carborane groups of the ligand prevent the coordination of a fifth and sixth atom, thus promoting the formation of tetracoordinated compounds.

Regarding their coordination geometries, four-coordinate Cu(II) compounds are known to display a diverse set of coordination geometries ranging from square planar to tetrahedral^{26,27}, although the tetrahedral geometry is more efficient at minimizing electronic repulsion. This distortion of the tetrahedral geometry, manifested as a flattening of the tetrahedron, is attributed to the Jahn-Teller effect generated by the d^9 electronic configuration of the Cu(II) atoms^{28–34}. The final degree of distortion of the resulting compounds depends on finely balanced factors such as steric effects, ligand-ligand repulsion, small crystal packing forces and hydrogen bonds^{29,32}. On the other hand, four-coordinate Zn(II) compounds, displaying a d^{10} electronic configuration, commonly adopt tetrahedral coordination geometries, as no Jahn-Teller effects are expected due to a full occupation of the degenerate orbitals^{32,35}.

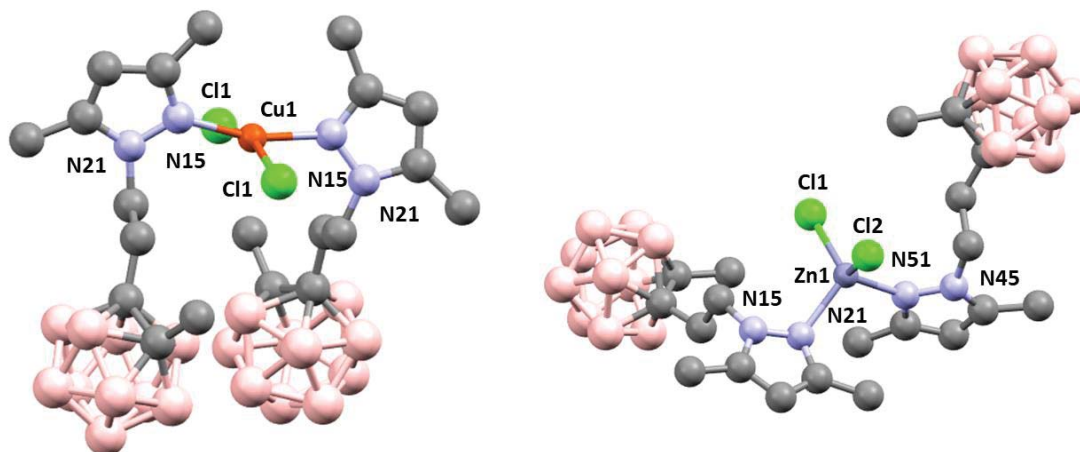


Figure 3.4.5 Compounds **24** (left) and **25** (right), showing all its non-hydrogen atoms and numbering scheme. Colour code: grey (C), pink (B), light blue (N), light green (Cl), orange (Cu), blue-grey (Zn).

Moreover, in **24**, the carborane substituents of the pyrazole protrude in the same direction, as the pyrazoles are coordinated in a *syn* fashion (dihedral angles between the mean plane of the pyrazoles is 21.63°), whereas in **25**, the pyrazoles coordinate in a distorted *anti* fashion (dihedral angles between the mean plane of the pyrazoles is 87.92°).

A search in the Cambridge Structural Database (CSD)²⁵ reveals a total of forty-seven crystal structures bearing the same *core* as **24**. Most of these compounds contain bis(pyrazole) ligands (twenty-six, 55.3 %) and twenty-one (44.7 %) contain monopyrazole ligands. Whereas in almost all other reported structures containing monopyrazole ligands the Cu(II) atom is located on a crystallographic center of inversion^{36,40}, for **24** it is located on a 2-fold axis. This is certainly unexpected, also for the fact that the carborane moieties are bulky and their proximity should be prevented. The search in the CSD only shows another structure containing a monopyrazole ligand (JEVXUD)⁴¹ with a very close arrangement of pyrazole moieties to that of **24**. However, a closer look to this structure shows that this structure has not been properly registered in the CSD, as the ligand in JEVXUD⁴¹ is, in fact, a bispyrazole (1,8-bis(3,5-dimethyl-1-*H*-pyrazolyl)-3,6-dithiaoctane), that acts as a bidentate ligand. For **25**, fifty-five crystal structures with the similar coordination features are found²⁵. Of them, only seventeen (30.9 %) contain monopyrazole ligands. The majority of these seventeen compounds (eleven, 64.7 %) display an *anti* coordination mode, just as compound **25**, while six (35.3 %) display a *syn* coordination. Therefore, the *syn* coordination mode for similar monopyrazole ligands is more common for Zn(II) compounds than for Cu(II) compounds, as **24** is the first example of a Cu(II) monopyrazole ligand with this conformation.

Relevant distances and angles for **24** and **25** are summarized in Table 3.4.2 and are in range of similar compounds reported in the literature^{36–39}.

Table 3.4.2 Selected bond lengths (Å) and angles (°) for **24** and **25**

24		25	
Cu(1)-N(21)#1	1.9966(19)	Zn(1)-Cl(1)	2.2311(13)
Cu(1)-N(21)	1.9966(19)	Zn(1)-Cl(2)	2.2311(17)
Cu(1)-Cl(1)	2.2413(19)	Zn(1)-N(21)	2.048(4)
		Zn(1)-N(51)	2.081(3)
Cl(1)-Cu(1)-Cl(1)#1	159.46(5)	Cl(2)-Zn(1)-Cl(1)	115.12(6)
N(21)-Cu(1)-Cl(1)	90.73(6)	N(21)-Zn(1)-Cl(1)	104.34(10)
N(21)#1-Cu(1)-Cl(1)	92.31(6)	N(21)-Zn(1)-Cl(2)	111.40(11)
N(21)#1-Cu(1)-Cl(1)#1	90.73(6)	N(21)-Zn(1)-N(51)	110.15(14)
N(21)-Cu(1)-Cl(1)#1	92.31(6)	N(51)-Zn(1)-Cl(1)	114.06(10)
N(21)#1-Cu(1)-N(21)	162.88(11)	N(51)-Zn(1)-Cl(2)	101.93(12)
#1: x, -y+1, z-1/2			

Molecular structure of {[HL9]₂[HgCl₄]} (27)

Suitable crystals for X-ray elucidation of the crystal structure of **27** were obtained *via* recrystallization in a CH₂Cl₂:Hexane mixture in a 1:1 ratio. It crystallizes in a monoclinic system and a P2₁ space group. It contains two crystallographically independent monomeric (HgCl₄)²⁻ anions and four crystallographically independent (HL9)⁺ cations (Figure 3.4.6) in its unit cell. In the (HgCl₄)²⁻ anions the metal centre displays a tetrahedral geometry ($\tau_4 = 0.89$ and 0.91^{24}), showing small differences in bond lengths and angles between both molecules. The Hg-Cl bond angles are within the range of reported (HgCl₄)²⁻ compounds (Table 3.4.3). A search in the CSD²⁵ reveals that there are a total of a hundred and seventeen reported crystal structures bearing the HgCl₄²⁻ anions. To the best of our knowledge, none of them contains a pyrazolium cation, although some imidazolinium cations are reported^{42–44}.

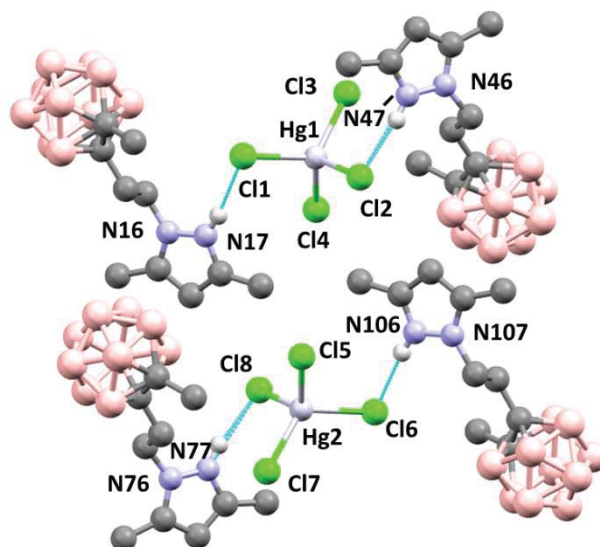


Figure 3.4.6 Compound **27**, showing all its non-hydrogen atoms and their corresponding numbering scheme. Colour code: grey (C), pink (B), light blue (N), light green (Cl), light-grey (Hg).

Table 3.4.3 Selected bond lengths (Å) and angles (°) for **27**

27			
Bond lengths (Å)			
Hg(1)-Cl(1)	2.5402(17)	Hg(2)-Cl(5)	2.5274(16)
Hg(1)-Cl(2)	2.5309(15)	Hg(2)-Cl(6)	2.5438(17)
Hg(1)-Cl(3)	2.4450(17)	Hg(2)-Cl(7)	2.4477(17)
Hg(1)-Cl(4)	2.4572(18)	Hg(2)-Cl(8)	2.4547(17)
Bond angles (°)			
Cl(1)-Hg(1)-Cl(2)	103.92(6)	Cl(5)-Hg(2)-Cl(6)	103.71(6)
Cl(1)-Hg(1)-Cl(3)	119.22(6)	Cl(7)-Hg(2)-Cl(5)	103.64(6)
Cl(1)-Hg(1)-Cl(4)	106.83(6)	Cl(7)-Hg(2)-Cl(6)	121.14(6)
Cl(2)-Hg(1)-Cl(3)	103.28(6)	Cl(7)-Hg(2)-Cl(8)	109.59(6)
Cl(2)-Hg(1)-Cl(4)	113.04(6)	Cl(8)-Hg(2)-Cl(5)	113.65(6)
Cl(3)-Hg(1)-Cl(4)	110.51(6)	Cl(8)-Hg(2)-Cl(6)	105.27(6)

Molecular structure of [Pd(L11)Cl₂] (29)

Suitable crystals for X-ray elucidation of the crystal structure of **29** were obtained *via* recrystallization in CH₃CN. It crystallizes in a triclinic system and a $\overline{P}1$ space group, showing a monomeric structure with a M:L11:Cl 1:1:2 ratio (Figure 3.4.7). It possesses a [Pd(N_{pz})₂Cl₂] *core*, which is reported in a hundred and twenty-five structures in the literature²⁵, forty-six of them (36.8 %) bearing chelate bispyrazole ligands. Ligand **L11** displays a *NN*-chelate behaviour, similar to the reported Pd(II) compounds bearing **L4** and **L5**⁴⁵ and other similar bispyrazole ligands synthesized in our group⁴⁶. Thus, the local environment of each metal consists of two nitrogen atoms provided by two different pyrazole moieties, and two chlorine atoms. The metal centre shows an almost perfect square planar geometry with a *trans* disposition ($\tau_4 = 0.024^{24}$). Relevant distances and angles are summarized in Table 3.4.4 and are in range of similar compounds reported in the literature^{45,46}.

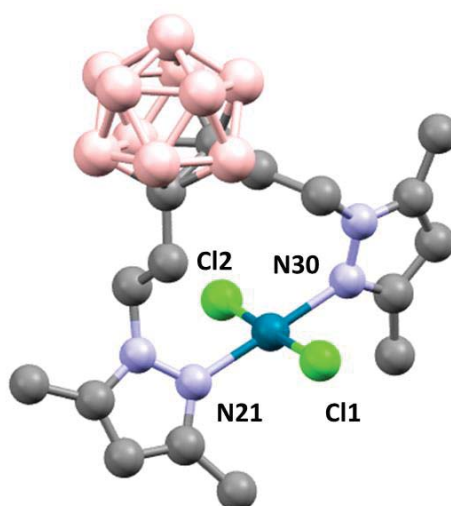


Figure 3.4.7 Compound **29**, showing all its non-hydrogen atoms and numbering scheme. Colour code: grey (C), pink (B), light blue (N), light green (Cl), turquoise (Pd).

Table 3.4.4 Bond lengths (Å) and angles (°) for **29**

29			
Bond lengths (Å)			
Pd(1)-Cl(1)	2.2972(2)	Pd(1)-N(21)	2.017(2)
Pd(1)-Cl(2)	2.3112(7)	Pd(1)-N(30)	2.014(2)
Bond Angles (°)			
Cl(1)-Pd(1)-Cl(2)	178.30(3)	N(21)-Pd(1)-Cl(1)	89.60(6)
N(21)-Pd(1)-Cl(2)	91.67(6)	N(30)-Pd(1)-Cl(1)	89.33(7)
N(30)-Pd(1)-Cl(2)	89.38(7)	N(30)-Pd(1)-N(21)	178.33(8)

3.4.2 Supramolecular structures of **24**, **25**, **27** and **29**

In the solid state, the different orientation of the coordinating pyrazole moieties in **24** (*syn*) and **25** (*anti*) (see previous section) has a dramatic effect regarding their intermolecular interactions. In **24**, the position of the carborane clusters and pyrazole rings prevents their participation in intermolecular interactions, resulting in a supramolecular structure formed by a stacking of 2D layers where different molecules interact *via* weak C-H \cdots H-B contacts between boron clusters and methyl groups of the ligands, forming helicoidal networks (Figure 3.4.8). These hydric-to-protic interactions, called dihydrogen bonds, owe to the hydric character of the B-H unit, which allows the formation of the dihydrogen bonds with H-X units, where X is an element with an electronegativity value higher than that of boron^{47,48}. In **25**, however, chlorine atoms are more accessible, and therefore, they participate in stronger C-H \cdots Cl interactions with the methyl groups of the ligand. This interaction results in the formation supramolecular helicoidal 1D-chains (Figure 3.4.9). Relevant intermolecular interactions are summarized in Table 3.4.5

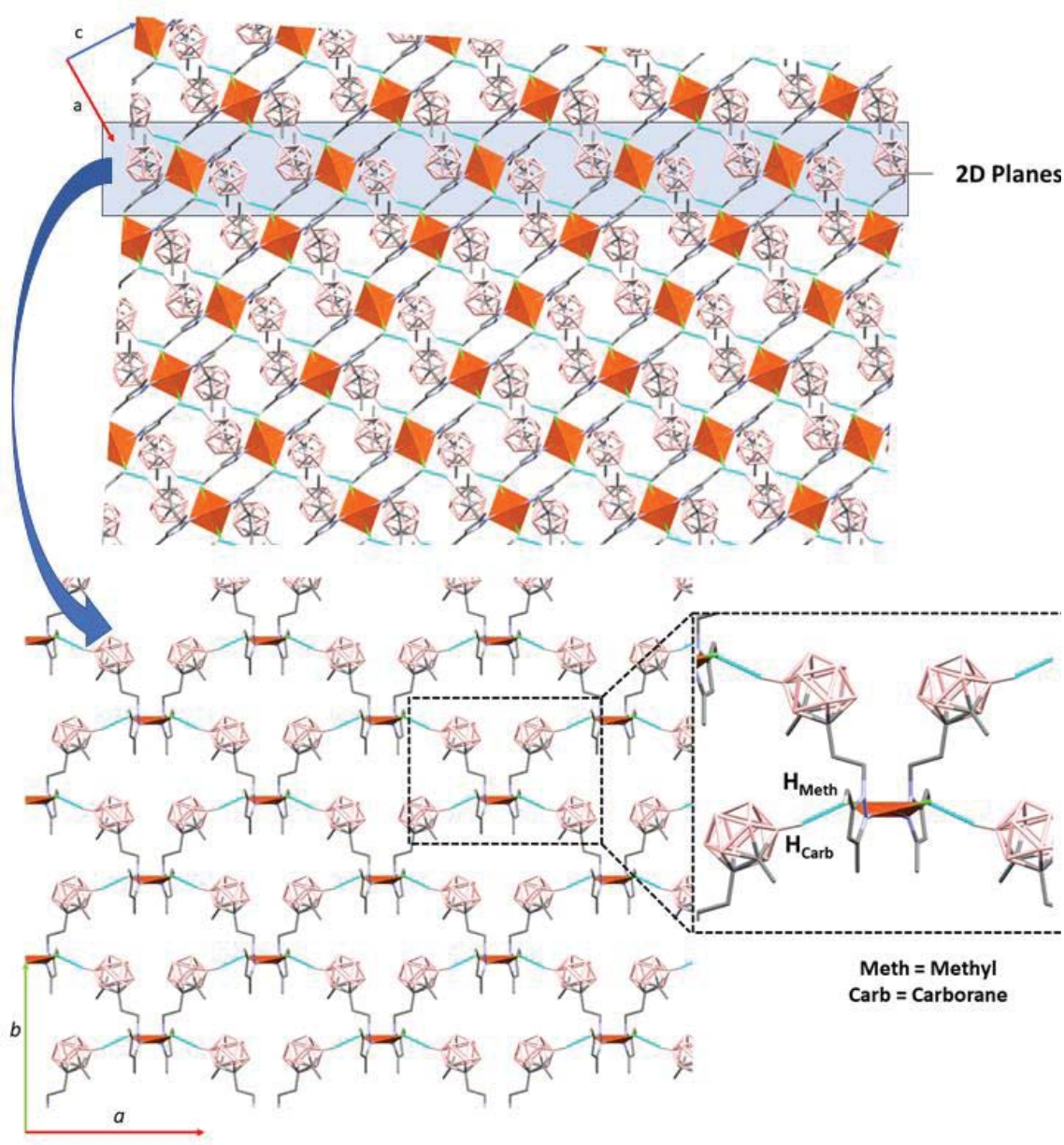


Figure 3.4.8 Supramolecular structure of **24**; view along *b* axis (top) and view of the 2D planes along *c* axis (bottom). Only hydrogen atoms participating in supramolecular interactions are shown. Colour code: grey (C), white (H), pink (B), light blue (N), light green (Cl), orange (Cu). Cu(II) atoms are also represented as orange polyhedra. Intermolecular interactions are represented as dashed light-blue lines.

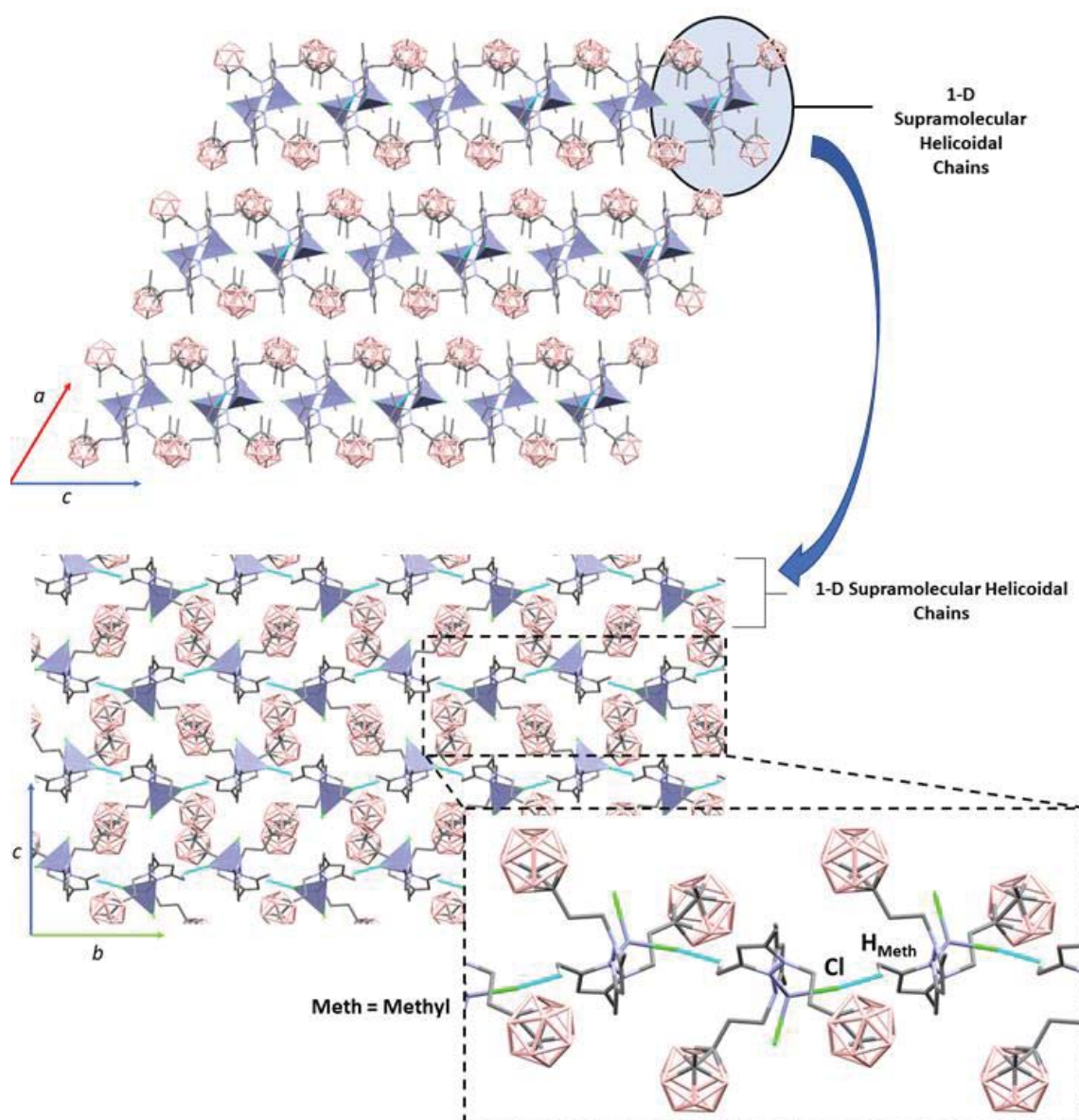


Figure 3.4.9 Supramolecular structure of **25**; view along *b* axis (top), view of the 1D-chains along *c* axis (bottom). Only hydrogen atoms participating in supramolecular interactions are shown. Colour code: grey (C), white (H), pink (B), light blue (N), light green (Cl), blue-grey (Zn). Zn(II) atoms are also represented as blue-grey polyhedra. Intermolecular interactions are represented as dashed light-blue lines.

The supramolecular structure of **27** could be described as a dense thread of parallel supramolecular 1-D chains. Each chain comprises exclusively Hg1 or Hg2 anions. They are held together thanks to a set of interactions involving the protonated pyrazole nitrogen and chlorine moieties as well as the chlorine moieties and the alkylic chain (Figure 3.4.10). Relevant intermolecular interactions are summarized in Table 3.4.5

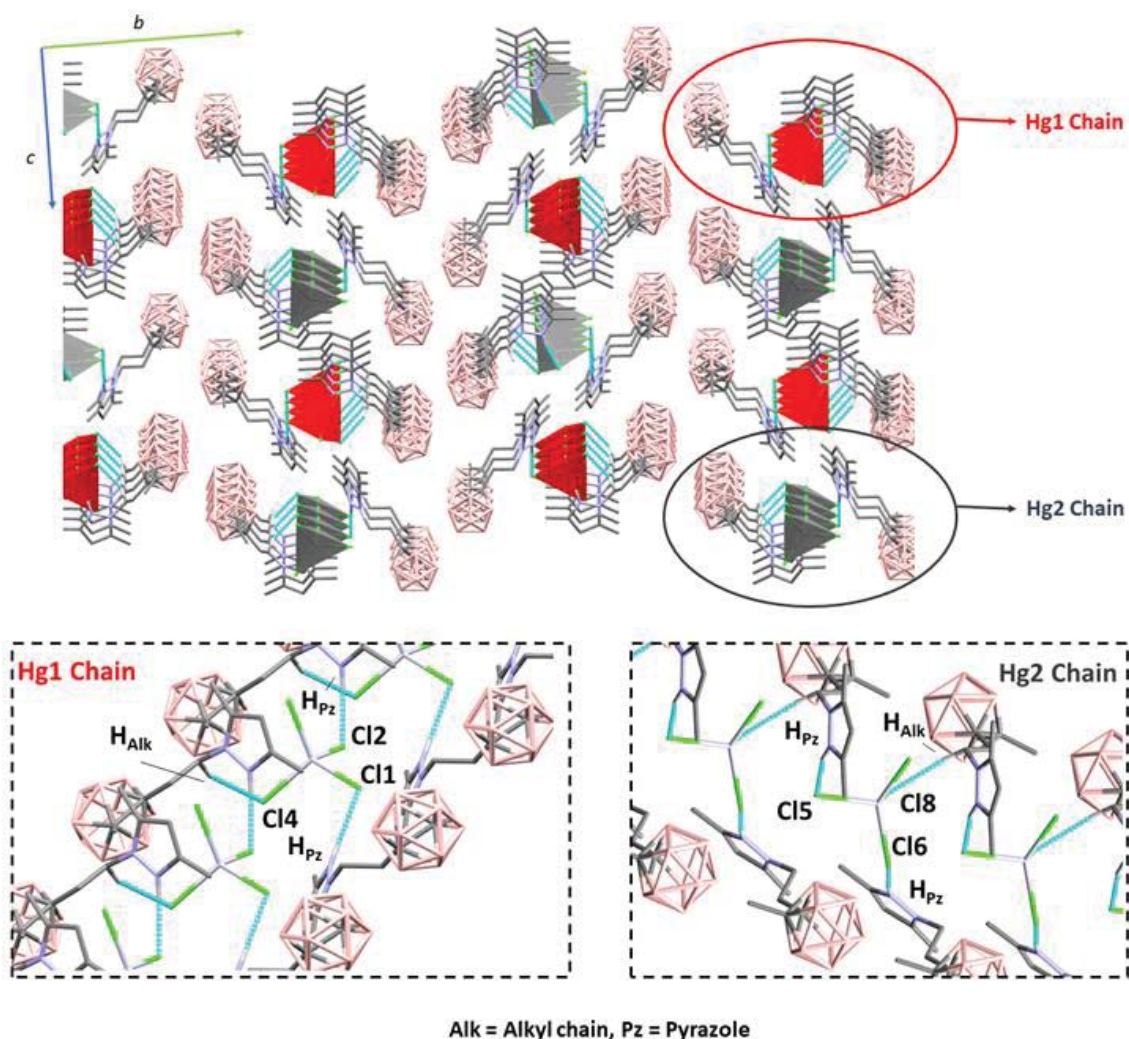


Figure 3.4.10 Supramolecular structure of compound **27**. Crystallographically independent anions are displayed as differently coloured (red for Hg1, grey for Hg2) polyhedrons. Colour code: grey (C), white (H), pink (B), light blue (N), light green (Cl), light grey (Hg). Intermolecular interactions are represented as dashed light-blue lines.

Regarding the supramolecular structure of **29**, two interactions promote the formation of 2D planes perpendicular to the *c* axis. The first and strongest interaction, responsible of the expansion along the *a* direction, is between a chlorine atom and an hydrogen atom of the alkylic chain. The second one, much weaker, is responsible for the expansion along the *b* direction and involves dihydrogen bonds between the pyrazole group and the carborane moiety (Figure 3.4.11). Relevant intermolecular interactions are summarized in Table 3.4.5.

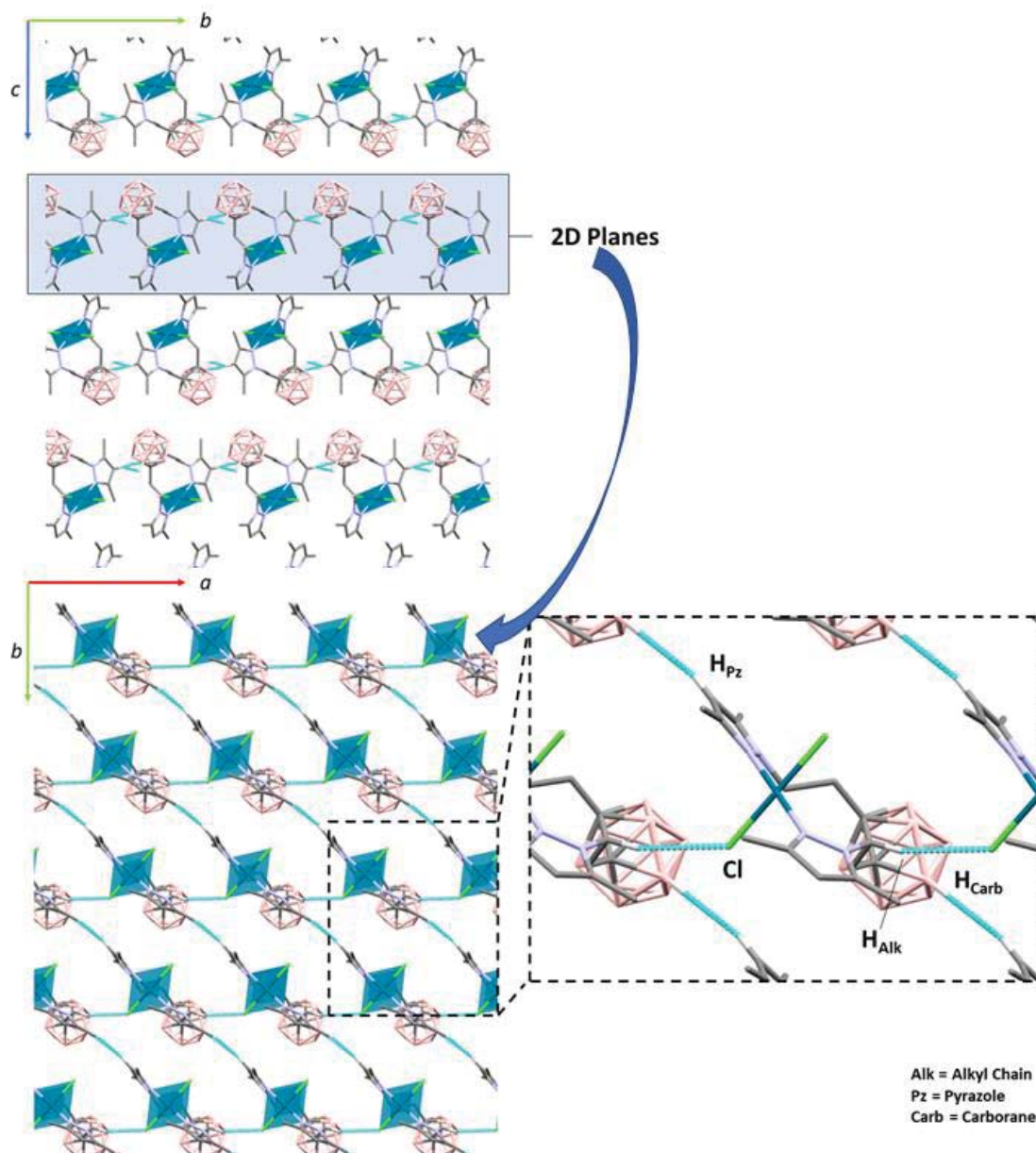


Figure 3.4.11 Supramolecular structure of **29**; view along *a* axis (top), view of the 2D planes along *c* axis (bottom). Only hydrogen atoms participating in intermolecular interactions are shown. View along *c* axis. Colour code: grey (C), white (H), pink (B), light blue (N), light green (Cl), turquoise (Pd). Pd(II) atoms are also represented as turquoise polyhedral. Intermolecular interactions are represented as dashed light-blue lines.

Table 3.4.5 Selected intermolecular interactions for **24**, **25**, **27** and **29**

	D-H...A (Å)	D-H (Å)	H-D...A (Å)	> D-H...A (°)
24				
C_{Meth}-H_{Meth}...H_{Carb}-B_{Carb}	2.372	0.960	3.061	128.29
25				
C_{Meth}-H_{Meth}...Cl	2.795	0.960	3.440	125.28
27				
N_{Pz}-H_{Pz}...Cl1	2.310	0.880	3.180	169.85
N_{Pz}-H_{Pz}...Cl2	2.225	0.881	3.092	168.05
C_{Alk}-H_{Alk}...Cl4	2.666	0.989	3.594	156.20
N_{Pz}-H_{Pz}...Cl5	2.219	0.879	3.081	166.60
N_{Pz}-H_{Pz}...Cl6	2.316	0.880	3.190	171.93
N_{Pz}-H_{Pz}...Cl1	2.310	0.880	3.180	169.85
29				
C_{Pz}-H_{Pz}...H_{Carb}-B	2.203	0.930	3.086	158.27
C_{Alk}-H_{Alk}...Cl	2.822	0.970	3.762	163.44

Meth = methyl, Carb = carborane, Pz = pyrazole, Alk = alkyl chain

The supramolecular structures of compounds **24**, **25**, **27** and **29** were further analysed using Hirshfeld surface calculations performed with CrystalExplorer 17.5⁴⁹. All surfaces have been calculated at a 0.5 e⁻au⁻³ isovalue.

For compound **24** the lack of red dots in the d_{norm} representation suggests that the present intermolecular interactions are weak or less directional in nature. This confirms that the supramolecular interactions in **24** are very weak. (Figure 3.4.12). For **25**, as intermolecular interactions are much stronger and directional, those clearly appear as red dots in the Hirshfeld surface showing the presence of C-H...Cl interactions (Figure 3.4.12). Fingerprint plots of both compounds show that the strongest interactions are H...H contacts, which imply almost the totality of the Hirshfeld surface for both compounds (82.4 % (**24**) and 84.1 % (**25**)). Minor Cl...H interactions (10.5 % (**24**), 10.2% (**25**)) are also identified. These appear as spikes, suggesting that these interactions are directional, albeit very weak. Lastly, for **25**, minor C...H interactions (4.4 %) appear as “wings” in their fingerprint plot, suggesting that some C-H... π interactions are also involved in the supramolecular scaffold.

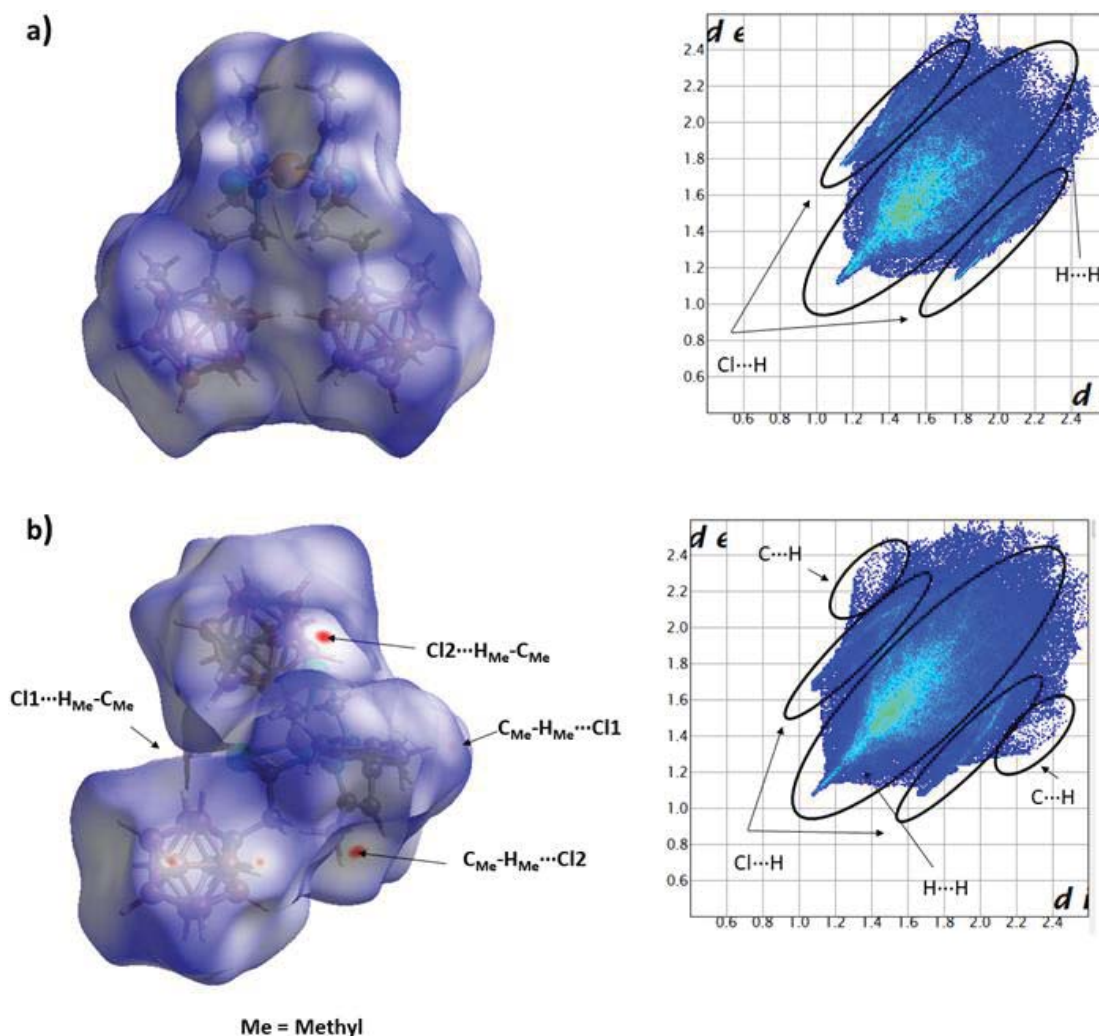


Figure 3.4.12 D_{norm} representation and fingerprint plot for compounds **24** (a). and **25** (b).

For compound **27**, the d_{norm} mapping and the 2D fingerprint plot has been carried out for individual components and for the association of components corresponding to the asymmetric unit (Figure 3.4.13). For the individual components, only the Hirshfeld surface of one HgCl_4^{2-} anion and one HL9^+ cation is shown as an example, as the rest of fingerprint plots and surfaces are similar. The asymmetric unit contains two HgCl_4^{2-} anions and four HL9^+ cations, as described in the previous section. As expected for the HgCl_4^{2-} anion, the fingerprint plot shows that most of the implied surface area belongs to $\text{H}\cdots\text{Cl}$ interaction (89-90 %), which appear as strong, sharp peaks. A smaller peak can also be identified, belonging to $\text{Cl}\cdots\text{N}$ interactions, and implying 4.5-5 % of the Hirshfeld surface. Regarding the HL9^+ cation, its fingerprint plot shows that $\text{H}\cdots\text{H}$ interactions (mostly those involving carborane clusters) account for 80-82 % of the implied surface, whereas ionic $\text{H}\cdots\text{Cl}$ interaction only account for 13-15 % of the implied surface.

However, $\text{H}\cdots\text{Cl}$ interactions appear as sharp peaks, suggesting that they are the strongest interactions. Regarding the asymmetric unit association, fingerprint plots reveal that $\text{Cl}\cdots\text{H}$ interactions play a notable role (16.8 % of implied Hirshfeld surface), appearing as well-defined spikes in the 2D fingerprint plot. Nonetheless, $\text{H}\cdots\text{H}$ interactions still represent most of the intermolecular forces in **27** (75.9 % of implied Hirshfeld surface).

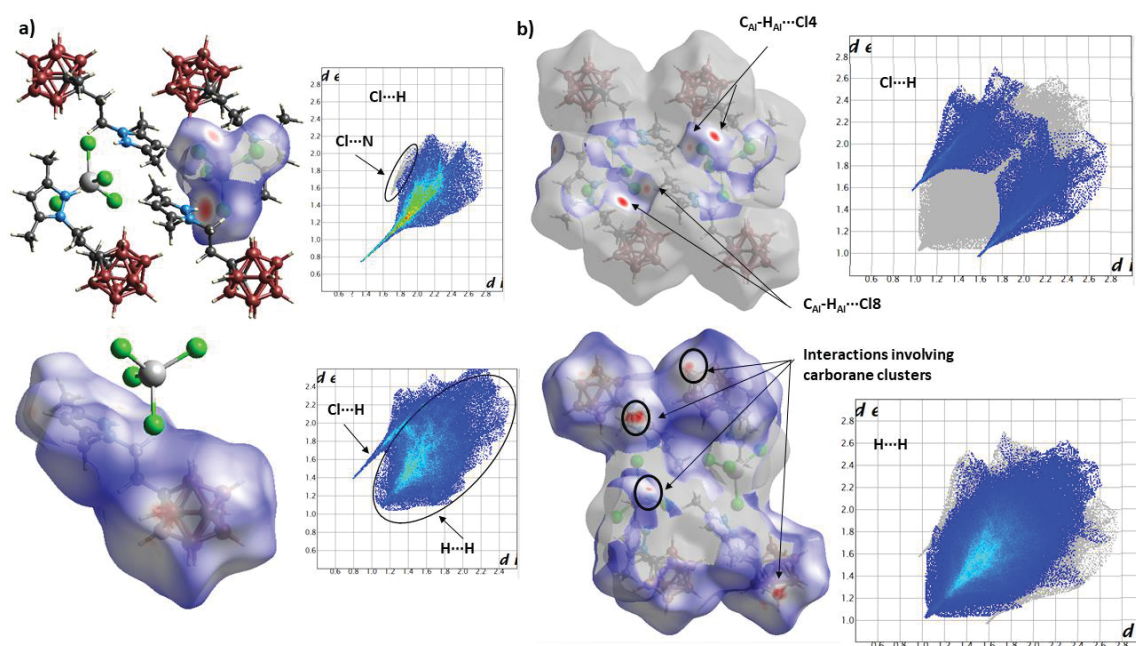


Figure 3.4.13 D_{norm} representation and fingerprint plots for compound **27** anion (top) and cation (bottom) (a). D_{norm} representation and fingerprint plots for **27** asymmetric unit, highlighting $\text{Cl}\cdots\text{H}$ (top) and $\text{H}\cdots\text{H}$ (bottom) interactions (b).

The d_{norm} representation (Figure 3.4.14) for compound **29** shows intense red spots over its chlorine atoms, alkylic chain atoms and the carborane cluster, confirming that those groups play key roles in holding its supramolecular scaffold, as mentioned previously. The analysis of its fingerprint plot (Figure 3.4.14) reveals that $\text{H}\cdots\text{H}$ interactions, centred in the carborane cluster, account for the majority of the implied surface (71.9 %), much like in compounds **24** and **25**, although the value of the implied surface is lower for **29**. However, in contrast to the aforementioned compounds, it appears as a more defined spike indicating a stronger directionality. On the other hand, $\text{H}\cdots\text{Cl}$ interactions also play a notable role (16.7% of the implied surface), identifiable as clearly defined sharp spikes in the 2D representation. The value of the surface implied is also higher than in **24** and **25**, suggesting that the overall supramolecular interactions are

stronger. Finally, the rest of the forces are $C\cdots H$ in nature, accounting for the remaining 8.0 % of the surface.

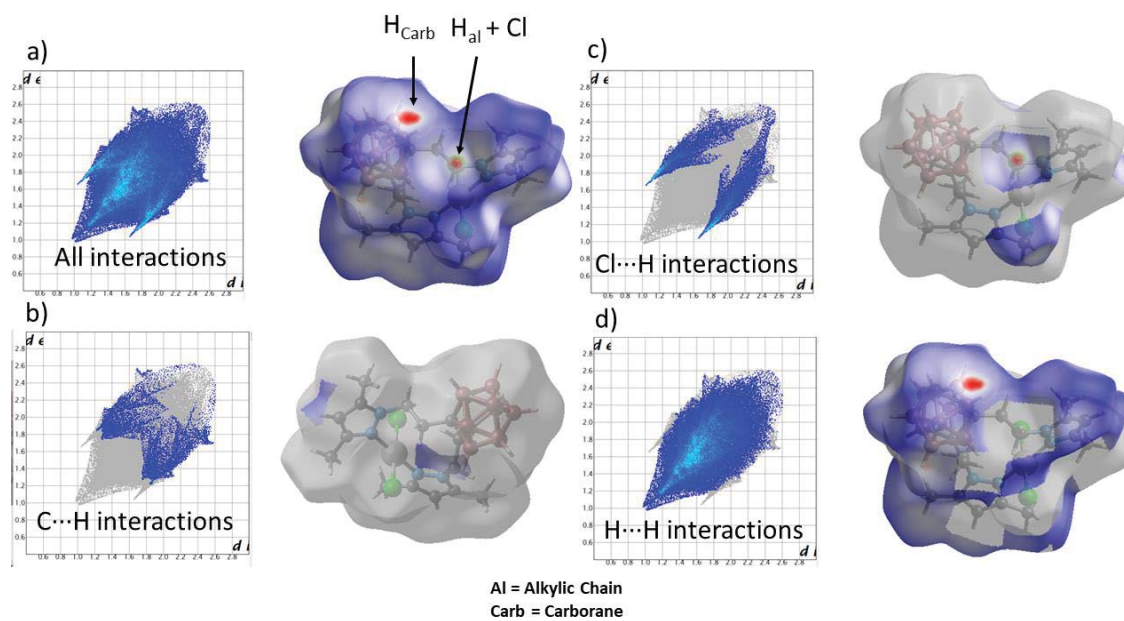


Figure 3.4.14 D_{norm} representation and fingerprint plots for compound **29** (a) and its decomposition in $C\cdots H$ (b), $\text{Cl}\cdots H$ (c) and $H\cdots H$ (d) interactions.

3.4.3 Summary and Conclusions

- ✓ The reactivity of **L9** against Cu(II), Zn(II), Cd(II) and Hg(II) and of **L10** and **L11** against Pd(II) has been assayed, resulting in the obtention of four coordination compounds (**24**, **25**, **28** and **29**) and two ionic salts (**26** and **27**).
- ✓ The isolated compounds have been characterized by analytical and spectroscopic techniques. Moreover, the crystal structures of **24**, **25**, **27** and **29** have been elucidated, allowing for a detailed study of their structure and supramolecular interactions.
- ✓ While **L9** shows a conventional coordination behavior against Cu(II) and Zn(II), it shows notable difficulties in coordinating to Cd(II) and Hg(II), as, in fact, no coordination compounds are obtained, but rather ionic salts. This fact can be attributed to the electron-withdrawing effect of the carborane moiety, which results in a lower basicity for the pyrazole ring.
- ✓ The supramolecular analysis of **24**, **25** and **29** shows that globular and spherical ligands such as carborane may prevent the formation of strong intermolecular interactions owing to their extensive occupation of conformational space, favoring the formation of weak C-H \cdots H-B interactions.
- ✓ Compounds **24**, **25**, **28** and **29** are the first reported examples of coordination compounds bearing *N*-alkylcarborane ligands.

References

- 1 L. I. Zakharkin, A. V. Grebennikov and L. A. Savina, *Izv. Akad. Nauk SSSR, Seriya Khimicheskaya*, 1968, 1130–1132.
- 2 L. I. Zakharkin and A. V. Grebennikov, *Zhurnal Obs. Khimii*, 1969, **39**, 575–579.
- 3 L. I. Zakharkin, A. V. Grebennikov and A. I. L’vov, *Izv. Akad. Nauk SSSR, Seriya Khimicheskaya*, 1970, 106–112.
- 4 N. Vázquez, V. Gómez-Vallejo and J. Llop, *Tetrahedron Lett.*, 2012, **53**, 4743–4746.
- 5 M. Rinaldi-Carmona, F. Barth, M. Héaulme, D. Shire, B. Calandra, C. Congy, S. Martinez, J. Maruani, G. Néliat, D. Caput, P. Ferrara, P. Soubrié, J. C. Brelière and G. Le Fur, *FEBS Lett.*, 1994, **350**, 240–244.
- 6 R. S. Padwal and S. R. Majumdar, *Lancet*, 2007, 369, 71–77.
- 7 A. Buzharevski, S. Paskas, M. Sárosi, M. Laube, P. Lönnecke, W. Neumann, S. Mijatovic, D. Maksimovic-Ivanic, J. Pietzsch and E. Hey-Hawkins, *ChemMedChem*, 2019, **14**, 315–321.
- 8 S. M. Ivanov and I. B. Sivaev, *J. Heterocycl. Chem.*, 2020, **57**, 1428–1434.
- 9 G. L. Rusinov, R. I. Ishmetova, S. G. Tolshchina, N. K. Ignatenko, I. N. Ganebnykh, P. A. Slepukhin, V. A. Ol’shevskaya, V. N. Kalinin and V. N. Charushin, *Russ. Chem. Bull.*, 2010, **59**, 116–121.
- 10 S. G. Tolshchina, R. I. Ishmetova, N. K. Ignatenko, A. V. Korotina, I. N. Ganebnykh, V. A. Ol’shevskaya, V. N. Kalinin and G. L. Rusinov, *Russ. Chem. Bull.*, 2011, **60**, 985–991.
- 11 H. Li, F. Bai, H. Yan and C. Lu, *Org. Lett.*, 2017, **19**, 862–865.
- 12 M. Frederick Hawthorne, A. Varadarajan, C. B. Knobler, S. Chakrabarti, R. J. Paxton, B. G. Beatty and F. L. Curtis, *J. Am. Chem. Soc.*, 1990, **112**, 5365–5366.
- 13 R. J. Paxton, B. G. Beatty, M. F. Hawthorne, A. Varadarajan, L. E. Williams, F. L. Curtis, C. B. Knobler, J. D. Beatty and J. E. Shively, *Proc. Natl. Acad. Sci.*, 1991, **88**, 3387–3391.

- 14 A. Varadarajan, S. E. Johnson, F. A. Gomez, S. Chakrabarti, C. B. Knobler and M. F. Hawthorne, *J. Am. Chem. Soc.*, 1992, **114**, 9003–9011.
- 15 J. Soldevila-Sanmartín, M. Guerrero, D. Choquesillo-Lazarte, J. Giner Planas and J. Pons, *Inorganica Chim. Acta*, 2020, **506**, 119549.
- 16 M. Guerrero, J. Pons, M. Font-Bardia, T. Calvet and J. Ros, *Aust. J. Chem.*, 2010, **63**, 958.
- 17 M. Guerrero, J. Pons, J. Ros, M. Font-Bardia, O. Vallcorba, J. Rius, V. Branchadell and A. Merkoçi, *CrystEngComm*, 2011, **13**, 6457.
- 18 A. M. Spokoyny, C. W. Machan, D. J. Clingerman, M. S. Rosen, M. J. Wiester, R. D. Kennedy, C. L. Stern, A. A. Sarjeant and C. A. Mirkin, *Nat. Chem.*, 2011, **3**, 590–596.
- 19 L. E. Riley, T. Krämer, C. L. McMullin, D. Ellis, G. M. Rosair, I. B. Sivaev and A. J. Welch, *Dalt. Trans.*, 2017, **46**, 5218–5228.
- 20 F. Di Salvo, M. Y. Tsang, F. Teixidor, C. Viñas, J. G. Planas, J. Crassous, N. Vanthuyne, N. Aliaga-Alcalde, E. Ruiz, G. Coquerel, S. Clevers, V. Dupray, D. Choquesillo-Lazarte, M. E. Light and M. B. Hursthouse, *Chem. Eur. J.*, 2014, **20**, 1081–1090.
- 21 W. J. Geary, *Coord. Chem. Rev.*, 1971, **7**, 81–122.
- 22 K. Nakamoto, *Handb. Vib. Spectrosc.*, 2006, 1872–1892.
- 23 M. Scholz and E. Hey-Hawkins, *Chem. Rev.*, 2011, **111**, 7035–7062.
- 24 L. Yang, D. R. Powell and R. P. Houser, *Dalt. Trans.*, 2007, 955–964.
- 25 F. H. Allen, *Acta Crystallogr. Sect. B Struct. Sci.*, 2002, **58**, 380–388.
- 26 R. R. Conry, in *Encyclopedia of Inorganic Chemistry*, John Wiley & Sons, Ltd, Chichester, UK, 2006.
- 27 R. R. Conry, in *Encyclopedia of Inorganic and Bioinorganic Chemistry*, John Wiley & Sons, Ltd, Chichester, UK, 2011.
- 28 M. H. M. Olsson, U. Ryde, B. O. Roos and K. Pierloot, *JBIC J. Biol. Inorg. Chem.*, 1998, **3**, 109–125.

- 29 P. R. Raithby, G. P. Shields, F. H. Allen and W. D. S. Motherwell, *Acta Crystallogr. Sect. B Struct. Sci.*, 2000, **56**, 444–454.
- 30 J. Cirera, P. Alemany and S. Alvarez, *Chem. - A Eur. J.*, 2004, **10**, 190–207.
- 31 S. Alvarez, P. Alemany, D. Casanova, J. Cirera, M. Llunell and D. Avnir, in *Coordination Chemistry Reviews*, 2005, vol. 249, pp. 1693–1708.
- 32 J. Cirera, E. Ruiz and S. Alvarez, *Inorg. Chem.*, 2008, **47**, 2871–2889.
- 33 S. Keinan and D. Avnir, *Inorg. Chem.*, 2001, **40**, 318–323.
- 34 L. R. Falvello, *J. Chem. Soc. - Dalt. Trans.*, 1997, 4463–4475.
- 35 S. J. Archibald, in *Comprehensive Coordination Chemistry II*, Elsevier, 2004, vol. 6, pp. 1147–1251.
- 36 P. Liebing, L. Wang, J. W. Gilje, L. Hilfert and F. T. Edelman, *Polyhedron*, 2019, **164**, 228–235.
- 37 C. P. Silva, H. C. S. Junior, I. F. Santos, A. M. R. Bernardino, R. A. A. Cassaro, M. A. Novak, M. G. F. Vaz and G. P. Guedes, *Inorganica Chim. Acta*, 2018, **482**, 395–401.
- 38 Q. Guo and U. Englert, *Cryst. Growth Des.*, 2016, **16**, 5127–5135.
- 39 J. Day, K. E. R. Marriott, C. A. Kilner and M. A. Halcrow, *New J. Chem.*, 2010, **34**, 52–60.
- 40 S. Kingsley, V. Chandrasekhar, C. D. Incarvito, M. K. Lam and A. L. Rheingold, *Inorg. Chem.*, 2001, **40**, 5890–5896.
- 41 W. G. Haanstra, W. A. J. W. Van Der Donk, W. L. Driessen, J. Reedijk, J. S. Wood and M. G. B. Drew, *J. Chem. Soc., Dalt. Trans.*
- 42 M. Jochriem, C. G. Kirchler, G. Laus, K. Wurst, H. Kopacka, T. Müller and H. Schottenberger, *Zeitschrift für Naturforsch. - Sect. B J. Chem. Sci.*, 2017, **72**, 617–626.
- 43 Á. García-Raso, J. J. Fiol, F. Bádenas, A. Tasada, X. Solans, M. Font-Bardia, M. G. Basallote, M. A. Máñez, M. J. Fernández-Trujillo and D. Sánchez, *J. Inorg. Biochem.*, 2003, **93**, 141–151.

- 44 J. Gómez-Segura, M. J. Prieto, M. Font-Bardia, X. Solans and V. Moreno, *Inorg. Chem.*, 2006, **45**, 10031–10033.
- 45 M. Guerrero, J. Pons, V. Branchadell, T. Parella, X. Solans, M. Font-Bardia and J. Ros, *Inorg. Chem.*, 2008, **47**, 11084–11094.
- 46 A. De León, M. Guerrero, J. García-Antón, J. Ros, M. Font-Bardía and J. Pons, *CrystEngComm*, 2013, **15**, 1762–1771.
- 47 R. Custelcean and J. E. Jackson, *Chem. Rev.*, 2001, **101**, 1963–1980.
- 48 M. A. Fox and A. K. Hughes, *Coord. Chem. Rev.*, 2004, 248, 457–476.
- 49 M. A. Spackman and D. Jayatilaka, *CrystEngComm*, 2009, **11**, 19–32.

3.5 Synthesis and characterization of new Cu(I) coordination compounds with *N*-pyrazole-carborane ligands

This chapter consists of four sections. The first one offers a brief introduction on the luminescent properties of Cu(I) compounds, their current fields of investigation and possible applications.

The second one reports the synthesis of Cu(I) compounds with **L9-L11** and a pyrazole-phenyl analogue (**L12**). All compounds have been fully characterized *via* analytical and spectroscopical techniques. Moreover, the crystal structures of all of them have been elucidated, allowing for a detailed study of their molecular and supramolecular structures.

In the third section, the solid state photophysical properties have been investigated, both experimentally and by TDDFT calculations.

The fourth section provides a summary of the work carried out in this chapter, as well as the obtained conclusions.

The TDDFT calculations presented in this section were carried out in collaboration with Prof. Eliseo Ruiz from the Universitat de Barcelona.

This work has been published in **Article 3**.

Article 3: *“Tuning the Architectures and Luminescence Properties of Cu(I) Compounds of Phenyl and Carboranyl Pyrazoles: The Impact of 2D versus 3D Aromatic Moieties in the Ligand Backbone”*

Joan Soldevila-Sanmartín, Eliseo Ruiz, Duane Choquesillo-Lazarte, Mark E. Light, Clara Viñas, Francesc Teixidor, Rosario Núñez, Josefina Pons, José G. Planas.

Journal of Materials Chemistry C, Advance Article (2021) DOI: 10.1039/D1TC01395E

3.5.1 Photoluminescent properties of Cu(I) compounds

Polynuclear Cu(I)-halide compounds have fascinated chemists for decades, their research dating back over a century, even before the incorporation of single-crystal X-ray crystallography into the arsenal of techniques used by researchers. Arguably, the most famous member of this family of coordination compounds is $\text{Cu}_4\text{I}_4\text{Py}_4$ (Py = Pyridine), which spurred the interest for this topic. This compound featured at the forefront of global research when Hardt and co-workers first reported their significant luminescent properties¹ and White and co-workers provided evidence for its cubane-like crystal structure². Since then, over a thousand Cu(I)-iodide crystal structures have been reported, according to the CCDC³. They feature a surprisingly variety of nuclearities, dimensionalities and topologies. They are usually classified according to their dimensionalities, which range from 0-D to 3-D aggregates and the structural motifs displayed by their *core* (Chart 3.5.1).

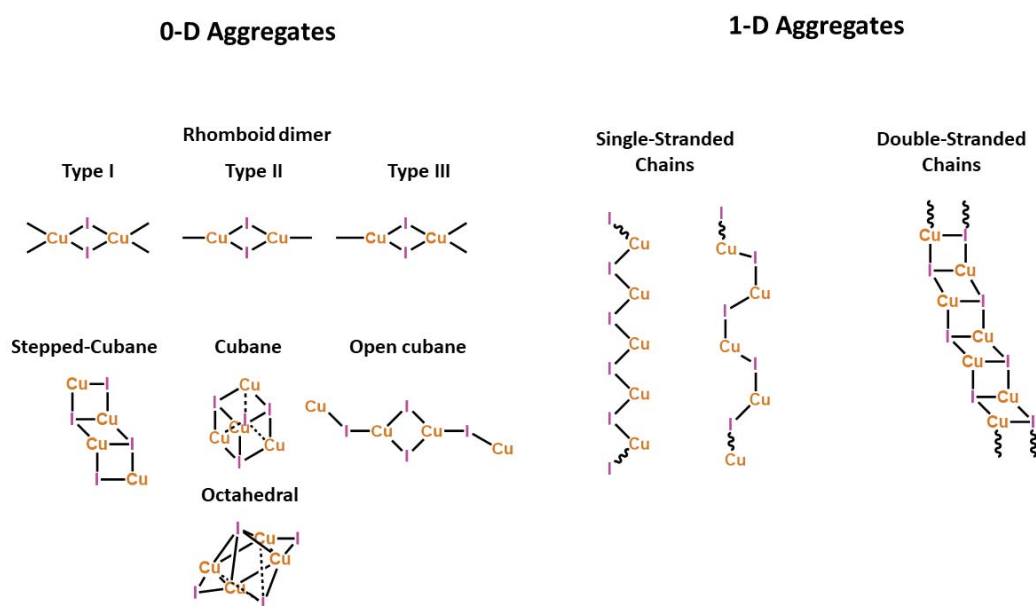


Chart 3.5.1 Schematic representation of some Cu(I)-iodide aggregates structural motifs

Regarding the 0-D aggregates, the simplest synthon, and the most common one, is the rhomboid dimer, which features three different coordination modes for the Cu(I) centres. The cubane and stepped-cubane motifs also feature among the most common synthons. Other less common motifs are the octahedral and the open-cubane. For their

one-dimensional aggregates it is worth mentioning the relatively rare single-stranded chain motifs (displaying different conformations, such as castellated or zigzag) and the more common double-stranded chain motifs (Chart 3.5.1).

The interest in Cu(I) compounds does not only stem from their structural variety, but also from their photophysical properties^{4–6}. As such, several Cu(I)-based materials are currently being investigated for their applications in lighting devices, such as light emitting diodes^{7–9}, light-emitting electrochemical cells (LECs)¹⁰, solar cells¹¹ or luminescent sensors^{12,13}.

However, these two fields of study are not isolated of each other and since the first reports on the luminescent properties of Cu(I) compounds¹, it has been observed that structural parameters greatly affect the photophysical properties of the resulting compounds. For instance, in cubane-like clusters a dual emission is observed arising from two different excited states. An iodide-to-ligand charge transfer (³XLCT, sometimes mixed with metal-to-ligand charge transfer, ³MLCT) gives rise to a high energy (HE) emission (ca. 450 nm) while a Cu₄I₄ cluster-centered (³CC) excited state yields a low energy (LE) emission (ca. 600 nm), which is related to Cu-Cu distances^{4,14}. In fact, this relationship between Cu-Cu distance and the LE emission gives rise to one of the most interesting properties of cubane compounds: thermochromism¹. However, this LE emission can be quenched using rigid ligands that prevent cluster relaxation, thus “blocking” this emission¹⁵, or fine-tuned using different heterocyclic donors¹⁶. In contrast, stair-step clusters only show HE emission, due to the presence of longer Cu-Cu distances¹⁷.

With regards to the ligands employed in the above mentioned polynuclear Cu(I) halides, nitrogen- (N-), sulfur- (S-) and phosphorus (P-) containing ligands are commonly found^{4,18–20}. Among them, structures with N-ligands (either monodentate or multidentate) are the most common ones and usually possess intriguing luminescent properties^{17,21}. Within the family of polynuclear Cu(I) compounds containing N-ligands, pyrazoles are significantly less studied, as the overwhelming majority of reports feature pyridines¹⁸. Furthermore, pyrazole ligands employed in such polynuclear Cu(I) compounds are deprotonated (pyrazolate ligands) or neutral pyrazolyl-pyridine/pyrimidine combinations^{18,22–26}. To our knowledge, there is only a handful of reports of Cu(I)

complexes bearing neutral monodentate *only*-pyrazole (not having other nitrogenated substituents)²⁷ or neutral polypyrazolyl ligands^{28–31}.

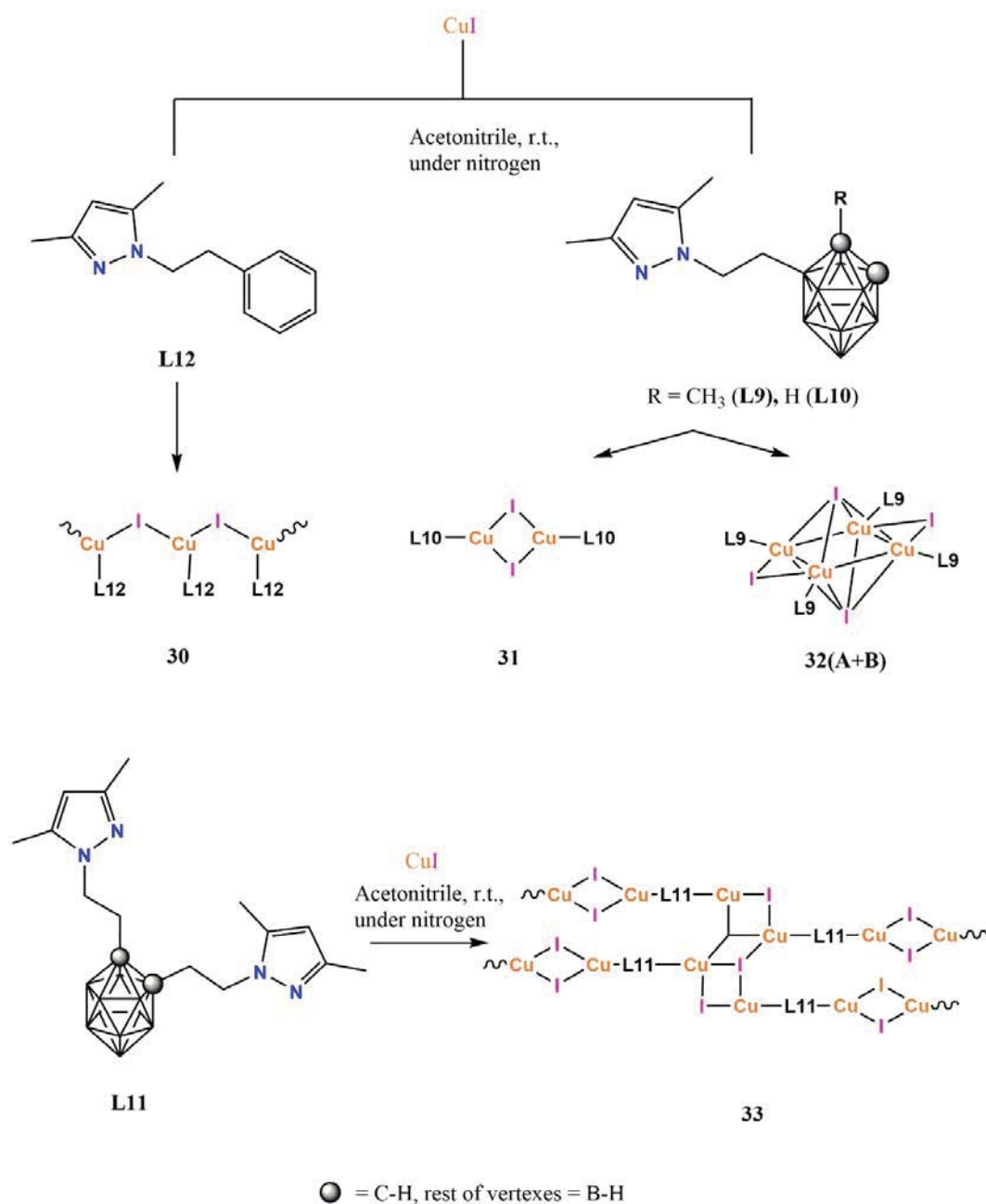
We were interested in exploring the impact of adding the icosahedral carborane clusters to the pyrazole backbone on their coordination to Cu(I) ions and their corresponding luminescence properties. Therefore, Cu(I) coordination compounds bearing **L9–L11** were synthesized (Scheme 3.5.1), characterized and their photophysical behaviour was studied. Moreover, for comparison purposes we also synthesized a Cu(I) compound bearing **L12**, which we identified as a commercial analogue of **L9** and **L10**, featuring a phenyl group *in lieu* of a carborane cage. We hoped that the resulting compounds would allow us to identify the effects induced by the presence of these two different groups. For instance, the introduction of the carborane moiety into a ligand backbone is expected to exert a weaker metal-heteroatom interaction with respect to the related phenyl derivative^{32–34}. In addition to that, different from classical rigid flat aromatic ligands, spherical-based linkers such as carborane can access to extensive conformational space by a combination of low-energy torsion of the substituents (e.g., aliphatic) and by the spherical core of the linker³⁵. Thus, for example, a spherical ligand shape could prevent the formation of intermolecular π - π staking interactions while favouring the weak dihydrogen bond interactions^{36,37}.

3.5.2 Cu(I) compounds of L9–L12

3.5.2.1 Synthesis

All reactions have been carried out by mixing **L9–L12** and CuI in a 1:1 ratio, using dry CH₃CN as solvent. After stirring (1 h to overnight, see Chapter 5: Experimental section), the solutions were concentrated under vacuum up to 1/5 of its original volume, resulting in the obtention of a white powder. If the product did not precipitate, the concentrated solutions were left to stand overnight in the fridge, resulting in the obtention of crystalline precipitates. Following this procedure, single crystals suitable for X-ray diffraction were obtained directly from the reaction mixtures. Their crystal structure elucidation revealed that each compound possessed a different molecular architecture (see below). Thus, a single stranded polymer of general formula {[Cu(**L12**)I]}_n (**30**), a dimer

of general formula $[\text{Cu}(\text{L10})\text{I}]_2$ (**31**) and a single stranded polymer bearing two different metal clusters of formula $\{[\text{Cu}_4(\text{L11})_2\text{I}_4] \cdot \text{CH}_3\text{CN}\}_n$ (**33**) were obtained (Scheme 3.5.1). For the synthesis of Cu(I) compounds involving **L9**, two different shaped crystals were grown simultaneously. Their crystal structure elucidation revealed the formation of two octahedral concomitant polymorphs of formula $[\text{Cu}(\text{L9})\text{I}]_4$ (**32A** and **32B**) (Scheme 3.5.1). All products were obtained in moderate to yields (42.1-60.1%), except for **31**, which was obtained in good yields (88.6%).



Scheme 3.5.1 Synthetic reactions carried out in this section. Compounds are shown with their numbering Scheme. Compound's **33** occluded solvents have been excluded for clarity.

3.5.2.2 Characterization

Compounds **30-33** have been characterized via Elemental analyses (EA), FTIR-ATR spectroscopy and ^1H , ^{11}B , $^{11}\text{B}\{^1\text{H}\}$ and $^{13}\text{C}\{^1\text{H}\}$ NMR spectroscopy whenever possible. Elemental analyses for compounds **30-33** agree with the molecular formulae obtained from the crystal structures.

- FTIR-ATR Spectroscopy

The FTIR-ATR spectra of compounds **30-33** show characteristic bands for pyrazole groups such as $[\nu(\text{C}=\text{C}/\text{C}=\text{N})_{\text{ar}}]$ (1556-1550 cm^{-1}), $[\delta(\text{C}=\text{C}/\text{C}=\text{N})_{\text{ar}}]$ (1465-1417 cm^{-1}), $[\delta(\text{C}-\text{H})_{\text{ip}}]$ (1049-1016 cm^{-1}) and $[\delta(\text{C}-\text{H})_{\text{oop}}]$ (801-660 cm^{-1})³⁸. For compounds containing carboranes, broad $[\nu(\text{B}-\text{H})]$ bands centred at 2572-2563 cm^{-1} are identified³⁸. The FTIR-ATR spectrum of **31** is shown as an example (Figure 3.5.1), while those of **30**, **32B** and **33** can be found in the SI section (Figures S3.5.1-S3.5.3).

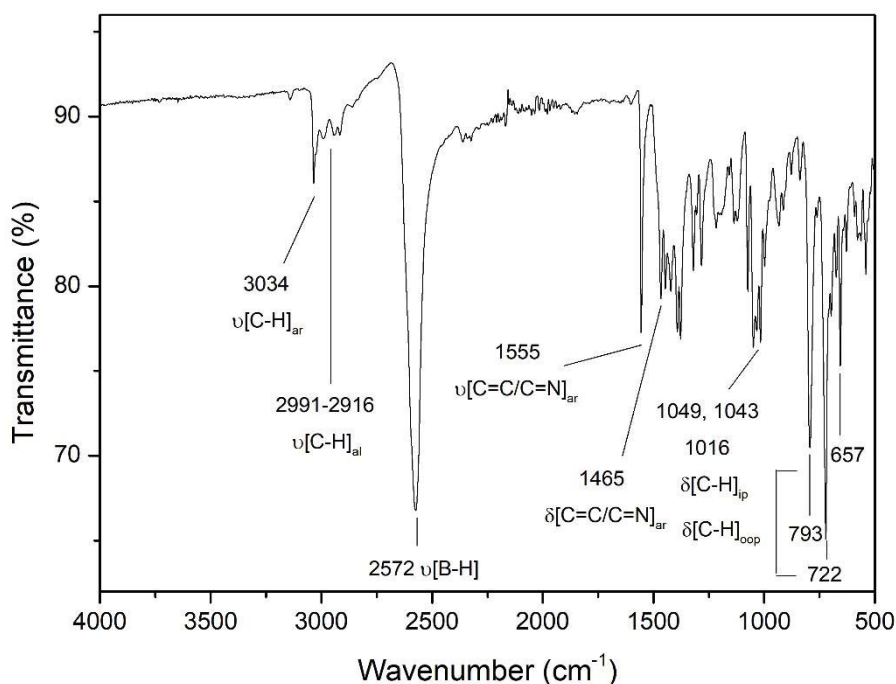


Figure 3.5.1 FTIR-ATR spectrum of compound **31**

- NMR Spectroscopy

^1H and $^{13}\text{C}\{^1\text{H}\}$ NMR spectra, as well as ^{11}B , $^{11}\text{B}\{^1\text{H}\}$ NMR spectra for compounds containing carboranes, were recorded using CD_3CN . Compound **30** was expected to be insoluble as it is a coordination polymer. The solids for this compound could however be solubilized in the NMR solvent. The recorded ^1H and $^{13}\text{C}\{^1\text{H}\}$ NMR spectra showed resonances that are consistent with free (uncoordinated) phenyl-pyrazol ligand. This data therefore suggests a weak Cu-N coordination in **30**, explaining the easy uncoordination of the ligand in CD_3CN .

For **31** and **32**, their ^1H NMR spectra are very similar to those of the ligand, showing only some slight upfield displacements for signals associated to 1-*H*-pyrazolyl fragment (5.82 ppm in both **31** and **32** vs. 5.77 ppm in the free ligand) or for $-\text{CH}_2\text{N}_{\text{Pz}}-$ fragment (4.18-4.13 ppm for **31** and **32** vs. 4.07-4.06 ppm for the free ligands).

Compound **33**, much like compound **30**, was also expected to be insoluble as it is a coordination polymer. However, the solids for this compound could also be solubilized. In contrast to compound **30**, the recorded ^1H NMR spectra displayed a noticeable upfield shifting for almost all signals, thus suggesting that the solubilization of the polymer results in the obtention of fragments still bearing coordinated Cu(I) atoms. As such, signals associated to 1-*H*-pyrazolyl fragment appears at 5.94 ppm (compared to 5.78 ppm in the free ligand) or those of the $-\text{CH}_2\text{CH}_2\text{N}_{\text{Pz}}-$ fragment appear at 4.43 and 2.97 ppm (4.09 and 2.79 ppm for the free ligand).

For all of them, the alkylic chain signals appear as multiplets in the regions of 4.43-4.13 and 2.97-2.76 ppm. As discussed for the free ligands (Chapter 3.1), their particular shapes owe to an AA'BB' spin system, caused by rigid conformation of the resulting compounds in solution. As an example, ^1H NMR spectra of **31** is shown (Figure 3.5.2) while those of **32** and fragments of **33** can be found in Annex I (Figures S3.5.4 and S3.5.5).

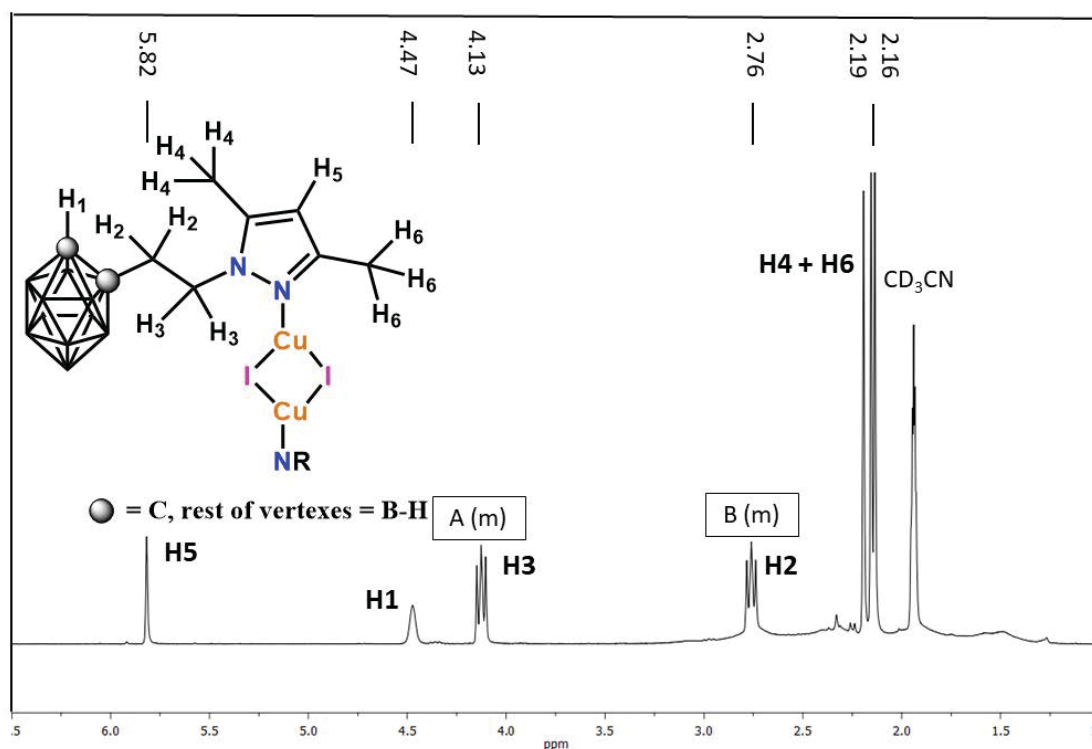


Figure 3.5.2 ^1H NMR spectrum of **31** (CD_3CN , 400.0 MHz)

Regarding the ^{11}B and $^{11}\text{B}\{^1\text{H}\}$ NMR spectra for **31-33**, the obtained signals are consistent with a *closo*-icosahedral geometry for boron cages, as discussed for their respective ligands. In the $^{11}\text{B}\{^1\text{H}\}$ NMR spectrum two resonances with a 2:8 pattern typical of homosubstituted *o*-carboranes can be identified for the fragments of **33**, while those of **31** and **32** display four and three resonances with a 1:1:2:6 and a 1:1:8 pattern, respectively, consistent with heterosubstituted *o*-carboranes. As an example, ^{11}B and $^{11}\text{B}\{^1\text{H}\}$ NMR spectra of **31** is shown (Figure 3.5.3), while those of **32** and fragments of **33** can be found in the SI section (Figures S3.5.6 and S3.5.7).

Lastly, $^{13}\text{C}\{^1\text{H}\}$ NMR spectra for **31-33** are consistent with the presence of the expected functional groups. Their spectra do not show any remarkable shifts on the signals, remaining very similar to those of the free ligands. As an example, the $^{13}\text{C}\{^1\text{H}\}$ NMR spectra of **31** is shown (Figure 3.5.4), while the spectra of **32** and the fragments of **33** can be found in the SI (Figures S3.5.8 and S3.5.9).

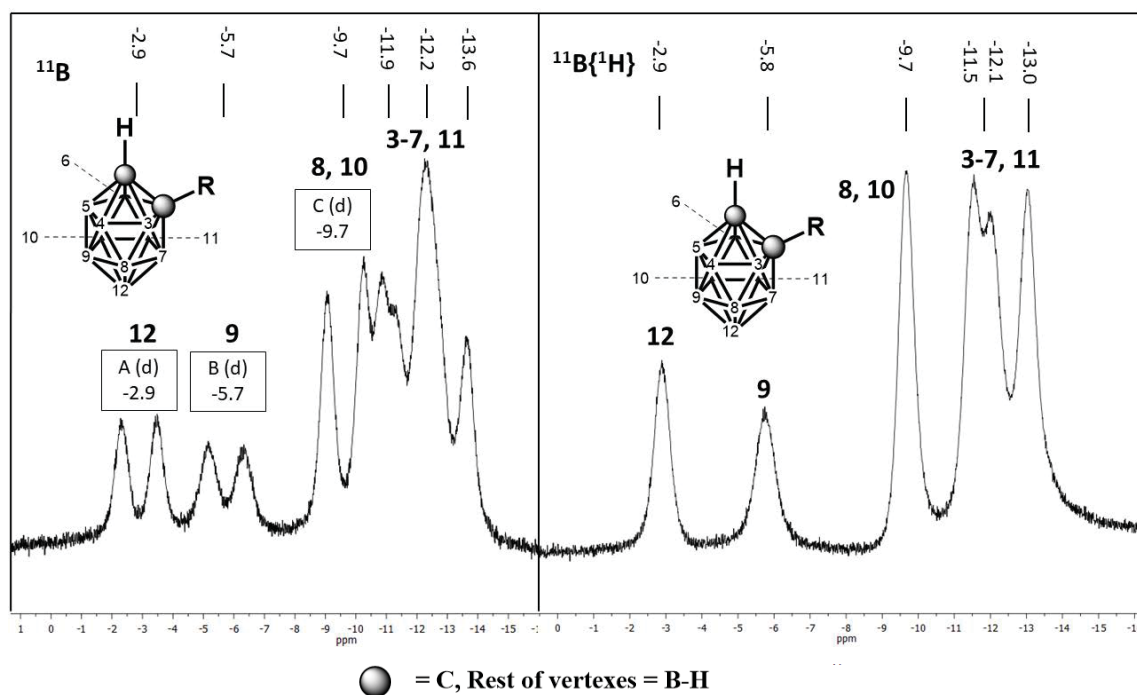


Figure 3.5.3 ^{11}B (left) and $^{11}\text{B}\{^1\text{H}\}$ (right) NMR spectrum of **31** (CD_3CN , 128.6 MHz)

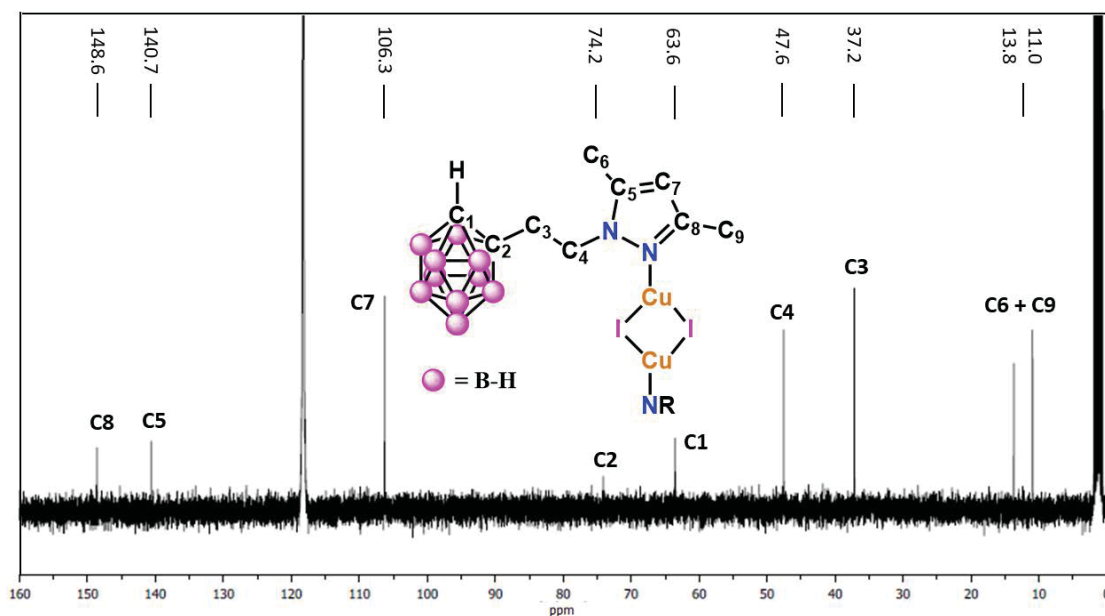


Figure 3.5.4 $^{13}\text{C}\{^1\text{H}\}$ NMR spectrum of **31** (CD_3CN , 100.6 MHz)

- Crystal and Extended structures

Crystal and Extended Structure of compound 30

Suitable crystals for single-crystal X-ray diffraction (SCXRD) of **30** were obtained *via* slow evaporation of its reaction mixture. Phase purity has been confirmed

via Powder X-ray Diffraction (PXRD, Figure S3.5.10). Its crystal structure elucidation revealed that **30** crystallizes in the monoclinic system in a $P2_1/c$ space group, displaying a split-stair polymeric structure. It possesses a trigonal-planar $[\text{Cu}(\text{N}_{\text{pz}})\text{I}_2]$ core, consisting of one nitrogen atom provided by **L12** and two bridging iodine atoms (Figure 3.5.5). Those iodine atoms bind together other Cu(I) metals, forming a single-stranded 1D chain along the a axis, with all **L12** ligands protruding in the same direction. This curious alignment can be attributed to the presence of pyrazole-pyrazole and phenyl-phenyl π - π stacking interactions, as proven by the observed distances between aromatic moieties (4.275 Å), as well as their completely parallel orientation (Figure 3.5.5). Relevant bond lengths and angles are summarized in Table 3.5.1.

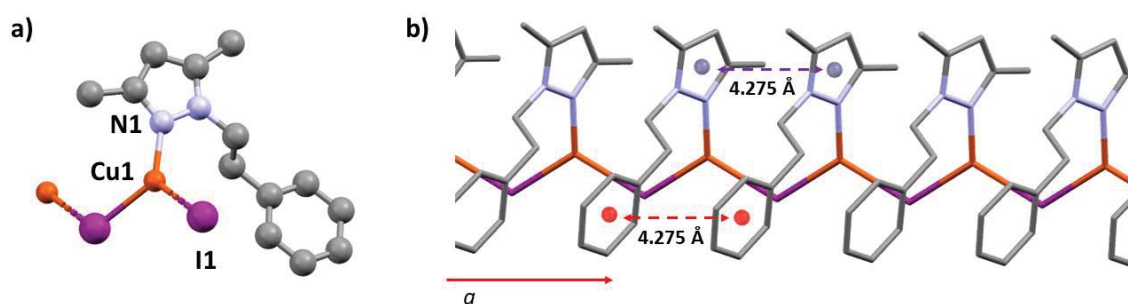


Figure 3.5.5 a. Compound **30**, showing all its non-hydrogen atoms and numbering scheme. b. Detail of π - π stacking interactions in **30**. Colour code: grey (C), light blue (N), orange (Cu), purple (I).

Single-stranded Cu(I) polymers are uncommon. Moreover, most of similar reported polymers have a tetrahedral geometry around its Cu(I) metal centre, and its auxiliary ligands are disposed in an alternating fashion rather than protruding towards the same direction as observed in **30**. In fact, a search in the CCDC database³⁹ reveals that there are only five reported polymers bearing a similar trigonal-planar Cu(I)-iodide polymer^{40–43}, all of them belonging to A.H. White's group. Moreover, all of them also feature the presence of planar aromatic rings involved in π - π interactions^{40–43}. Thus, the obtention of this rare topology in **30** may owe to the presence of strong π - π interactions stabilizing this polymeric chain, and therefore preventing the obtention of other more common structural motifs.

The main supramolecular motif of **30** is the presence of corrugated bidimensional sheets parallel to the ab plane. Once again, the role of aromatic groups is key in the

extended features of **30**, as this scaffold is held together thanks to the presence of two reciprocal C-H \cdots π interactions between phenyl and pyrazolyl groups of different chains (Figure 3.5.6). Thus, the aromatic groups are key in both determining the molecular structure of the compound as well as its self-assembly. Relevant supramolecular interactions are summarized in Table 3.5.1.

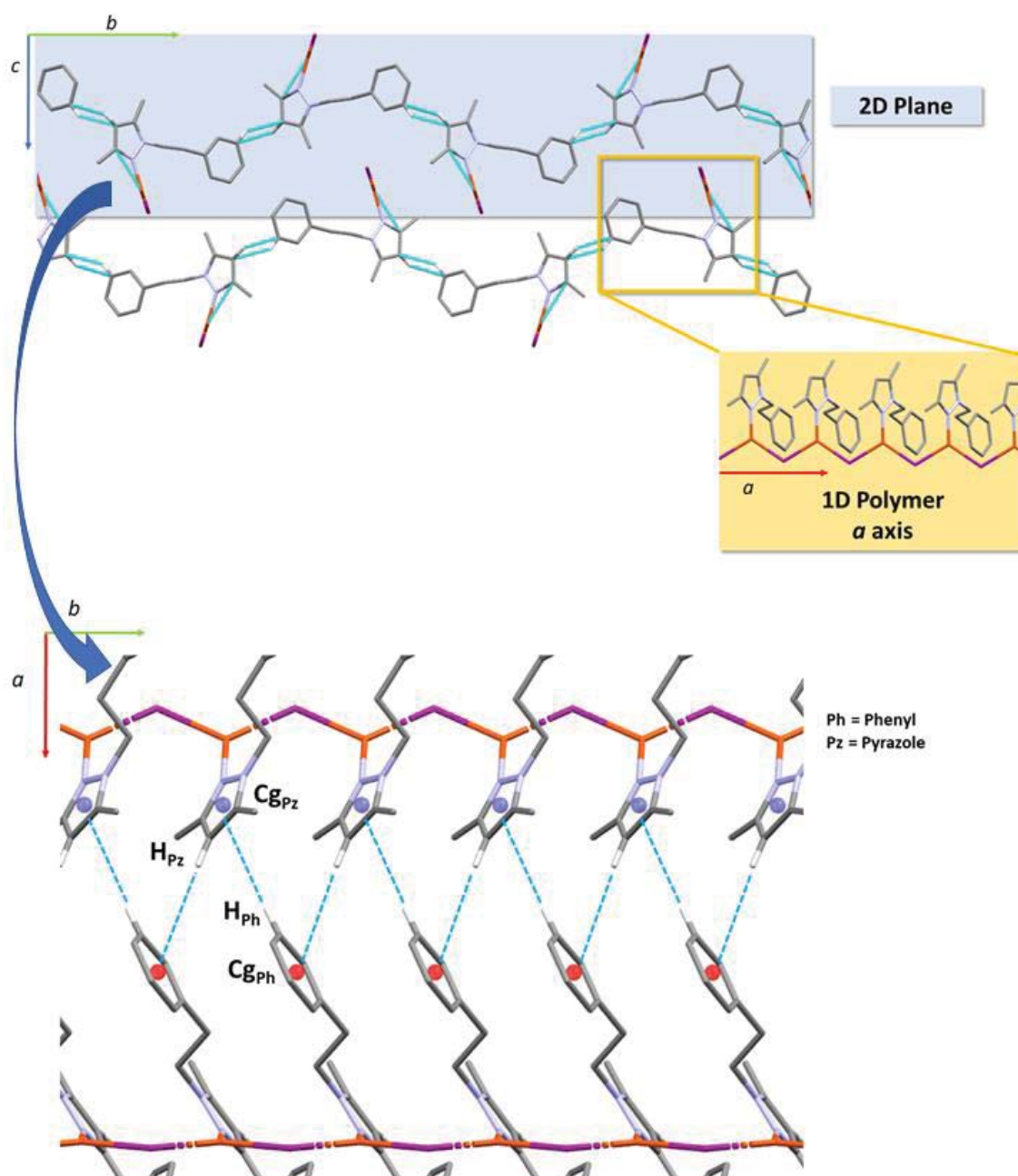


Figure 3.5.6 Supramolecular structure of compound **30**, view along the *a* axis (top). Detail of the supramolecular interactions between 1D polymers in the 2D planes, view along *c* axis (bottom). Colour code: grey (C), pink (B), light blue (N), orange (Cu), purple (I)

Table 3.5.1 Bond lengths (Å), angles (°) and intermolecular interactions for **30**

30				
Bond lengths (Å)				
Cu(1)-I(1)	2.5538(6)	Cu(1)-N(1)	1.971(4)	
Cu(1)-I(1)#1	2.5499(6)	Cu(1)⋯Cu(1)	4.275	
Bond Angles (°)				
Cu(1)#1-I(1)-Cu(1)	113.77(2)	N(1)-Cu(1)-I(1)	120.31(11)	
I(1)#2-Cu(1)-I(1)	113.78(2)	N(1)-Cu(1)-I(1)#2	125.88(11)	
Intermolecular interactions				
D-H⋯A	H⋯A (Å)	D-H (Å)	D⋯A (Å)	> D-H⋯A (°)
C _{Pz} -H _{Pz} ⋯Cg _{Ph}	3.555	0.950	4.476	163.97
C _{Ph} -H _{Ph} ⋯Cg _{Pz}	3.520	0.950	4.397	154.67
#1: x+1, y, z #2 : x-1, y, z				
Pz = pyrazole, Ph = phenyl				
Cg _{Ph} = C8-C13, Cg _{Pz} = C1-C3-C4-N1-N2				

Crystal and Extended Structure of compound 31

Compound **31** crystallizes in the monoclinic system, in the $P\bar{1}$ space group. Phase purity has been confirmed *via* PXRD (Figure S3.5.11). Its single crystal structure elucidation revealed that **30** consists of two crystallographically independent rhomboid dimeric molecules featuring very short Cu⋯Cu distances (2.4728(8) for molecule **A** and 2.5158(9) Å for molecule **B** (Figure 3.5.7). In those, iodine atoms act as μ_2 bidentate bridging ligands and **L10** acts as a monodentate ligand. As the Cu₂I₂ framework lies in the middle of an inversion centre, the pyrazole-carborane ligands protrude facing opposite directions, in an *anti*- conformation, their pyrazole ring's ligand being coplanar. Moreover, this plane defined by the pyrazole ring's is nearly perpendicular to that of the Cu₂I₂ plane (84.54°).

Rhomboid dimers are one of the most prevalent Cu(I) motifs, with over five-hundred structures reported in the CCDC³⁹, but the majority of them feature type I rhomboid dimers (75 %, Chart 3.5.1), and only 20 % of them featuring type II rhomboid dimers (Chart 3.5.1)⁴⁴. Relevant bond lengths and angles for compound **31** are

summarized in Table 3.5.2. They are in range of the distances reported for similar Cu-I rhomboid dimers^{45,46,26}.

Table 3.5.2 Bond lengths (Å), angles (°) and intermolecular interactions for **31**

31				
Molecule A		Molecule B		
Bond lengths (Å)				
Cu(1A)-I(1A)	2.5426(7)	Cu(1B)-I(1B)	2.5439(7)	
Cu(1A)-I(1A)#1	2.6084(7)	Cu(1B)-I(1B)#2	2.6107(7)	
Cu(1A)-N(21)	1.954(3)	Cu(1B)-N(21B)	1.963(3)	
Cu(1A)⋯Cu(1A)#1	2.4726(9)	Cu(1B)⋯Cu(1B)#2	2.5158(9)	
Bond Angles (°)				
Cu(1A)#1-Cu(1A)-I(1A)	62.66(2)	Cu(1B)#2-Cu(1B)-I(1B)	62.12(2)	
Cu(1A)#1-Cu(1A)-I(1A)#1	59.98(2)	Cu(1B)#2-Cu(1B)-I(1B)#2	59.46(2)	
I(1A)-Cu(1A)-I(1A)#1	122.64(2)	I(1B)-Cu(1B)-I(1B)#2	121.59(2)	
N(21A)-Cu(1A)-I(1A)	122.31(10)	N(21B)-Cu(1B)-I(1B)	124.68(8)	
N(21A)-Cu(1A)-I(1A)#1	114.99(9)	N(21B)-Cu(1B)-I(1B)#2	113.61(8)	
N(21A)-Cu(1A)-Cu(1A)#1	174.46(10)	N(21B)-Cu(1B)-Cu(1B)#2	172.26(9)	
Cu(1A)-I(1A)-Cu(1A)#1	57.36(2)	Cu(1B)-I(1B)-Cu(1B)#2	58.41(2)	
Intermolecular interactions				
D-H⋯A	H⋯A (Å)	D-H (Å)	D⋯A (Å)	> D-H⋯A (°)
C _{Carb} -H _{Carb} ⋯N _{Pz}	2.729	1.100	3.656	141.65
#1: -x+1, -y+1, -z+1 #2: -x, -y+1, -z+2				
Pz = pyrazole, Carb = carborane				

The supramolecular assembly of **31** is based around supramolecular 1-D chains. In these chains, molecules A and B alternate, held together by C-H⋯N interactions involving pyrazole rings and carborane moieties. Finally, they assemble in a parallel fashion along *a* and *c* crystallographic directions, forming a dense network (Figure 3.5.8). Relevant supramolecular interactions are summarized in Table 3.5.2.

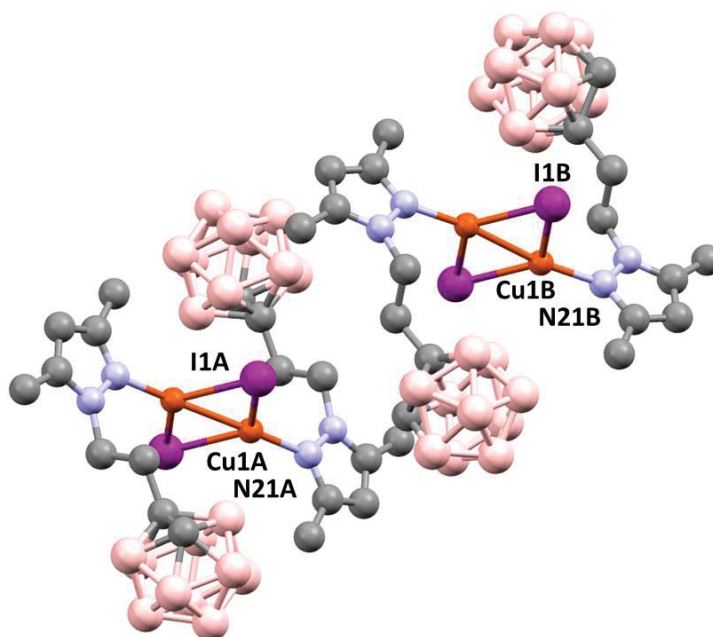


Figure 3.5.7 Compound **31**, showing all its relevant atoms and numbering scheme (top). Colour code: grey (C), pink (B), light blue (N), orange (Cu), purple (I)

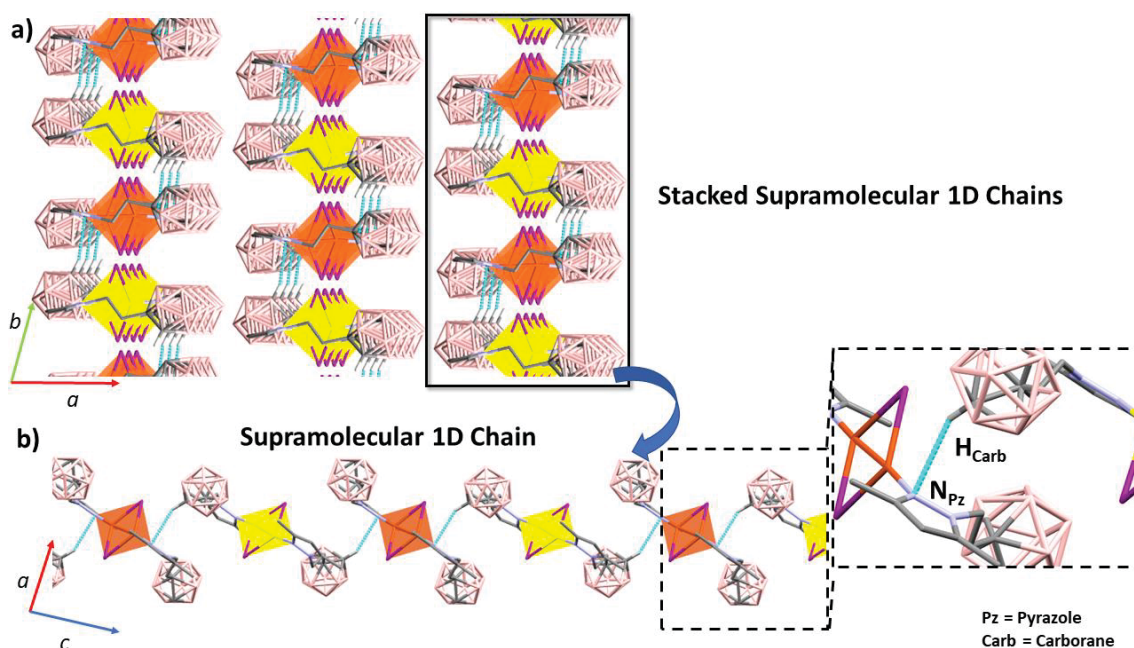


Figure 3.5.8 Packing of supramolecular 1D-Chains in **31**, view along *c* axis (a). Detail of the 1D-Chains, view along *b* axis (b). Only hydrogen atoms participating in the supramolecular interactions are shown. Colour code: grey (C), white (H), pink (B), purple (I), orange (Cu), yellow (Cu). CuI frameworks are depicted in the polyhedral mode, orange for molecule A and yellow for molecule B. Supramolecular interactions are depicted as dashed light-blue lines.

Crystal and Extended Structure of compounds 32A and 32B

Single crystals of compounds **32A** and **32B** crystallize concomitantly after recrystallization in dry CH₃CN. It was observed that the bulk powder contained a mixture of both compounds (Figure 3.5.9). Further synthetic efforts allowed for the isolation of **32B** (Figure S3.5.12), but compound **32A** has not been isolated as a pure phase. It was also observed that recrystallization of pure **32B** also resulted in the concomitant precipitation of both polymorphs. Although single crystal X-ray diffractions measurements were performed for both, the crystal structure of **32B** could not be fully resolved as the data was not good enough ($R = 10\%$). Nevertheless, although preliminary, the data is sufficient to prove that **32A** and **32B** are polymorphs. As shown in Figure 3.5.10, both compounds show a very similar tetranuclear structure of the rare octahedral variety. Whereas there are two crystallographically independent molecules in **32B**, there is only one in **32A** (Figure 3.5.10).

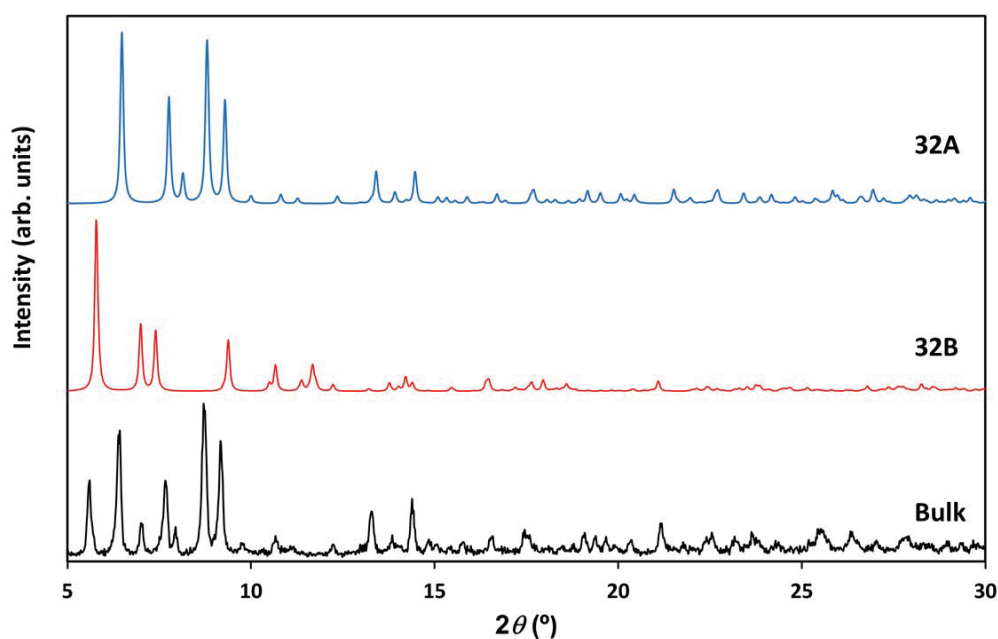


Figure 3.5.9 PXRD pattern of bulk mixture of **32A** and **32B** (black, bottom). PXRD patterns calculated from the solved crystal structure at 100(2) K for **32A** (blue, top) and **32B** (red, middle) as a reference.

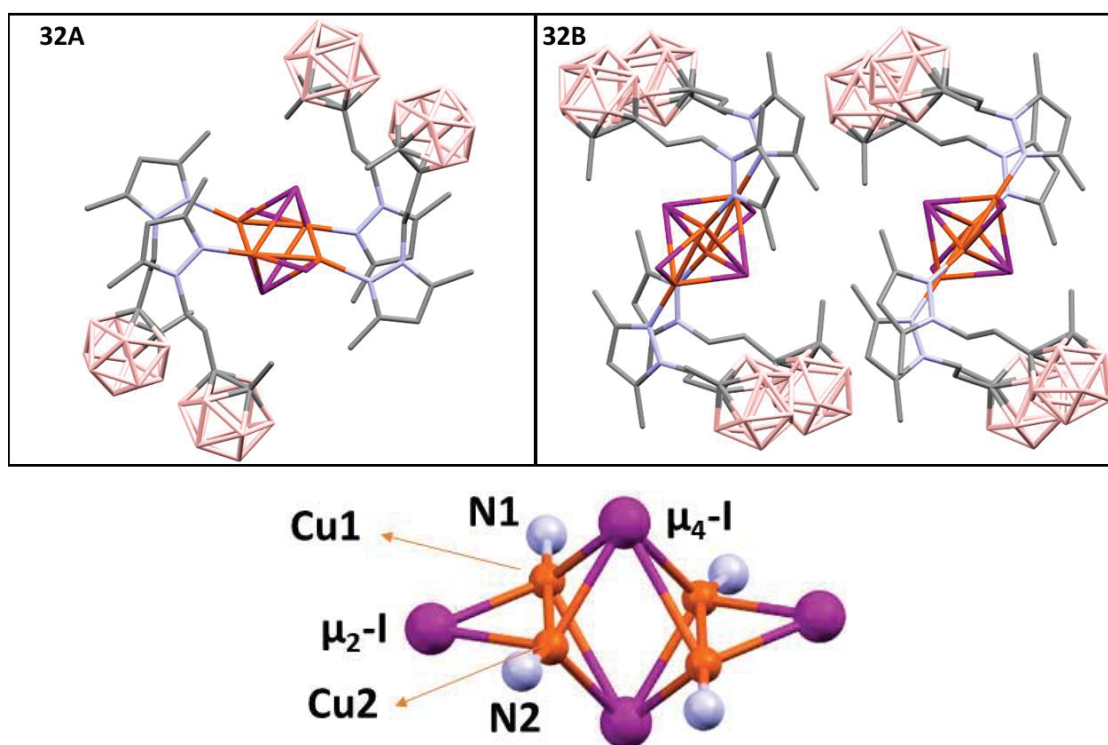


Figure 3.5.10 Compounds **32A** and **32B**, showing all their non-hydrogen atoms (top). Detail of the octahedral core, showing their numbering scheme. Colour code: grey (C), pink (B), light blue (N), orange (Cu), purple (I).

A search in the CCDC database³⁹ reveals a total of twenty-six octahedral Cu_4I_4 clusters, almost all of them bearing bidentate ligands. Most of them bear neutral ligands containing pyridine/imidazole and phosphine ($\text{N}^{\wedge}\text{P}$) or diphosphine ($\text{P}^{\wedge}\text{P}$) groups^{15,47–56}. In a recent publication (2018)⁵⁷, Ya-Dong *et al.* synthesized a family of zwitterionic bidentate $\text{N}^{\wedge}\text{N}$ pyrazolate ligands, and reported for the first time the resulting octahedral $\text{Cu}(\text{I})$ compounds bearing pyrazoles. There is only one reported example of an octahedral $\text{Cu}(\text{I})$ structure bearing a monodentate ligand, published in 2014 by Han *et al.*⁵⁸, using a carbene. Thus, compounds **32A** and **32B** are the first examples of octahedral compounds bearing a neutral monodentate N-donor ligand. Compared to the huge number of $\text{Cu}(\text{I})$ -halide cubane-like structure, these statistics highlights the uniqueness of this architecture. The scarcity of reports bearing octahedral $\text{Cu}(\text{I})$ -halide clusters can be attributed to the fact that their formation is energetically unfavourable when compared to cubane *cores*, as demonstrated by theoretical calculations⁴⁸.

In **32A**, the Cu_4 arrays form slightly distorted parallelograms, with angles ranging from 81.93° – 98.07° . Thus, each molecule presents two distinct Cu–Cu distances, a short

(2.5917(8) Å) and a long one (2.9289(98) Å). These parallelograms are axially capped by two μ_4 -iodides (Cu-I distances ranging from 2.7027(7)-3.1044(8) Å), while two μ_2 -iodine atoms lie at the short side of the parallelogram, being almost coplanar with the metal centres (Cu-I distances ranging from 2.5662(6)-2.647(6) Å). The ligands protrude out of the Cu₄I₄ octahedral *core*, in a curious disposition (Cu-N distances ranging from 1.984(4)-1.990(4) Å). Both pyrazole rings in the same long side face the same direction, in a *syn* configuration, and are almost parallel to each other (angles of the plane defined by the pyrazole rings being 14.23°). The short distance between their centroids (3.910 Å) suggest an intramolecular π - π stacking interaction, which may be responsible for this disposition. Relevant bond distances in the octahedral core are summarized in Table 3.5.3. Detailed information on bond lengths and angles for compound **32A** is reported in Table S3.5.1. Although the Cu-N and Cu-I bond lengths are in the range of the similar reported octahedral compounds bearing bidentate N[^]N ligands⁵⁷, their Cu-Cu “long” distances are somewhat longer, which range from 2.834(4) Å to 2.920(15) Å in compounds bearing bidentate N[^]N ligands⁵⁷, compared to the 2.9289(9) Å in **32A**. This fact may be of capital importance, as photophysical properties of similar compounds are greatly influenced by the structure of the CuI framework.

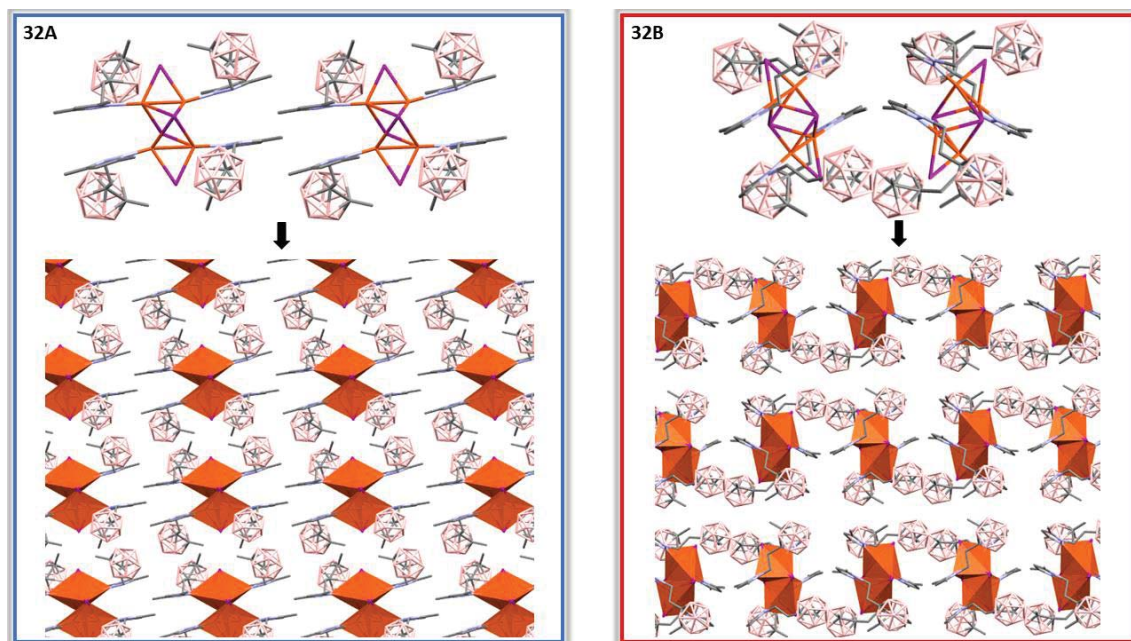
Table 3.5.3 Bond lengths (Å) in the octahedral *core* for **32A**

Cu-N	Cu-I μ_4	Cu-I μ_2	Cu-Cu
	3.1044(8)		
1.984(4)	2.9685(6)	2.5662(6)	2.5917(8)
1.990(4)	2.7437(6)	2.6474(6)	2.9289(9)
	2.7027(7)		

The differences between polymorphs **32A** and **32B** are made obvious when their supramolecular scaffolds are studied, displaying a notable difference between the relative positions of adjacent molecules (Figure 3.5.11). In **32A**, this scaffold is held together thanks to C-H \cdots I interaction involving methyl groups and coordinated μ_2 -Iodine atoms, while weak C-H \cdots H-B, where methyl groups and pyrazole moieties are also identified (Table 3.5.4).

Table 3.5.4 Intermolecular interactions for **32A**

32A				
D-H...A	H...A (Å)	D-H (Å)	D...A (Å)	> D-H...A (°)
B_{Carb}-H_{Carb}...H_{Me}	2.448	1.120	3.027	110.43
C_{Me}-H_{Me}...μ₂-I	3.019	0.980	3.961	161.68
Me = Methyl, Pz = Pyrazole, Carb = Carborane				

**Figure 3.5.11** Packing of compounds **32A** and **32B**. Colour code: grey (C), pink (B), light blue (N), purple (I). Cu(I) polynuclear clusters are depicted as orange polyhedra.*Crystal and Extended Structure of compound 33*

For **33** it was possible to obtain crystals suitable for SCXRD *via* slow evaporation of the reaction mixture. Its crystal structure elucidation revealed that **33** crystallizes in the monoclinic system and the $P2_1/c$ space group. Phase purity has been confirmed *via* PXRD (Figure S3.5.13). Its structure is rather interesting, as it is a coordination polymer containing two different CuI arrays: a dimeric (Cu_2I_2), and a tetrameric (Cu_4I_4) one (Figure 3.5.12).

Upon closer inspection, the rhomboid dimeric centre is identified as a type II (Chart 3.5.1), which account only for 20 % of the reported Cu(I) rhomboid dimers⁴⁴. It is very much alike as the centre for compound **31**, with the pyrazole moiety coordinating in a monodentate fashion and bridging μ_2 -I atoms. Regarding its Cu_4I_4 framework, although

their Cu(I) atoms are also arranged in a parallelogram, much like octahedral tetramers, the iodine atoms coordinate in μ_2 and μ_3 bridging modes, instead of μ_4 , thus displaying the stepped-cubane geometry.

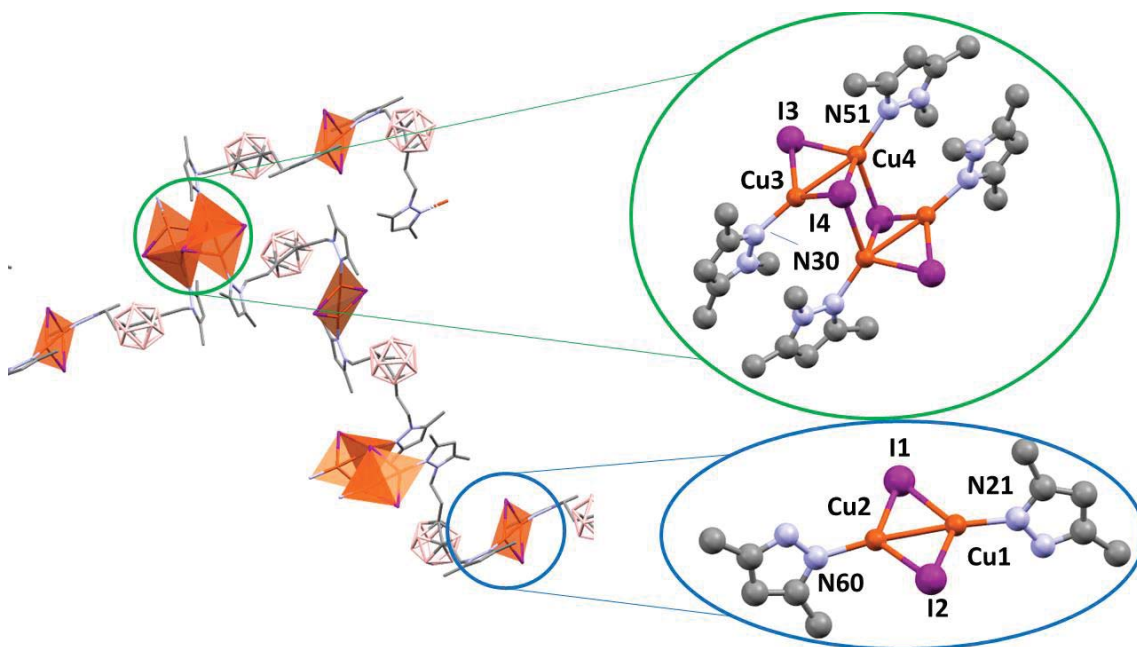


Figure 3.5.12 Polymeric compound **33**. Detail of the two different CuI cores. Colour code: grey (C), pink (B), light blue (N), orange (Cu), purple (I). Polynuclear Cu(I) clusters are also depicted as orange polyhedral.

Although both types of cluster have been reported²⁰, to the best of our knowledge this is the first example of both types combined in a coordination polymer. Both *cores* feature short Cu-Cu distances (2.5583(10) Å and 2.6373(12) Å), implying some attractive interactions between closed shell d^{10} metal ions⁵⁹. Relevant bond lengths and angles are summarized in Table 3.5.5. They are in range of the reported distances for similar rhomboid dimeric^{26,45,46} and stepped-cubane compounds^{59–61}.

Each dimeric *core* is bridged by two different **L11** ligands to two stepped cubane *cores*, while each stepped-cubane *core* is bridged by four **L11** ligands to four dimeric *cores*. The ligand adopts two distinct conformations which alternate along the structure. In conformation I (Figure 3.5.13, top-right), pyrazole rings possess a distorted *anti*-configuration and lie almost perpendicular to each other (angle between planes defined by pyrazole rings being 84.02°), whereas in conformation II (Figure 3.5.13, top-right), pyrazole ligands lie in an *anti*- configuration, at a much less perpendicular angle (42.76°).

This arrangement affords a bidimensional layer, where dimeric *cores* are arranged in a zig-zag pattern and stepped cubane *cores* in a linear one. These patterns are stacked in an ABA'B' fashion (Figure 3.5.13, top-left). Finally, the bidimensional layers are assembled in a parallel fashion (Figure 3.5.13, bottom).

Table 3.5.5 Selected bond lengths (Å) and angles (°) for **33**

33					
Bond lengths (Å)					
Cu(1)-I(1)	2.5523(9)	Cu(2)-N(60)	1.979(4)	Cu(4)-I(3)	2.5547(10)
Cu(1)-I(2)	2.5853(9)	Cu(3)-I(3)	2.6351(10)	Cu(4)-I(4)	2.5991(10)
Cu(1)-N(21)	1.966(4)	Cu(3)-I(4)	2.8614(9)	Cu(4)-N(30)#2	1.987(5)
Cu(2)-I(1)	2.5772(9)	Cu(3)-I(4)#1	2.7128(9)	Cu(1)-Cu(2)	2.5583(10)
Cu(2)-I(2)	2.5421(10)	Cu(3)-N(51)	1.998(4)	Cu(3)-Cu(4)	2.6373(12)
Bond angles (°)					
Cu(2)-Cu(1)-I(2)	59.23(3)	N(21)-Cu(1)-I(2)	122.77(13)	Cu(4)-Cu(3)-I(4)#1	81.53(3)
I(1)-Cu(1)-I(2)	119.55(3)	I(2)-Cu(2)-I(1)	120.26(3)	Cu(4)-Cu(3)-I(4)	56.24(3)
N(21)-Cu(1)-Cu(2)	175.11(14)	N(60)-Cu(2)-Cu(1)	173.37(15)	I(3)-Cu(3)-Cu(4)	57.97(3)
N(21)-Cu(1)-I(1)	117.67(13)	N(60)-Cu(2)-I(1)	114.33(15)	I(3)-Cu(3)-I(4)	107.66(3)
I(2)-Cu(2)-Cu(1)	60.91(3)	N(60)-Cu(2)-I(2)	125.34(15)	I(3)-Cu(3)-I(4)#1	103.59(3)
I(1)-Cu(1)-Cu(2)	60.57(3)	Cu(1)-Cu(2)-I(1)	59.60(3)	I(4)#1-Cu(3)-I(4)	93.48(3)
N(51)-Cu(3)-Cu(4)	152.84(13)	N(51)-Cu(3)-I(3)	112.84(13)	N(51)-Cu(3)-I(4)#1	125.20(13)
N(51)-Cu(3)-I(4)	111.61(13)	I(3)-Cu(4)-Cu(3)	60.97(3)	I(3)-Cu(4)-I(4)	118.94(3)
I(4)-Cu(4)-Cu(3)	66.24(3)	N(30)#2-Cu(4)-Cu(3)	170.21(18)	N(30)#2-Cu(4)-I(3)	119.77(14)
N(30)#2-Cu(4)-I(4)	117.54(14)	Cu(1)-I(1)-Cu(2)	59.83(2)	Cu(2)-I(2)-Cu(1)	59.85(2)
Cu(4)-I(3)-Cu(3)	61.06(3)	Cu(3)#1-I(4)-Cu(3)	86.52(3)	Cu(4)-I(4)-Cu(3)#1	77.50(3)
Cu(4)-I(4)-Cu(3)	57.52(3)				
#1 -x,-y+2,-z+1 #2 -x+1,y+1/2,-z+3/2 #3 -x+1,y-1/2,-z+3/2					

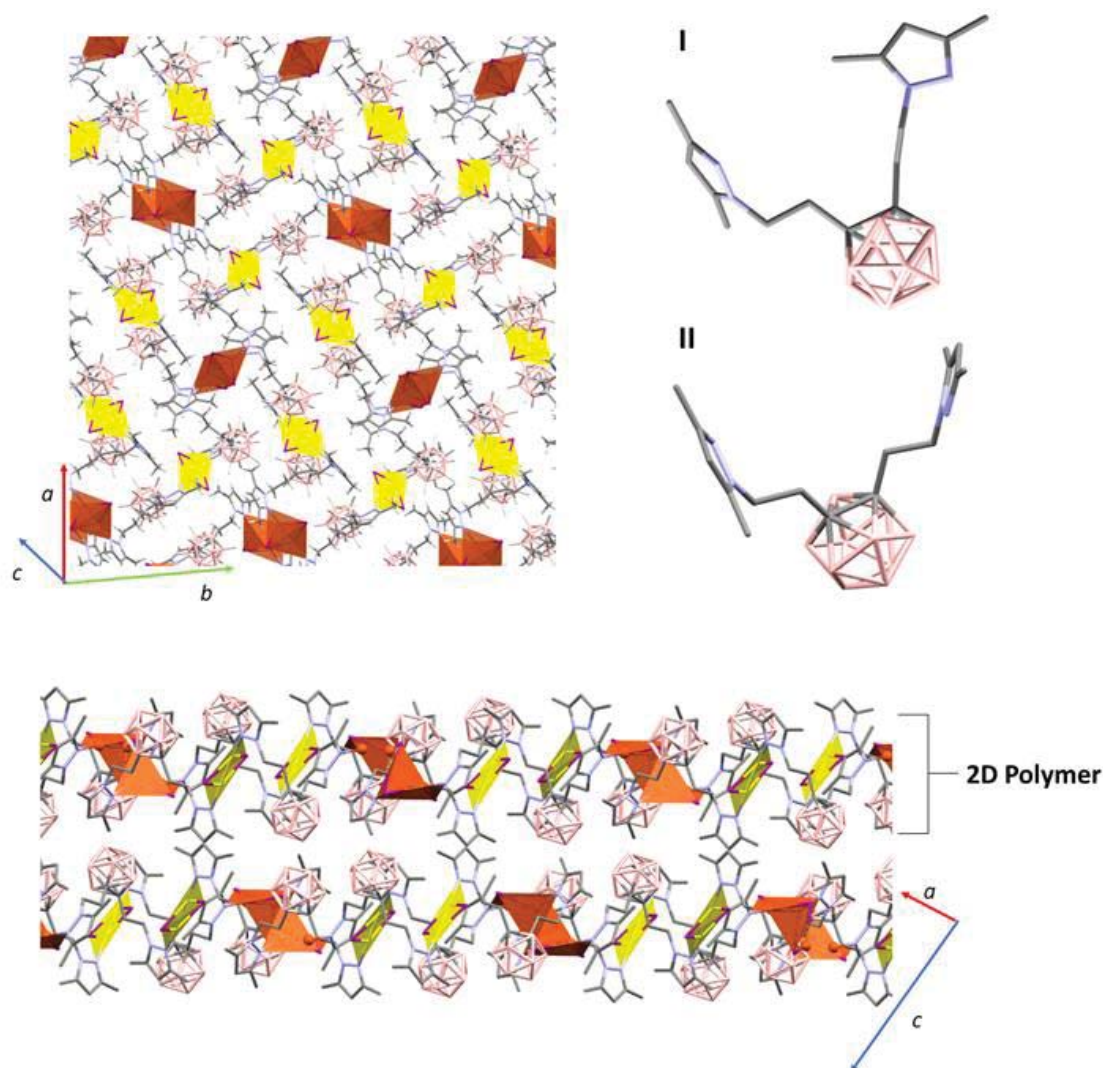


Figure 3.5.13 Bidimensional layer in **33** (top-right). Polinuclear Cu(I) clusters are depicted in the polyhedral mode, dimeric ones highlighted in yellow, tetrameric ones in orange (top-left). Stacking of 2D-polymeric layers, view along b axis (bottom). Conformations of **L11** in compound **33** (right). Colour code: grey (C), pink (B), light blue (N), orange (Cu), purple (I). Occluded CH₃CN solvent molecules and hydrogen atoms are omitted for clarity.

3.5.3 Photophysical studies for compounds 30-33

Compounds **30-33** are white crystalline solids under ambient light. However, even at room temperature (RT) and at the naked eye, they show solid-state photoluminescence when lit with a UV lamp. Intrigued by this fact, we studied their photoluminescent properties. First, we recorded their absorption spectra in solid-state at RT (Figure 3.5.14). All compounds show broad absorption bands, which are especially noticeable on compounds **32B** and **33**. Overall, two distinct absorption regions are identified; a HE one from 200-320 nm and a LE from 320-410 nm. For polymer **30**, its main absorption bands

are in the HE region (224, 269 and 290 nm), although it also displays a shoulder at lower energy (369 nm). For complex **31**, on the other hand, its absorption maximum is in the LE region (363 nm). Complexes **32B** and **33** show broad bands encompassing both regions, and, in fact, the broad absorption band of **33** seems to correspond to the combined absorption spectra for **31** and **32B**. Results are summarized in Table 3.5.6. For similar Cu(I)-iodide pyrazole compounds, absorption bands at HE have been associated to $\pi \rightarrow \pi^*$ transitions centred in the pyrazole ligands⁶², whereas lower energy absorptions have been attributed to a mixture of halide-to-ligand and metal-to-ligand charge transfers ((X+M)LCT) transfers⁶². The UV-Vis spectra for ligands **L9-L12** only display absorption bands in the HE region (Figure S3.5.14), supporting the previous statement.

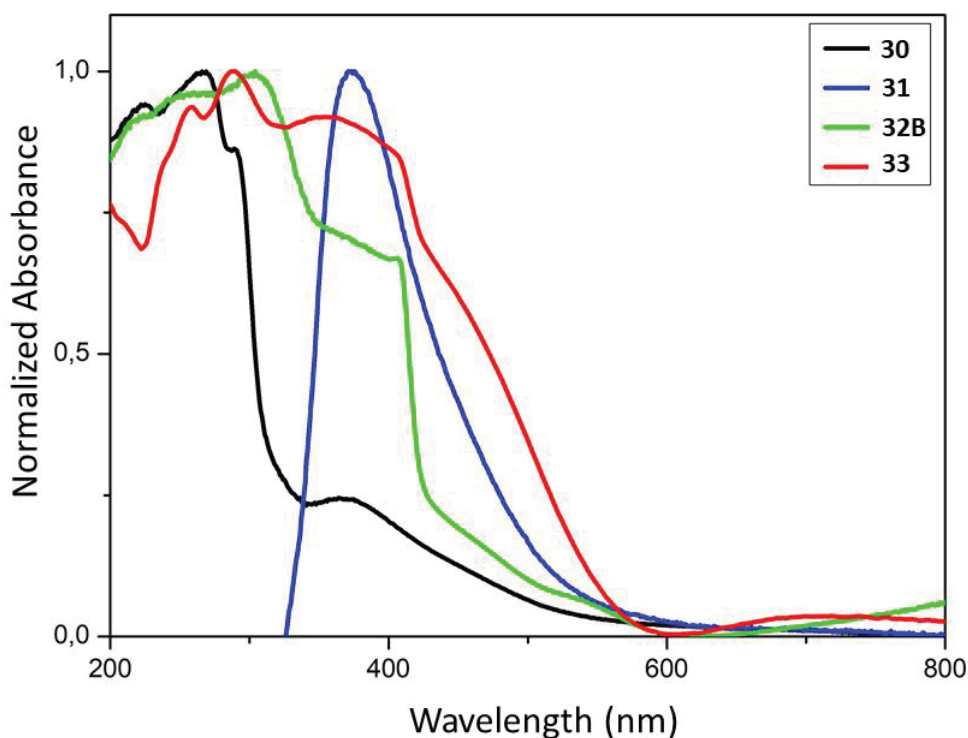


Figure 3.5.14 Solid-state UV-Vis spectra of **30-33** at RT.

The excitation and emission spectra and its Photoluminescent Quantum Yield Efficiency (PLQY, Φ_F) for **30-33** in the solid state were also measured, the results are summarized in Table 3.5.6. All the resulting emission spectra are broad and unstructured, as commonly seen with related Cu(I)-halide compounds, owing to their charge-transfer (CT) origin⁴ (Figure 3.5.15). These CT emissions are known to stem from a variety of sources, such as halide-to-ligand charge transfer (XLCT),^{5,63} metal-to-ligand charge transfer (MLCT)^{5,63} intra-ligand charge transfer (ILCT)⁶⁴, and, for compounds containing

Cu(I) clusters, a cluster-centred excited state of d-s character (CC)⁶³. As such, their photophysical properties bear a strong intrinsic relationship with their structural features.

Table 3.5.6 Photophysical data for **30-33**

Compound	UV-Vis maximum absorbance (nm)	Excitation (λ_{max} , nm)	Emission (λ_{max} , nm)	Φ_F
30	290	283	460, 609	0.038
31	363	340	483	0.665
32B	306	318	517	0.049
33	349	336	467	0.137

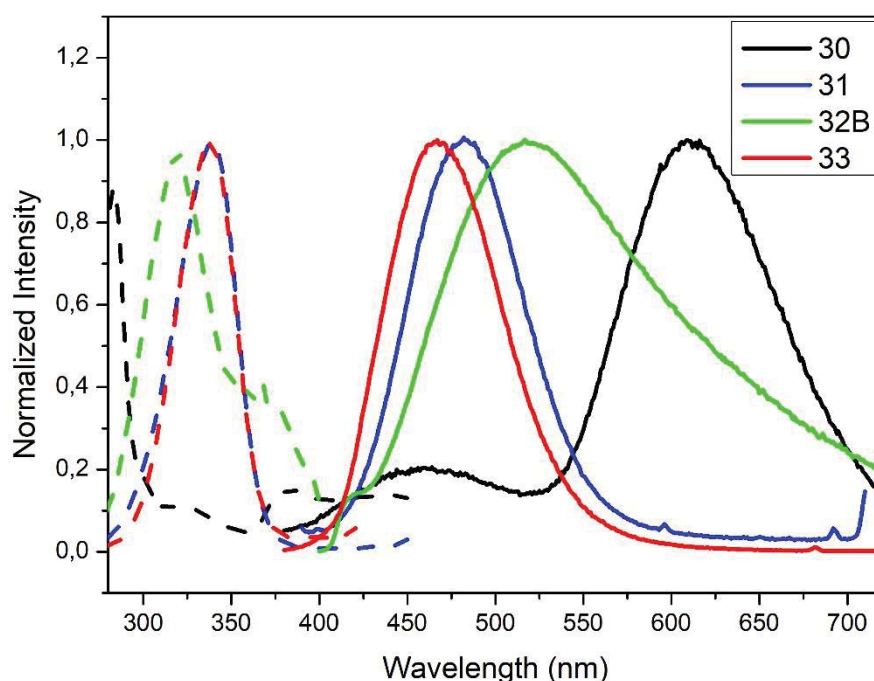


Figure 3.5.15 Excitation (dashed lines) and Emission (solid lines) spectra for compounds **1-4** in the solid state at 298K.

Crystalline solid of polymer **30** exhibits dual emission in the blue (460 nm, HE) and in the orange ($\lambda_{\text{em}} = 609$ nm, LE) regions of the visible spectra upon excitation at 283 nm with a low quantum yield of 4% (Table 3.5.6). Contrary to Cu(I)-iodide rhomboid dimers or tetramers, photophysical studies of single-stranded Cu(I)-iodide polymers are scarce. The first one was reported by Cariati *et al.* in 2002⁶⁵, and since, only few others have been found^{30,31,46,66}. As Cu-Cu bond length is the primary factor governing CC excited states in Cu(I) clusters⁴, their long distances in **30** (4.275 Å, Table 3.5.1), being larger than the sum of their Van der Waals radii (2.8 Å), seem to preclude them as the

source of its emission. Thus, according to the few reports on similar single-stranded Cu(I) polymers, the HE emission is attributed to a mixture of $^3\text{XLCT}$ and $^3\text{MLCT}$ ^{30,31,66}, whereas the LE emission is attributed to $^3\text{XMCT}$ ⁶⁷. Note that there are only two cases of double emission in single-stranded Cu(I) polymers, both reported by Cariatì *et al.* in 2002⁶⁵. Although similar results have been reported for double-stranded or grid-like Cu(I) polymers^{68,69}, direct extrapolation should be avoided, as the latter can possess ^3CC based-emission^{67,70} and display completely different structures. However, by examining other studies, such as the one by Khatri *et al.* for the similar 2D grid-like $[\text{CuBr}(\text{pyz})]_n$ (pyz = pyrazine) and $[\text{CuBr}(\text{quinz})]_n$ (quinz = quinazoline)⁷¹, we can tentatively assume that the HOMO is based on a mix of halide and metal orbitals, while the LUMO is dominated by π^* ligand orbitals. This (X+M)LCT to an antibonding LUMO could explain the large resulting Stokes Shift (ca. 19000 cm^{-1}), as it would promote a bond and geometrical change⁷¹. This fact is also consistent with its low measured quantum efficiency value.

Molecular complexes **31** and **32B** emit at high energies, in the blue-to-yellow region (450–520 nm), of the visible spectrum (Figure 3.5.15 and Table 3.5.6). Crystalline powder of complex **31** exhibits an outstanding blue emission compared to other analogues⁴⁶, with a maximum at 483 nm upon excitation at 340 nm, and an absolute quantum yield (Φ_F) of 66.5%. As explained before, of the reported Cu(I) rhomboid dimers, a 75 % are type I (Chart 3.5.1), while only a 20 % of them belong to type II, such as **31** (Chart 3.5.1)^{39,44}. Thus, the photophysical properties type I rhomboid dimers have been extensively studied. Among these studies, the ones performed by Bräse's group^{9,16,72,73} on rhomboid dimers containing bidentate $\text{N}_{\text{pyridine}},\text{P}$ -heteroleptic are specially remarkable. Their analyses have revealed that HOMO orbitals are mainly centred in the Cu_2X_2 framework and HOMO orbitals in the pyridine ligand. Thus, their emission stems mainly from (X+M)LCT, and can be tuned by slightly modifying the pyridine ligands^{9,16,72,73}. As dimeric Cu(I) compounds with tri-coordinated metal centres, such as **31**, are much less studied, we decided to perform TDDFT calculations (*vide infra*).

Crystalline solid of complex **32B** shows a very broad emission band with maximum at 517 nm upon excitation at 318 nm at room temperature with absolute Φ_F of 5% (Fig 3.5.15, Table 3.5.6). The latter is significantly lower than those reported for some homologous complexes^{48,56}. For other reported octahedral complexes, dual emission has been observed, that is a LE emission (560–620 nm) dominating at room temperature and a HE emission (420–520 nm) dominating at lower temperatures^{15,48,54}. By analogy with

the more studied $\text{Cu}_4\text{I}_4\text{L}_x$ ($x = 2-4$) cubane clusters, those have been attributed to ^3CC transitions and $^3\text{XLCT}$ transitions respectively^{17,53,56}. However, recent studies have shown other octahedral clusters displaying single LE or HE emission bands which are largely temperature independent^{50,57}, a phenomenon known as rigidochromism, or only displaying HE emission^{48,74}. Complex **32B** seems to fall under this behavior, as no dual emission is observed. Since photophysical studies of octahedral clusters are rare, and differing photophysical behaviours have been observed, we performed TDDFT calculations for **32B** (*vide infra*).

Crystalline solid of multinuclear coordination polymer **33** exhibits blue emission with a maximum at 467 nm upon excitation at 336 nm and absolute quantum yield of 13.7% (Figure 3.5.15, Table 3.5.6). It is noteworthy that both the emission and excitation spectra of **33** are quite like that of complex **31** (Cu_2I_2 units). In one of the few reports featuring Cu(I) compounds containing different metal clusters⁷⁵, it was observed that its photoluminescent behaviour was a combination of that of its constituent parts. Thus, assuming a similar behaviour for **33**, it seems that the emission originating in the rhomboid dimeric *core* dominates over that originating in the stepped cubane *core*. Coupled with the high Φ_F observed for **31**, compared to the low Φ_F observed for the tetranuclear cluster in **32B**, it seems to suggest that tetranuclear clusters bearing this kind of ligand have lower Φ_F than their dimeric counterparts. Thus, we assume the emission for both **4** and **2** originate in the dimeric units. On this basis, the TDDFT calculations performed for **31** can also shed light on the photophysical behaviour of **33**.

- TDDFT calculations for compounds **31** and **32B**

In order to analyse and fully understand the photophysical properties of the molecular systems, time-dependent density functional theory (TDDFT) calculations were performed using Gaussian16 program⁷⁶, with the B3LYP functional^{77,78} using the Def2TZV basis set⁷⁹ for **31** and **32B**. The TDDFT calculations were employed only for the discrete molecules because for periodic structures would be mandatory to employ discrete models that usually lead to non-realistic results. The deexcitations energies are calculated by optimizing the structure of the excited triplet state and using such optimized geometry to perform a singlet calculation. Such procedure is employed because TDDFT calculations must be performed in the singlet ground state.

First, the optical absorption properties were investigated. For compound **31**, which has absorption and excitation peaks at 363 and 340 nm, respectively (Table 3.5.6), the calculated TDDFT values at B3LYP level show the first non-zero extinction coefficient at 321 nm. The excitation takes place from the HOMO to the LUMO+1 (Figure 3.5.16), and it can be described as a (X+M)LCT transfer from the Cu_2I_2 framework to the ligand, much in the same manner as the tetracoordinated rhomboid dimers studied by Bräse's group^{9,16,72,73,80}. In the case of complex **32B**, there are four calculated excitations that have non-zero extinction coefficient in the same region than the experimental results. They correspond to transitions between a mixture of the three last occupied orbitals (HOMO, HOMO-1 and HOMO-2, Figure 3.5.16) with large contribution of iodine and copper atoms to the first empty orbitals (LUMO, LUMO+1, LUMO+2 and LUMO+3, Figure 3.5.17), which are mainly ligand-based. The calculated excitation values are 318, 312, 305 and 298 nm. Such values are in good agreement with the experimental absorption and excitation peaks of 306 and 318 nm, respectively. The nature of such excitation is clearly a (X+M)LCT transfer from the Cu_4I_4 framework to the ligand.

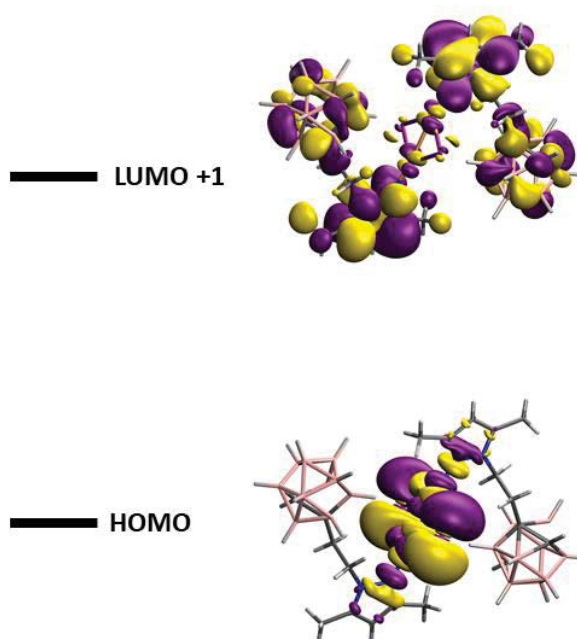
31

Figure 3.5.16 Orbitals involved in the absorption processes for **31**. Colour code: grey (C), pink (B), light blue (N), orange (Cu), purple (I).

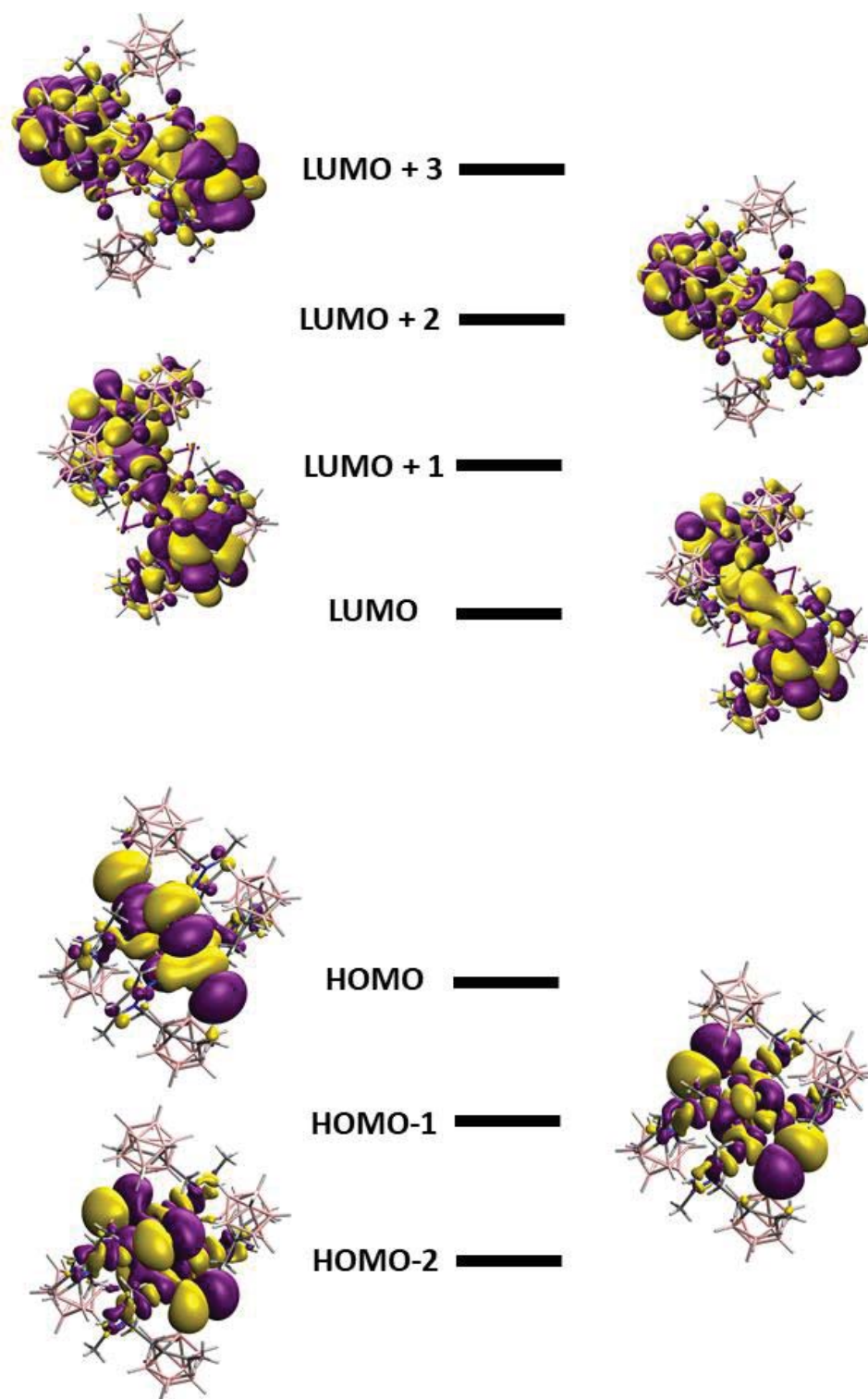
32B

Figure 3.5.17 Orbitals involved in the absorption processes for **32B** (right). Colour code: grey (C), pink (B), light blue (N), orange (Cu), purple (I).

Previously, it has been reported that the deexcitation in these kinds of systems are through triplet states with long excited state lifetimes. The theoretical analysis of the emission spectra was done by optimizing the structure of the wavefunction corresponding

to the triplet state (See experimental section for details). The structure of the optimized triplet excited state from **31** is very distorted with non-bridging iodide ligands (see Fig. 3.5.17), as already reported for other Cu_2I_2 systems⁷⁵. Moreover, the $\text{Cu}\cdots\text{Cu}$ distance was shorter in the optimized triplet excited state (2.346 Å) compared to that of the experimental (2.516 Å) and optimized singlet ground state (2.593 Å). The results indicate that the emission is from the LUMO orbital to HOMO-1 and HOMO-2 (Figure 3.5.18). There are triplet excitations (542, 498 and 487 nm) that are close to the experimental emission peak (483 nm). The analysis of the orbitals involved in such deexcitation transitions reveals that they basically occur among the Cu_2I_2 orbitals. The LUMO is mainly a combination of 4s copper orbitals while HOMO-1 and HOMO-2 correspond to bonding d-d orbitals (for $\text{dx}^2\text{-y}^2$ and dz^2 pairs) of copper mixed with large contributions of p orbitals of the iodine atoms. Thus, such deexcitation transitions could be described as cluster-centred excited state of d-s transition in origin. A similar result was observed for an adduct containing Cu_2I_2 and Cu_3 -pyrazolate clusters⁷⁵. Those results are particularly interesting, as many studies concerning similar dimers attributed their photophysical behaviour to (X+M)LCT in origin^{45,81,82}, on the basis of the results published for tetra-coordinated dimer by Bräse's group^{9,16,72,73}. Thus, our results suggest that tetra-coordinated and tri-coordinated Cu_2I_2 clusters follow a different emission behaviour.

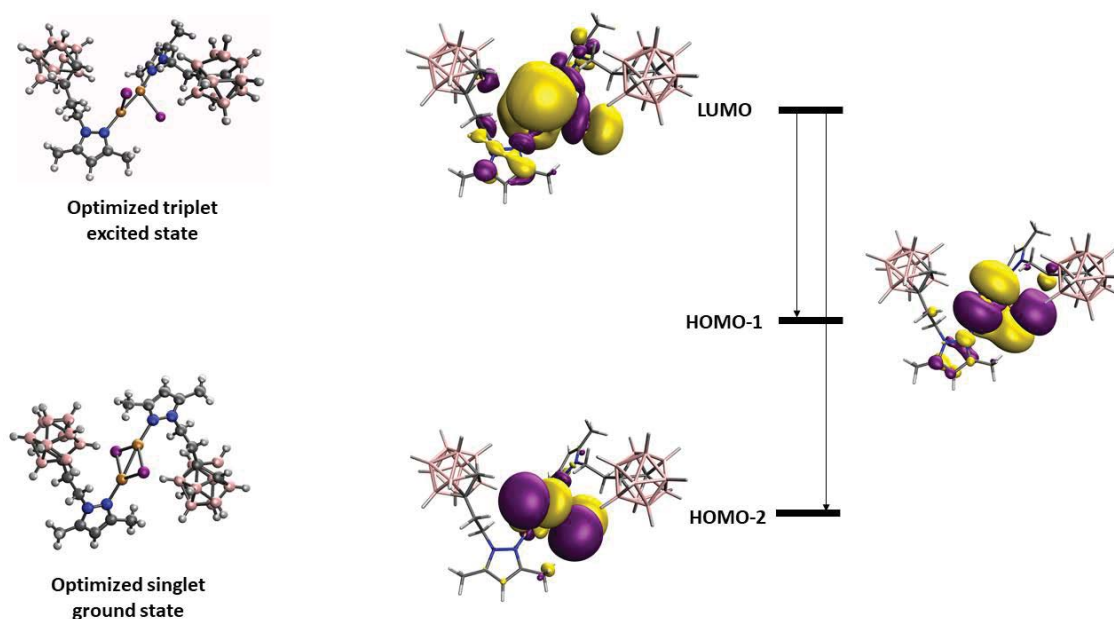


Figure 3.5.18 Optimized structure in the triplet excited state (top left) and singlet ground state (bottom left) for **31**. Orbitals involved in the emission process for **31** (right). Colour code: grey (C), pink (B), light blue (N), orange (Cu), purple (I).

Regarding compound **32**, the optimization of the excited triplet state resulted in the observation of a huge distortion in the structure of the Cu_4I_4 framework. In this optimized structure, two metal-metal interactions are broken, and the iodides coordination modes changes from μ_2 - and μ_4 -bridging to μ_1 -terminal. The calculation of the vertical excitations using TDDFT of the triplet excited state to the singlet ground state gives triplet emissions at 483 and 475 nm, compared to the experimental emission band at 517 nm (Table 3.5.6). The analysis of the orbital involved indicates a deexcitation of the LUMO orbital, mainly based in the central Cu-I framework, to HOMO and HOMO-1 orbitals, also centred in the Cu-I framework (Figure 3.5.19). Thus, as for **31**, the deexcitation process is through a ^3CC state. This huge distortion of the structure is consistent with both its large Stokes shift (ca. 12000 cm^{-1} , Table 3.5.6) and its low Φ_F (5%, Table 3.5.6).

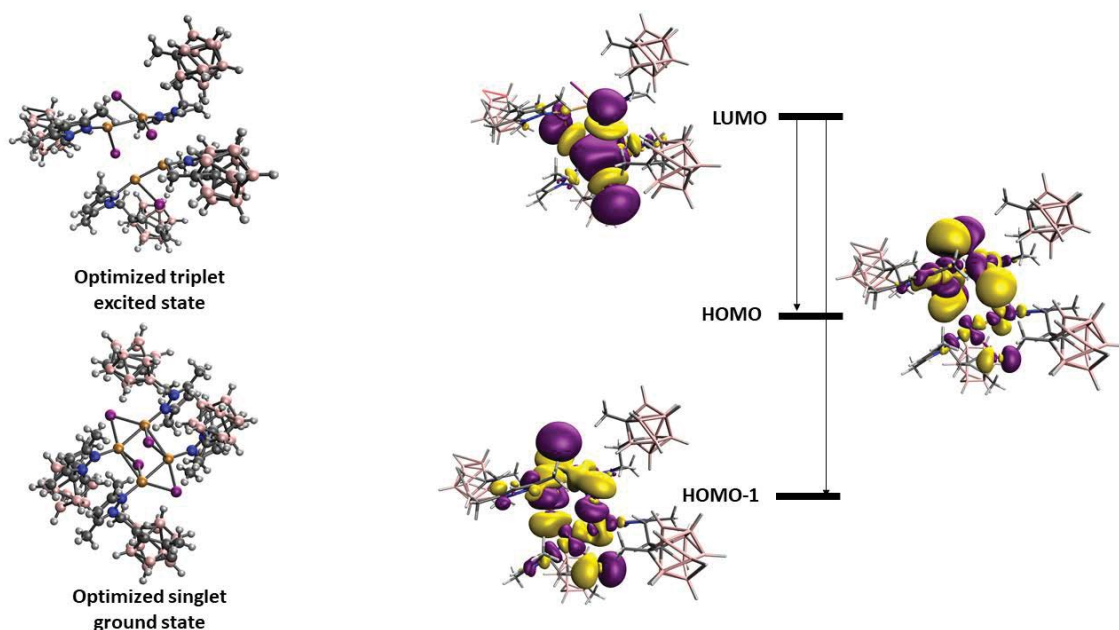


Figure 3.5.2 Optimized structure in the triplet excited state (top left) and singlet ground state (bottom left) for **32**. Orbitals involved in the emission process for **32** (right). Colour code: grey (C), pink (B), light blue (N), orange (Cu), purple (I).

To the best of our knowledge, this is the first example of such behaviour for type of octahedral compounds and could be attributed to the fact that monodentate ligands allow this huge distortion, whereas those octahedral compounds bearing bidentate ligands, which are the majority of the reported ones, are stabilized by them, preventing this distortion in the triplet excited state. Moreover, these results also depart from the classical assumption that octahedral Cu_4I_4 clusters behave similarly to cubane clusters, with a HE emission caused by a $(X+M)\text{LCT}$ and LE emission caused by a ${}^3\text{CC}$ state. Thus, these results highlight that more efforts in the rationalisation of the photophysical behaviour of octahedral clusters are needed.

3.5.4 Summary and Conclusions

- ✓ Four new Cu(I) compounds bearing ligands **L9-L12** were isolated and fully characterized

- ✓ Elucidation of their crystal structure revealed a remarkable structural variety. They feature different structural motifs: polymeric single-stranded zigzag chain (**30**), molecular rhomboid dimer (**31**), molecular octahedral (**32**) and a coordination polymer supporting two distinct structural motifs: rhomboid dimer and stepped cubane (**33**)

- ✓ Reports on compounds bearing two of the featured structural motifs, single-stranded zigzag chain (**30**) and octahedral (**32**) are notably scarce. Moreover, this is the first octahedral compound bearing a monodentate neutral ligand (**32**) and the first example of a polymer bearing the rhomboid dimer and stepped cubane motifs (**33**).

- ✓ The substitution of the phenyl moiety (**L12**) for a carborane one (**L9** and **L10**) resulted in a complete change of the structural motifs of the resulting compounds. Thus, for **L12** a coordination polymer was obtained (**30**), the structure of which seems to require the presence of π - π interactions for its formation. Such interactions are not possible for **L9** and **L10**, and thus molecular compounds are obtained.

- ✓ The photophysical behavior of this family of compounds has been studied. Their emission covers a wide spectrum, from blue to red. Compound **30** exhibits dual emission and a large Stokes shift ($\approx 19000\text{ cm}^{-1}$), attributed to a CT to an antibonding LUMO.

- ✓ Compounds **31** and **33** exhibit almost identical emission behavior, suggesting that the emission in **33** is dominated by the Cu_2I_2 core. This is supported by the fact that for this family of compounds the rhomboid dimer core has a notable Φ_F (65%), whereas the tetranuclear core in **32B** has an extremely poor Φ_F (5%).

✓ TDDFT calculations showed that the emission in **31** is through a ^3CC state, showing a notable difference compared to the more studied type I rhomboid dimeric compounds (Chart 3.5.1), whose emission is attributed to $(\text{X}+\text{M})\text{LCT}$. Thus, our studies suggest that type I and type II rhomboid dimers (Chart 3.5.1) possess different photophysical behavior, and that of the later can not be explained on the basis of the former in a general manner.

✓ For compound **32** TDDFT calculations revealed that its *core* is completely cleaved in the excited stated, accounting for the lack of a dual emission, its low Φ_{F} and its large Stokes shift. To the best of our knowledge, it is the first time that such behavior is reported, and it could be attributed to the presence of a monodentate ligand, whereas in all other photoluminescence studies of similar structures they bear bidentate ligands. Therefore, it seems that bidentate ligands may prevent the cleavage of the cluster in the triplet excited state, whereas the monodentate ligands are not rigid enough to prevent it.

References

- 1 H. D. Hardt and A. Pierre, *Zeitschrift für Anorg. und Allg. Chemie*, 1973, **402**, 107–112.
- 2 C. L. Raston and A. H. White, *J. Chem. Soc., Dalt. Trans.*, 1976, **0**, 2153–2156.
- 3 C. R. Groom, I. J. Bruno, M. P. Lightfoot and S. C. Ward, *Acta Crystallogr. Sect. B*, 2016, **72**, 171–179.
- 4 P. C. Ford, E. Cariati and J. Bourassa, *Chem. Rev.*, 1999, **99**, 3625–3648.
- 5 V. W.-W. Yam and K. K.-W. Lo, *Chem. Soc. Rev.*, 1999, **28**, 323–334.
- 6 J. Troyano, F. Zamora and S. Delgado, *Chem. Soc. Rev.*, 2021, **50**, 4606–4628.
- 7 C. Bizzarri, E. Spuling, D. M. Knoll, D. Volz and S. Bräse, *Coord. Chem. Rev.*, 2018, **373**, 49–82.
- 8 W. Liu, Y. Fang and J. Li, *Adv. Funct. Mater.*, 2018, **28**, 1705593.
- 9 D. Volz, Y. Chen, M. Wallesch, R. Liu, C. Fléchon, D. M. Zink, J. Friedrichs, H. Flügge, R. Steininger, J. Göttlicher, C. Heske, L. Weinhardt, S. Bräse, F. So and T. Baumann, *Adv. Mater.*, 2015, **27**, 2538–2543.
- 10 M. Alkan-Zambada, S. Keller, L. Martínez-Sarti, A. Prescimone, J. M. Junquera-Hernández, E. C. Constable, H. J. Bolink, M. Sessolo, E. Ortí and C. E. Housecroft, *J. Mater. Chem. C*, 2018, **6**, 8460–8471.
- 11 Y. Liu, S.-C. Yiu, C.-L. Ho and W.-Y. Wong, *Coord. Chem. Rev.*, 2018, **375**, 514–557.
- 12 J. Conesa-Egea, F. Zamora and P. Amo-Ochoa, *Coord. Chem. Rev.*, 2019, **381**, 65–78.
- 13 O. S. Wenger, *Chem. Rev.*, 2013, **113**, 3686–3733.
- 14 Q. Benito, X. F. Le Goff, G. Nocton, A. Fargues, A. Garcia, A. Berhault, S. Kahlal, J.-Y. Saillard, C. Martineau, J. Trébosc, T. Gacoin, J.-P. Boilot and S. Perruchas, *Inorg. Chem.*, 2015, **54**, 4483–4494.
- 15 E. I. Musina, A. V. Shamsieva, I. D. Strelnik, T. P. Gerasimova, D. B.

- Krivolapov, I. E. Kolesnikov, E. V. Grachova, S. P. Tunik, C. Bannwarth, S. Grimme, S. A. Katsyuba, A. A. Karasik and O. G. Sinyashin, *Dalt. Trans.*, 2016, **45**, 2250–2260.
- 16 D. M. Zink, T. Baumann, J. Friedrichs, M. Nieger and S. Bräse, *Inorg. Chem.*, 2013, **52**, 13509–13520.
- 17 L. Maini, P. P. Mazzeo, F. Farinella, V. Fattori and D. Braga, *Faraday Discuss.*, 2014, **170**, 93–107.
- 18 E. Cariati, E. Lucenti, C. Botta, U. Giovanella, D. Marinotto and S. Righetto, *Coord. Chem. Rev.*, 2016, **306**, 566–614.
- 19 V. W.-W. Yam, V. K.-M. Au and S. Y.-L. Leung, *Chem. Rev.*, 2015, **115**, 7589–7728.
- 20 R. Peng, M. Li and D. Li, *Coord. Chem. Rev.*, 2010, **254**, 1–18.
- 21 X. Zhang, W. Liu, G. Z. Wei, D. Banerjee, Z. Hu and J. Li, *J. Am. Chem. Soc.*, 2014, **136**, 14230–14236.
- 22 K. A. Vinogradova, V. P. Krivopalov, E. B. Nikolaenkova, N. V. Pervukhina, D. Y. Naumov, M. I. Rakhmanova, E. G. Boguslavsky, L. A. Sheludyakova and M. B. Bushuev, *Polyhedron*, 2013, **57**, 1–13.
- 23 J. C. Li, H. X. Li, H. Y. Li, W. J. Gong and J. P. Lang, *Cryst. Growth Des.*, 2016, **16**, 1617–1625.
- 24 M. Yang, X.-L. Chen and C.-Z. Lu, *Dalt. Trans.*, 2019, **48**, 10790–10794.
- 25 S.-Z. Zhan, T. Feng, W. Lu, M. R. Razali and D. Li, *Cryst. Growth Des.*, 2018, **18**, 7663–7673.
- 26 J.-H. Wang, M. Li, J. Zheng, X.-C. Huang and D. Li, *Chem. Commun.*, 2014, **50**, 9115–9118.
- 27 F. Wu, H. Tong, K. Wang, X. Zhang, J. Zhang, W.-K. Wong and X. Zhu, *J. Coord. Chem.*, 2016, **69**, 926–933.
- 28 A. Tarassoli, V. Nobakht, E. Baladi, L. Carlucci and D. M. Proserpio, *CrystEngComm*, 2017, **19**, 6116–6126.

- 29 J. He, J. Duan, H. Shi, J. Huang, J. Huang, L. Yu, M. Zeller, A. D. Hunter and Z. Xu, *Inorg. Chem.*, 2014, **53**, 6837–6843.
- 30 W.-X. Wang, L. Wang, H.-X. Li, H.-Y. Li and J.-P. Lang, *Zeitschrift für Anorg. und Allg. Chemie*, 2013, **639**, 618–625.
- 31 H.-Y. Li, Y. Zhang, Y.-C. Ding, M. Wang, L.-X. Dai and J.-P. Lang, *J. Mol. Struct.*, 2011, **996**, 90–94.
- 32 A. M. Spokoyny, C. W. Machan, D. J. Clingerman, M. S. Rosen, M. J. Wiester, R. D. Kennedy, C. L. Stern, A. A. Sarjeant and C. A. Mirkin, *Nat. Chem.*, 2011, **3**, 590–596.
- 33 L. E. Riley, T. Krämer, C. L. McMullin, D. Ellis, G. M. Rosair, I. B. Sivaev and A. J. Welch, *Dalt. Trans.*, 2017, **46**, 5218–5228.
- 34 F. Di Salvo, M. Y. Tsang, F. Teixidor, C. Viñas, J. G. Planas, J. Crassous, N. Vanthuyne, N. Aliaga-Alcalde, E. Ruiz, G. Coquerel, S. Clevers, V. Dupray, D. Choquesillo-Lazarte, M. E. Light and M. B. Hursthouse, *Chem. Eur. J.*, 2014, **20**, 1081–1090.
- 35 F. Tan, A. López-Periago, M. E. Light, J. Cirera, E. Ruiz, A. Borrás, F. Teixidor, C. Viñas, C. Domingo and J. G. Planas, *Adv. Mater.*, 2018, **30**, 1800726.
- 36 M. A. Fox and A. K. Hughes, *Coord. Chem. Rev.*, 2004, **248**, 457–476.
- 37 J. G. Planas, C. Vinas, F. Teixidor, A. Comas-Vives, G. Ujaque, A. Lledos, M. E. Light and M. B. Hursthouse, *J. Am. Chem. Soc.*, 2005, **127**, 15976–15982.
- 38 K. Nakamoto, *Handb. Vib. Spectrosc.*, 2006, 1872–1892.
- 39 F. H. Allen, *Acta Crystallogr. Sect. B Struct. Sci.*, 2002, **58**, 380–388.
- 40 J. A. Campbell, C. L. Raston and A. H. White, *Aust. J. Chem.*, 1977, **30**, 1937–1945.
- 41 P. C. Healy, C. Pakawatchai, C. L. Raston, B. W. Skelton and A. H. White, *J. Chem. Soc. Dalt. Trans.*, 1983, 1905–1916.
- 42 P. Healy, J. Kildea, B. Skelton and A. White, *Aust. J. Chem.*, 1989, **42**, 115.
- 43 L. M. Engelhardt, P. C. Healy, J. D. Kildea, B. W. Skelton and A. H. White,

- Aust. J. Chem.*, 1989, **42**, 933–943.
- 44 K. Tsuge, Y. Chishina, H. Hashiguchi, Y. Sasaki, M. Kato, S. Ishizaka and N. Kitamura, *Coord. Chem. Rev.*, 2016, **306**, 636–651.
- 45 A. V. Artem'ev, E. P. Doronina, M. I. Rakhmanova, O. A. Tarasova, I. Y. Bagryanskaya and N. A. Nedolya, *Inorg. Chem. Front.*, 2019, **6**, 671–679.
- 46 A. V. Artem'ev, D. G. Samsonenko and O. V. Antonova, *Polyhedron*, 2018, **151**, 171–176.
- 47 D. M. Zink, T. Grab, T. Baumann, M. Nieger, E. C. Barnes, W. Kloppe and S. Bräse, *Organometallics*, 2011, **30**, 3275–3283.
- 48 Z. Liu, P. I. Djurovich, M. T. Whited and M. E. Thompson, *Inorg. Chem.*, 2012, **51**, 230–236.
- 49 L. Maini, D. Braga, P. P. Mazzeo and B. Ventura, *Dalt. Trans.*, 2012, **41**, 531–539.
- 50 P. Boden, P. Di Martino-Fumo, J. M. Busch, F. R. Rehak, S. Steiger, O. Fuhr, M. Nieger, D. Volz, W. Kloppe, S. Bräse and M. Gerhards, *Chem. - A Eur. J.*, 2020, chem.202004539.
- 51 A. Camus, G. Nardin and L. Randaccio, *Inorganica Chim. Acta*, 1975, **12**, 23–32.
- 52 N. Mézailles, P. Le Floch, K. Waschbüsch, L. Ricard, F. Mathey and C. P. Kubiak, *J. Organomet. Chem.*, 1997, **541**, 277–283.
- 53 S. Naik, J. T. Mague and M. S. Balakrishna, *Inorg. Chem.*, 2014, **53**, 3864–3873.
- 54 E. W. Emerson, M. F. Cain, M. D. Sanderson, C. B. Knarr, D. S. Glueck, J. C. Ahern, H. E. Patterson and A. L. Rheingold, *Inorganica Chim. Acta*, 2015, **427**, 168–172.
- 55 I. Avinash, S. Parveen and G. Anantharaman, *Inorg. Chem.*, 2020, **59**, 5646–5661.
- 56 W.-F. Fu, X. Gan, C.-M. Che, Q.-Y. Cao, Z.-Y. Zhou and N. N.-Y. Zhu, *Chem. - A Eur. J.*, 2004, **10**, 2228–2236.
- 57 Y.-D. Yu, L.-B. Meng, Q.-C. Chen, G.-H. Chen and X.-C. Huang, *New J. Chem.*,

- 2018, **42**, 8426–8437.
- 58 X. Han, Z. Weng, D. J. Young, G.-X. Jin and T. S. Andy Hor, *Dalt. Trans.*, 2014, **43**, 1305–1312.
- 59 G. F. Manbeck, W. W. Brennessel, C. M. Evans and R. Eisenberg, *Inorg. Chem.*, 2010, **49**, 2834–2843.
- 60 S.-Q. Bai, L. Jiang, D. J. Young and T. S. A. Hor, *Dalt. Trans.*, 2015, **44**, 6075–6081.
- 61 T. Yoneda, C. Kasai, Y. Manabe, M. Tsurui, Y. Kitagawa, Y. Hasegawa, P. Sarkar and Y. Inokuma, *Chem. – An Asian J.*, 2020, **15**, 601–605.
- 62 T. N. Sorrell and A. S. Borovik, *Inorg. Chem.*, 1987, **26**, 1957–1964.
- 63 M. Vitale and P. C. Ford, *Coord. Chem. Rev.*, 2001, **219**, 3–16.
- 64 A. Acosta, J. I. Zink and J. Cheon, *Inorg. Chem.*, 2000, **39**, 427–432.
- 65 E. Cariati, D. Roberto, R. Ugo, P. C. Ford, S. Galli and A. Sironi, *Chem. Mater.*, 2002, **14**, 5116–5123.
- 66 J. Zhao, D. Shi, H. Cheng, L. Chen, P. Ma and J. Niu, *Inorg. Chem. Commun.*, 2010, **13**, 822–827.
- 67 A. Aguirrechu-Comerón, R. Hernández-Molina, P. Rodríguez-Hernández, A. Muñoz, U. R. Rodríguez-Mendoza, V. Lavín, R. J. Angel and J. Gonzalez-Platas, *Inorg. Chem.*, 2016, **55**, 7476–7484.
- 68 I. L. Malaestean, V. C. Kravtsov, J. Lipkowski, E. Cariati, S. Righetto, D. Marinotto, A. Forni and M. S. Fonari, *Inorg. Chem.*, 2017, **56**, 5141–5151.
- 69 J. López, J. G. Platas, U. R. Rodríguez-Mendoza, J. I. Martínez, S. Delgado, G. Lifante-Pedrola, E. Cantelar, R. Guerrero-Lemus, C. Hernández-Rodríguez and P. Amo-Ochoa, *Inorg. Chem.*, 2021, **60**, 1208–1219.
- 70 K. Hassanein, P. Amo-Ochoa, C. J. Gómez-García, S. Delgado, O. Castillo, P. Ocón, J. I. Martínez, J. Perles and F. Zamora, *Inorg. Chem.*, 2015, **54**, 10738–10747.
- 71 N. M. Khatri, M. H. Pablico-Lansigan, W. L. Boncher, J. E. Mertzman, A. C.

- Labatete, L. M. Grande, D. Wunder, M. J. Prushan, W. Zhang, P. S. Halasyamani, J. H. S. K. Monteiro, A. De Bettencourt-Dias and S. L. Stoll, *Inorg. Chem.*, 2016, **55**, 11408–11417.
- 72 D. Volz, D. M. Zink, T. Bocksrocker, J. Friedrichs, M. Nieger, T. Baumann, U. Lemmer and S. Bräse, *Chem. Mater.*, 2013, **25**, 3414–3426.
- 73 D. Volz, M. Wallesch, S. L. Grage, J. Göttlicher, R. Steininger, D. Batchelor, T. Vitova, A. S. Ulrich, C. Heske, L. Weinhardt, T. Baumann and S. Bräse, *Inorg. Chem.*, 2014, **53**, 7837–7847.
- 74 K. Chen, J. Shearer and V. J. Catalano, *Inorg. Chem.*, 2015, **54**, 6245–6256.
- 75 S.-Z. Zhan, X. Jiang, J. Zheng, X.-D. Huang, G.-H. Chen and D. Li, *Dalt. Trans.*, 2018, **47**, 3679–3683.
- 76 M. J. Frisch, G. W. Trucks, H. B. Schlegel, G. E. Scuseria, M. a. Robb, J. R. Cheeseman, G. Scalmani, V. Barone, G. a. Petersson, H. Nakatsuji, X. Li, M. Caricato, a. V. Marenich, J. Bloino, B. G. Janesko, R. Gomperts, B. Mennucci, H. P. Hratchian, J. V. Ortiz, a. F. Izmaylov, J. L. Sonnenberg, Williams, F. Ding, F. Lipparini, F. Egidi, J. Goings, B. Peng, A. Petrone, T. Henderson, D. Ranasinghe, V. G. Zakrzewski, J. Gao, N. Rega, G. Zheng, W. Liang, M. Hada, M. Ehara, K. Toyota, R. Fukuda, J. Hasegawa, M. Ishida, T. Nakajima, Y. Honda, O. Kitao, H. Nakai, T. Vreven, K. Throssell, J. a. Montgomery Jr., J. E. Peralta, F. Ogliaro, M. J. Bearpark, J. J. Heyd, E. N. Brothers, K. N. Kudin, V. N. Staroverov, T. a. Keith, R. Kobayashi, J. Normand, K. Raghavachari, a. P. Rendell, J. C. Burant, S. S. Iyengar, J. Tomasi, M. Cossi, J. M. Millam, M. Klene, C. Adamo, R. Cammi, J. W. Ochterski, R. L. Martin, K. Morokuma, O. Farkas, J. B. Foresman and D. J. Fox, 2016, Gaussian 16, Revision C.01, Gaussian, Inc., Wallin.
- 77 A. D. Becke, *J. Chem. Phys.*, 1993, **98**, 5648–5652.
- 78 F. Weigend and R. Ahlrichs, *Phys. Chem. Chem. Phys.*, 2005, **7**, 3297–3305.
- 79 F. Weigend, *Phys. Chem. Chem. Phys.*, 2006, **8**, 1057–1065.
- 80 J. M. Busch, D. S. Koshelev, A. A. Vashchenko, O. Fuhr, M. Nieger, V. V. Utochnikova and S. Bräse, *Inorg. Chem.*, 2021, **60**, 2315–2332.

- 81 S. Demir, B. Eren and M. Hołyńska, *J. Mol. Struct.*, 2015, **1081**, 304–310.
- 82 S. Jana and S. Chattopadhyay, *Polyhedron*, 2014, **81**, 298–307.

4. Conclusions

4. Conclusions

During this PhD work, twelve pyrazole-bearing ligands (**L1-L12**) have been employed. Only **L12** is a commercial product, the rest have been synthesized. Of them, six have been reported for the first time in this thesis. They can be classified in two distinct families: three ligands (**L6-L8**) belong to the bispyrazole ether family and three of them (**L9-L11**) to the pyrazole-carborane family. The synthesis of the latter has been particularly challenging, as it has been found that the reaction occurs between several competing processes. Through the isolation and characterization of the resulting sub-products, those have been identified and their synthetic pathways have been proposed. All new ligands have been characterized by analytical and spectroscopic methods, confirming their obtention. In this way, two of the main objectives proposed for this PhD (see chapter 2) have been successfully achieved.

The reactivity of *N*-hydroxyalkylpyrazole ligands **HL1-HL3**, which feature methyl, phenyl and 2-pyridyl groups in positions 3- and 5-, respectively, with three different Cu(II) salts ($\text{CuCl}_2 \cdot 2\text{H}_2\text{O}$, $\text{Cu}(\text{NO}_3)_2 \cdot 3\text{H}_2\text{O}$ and $\text{Cu}(\text{CH}_3\text{COO})_2 \cdot \text{H}_2\text{O}$) has been assayed. This resulted in the obtention of nine coordination compounds (**1-9**), eight of them reported for the first time. The resulting compounds show a notable structural variability, as ionic, monomeric, dimeric, and polymeric topologies can be observed. From their study and the study of the related bibliography, it can be inferred that the protonation or deprotonation of the alcohol moiety plays a key role in the topology of the obtained complexes. As such, when the alcohol group is protonated, monomers or ionic compounds are obtained, whereas when it is deprotonated, dimers are isolated. Moreover, it has been observed that the inclusion of polydentate auxiliary ligands, such as nitrate, could result in the obtention of polymeric compounds (as compound **5**), whereas the use of monodentate or chelate ligands prevents the formation of complexes of higher nuclearity. These observations pave the way for further developments on this field, such as purposeful synthesis of dimers or monomers *via* control of the reaction media pH and the use of different auxiliary ligands to link these dimeric or monomeric units into polymers. Lastly, the magneto-structural correlation for the dimeric compounds have been studied. All of them have an antiferromagnetic behaviour, the magnitude of which has been rationalised according to structural parameters such as Cu-O-Cu angles, Cu-O-

C torsion angles (τ) or the hinge distortion of the plane defined by the Cu(II) and the oxygen atoms.

For bispyrazole ether ligands **L4** and **L5**, ten new coordination compounds (**10-19**) bearing metal centres such as Co(II), Cu(II), Zn(II), Cd(II) and Hg(II) have been synthesized. It has been determined that the substituent position is the key factor governing the topology of the resulting compounds. In this case, the *para*-substitution (**L4**) results in the obtention of exclusively metalacyclic motifs, whereas the *ortho*-substitution (**L5**) results in the obtention of polymeric/dimeric motifs. Regarding this last ligand, it also displayed different coordination modes depending on the metal, owing to the different behaviour of the oxygen atoms. Hence, the ligand adopts a *NN'*-bridging conformation for Co(II) and Zn(II) compounds, a *NON'*-chelate and bridging conformation for Cd(II) and Hg(II) and a *NOO'N'*-chelate and bridging conformation for Cu(II). Thus, the objective of proving the coordination versatility of these ligands has been successfully achieved, as they displayed new conformations and coordination modes when compared to the previous results. The study of the obtained crystal structures has allowed to rationalise them based on a set of structural parameters. In particular, it was found that the angle between the coordinating nitrogen atoms and the centroid of the phenyl rings (θ) was the best suited to describe their behaviour. The comparison of these results with other reported accounts showed that the θ parameter can be used in the purposeful design of pyrazole ligands that favour a certain structural motif.

Regarding this same family of ligands, the reactivity of **L6-L8** against Pd(II) has been assayed. Unfortunately, it has been not possible to elucidate the crystal structures of the resulting compounds (**20-23**), and thus the analysis of the effect of the phenyl substituents in positions 3- and 5- has not been possible. However, the spectroscopical and analytic analysis has allowed us to provide some structural propositions for them. Furthermore, it has been observed that while for ligands **L6** and **L7** only one product is obtained (most likely a monomer), the reaction with **L8** results in the obtention of a mixture of products, the majoritarian ones being probably a monomer ($\approx 62\%$ yield) and a dimer ($\approx 18\%$ yield).

In this thesis, the first examples of coordination compounds bearing *N*-alkylcarborane ligands have been reported. Thus, six complexes (**24-29**) bearing Pd(II), Cu(II), Zn(II), Cd(II) and Hg(II) metal centres have been isolated and characterized. It is

worth mentioning that **L9** shows notable difficulties when reacting with Cd(II) and Hg(II), as, in fact, no coordination compounds are obtained, but rather ionic salts. This fact can be attributed to the electron-withdrawing effect of the carborane moiety, which results in a lower basicity for the pyrazole ring. The study of their supramolecular network also revealed that the globular nature of the carborane ligand prevent the formation of strong molecular interactions, favouring the formation of weak C-H \cdots H-B interactions.

Lastly, a series of CuI coordination compounds (**30-33**) were synthesized. Besides the pyrazole-carborane ligands (**L9-L11**), a pyrazole-phenyl ligand (**L12**), was used as a benchmark for the observation of the effect of the carborane moieties in the resulting compounds. The differences between ligands, which are particularly minimal between **L9** and **L10** (substitution of a -CH₃ group (**L9**) for a -H atom (**L10**)) had a profound impact on the resulting compound which showed a notable structural diversity as each one had a different structural motif. Moreover, some of the resulting morphologies are extremely rare. For instance, a single-stranded chain polymer, of which there are only three other reported compounds, an octahedral tetramer bearing a monodentate ligand, of which there is only one other reported example, and the first polymer simultaneously bearing the stepped cubane and the rhomboid dimeric *core* in its structure were obtained. Since some of the topologies were so rare, studying their photoluminescent behaviour is of great interest. Thus, their solid-state emission was studied, and the origin of their emissive properties was rationalized thanks to TDDFT calculations and by comparison with other published reports. The results were remarkable as it was possible to demonstrate a ³CC origin for the emission of a tri-coordinated rhomboid dimer, while in previous reports this was usually attributed to a (X+M)LCT by analogy with the more studied tetracoordinated rhomboid dimers. For the octahedral cluster, it was found that in the excited state the cluster is cleaved, explaining its large Stokes shift. It is the first time that this behaviour is observed for such clusters, indicating that more efforts are needed in order to rationalize their luminescent properties. Overall, a new understanding on some significant aspects of the luminescence of rare Cu(I) clusters was achieved, and the relationship between their structure and emissive properties studied.

The results in this thesis have allowed to expand the knowledge in the coordination behaviour of pyrazole-derived ligands. Besides working with previously synthesized ligands of the *N*-hydroxyalkylpyrazole and bispyrazole ether families, the latter has been expanded with the inclusion of three new ligands. Moreover, this work has

also resulted in the development of *N*-alkylpyrazole carboranes, a previously unreported new set of ligands. These results highlight the versatility of pyrazoles in the field of ligand design, as they act as a framework upon which different substituent groups can be easily grafted. Their cyclic nature and different reactive positions (1-, 3-, 4- and 5-) allowed a great degree of control between the orientations and relative distances of the substituents. Moreover, in contrast with other aromatic groups such as phenyls, the presence of *N*-donors embedded in their structure also allow the pyrazole itself to coordinate to metal centres. In addition, over thirty coordination compounds have been synthesized, allowing to study the influence of the different substituents in positions 1-, 3- and 5- on the structural features of the resulting metal complexes and their properties. Finally, some of the metal complexes properties have been rationalized based on the complex structure, which in turn is intrinsically related to the ligands' substituents and morphology, allowing to establish a direct link between these three features.

5. Experimental Section

5. Experimental Section

- Materials and general details

Anhydrous metal(II) chloride (Metal = copper(II), zinc(II), cadmium(II) and mercury(II)), cobalt(II) chloride hexahydrate ($\text{CoCl}_2 \cdot 6\text{H}_2\text{O}$), Copper(II) chloride dihydrate ($\text{CuCl}_2 \cdot 2\text{H}_2\text{O}$), copper(II) nitrate trihydrate ($\text{Cu}(\text{NO}_3)_2 \cdot 3\text{H}_2\text{O}$), copper(II) acetate monohydrate ($\text{Cu}(\text{MeCO}_2)_2 \cdot \text{H}_2\text{O}$), acetylacetone, 2-hydroxyethylhydrazine, aqueous ammonia 30%, sodium hydride, α, α -dibromo-*p*-xylene, α -dibromo-*o*-xylene, absolute ethanol (EtOH) methanol (MeOH), diethyl ether (Et_2O), hexane, chloroform (CHCl_3), acetonitrile (CH_3CN) and dichloromethane (CH_2Cl_2) were purchased from Sigma Aldrich and used without further purification. Dry CH_3CN was prepared using 3 Å activated molecular sieves and kept under dinitrogen atmosphere for 48 h. Spectroscopic grade acetonitrile (CH_3CN) was purchased from ROMIL-SpS and used without further purification. Deuterated solvents were bought from Eurisotop and used as received. All other chemicals are commercially available and were used as received.

Powder X-ray patterns (PXRD) were measured using a Siemens D5000 apparatus (with 40 kW and 45 mA using $\text{Cu } k_\alpha$ radiation with $\lambda = 1.5406 \text{ \AA}$), unless otherwise noted. Patterns were recorded from $2\theta = 5^\circ$ to 40° with a step scan of 0.02° counting for 1 s at each step. Elemental analyses (C, H, N) were carried out on a Thermo Scientific Flash 2000 CHNS Analyser. FTIR-ATR spectra were recorded on a high-resolution spectrometer FT-IR Perkin Elmer spectrum One equipped with a universal attenuated total reflectance (ATR) accessory with a diamond window in the range of $4000\text{--}500 \text{ cm}^{-1}$. ^1H NMR, ^{11}B NMR, $^{11}\text{B}\{^1\text{H}\}$ NMR and $^{13}\text{C}\{^1\text{H}\}$ NMR, HSQC-NMR and DOSY-NMR spectra were recorded on a NMR-FT Bruker 400 MHz spectrometer using deuterated chloroform (CDCl_3) or acetonitrile (CD_3CN) at 298 K. Chemical shifts are reported in ppm and referenced to the residual solvent peak for ^1H and $^{13}\text{C}\{^1\text{H}\}$ NMR or to $\text{BF}_3 \cdot \text{OEt}_2$ as an external standard for ^{11}B and $^{11}\text{B}\{^1\text{H}\}$ NMR. Chemical shifts are reported in ppm and coupling constants in Hertz. Multiplets nomenclature is as follows: s, singlet; d, doublet; t, triplet; br, broad; m, multiplet.

5.1 Experimental Section for 3.1

- Materials and general details

Synthetic procedures for **L6-L11** were carried out under dinitrogen atmosphere using standard Schlenk techniques. Tetrahydrofuran (THF) and toluene were purchased from Carlo Erba reagents S.A. and distilled from Na/Benzophenone prior to use. 3,5-dimethyl-1-(2-toluene-*p*-sulfonyloxyethyl)pyrazole and 1-(2-hydroxyethyl)-3,5-diphenylpyrazole (**HL2**) were synthesized according to the reported procedures^{1,2}.

- Synthetic Procedures

Synthesis of L6-L8

A solution of **HL2** (0.658 g, 2.49 mmol) in dry toluene (15 mL) was slowly added to a suspension of NaH (0.185 g, 57.7%, 4.45 mmol) in dry toluene (15 mL) and kept under reflux conditions for 4 h. After that period, a solution of α,α -dibromo-*x*-xylene (*x* = *para* (**L6**), *meta* (**L7**), *ortho* (**L8**)) (0.327 g, 1.24 mmol) in dry toluene (20 mL) was added dropwise under vigorous stirring. The resulting solution was kept under reflux conditions for 96 h. After cooling down, 10 mL of distilled water were added dropwise to destroy excess NaH. The solvents were then evaporated under reduced pressure. The residue was taken up in water (40 mL) and extracted with CHCl₃ (3x20 mL). The organic layers were dried with anhydrous MgSO₄ and evaporated under reduced pressure.

L6. Yield: 48.43% (0.379 g). Elemental analysis calc. (%) for C₄₂H₃₈N₄O₂ (630.30): C 79.97; H 6.07; N 8.88. Found: C 80.12; H 5.85; N 8.54. M.p.: 20-25 °C. FTIR-ATR (wavenumber, cm⁻¹): 3053(m) [v(C-H)_{ar}], 2923-2856(m) [v(C-H)_{al}], 1604(w), 1547(m) [v(C=C/C=N)_{ar}], 1491(w), 1483(m), 1461(s) [δ (C=C/C=N)_{ar}], 1437(w), 1417(w), 1363(m), 1295(w), 1277(w), 1200(w), 1174(w), 1096 and 1091(s) [v(C-O-C)] + [δ (C-H)_{ip}], 1050(m), 1025(w), 1008(w), 956(w), 916(w), 876(w), 839(m), 802(m), 758(vs) [δ (C-H)_{oop}], 692(vs) [δ (C-H)_{oop}], 615(w), 569(w). ¹H NMR (CDCl₃, 400 MHz, ppm): δ = 7.84 (m, 4H, *H*_{Ph-Pz-orto}), 7.53 (m, 4H, *H*_{Ph-Pz-orto}), 7.43 (m, overlapping signals 10H, *H*_{Ph-Pz}), 7.31 (m, 2H, *H*_{Ph-Pz-para}), 7.10 (s, 4H, CH₂O-*Ph-H*-OCH₂), 6.59 (s, 2H, CH(Pz)), 4.40 (s, 4H, OCH₂Ph) 4.34 (t, 4H, ³*J* = 5.61 Hz, N_{Pz}CH₂CH₂O), 3.95 (t, 4H, ³*J* = 5.61 Hz, N_{Pz}CH₂CH₂O). ¹³C {¹H} NMR (CDCl₃, 100.6 MHz, ppm): δ = 151.0, 146.1

(Pz-C), 137.5 (CH₂O-Ph-OCH₂), 133.6, 130.8 (Ph-Pz), 129.4, 128.7, 127.8 (C_{Ph-H-Pz}), 127.6 (CH₂O-Ph-H-OCH₂), 125.8 (C_{Ph-H-Pz-meta}), 103.5 (CH(Pz)), 73.0 (Ph-CH₂O), 69.0 (N_{Pz}CH₂CH₂O), 49.4 (N_{Pz}CH₂CH₂O).

L7. Yield: 56.07% (0.440 g). Elemental analysis calc. (%) for C₄₂H₃₈N₄O₂ (630.30): C 79.97; H 6.07; N 8.88. Found: C 79.35; H 6.04; N 8.71. M.p.: 20-25 °C. FTIR-ATR (wavenumber, cm⁻¹): 3053(m) [ν(C-H)_{ar}], 2918-2852(m) [ν(C-H)_{al}], 1604(w), 1546(m) [ν(C=C/C=N)_{ar}], 1483(m), 1461(s) [δ(C=C/C=N)_{ar}], 1437(m), 1415(w), 1363(m), 1296(w), 1277(w), 1259(w), 1237(w), 1198(w), 1177(w), 1115(w), 1108(s) and 1089(s) [ν(C-O-C)] + [δ(C-H)_{ip}], 1051(m), 1025(w), 957(m), 915(w), 881(w), 796(m), 759(vs) [δ(C-H)_{oop}], 692(vs) [δ(C-H)_{oop}], 655(w), 615(w), 580(w), 570(w). ¹H NMR (CDCl₃, 400 MHz, ppm): δ = 7.85 (m, 4H, H_{Ph-Pz-orto}), 7.52 (m, 4H, H_{Ph-Pz-orto}), 7.42 (m, overlapping signals 10H, H_{Ph-Pz}), 7.32 (m, 2H, H_{Ph-Pz-para}), 7.19 (m, 1H, CH₂O-Ph-H-OCH₂), 7.08 (d, 2H, ³J = 7.51 Hz, CH₂O-Ph-H-OCH₂), 7.03 (s, 1H, CH₂O-Ph-H-OCH₂), 6.58 (s, 2H, CH(Pz)), 4.38 (s, 4H, OCH₂Ph) 4.32 (t, 4H, ³J = 5.70 Hz, N_{Pz}CH₂CH₂O), 3.92 (t, 4H, ³J = 5.70 Hz, N_{Pz}CH₂CH₂O). ¹³C {¹H} NMR (CDCl₃, 100.6 MHz, ppm): δ = 151.0, 146.1 (Pz-C), 138.3 (CH₂O-Ph-OCH₂), 133.7, 130.8 (Ph-Pz), 129.4, 128.7, 128.6, 128.5, 127.8 (C_{Ph-H-Pz}), 128.5, 126.8, 126.7 (CH₂O-Ph-H-OCH₂), 125.8 (C_{Ph-H-Pz-meta}), 103.5 (CH(Pz)), 73.1 (Ph-CH₂O), 69.1 (N_{Pz}CH₂CH₂O), 49.4 (N_{Pz}CH₂CH₂O).

L8. Yield: 46.26% (0.362 g). Elemental analysis calc. (%) for C₄₂H₃₈N₄O₂ (630.30): C 79.97; H 6.07; N 8.88. Found: C 79.69; H 5.97; N 8.72. M.p.: 20-25 °C. FTIR-ATR (wavenumber, cm⁻¹): 3056(m) [ν(C-H)_{ar}], 2919-2854(m) [ν(C-H)_{al}], 1604(w), 1548(m) [ν(C=C/C=N)_{ar}], 1482(m), 1460(s) [δ(C=C/C=N)_{ar}], 1438(m), 1415(w), 1354(m), 1296(w), 1276(w), 1235(w), 1215(w), 1185(w), 1115(w), 1090(s) [ν(C-O-C)] + [δ(C-H)_{ip}], 1050(m), 1026(m), 1007(w), 957(m), 914(w), 799(w), 755(vs) [δ(C-H)_{oop}], 692(vs) [δ(C-H)_{oop}], 616(w), 584(w), 570(w). ¹H NMR (CDCl₃, 400 MHz, ppm): δ = 7.85 (m, 4H, H_{Ph-Pz-orto}), 7.47-7.39 (m, overlapping signals 14H, H_{Ph-Pz}), 7.31 (m, 2H, H_{Ph-Pz-para}), 7.19 (s, 4H, CH₂O-Ph-H-OCH₂), 6.58 (s, 2H, CH(Pz)), 4.36 (s, 4H, OCH₂Ph) 4.27 (t, 4H, ³J = 5.53 Hz, N_{Pz}CH₂CH₂O), 3.85 (t, 4H, ³J = 5.53 Hz, N_{Pz}CH₂CH₂O). ¹³C {¹H} NMR (CDCl₃, 100.6 MHz, ppm): δ = 150.8, 146.9 (Pz-C), 136.2 (CH₂O-Ph-OCH₂), 133.7, 130.8 (Ph-Pz), 129.4, 128.8, 128.7, 128.6 (C_{Ph-H-Pz}), 128.6, 128.5 (CH₂O-Ph-H-OCH₂), 125.7 (C_{Ph-H-Pz-meta}), 103.5 (CH(Pz)), 70.7 (Ph-CH₂O), 69.0 (N_{Pz}CH₂CH₂O), 49.3 (N_{Pz}CH₂CH₂O).

Synthesis of **L9**

n-BuLi (2.70 mL, 1.50 M in hexane, 4.05 mmol) was added dropwise to a solution of 1-methyl-*o*-carborane (0.834 g, 3.27 mmol) in dry THF (20 mL) under a nitrogen atmosphere at 0°C (ice/water bath). The solution was stirred for 45 minutes at 0°C and 45 minutes at r.t. resulting in a pale-yellow suspension. Next, a solution of 3,5-dimethyl-1-(2-toluene-*p*-sulfonyloxyethyl)pyrazole (1.00 g, 3.74 mmol) in dry THF (20 mL) under an inert atmosphere was carefully cannulated over the lithiate at 0°C (ice/water bath). The mixture was stirred overnight under an inert atmosphere, letting it warm naturally to r.t. After quenching the reaction by using a saturate aqueous solution of NH₄Cl (10 mL), the aqueous phase was extracted using Et₂O (3 x 20 mL) and the organic layers were dried over anhydrous MgSO₄. **L9** was purified by preparative TLC (eluent = Ethyl Acetate / Hexane 2:3, *R_f* = 0.47). The product was extracted from the corresponding silica portions with THF and obtained as white powders on solvent evaporation. Crystals suitable for SCXRD were obtained *via* slow evaporation of the latter THF solutions.

L9. Yield: 36 % (0.326 g). Elem. Anal. Calc. for C₁₀H₂₄B₁₀N₂ (280.42): C 42.83, H 8.63, N 9.99. Found: C 42.59, H 8.33, N 9.69. M.p.: 138-142 °C. ATR-FTIR (wavenumber, cm⁻¹): 3134-3061 (w) [ν(C-H)_{ar}], 2978-2858 (w) [ν(C-H)_{al}], 2571 (s) [ν(B-H)], 1554 (s) [ν(C=C/C=N)_{ar}], 1482 (w), 1463 (m), 1452 (s) [δ(C=C)/δ(C=N)_{ar}], 1421 (s), 1388 (s), 1372 (w), 1317 (w), 1299 (w), 1278 (m), 1218 (w), 1177 (w), 1161 (w), 1129 (w), 1088 (w), 1024 (s) [δ(C-H)_{ip}], 977 (w), 946 (w), 921 (w), 779 (s) [δ(C-H)_{oop}], 726 (s) [δ(C-H)_{oop}], 666 (m), 648 (m), 550 (m). ¹H NMR (CD₃CN, 400.0 MHz): δ = 5.77 (s, 1H, CH(Pz)), 4.07 (m, 2H, N_{Pz}CH₂CH₂C_{carb}, ²*J*_{AA'} = -6.0 Hz, ³*J*_{AB} = 12.7 Hz, ³*J*_{AB'} = 3.4 Hz, ³*J*_{A'B} = 8.8 Hz, ³*J*_{A'B'} = 11.7 Hz), 2.72 (m, 2H, N_{Pz}CH₂CH₂C_{carb}, ²*J*_{BB'} = -5.4 Hz, ³*J*_{AB} = 12.7 Hz, ³*J*_{AB'} = 3.4 Hz, ³*J*_{A'B} = 8.8 Hz, ³*J*_{A'B'} = 11.7 Hz), 2.19 (s, 3H, CH₃(Carb)), 2.08 and 2.07 (s, 6H, CH₃(Pz)). ¹¹B NMR (CDCl₃, 128.6 MHz): δ = -4.42 (br d, ¹*J*_{BH} = 157.3 Hz, 1B), -6.18 (br d, ¹*J*_{BH} = 151, 1B), -8.23 to -11.40, overlapping signals (8B). ¹¹B{¹H} NMR (CD₃CN, 128.6 MHz): δ = -4.4 (br s, 1B), -6.2 (br s, 1B), -8.9 to -10.8, overlapping signals (8B). ¹³C{¹H} NMR (CD₃CN, 100.6 MHz): δ = 148.2 and 140.1 (Pz-C), 106.9 (CH(Pz)), 47.7 (N_{Pz}CH₂CH₂C_{carb}), 36.1 (N_{Pz}CH₂CH₂C_{carb}), 23.6 (CH₃(Carb)), 13.6 and 11.1 (CH₃(Pz)). UV-Vis: (CH₃CN, 2.1 · 10⁻⁵ M) λ_{max} (ε (M⁻¹cm⁻¹)) = 196 nm (1012).

S1. ¹H NMR (AcD₆, 400.0 MHz): δ = 2.67 (s, 4H, C_{carb}CH₂CH₂C_{carb}), 2.22 (s, 3H, CH₃(Carb)). ¹¹B NMR (AcD₆, 128.6 MHz): δ = -2.3 to -5.6 overlapping signals (2B), -6.8

to -10.3, overlapping signals (8B). $^{11}\text{B}\{^1\text{H}\}$ NMR (CDCl_3 , 128.6 MHz): δ = -2.96 (br s, 1B), -4.68 (br s, 1B), -7.68 to -9.44, overlapping signals (8B).

S2. See ANNEX I and references sections³.

Synthesis of L10 and L11

A similar procedure as that described above was followed: *n*-BuLi (4.70 mL, 1.50 M in hexane, 7.05 mmol), *o*-carborane (0.456 g, 3.16 mmol) in dry THF (20 mL) and 3,5-dimethyl-1-(2-toluene-*p*-sulfonyloxyethyl)pyrazole (1.696 g, 6.33 mmol) in dry THF (20 mL). Then, the mixture was quenched using a saturate aqueous solution of NH_4Cl (10 mL). The aqueous phase was extracted using CHCl_3 (3 x 20 mL) and the organic layers were dried over anhydrous MgSO_4 . The desired products were purified by preparative TLC (**L10**, eluent = Ethyl Acetate / Chloroform 1:4, R_f = 0.76; **L11**, eluent = Ethyl Acetate / Hexane 9:1, R_f = 0.68). The products were extracted from the corresponding silica portions with CHCl_3 and obtained as white powders on solvent evaporation. The products were washed with cold Hexane (2 mL) and dried under vacuum.

L10. Yield: 33 % (0.622 g). Elem. Anal. Calc. for $\text{C}_9\text{H}_{22}\text{B}_{10}\text{N}_2$ (266.39): C 40.58, H 8.32, N 14.01. Found: C 40.49, H 8.23, N 13.85. M.p.: 172-176 °C. ATR-FTIR (wavenumber, cm^{-1}): 2982-2917 (w) [$\nu(\text{C-H})_{\text{al}}$], 2561 (s) [$\nu(\text{B-H})$], 2551 (s) [$\nu(\text{B-H})$], 1555 (s) [$\nu(\text{C}=\text{C}/\text{C}=\text{N})_{\text{ar}}$], 1489 (w), 1466 (m), 1442 (m), 1425 (s) [$\delta(\text{C}=\text{C})/\delta(\text{C}=\text{N})_{\text{ar}}$], 1377 (w), 1372 (m), 1321 (m), 1282 (w), 1218 (w), 1139 (w), 1071 (m), 1024 (s) [$\delta(\text{C-H})_{\text{ip}}$], 988 (w), 937 (w), 903 (w), 835 (w), 789 (vs) [$\delta(\text{C-H})_{\text{oop}}$], 719 (vs) [$\delta(\text{C-H})_{\text{oop}}$] and [$\nu(\text{B-B})$], 673 (w), 656 (w), 640 (w), 556 (w), 540 (w). ^1H NMR (CD_3CN , 400.0 MHz): δ = 5.84 (s, 1H, $\text{CH}(\text{Pz})$), 4.43 (br, 1H, $\text{C}_{\text{carb}}\text{-H}$) 4.06 (m, 2H, $\text{N}_{\text{Pz}}\text{CH}_2\text{CH}_2\text{C}_{\text{carb}}$), 2.75 (m, 2H, $\text{N}_{\text{Pz}}\text{CH}_2\text{CH}_2\text{C}_{\text{carb}}$), 2.19 (s, 3H, Pz-CH_3), 2.10 (s, 3H, Pz-CH_3). ^{11}B NMR (CD_3CN , 128.6 MHz) δ = -2.75 (br d, $^1J_{\text{BH}}$ = 155.0, 1B), -5.67 (br d, $^1J_{\text{BH}}$ = 155.0, 1B), -9.66 (br d, $^1J_{\text{BH}}$ = 149.5, 2B), -10.2 to -13.6, overlapping signals (6B). $^{11}\text{B}\{^1\text{H}\}$ NMR (CD_3CN , 128.6 MHz) δ = -2.88 (br s, 1B), -5.75 (br s, 1B), -9.65 (s, 2B), -11.15 to -13.0, overlapping signals (6B). $^{13}\text{C}\{^1\text{H}\}$ NMR (CD_3CN , 100.6 MHz): δ = 147.6, 145.5 (Pz-C), 108.1 (Pz-CH), 73.0 ($\text{C}_{\text{carb}}\text{-CH}_2\text{R}$), 63.7 ($\text{C}_{\text{carb}}\text{-H}$), 47.3 ($\text{C}_{\text{carb}}\text{-CH}_2\text{CH}_2\text{N}_{\text{Pz}}$), 36.5 ($\text{C}_{\text{carb}}\text{-CH}_2\text{CH}_2\text{N}_{\text{Pz}}$), 11.8, 11.2 ($\text{CH}_3(\text{Pz})$). UV-Vis: (CH_3CN , $6.5 \cdot 10^{-5}$ M) λ_{max} (ϵ ($\text{M}^{-1}\text{cm}^{-1}$)) = 201 nm (6380).

L11. Yield: 13 % (0.184 g). Elem. Anal. Calc. for $C_{16}H_{32}B_{10}N_4$ (388.56): C 49.46, H 8.30, N 14.01. Found: C 49.32, H 8.17, N 13.92. M.p.: 110-115 °C. ATR-FTIR (wavenumber, cm^{-1}): 3128 (w) [$\nu(C-H)_{ar}$], 2996-2856 (w) [$\nu(C-H)_{al}$], 2563 (br, vs) [$\nu(B-H)$], 1552 (s) [$\nu(C=C/C=N)_{ar}$], 1450 (s), 1416 (s) [$\delta(C=C)/\delta(C=N)_{ar}$], 1383 (s), 1365(s), 1315(s), 1258 (s), 1213 (m), 1173 (w), 1135 (w), 1080 (w), 1062 (w), 1020 (m) [$\delta(C-H)_{ip}$], 981 (m), 980 (m), 788 (vs) [$\delta(C-H)_{oop}$], 717 (vs) [$\delta(C-H)_{oop}$], 670 (vs) [$\delta(C-H)_{oop}$], 632 (m), 534 (m). 1H NMR (CD_3CN , 400.0 MHz): δ = 5.78 (s, 2H, $CH(Pz)$), 4.09 (m, 4H, $N_{Pz}CH_2CH_2C_{carb}$), 2.79 (m, 4H, $N_{Pz}CH_2CH_2C_{carb}$), 2.21 (s, 12H, $CH_3(Pz)$). ^{11}B NMR (CD_3CN , 128.6 MHz): δ = -4.07 (br d, $^1J_{BH}$ = 149.4, 1B), -9.34 to -11.64, overlapping signals (8B). $^{11}B\{^1H\}$ RMN (CD_3CN , 128.6 MHz): δ = -4.07 (br s, 2B), -9.8 and -11.3 overlapping signals (8B). $^{13}C\{^1H\}$ NMR (CD_3CN , 100.6 MHz): δ = 147.3 and 139.3 ($Pz-C$), 106.0 ($CH(Pz)$), 78.0 (C_{carb}), 46.6 ($N_{Pz}CH_2CH_2C_{carb}$), 33.9 ($N_{Pz}CH_2CH_2C_{carb}$), 12.5 and 10.0 ($CH_3(Pz)$). UV-Vis: (CH_3CN , $5.2 \cdot 10^{-5}$ M) λ_{max} (ϵ ($M^{-1}cm^{-1}$)) = 214 nm (6231).

5.2 Experimental Section for 3.2

- Materials and general details

Reactions and manipulation were carried out in air at room temperature (r.t.) unless otherwise noted. Ligands **HL1**, **HL2** and **HL3** ligand were synthesized as described in the literature⁴⁻⁶.

Conductivity measurements were performed at r.t. in MeOH (**1-4**·(CH_2Cl_2)(H_2O), **6** and **9**), CH_3CN (**7**·($2CH_3CN$) and **8**· H_2O) or DMF (**5**) solutions ($\approx 1 \cdot 10^{-3}$ M), using an EC-Meter BASIC 30 (Crisson Instruments) conductometer. The electronic spectra in MeOH (**1-4**·(CH_2Cl_2)(H_2O), **9**), CH_3CN (**7**·($2CH_3CN$) and **8**· H_2O) or DMF (**5**) solutions ($5.69 \cdot 10^{-4}$ - $1.33 \cdot 10^{-3}$ M) were run on a JASCO V-780 UV-Visible/NIR Spectrophotometer with a quartz cell having a path length of 1 cm in the range of 500-1100 nm. Simultaneous TG/DTA determinations were carried out in a Netzsch STA 409 instrument, with an aluminium oxide (Al_2O_3) crucible and heating at $5 K \cdot min^{-1}$ from 298 to 723 K, under a nitrogen atmosphere with a flow rate of $80 mL \cdot min^{-1}$. Aluminium oxide powder (PerkinElmer 0419-0197) was used as a standard. Magnetic measurements from 5 K to 300 K were carried out with a Quantum Design MPMS-5S SQUID spectrometer using a

100 Oe field. The experimental susceptibilities were corrected for the diamagnetism of the constituent atoms⁷ and effects of the capsule container.

- Synthetic Procedures

Synthesis of [CuCl(μ -L1)]₂ (1) and [CuCl(HL1)₂]Cl (2)

To a solution of **HL1** (2.60 mmol, 0.365 g) in MeOH (10 mL), a solution of CuCl₂·2H₂O (2.62 mmol, 0.446 g) in MeOH (10 mL) was added dropwise. The resulting dark green solution was stirred for 48 h at RT. After that period, a dark blue precipitate appeared (**1**), which was filtered off and dried under vacuum. The remaining mother liquors were concentrated until a dark green oil appeared, which after treatment with Et₂O, resulted in dark green solid (**2**). This solid was filtered off, washed with Et₂O and dried under vacuum. Suitable crystals for X-ray diffraction of compound **1** were obtained by recrystallization in an acetone:hexane 1:1 mixture for three weeks. Suitable crystals for X-ray diffraction of **2** were obtained by slow diffusion of hexane to a CHCl₃ solution.

1. Yield: 7.4 % (0.046 g). Elem. Anal. Calc. for C₁₄H₂₂Cl₂Cu₂N₄O₂ (476.33 g/mol): C 35.30; H 4.65; N 11.76. Found: C 35.22; H 4.58; N 11.57 %. Conductivity ($\Omega^{-1}\cdot\text{cm}^2\cdot\text{mol}^{-1}$ 1.4·10⁻³ M in MeOH): 20. FTIR-ATR (wavenumber, cm⁻¹): 3012(w) [ν (C-H)_{ar}], 2924-2873(w) [ν (C-H)_{al}], 1548(m) [ν (C=C/C=N)]_{ar}, 1469(m), 1421(m), 1389(m) [δ (C=C/C=N)]_{ar}, 1326(w), 1301(m), 1227(w), 1158 (m), 1140(w), 1082(m), 1058(s) [δ (C-H)_{ip}], 995(w), 895(s) [δ (C-H)_{oop}], 775(s) [δ (C-H)_{oop}], 626(s) [δ (C-H)_{oop}]. UV-Vis: (MeOH, 1.09·10⁻³ M) λ_{max} (ϵ (M⁻¹cm⁻¹)) = 696 nm (59).

2. Yield: 76.8 % (0.414 g). Elem. Anal. Calc. for C₁₄H₂₄Cl₂CuN₄O₂ (414.81 g/mol): C 40.54; H 5.83; N 13.51. Found: C 40.48; H 5.80; N 13.30 %. Conductivity ($\Omega^{-1}\cdot\text{cm}^2\cdot\text{mol}^{-1}$ 9.9·10⁻³ M in MeOH): 94. FTIR-ATR (wavenumber, cm⁻¹): 3123(br)-3089(br) [ν (OH)], 2940-2627(w) [ν (C-H)_{al}], 1551(m) [ν (C=C/C=N)]_{ar}, 1468(m), 1421(m), 1395(m) [δ (C=C/C=N)]_{ar}, 1329(w), 1306(m), 1261(w), 1225(w), 1158 (w), 1141(w), 1079(m), 1063(s), 1044(s) [δ (C-H)_{ip}], 875(s) [δ (C-H)_{oop}], 834(m), 805(s) [δ (C-H)_{oop}], 691(s) [δ (C-H)_{oop}]. UV-Vis: (MeOH, 1.04·10⁻³ M) λ_{max} (ϵ (M⁻¹cm⁻¹)) = 840 nm (46).

Synthesis of $\{[CuCl(\mu-L2)]_2 \cdot (HL2) (3 \cdot HL2)\}$

To a solution of **HL2** (1.01 mmol, 0.266 g) in MeOH (15 mL), a solution of $CuCl_2 \cdot 2H_2O$ (1.00 mmol, 0.171 g) in MeOH (10 mL) was added dropwise. The resulting dark green solution was stirred for 48 h at RT. After that period, the solution was concentrated up to 5 mL and left overnight on the fridge, which resulted in the formation of a dark green solid. This solid was filtered off, washed with cold Et_2O (5 mL) and dried under vacuum. Suitable crystals for X-ray diffraction of compound **3** were obtained by recrystallization in MeOH for six days.

3·HL2. Yield: 27.9 % (0.090 g). Elem. Anal. Calc. for $C_{85}H_{76}Cl_4Cu_4N_2O_5$ (1713.56 g/mol): C 59.32; H 4.19; N 8.12. Found: C 59.22; H 4.08; N 7.95 %. Conductivity ($\Omega^{-1} \cdot cm^2 \cdot mol^{-1}$ $1.06 \cdot 10^{-3}$ M in MeOH): 57. FTIR-ATR (wavenumber, cm^{-1}): 3331(br) [$\nu(O-H)$], 3056(w) [$\nu(C-H)_{ar}$], 2941-2851(w) [$\nu(C-H)_{al}$], 1576(m) [$\nu(C=C/C=N)_{ar}$], 1551(m) [$\nu(C=C/C=N)_{ar}$], 1469(m), 1464(m) [$\delta(C=C/C=N)_{ar}$], 1451(m) [$\delta(C=C/C=N)_{ar}$], 1374(m), 1298(m), 1278(m), 1235(w), 1202(w), 1160 (w), 1102(w), 1073(m) [$\delta(C-H)_{ip}$], 1016(m) [$\delta(C-H)_{ip}$], 965(w), 922(w), 879(w), 809(w), 761(vs) [$\delta(C-H)_{oop}$], 695(vs) [$\delta(C-H)_{oop}$], 614(w), 580(w), 519(w). UV-Vis: (MeOH, $8.92 \cdot 10^{-4}$ M) λ_{max} ($\epsilon(M^{-1}cm^{-1})$) = 769 nm (66).

Synthesis of $[CuCl_2(HL3)] \cdot (CH_2Cl_2)(H_2O) (4 \cdot (CH_2Cl_2)(H_2O))$

To a solution of **HL3** (0.635 mmol, 0.169 g) in MeOH (10 mL), a solution of $CuCl_2 \cdot 2H_2O$ (0.635 mmol, 0.285 g) in MeOH (20 mL) was added dropwise. The resulting dark green solution was stirred for 48 h at RT. After that period, a green precipitate appeared, which was filtered off and dried under vacuum. Suitable crystals for X-ray diffraction of compound **4** were obtained by recrystallization in CH_2Cl_2 for two weeks. Although the molecular formula of **4·(CH₂Cl₂)(H₂O)** has been established after resolution of its crystal structure by single crystal X-ray diffraction, this compound loses solvent molecules after being removed from solution. For this reason, we found that the manipulation required to prepare the sample for EA unavoidably leads to the loss of CH_2Cl_2 solvent molecules. Thus, EA results were adjusted considering a **4·H₂O** molecular relation.

4·H₂O. Yield: 72.2 % (0.231 g). Elem. Anal. Calc. for $C_{14}H_{12}Cl_2CuN_4O_2$ (406.75 g/mol): C 41.34; H 3.96; N 13.77. Found: C 41.27; H 4.08; N 13.49 %. Conductivity ($\Omega^{-1} \cdot cm^2 \cdot mol^{-1}$ $1.3 \cdot 10^{-3}$ M in MeOH): 14. FTIR-ATR (wavenumber, cm^{-1}): 3532(br) [$\nu(O-$

H)], 3246(br) [$\nu(\text{O-H})$], 3113(m)-3032(m) [$\nu(\text{C-H})_{\text{ar}}$], 2969(w)-2932(w) [$\nu(\text{C-H})_{\text{al}}$], 1609(m) [$\nu(\text{C}=\text{C}/\text{C}=\text{N})_{\text{ar}}$], 1586(m) [$\nu(\text{C}=\text{C}/\text{C}=\text{N})_{\text{ar}}$], 1567(m) [$\nu(\text{C}=\text{C}/\text{C}=\text{N})_{\text{ar}}$], 1466(w), 1442(m) [$\delta(\text{C}=\text{C}/\text{C}=\text{N})_{\text{ar}}$], 1438(s) [$\delta(\text{C}=\text{C}/\text{C}=\text{N})_{\text{ar}}$], 1380(m), 1351(m), 1314(w), 1286(m), 1252(w), 1229(w), 1161 (m), 1043(s) [$\delta(\text{C-H})_{\text{ip}}$], 1013(m), 978(m), 880(w), 848(m), 826(m), 795(m), 781(s) [$\delta(\text{C-H})_{\text{oop}}$], 741(w), 738(m), 685(m), 659(w), 626(m). UV-Vis: (MeOH, $1.32 \cdot 10^{-3}$ M) $\lambda_{\text{max}} (\epsilon(\text{M}^{-1}\text{cm}^{-1})) = 769 \text{ nm} (68)$.

Synthesis of $\{[\text{Cu}(\mu\text{-NO}_3)(\mu\text{-L1})]_2\}_n$ (5) and $[\text{Cu}(\text{NO}_3)(\text{HL1})_2]\text{NO}_3$ (6)

To a solution of **HL1** (2.01 mmol, 0.280 g) in MeOH (10 mL), a solution of $\text{Cu}(\text{NO}_3)_2 \cdot 3\text{H}_2\text{O}$ (2.02 mmol, 0.481 g) in MeOH (10 mL) was added dropwise, resulting in a green solution which was stirred for 12 h. under reflux conditions. Upon cooling, a light blue powder (**5**) appeared, which was filtered off, washed twice with cold Et_2O and dried under vacuum. The filtrate was concentrated under vacuum until a green oil was obtained. After the addition of 5 mL of Et_2O , a green powder precipitated (**6**). Suitable crystals for X-ray diffraction of **5** were obtained by recrystallization in CH_3CN for three weeks. Suitable crystals for X-ray diffraction of **6** were obtained by recrystallization in MeOH for one month.

5. Yield: 71.4 % (0.380 g). Elem. Anal. Calc. for $\text{C}_{14}\text{H}_{22}\text{Cu}_2\text{N}_6\text{O}_8$ (529.46 g/mol): C 31.76; H 4.19; N 24.17. Found: C 31.88; H 4.17; N 23.98 %. Conductivity ($\Omega^{-1} \cdot \text{cm}^2 \cdot \text{mol}^{-1}$ $1.1 \cdot 10^{-3}$ M in DMF): 36. FTIR-ATR (wavenumber, cm^{-1}): 2972-2865(w) [$\nu(\text{C-H})_{\text{al}}$], 1750(w)-1732(w) [$\nu_1+\nu_4(\text{NO}_3)$], 1549(s) [$\nu(\text{C}=\text{C}/(\text{C}=\text{N})_{\text{ar}}$], 1495(w), 1454(s) [$\nu(\text{NO}_3)$], 1403(m) [$\delta(\text{C}=\text{C}/\text{C}=\text{N})_{\text{ar}}$], 1373(w), 1351(w), 1304(w), 1268(s) [$\nu(\text{NO}_3)$], 1229(w), 1156(w), 1140(m), 1081(w), 1066(s) [$\delta(\text{C-H})_{\text{ip}}$], 1022(m), 997(m), 971(w), 894(m) [$\delta(\text{C-H})_{\text{oop}}$], 790(w), 777(m) [$\delta(\text{C-H})_{\text{oop}}$], 749(w), 632(m), 602(m), 599(m). UV-Vis: (DMF, $1.17 \cdot 10^{-3}$ M) $\lambda_{\text{max}} (\epsilon(\text{M}^{-1}\text{cm}^{-1})) = 681 \text{ nm} (112)$.

6. Yield: 4.2 % (0.020 g). Elem. Anal. Calc. for $\text{C}_{14}\text{H}_{24}\text{CuN}_6\text{O}_8$ (467.9 g/mol): C 35.94; H 5.17; N 17.96. Found: C 35.71; H 4.98; N 17.69 %. Conductivity ($\Omega^{-1} \cdot \text{cm}^2 \cdot \text{mol}^{-1}$ $1.2 \cdot 10^{-3}$ M in MeOH): 111. FTIR-ATR (wavenumber, cm^{-1}): 3191(br)-3149(br) [$\nu(\text{OH})$], 2858-2651(w) [$\nu(\text{C-H})_{\text{al}}$], 1770(w)-1718(w) [$\nu_1+\nu_4(\text{NO}_3)$], 1555(s) [$\nu(\text{C}=\text{C}/\text{C}=\text{N})_{\text{ar}}$], 1500(w), 1442(s) [$\nu(\text{N-O}_3)$], 1403(s) [$\delta(\text{C}=\text{C}/\text{C}=\text{N})_{\text{ar}}$], 1350(m), 1280(s)

$[\nu(\text{N-O}_3)]$, 1155(w), 1142(w), 1086(w), 1056(w), 1042(w), 1019(m) $[\delta(\text{C-H})_{\text{ip}}]$, 993(w), 963(w), 881(m) $[\delta(\text{C-H})_{\text{oop}}]$, 810(m) $[\delta(\text{C-H})_{\text{oop}}]$, 781(m) $[\delta(\text{C-H})_{\text{oop}}]$, 646(w).

Synthesis of $\text{Cu}(\text{NO}_3)(3,5\text{-DPP})(\mu\text{-L2})_2 \cdot 2(\text{CH}_3\text{CN})$ ($3 \cdot 2\text{CH}_3\text{CN}$, $3,5\text{-DPP} = 3,5\text{-diphenylpyrazole}$)

To a solution of **HL2** (1.69 mmol, 0.474 g) in MeOH (20 mL), a solution of $\text{Cu}(\text{NO}_3)_2 \cdot 3\text{H}_2\text{O}$ (1.79 mmol, 0.432 g) in MeOH (20 mL) was added dropwise. The resulting dark green solution was stirred for 48h at r.t. After that period, the solution was concentrated up to 5 mL, and left standing to evaporate for four days. Then, the green precipitate was filtered off, washed with 5 mL of cold Et_2O and dried under vacuum. Recrystallization of this solid in CH_3CN for two weeks yielded suitable crystals for X-ray diffraction.

7·(2CH₃CN). Yield: 89.55 % (0.492 g). Elem. anal. Calc. for $\text{C}_{68}\text{H}_{60}\text{Cu}_2\text{N}_{12}\text{O}_8$ (1300.36 g/mol): C 62.81; H 4.65; N 12.93. Found: C 62.59; H 4.36; N 12.78%. Conductivity ($\Omega^{-1} \cdot \text{cm}^2 \cdot \text{mol}^{-1}$ $5.69 \cdot 10^{-4}$ M in CH_3CN): 44. FTIR-ATR (wavenumber, cm^{-1}): 3122(w) $[\nu(\text{N-H})]$, 3061(w) $[\nu(\text{C-H})_{\text{ar}}]$, 2915(w)-2863(w) $[\nu(\text{C-H})_{\text{al}}]$, 2254(m) $[\nu(\text{CN})]$, 1750-1741(w) $[\nu_1 + \nu_4 (\text{NO}_3)]$ 1577(s) $[\nu(\text{C}=\text{N})]_{\text{ar}}$, 1557(s) $[\nu(\text{C}=\text{N})]_{\text{ar}}$, 1551(s) $[\nu(\text{C}=\text{N})]_{\text{ar}}$, 1478(m), 1464(m) $[\delta(\text{C}=\text{C}/\text{C}=\text{N})]_{\text{ar}}$, 1441(m), 1389(vs) $[\nu(\text{NO}_3)]$, 1300(vs) $[\nu(\text{NO}_3)]$, 1233(w), 1204(w), 1161(m), 1104(m), 1076(s) $[\delta(\text{C-H})_{\text{ip}}]$, 1038(m), 1028(m), 1016(m), 990(m), 986(m), 968(w), 954(w), 910(m), 843(w), 811(w), 758(vs) $[\delta(\text{C-H})_{\text{oop}}]$, 705(w), 689(vs) $[\delta(\text{C-H})_{\text{oop}}]$, 669 (m), 648(w), 579(m). UV-Vis: (CH_3CN , $5.69 \cdot 10^{-4}$ M) $\lambda_{\text{max}} (\epsilon(\text{M}^{-1}\text{cm}^{-1})) = 728 (154)$

Synthesis of $[\text{Cu}(\text{H}_2\text{O})(3,5\text{-DPyP})]_2(\text{NO}_3)_2 \cdot (\text{H}_2\text{O})$ ($8 \cdot \text{H}_2\text{O}$), $3,5\text{-DPyP} = 3,5\text{-di}(2\text{-pyridyl})\text{pyrazole}$

To a solution of **HL3** (0.368 mmol, 0.098 g) in MeOH (20 mL), a solution of $\text{Cu}(\text{NO}_3)_2 \cdot 3\text{H}_2\text{O}$ (0.389 mmol, 0.094 g) in MeOH (20 mL) was added dropwise. The resulting dark green solution was stirred for 48h at r.t. After that period, the solution was concentrated up to 5 mL, and left in the fridge for two days. Then, the green precipitate was filtered off, washed with 5 mL of cold Et_2O and dried under vacuum.

Recrystallization of this solid in a $\text{CH}_3\text{CN}:\text{CHCl}_3$ mixture (3:1 ratio) for one month yielded suitable crystals for X-ray diffraction.

8·H₂O. Yield: 71.24 % (0.098 g). Elem. anal. Calc. for $\text{C}_{26}\text{H}_{24}\text{Cu}_2\text{N}_{10}\text{O}_9$ (747.63 g/mol): C 41.77; H 3.24; N 18.74. Found: C 41.62; H 3.30; N 18.53%. Conductivity ($\Omega^{-1}\cdot\text{cm}^2\cdot\text{mol}^{-1}$ $6.95\cdot 10^{-4}$ M in CH_3CN): 219. FTIR-ATR (wavenumber, cm^{-1}): 3301(br) [$\nu(\text{OH})$], 3099(w)-2952(w) [$\nu(\text{C-H})_{\text{ar}}+\nu(\text{C-H})_{\text{al}}$], 1749(w) [$\nu_1 + \nu_4 (\text{NO}_3)$], 1614(s) [$\nu(\text{C}=\text{N})$]_{ar}, 1588(s) [$\nu(\text{C}=\text{N})$]_{ar}, 1569(s) [$\nu(\text{C}=\text{N})$]_{ar}, 1472(m), 1461(m) [$\delta(\text{C}=\text{C}/\text{C}=\text{N})$]_{ar}, 1435(s) [$\nu(\text{NO}_3)$], 1406(m), 1361(m), 1271(vs) [$\nu(\text{NO}_3)$], 1158(m), 1053(w), 1046(m), 1036(s) [$\delta(\text{C-H})_{\text{ip}}$], 1017(m), 993(m), 980(w), 955(m), 891(w), 870(m), 840(w), 820(m), 799(m), 781(vs) [$\delta(\text{C-H})_{\text{oop}}$], 750(s) [$\delta(\text{C-H})_{\text{oop}}$], 716(m), 984(m), 656(m), 648(m), 626(m), 596(m). UV-Vis: (CH_3CN , $6.95\cdot 10^{-4}$ M) $\lambda_{\text{max}}(\epsilon(\text{M}^{-1}\text{cm}^{-1})) = 709 \text{ nm} (119)$

Synthesis of [Cu(MeCO₂)(μ-L1)]₂·6H₂O (9·6H₂O)

To a solution of **HL1** (2.410 mmol, 0.338 g) in MeOH (20 mL), a solution of $\text{Cu}(\text{MeCO}_2)_2\cdot\text{H}_2\text{O}$ (2.40 mmol, 0.481 g) in MeOH (25 mL) was added dropwise. In addition, 0.1 mL of aqueous ammonia 30% were added to the previous solution. The resulting blue solution was stirred for 48h at r.t. After that period, the solution was concentrated up to 5 mL, and 20 mL of Et_2O were added. After 20 minutes, a blue precipitate appeared. The resulting solution was kept overnight on the fridge. Then, the blue precipitate was filtered off, washed with 5 mL of cold Et_2O and dried under vacuum (**9**). Recrystallization of this solid in MeOH for 36h yielded suitable crystals for X-ray diffraction of molecular formula $[\text{Cu}(\text{MeCO}_2)(\mu\text{-L1})]_2\cdot 6\text{H}_2\text{O}$ (**9**·6H₂O). Although the molecular formula of **9** has been established after resolution of its crystal structure by single crystal X-ray diffraction, this compound loses solvent molecules after being removed from solution. For this reason, we found that the manipulation required to prepare the sample for EA unavoidably leads to the loss of two water solvent molecules. Thus, EA results were adjusted considering a **9**·4H₂O molecular relation.

9·4H₂O. Yield: 44.7 % (0.281 g). Elem. anal. Calc. for $\text{C}_{18}\text{H}_{36}\text{Cu}_2\text{N}_4\text{O}_8$ (595.59 g/mol): C 36.29; H 6.09; N 9.40. Found: C 36.14; H 6.16; N 9.13%. Conductivity ($\Omega^{-1}\cdot\text{cm}^2\cdot\text{mol}^{-1}$ $9.6\cdot 10^{-3}$ M in MeOH): 28. FTIR-ATR (wavenumber, cm^{-1}): 3473(br) [$\nu(\text{OH})$], 3368(br) [$\nu(\text{OH})$], 3269(br) [$\nu(\text{OH})$], 2967(w)-2825(w) [$\nu(\text{C-H})_{\text{al}}$], 1585(s)

$[\nu(\text{C}=\text{C}/\text{C}=\text{N})]_{\text{ar}}$, 1547(s) $[\nu(\text{COO})_{\text{as}}]$, 1470(w), 1417(s) $[\nu(\text{COO})_{\text{s}}]$, 1389(s) $[\delta(\text{C}=\text{C}/\text{C}=\text{N})]_{\text{ar}}$, 1328(m), 1303(m), 1228(m), 1154(w), 1138(w), 1086(s) $[\delta(\text{C}-\text{H})_{\text{ip}}]$, 1069(m), 967(w), 924(w), 894(s), 782(s) $[\delta(\text{C}-\text{H})_{\text{oop}}]$, 679(s) $[\delta(\text{C}-\text{H})_{\text{oop}}]$, 625(s), 579(s). UV-Vis: (MeOH, $9.93 \cdot 10^{-4}$ M) λ_{max} ($\epsilon(\text{M}^{-1}\text{cm}^{-1})$) = 670 nm (113).

5.3 Experimental Section for 3.3

- Materials and general details

All reactions and manipulations were carried out in air. Ligands **L4**, **L5** and $[\text{Pd}(\text{CH}_3\text{CN})_2\text{Cl}_2]$ were synthesised as described in the literature.^{8–10} The electronic spectra were run on a Varian Cary 500 spectrophotometer, using spectroscopic grade CH_3CN , in a normal quartz cell having a path length of 10 mm in the range of 200–800 nm, with concentrations between $1.05 \cdot 10^{-4}$ – $1.34 \cdot 10^{-4}$ M at room temperature (r.t.) for compounds **10–12** and **15–17**. Electronic spectra in acetone (**13**), CH_2Cl_2 (**18**) and MeOH (**14** and **19**) solutions ($\sim 1.1 \cdot 10^{-3}$ M) were run on a JASCO UV-Visible/NIR Spectrophotometer with a quartz cell having a path length of 1 cm in the range of 500–1000 nm. The fluorescence emission and excitation spectra were recorded in a Varian Cary Eclipse Fluorescence Spectrometer at r.t., equipped with a quartz cell having a path length of 10 mm. The samples were excited at 260 nm and the emission was recorded in the range of 270–600 nm in spectroscopic grade CH_3CN ($4.87 \cdot 10^{-4}$ M for **L4**, $5.02 \cdot 10^{-4}$ M for **L5** and $1.21 \cdot 10^{-4}$ – $1.38 \cdot 10^{-4}$ M for **10–12** and **15–17**). The dilution effects of the obtained data were corrected using Origin Pro 8 software.

- Synthetic Procedures

*Synthesis of the complexes $[\text{M}(\text{L4})\text{Cl}_2]_2$ [$\text{M} = \text{Zn(II)}$ (**10**), Cd(II) (**11**), Hg(II) (**12**), Cu(II) (**14**)] and $[\text{Co}(\text{L4})\text{Cl}_2]_2 \cdot 1/2\text{H}_2\text{O}$ (**13**)*

An absolute EtOH (20 mL) solution of MCl_2 ($\text{M} = \text{Zn(II)}$, 0.690 mmol: 0.094 g (**10**); $\text{M} = \text{Cd(II)}$, 0.127 g (**11**); $\text{M} = \text{Hg(II)}$, 0.187 g (**12**), $\text{M} = \text{Cu(II)}$, 0.093 g) or $\text{CoCl}_2 \cdot 6(\text{H}_2\text{O})$ (0.165 g, 0.692 mmol (**13**)), was added dropwise to a solution of **L4** (0.692 mmol, 0.265 g) in absolute EtOH (20 mL). The resulting solutions were stirred for 48 h

at r.t. (**10-12**, **14**) or under reflux conditions (**13**) After that period, the solutions were concentrated under vacuum up to 10 mL and left to evaporate until solids precipitated. The resulting solids were filtered off, washed with 5 mL of cold Et₂O and dried under vacuum. Suitable crystals for X-ray diffraction were obtained by letting an EtOH solution of the powder crystallize at r.t. for sixteen (**10**), nineteen (**11**) or twenty (**12**) days or *via* recrystallization in a CHCl₃:MeOH:Acetone mixture in a 1:1:1 ratio (**13**).

10. Yield: 74.1% (0.265 g). Elemental analysis calc. (%) for C₄₄H₆₀Zn₂Cl₄N₈O₄ (1037.54): C 50.93; H 5.83; N 10.80. Found: C 50.74; H 5.85; N 10.71. FTIR-ATR (wavenumber, cm⁻¹): 2935-2853(m) [ν(C-H)_{al}], 1551(s) [ν(C=C)_{ar}/ν(C=N)_{ar}], 1479(w), 1457(w), 1455(m), 1424(m) [δ(C=C)_{ar}/δ(C=N)_{ar}], 1375(w), 1371(w), 1345(m), 1306(m), 1266(w), 1254(w), 1209(m), 1099(s) [ν(C-O-C)], 1067(m), 1033(s) [δ(C-H)_{ip}], 873(w), 843(m), 816(s) [δ(C-H)_{oop}], 772(s) [δ(C-H)_{oop}], 650(w), 631(s). ¹H NMR (CDCl₃, 400 MHz, ppm): δ = 7.26 (overlapped with CDCl₃, br, 4H, *Ph*), 5.97 (s, 2H, *CH*(Pz)), 4.72 (br, 4H, OCH₂Ph), 4.53 (s, 4H, N_{Pz}CH₂CH₂O), 3.84 (br, 4H, N_{Pz}CH₂CH₂O), 2.34 (s, 6H, CH₃(Pz)), 2.29 (s, 6H, CH₃(Pz)). ¹³C {¹H} NMR (CDCl₃, 100.6 MHz, ppm): δ = 150.4, 143.5 (Pz-C), 136.3 (*Ph*-CH₂O), 128.8 (*Ph*-H), 107.1 (*CH*(Pz)), 73.8 (Ph-CH₂O), 69.2 (N_{Pz}CH₂CH₂O), 47.8 (N_{Pz}CH₂CH₂O), 13.4, 11.6 (CH₃(Pz)). UV-Vis: (CH₃CN, 1.07·10⁻⁴ M) λ_{max} (ε (M⁻¹cm⁻¹)) = 221 nm (8.4·10⁴), 277 (shoulder, 1.6·10⁴). Fluorescence (CH₃CN): λ_{ex} = 260 nm, λ_{em} = 283 nm.

11. Yield: 73.6% (0.287 g). Elemental analysis calc. (%) for C₄₄H₆₀Cd₂Cl₄N₈O₄ (1131.60): C 46.70; H 5.34; N 9.90. Found: C 46.55; H 5.20; N 9.60. FTIR-ATR (wavenumber, cm⁻¹): 3188(w) [ν(C-H)_{ar}], 2951-2851(s) [ν(C-H)_{al}], 1547(s) [ν(C=C)_{ar}/ν(C=N)_{ar}], 1496(w), 1465(s), 1440(w), 1423(s) [δ(C=C)_{ar}/δ(C=N)_{ar}], 1397(w), 1387(w), 1376(m), 1373(m), 1357(w), 1307(m), 1267(w), 1254(w), 1207(m), 1162(w), 1112(m), 1105(s) [ν(C-O-C)], 1065(m), 1043(m) [δ(C-H)_{ip}], 1013(m), 982(w), 870(m), 836(m), 816(s) [δ(C-H)_{oop}], 762(s) [δ(C-H)_{oop}], 649(w), 628(m). ¹H NMR (CDCl₃, 400 MHz, ppm): δ = 7.16 (s, 4H, *Ph*), 5.79 (s, 2H, *CH*(Pz)), 4.47 (s, 4H, OCH₂Ph), 4.17 (t, 4H, ³J = 5.8 Hz, N_{Pz}CH₂CH₂O), 3.78 (t, 4H, ³J = 5.7 Hz, N_{Pz}CH₂CH₂O), 2.24 (s, 6H, CH₃(Pz)), 2.22 (s, 6H, CH₃(Pz)). ¹³C {¹H} NMR (CDCl₃, 100.6 MHz, ppm): δ = 147.8, 140.3 (Pz-C), 137.6 (*Ph*-CH₂O), 127.7 (*Ph*-H), 106.1 (*CH*(Pz)), 73.1 (Ph-CH₂O), 69.4 (N_{Pz}CH₂CH₂O), 48.7 (N_{Pz}CH₂CH₂O), 13.7, 11.4 (CH₃(Pz)). UV-Vis: (CH₃CN, 1.17·10⁻⁴ M) λ_{max} (ε (M⁻¹cm⁻¹)) = 230 nm (7.5·10⁴), 277 (shoulder, 7.1·10³). Fluorescence (CH₃CN): λ_{ex} = 260 nm, λ_{em} = 282 nm.

12. Yield: 61.7% (0.275 g). Elemental analysis calc. (%) for $C_{44}H_{60}Hg_2Cl_4N_8O_4$ (1307.98): C 40.40; H 4.62; N 8.57. Found: C 40.27; H 4.54; N 8.30. FTIR-ATR (wavenumber, cm^{-1}): 3117(w) [$\nu(C-H)_{ar}$], 2959-2861(s) [$\nu(C-H)_{al}$], 1547(s) [$\nu(C=C)_{ar}/\nu(C=N)_{ar}$], 1494(w), 1463(m), 1423(m) [$\delta(C=C)_{ar}/\delta(C=N)_{ar}$], 1387(w), 1376(m), 1347(w), 1307(m), 1266(m), 1207(m), 1122(s), 1105(s) [$\nu(C-O-C)$], 1065(m), 1040(m) [$\delta(C-H)_{ip}$], 1014(m), 870(w), 821(m), 816(s) [$\delta(C-H)_{oop}$], 763(w), 630(m), 533(m). 1H NMR ($CDCl_3$, 400 MHz, ppm): δ = 7.15 (s, 4H, *Ph*), 5.90 (s, 2H, *CH*(Pz)), 4.47 (s, 4H, *OCH*₂Ph), 4.33 (t, 4H, 3J = 5.26 Hz, $N_{Pz}CH_2CH_2O$), 3.79 (t, 4H, 3J = 5.33 Hz, $N_{Pz}CH_2CH_2O$), 2.31 (s, 6H, *CH*₃(Pz)), 2.27 (s, 6H, *CH*₃(Pz)). $^{13}C\{^1H\}$ NMR ($CDCl_3$, 100.6 MHz, ppm): δ = 147.7, 141.2 (Pz-C), 137.3 (*Ph*-CH₂O), 128.1 (*Ph*-H), 107.0 (*CH*(Pz)), 73.1 (*Ph*-CH₂O), 68.8 ($N_{Pz}CH_2CH_2O$), 48.7 ($N_{Pz}CH_2CH_2O$), 13.3, 11.4 (*CH*₃(Pz)). UV-Vis: (CH_3CN , $1.05 \cdot 10^{-4}$ M) λ_{max} (ϵ ($M^{-1}cm^{-1}$)) = 275 ($2.3 \cdot 10^3$). Fluorescence (CH_3CN): λ_{ex} = 260 nm, λ_{em} = 286 nm.

13. Yield: 69.3 % (0.248 g) Elem anal. Calc. for $C_{88}H_{122}Cl_8N_{16}O_9Co_4$ (2067.33): C 51.13, H 5.95, N 10.84. Found: C 50.98, H 5.87, N 10.76. FTIR-ATR (wavenumber, cm^{-1}): 3385(br) [$\nu(O-H)$], 2963(w)-2867(w) [$\nu(C-H)_{al}$], 1550(s) [$\nu(C=C/C=N)_{ar}$], 1466(m), 1446(m) 1427(m) 1420(s) [$\delta(C=C/C=N)_{ar}$], 1373(s), 1308(m), 1265(w), 1252(w), 1208(m), 1164(w), 1117(s) and 1105(vs) [$\nu(C-O-C)$], 1066(s) [$\delta(C-H)_{ip}$], 1045(s), 872(w), 839(w), 815(s) [$\delta(C-H)_{oop}$], 762(s) [$\delta(C-H)_{oop}$], 632(m), 533(w). UV-Vis (Acetone, $9.44 \cdot 10^{-4}$ M) λ_{max} ($\epsilon(M^{-1}cm^{-1})$) = 664 nm (403), 585 nm (shoulder, 303).

14. Yield: 60.3 % (0.215 g). Elem. Anal. Calc. for $C_{44}H_{60}Cl_4N_8O_4Cu_2$ (1033.90): C 51.11, H 5.85, N 10.84. Found: C 51.18, H 5.76, N 10.61. FTIR-ATR (wavenumber, cm^{-1}): 2915(w)-2873(w) [$\nu(C-H)_{al}$], 1555(s) [$\nu(C=C/(C=N))_{ar}$], 1495(w), 1467(m), 1421(m) [$\delta(C=C)$, $\delta(C=N)_{ar}$], 1395(s), 1353(s), 1306(m), 1258(m), 1219(m), 1215(w), 1091(s) [$\nu(C-O-C)$], 1065(s) [$\delta(C-H)_{ip}$], 1058(s) [$\delta(C-H)_{ip}$], 1014(s), 988(m), 871(m), 835(s) [$\delta(C-H)_{oop}$], 786(s) [$\delta(C-H)_{oop}$], 756(s) [$\delta(C-H)_{oop}$], 624(m), 592(w), 524(m). UV-Vis (MeOH, $1.12 \cdot 10^{-3}$ M) λ_{max} ($\epsilon(M^{-1}cm^{-1})$) = 875 nm (78).

Synthesis of $\{[M(L5)Cl_2] \cdot 1/2H_2O\}_n$ [$M = Zn(II)$ (15**), $Co(II)$ (**18**) and $\{[M(L5)Cl_2] \cdot 1/2EtOH\}_n$ [$M = Cd(II)$ (**16**), $Hg(II)$ (**17**)]**

An absolute EtOH (20 mL) solution of MCl_2 (0.934 mmol: 0.127 g (**15**); 0.171 g (**16**); 0.254 g (**17**)) or $CoCl_2 \cdot 6(H_2O)$ (0.518 mmol, 0.222 g (**18**)) was added dropwise to a solution of **L5** (0.357 g, 0.934 mmol) in absolute EtOH (20 mL). The resulting solutions were stirred for 48 h. at RT (**15-17**) or under reflux conditions (**18**). During this time, the solution for **18** shifted from a deep violet colour to a light blue. After that period, the solutions were concentrated up to 10 ml and left to evaporate until precipitates appeared, which were filtered off, washed with 5 mL of cold Et_2O and dried under vacuum. Suitable crystals for X-ray diffraction were obtained by letting an EtOH solution of the white powder crystallize at r.t. for twelve (**15**), twenty-five (**16**) or eleven days in the fridge for **17** or by layering a CH_2Cl_2 solution of **18** with hexane and leaving it in the fridge at 4°C for one month.

15. Yield: 92.9% (0.458 g). Elemental analysis calc. (%) for $C_{44}H_{62}Zn_2Cl_4N_8O_5$ (1055.55): C 50.06; H 5.92; N 10.62. Found: C 49.96; H 5.64; N 10.33. FTIR-ATR (wavenumber, cm^{-1}): 3600-3200(br) [$\nu(O-H)$], 3125(w) [$\nu(C-H)_{ar}$], 2954-2855(s) [$\nu(C-H)_{al}$], 1554(m) [$\nu(C=C)_{ar}/\nu(C=N)_{ar}$], 1470(w), 1440(m), 1420(m) [$\delta(C=C)_{ar}/\delta(C=N)_{ar}$], 1385(w), 1374(m), 1353(m), 1314(w), 1286(w), 1261(w), 1220(w), 1218(w), 1189(w), 1168(w), 1148(w), 1124(s), 1105(s) [$\nu(C-O-C)$], 1065(m), 1050(s) [$\delta(C-H)_{ip}$], 1014(w), 876(w), 816(m), 786(s) [$\delta(C-H)_{oop}$], 758(s) [$\delta(C-H)_{oop}$], 656(m), 634(m). 1H NMR ($CDCl_3$, 400 MHz, ppm): δ = 7.25 (s, 4H, *Ph*), 5.95 (s, 2H, *CH(Pz)*), 4.67 (t, 4H, 3J = 5.6 Hz, $N_{Pz}CH_2CH_2O$), 4.40 (s, 4H, OCH_2Ph), 3.84 (br, 4H, $N_{Pz}CH_2CH_2O$), 2.32 (s, 6H, $CH_3(Pz)$), 2.25 (s, 6H, $CH_3(Pz)$). $^{13}C\{^1H\}$ NMR ($CDCl_3$, 100.6 MHz, ppm): δ = 150.1, 144.0 (*Pz-C*), 136.1 (*Ph-CH_2O*), 128.2, 128.1 (*Ph-H*), 107.4 (*CH(Pz)*), 69.9 (*Ph-CH_2O*), 68.7 ($N_{Pz}CH_2CH_2O$), 48.5 ($N_{Pz}CH_2CH_2O$), 13.7, 11.7 ($CH_3(Pz)$). UV-Vis: (CH_3CN , $1.26 \cdot 10^{-4} M$) λ_{max} ($\epsilon(M^{-1}cm^{-1})$) = 218 nm ($1.84 \cdot 10^4$), 251(shoulder, $1.7 \cdot 10^3$). Fluorescence (CH_3CN): λ_{ex} = 260 nm, λ_{em} = 286 nm.

16. Yield: 88.3% (0.486 g). Elemental analysis calc. (%) for $C_{23}H_{33}CdCl_2N_4O_{2.5}$ (588.83): C 46.91; H 5.65; N 9.52. Found: C 46.87; H 5.61; N 9.22. FTIR-ATR (wavenumber, cm^{-1}): 3496(br) [$\nu(O-H)$], 2965-2866(m) [$\nu(C-H)_{al}$], 1550(s) [$\nu(C=C)_{ar}/\nu(C=N)_{ar}$], 1468(w), 1447(m) [$\delta(C=C)_{ar}/\delta(C=N)_{ar}$], 1422(m) [$\delta(C=C)_{ar}/\delta(C=N)_{ar}$], 1374(s), 1356(w), 1315(w), 1300(w), 1281(w), 1256(w), 1209(w),

1184(w), 1123(s), 1101(s) [$\nu(\text{C-O-C})$], 1069(m), 1036(s) [$\delta(\text{C-H})_{\text{ip}}$], 1019(m), 993(w), 838(w), 811(w), 791(m) [$\delta(\text{C-H})_{\text{oop}}$], 751(s) [$\delta(\text{C-H})_{\text{oop}}$], 631(m). ^1H NMR (CDCl_3 , 400 MHz, ppm): δ = 7.22 (m, 4H, *Ph*), 5.85 (s, 2H, *CH*(Pz)), 4.40 (s, 4H, *OCH*₂Ph), 4.32 (br, 4H, *N*_{Pz}*CH*₂*CH*₂O), 3.75 (t, 4H, 3J = 5.6 Hz, *N*_{Pz}*CH*₂*CH*₂O), 2.32 (s, 6H, *CH*₃(Pz)), 2.23 (s, 6H, *CH*₃(Pz)). $^{13}\text{C}\{^1\text{H}\}$ NMR (CDCl_3 , 100.6 MHz, ppm): δ = 148.6, 148.2 (Pz-C), 136.2 (*Ph-CH*₂O), 128.8, 128.0 (*Ph-H*), 105.6 (*CH*(Pz)), 71.8 (*Ph-CH*₂O), 69.3 (*N*_{Pz}*CH*₂*CH*₂O), 48.6 (*N*_{Pz}*CH*₂*CH*₂O), 13.6, 11.4 (*CH*₃(Pz)). UV-Vis: (CH_3CN , $1.05 \cdot 10^{-4}$ M) λ_{max} (ϵ ($\text{M}^{-1}\text{cm}^{-1}$)) = 219 nm ($1.52 \cdot 10^4$). Fluorescence (CH_3CN): λ_{ex} = 260 nm, λ_{em} = 286 nm.

17. Yield: 24.5% (0.155 g). Elemental analysis calc. (%) for $\text{C}_{23}\text{H}_{33}\text{HgCl}_2\text{N}_4\text{O}_{2.5}$ (677.02): C 40.80; H 4.98; N 8.27. Found: C 40.70; H 4.76; N 8.05. FTIR-ATR (wavenumber, cm^{-1}): 3515(br) [$\nu(\text{O-H})$], 2925-2863(m) [$\nu(\text{C-H})_{\text{al}}$], 1550(s) [$\nu(\text{C=C})_{\text{ar}}/\nu(\text{C=N})_{\text{ar}}$], 1489(w), 1469(w), 1442(s), 1420(m) [$\delta(\text{C=C})_{\text{ar}}/\delta(\text{C=N})_{\text{ar}}$], 1375(s), 1356(m), 1281(m), 1255(w), 1216(w), 1209(w), 1184(w), 1123(s), 1101(s) [$\nu(\text{C-O-C})$], 1068(m), 1027(s) [$\delta(\text{C-H})_{\text{ip}}$], 1022(m), 984(w), 874(w), 843(w), 805(m) [$\delta(\text{C-H})_{\text{oop}}$], 752(s) [$\delta(\text{C-H})_{\text{oop}}$], 658(w), 631(m). ^1H NMR (CDCl_3 , 400 MHz, ppm): δ = 7.24 (m, 4H, *Ph*), 5.86 (s, 2H, *CH*(Pz)), 4.46 (s, 4H, *OCH*₂Ph), 4.33 (t, 4H, 3J = 5.3 Hz, *N*_{Pz}*CH*₂*CH*₂O), 3.71 (t, 4H, 3J = 5.4 Hz, *N*_{Pz}*CH*₂*CH*₂O), 2.29 (s, 6H, *CH*₃(Pz)), 2.20 (s, 6H, *CH*₃(Pz)). $^{13}\text{C}\{^1\text{H}\}$ NMR (CDCl_3 , 100.6 MHz, ppm): δ = 142.4, 141.5 (Pz-C), 136.0 (*Ph-CH*₂O), 129.3, 128.3 (*Ph-H*), 106.2 (*CH*(Pz)), 71.3 (*Ph-CH*₂O), 69.3 (*N*_{Pz}*CH*₂*CH*₂O), 48.4 (*N*_{Pz}*CH*₂*CH*₂O), 13.6, 11.5 (*CH*₃(Pz)). UV-Vis: (CH_3CN , $1.34 \cdot 10^{-4}$ M) λ_{max} (ϵ ($\text{M}^{-1}\text{cm}^{-1}$)) = 219 nm ($1.66 \cdot 10^4$). Fluorescence (CH_3CN): λ_{ex} = 260 nm, λ_{em} = 286 nm.

18. Yield: 41.8 % (0.407 g) Elem anal. Calc. for $\text{C}_{44}\text{H}_{62}\text{Cl}_4\text{N}_8\text{O}_5\text{Co}_2$ (1042.67): C 50.68, H 5.99, N 10.75. Found: C 50.75, H 5.78, N 10.43. FTIR-ATR (wavenumber, cm^{-1}): 3370(br) [$\nu(\text{O-H})$], 2963(w)-2869(w) [$\nu(\text{C-H})_{\text{al}}$], 1552(s) [$\nu(\text{C=C/C=N})_{\text{ar}}$], 1466(m), 1440(m) [$\delta(\text{C=C/C=N})_{\text{ar}}$], 1420(m), 1371(m), 1352(s), 1311(w), 1263(w), 1218(m), 1186(m), 1124(m), 1100(s) and 1094(vs) [$\delta(\text{C-H})_{\text{ip}}$] + [$\nu(\text{C-O-C})$], 1066(s), 1048(s), 876(w), 813(w), 790(s) [$\delta(\text{C-H})_{\text{oop}}$], 760(vs) [$\delta(\text{C-H})_{\text{oop}}$], 637(w), 524(w). UV-Vis (CH_2Cl_2 , $1.06 \cdot 10^{-3}$ M) λ_{max} (ϵ ($\text{M}^{-1}\text{cm}^{-1}$)) = 651 nm (360), 587 nm (shoulder, 231).

Synthesis of [Cu₂(L5)Cl₄] (19)

A solution of anhydrous CuCl₂ (0.427 g, 3.17 mmol) in absolute EtOH (40 ml) was added to a solution of **L5** (1.216 g, 3.18 mmol) in absolute EtOH (40 ml). A green precipitate appeared immediately. The solution was left to stir for 4 hours. After that period, the green precipitate was filtered off, washed with 5 ml of cold Et₂O and dried under air.

Suitable crystals for SCRXD for **19** were obtained *via* recrystallization in EtOH for one month.

19. Yield: 71.6 % (0.749 g). Elem. Anal. Calc. for C₂₂H₃₀Cl₄N₄O₂Cu₂ (651.40): C 40.56, H 4.64, N 8.60. Found: C 40.30, H 4.74, N 8.35. FTIR-ATR (wavenumber, cm⁻¹): 2939(w)-2872(w) [ν(C-H)_{al}], 1555(s) [ν(C=C/C=N)]_{ar}, 1472(m), 1440(m) [δ(C=C/C=N)]_{ar}, 1396(m), 1357(w), 1315(s), 1254(m), 1228(w), 1215(w), 1188(w), 1143(w), 1103(s) [ν(C-O-C)], 1058(s) [δ(C-H)_{ip}], 1014(s), 993(s), 840(s) [δ(C-H)_{oop}], 818(m), 785(s) [δ(C-H)_{oop}], 744(s) [δ(C-H)_{oop}], 635(m), 624(m). UV-Vis (MeOH, 1,25·10⁻³ M) λ_{max} (ε(M⁻¹cm⁻¹)) = 678 nm (75), 867 nm (shoulder, 49).

Synthesis of [Pd(LX)Cl₂] (LX = L6 (20), L7 (21), L8 (22)) and [Pd(L8)Cl₂]₂ (23)

A solution of [Pd(CH₃CN)₂Cl₂] (0.067 g, 0.258 mmol (**20**), 0.042 g, 0.162 mmol (**21**), 0.066 g, 0.250 mmol (**22** and **23**)) in dry CH₃CN (20 mL) was added to a solution of the corresponding ligand (**L6**, 0.174 g, 0.275 mmol (**20**), **L7**, 0.103 g, 0.163 mmol (**21**), **L8**, 0.159 g, 0.250 mmol (**22** and **23**)), in dry CH₃CN (10 mL). The solution was refluxed for 120 h. After that period, the solution was concentrated up to 5 mL and left in the fridge for 24h. After that period an orange solid precipitated, which was filtered off and dried under vacuum. Compounds **22** and **23** were obtained as a mixture, and it has not been possible to isolate them separately.

20. Yield: 38.15 % (0.085 g). FTIR-ATR (wavenumber, cm⁻¹): 3659(w) [ν(O-H)], 2987(s)-2900(s) [ν(C-H)_{al}], 1552(m) [ν(C=C/C=N)]_{ar}, 1481(m), 1464(m), 144(m) [δ(C=C/C=N)]_{ar}, 1386(w), 1380(w), 1302(w), 1277(w), 1257(w), 1198(w), 1074(vs, br) [ν(C-O-C) + [δ(C-H)_{ip}], 1015(s), 921(w), 805(w), 759(vs) [δ(C-H)_{oop}], 694(vs) [δ(C-H)_{oop}], 607(w), 589(w). ¹H NMR (CDCl₃, 400 MHz, ppm): δ = 8.20 (m, 4H,

H_{Ph-Pz-orto}), 7.52-7.31 (overlapping signals, 16H, *H_{Ph-Pz}*), 7.09 (s, 4H, CH₂O-*Ph-H*-OCH₂), 6.33 (s, 2H, CH(Pz)), 4.93 (m, 4H, N_{Pz}CH₂CH₂O), 4.29 (s, 4H, OCH₂Ph), 4.09 (t, 4H, ³*J* = 4.9 Hz, N_{Pz}CH₂CH₂O). ¹³C{¹H} NMR (CDCl₃, 100.6 MHz, ppm): δ = 154.9, 150.0 (Pz-C), 137.6, 132.8, (*Ph-Pz*), 130.0, 129.8, 129.7, 129.5, 128.7, 127.7 (*C_{Ph-Pz}* and CH₂O-*Ph-H*-OCH₂), 108.6 (CH(Pz)), 72.8 (Ph-CH₂O), 68.2 (N_{Pz}CH₂CH₂O), 50.7 (N_{Pz}CH₂CH₂O).

21. Yield: 31.24 % (0.041 g). FTIR-ATR (wavenumber, cm⁻¹): 3054(w)-3024(w) [ν(C-H)_{ar}], 2944(w)-2849(w) [ν(C-H)_{al}], 1604(w), 1577(w), 1552(m) [ν(C=C/C=N)]_{ar}, 1480(m), 1464(m), 1445(m) [δ(C=C/C=N)]_{ar}, 1379(m), 1364(w), 1300(w), 1279(w), 1235(w), 1198(w), 1155(w), 1100(s) [ν(C-O-C)], 1072(s) [δ(C-H)_{ip}], 1015(w), 920(w), 886(w), 845(w), 802(w), 758(vs) [δ(C-H)_{oop}], 694(vs) [δ(C-H)_{oop}], 616(w), 584(w). ¹H NMR (CDCl₃, 400 MHz, ppm): δ = 8.18 (m, 4H, *H_{Ph-Pz-orto}*), 7.50-7.31 (overlapping signals 16H, *H_{Ph-Pz}*), 7.25 (m, overlapped with CDCl₃, 1H, CH₂O-*Ph-H*-OCH₂), 7.06 (d, 3H, ³*J* = 7.07 Hz, CH₂O-*Ph-H*-OCH₂), 6.97 (s, 1H, CH₂O-*Ph-H*-OCH₂), 6.32 (s, 2H, CH(Pz)), 4.92 (t, 4H, ³*J* = 4.81 Hz, N_{Pz}CH₂CH₂O), 4.28 (s, 4H, OCH₂Ph), 4.09 (t, 4H, ³*J* = 4.81 Hz, N_{Pz}CH₂CH₂O). ¹³C{¹H} NMR (CDCl₃, 100.6 MHz, ppm): δ = 154.9, 150.0 (Pz-C), 138.3, 132.8 (*Ph-Pz*), 130.0, 129.7, 129.6, 129.4, 129.2, 128.7, 128.2, 127.0 (*C_{Ph-Pz}* and CH₂O-*Ph-H*-OCH₂), 108.6 (CH(Pz)), 73.0 (Ph-CH₂O), 68.2 (N_{Pz}CH₂CH₂O), 50.7 (N_{Pz}CH₂CH₂O).

22. FTIR-ATR (wavenumber, cm⁻¹): 3659 [ν(O-H)], 3013(s)-28881(s) [ν(C-H)_{al}], 1552(m) [ν(C=C/C=N)]_{ar}, 1454(m), 1447(m) [δ(C=C/C=N)]_{ar}, 1381(m), 1301(w), 1279(w), 1197(w), 1183(w), 1157(w), 1097 and 1071(vs, br) [ν(C-O-C) + [δ(C-H)_{ip}], 1015(m), 919(w), 806(w), 756(vs) [δ(C-H)_{oop}], 694 (vs) [δ(C-H)_{oop}], 587(w). ¹H NMR (CDCl₃, 400 MHz, ppm): δ = 8.21 (m, 4H, *H_{Ph-Pz-orto}*), 7.50-7.24 (overlapping signals 16H, *H_{Ph-Pz}*), 7.13 (m, overlapped with CDCl₃, 4H, CH₂O-*Ph-H*-OCH₂), 6.33 (s, 2H, CH(Pz)), 4.93 (br), 4.17 (s, 4H, OCH₂Ph), 4.01 (br).

23. FTIR-ATR (wavenumber, cm⁻¹): 3659 [ν(O-H)], 3013(s)-28881(s) [ν(C-H)_{al}], 1552(m) [ν(C=C/C=N)]_{ar}, 1454(m), 1447(m) [δ(C=C/C=N)]_{ar}, 1381(m), 1301(w), 1279(w), 1197(w), 1183(w), 1157(w), 1097 and 1071(vs, br) [ν(C-O-C) + [δ(C-H)_{ip}], 1015(m), 919(w), 806(w), 756(vs) [δ(C-H)_{oop}], 694 (vs) [δ(C-H)_{oop}], 587(w). ¹H NMR (CDCl₃, 400 MHz, ppm): δ = 8.11 (m, 4H, *H_{Ph-Pz-orto}*), 7.50-7.24 (overlapping signals 16H, *H_{Ph-Pz}*), 7.13 (m, overlapped with CDCl₃, 4H, CH₂O-*Ph-H*-OCH₂), 6.38 (s, 2H,

$CH(Pz)$), 5.42 (t, 4H, $^3J = 7.79$ Hz, $N_{Pz}CH_2CH_2O$), 4.72 (s, 4H, OCH_2Ph), 4.43 (t, 4H, $^3J = 7.79$ Hz, $N_{Pz}CH_2CH_2O$).

5.4 Experimental Section for 3.4

- Materials and general details

Ligands **L9-L11** were synthesized as described in section 5.1 in this chapter. Samples of $[Pd(CH_3CN)_2Cl_2]$ were prepared as described in the literature¹⁰. The rest of the reactants are commercially available and were used as received.

- Synthetic Procedures

Synthesis of $[Cu(L9)Cl_2]_2$ (24)

A solution of anhydrous $CuCl_2$ (0.018 g, 0.135 mmol) in absolute EtOH (10 mL) was added to a solution of **L6** (0.072 g, 0.271 mmol) in absolute EtOH (10 mL). The resulting green solution was stirred for 48 h at r.t. After that period, the solution was concentrated under vacuum up to 5 mL. Then, it was kept overnight in the fridge at 4°C. After this period, cubic green crystals precipitated, which were filtered off, cleaned with 5 mL cold Et_2O and dried under vacuum. Those same crystals were suitable for X-ray diffraction.

24. Yield: 80.7% (0.076 g). Elemental analysis calc. (%) for $C_{20}H_{48}B_{20}CuCl_2N_4$ (695.28): C 34.55; H 6.96; N 8.06. Found: C 34.31; H 6.97; N 7.97. Conductivity ($\Omega^{-1} \cdot cm^2 \cdot mol^{-1}$ 1.25 $\cdot 10^{-3}$ M in MeOH): 66 FTIR-ATR (wavenumber, cm^{-1}): 3124(w) [$\nu(C-H)_{ar}$], 3088(w) [$\nu(C-H)_{ar}$], 2965-2921(w) [$\nu(C-H)_{al}$], 2580(vs) [$\nu(B-H)$], 1556(s) [$\nu(C=C)_{ar}/\nu(C=N)_{ar}$], 1460(vs) [$\delta(C=C)_{ar}/\delta(C=N)_{ar}$], 1443(m), 1398(m), 1390(s), 1322(m), 1287(w), 1189(w), 1165(w), 1161(w), 1061(w), 1053(m), 1030(s) [$\delta(C-H)_{ip}$], 1026(s) [$\delta(C-H)_{ip}$], 949(w), 813(vs) [$\delta(C-H)_{oop}$], 730(vs) [$\delta(C-H)_{oop}$], 672(m), 639(s), 547(m).

Synthesis of [Zn(L9)Cl₂]₂ (25)

A solution of anhydrous ZnCl₂ (0.032 g, 0.235 mmol) in absolute EtOH (10 mL) was added to a solution of **L6** (0.125 g, 0.467 mmol) in absolute EtOH (10 mL). The resulting solution was stirred for 24 h at r.t. After that period, the solution was concentrated under vacuum until a white precipitate appeared. This precipitate was filtered off, cleaned with 5 mL cold Et₂O and dried under vacuum. Crystals were suitable for X-ray diffraction were obtained by recrystallization of the obtained product in Et₂O in the fridge at 4°C.

25. Yield: 79.4% (0.136 g). Elemental analysis calc. (%) for C₂₀H₄₈B₂₀ZnCl₂N₄ (697.14): C 34.46; H 6.94; N 8.04. Found: C 34.68; H 6.84; N 8.25. Conductivity ($\Omega^{-1}\cdot\text{cm}^2\cdot\text{mol}^{-1}$ 1.10·10⁻³ M in MeOH): 29. FTIR-ATR (wavenumber, cm⁻¹): 2980-2917(w) [v(C-H)_{al}], 2570(vs) [v(B-H)], 1553(s) [v(C=C)_{ar}/v(C=N)_{ar}], 1464(s) [δ(C=C)_{ar}/δ(C=N)_{ar}], 1422(m), 1388(s), 1317(w), 1283(w), 1278(m), 1218(w), 1179(w), 1159(w), 1129(w), 1084(w), 1025(s) [δ(C-H)_{ip}], 975(w), 946(w), 921(w), 902(w), 780(s) [δ(C-H)_{oop}], 728(s) [δ(C-H)_{oop}], 666(m), 647(m), 588(w), 551(m). ¹H NMR (CDCl₃, 400 MHz, ppm): δ = 5.96 (s, 1H, CH(Pz)), 4.66 (br, 2H, C_{carb}CH₂CH₂N_{Pz}), 2.70 (m, 2H, ²J_{BB'} = -8.3 Hz, ³J_{AB} = 11.2 Hz, ³J_{A'B} = 7.2 Hz, ³J_{AB'} = 4.0 Hz, ³J_{A'B'} = 13.7 Hz, C_{carb}CH₂CH₂N_{Pz}), 2.31, 2.17 (s, 3H, CH₃-Pz), 2.06 (s, 3H, CH₃-C_{carb}). ¹¹B NMR (CDCl₃, 128.6 MHz, ppm) δ = -3.62 (d, ¹J_{BH} = 150.1 Hz, 1B, B-H), -5.85 (d, ¹J_{BH} = 147.7 Hz, 1B, B-H), -9.48 to -10.44, overlapping signals (8B, B-H, B-C). ¹¹B{¹H} NMR (CDCl₃, 128.6 MHz, 298K): δ = -3.63 (s, 1B, B-H), -5.90 (s, 1B, B-H), -10.07 (b, 8B, B-H, B-C). ¹³C{¹H} NMR (CDCl₃, 100.6 MHz, ppm): δ = 108.1 (CH-Pz), 76.0, 74.1 (C_{carb}), 47.0 (N_{Pz}CH₂CH₂C_{carb}), 34.6 (N_{Pz}CH₂CH₂C_{carb}), 23.8 (CH₃-C_{carb}), 13.3, 11.5 (CH₃-Pz).

Synthesis of {[HL9]₂[CdCl₄]}₂ (26)

A solution of anhydrous CdCl₂ (0.029 g, 0.158 mmol) in absolute EtOH (10 mL) was added to a solution of **L9** (0.085 g, 0.320 mmol) in absolute EtOH (10 mL). The resulting solution was acidified up to pH = 1-2 using HCl, and stirred for 6 h at RT. After that period, the solution was concentrated under vacuum up to 3 mL. Then, the solution was left in the fridge at 4°C for a week, resulting in the obtention of a white precipitate. It was filtered off, cleaned with cold Et₂O and dried under vacuum.

26. Yield: 66.0 % (0.085 g). Elemental analysis calc. (%) for $C_{20}H_{50}B_{20}CdCl_4N_4$ (817.08): C 29.40; H 6.17; N 6.86. Found: C 29.47; H 6.29; N 6.42. Conductivity ($\Omega^{-1}\cdot\text{cm}^2\cdot\text{mol}^{-1}$ 9.30 $\cdot 10^{-3}$ M in MeOH): 174. FTIR-ATR (wavenumber, cm^{-1}): 3128-2788(br, m) $[\nu(\text{C-H})_{\text{ar}}] + [\nu(\text{C-H})_{\text{al}}] + [\nu(\text{N-H})]$, 2560(br, vs) $[\nu(\text{B-H})]$, 1595(m) $[\nu(\text{C}=\text{C})_{\text{ar}}/\nu(\text{C}=\text{N})_{\text{ar}}]$, 1478(w), 1391(br, vs) $[\delta(\text{C}=\text{C})_{\text{ar}}/\delta(\text{C}=\text{N})_{\text{ar}}]$, 1286(w), 1215(w), 1160(w), 1154(m), 1026(m) $[\delta(\text{C-H})_{\text{ip}}]$, 951(w), 919(w), 851(m), 827(m), 729(s) $[\delta(\text{C-H})_{\text{oop}}]$, 720(m), 665(w), 646(w). ^1H NMR (CDCl_3 , 400 MHz, ppm): δ = 6.13 (s, 1H, $\text{CH}(\text{Pz})$), 4.51 (br, 2H, $\text{C}_{\text{carb}}\text{CH}_2\text{CH}_2\text{N}_{\text{Pz}}$), 3.00 (br, 2H $\text{C}_{\text{carb}}\text{CH}_2\text{CH}_2\text{N}_{\text{Pz}}$), 2.49, 2.40 (s, 3H, $\text{CH}_3\text{-Pz}$), 2.28 (s, 3H, $\text{CH}_3\text{-C}_{\text{carb}}$). ^{11}B NMR (CDCl_3 , 128.6 MHz, ppm) δ = -3.37 (d, $^1J_{\text{BH}}$ = 130.1 Hz, 1B, B-H), -5.72 (d, $^1J_{\text{BH}}$ = 152.8 Hz, 1B, B-H), -10.5 to -11.8, overlapping signals (8B, B-H , B-C). $^{11}\text{B}\{^1\text{H}\}$ NMR (CDCl_3 , 128.6 MHz, 298K): δ = -3.47 (s, 1B, B-H), -5.79 (s, 1B, B-H), -9.61 to -11.1, overlapping signals (8B, B-H , B-C). $^{13}\text{C}\{^1\text{H}\}$ NMR (CDCl_3 , 100.6 MHz, ppm): δ = 147.0, 142.7 (Pz-C), 107.3 (CH-Pz), 76.2, 73.4 (C_{carb}), 47.2 ($\text{N}_{\text{Pz}}\text{CH}_2\text{CH}_2\text{C}_{\text{carb}}$), 34.6 ($\text{N}_{\text{Pz}}\text{CH}_2\text{CH}_2\text{C}_{\text{carb}}$), 24.1 ($\text{CH}_3\text{-C}_{\text{carb}}$), 12.6, 11.4 ($\text{CH}_3\text{-Pz}$).

Synthesis of $\{[\text{HL9}]_2[\text{HgCl}_4]\}_2$ (27)

A solution of anhydrous HgCl_2 (0.022 g, 0.081 mmol) in absolute EtOH (10 mL) was added to a solution of **L6** (0.043 g, 0.161 mmol) in absolute EtOH (10 mL). The resulting solution was acidified to pH = 1-2 with HCl and stirred for 6 h at RT. After that period, the solution was concentrated under vacuum up to 5 mL. The solution was kept overnight in the fridge at 4°C. After that period a white precipitate appeared, which was filtered off, cleaned with 5 mL cold Et_2O and dried under vacuum. Crystals were suitable for X-ray diffraction were obtained by recrystallization of the obtained product in a CH_2Cl_2 :Hexane mixture.

27. Yield: 62.4% (0.023 g). Elemental analysis calc. (%) for $C_{20}H_{50}B_{20}\text{HgCl}_4N_4$ (905.23): C 26.54; H 5.57; N 6.19. Found: C 26.66; H 5.72; N 5.92. Conductivity ($\Omega^{-1}\cdot\text{cm}^2\cdot\text{mol}^{-1}$ 9.07 $\cdot 10^{-3}$ M in MeOH): 184. FTIR-ATR (wavenumber, cm^{-1}): 3191(w), 3127(w) $[\nu(\text{C-H})_{\text{ar}}]$, 2984-2848(w) $[\nu(\text{C-H})_{\text{al}}] + [\nu(\text{N-H})]$, 2782(w), 2580(vs) $[\nu(\text{B-H})]$, 1595(s) $[\nu(\text{C}=\text{C})_{\text{ar}}/\nu(\text{C}=\text{N})_{\text{ar}}]$, 1516(w), 1471(w), 1445(w), 1432(s) $[\delta(\text{C}=\text{C})_{\text{ar}}/\delta(\text{C}=\text{N})_{\text{ar}}]$, 1392(w), 1380(w), 1345(m), 1284(s), 1218(w), 1154(s), 1084(w), 1040(w), 1027(s) $[\delta(\text{C-H})_{\text{ip}}]$, 991(w), 951(w), 848(m), 825(m), 784(w), 729(vs) $[\delta(\text{C-H})_{\text{oop}}]$, 664(w), 645(w), 608(w), 544(w). ^1H NMR (CDCl_3 , 128.6 MHz, ppm): δ = 6.03 (s, 1H, $\text{CH}(\text{Pz})$), 4.40 (m,

2H, $\text{RCH}_2\text{CH}_2\text{Pz}$), 2.87 (m, 2H, $\text{RCH}_2\text{CH}_2\text{Pz}$), 2.40, 2.35 (s, 3H, $\text{CH}_3(\text{Pz})$), 2.16 (s, 3H, $\text{CH}_3(\text{carborane})$). ^{11}B NMR (CDCl_3 , 128.6 MHz, ppm) δ = -3.59 (d, $^1J_{\text{BH}}$ = 152.5 Hz, 1B, B-H), -5.58 (d, $^1J_{\text{BH}}$ = 154.0 Hz, 1B, B-H), -8.91 to -11.63, overlapping signals (8B, B-H, B-C). $^{11}\text{B}\{^1\text{H}\}$ NMR: (CDCl_3 , 400 MHz, 298K), δ = -3.59 (s, 1B, B-H), -5.61 (s, 1B, B-H), -9.57 to -11.0 (m, 8B, B-H, B-C). $^{13}\text{C}\{^1\text{H}\}$ NMR (CDCl_3 , 100.6 MHz, ppm): δ = 147.9, 141.1 (Pz-C), 106.6 (CH-Pz), 75.7, 74.3 (C_{carb}), 47.1 ($\text{N}_{\text{Pz}}\text{CH}_2\text{CH}_2\text{C}_{\text{carb}}$), 34.6 ($\text{N}_{\text{Pz}}\text{CH}_2\text{CH}_2\text{C}_{\text{carb}}$), 23.7 ($\text{CH}_3\text{-C}_{\text{carb}}$), 13.0, 11.1 ($\text{CH}_3\text{-Pz}$).

Synthesis of $[\text{Pd}(\text{L10})_2\text{Cl}_2]$ (28)

A solution of $[\text{Pd}(\text{CH}_3\text{CN})_2\text{Cl}_2]$ (0.119 g, 0.457 mmol) in acetonitrile (10 mL) was added to a solution of **L10** (0.248 g, 0.922 mmol) in acetonitrile (10 mL). The resulting solution was stirred for 24 h at r.t. After that period, the solution was concentrated under vacuum up to 5 mL. The solution was kept for three days in the fridge at 4°C. After that period a yellow precipitate appeared, which was filtered off, cleaned with 5 mL cold Et_2O and dried under vacuum.

28. Yield: 49.3% (0.160 g). Elemental analysis calc. (%) for $\text{C}_{18}\text{H}_{44}\text{B}_{20}\text{PdCl}_2\text{N}_4$ (710.11): C 30.44; H 6.25; N 7.89. Found: C 30.15; H 6.29; N 8.04. Conductivity ($\Omega^{-1}\cdot\text{cm}^2\cdot\text{mol}^{-1}$ 9.82 $\cdot 10^{-3}$ M in CH_3CN): 20. FTIR-ATR (wavenumber, cm^{-1}): 3139(w) [$\nu(\text{C-H})_{\text{ar}}$], 3025-2900(br, vs) [$\nu(\text{C-H})_{\text{al}}$], 2590(br, vs) [$\nu(\text{B-H})$], 1559(m) [$\nu(\text{C}=\text{C})_{\text{ar}}/\nu(\text{C}=\text{N})_{\text{ar}}$], 1454(m) [$\delta(\text{C}=\text{C})_{\text{ar}}/\delta(\text{C}=\text{N})_{\text{ar}}$], 1395(br, vs), 1334(m), 1288(w), 1284(w), 1228(w), 1075(vs) [$\delta(\text{C-H})_{\text{ip}}$], 1055 (s) [$\delta(\text{C-H})_{\text{ip}}$], 1035(s) [$\delta(\text{C-H})_{\text{ip}}$], 910(w), 902(w), 880(w), 825(m), 795(vs) [$\delta(\text{C-H})_{\text{oop}}$], 729(vs) [$\delta(\text{C-H})_{\text{oop}}$], 657(m) [$\delta(\text{C-H})_{\text{oop}}$], 596(w), 564(w), 526(w). ^1H NMR (CDCl_3 , 128.6 MHz, ppm): δ = 5.98 (s, 1H, $\text{CH}(\text{Pz})$), 5.00 (m, 2H, $\text{RCH}_2\text{CH}_2\text{Pz}$), 3.91 (br, 1H, $\text{C}_{\text{carb}}\text{-H}$), 3.00 (m, 2H, $\text{RCH}_2\text{CH}_2\text{Pz}$), 2.85, 2.29 (s, 3H, $\text{CH}_3(\text{Pz})$). ^{11}B NMR (CDCl_3 , 128.6 MHz, ppm) δ = -2.13 (d, $^1J_{\text{BH}}$ = 119.5 Hz, 1B, B-H), -4.63 (m, B-H), -8.82 to -12.0, overlapping signals (8B, B-H, B-C). $^{11}\text{B}\{^1\text{H}\}$ NMR: (CDCl_3 , 400 MHz, 298K), δ = -2.09 (s, 1B, B-H), -4.88 (s, 1B, B-H), -9.33 (s, 2B, B-H), -12.1 (m, 6B, B-H, B-C). $^{13}\text{C}\{^1\text{H}\}$ NMR (CDCl_3 , 100.6 MHz, ppm): δ = 151.3, 143.5 (Pz-C), 109.0 (CH-Pz), 71.3 ($\text{C}_{\text{carb}}\text{-C}$), 62.3 ($\text{C}_{\text{carb}}\text{-H}$), 48.6 ($\text{N}_{\text{Pz}}\text{CH}_2\text{CH}_2\text{C}_{\text{carb}}$), 36.5 ($\text{N}_{\text{Pz}}\text{CH}_2\text{CH}_2\text{C}_{\text{carb}}$), 15.6, 11.9 ($\text{CH}_3\text{-Pz}$).

Synthesis of [Pd(L11)Cl₂] (29)

A solution of [Pd(CH₃CN)₂Cl₂] (0.029 g, 0.112 mmol) in acetonitrile (10 mL) was added to a solution of **L11** (0.042 g, 0.109 mmol) in acetonitrile (10 mL). The resulting solution was stirred for 24 h at r.t. After that period, the solution was concentrated under vacuum up to 5 mL. The solution was kept overnight in the fridge at 4°C. After that period a white precipitate appeared, which was filtered off, cleaned with 5 mL cold Et₂O and dried under vacuum. Crystals were suitable for X-ray diffraction were obtained by recrystallization of the obtained product in CH₂Cl₂.

29. Yield: 68.1% (0.042 g). Elemental analysis calc. (%) for C₁₆H₃₂B₁₀PdCl₂N₄ (565.85): C 33.84; H 5.70; N 9.90. Found: C 33.96; H 5.82; N 9.60. Conductivity (Ω⁻¹·cm²·mol⁻¹ 1.05·10⁻³ M in CH₃CN): 12. FTIR-ATR (wavenumber, cm⁻¹): 3139(m) [ν(C-H)_{ar}], 2997-2850(m) [ν(C-H)_{al}] 2566(vs, br) [ν(B-H)], 1577(vs) [ν(C=C)_{ar}/ν(C=N)_{ar}], 1473(w), 1458(s), 1420(vs) [δ(C=C)_{ar}/δ(C=N)_{ar}], 1402(s), 1333(s), 1282(s), 1229(m), 1155(w), 1067(w), 1040(w), 1021(m) [δ(C-H)_{ip}], 963(w), 961(w), 905(w), 844(w), 811(vs) [δ(C-H)_{oop}], 794(vs) [δ(C-H)_{oop}], 732(vs) [δ(C-H)_{oop}], 658(vs) [δ(C-H)_{oop}], 545(m). ¹H NMR (CDCl₃, 128.6 MHz, ppm): δ = 5.90 (s, 1H, CH(Pz)), 4.98 (m, 2H, RCH₂CH₂Pz), 3.72 (m, 2H, RCH₂CH₂Pz), 2.73, 2.30 (s, 3H, CH₃(Pz)). ¹¹B NMR (CDCl₃ 128.6 MHz, ppm) δ = -4.01 (s, 2B, B-H), -9.96 (s, 8B, B-H). ¹¹B{¹H} NMR: (CDCl₃, 400 MHz, 298K), δ = -3.99 (s, 2B, B-H), -9.96 (s, 8B, B-H, B-C). ¹³C{¹H} NMR (CDCl₃, 100.6 MHz, ppm): δ = 151.1, 143.2 (Pz-C), 107.8 (CH-Pz), 76.9 (C_{carb}), 47.6 (N_{Pz}CH₂CH₂C_{carb}), 34.4 (N_{Pz}CH₂CH₂C_{carb}), 14.8, 11.7 (CH₃-Pz).

5.5 Experimental Section for 3.5

- Materials and general details

All reactions and manipulations for **30-33** were carried out under dinitrogen atmosphere using standard Schlenk techniques unless noted. Tetrahydrofuran (THF) was purchased from Carlo Erba Reagents S.A. and distilled from Na/Benzophenone prior to use. Commercial grade acetonitrile (CH₃CN) was purchased from Merck and dried using 3 Å activated molecular sieves under dinitrogen atmosphere for 48 h. Spectroscopic grade methanol (MeOH) was purchased from ROMIL-SpS and used without further

purification. 3,5-dimethyl-1-(2-toluene-*p*-sulfonyloxyethyl)pyrazole) was synthesized according to reported procedures¹. Ligand **L12** and all other chemicals were commercially available and used as received.

For **33**, PXRD pattern was measured using a Malvern PANalytical X'pert PRO Material Powder Diffractometer (with 45 kW and 40 mA using Cu k_{α} radiation with $\lambda = 1.5406 \text{ \AA}$). The pattern was recorded in transmission mode from $2\theta = 2.5^{\circ}$ to 40° with a step scan of 0.03° counting for 200s at each step. This diffractometer was equipped with a capillary spinner and the sample was placed inside a borosilicate glass capillary with an outer diameter of 0.7 mm. The electronic spectra of **L9-L12** in CH_3CN ($1.45 \cdot 10^{-5} \text{ M} - 6.5 \cdot 10^{-5} \text{ M}$) were run on a JASCO V-780 UV-Visible/NIR spectrophotometer with a quartz cell having a path length of 1 cm in the range of 190-600 nm. Solid-state electronic spectra were run on a JASCO V-780 UV-Visible/NIR spectrophotometer equipped with a 60 mm integrating sphere model ISN-901i/A001461872. Solid-state emission and excitation spectra were run on a NanologTM Horib Jobin Yvon IHR320 fluorimeter. Quantum yields for compounds **30-33** in the solid state were measured on a Hamamatsu Absolute PL Quantum Yield Spectrometer C9920-O2G.

- Synthetic Procedures

*Synthesis of $[\text{Cu}(\text{L12})\text{I}]_n$ (**30**)*

A solution of anhydrous CuI (0.019 g, 0.098 mmol) and **L12** (0.020 g, 0.098 mmol) in dry CH_3CN (20 mL) was stirred at RT until all CuI was dissolved. After that period, the solvent was evaporated under vacuum, resulting in pure **24** as a white powder. Suitable crystal for SCXRD were obtained *via* slow evaporation of the solvent.

30. Yield: 60.1 % (0.023 g) Elem anal. Calc. for $\text{C}_{13}\text{H}_{16}\text{IN}_2\text{Cu}$ (390.72): C 39.96, H 4.13, N 7.17. Found: C 39.83, H 4.10, N 7.14. ATR-FTIR (wavenumber, cm^{-1}): 3126-3030 (w) [$\nu(\text{C-H})_{\text{ar}}$], 2978-2855 (w) [$\nu(\text{C-H})_{\text{al}}$], 1550 (s) [$\nu(\text{C}=\text{C}/\text{C}=\text{N})_{\text{ar}}$], 1496 (m), 1488 (m), 1462 (m), 1453 (s) [$\delta(\text{C}=\text{C})/\delta(\text{C}=\text{N})_{\text{ar}}$], 1421 (w), 1388 (m), 1371 (w), 1357 (m), 1310 (m), 1253 (m), 1152 (w), 1075 (w), 1047 (m) [$\delta(\text{C-H})_{\text{ip}}$], 1031 (m) [$\delta(\text{C-H})_{\text{ip}}$], 904 (w), 801 (s) [$\delta(\text{C-H})_{\text{oop}}$], 746 (s) [$\delta(\text{C-H})_{\text{oop}}$], 696 (s) [$\delta(\text{C-H})_{\text{oop}}$] and 687 (s) [$\delta(\text{C-H})_{\text{oop}}$].

UV-Vis: (solid state) $\lambda_{\text{max}} = 290$ nm. Fluorescence (solid state): $\lambda_{\text{ex}} = 283$ nm, $\lambda_{\text{em}} = 609$ nm.

Synthesis of [Cu(L10)I]₂ (31)

A solution of anhydrous CuI (0.127 g, 0.640 mmol) and **L10** (0.170 g, 0.640 mmol) in dry CH₃CN (20 mL) was stirred overnight. Then, the resulting solution was filtered, concentrated up to 5 mL and left standing overnight in the fridge, which provided a white precipitate. The precipitate was filtered, washed with cold Et₂O and dried under vacuum.

31. Yield: 88.6 % (0.259 g) Elem anal. Calc. for C₁₈H₄₄B₂₀I₂N₄Cu₂ (913.69): C 23.66, H 4.85, N 6.13. Found: C 23.88, H 4.97, N 6.10. ATR-FTIR (wavenumber, cm⁻¹): 3034 (w) [$\nu(\text{C-H})_{\text{ar}}$], 2986-2913 (w) [$\nu(\text{C-H})_{\text{al}}$], 2572 (vs) [$\nu(\text{B-H})$], 1555 (s) [$\nu(\text{C}=\text{C}/\text{C}=\text{N})_{\text{ar}}$], 1466 (m) [$\delta(\text{C}=\text{C})/\delta(\text{C}=\text{N})_{\text{ar}}$], 1445 (m), 1421 (w), 1392 (m), 1377 (m), 1319 (m), 1283 (m), 1215 (w), 1136 (w), 1119 (m), 1075 (w), 1049 (m) [$\delta(\text{C-H})_{\text{ip}}$], 1043 (m) [$\delta(\text{C-H})_{\text{ip}}$], 1016 (m) [$\delta(\text{C-H})_{\text{ip}}$], 997 (w), 932 (w), 916 (w), 877 (w), 839 (w), 794 (vs) [$\delta(\text{C-H})_{\text{oop}}$], 722 (vs) [$\delta(\text{C-H})_{\text{oop}}$], 697 (w), 674 (w), 656 (m) [$\delta(\text{C-H})_{\text{oop}}$], 582 (w), 561 (w) and 541 (w). ¹H NMR (CD₃CN, 400.0 MHz): $\delta = 5.82$ (s, 1H, CH(Pz)), 4.47 (br s, 1H, C_{carb}-H) 4.13 (m, 2H, N_{Pz}CH₂CH₂C_{carb}), 2.76 (m, 2H, N_{Pz}CH₂CH₂C_{carb}), 2.19 (s, 3H, Pz-CH₃), 2.16 (s, 3H, Pz-CH₃). ¹¹B NMR (CD₃CN, 128.6 MHz) $\delta = -2.86$ (br d, ¹J_{BH} = 146, 1B), -5.72 (br d, ¹J_{BH} = 146, 1B), -9.7 (br d, ¹J_{BH} = 158.9, 2B), -10.9 to -13.7, overlapping signals (6B). ¹¹B{¹H} NMR (CD₃CN, 128.6 MHz) $\delta = -2.9$ (br s, 1B), -5.80 (br s, 1B), -9.7 (br s, 2B), -11.5 (br s, 2B), -12.1 (br s, 2B), -13.0 (br s, 2B). ¹³C{¹H} NMR (CD₃CN, 100.6 MHz): $\delta = 148.6$, 140.7 (Pz-C), 106.3 (Pz-CH), 74.2 (C_{carb}-CH₂R), 63.6 (C_{carb}-H), 47.6 (C_{carb}-CH₂CH₂N_{Pz}), 37.2 (C_{carb}-CH₂CH₂N_{Pz}), 13.8, 11.0 (CH₃(Pz)). UV-Vis: (solid state) $\lambda_{\text{max}} = 363$ nm. Fluorescence (solid state): $\lambda_{\text{ex}} = 340$ nm, $\lambda_{\text{em}} = 483$ nm.

Synthesis of [Cu(L9)I]₄ (32B)

A solution of anhydrous CuI (0.037 g, 0.188 mmol) and **L9** (0.051 g, 0.188 mmol) in dry CH₃CN (20 mL) was stirred for 1 h. at r.t. under nitrogen. After that period, the solvent was evaporated under nitrogen, resulting in a white powder. Suitable crystals for SCRXD were obtained via recrystallization of a solution of the white powder in dry CH₃CN.

32. Yield: 58.5 % (0.052 g) Elem anal. Calc. for $C_{40}H_{96}B_{40}N_8I_4Cu_4$ (1883.48): C, 25.51 H, 5.14; N, 5.95. Found: C, 25.21; H, 4.98; N 5.85. ATR-FTIR (wavenumber, cm^{-1}): 2984-2917 (w) [$\nu(C-H)_{ar}$], 2563 (s) [$\nu(B-H)$], 1556 (s) [$\nu(C=C/C=N)_{ar}$], 1467(w), 1445 (s) [$\delta(C=C/C=N)_{ar}$], 1418 (s) [$\delta(C=C/C=N)_{ar}$], 1376 (m), 1324 (m), 1280 (m), 1041 (m) [$\delta(C-H)_{ip}$], 1023 (m) [$\delta(C-H)_{ip}$], 779 (s) [$\delta(C-H)_{oop}$], 729 (s) [$\delta(C-H)_{oop}$], 676 (w), 663 (w), 647 (w) and 633 (w). 1H NMR (CD_3CN , 400.0 MHz): δ = 5.82 (s, 1H, $CH(Pz)$), 4.18 (m, 2H, $N_{Pz}CH_2CH_2C_{carb}$), 2.71 (m, 2H, $N_{Pz}CH_2CH_2C_{carb}$), 2.22 (s, 3H, $CH_3(Pz)$), 2.15 (s, 3H, $CH_3(Pz)$), 2.10 (s, 3H, $CH_3(Carb)$). ^{11}B NMR (CD_3CN , 128.6 MHz): δ = -4.46 (br d, $^1J_{BH}$ = 185, 1B), -6.09 (br d, $^1J_{BH}$ = 143 Hz, 1B), -8.2 to -11.98 overlapping signals, (8B, $B-H$). $^{11}B\{^1H\}$ NMR (CD_3CN , 128.6 MHz): δ = -4.40 (br s, 1B), -6.09 (br s, 1B), -8.90 to -10.8, overlapping signals (8B). $^{13}C\{^1H\}$ NMR (CD_3CN , 100.6 MHz): δ = 148.6 and 140.6 ($Pz-C$), 106.2 ($CH(Pz)$), 77.4 and 76.8 ($C_{carb}-CR$), 47.8 ($N_{Pz}CH_2CH_2C_{carb}$), 35.0 ($N_{Pz}CH_2CH_2C_{carb}$), 23.7 (CH_3C_{carb}), 13.8 and 11.1 ($CH_3(Pz)$). UV-Vis: (solid state) λ_{max} = 306 nm. Fluorescence (solid state): λ_{ex} = 318 nm, λ_{em} = 517 nm.

Synthesis of $\{[Cu_4(L11)_2I_4] \cdot (CH_3CN)\}_n$ (33)

A solution of anhydrous CuI (0.100 g, 0.525 mmol) and **L11** (0.082 g, 0.210 mmol) in dry CH_3CN (20 mL) was stirred for 3 h at RT under nitrogen. Then, the resulting solution was filtered, concentrated up to 5 mL and left standing overnight in the fridge, which provided a white precipitate. The precipitate was filtered, washed with cold Et_2O and dried under vacuum.

33. Yield: 42.1 % (0.068 g) Elem anal. Calc. for $C_{34}H_{67}B_{20}N_9I_4Cu_4$ (1538.92): C, 25.85 H, 4.27; N, 7.98. Found: C, 25.67; H, 4.19; N 7.86. ATR-FTIR (wavenumber, cm^{-1}): 3132 (w) [$\nu(C-H)_{ar}$], 2990-2918 (w) [$\nu(C-H)_{al}$], 2572 (vs) [$\nu(B-H)$], +1555 (s) [$\nu(C=C/C=N)_{ar}$], 1464 (m), 1436 (m), 1417 (s) [$\delta(C=C/C=N)_{ar}$], 1376 (s), 1317 (m), 1285 (w), 1248 (m), 1219 (w), 1154 (w), 1113 (w), 1071 (w), 1066 (w), 1036 (s) [$\delta(C-H)_{ip}$], 998 (m), 982 (m), 798 (vs) [$\delta(C-H)_{oop}$], 795 (vs) [$\delta(C-H)_{oop}$], 730 (s) [$\nu(B-B)$], 672 (s) [$\delta(C-H)_{oop}$], 660 (s) [$\delta(C-H)_{oop}$], 544 (m), 526 (m). UV-Vis: (solid state) λ_{max} = 349 nm. Fluorescence (solid state): λ_{ex} = 336 nm, λ_{em} = 467 nm.

5.6 Crystallographic Data

Molecular graphics were generated using Mercury Software^{11,12} with POV-Ray package¹³. Colour codes for all molecular graphics are: pink (B), grey (C), red (O), light-blue (N), white (H), dark blue (Co), orange (Cu), violet (I), blue-grey (Zn), bone (Cd), light grey (Hg), turquoise (Pd) light green (Cl).

Single Crystals suitable for X-ray diffraction (SCXRD) were prepared under inert conditions immersed in perfluoropolyether or paratone as protecting oil for manipulation and mounted on MiTeGen MicromountsTM.

For crystals of **L9**, **S1**, **10-12**, **18**, **27**, **30** and **32A** data were collected at BL13 (XALOC)¹⁴ at the ALBA synchrotron with an undulator source and channel-cut Si(111) monochromator and Kirkpatrick-Baez focusing mirrors with a selected wavelength of 0.82654 Å (**S1**), 0.72932 Å (**L9**, **10-12**, **18**, **27**, **30** and **32A**). An MD2M-Maatel diffractometer fitted with a Dectris Pilatus 6M detector was employed. The samples were kept at 100 K with an Oxford Cryosystems 700 series Cryostream.

For crystals of **1-9·6H₂O**, **13**, **15-17**, **19**, **24**, **25**, **29**, **31** and **33** data were collected with a Bruker D8 diffractometer with a graphite monochromated MoK α radiation (λ = 0.71073 Å, **16**, **17**, **29**, **31** and **33**) or CuK α radiation (λ = 1.54178 Å, **15**, **24** and **25**).

For crystals of **1-9·6H₂O**, **13** and **19** data were collected on a D8 Venture system with a multilayer monochromator and a Mo microfocus (λ = 0.71073 Å).

For **L9**, cell parameters were retrieved using the **CrysAlisPro**¹⁵ software and refined using **CrysAlisPro**¹⁵. Data reduction was performed using the **CrysAlisPro**¹⁵ software which corrects for Lorentz polarisation. A multi-scan absorption correction was performed using **CrysAlisPro**¹⁵. Empirical absorption correction using spherical harmonics, implemented in SCALE3 ABSPACK scaling algorithm. The structure was solved in the space group *P2₁/c* (# 14) by Intrinsic Phasing using the **ShelXT**¹⁶ structure solution program and refined by Least Squares using version 2014/7 of **ShelXL**¹⁷. All non-hydrogen atoms were refined anisotropically. Hydrogen atom positions were calculated geometrically and refined using the riding model. **L9** was refined as a 2-component perfect twin.

Data for **S1**, **10-12**, **15-18**, **24**, **27**, **29-31**, **32A** and **33** was processed with APEX3 suite (Bruker APEX3. APEX3 V2019.1; Bruker-AXS: Madison, WI, USA, 2019). The structures were solved by Intrinsic Phasing using the ShelXT program¹⁶, which revealed the position of all non-hydrogen atoms. These atoms were refined on F2 by a full-matrix least-squares procedure using anisotropic displacement parameter¹⁶. All hydrogen atoms were located in difference Fourier maps and included as fixed contributions riding on attached atoms with isotropic thermal displacement parameters 1.2 or 1.5 times those of the respective atom. The OLEX2 software was used as a graphical interface¹⁸. The contribution of the disordered solvent molecules to the diffraction pattern in **16** and **17** could not be rigorously included in the model and were consequently removed with the SQUEEZE routine of PLATON¹⁹ (0.5 molecules of EtOH for **16** and **17**). This contribution has been included in the empirical formula to give the correct calculated density, absorption coefficient and molecular weight. Compound **16** was treated as a two-component non-merohedral twin; the exact twin matrix identified by the integration program was found to be $-1\ 0\ -0.5\ 0\ -1\ 0\ 0\ 0\ 1$. The structure of **16** was solved using direct methods with only the non-overlapping reflections of component 1. The structure was refined using the HKLF 5 routine with all reflections of component 1 (including the overlapping ones), resulting in a BASF value of 0.317.

For compounds **1-9**·6H₂O, **13** and **19**, the frames were integrated with the Bruker SAINT software package using a narrow-frame algorithm. The structures were solved and refined using the Bruker SHELXTL Software Package¹⁷. Data were corrected for absorption effects using the Multi-Scan method (SADABS)²⁰.

Crystallographic data for the elucidated crystal structures are gathered in Tables 5.1-5.10.

Table 5.1 Crystallographic data for compounds **L9** and **S1**.

Formula	C ₁₀ H ₂₄ B ₁₀ N ₂ (L9)	C ₈ H ₃₀ B ₂₀ (S1)
Formula Weight	280.41	342.52
Temperature (K)	100(2)	100(2)
Wavelength (Å)	0.72932	0.82654
System, space group	Monoclinic, P2 ₁ /c	Orthorhombic, Pbca
a (Å)	10.8644(2)	10.8654(4)
b (Å)	20.6842(3)	13.6431(6)
c (Å)	7.79360(10)	13.8271(6)
α (°)	90	90
β (°)	106.795(2)	90
γ (°)	90	90
U (Å ³) / Z	1676.68(5) / 4	2049.70(15) / 4
D _{calc} (g cm ⁻³) / μ (mm ⁻¹)	1.111 / 0.059	1.110 / 0.063
F(000)	592	712
Crystal size (mm ³)	0.20x0.20x0.20	0.12x0.15x0.16
hkl ranges	-14≤h≤14, -27≤k≤27, -10≤l≤10	-12≤h≤12, -16≤k≤16, -16≤l≤16
2θ Range (°)	3.107 to 29.515	3.473 to 29.458
Reflections collected/unique/ [R _{int}]	4322/4322 [R(int)=1]	21086/1720 [R(int)=0.0380]
Completeness to θ (%)	99.70	94.8
Absorption correction	Empirical using spherical harmonics	Semi-empirical from equivalents
Max. and min. trans.	1.00000 and 0.60412	0.0124 and 0.0014
Data/restraints/parameters	3937/0/202	1720/0/128
Goodness-of-fit on F ²	1.056	1.077
Final R indices [I>2σ (I)]	R ₁ = 0.0703 wR ₂ = 0.2097	R ₁ = 0.0781 wR ₂ = 0.2286
R indices (all data)	R ₁ = 0.0735 wR ₂ = 0.2152	R ₁ = 0.0786 wR ₂ = 0.2294
Largest diff. peak and hole (e Å ⁻³)	+0.405, -0.402	+0.301, -0.234

Table 5.2 Crystallographic data for compounds **1-3·HL2**.

Formula	C ₁₄ H ₂₂ Cl ₂ Cu ₂ N ₄ O ₂ (1)	C ₁₄ H ₂₄ Cl ₂ CuN ₄ O ₂ (2)	C ₈₅ H ₇₆ Cl ₄ Cu ₄ N ₁₀ O ₅ (3·HL2)
Formula Weight	476.33	414.81	1713.51
Temperature (K)	100(2)	293(2)	100(2)
Wavelength (Å)	0.71073	0.71073	0.71073
System, space group	Triclinic, P $\bar{1}$	Orthorhombic, Pccn	Monoclinic C2/c
a (Å)	4.290(2)	23.8198(12)	32.071(3)
b (Å)	8.2451(4)	10.6354(5)	12.8910(12)
c (Å)	12.9432(6)	14.6124(8)	21.3823(19)
α (°)	82.066(2)	90	90
β (°)	87.584(2)	90	120.051(3)
γ (°)	79.200(2)	90	90
U (Å ³) / Z	446.28(4) / 1	3701.8(3) / 8	7651.8(12) / 4
D _{calc} (g cm ⁻³) / μ (mm ⁻¹)	1.772 / 2.697	1.489 / 1.482	1.487 / 1.297
F(000)	242	1720	3520
Crystal size (mm ³)	0.205 x 0.144 x 0.060	0.163 x 0.140 x 0.078	0.126 x 0.071 x 0.046
hkl ranges	-6 ≤ h ≤ 6 -11 ≤ k ≤ 11 -18 ≤ l ≤ 18	-33 ≤ h ≤ 34 -15 ≤ k ≤ 15 -20 ≤ l ≤ 20	-40 ≤ h ≤ 40, -16 ≤ k ≤ 16, -26 ≤ l ≤ 26
2 θ Range (°)	3.168 to 30.593	2.518 to 30.601	2.475 to 26.541
Reflections collected/unique/ [R _{int}]	23008/ 2733 / 0.0223	163709 / 5675 / 0.0526	67297 / 7851 / 0.081
Completeness to θ (%)	99.3	93.2	99.1
Absorption correction	Semi-empirical	Semi-empirical	Semi-empirical
Max. and min. trans.	0.7461 and 0.6649	0.7461 and 0.6897	0.7454 and 0.6969
Data/restraints/parameters	2733/1/111	5675/1/212	7851 / 7 / 501
Goodness-of-fit on F ²	1.100	1.086	0.984
Final R indices [I > 2 σ (I)]	R1 = 0.0162, wR2 = 0.0432	R1 = 0.0280, wR2 = 0.0632	R1 = 0.0358 wR2 = 0.0878
R indices (all data)	R1 = 0.0175, wR2 = 0.0439	R1 = 0.0361, wR2 = 0.0663	R1 = 0.0583 wR2 = 0.0972
Largest diff. peak and hole (e Å ⁻³)	0.444 and -0.409	0.460 and -0.426	1.512 and -0.472

Table 5.3 Crystallographic data for compounds **4·(CH₂Cl₂)(H₂O)-6**.

Formula	C ₁₆ H ₁₈ Cl ₄ CuN ₄ O ₂ (4·(CH ₂ Cl ₂)(H ₂ O))	C ₇ H ₁₁ CuN ₃ O ₄ (5)	C ₁₄ H ₂₄ CuN ₆ O ₈ (6)
Formula Weight	503.68	264.73	467.93
Temperature (K)	100(2)	100(2)	100(2)
Wavelength (Å)	0.71073	0.71073	0.71073
System, space group	Triclinic, P $\bar{1}$	Monoclinic, P2 ₁ /c	Monoclinic, P2 ₁ /c
a (Å)	7.1504(7)	13.880(2)	29.965(4)
b (Å)	11.4516(10)	4.7765(9)	8.0447(12)
c (Å)	13.4558(11)	16.127(3)	23.742(4)
α (°)	115.148(3)	90	90
β (°)	94.615(3)	114.798(6)	92.447(3)
γ (°)	93.934(3)	90	90
U (Å ³) / Z	987.66(15) / 2	970.6(3) / 4	2028.03 / 4
D _{calc} (g cm ⁻³) / μ (mm ⁻¹)	1.694 / 1.667	1.812 / 2.249	1.533 / 1.131
F(000)	510	540	972
Crystal size (mm ³)	0.348 x 0.158 x 0.092	0.314 x 0.120 x 0.031	0.241 x 0.068 x 0.047
hkl ranges	-10 ≤ h ≤ 10, -16 ≤ k ≤ 16, -19 ≤ l ≤ 19	-19 ≤ h ≤ 19 -6 ≤ k ≤ 6 -22 ≤ l ≤ 23	-22 ≤ h ≤ 22 0 ≤ k ≤ 11 0 ≤ l ≤ 16
2 θ Range (°)	3.082 to 30.620	2.566 to 30.613	2.312 to 27.565
Reflections collected/unique/ [R _{int}]	38694 / 5964 / 0.0253	12549 / 2916 / 0.0561	4667 / 4667 / 0.1826
Completeness to θ (%)	98.4	99.7	99.6
Absorption correction	Semi-empirical	Semi-empirical	Semi-empirical
Max. and min. trans.	0.7461 and 0.6694	0.7461 and 0.6202	0.7456 and 0.6571
Data/restraints/parameters	5964 / 3 / 250	2916/0/138	4667/0/257
Goodness-of-fit on F ²	1.080	1.056	0.855
Final R indices [I > 2 σ (I)]	R1 = 0.0193 wR2 = 0.0529	R1 = 0.0490, wR2 = 0.0864	R1 = 0.0329, wR2 = 0.0488
R indices (all data)	R1 = 0.0204 wR2 = 0.00541	R1 = 0.0699, wR2 = 0.0931	R1 = 0.0748, wR2 = 0.0549
Largest diff. peak and hole (e Å ⁻³)	0.460 and -0.399	0.800 and -1.146	0.378 and -0.660

Table 5.4 Crystallographic data for compounds **7·2CH₃CN·9·6H₂O**.

Formula	C ₆₈ H ₆₀ Cu ₂ N ₁₂ O ₈ (3·7(CH ₃ CN))	C ₂₆ H ₂₄ Cu ₂ N ₁₀ O ₉ (8·H ₂ O)	C ₁₈ H ₄₀ Cu ₂ N ₄ O ₁₂ (9·6H ₂ O)
Formula Weight	1300.36	747.63	631.62
Temperature (K)	100(2)	100(2)	150(2)
Wavelength (Å)	0.71073	0.71073	0.71073
System, space group	Triclinic, P-1	Orthorhombic, Fddd	Monoclinic, P2 ₁ /c
a (Å)	9.8155(9)	18.360(2)	10.5582(5)
b (Å)	12.1884(12)	23.625(2)	14.3727(6)
c (Å)	13.9385(14)	27.038(3)	9.1424(4)
α (°)	67.033(4)	90	90
β (°)	87.810(4)	90	90.643(2)
γ (°)	84.075(4)	90	90
U (Å ³) / Z	1527.1(3) / 1	11728(2) / 16	1387.27(11) / 2
D _{calc} (g cm ⁻³) / μ (mm ⁻¹)	1.414 / 0.764	1.694 / 1.523	1.512 / 1.595
F(000)	674	6080	660
Crystal size (mm ³)	0.150x0.080x0.060	0.120x0.090x0.060	0.313 x 0.076 x 0.057
hkl ranges	-13≤h≤14 -17≤k≤17 -19≤l≤19	-26≤h≤26 -34≤k≤34 -39≤l≤35	-15≤h≤15 -20≤k≤18 -13≤l≤13
2θ Range (°)	2.086 to 30.549	2.290 to 31.063	2.394 to 30.579
Reflections collected/unique/ [R _{int}]	63778/ 9331 / 0.0355	70856 / 4701 / 0.1015	45761 / 4228 / 0.0270
Completeness to θ (%)	99.8	99.9	99.1
Absorption correction	Semi-empirical	Semi-empirical	Semi-empirical
Max. and min. trans.	0.7461 and 0.6980	0.7462 and 0.6972	0.7461 and 0.6182
Data/restraints/parameters	9331 / 0 / 407	4701 / 3 / 243	4228/10/184
Goodness-of-fit on F ²	1.073	1.089	1.132
Final R indices [I>2σ (I)]	R1 = 0.0331 wR2 = 0.0805	R1 = 0.0725 wR2 = 0.1923	R1 = 0.0232, wR2 = 0.0592
R indices (all data)	R1 = 0.0405 wR2 = 0.0872	R1 = 0.1381 wR2 = 0.2630	R1 = 0.0276, wR2 = 0.0616
Largest diff. peak and hole (e Å ⁻³)	1.694 and -0.565	1.227 and -0.786	0.427 and -0.470

Table 5.5 Crystallographic data for compounds **10-12**.

Formula	C ₄₄ H ₆₀ Zn ₂ Cl ₄ N ₈ O ₄ (10)	C ₄₄ H ₆₀ Cd ₂ Cl ₄ N ₈ O ₄ (11)	C ₄₄ H ₆₀ Hg ₂ Cl ₄ N ₈ O ₄ (12)
Formula Weight	1037.54	1131.60	1307.98
Temperature (K)	100(2)	100(2)	100(2)
Wavelength (Å)	0.72932	0.72929	0.72931
System, space group	Monoclinic, P2 ₁ /n	Monoclinic, P2 ₁ /n	Monoclinic P2 ₁ /n
a (Å)	9.5030(4)	9.5328(8)	9.5573(4)
b (Å)	19.1113(9)	19.3000(16)	19.2939(7)
c (Å)	13.3218(6)	13.5436(11)	13.5592(5)
α (°)	90	90	90
β (°)	96.203(2)	97.179(2)	97.3560(10)
γ (°)	90	90	90
U (Å ³) / Z	2405.27(19) / 2	2472.3(4) / 2	2479.71(17) / 2
D _{calc} (g cm ⁻³) / μ (mm ⁻¹)	1.433 / 1.353	1.520 / 1.196	1.752 / 6.872
F(000)	1080	1152	1280
Crystal size (mm ³)	0.12x0.1x0.1	0.11x0.1x0.1	0.1x0.1x0.08
hkl ranges	-11 ≤ h ≤ 11, -22 ≤ k ≤ 22, -15 ≤ l ≤ 15	-11 ≤ h ≤ 11, -23 ≤ k ≤ 23, -16 ≤ l ≤ 16	-11 ≤ h ≤ 11, -22 ≤ k ≤ 22, -16 ≤ l ≤ 16
2θ Range (°)	1.920 to 25.773	2.461 to 25.812	1.894 to 25.728
Reflections collected/unique/ [R _{int}]	17476 / 4097 / 0.0516	19112 / 4111 / 0.0646	42758/ 4370 / 0.0719
Completeness to θ (%)	95.9	93.2	99.6
Absorption correction	Semi-empirical from equivalents	Semi-empirical from equivalents	Semi-empirical from equivalents
Max. and min. trans.	0.0189 and 0.0048	0.0922 and 0.0385	0.0961 to 0.0280
Data/restraints/parameters	4097 / 0 / 284	4111 / 0 / 284	4370 / 0 / 285
Goodness-of-fit on F ²	1.064	1.074	1.174
Final R indices [I > 2σ (I)]	R1 = 0.0457 wR2 = 0.1320	R1 = 0.0672 wR2 = 0.1866	R1 = 0.0695 wR2 = 0.1714
R indices (all data)	R1 = 0.0466 wR2 = 0.1344	R1 = 0.0688 wR2 = 0.1906	R1 = 0.0707 wR2 = 0.1738
Largest diff. peak and hole (e Å ⁻³)	1.134 and -0.723	1.108 and -0.889	2.049 and -4.641

Table 5.6 Crystallographic data for compounds **13**, **15** and **16**.

Formula	C ₈₈ H ₁₂₂ Co ₄ Cl ₈ N ₁₆ O ₉ (13)	C ₄₄ H ₆₂ Zn ₂ Cl ₄ N ₈ O ₅ (15)	C ₂₃ H ₃₃ CdCl ₂ N ₄ O _{2.5} (16)
Formula Weight	2067.33	1055.55	588.83
Temperature (K)	100(2)	100.0	100(2)K
Wavelength (Å)	0.71073	1.54178	0.71073
System, space group	Monoclinic, P2 ₁ /n	Monoclinic, C2/c	Monoclinic, P2 ₁ /n
a (Å)	9.4978(5)	29.965(4)	11.1004(3)
b (Å)	19.0963(10)	8.0447(12)	12.9995(3)
c (Å)	13.2916(7)	23.742(4)	18.6202(5)
α (°)	90	90	90
β (°)	96.227(2)	122.071(7)	101.2850(10)
γ (°)	90	90	90
U (Å ³) / Z	2396.5(2) / 1	4849.9(12) / 4	2634.94(12) / 4
D _{calc} (g cm ⁻³) / μ (mm ⁻¹)	1.432 / 0.966	1.446 / 3.665	1.484 / 1.060
F(000)	1078	2200	1204
Crystal size (mm ³)	0.267 x 0.171 x 0.160	0.1 x 0.08 x 0.08	0.12 x 0.1 x 0.08
hkl ranges	-13 ≤ h ≤ 13, -27 ≤ k ≤ 27, -19 ≤ l ≤ 18	-35 ≤ h ≤ 35, -7 ≤ k ≤ 9, -28 ≤ l ≤ 27	-14 ≤ h ≤ 14, 0 ≤ k ≤ 16, 0 ≤ l ≤ 24
2θ Range (°)	2.784 to 30.550	3.481 to 66.860	1.923 to 27.494
Reflections collected/unique/ [R _{int}]	50359 / 7258 / 0.0290	15452 / 4279 / 0.0653	5995 / 5995 / 0.0945
Completeness to θ (%)	99.1	99.3	99.1
Absorption correction	Semi-empirical from equivalents	Semi-empirical from equivalents	Semi-empirical From equivalents
Max. and min. trans.	0.7461 and 0.6938	0.7528 and 0.6573	0.745684 and 0.349755
Data/restraints/parameters	7258 / 3 / 299	4279 / 0 / 289	5995 / 0 / 285
Goodness-of-fit on F ²	1.068	1.058	1.057
Final R indices [I > 2σ (I)]	R1 = 0.0251 wR2 = 0.0633	R1 = 0.0452 wR2 = 0.0909	R1 = 0.0547 wR2 = 0.1695
R indices (all data)	R1 = 0.0307 wR2 = 0.0683	R1 = 0.0766 wR2 = 0.1033	R1 = 0.0589 wR2 = 0.1799
Largest diff. peak and hole (e Å ⁻³)	0.414 and -0.449	0.356 and -0.527	1.961 and -1.256

Table 5.7 Crystallographic data for compounds **17-19**.

Formula	C ₂₃ H ₃₃ HgCl ₂ N ₄ O _{2.5} (17)	C ₄₄ H ₆₂ Co ₂ Cl ₄ N ₈ O ₅ (18)	C ₂₂ H ₃₀ Cu ₂ Cl ₂ N ₄ O ₂ (19)
Formula Weight	677.02	1042.67	651.40
Temperature (K)	298(2)K	100(2)	283(2)
Wavelength (Å)	0.71073	0.7293	0.71073
System, space group	Monoclinic, P2 ₁ /n	Monoclinic, C ₂ /c	Orthorhombic, Cmc2 ₁
a (Å)	11.1617(19)	29.9778(10)	21.873(16)
b (Å)	13.094(2)	8.0411(3)	7.781(4)
c (Å)	18.698(4)	23.7682(8)	15.377(7)
α (°)	90	90	90
β (°)	99.661(7)	122.0530(10)	90
γ (°)	90	90	90
U (Å ³) / Z	2693.8(8) / 4	4856.0(3) / 4	2617(3) / 4
D _{calc} (g cm ⁻³) / μ (mm ⁻¹)	1.669 / 5.940	1.426 / 1.017	1.699 / 2.062
F(000)	1332	2176	1352
Crystal size (mm ³)	0.1 x 0.1 x 0.08	0.12 x 0.1 x 0.1	0.068 x 0.062 x 0.043
hkl ranges	-13 ≤ h ≤ 13, -15 ≤ k ≤ 15, -20 ≤ l ≤ 22	-35 ≤ h ≤ 35, -9 ≤ k ≤ 9, -28 ≤ l ≤ 28	-28 ≤ h ≤ 28, -10 ≤ k ≤ 10, -19 ≤ l ≤ 19
2θ Range (°)	2.418 to 25.026	3.481 to 66.860	2.649 to 27.572
Reflections collected/unique/ [R _{int}]	37205/ 4760 / 0.1006	33398 / 4269 / 0.0520	15100 / 3080 / 0.2017
Completeness to θ (%)	99.8	99.4	99.9
Absorption correction	Semi-empirical From equivalents	Semi-empirical from equivalents	Semi-empirical from equivalents
Max. and min. trans.	0.7454 and 0.4502	0.0298 and 0.0098	0.7454 and 0.5078
Data/restraints/parameters	4760 / 0 / 284	4269 / 0 / 289	3080 / 1 / 159
Goodness-of-fit on F ²	1.011	1.039	1.029
Final R indices [I > 2σ (I)]	R1 = 0.0409 wR2 = 0.0719	R1 = 0.0379 wR2 = 0.1115	R1 = 0.0607 wR2 = 0.0997
R indices (all data)	R1 = 0.0800 wR2 = 0.0844	R1 = 0.0382 wR2 = 0.1118	R1 = 0.1282 wR2 = 0.1196
Largest diff. peak and hole (e Å ⁻³)	0.851 and -0.977	0.568 and -0.457	0.805 and -0.679

Table 5.8 Crystallographic data for compounds **24**, **25** and **27**.

Formula	C ₂₀ H ₄₈ B ₂₀ N ₄ CuCl ₂ (24)	C ₂₀ H ₄₈ B ₂₀ N ₄ ZnCl ₂ (25)	C ₂₀ H ₅₀ B ₂₀ N ₄ HgCl ₄ (27)
Formula Weight	695.26	697.09	905.23
Temperature (K)	298(2)	298(2)	100(2)
Wavelength (Å)	1.54178	1.54178	0.7293
System, space group	Monoclinic, C2/c	Monoclinic, P2 ₁ /c	Monoclinic, P2 ₁
a (Å)	23.571(6)	16.032(4)	7.5892(3)
b (Å)	13.290(5)	14.306(4)	32.6382(13)
c (Å)	14.597(4)	18.071(5)	16.4317(7)
α (°)	90	90	90
β (°)	125.225(8)	113.365(4)	97.0673(11)
γ (°)	90	90	90
U (Å ³) / Z	3735(2) / 4	3804.18(19) / 4	4039.2(3) / 4
D _{calc} (g cm ⁻³) / μ (mm ⁻¹)	1.236 / 2.281	1.217 / 2.326	1.489 / 4.354
F(000)	1436	1440	1784
Crystal size (mm ³)	0.12x0.12x0.11	0.14x0.12x0.12	0.12x0.12x0.08
hkl ranges	-28 ≤ h ≤ 27, -12 ≤ k ≤ 15, -17 ≤ l ≤ 16	-16 ≤ h ≤ 19, -15 ≤ k ≤ 16, -21 ≤ l ≤ 21	-9 ≤ h ≤ 9, -42 ≤ k ≤ 42, -21 ≤ l ≤ 21
2θ Range (°)	4.042 to 66.604	3.003 to 66.617	2.563 to 28.266
Reflections collected/unique/ [R _{int}]	18039/3286 [R(int)=0.0432]	28053/6695 [R(int)=0.0914]	59249/17402/ [R(int)=0.0271]
Completeness to θ (%)	99.6	99.6	95.3
Absorption correction	Semi-empirical from equivalents	Semi-empirical from equivalents	Semi-empirical from equivalents
Max. and min. trans.	0.7528 and 0.4768	0.7528 and 0.4823	0.0298 and 0.0090
Data/restraints/parameters	3286/0/216	6695/0/430	17402/1/895
Goodness-of-fit on F ²	1.111	1.021	1.047
Final R indices [I > 2σ (I)]	R ₁ = 0.0547 wR ₂ = 0.1517	R ₁ = 0.0629 wR ₂ = 0.1557	R ₁ = 0.0293 wR ₂ = 0.0695
R indices (all data)	R ₁ = 0.0559 wR ₂ = 0.1541	R ₁ = 0.1040 wR ₂ = 0.1824	R ₁ = 0.0300 wR ₂ = 0.0704
Largest diff. peak and hole (e Å ⁻³)	+0.228, -0.840	+0.734, -0.566	+0.964, -1.475

Table 5.9 Crystallographic data for compounds **29-31**

Formula	C ₁₆ H ₃₂ B ₁₀ PdCl ₂ N ₄ (29)	C ₁₃ H ₁₆ CuIN ₂ (30)	C ₁₈ H ₄₄ B ₂₀ Cu ₂ I ₂ N ₄ (31)
Formula Weight	565.85	390.72	913.65
Temperature (K)	298(2)	100(2)	298(2)
Wavelength (Å)	0.71073	0.72932	0.71073
System, space group	Triclinic, P $\bar{1}$	Monoclinic, P2 ₁ /c	Triclinic, P $\bar{1}$
a (Å)	8.1091(8)	4.2749(3)	10.361(2)
b (Å)	8.1123(5)	19.9244(15)	12.195(2)
c (Å)	20.7127(14)	16.0826(11)	15.412(3)
α (°)	85.855(2)	90	98.412(6)
β (°)	81.902(4)	97.106(2)	91.117(6)
γ (°)	80.528(4)	90	96.772(6)
U (Å ³) / Z	1328.89(18) / 2	1359.31(17) / 4	1911.6(6) / 2
D _{calc} (g cm ⁻³) / μ (mm ⁻¹)	1.414 / 0.913	1.909 / 4.101	1.587 / 2.748
F(000)	572	760	888
Crystal size (mm ³)	0.14 x 0.12 x 0.12	0.1x0.1x0.08	0.13x0.13x0.11
hkl ranges	-10 \leq h \leq 10, -10 \leq k \leq 10, -26 \leq l \leq 26	-5 \leq h \leq 5, -23 \leq k \leq 23, -19 \leq l \leq 19	-13 \leq h \leq 13, -15 \leq k \leq 15, -19 \leq l \leq 19
2 θ Range (°)	2.689 to 27.563	1.678 to 25.718	1.981 to 27.522
Reflections collected/unique/ [R _{int}]	19758 / 6085/ [R(int)=0.0417]	28558 / 2381 / 0.0937	50381 / 8766 / 0.0594
Completeness to θ (%)	99.5	99.9	99.9
Absorption correction	Semi-empirical from equivalents	Semi-empirical from equivalents	Semi-empirical from equivalents
Max. and min. trans.	0.7456 and 0.5150	0.4910 and 0.2737	0.7456 and 0.4209
Data/restraints/parameters	6085 / 0 / 302	2381 / 0 / 159	8766 / 0 / 419
Goodness-of-fit on F ²	1.070	1.059	1.020
Final R indices [I>2 σ (I)]	R1= 0.0345 wR2= 0.0807	R1= 0.0451 wR2= 0.1262	R1= 0.0408 wR2= 0.0774
R indices (all data)	R1= 0.0436 wR2= 0.0846	R1= 0.0460 wR2= 0.1268	R1= 0.0762 wR2= 0.0892
Largest diff. peak and hole (e Å ⁻³)	0.462 and -0.945	1.499 and -0.995	0.693 and -0.692

Table 5.10 Crystallographic data for compounds **32A** and **33**

Formula	C ₂₀ H ₄₈ B ₂₀ Cu ₂ I ₂ N ₄ (32A)	C ₃₄ H ₆₇ B ₂₀ Cu ₄ I ₄ N ₉ (33)
Formula Weight	941.70	1579.92
Temperature (K)	100(2)	298(2)
Wavelength (Å)	0.7293	0.71073
System, space group	Triclinic, P $\bar{1}$	Monoclinic, P2 ₁ /c
a (Å)	12.0222(8)	13.3779(13)
b (Å)	12.9633(8)	19.272(2)
c (Å)	14.3391(9)	23.825(2)
α (°)	72.561(2)	90
β (°)	78.697(2)	99.679(2)
γ (°)	64.922(2)	90
U (Å ³) / Z	1924.2(9) / 2	6055.0(10) / 4
D _{calc} (g cm ⁻³) / μ (mm ⁻¹)	1.625 / 2.835	1.733 / 3.460
F(000)	920	3048
Crystal size (mm ³)	0.11x0.1x0.1	0.11x0.1x0.1
hkl ranges	-14 \leq h \leq 14, -15 \leq k \leq 15, -17 \leq l \leq 17	-17 \leq h \leq 17, -25 \leq k \leq 24, -28 \leq l \leq 30
2 θ Range (°)	2.555 to 25.728	2.285 to 27.522
Reflections collected/unique/ [R _{int}]	46530 / 6686 / 0.0917	137504 / 13904 / 0.1346
Completeness to θ (%)	98.5	99.9
Absorption correction	Semi-empirical from equivalents	Semi-empirical from equivalents
Max. and min. trans.	0.0285 and 0.0068	0.7456 and 0.3935
Data/restraints/parameters	6686 / 0 / 440	13904 / 0 / 622
Goodness-of-fit on F ²	1.110	1.014
Final R indices [I $>2\sigma$ (I)]	R1= 0.0541 wR2= 0.1341	R1= 0.0509 wR2= 0.1006
R indices (all data)	R1= 0.0551 wR2= 0.1352	R1= 0.1028 wR2= 0.1183
Largest diff. peak and hole (e Å ⁻³)	2.361 and -1.693	1.137 and -0.952

References

- 1 W. G. Haanstra, W. L. Driessen, J. Reedijk, U. Turpeinen and R. Hämäläinen, *J. Chem. Soc. Dalton Trans.*, 1989, 2309–2314.
- 2 S. Muñoz, J. Pons, J. Ros, M. Font-Bardia, C. A. Kilner and M. A. Halcrow, *Inorganica Chim. Acta*, 2011, **373**, 211–218.
- 3 H. Ochi, T. Miyasaka and K. Arakawa, *Yakugaku Zasshi*, 1978, **98**, 165–171.
- 4 H. L. Blonk, W. L. Driessen and J. Reedijk, *J. Chem. Soc., Dalton Trans.*, 1985, 1699–1705.
- 5 F. Bondavalli, O. Bruno, A. Ranise, P. Schenone, P. Addonizio, V. De Novellis, A. Loffreda and E. Marmo, *Farm. Ed. Sci.*, 1988, **43**, 725–743.
- 6 M. Guerrero, T. Calvet, M. Font-Bardia and J. Pons, *Polyhedron*, 2016, **119**, 555–562.
- 7 G. A. Bain and J. F. Berry, *J. Chem. Educ.*, 2008, **85**, 532.
- 8 M. Guerrero, J. García-Antón, M. Tristany, J. Pons, J. Ros, K. Philippot, P. Lecante and B. Chaudret, *Langmuir*, 2010, **26**, 15532–15540.
- 9 M. Guerrero, J. Pons, V. Branchadell, T. Parella, X. Solans, M. Font-Bardia and J. Ros, *Inorg. Chem.*, 2008, **47**, 11084–11094.
- 10 S. Komiya, *Synthesis of Organometallic Compounds*, John Wiley & Sons, Ltd, Chichester, West Sussex, England.
- 11 C. F. Macrae, P. R. Edgington, P. McCabe, E. Pidcock, G. P. Shields, R. Taylor, M. Towler and J. van de Streek, *J. Appl. Crystallogr.*, 2006, **39**, 453–457.
- 12 C. F. Macrae, I. J. Bruno, J. A. Chisholm, P. R. Edgington, P. McCabe, E. Pidcock, L. Rodriguez-Monge, R. Taylor, J. van de Streek and P. A. Wood, *J. Appl. Crystallogr.*, 2008, **41**, 466–470.
- 13 C. Cason, T. Froehlich and C. Lipka, *Persistence Vis. Pty. Ltd., Williamstown, Victoria, Aust. (version 3.7)*.
- 14 J. Juanhuix, F. Gil-Ortiz, G. Cuní, C. Colldelram, J. Nicolás, J. Lidón, E. Boter,

- C. Ruget, S. Ferrer and J. Benach, *J. Synchrotron Radiat.*, 2014, **21**, 679–689.
- 15 Rigaku, 2015.
- 16 G. M. Sheldrick, *Acta Crystallogr. Sect. A Found. Adv.*, 2015, **71**, 3–8.
- 17 G. M. Sheldrick, *Acta Crystallogr. Sect. C Struct. Chem.*, 2015, **71**, 3–8.
- 18 O. V. Dolomanov, L. J. Bourhis, R. J. Gildea, J. A. K. Howard and H. Puschmann, *J. Appl. Crystallogr.*, 2009, **42**, 339–341.
- 19 A. L. Spek, *J. Appl. Crystallogr.*, 2003, **36**, 7–13.
- 20 L. Krause, R. Herbst-Irmer, G. M. Sheldrick and D. Stalke, *J. Appl. Crystallogr.*, 2015, **48**, 3–10.

ANNEX I: Spectra and Additional Information

Annex for Section 3.1

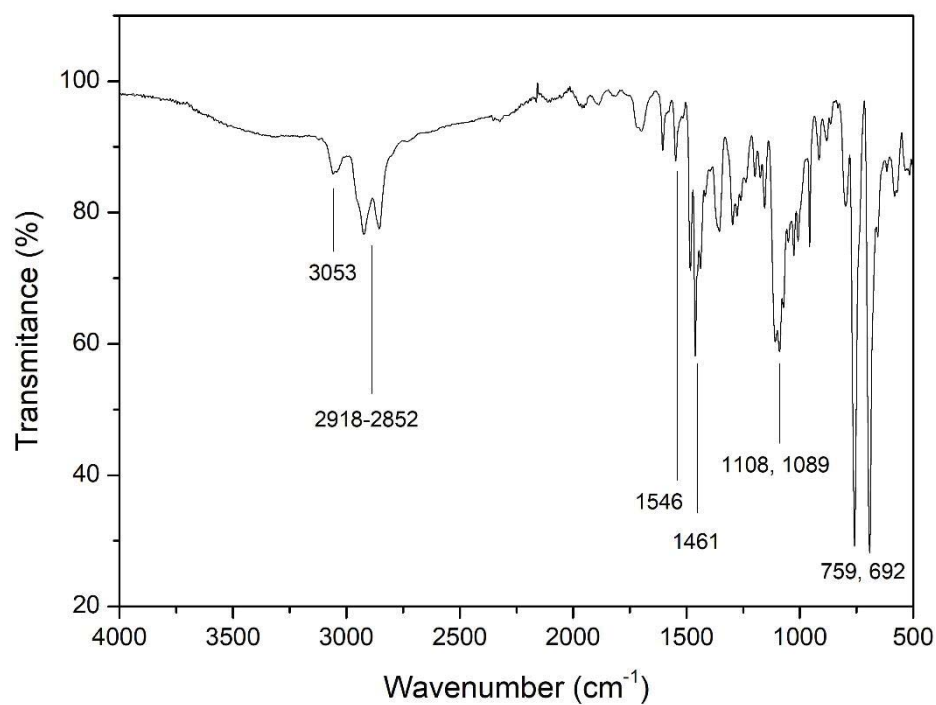


Figure S3.1.1 FTIR-ATR spectrum of L7

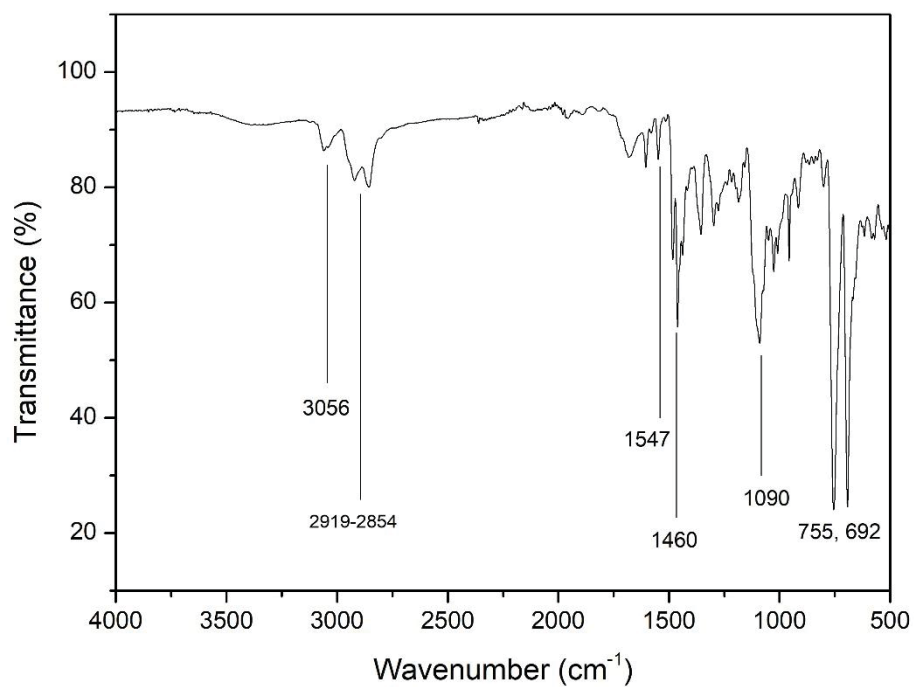


Figure S3.1.2 FTIR-ATR spectrum of L8

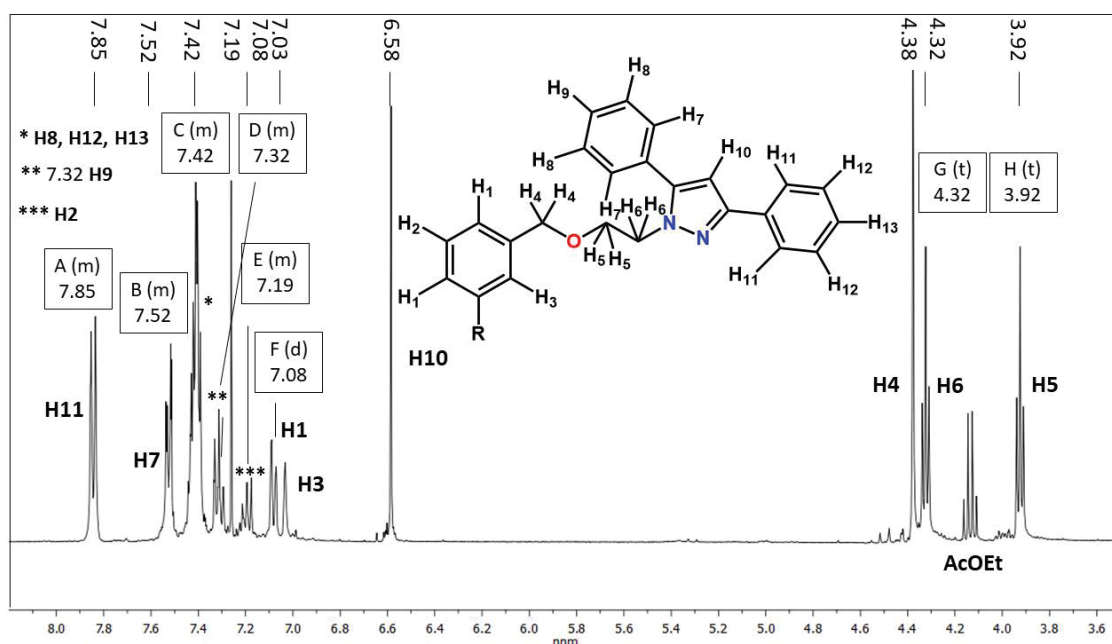


Figure S3.1.3 ^1H NMR spectrum of **L7** (CDCl_3 , 400.0 MHz)

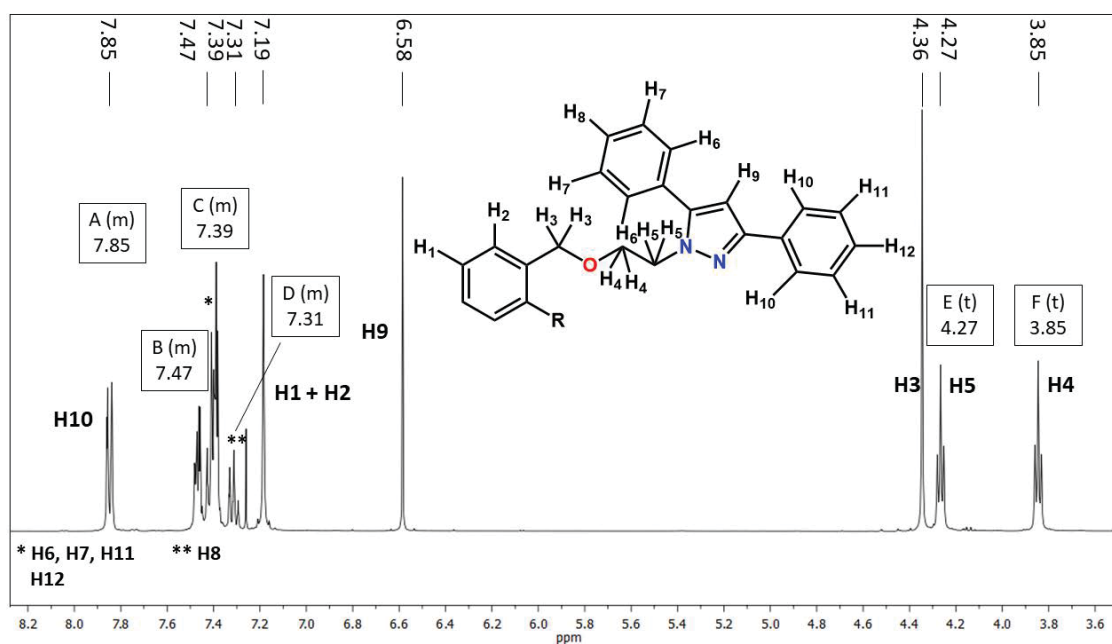


Figure S3.1.4 ^1H NMR spectrum of **L8** (CDCl_3 , 400.0 MHz)

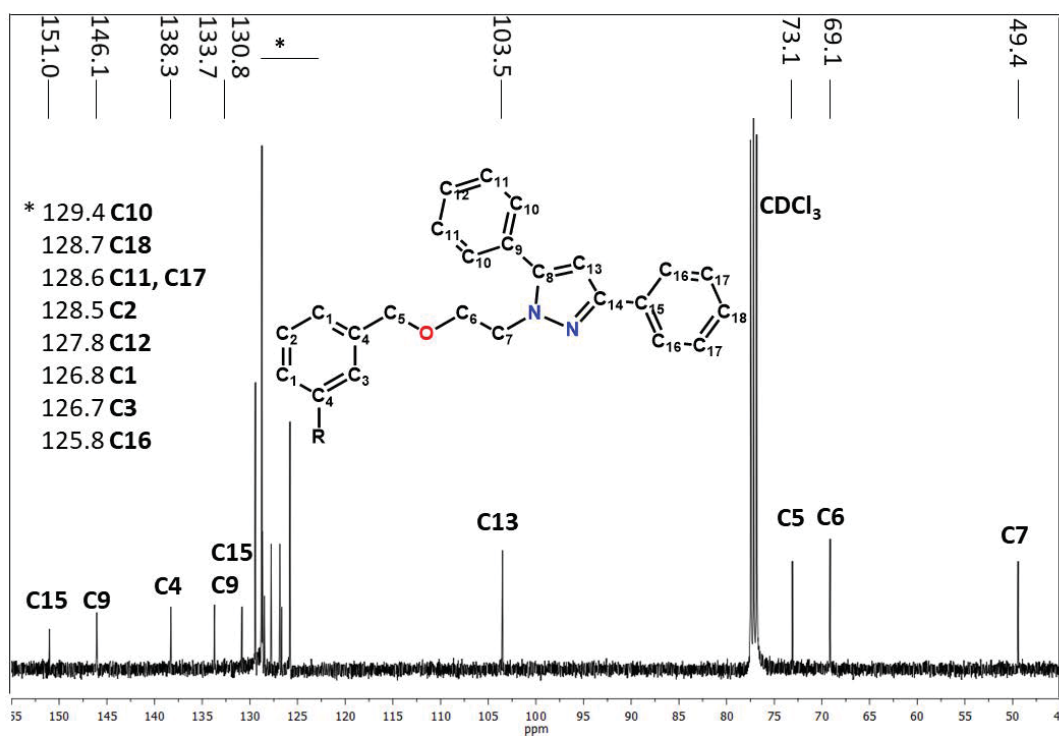


Figure S3.1.5 $^{13}\text{C}\{^1\text{H}\}$ NMR spectrum of L7 (CDCl₃, 100.6 MHz)

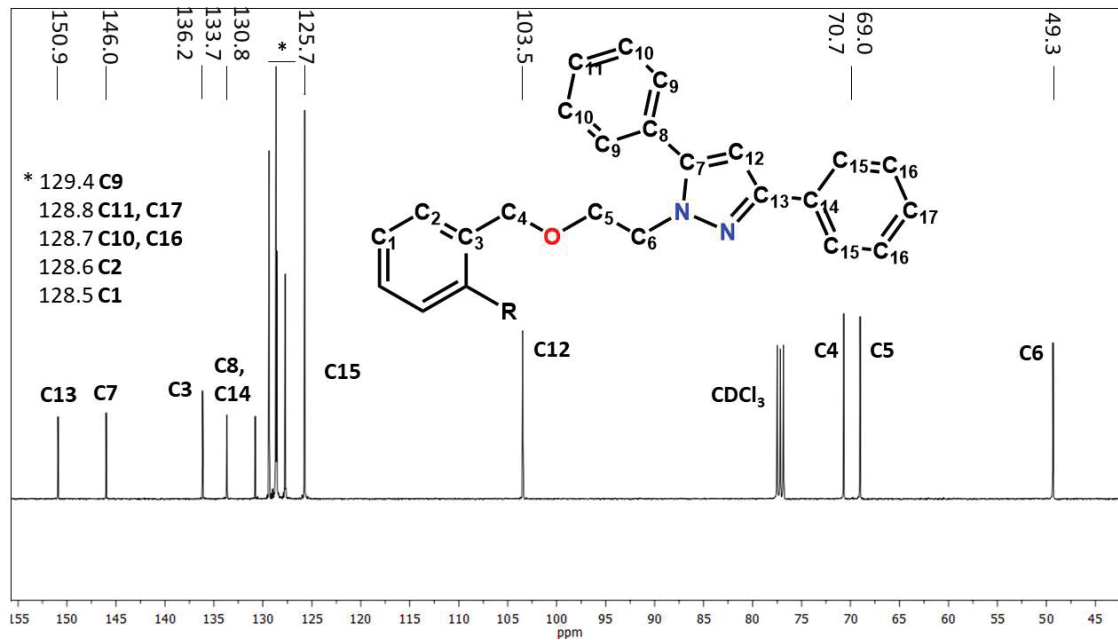


Figure S3.1.6 $^{13}\text{C}\{^1\text{H}\}$ NMR spectrum of L8 (CDCl₃, 100.6 MHz)

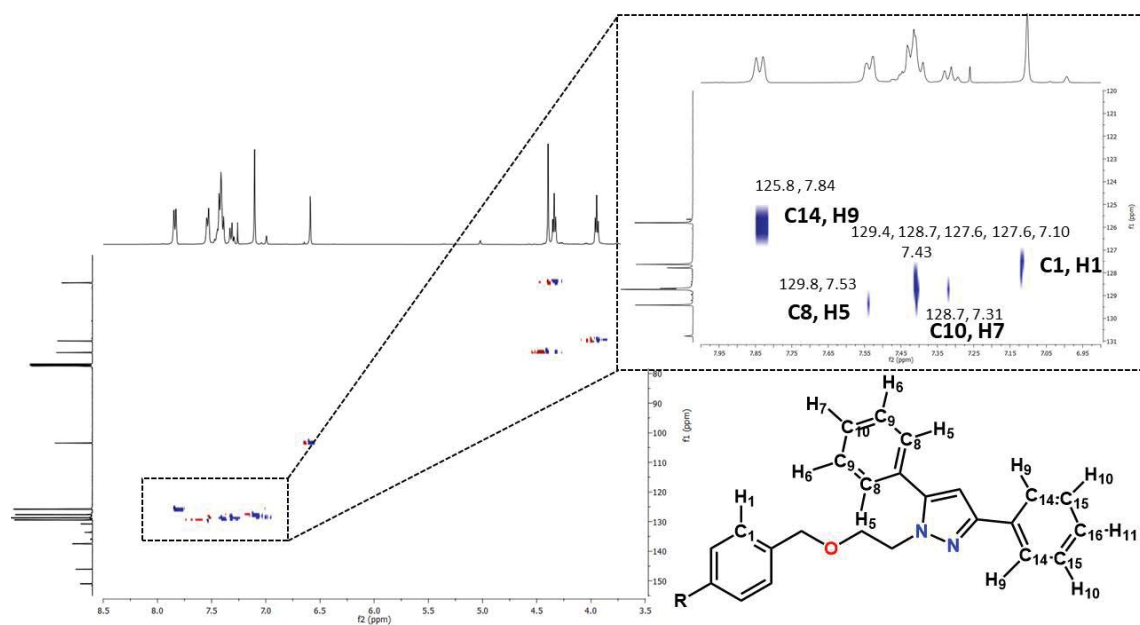


Figure S3.1.7 HSQC NMR spectrum of **L6** (CDCl₃ 400.0 and 100.6 MHz)

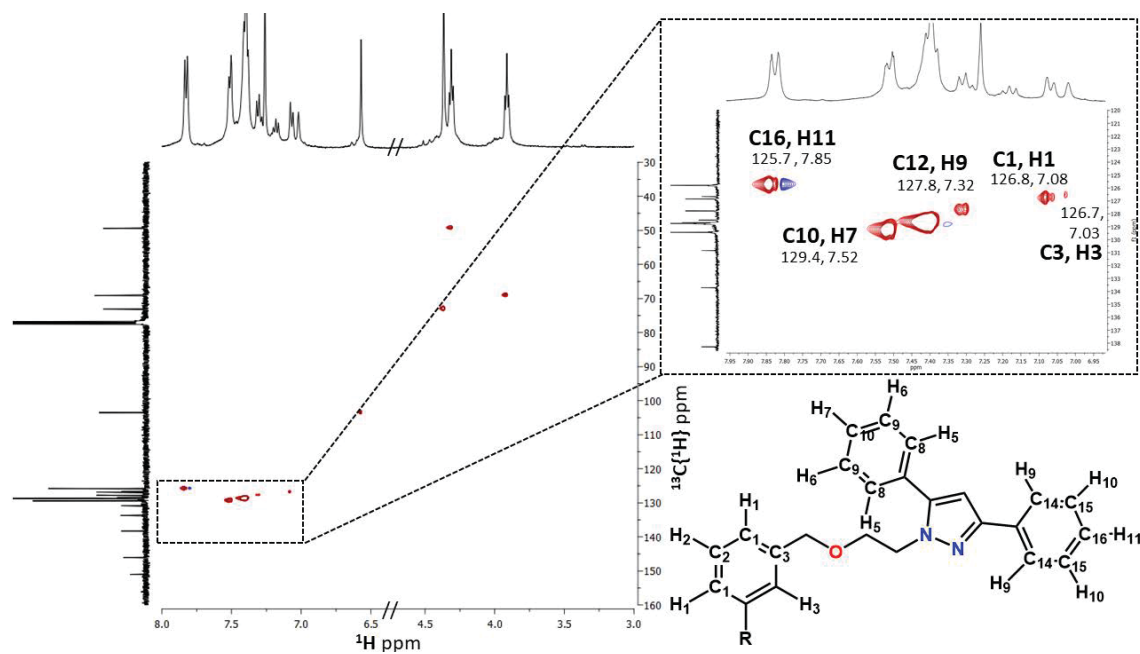


Figure S3.1.8 HSQC NMR spectrum of **L7** (CDCl₃ 400.0 and 100.6 MHz)

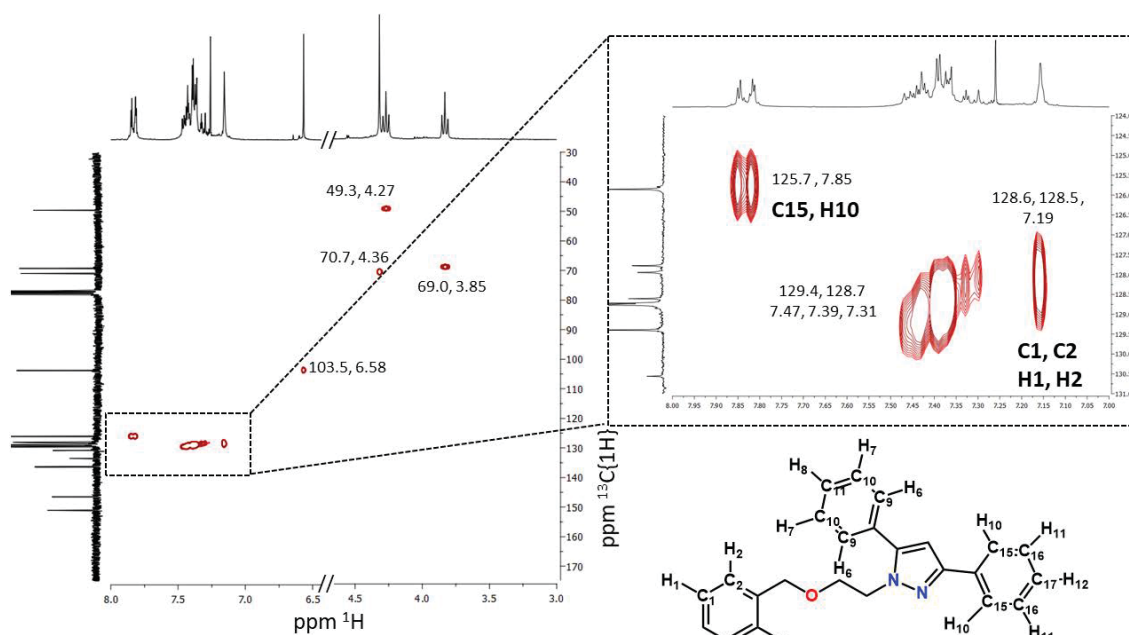


Figure S3.1.9 HSQC NMR spectrum of **L8** (CDCl₃, 400.0 and 100.6 MHz)

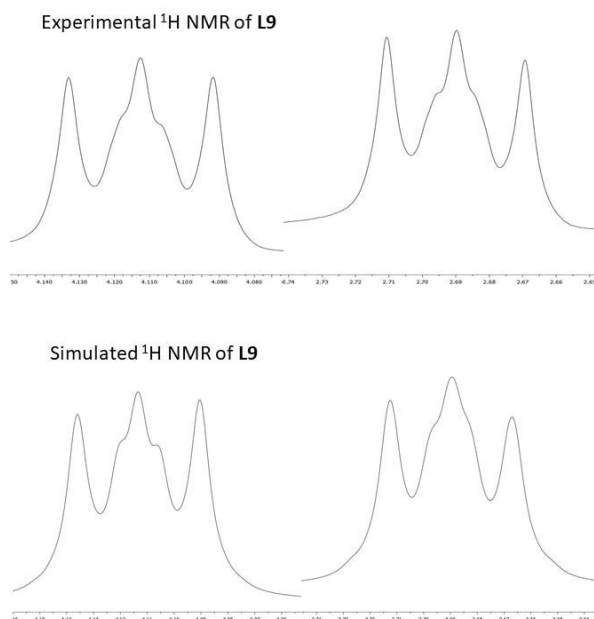


Figure S3.1.10 Detail of the AA'BB' multiplets for L9. Comparison between simulated and experimental spectra (CD_3CN , 400.0 MHz)

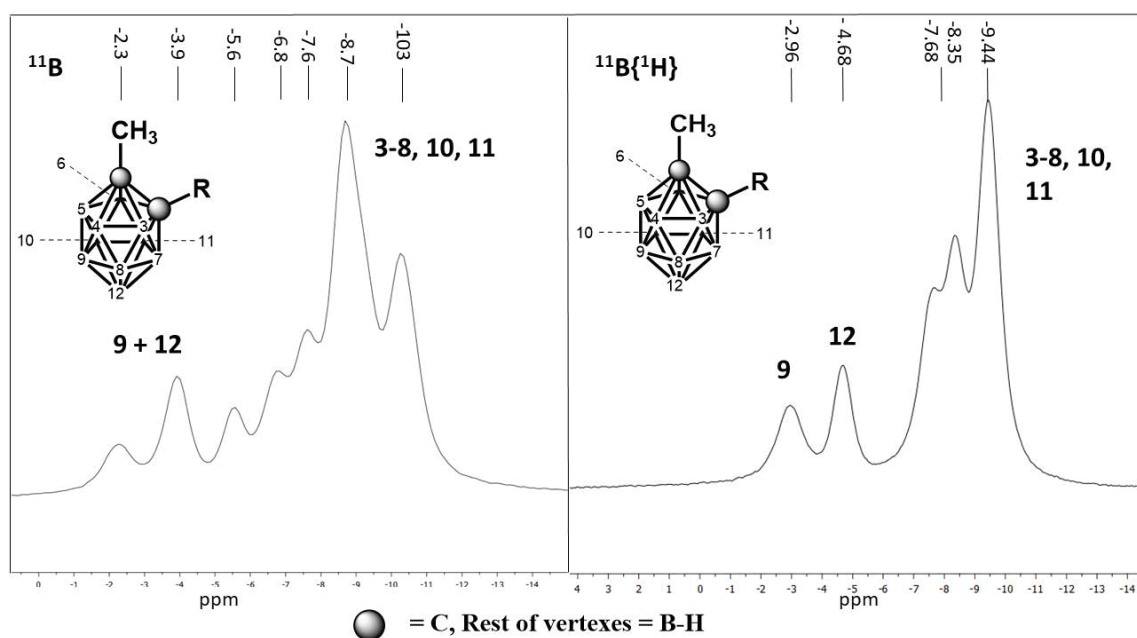


Figure S3.1.11 ^{11}B (left) and $^{11}\text{B}\{^1\text{H}\}$ NMR (right) spectra of S1 (AcD_6 , 128.6 MHz)

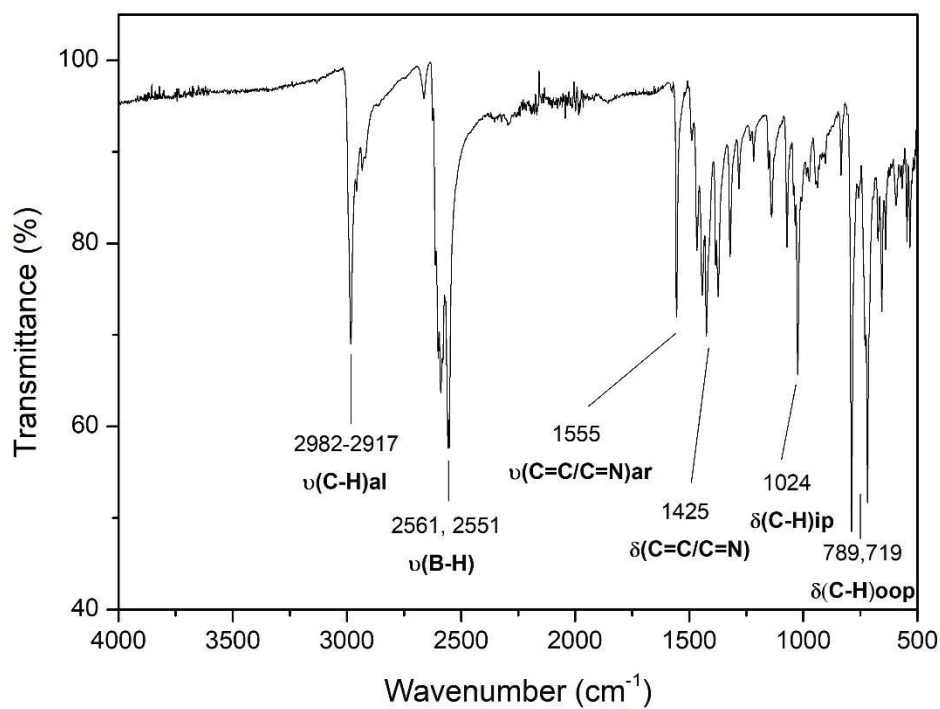


Figure S3.1.12 FTIR-ATR spectrum of L10

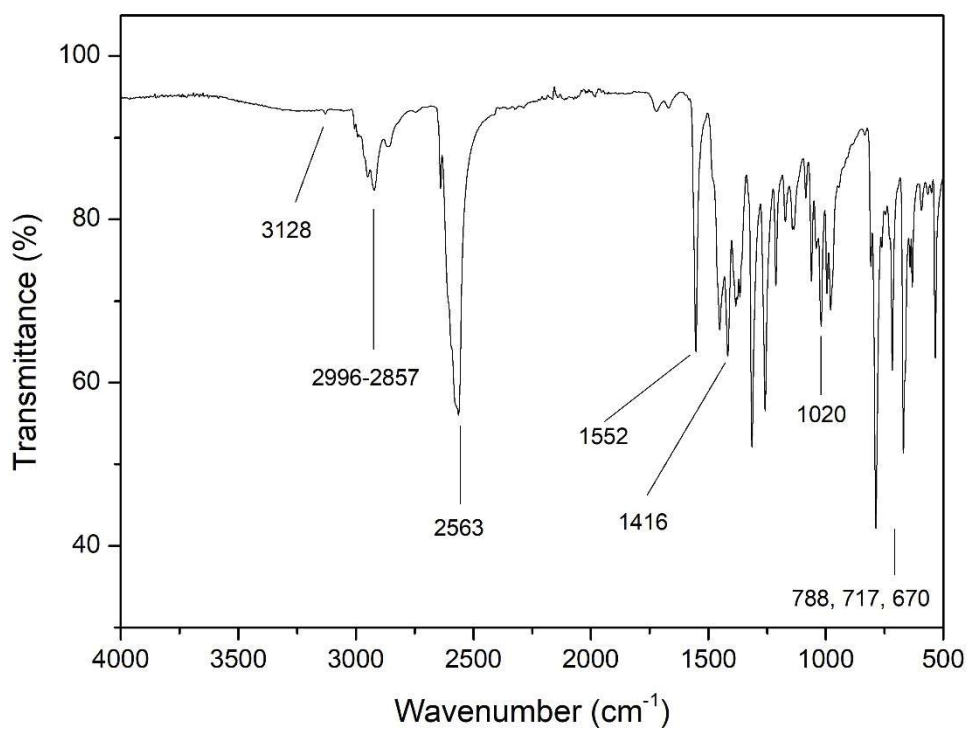


Figure S3.1.13 FTIR-ATR spectrum of L11

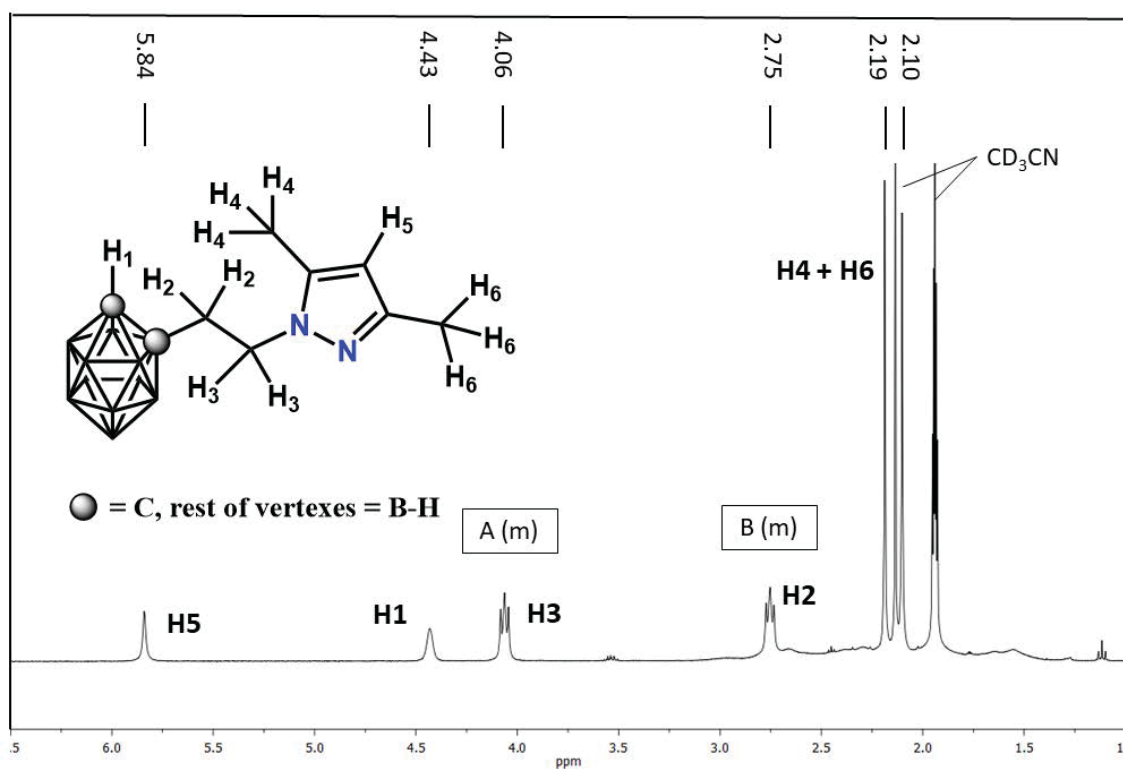


Figure S3.1.11 ¹H NMR spectrum of **L10** (CD₃CN, 400.0 MHz)

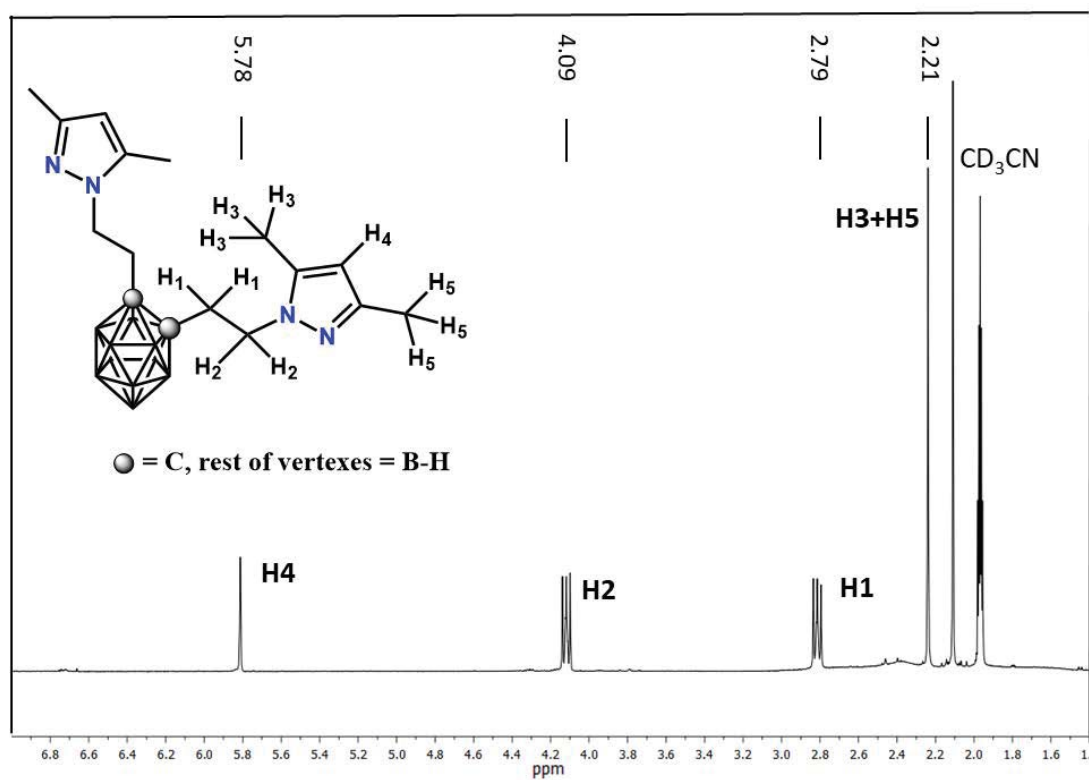


Figure S3.1.12 ¹H NMR spectrum for **L11** (CD₃CN, 400.0 MHz)

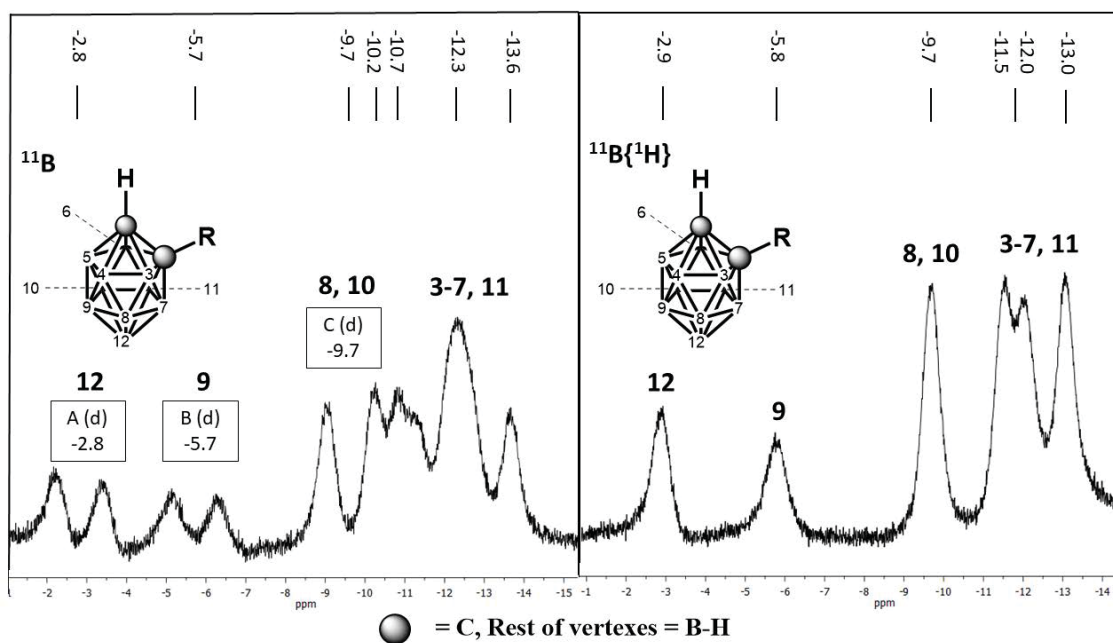


Figure S3.1.16 ^{11}B (left) and $^{11}\text{B}\{^1\text{H}\}$ NMR (right) spectra for L10 (CD_3CN , 128.6 MHz)

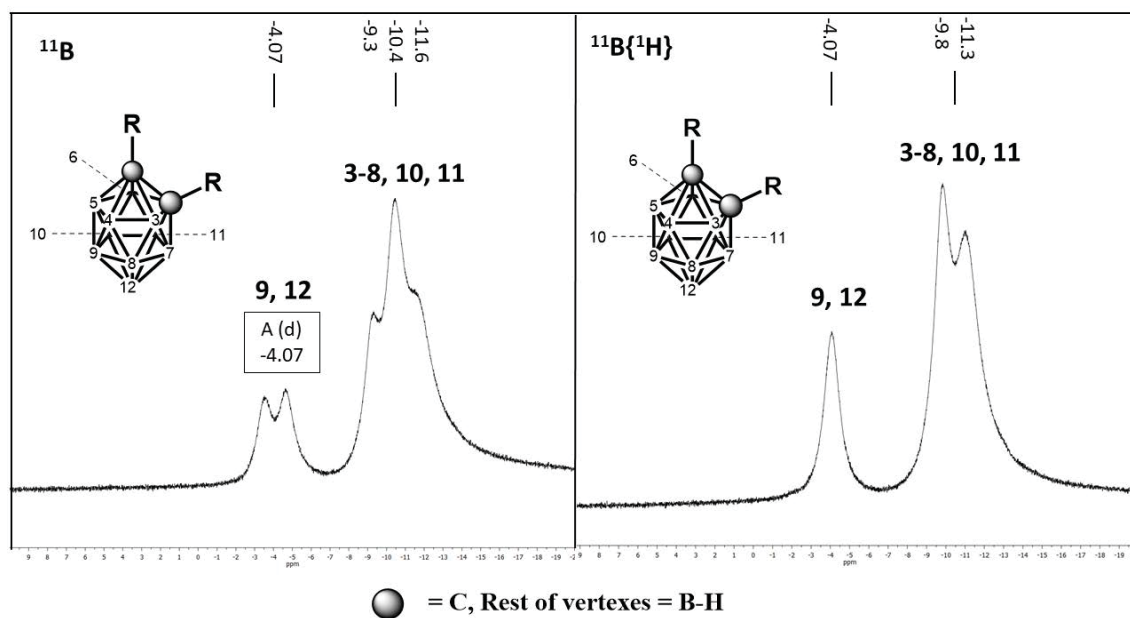


Figure S3.1.13 ^{11}B (left) and $^{11}\text{B}\{^1\text{H}\}$ NMR (right) spectra for L11 (CD_3CN , 128.6 MHz)

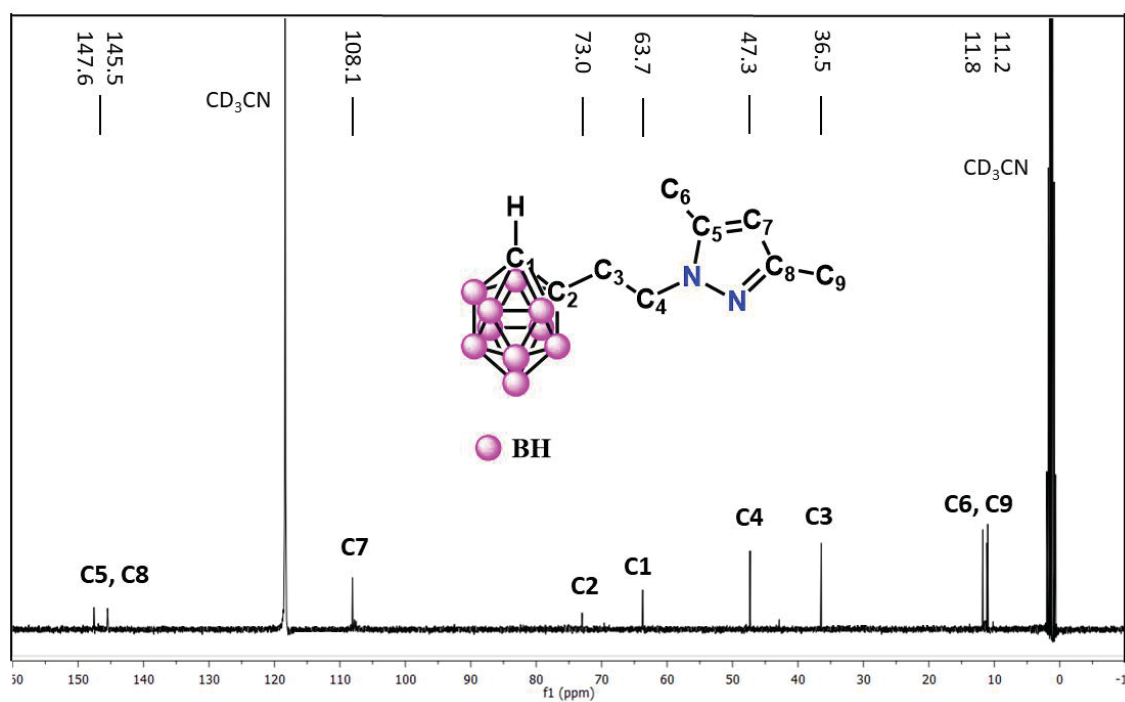


Figure S3.1.14 $^{13}\text{C}\{^1\text{H}\}$ NMR spectrum of L10 (CD_3CN , 100.6 MHz).

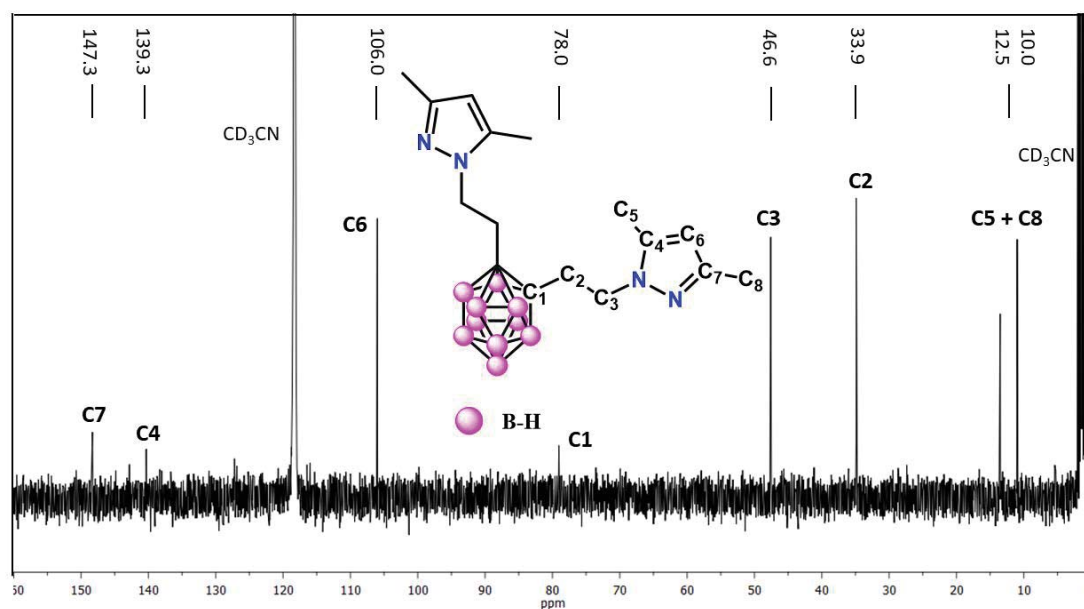
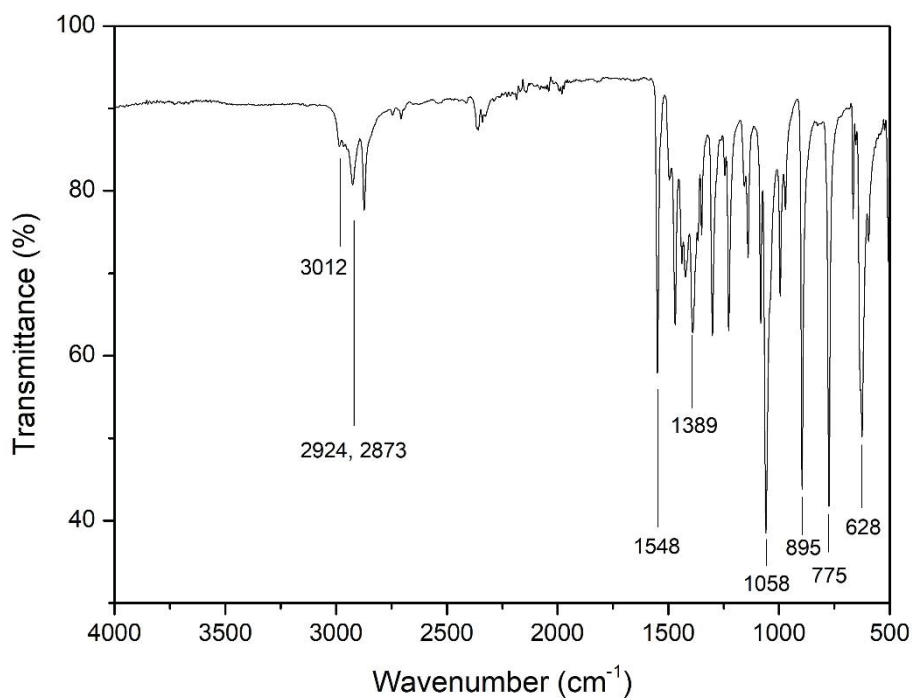
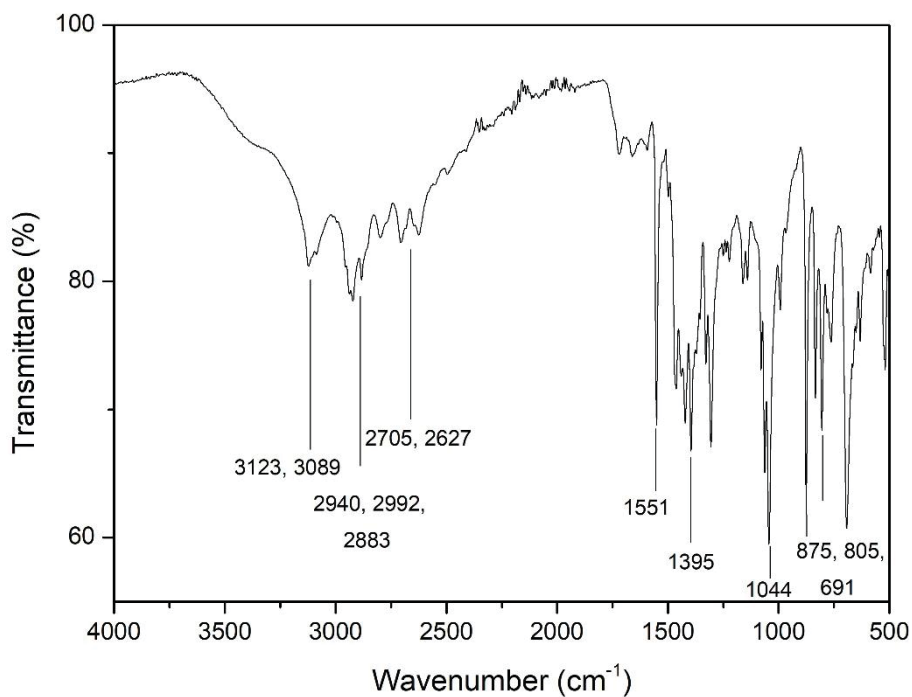


Figure S3.1.15 $^{13}\text{C}\{^1\text{H}\}$ RMN spectrum for L11 (CD_3CN , 100.6 MHz)

Annex for Section 3.2**Figure S3.2.1** FTIR-ATR spectrum of **1****Figure S3.2.2** FTIR-ATR spectrum of **2**

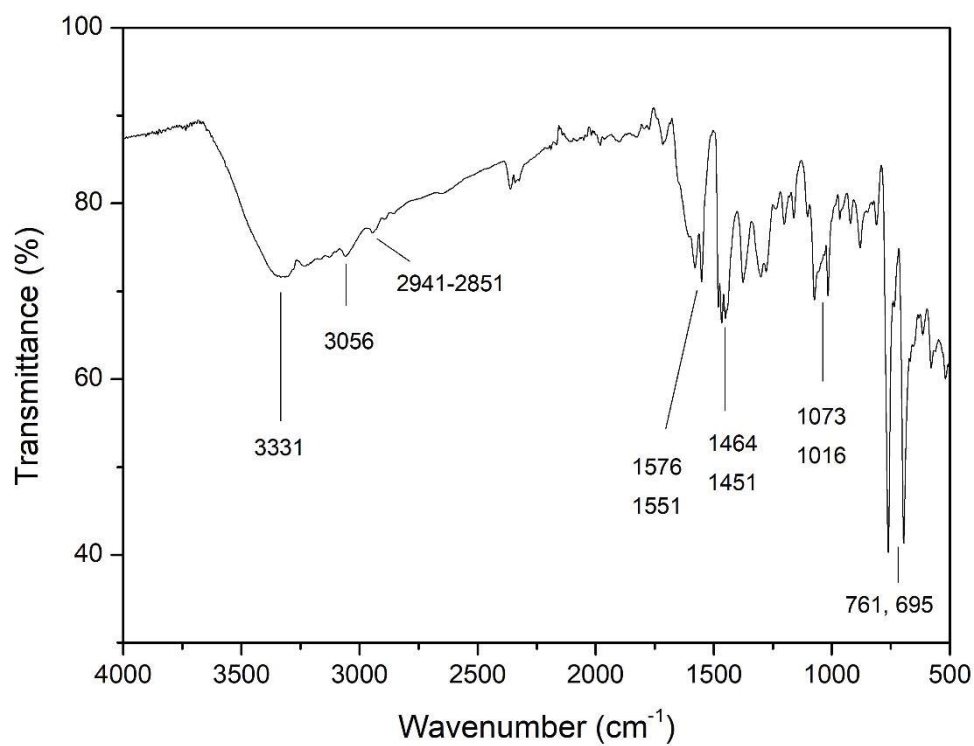


Figure S3.2.3 FTIR-ATR spectrum of **3·HL2**

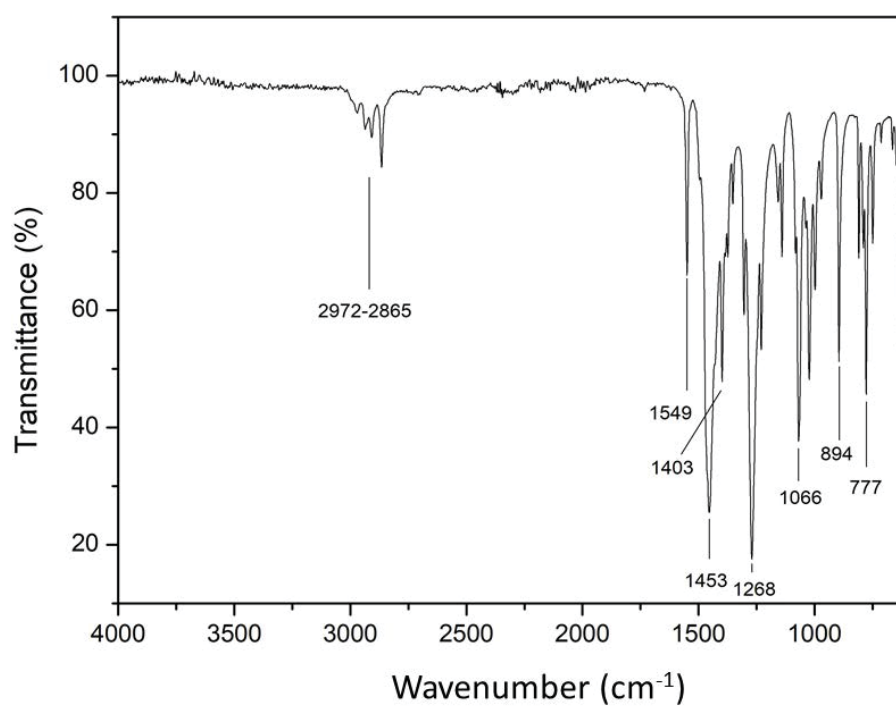


Figure S3.2.4 FTIR-ATR spectrum of **5**.

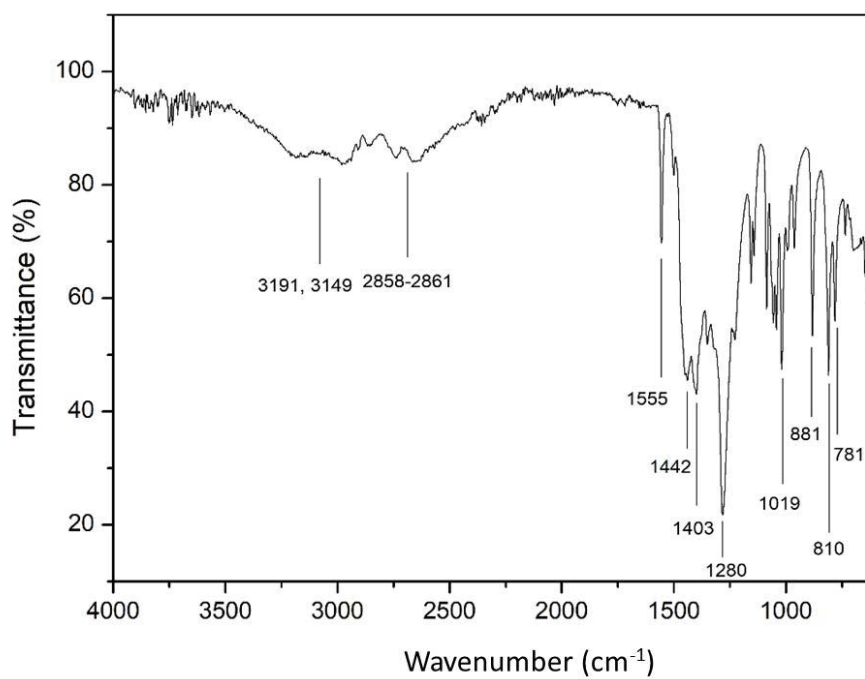


Figure S3.2.5 FTIR-ATR spectrum of **6**.

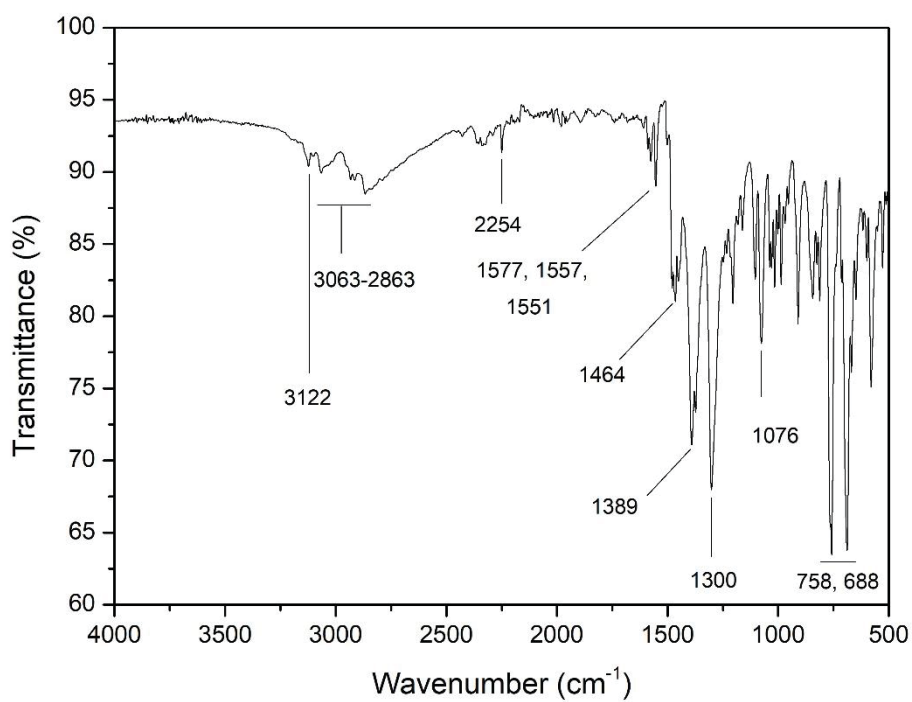


Figure S3.2.6 FTIR-ATR spectrum of **7·2(CH₃CN)**.

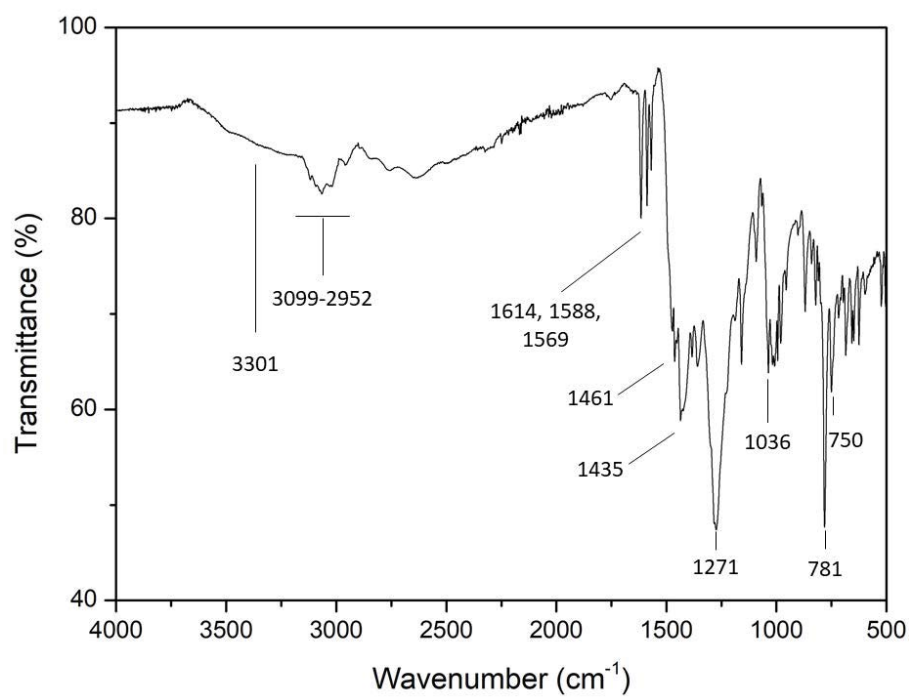


Figure S3.2.7 FTIR-ATR spectrum of $8 \cdot H_2O$.

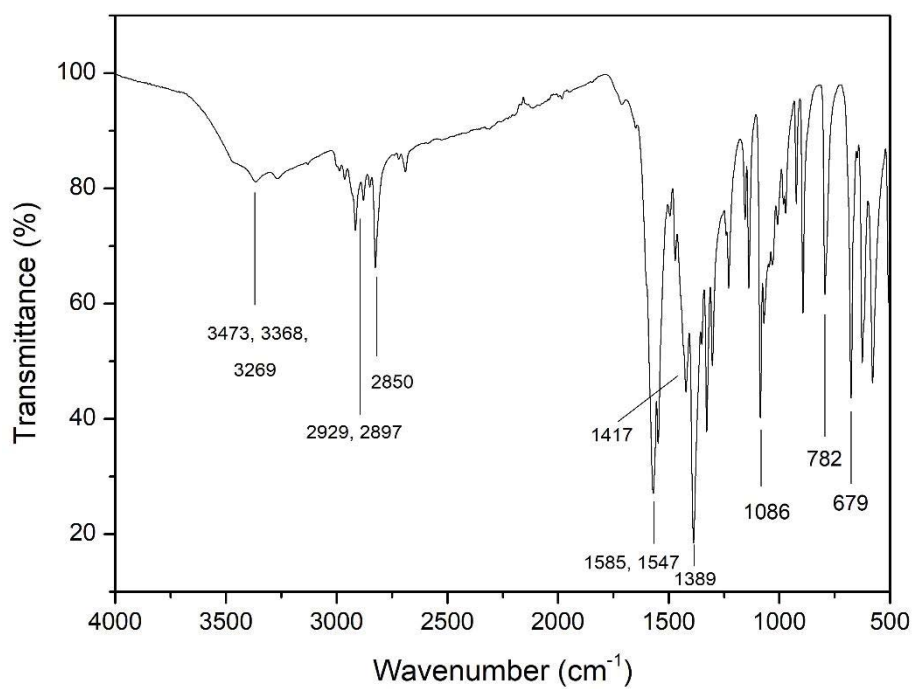


Figure S3.2.8 FTIR-ATR spectrum of $9 \cdot 6H_2O$.

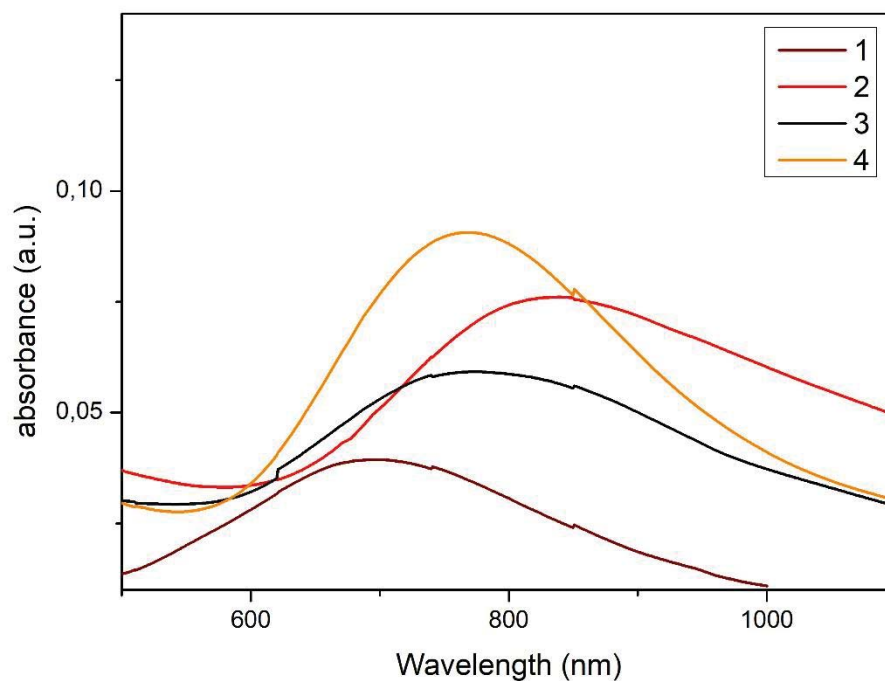


Figure S3.2.9 UV-Vis spectra of **1-4**·(CH₂Cl₂)(H₂O) (MeOH, $8.92 \cdot 10^{-3}$ - $1.33 \cdot 10^{-3}$ M)

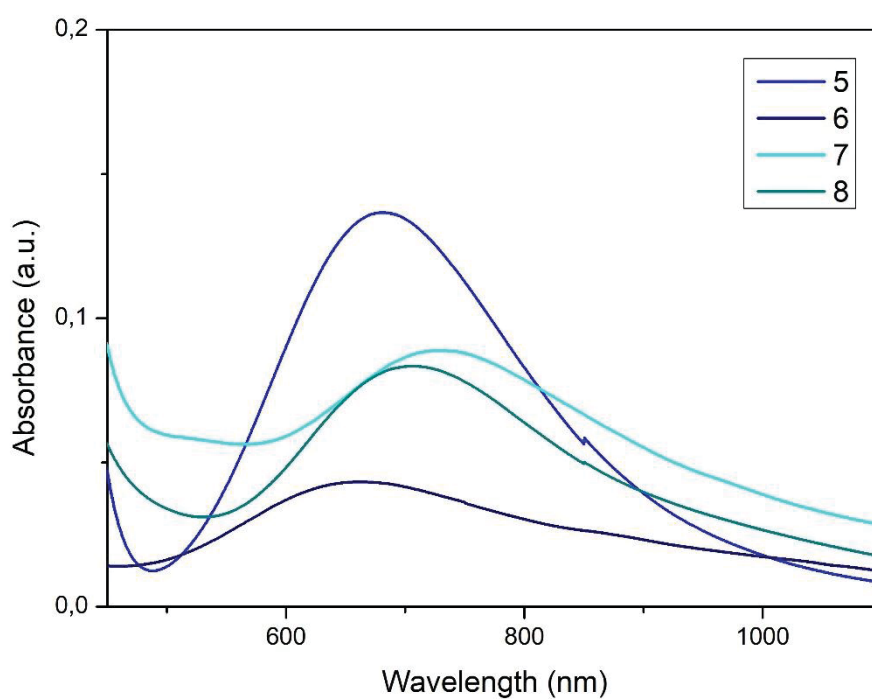


Figure S3.2.10 UV-Vis spectra of **5** (DMF; $1.10 \cdot 10^{-3}$ M), **6** (MeOH, $1.37 \cdot 10^{-3}$ M), **7**·2CH₃CN and **8**·H₂O (CH₃CN, $5.69 \cdot 10^{-4}$ M and $6.95 \cdot 10^{-4}$ M, respectively)

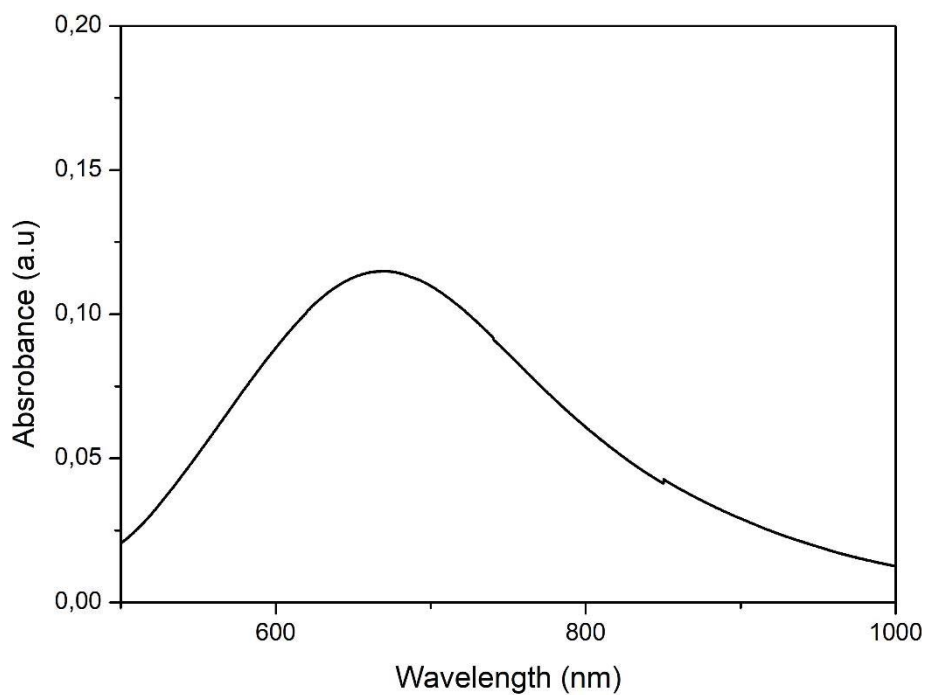


Figure S3.2.11 UV-Vis spectrum of compound **9** (MeOH, $9.93 \cdot 10^{-4}$ M).

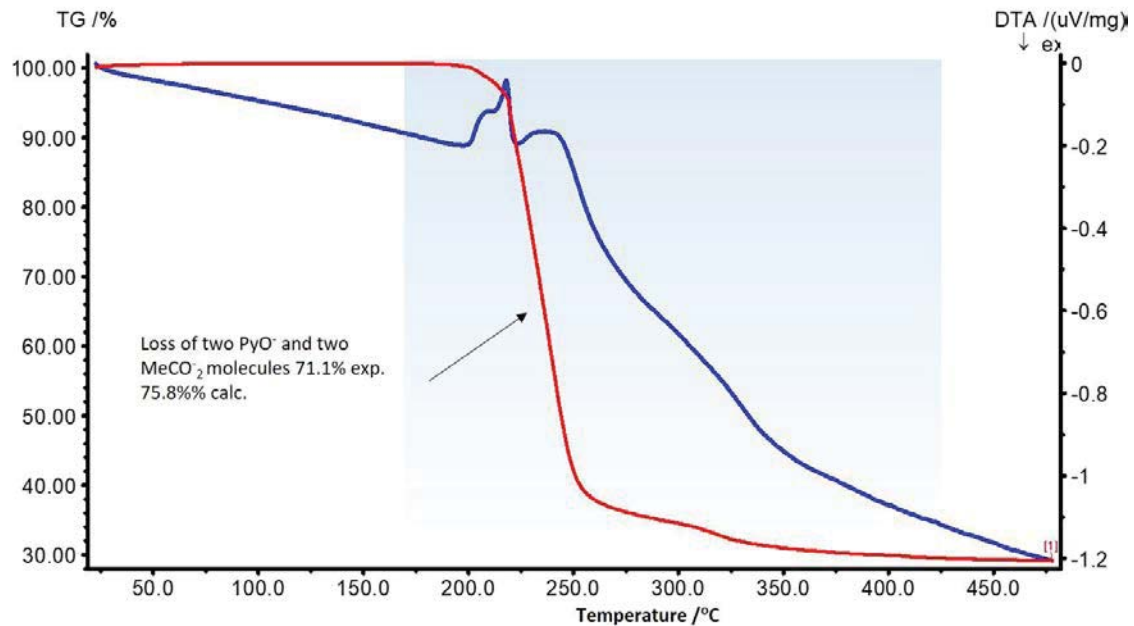


Figure S3.2.11 TGA/DTA Analysis of compound $[\text{Cu}(\text{CH}_3\text{COO})(\mu\text{-L1})_2]$ (**9**, “dry” phase)

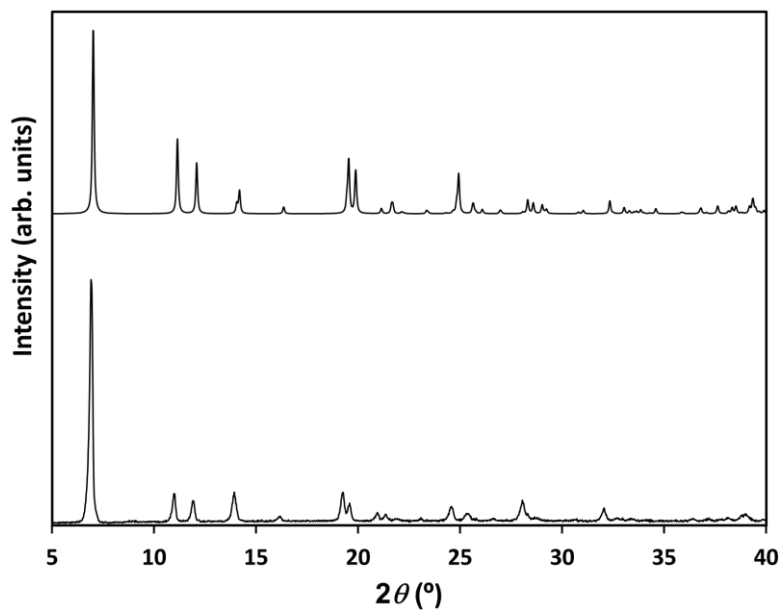


Figure S3.2.13 X-ray diffractogram of $\{[\text{Cu}(\mu\text{-NO}_3)(\mu\text{-L1})]_2\}_n$ (**5**, bottom) measured at r.t. Calculated pattern from resolved crystal structure is also included (top) as a reference, from monocrystal measured at 100 K.

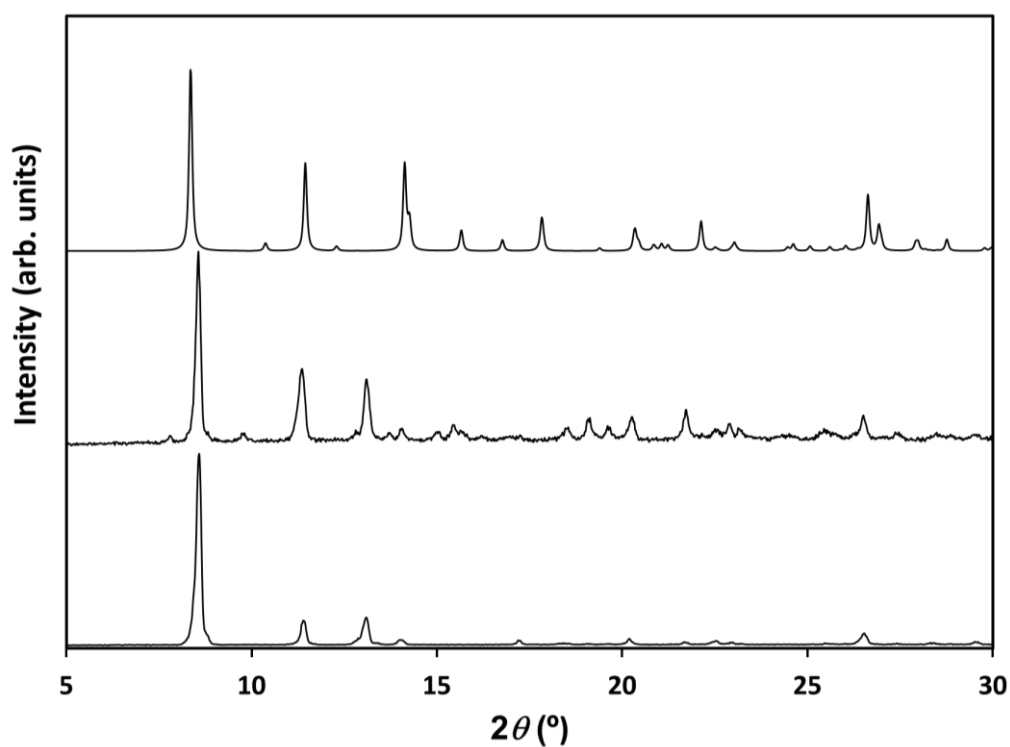


Figure S3.2.14 X-ray diffractogram of **9**·4H₂O (middle) and **9** (dry phase, bottom) measured at r.t. Calculated pattern from resolved crystal structure **9**·6H₂O (crystal) is also included (top) as a reference, from monocrystal measured at 150 K.

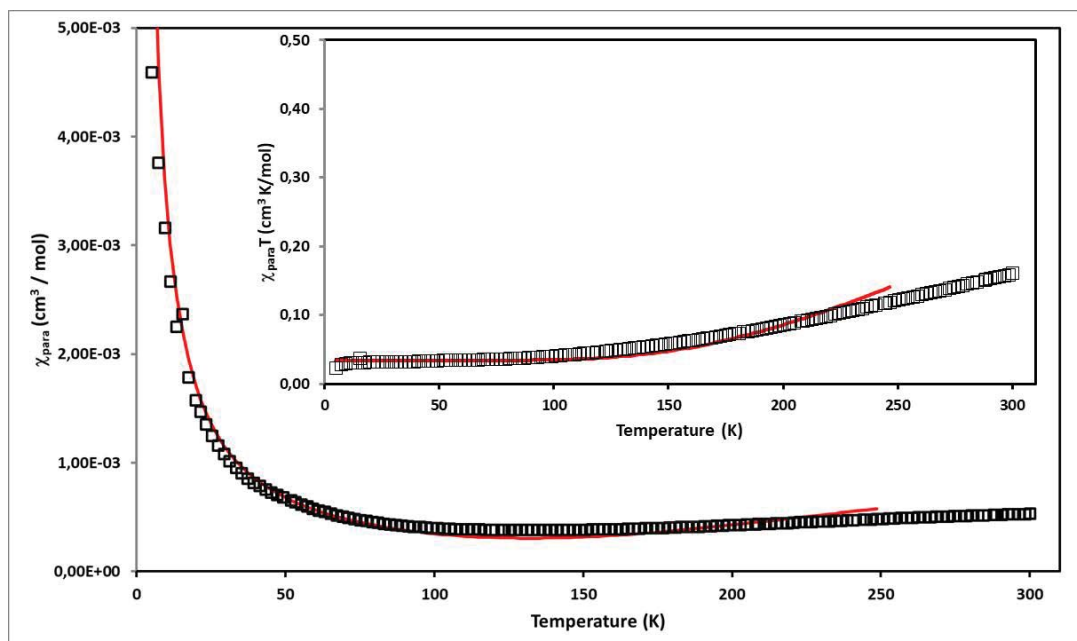


Figure S3.2.15 Thermal variation of χ_{ρ} and $\chi_{\rho}T$ (inset) for **9**. Solid line represents the best fit for the proposed model (see text).

Annex for Section 3.3

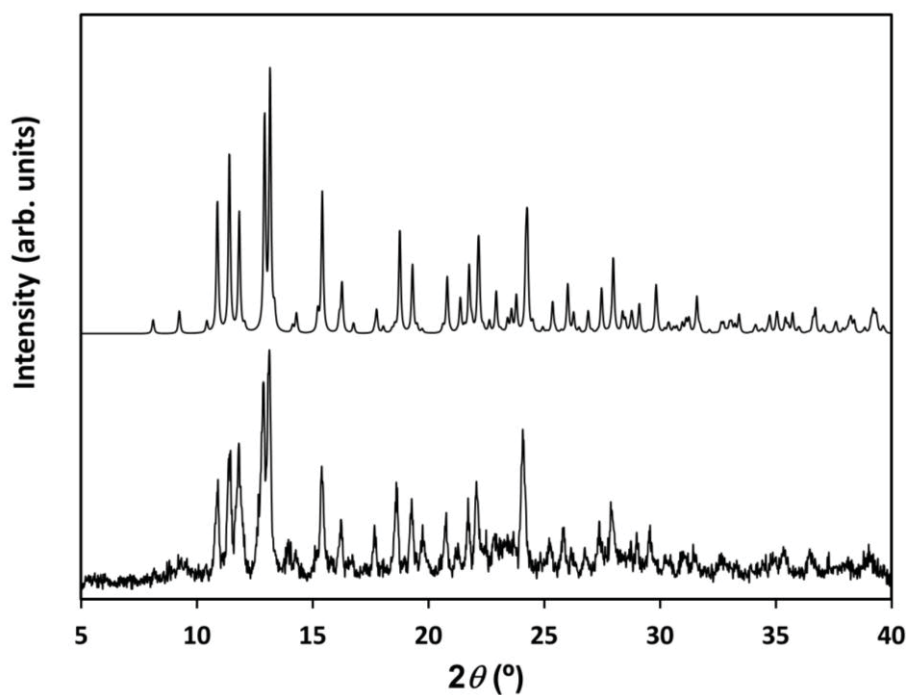


Figure S3.3.1 X-ray diffractogram of $[\text{Zn}(\text{L4})\text{Cl}_2]_2$ (**10**, bottom) measured at 298 K. Calculated pattern from resolved crystal structure is also included (top) as a reference, from monocrystal XRD measured at 100(2) K.

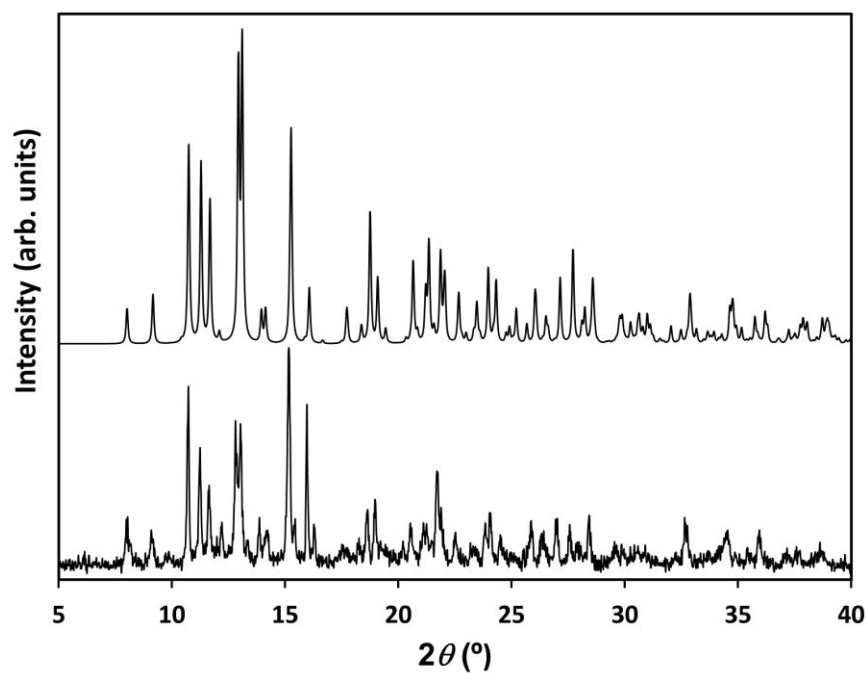


Figure S3.3.2 X-ray diffractogram of $[\text{Cd}(\text{L4})\text{Cl}_2]_2$ (**11**, bottom) measured at 298 K. Calculated pattern from resolved crystal structure is also included (top) as a reference, from monocrystal XRD measured at 100(2) K.

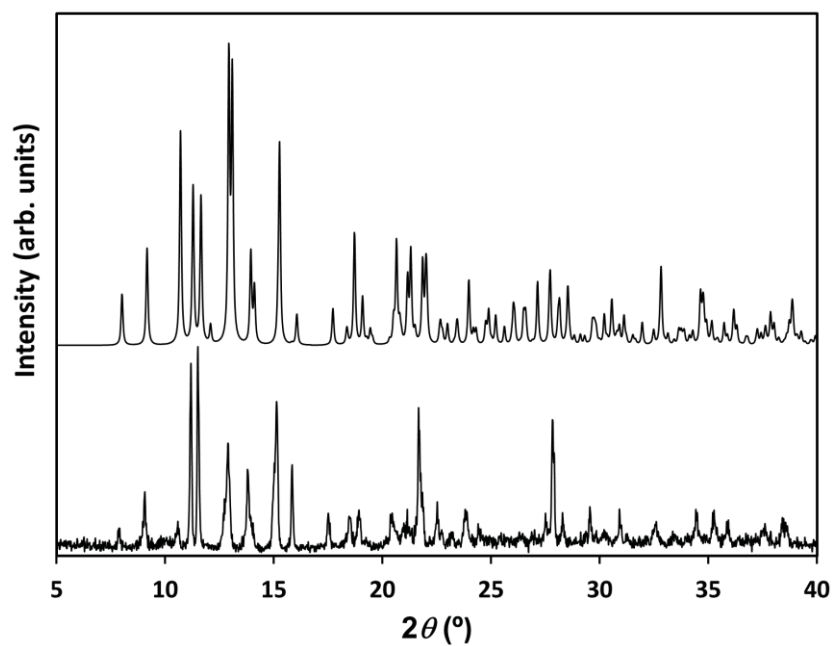


Figure S3.3.3 X-ray diffractogram of $[\text{Hg}(\text{L4})\text{Cl}_2]_2$ (**12**, bottom) measured at 298 K. Calculated pattern from resolved crystal structure is also included (top) as a reference, from monocrystal XRD measured at 100(2) K

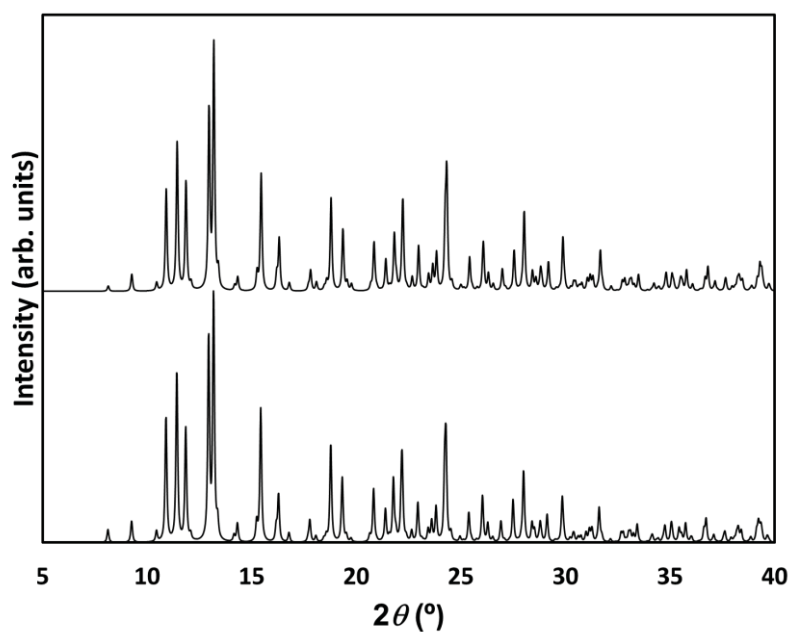


Figure S3.3.4 X-ray diffractogram of $[\text{Co}(\text{L4})\text{Cl}_2]_2 \cdot 1/2(\text{H}_2\text{O})$ (**13**, bottom) measured at r.t. Calculated pattern from resolved crystal structure is also included (top) as a reference, from monocrystal XRD measured at 100(2) K.

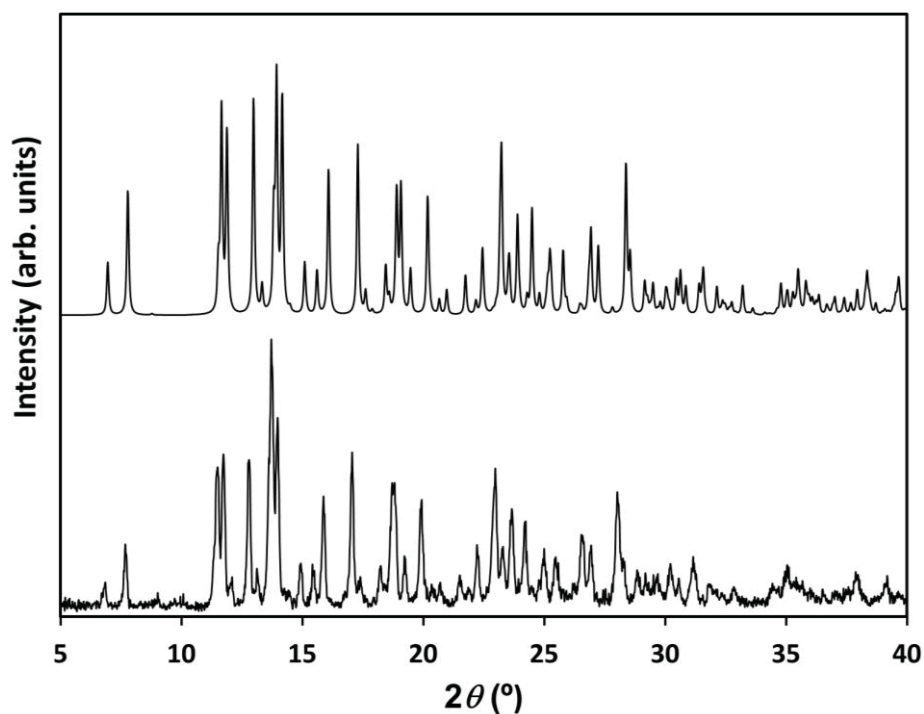


Figure S3.3.5 X-ray diffractogram of $\{[\text{Zn}(\text{L5})\text{Cl}_2] \cdot 1/2\text{H}_2\text{O}\}_n$ (**15**, bottom) measured at 298 K. Calculated pattern from resolved crystal structure is also included (top) as a reference, from monocystal XRD measured at 100.0 K.

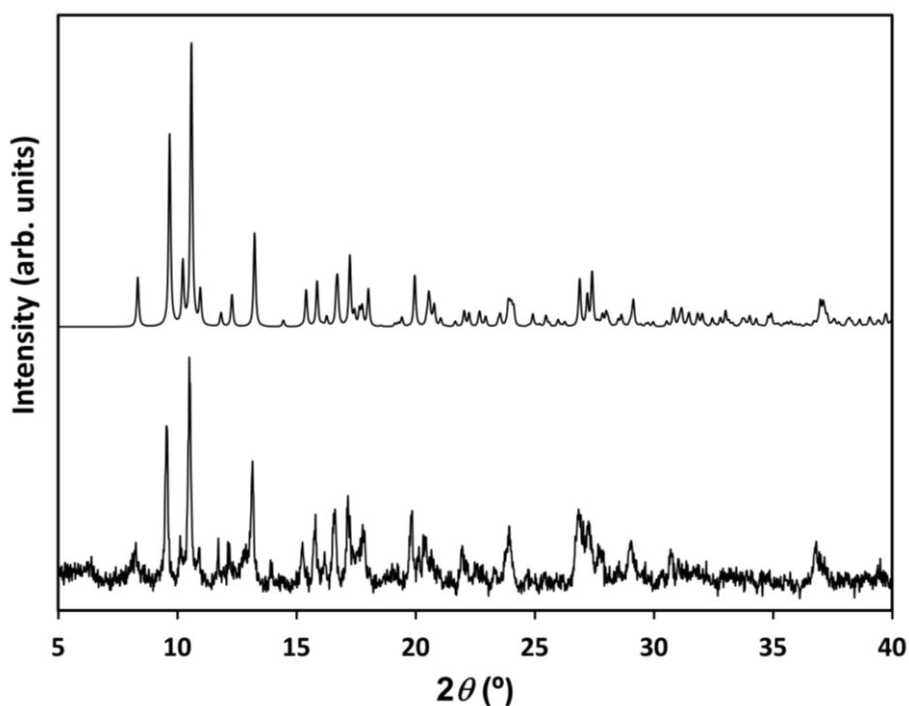


Figure S3.3.6 X-ray diffractogram of $\{[\text{Cd}(\text{L5})\text{Cl}_2] \cdot 1/2\text{EtOH}\}_n$ (**16**, bottom) measured at 298 K. Calculated pattern from resolved crystal structure is also included (top) as a reference, from monocystal XRD measured at 100(2) K.

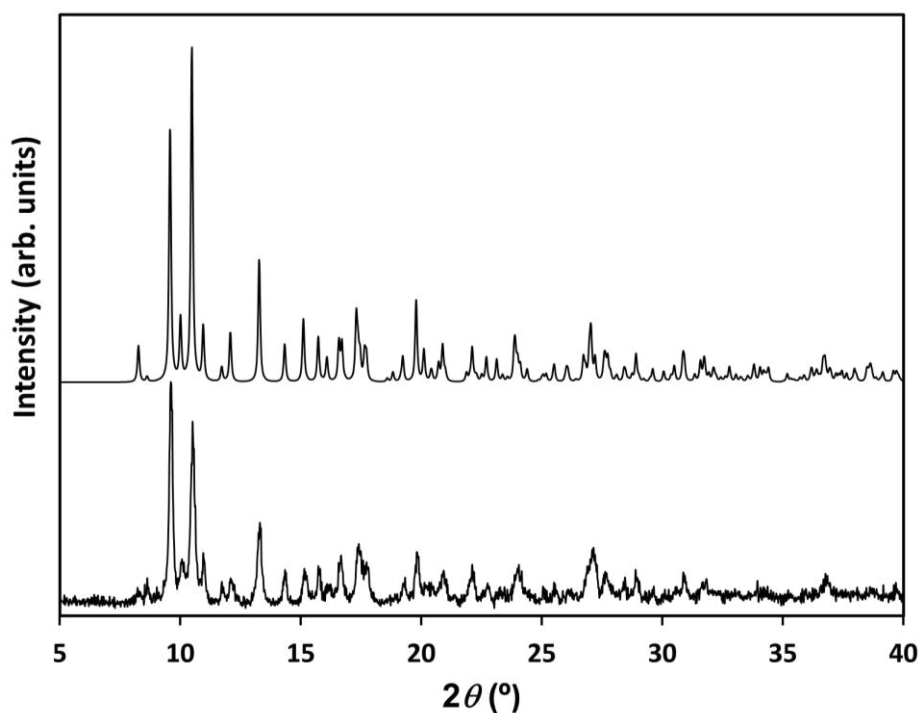


Figure S3.3.7 X-ray diffractogram of $\{[\text{Hg}(\text{L5})\text{Cl}_2] \cdot 1/2\text{EtOH}\}_n$ (**17**, bottom) measured at 298 K. Calculated pattern from resolved crystal structure is also included (top) as a reference, from monocystal XRD measured at 298(2) K.

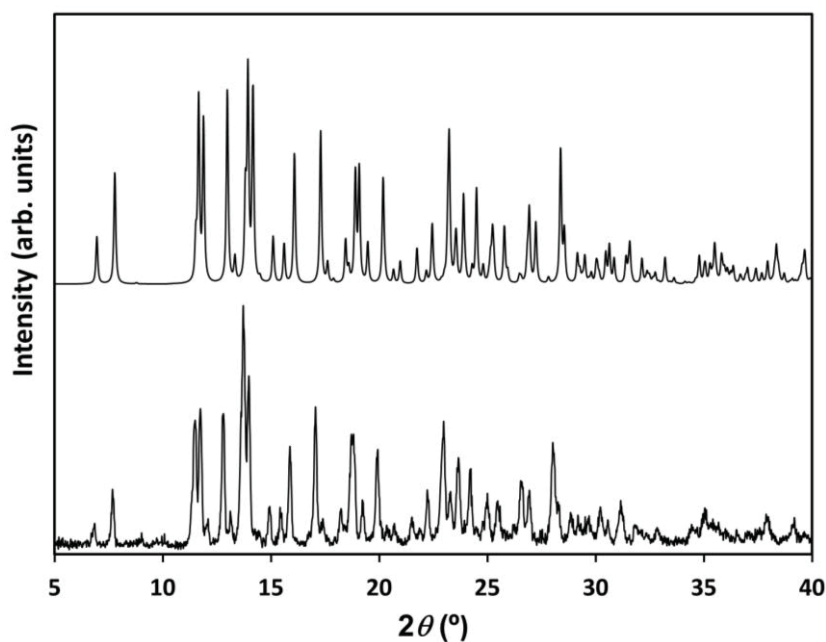


Figure S3.3.8 X-ray diffractogram of $\{[\text{Co}(\text{L5})\text{Cl}_2] \cdot 1/2\text{H}_2\text{O}\}_n$ (**18**, bottom) measured at r.t. Calculated pattern from resolved crystal structure is also included (top) as a reference, from monocystal XRD measured at 100(2) K.

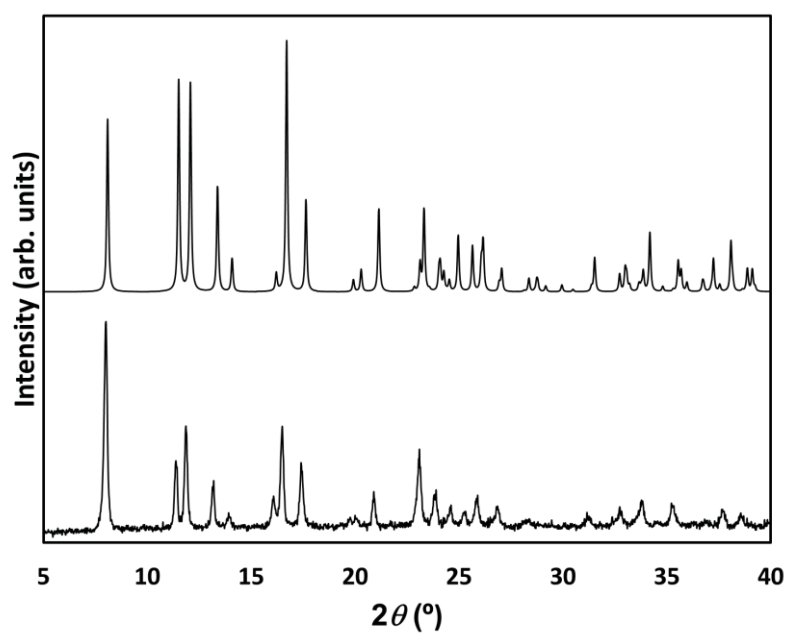


Figure S3.3.9. X-ray diffractogram of $[\text{Cu}_2(\text{L5})\text{Cl}_4]$ (**19**, bottom) measured at r.t. Calculated pattern from resolved crystal structure is also shown (top) as a reference, from monocystal XRD measured at 293(2) K.

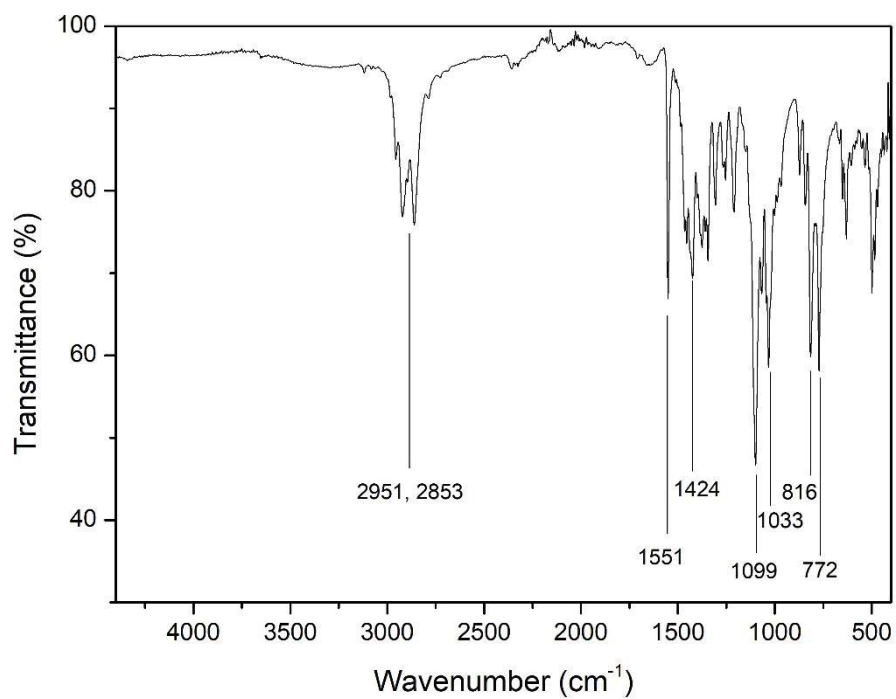


Figure S3.3.10 FTIR-ATR spectrum of compound **10**

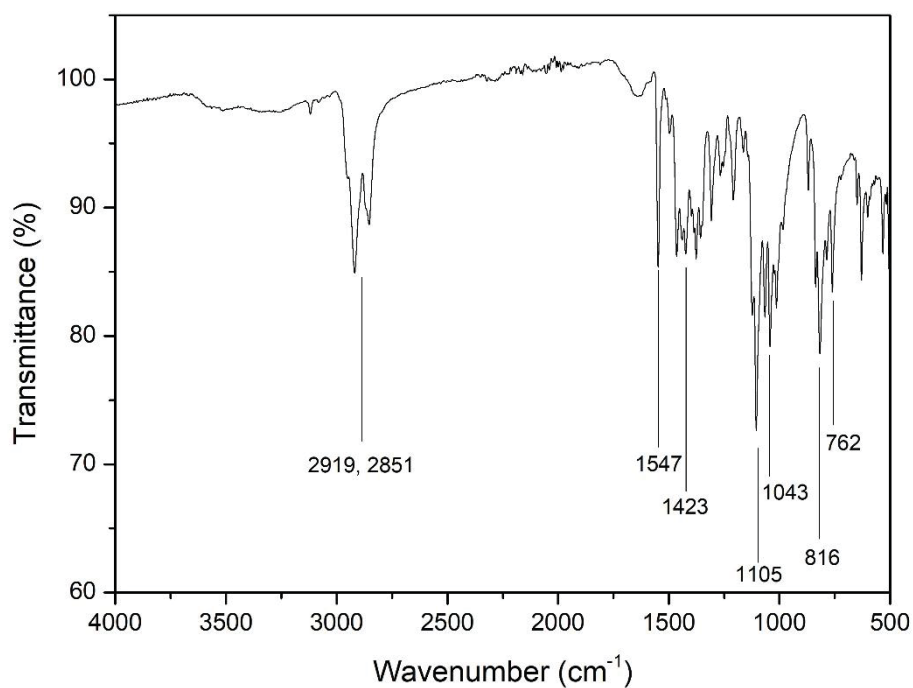


Figure S3.3.11 FTIR-ATR spectrum of compound **11**

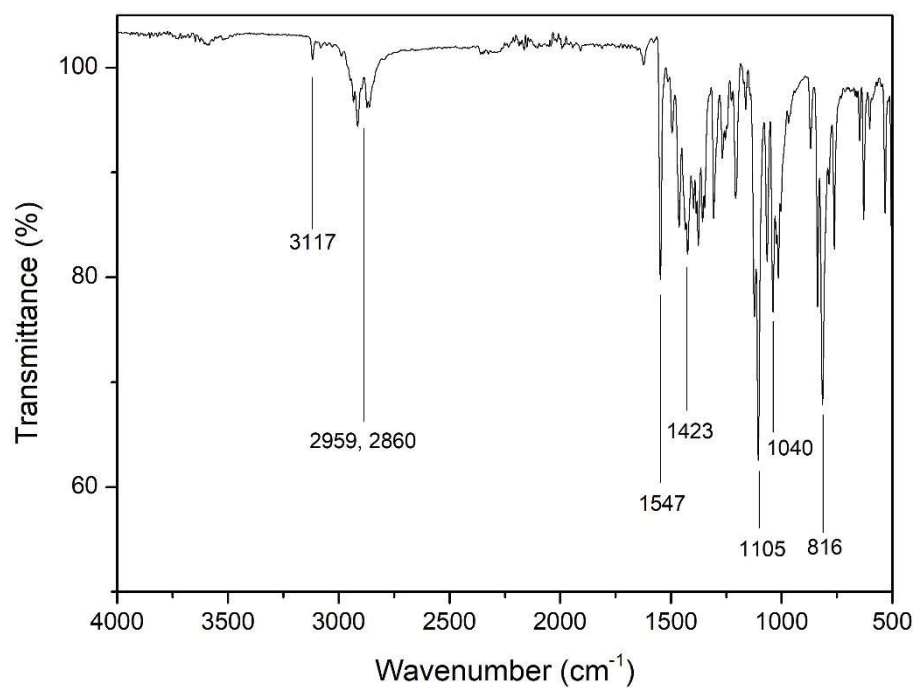


Figure S3.3.12 FTIR-ATR spectrum of compound 12

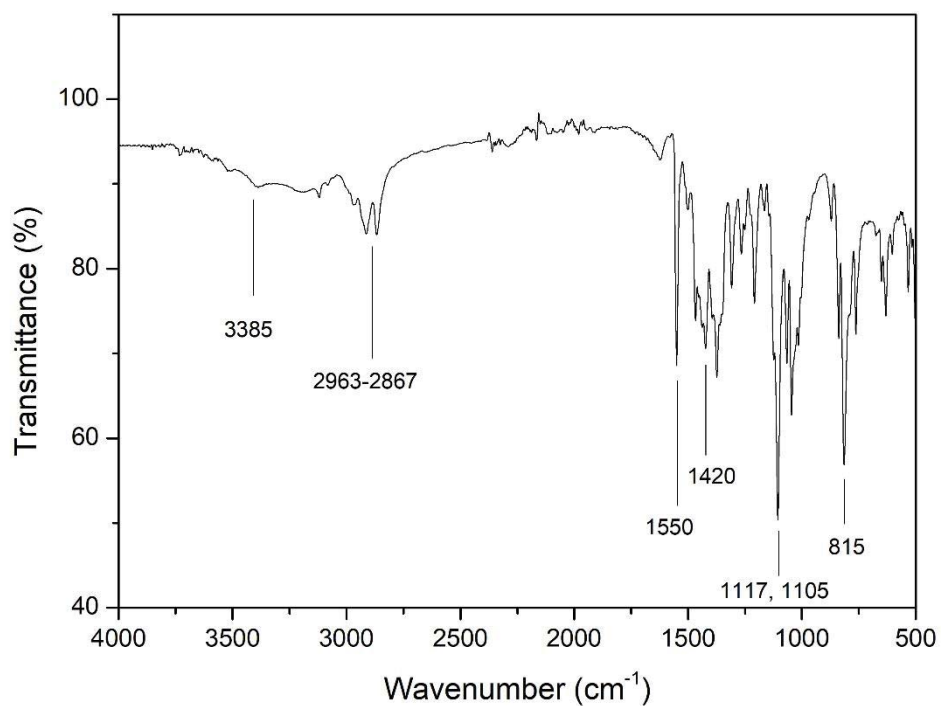


Figure S3.3.13 FTIR-ATR spectrum of compound 13

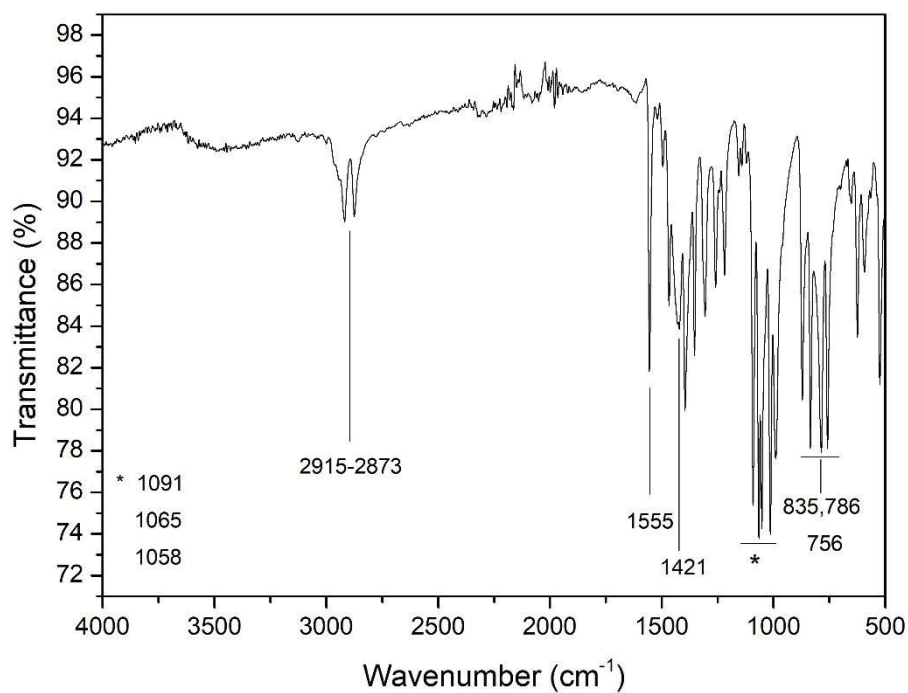


Figure S3.3.14 FTIR-ATR spectrum of compound **14**

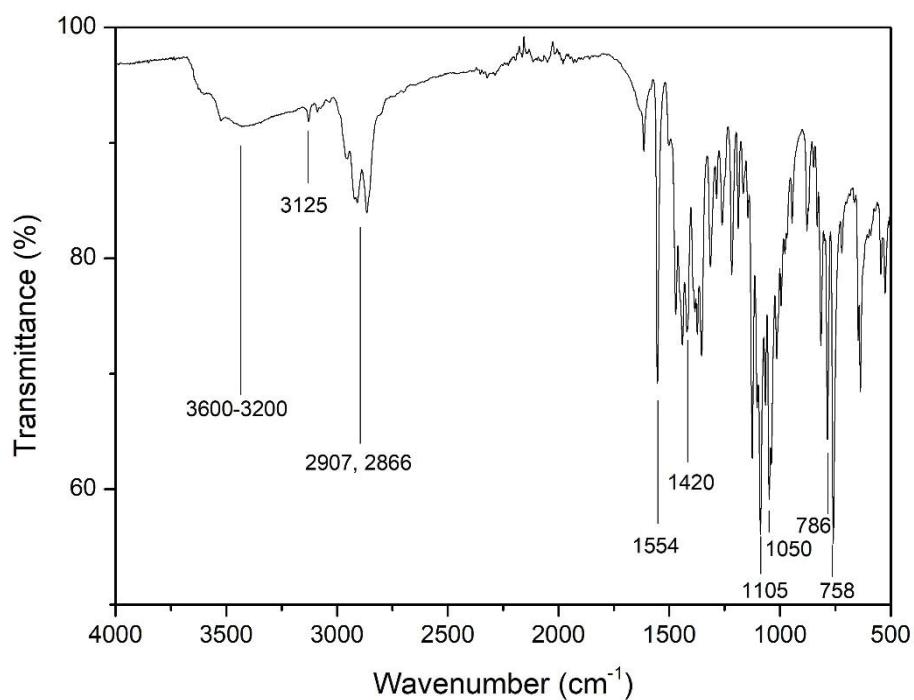


Figure S3.3.15 FTIR-ATR spectrum of compound **15**

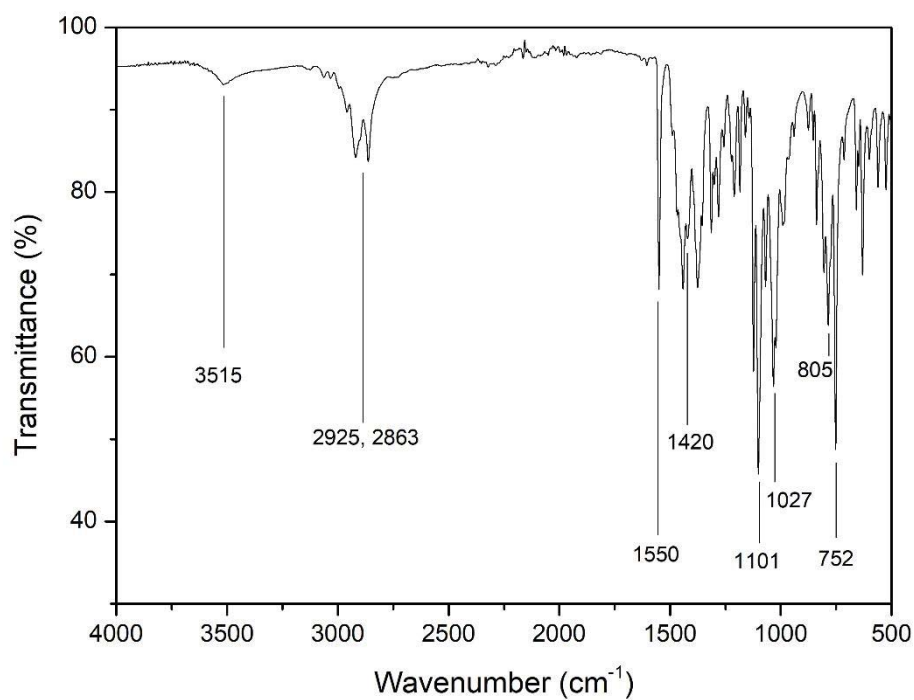


Figure S3.3.16 FTIR-ATR spectrum of compound 17

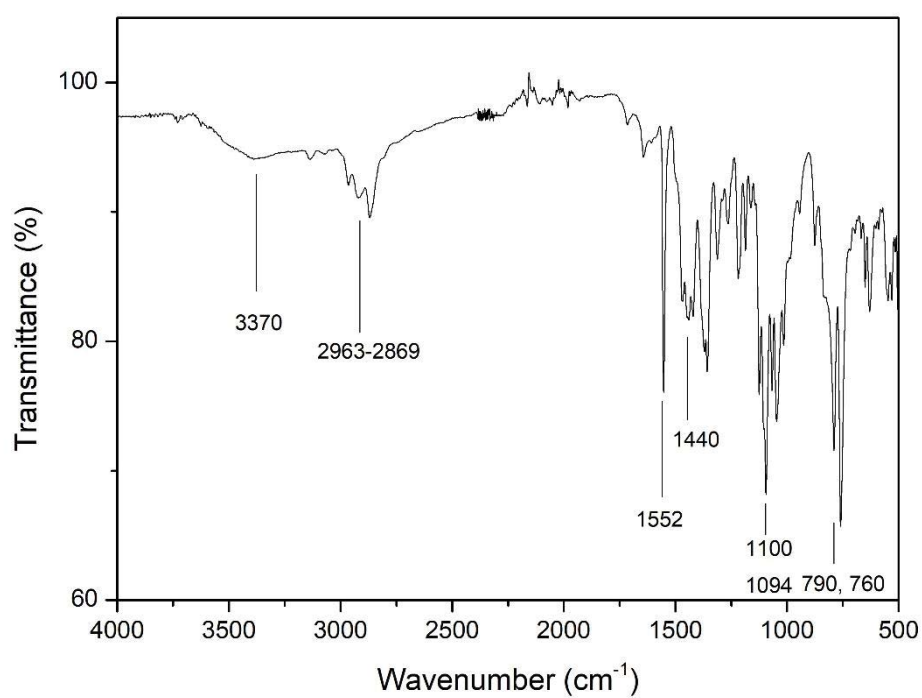


Figure S3.3.17 FTIR-ATR spectrum of compound 18

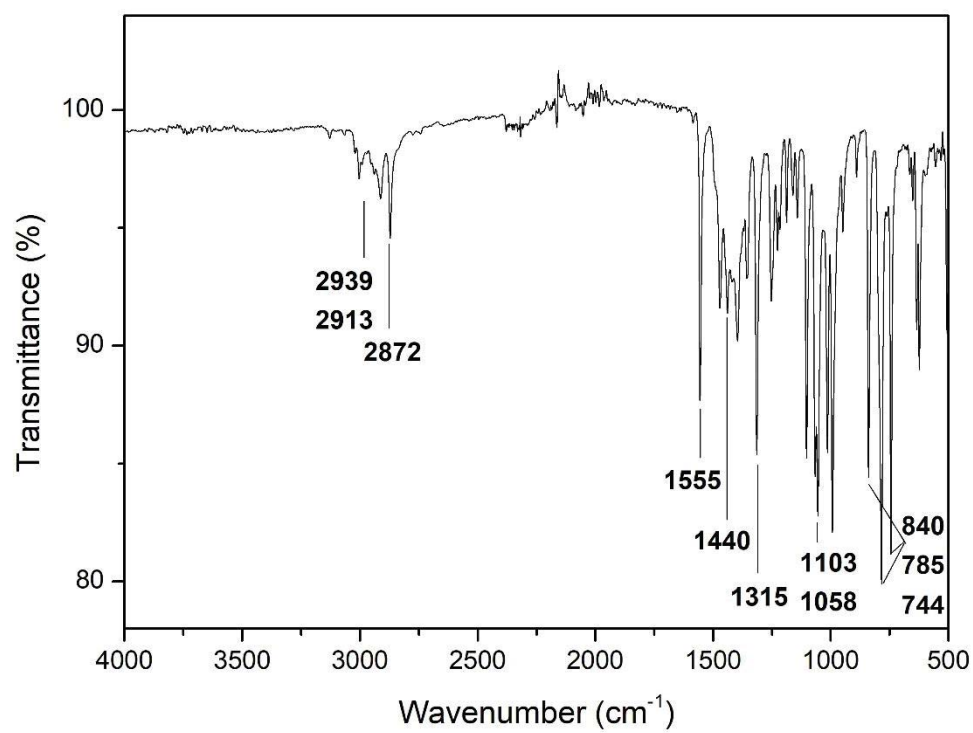


Figure S3.3.18 FTIR-ATR spectrum of compound **19**

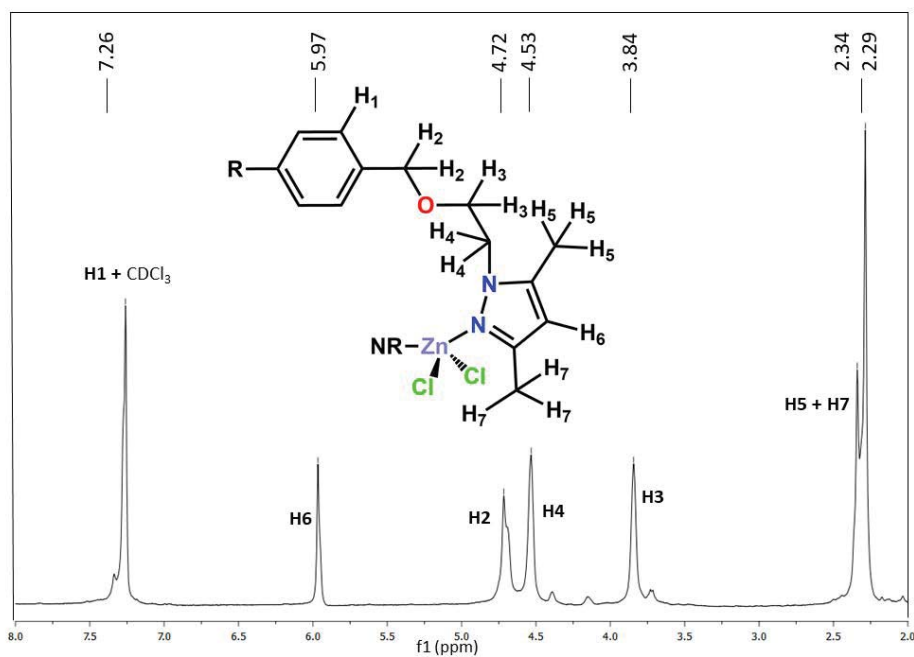


Figure S3.3.19 ¹H NMR spectrum of **10** (CDCl₃, 400.0 MHz)

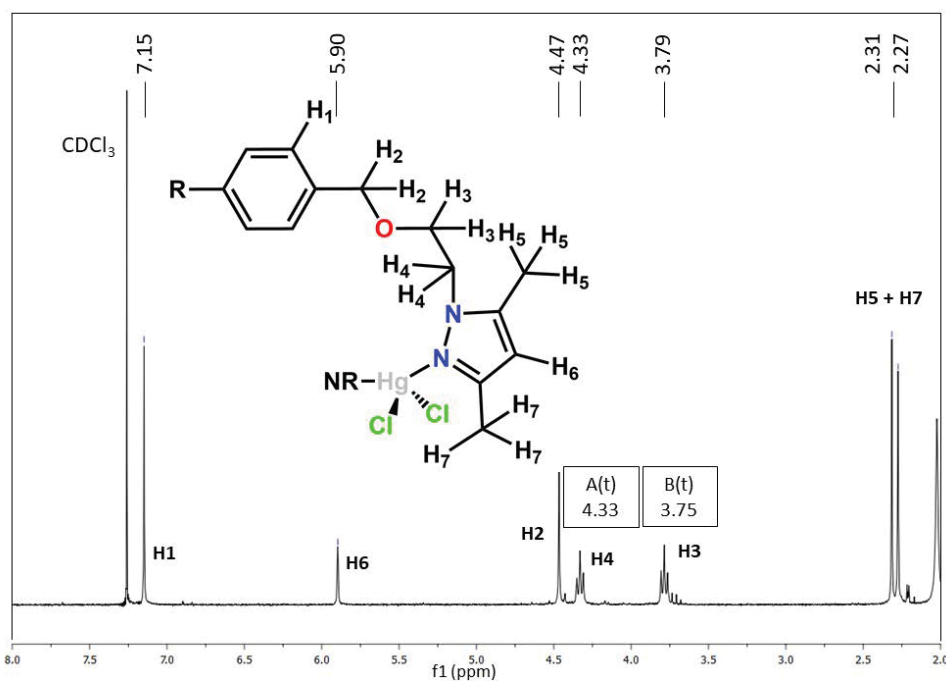


Figure S3.3.20 ¹H NMR spectrum of compound **12** (CDCl₃, 400.0 MHz)

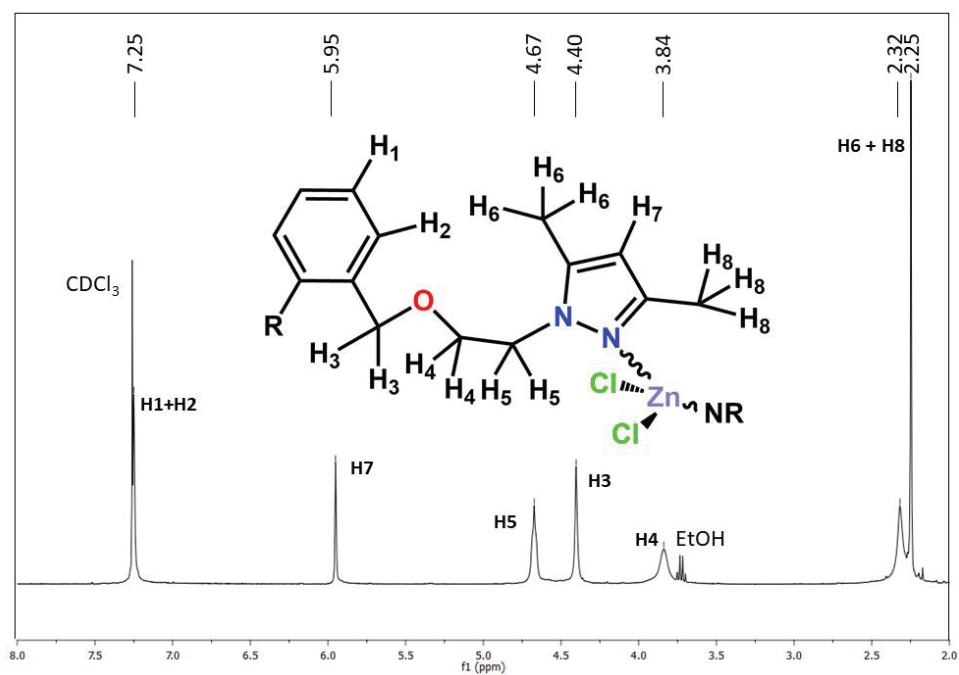


Figure S3.3.21 ¹H NMR spectrum of compound **15** (CDCl₃, 400.0 MHz)

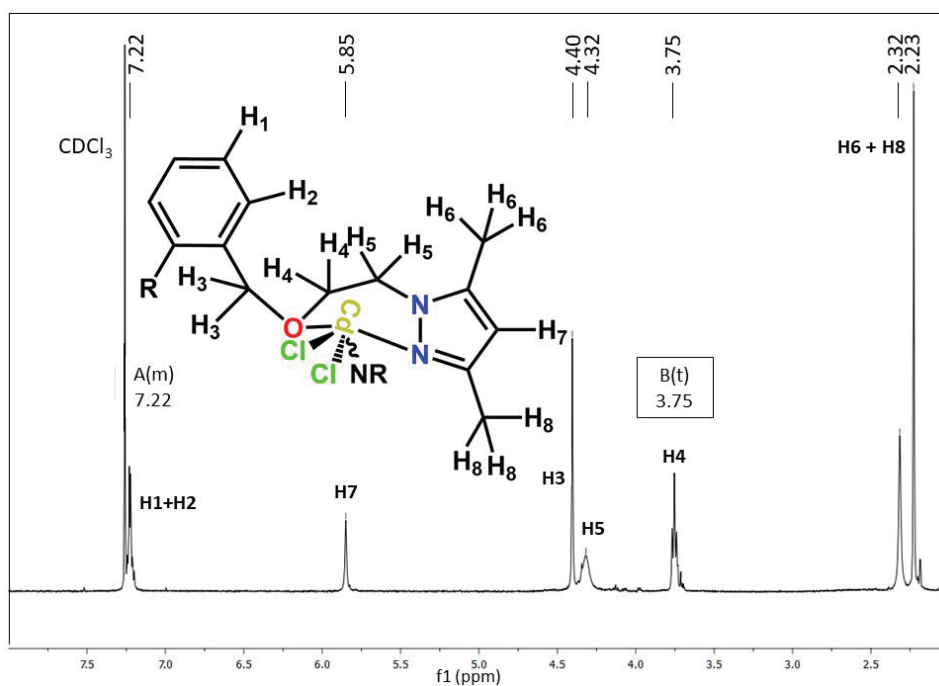


Figure S3.3.22 ¹H NMR spectrum of compound **16** (CDCl₃, 400.0 MHz)

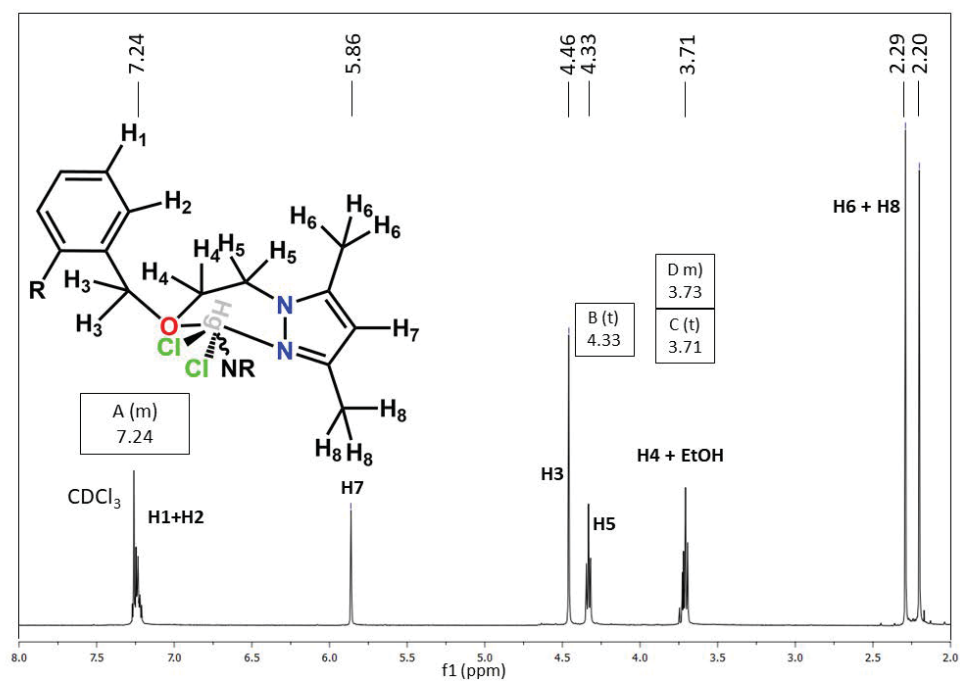


Figure S3.3.23 ¹H NMR spectrum of compound **17** (CDCl₃, 400.0 MHz)

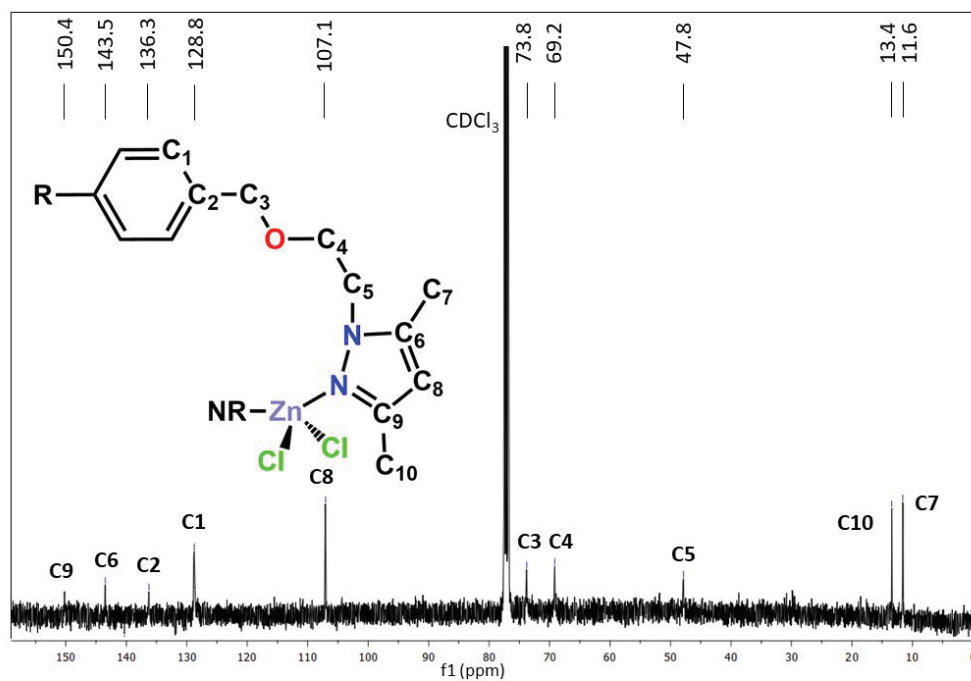


Figure S3.3.24 ¹³C{¹H} NMR spectrum of compound **10** (CDCl₃, 100.6 MHz)

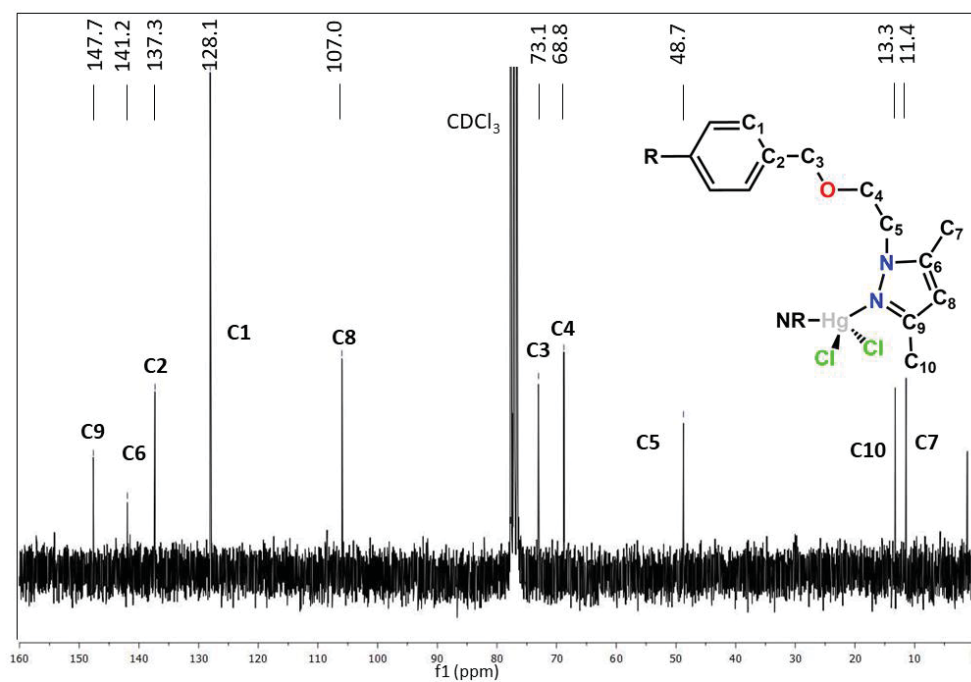


Figure S3.3.25 ¹³C{¹H} NMR spectrum of compound **12** (CDCl₃, 100.6 MHz)

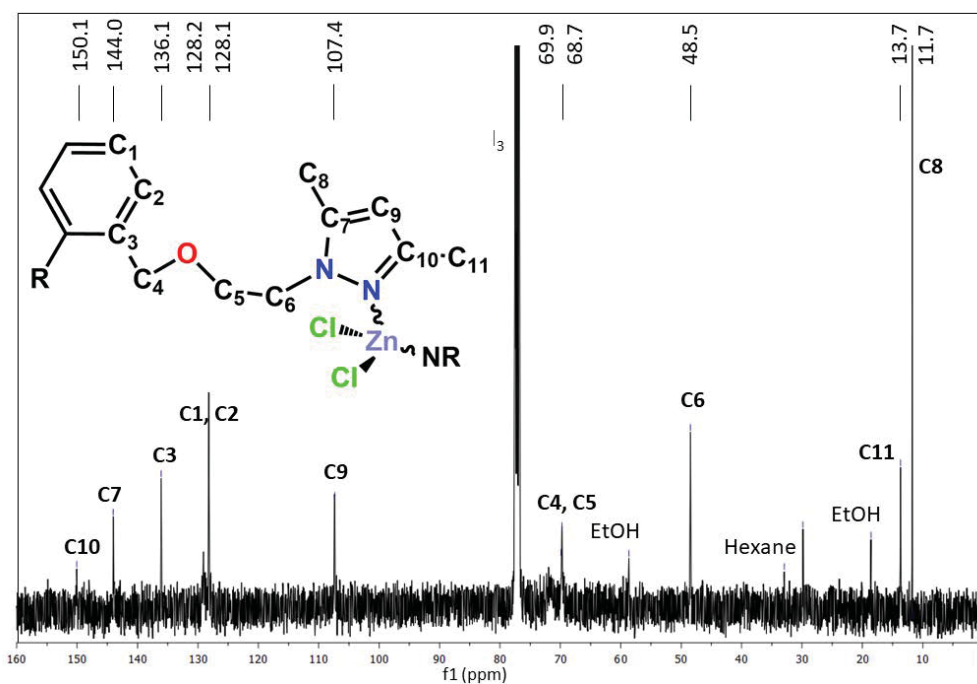


Figure S3.3.26 $^{13}\text{C}\{^1\text{H}\}$ NMR spectrum of compound **15** (CDCl_3 , 100.6 MHz)

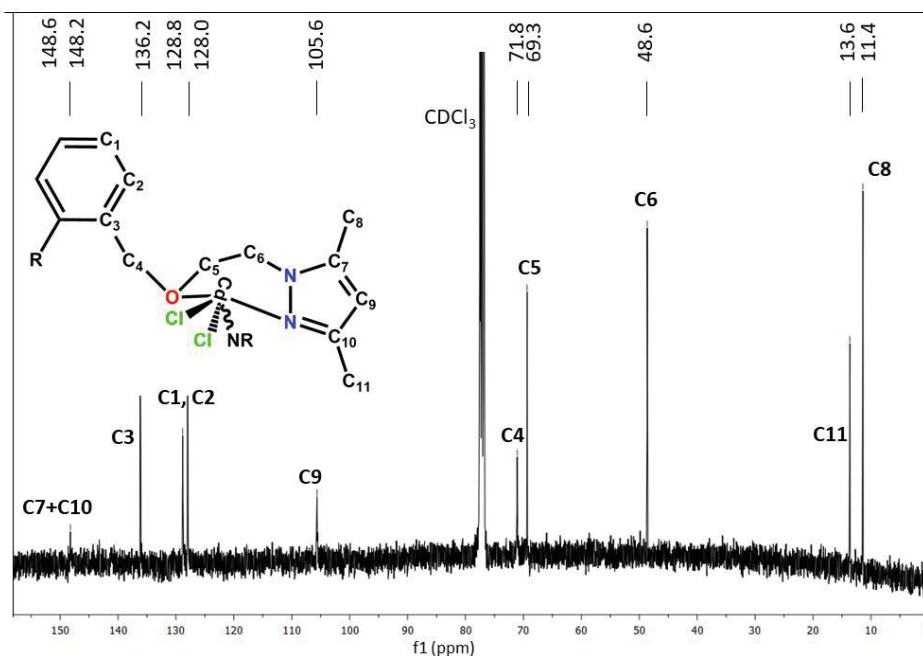


Figure S3.3.27 $^{13}\text{C}\{^1\text{H}\}$ NMR of compound **16** (CDCl_3 , 100.6 MHz)

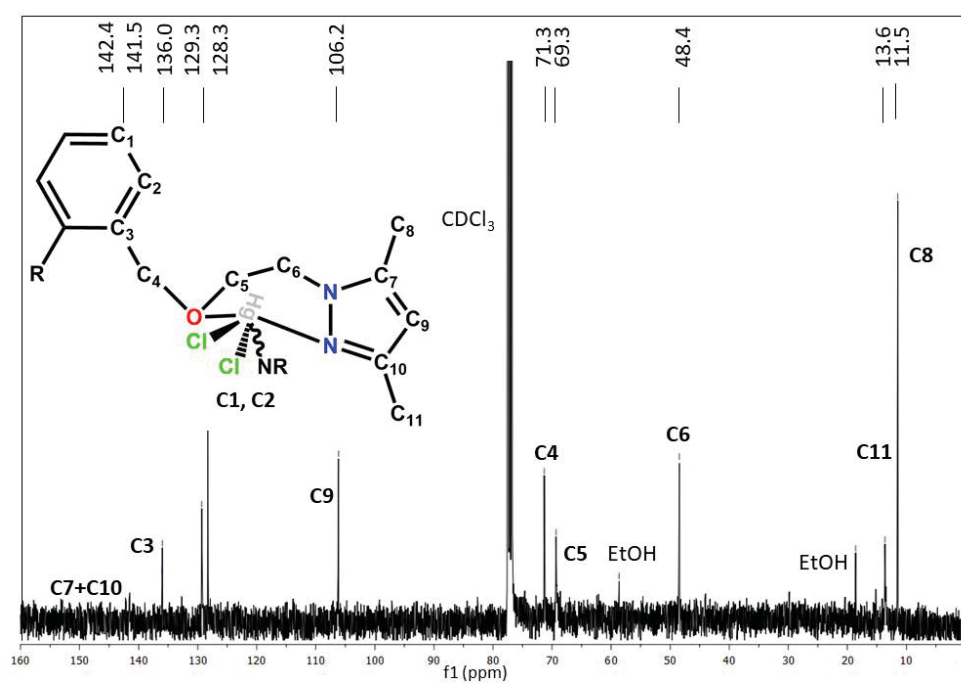


Figure S3.3.28 $^{13}\text{C}\{^1\text{H}\}$ NMR spectrum of compound **17** (CDCl_3 , 100.6 MHz)

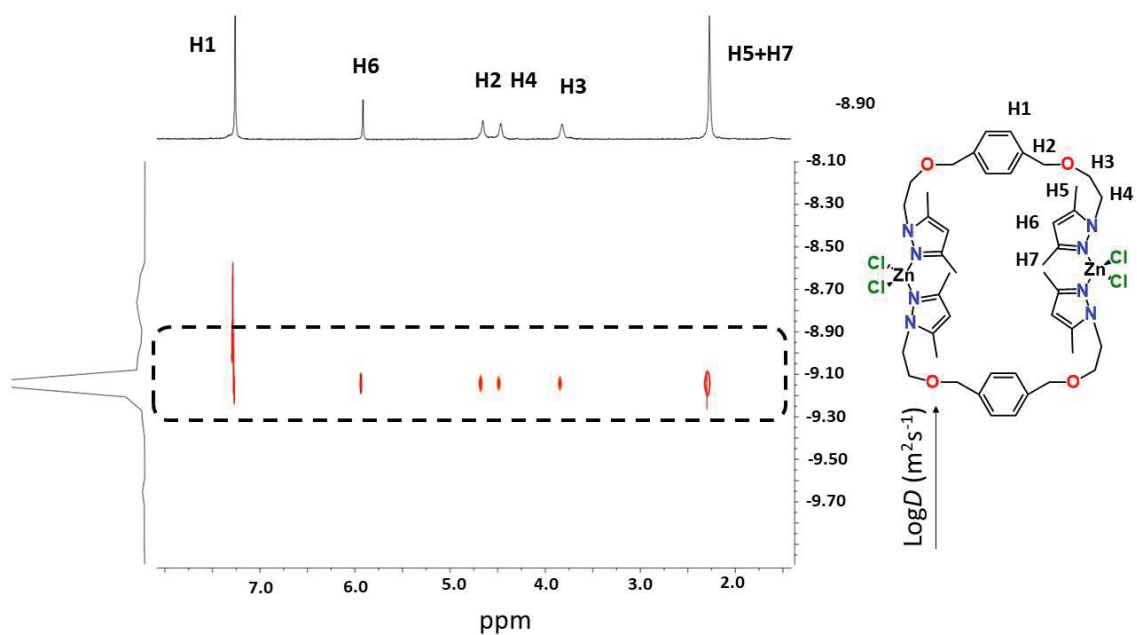


Figure S3.3.29 DOSY-NMR spectra of **10** (400 MHz, CDCl₃)

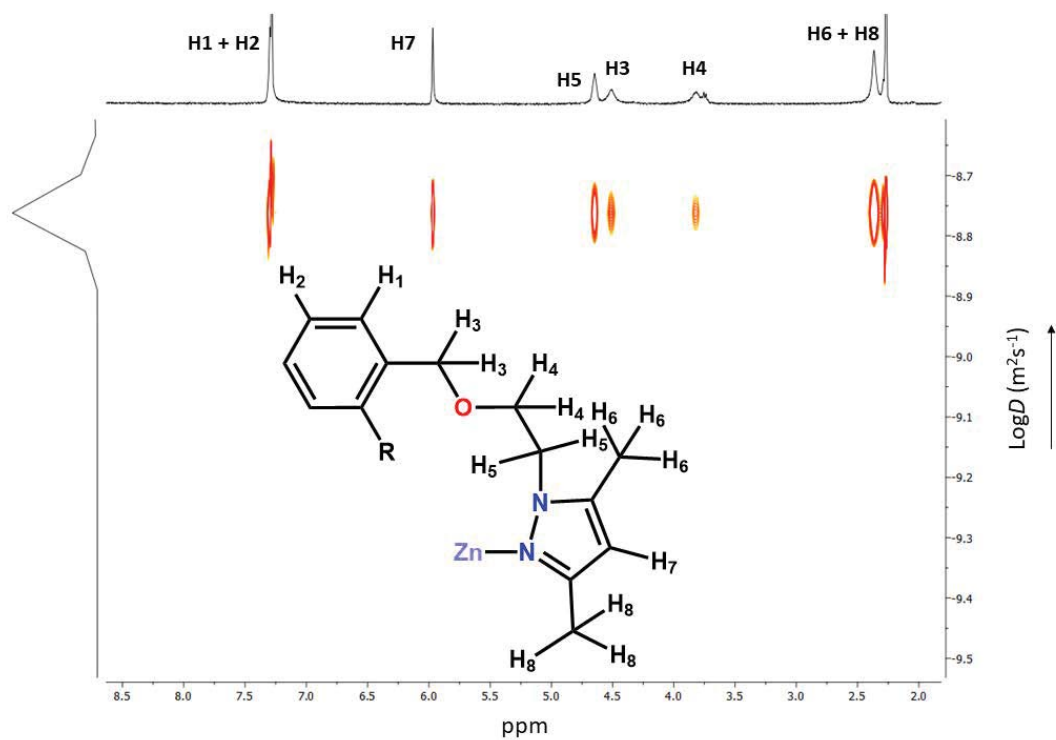


Figure S3.3.30 DOSY-NMR spectra of **15** (400 MHz, CDCl₃)

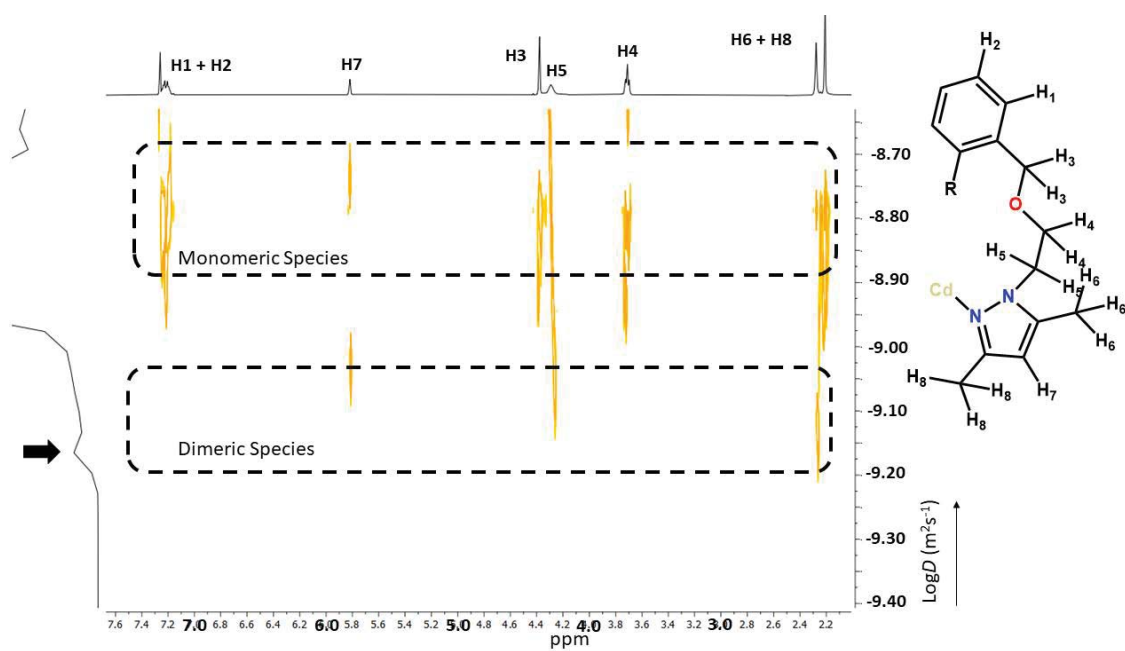


Figure S3.3.31 DOSY NMR spectrum of **16** (400 MHz, CDCl_3). Note the minor diffusion peak at $D = 6.59 \cdot 10^{-10} \text{ m}^2\text{s}^{-1}$, highlighted with a black arrow

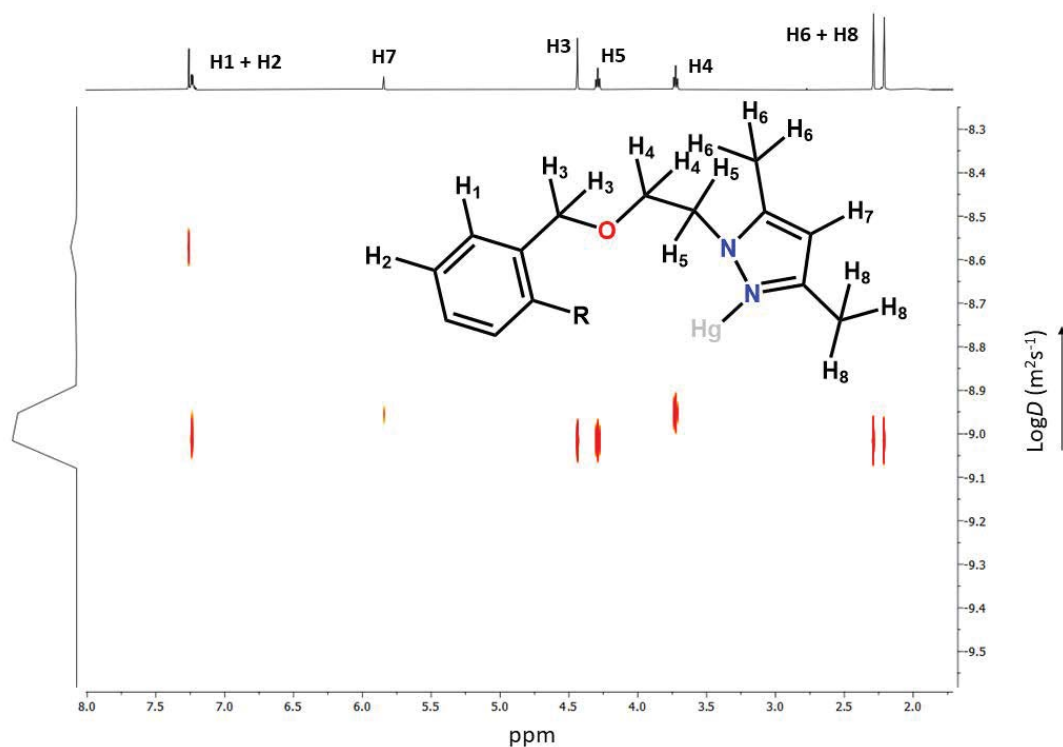


Figure S3.3.32 DOSY NMR spectrum of **17** (400 MHz, CDCl_3)

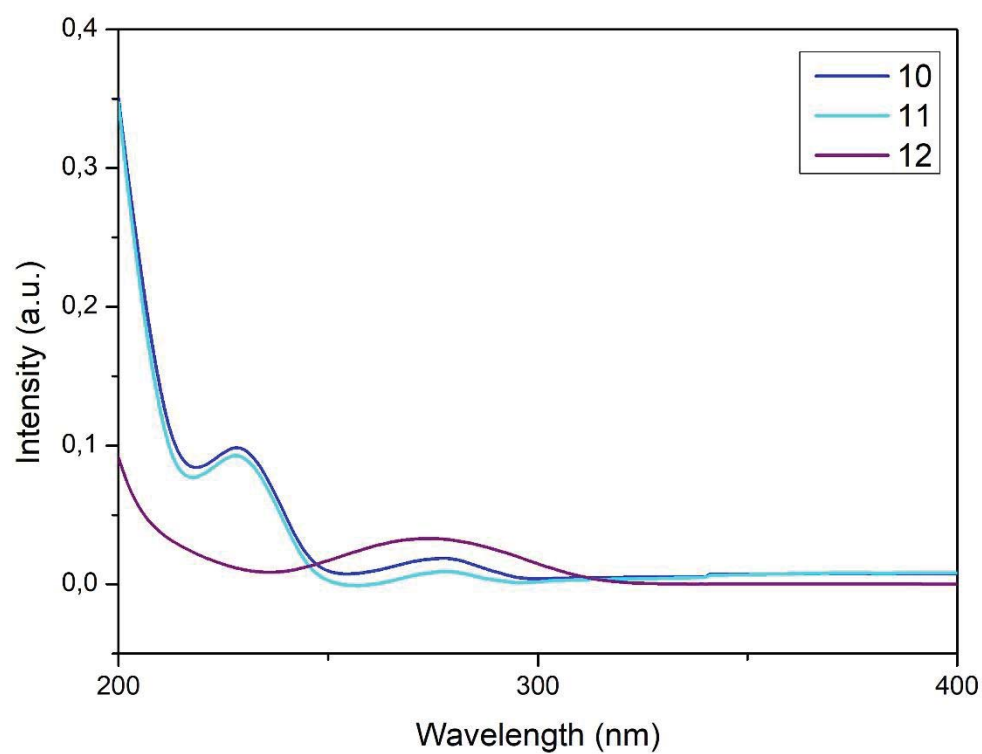


Figure S.3.3.33 UV-Vis spectra of **10-12** (CH₃CN, $\sim 1 \cdot 10^{-6}$ M) measured at RT.

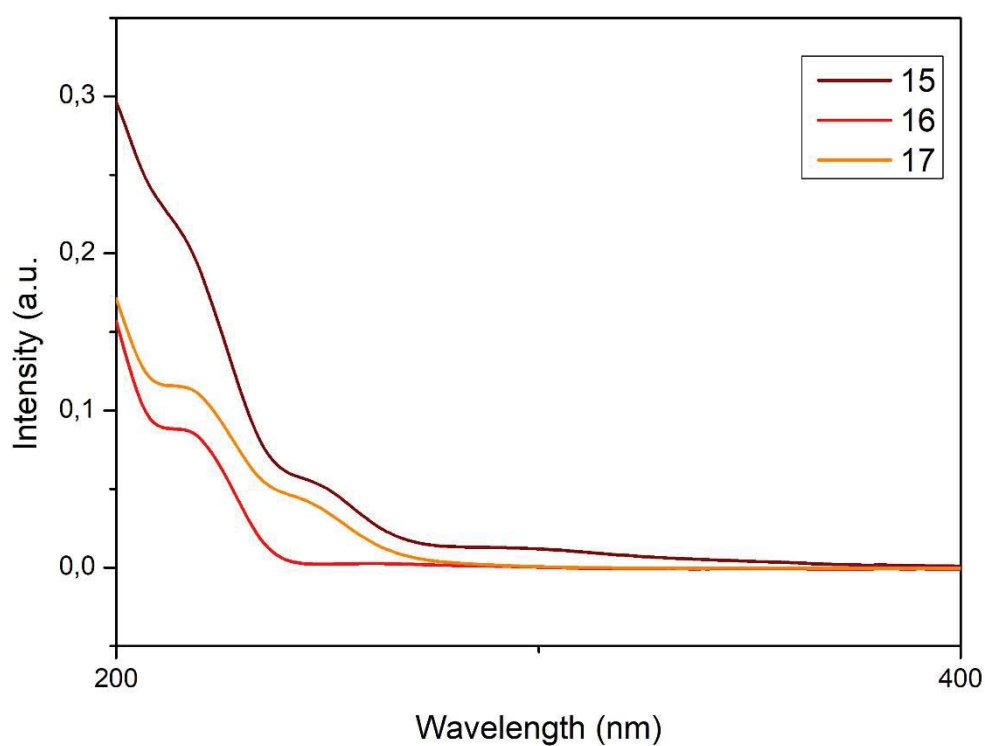


Figure S.3.3.34 UV-Vis spectra of **15-17** (CH₃CN, $\sim 3 \cdot 10^{-6}$ M) measured at RT.

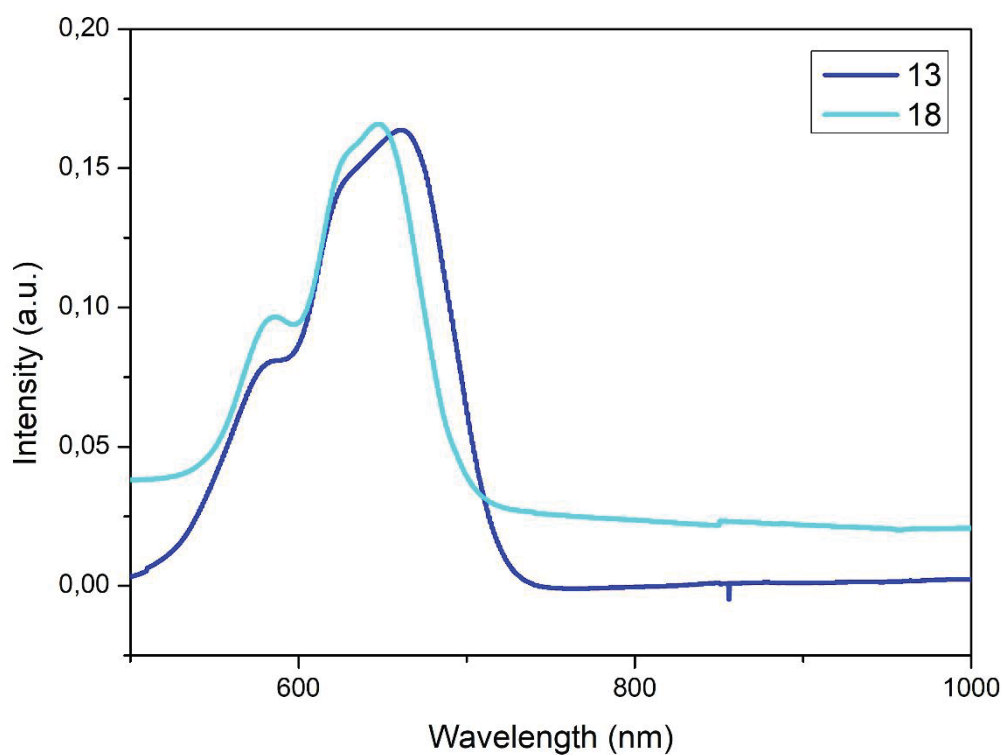


Figure S3.3.35 UV-Vis spectra of **13** (acetone, $9.44 \cdot 10^{-4}$ M) and **18** (CH_2Cl_2 , $1.06 \cdot 10^{-3}$ M) measured at RT.

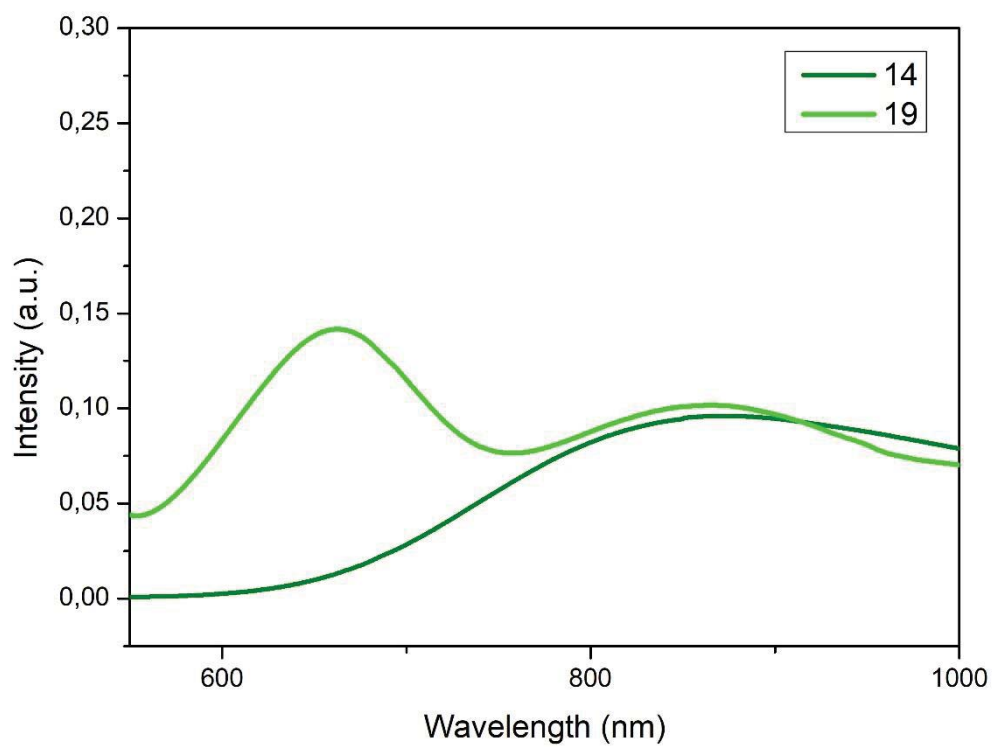


Figure S3.3.36 UV-Vis spectra of **14** ($1.12 \cdot 10^{-3}$ M) and **19** ($1.25 \cdot 10^{-3}$ M) in MeOH measured at RT.

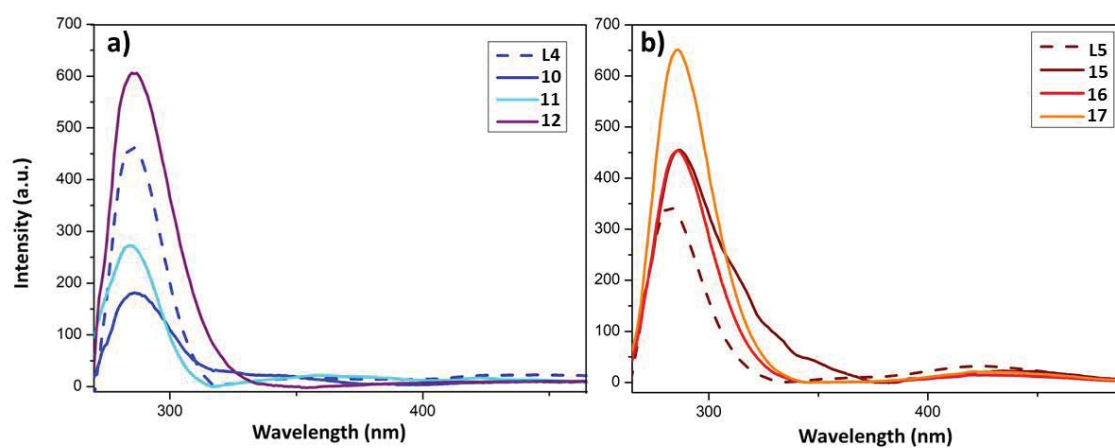


Figure S3.3.37 Emission spectra of **L4**, **L5**, **10-12** and **15-17** recorded in CH_3CN at RT.

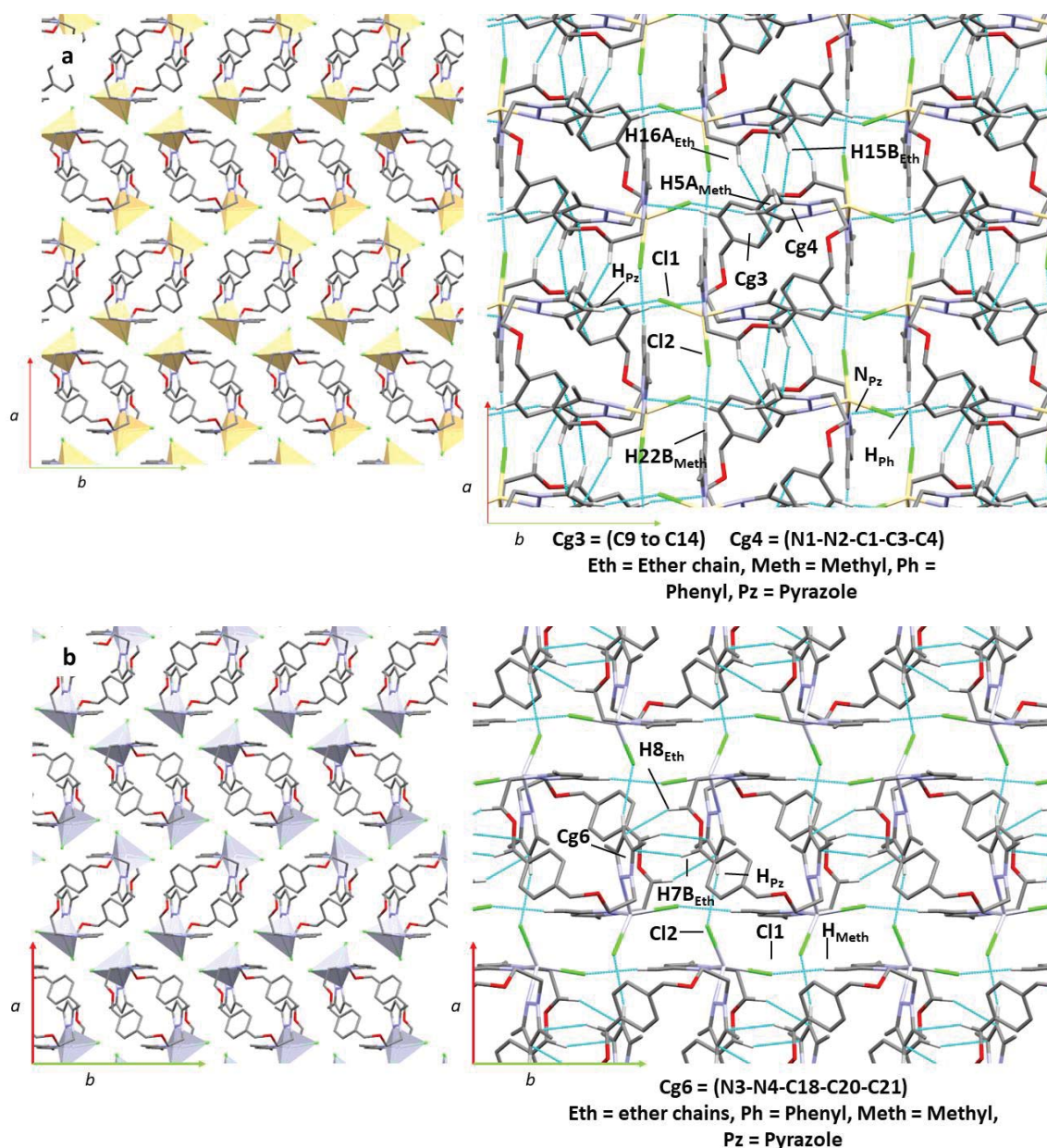


Figure S3.3.37 a. Supramolecular structure of **11**, view along *c* axis (right). Detail of the non-bonding interactions in **11**, view along *c* axis (left). **b.** Supramolecular structure of **12**, view along *c* axis (right). Detail of the non-bonding interactions in **12**, view along *c* axis (left). Colour code: grey (C), white (H), light blue (N), light green (Cl), bone (Cd), light-grey (Hg). Cd(II) and Hg(II) atoms are also represented as bone or light-grey polyhedral, respectively. Intermolecular interactions are represented as dashed light-blue lines. Only hydrogen atoms participating in intermolecular interactions are shown.

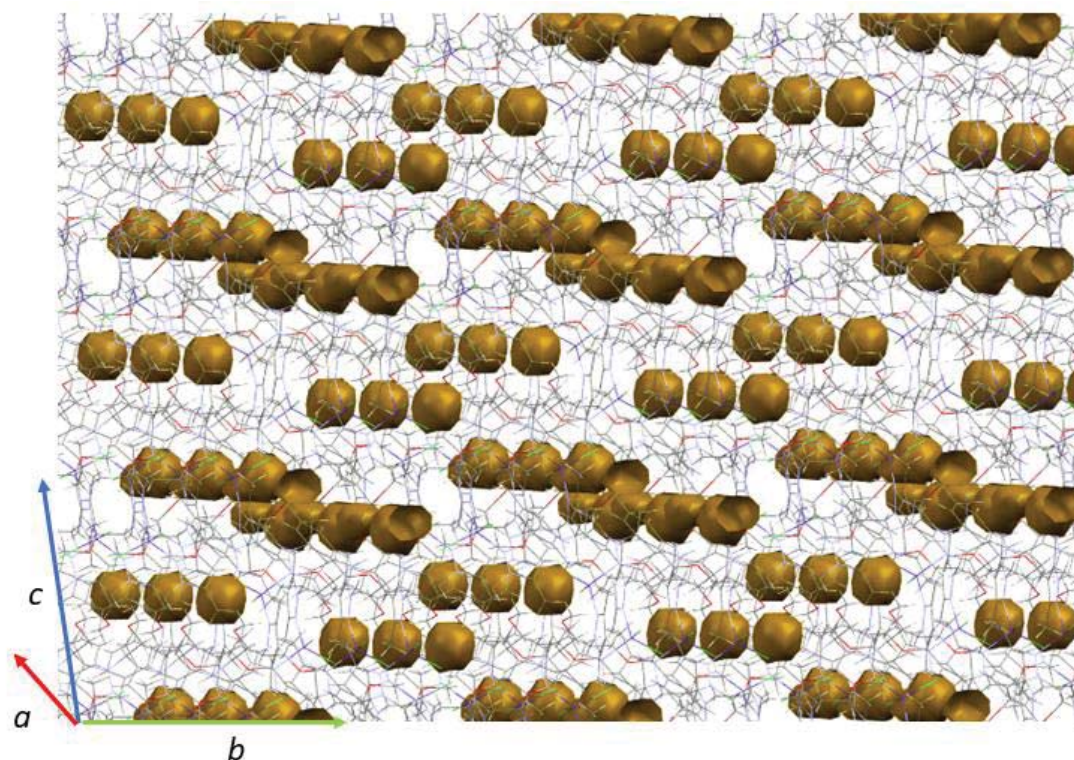


Figure S.3.3.38 Voids representation in **13**. Colour code: grey (C), white (H), light blue (N), light green (Cl), blue (Co). Cavities are represented in light brown.

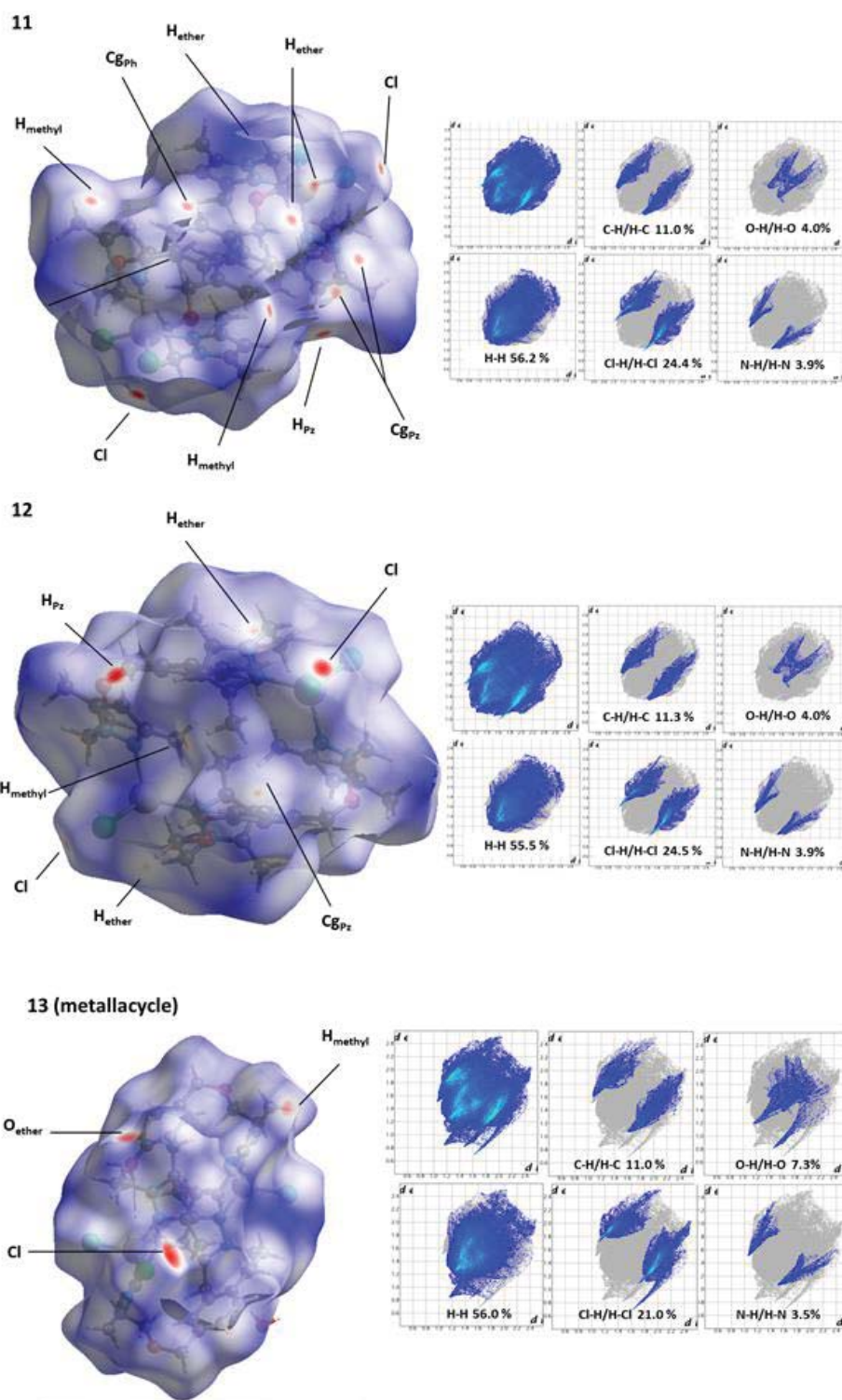


Figure S3.3.40 Hirshfeld surface mapped in d_{norm} representation of **11** (top-left) and **12** (middle-left) and metallacyclic component of **13** (bottom-left). Surface transparency has been enabled and relevant atoms labelled. Fingerprint plot of **11** (top-right) and **12** (middle-left) and metallacyclic component of **13** (bottom-left).

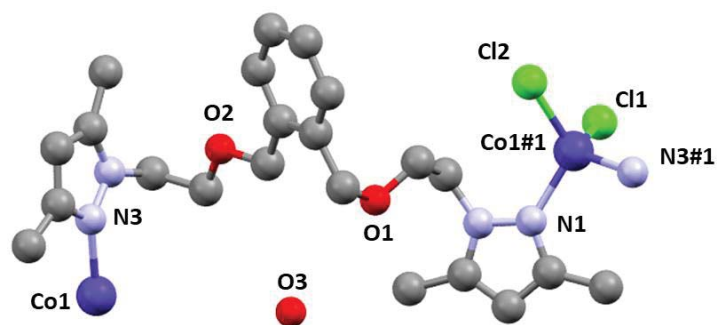


Figure S3.3.39 Compound **18**, showing all its non-hydrogen atoms and numbering scheme. Colour code: grey (C), white (H), light blue (N), light green (Cl), blue (Co).

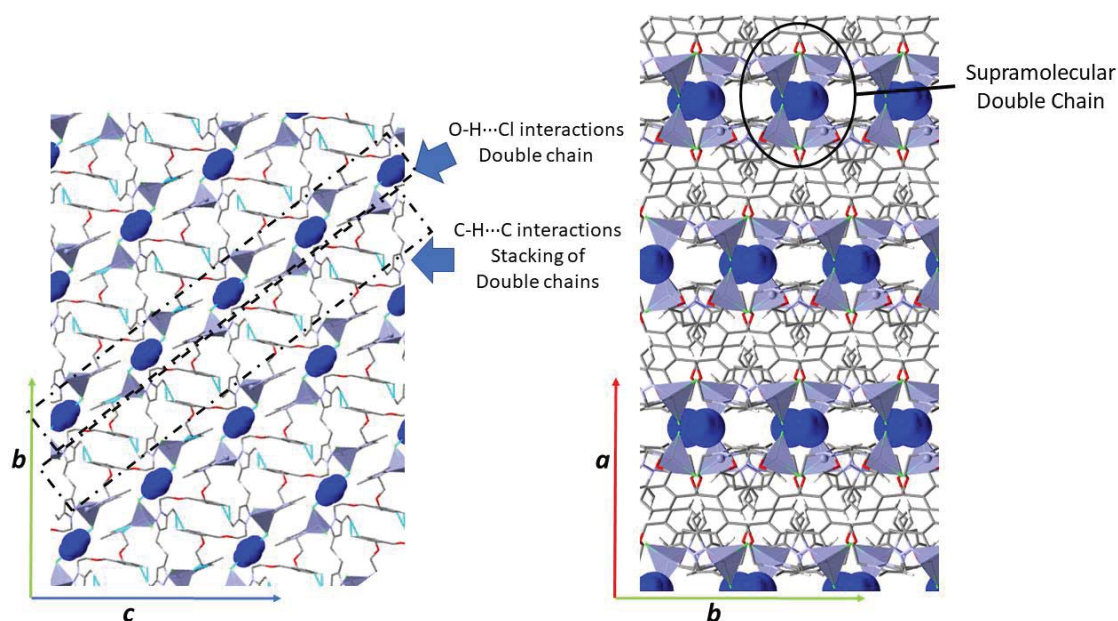


Figure S3.3.40 Detail of the H-bond interactions in **15**, showing only hydrogen atoms involved in intermolecular interactions. View along *b* axis. Colour code: grey (C), white (H), light blue (N), light green (Cl), grey-blue (Zn). Water molecules are highlighted in blue and represented in spacefill mode. Zn(II) atoms are also represented as blue-grey polyhedra. Intermolecular interactions are represented as dashed light-blue lines. Only hydrogen atoms participating in intermolecular interactions are shown.

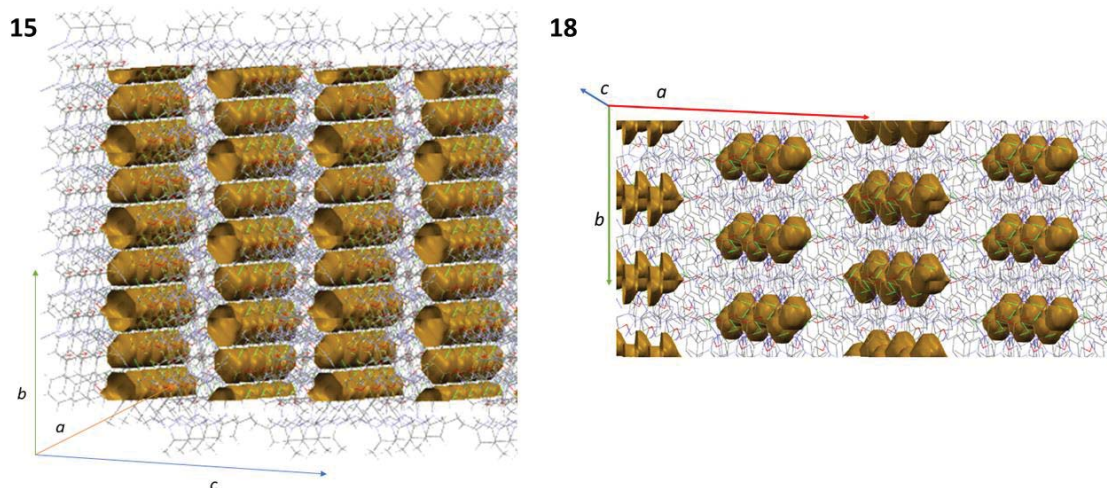


Figure S3.3.41 Voids representation in **15** (91.22 \AA^3 , 1.9 % of unit cell) and **18** (86.91 \AA^3 , 1.8 % of unit cell). Colour code: grey (C), white (H), light blue (N), light green (Cl), light-grey (Zn), blue (Co). Cavities are represented in light brown.

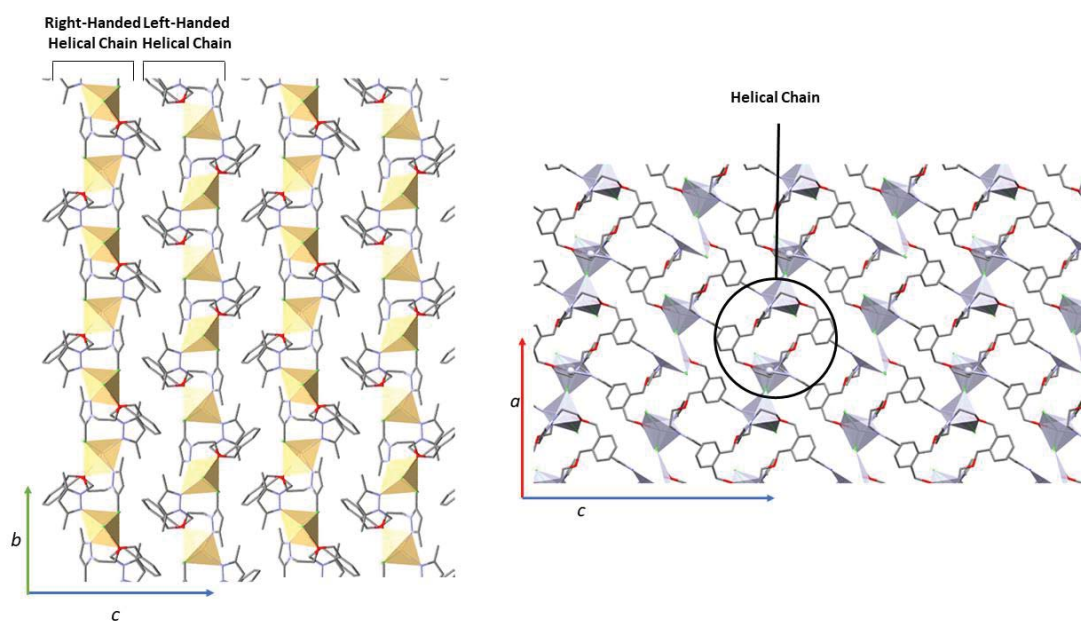


Figure S3.3.42 Supramolecular structure of **16** (left, view along a axis) and **17** (right, view along b axis). Occluded solvent molecules have been removed for clarity. Colour code: grey (C), white (H), light blue (N), light green (Cl), bone (Cd), grey (Hg). Cd(II) and Hg(II) atoms are also represented as bone or grey polyhedra, respectively.

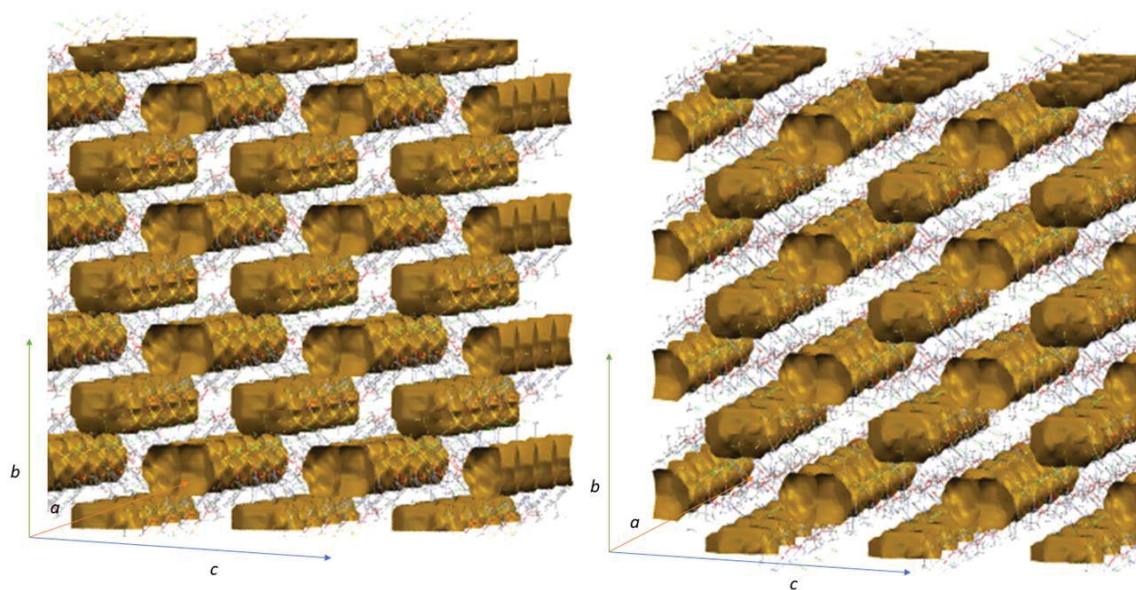


Figure S3.3.43 Voids representation (227.28 \AA^3 , 8.6 % of unit cell) in **16** (left) and (229.75 \AA^3 , 8.5 % of unit cell) **17** (right). Colour code: grey (C), white (H), light blue (N), light green (Cl), bone (Cd), grey (Hg). Cavities are represented in light brown.

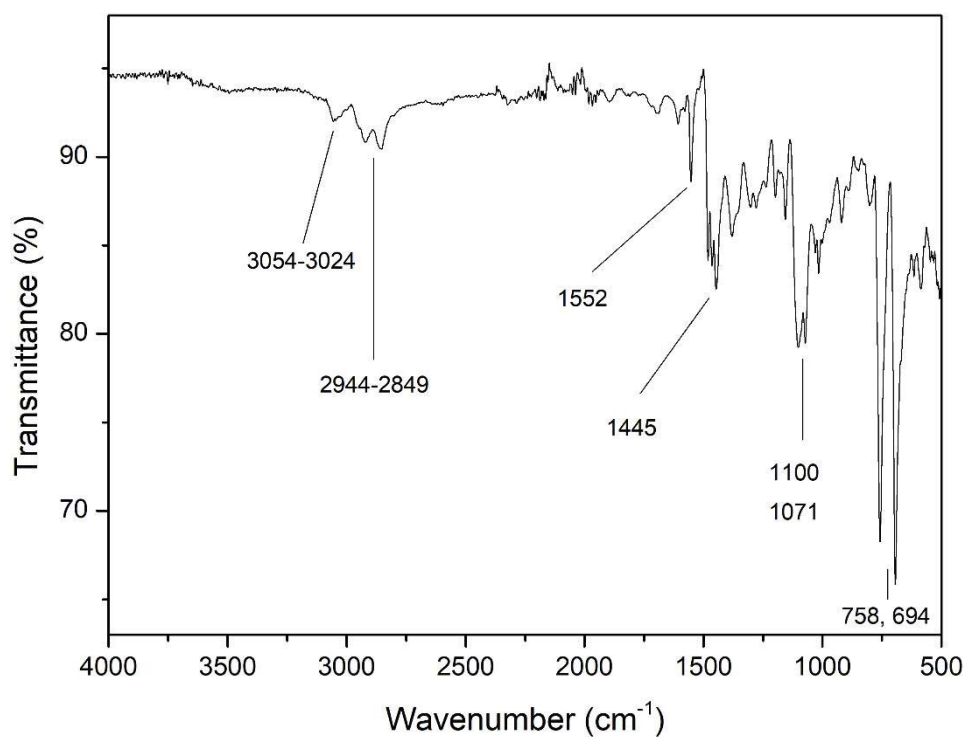


Figure S3.3.44 FTIR-ATR spectrum of compound **21**

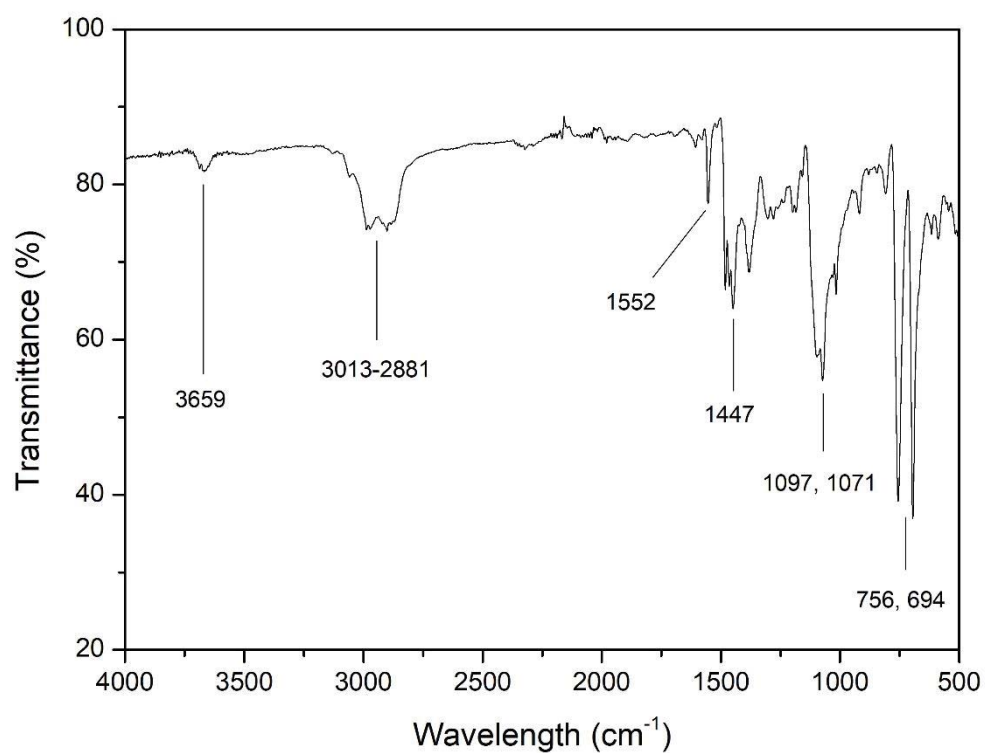


Figure S3.3.45 FTIR-ATR spectra of compounds **22** and **23** mixture

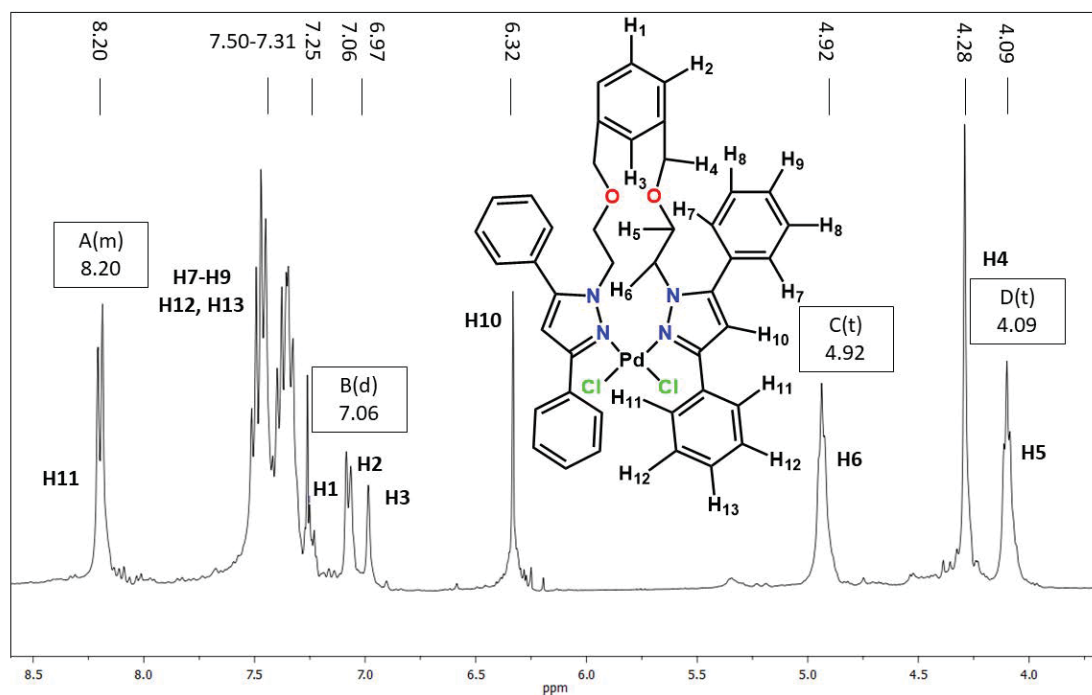


Figure S.3.3.46 ¹H NMR spectrum of compound **21** (CDCl₃, 400.0 MHz).

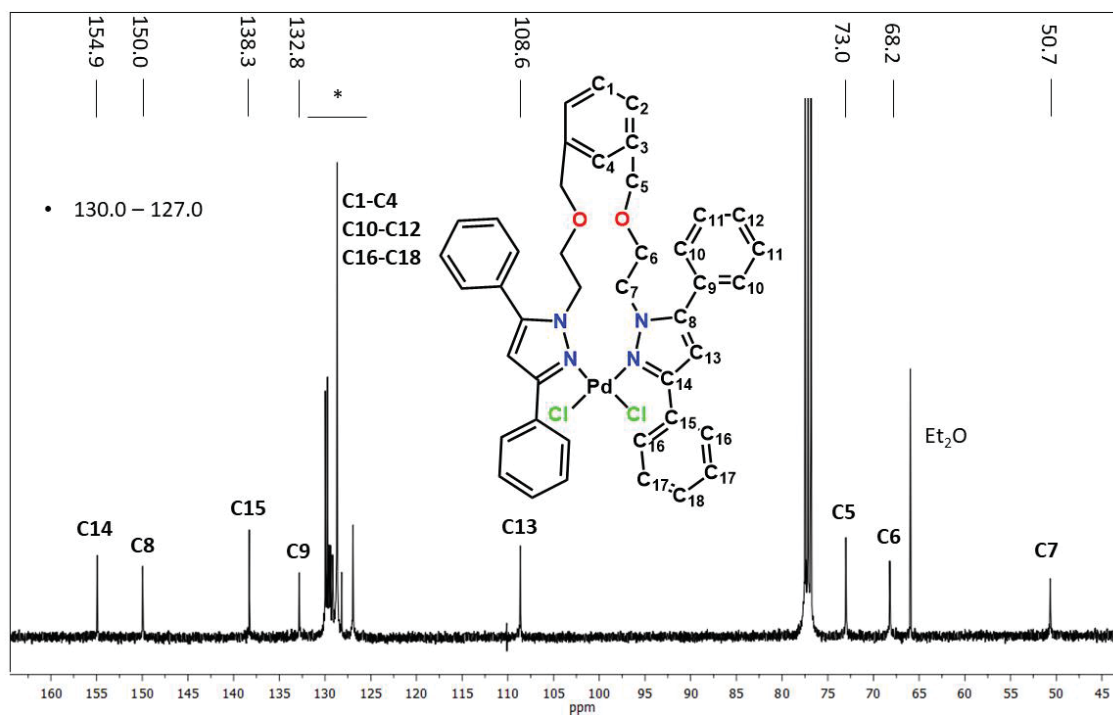


Figure S.3.3.47 ¹³C{¹H} NMR spectrum of compound **21** (CDCl₃, 100.6 MHz).

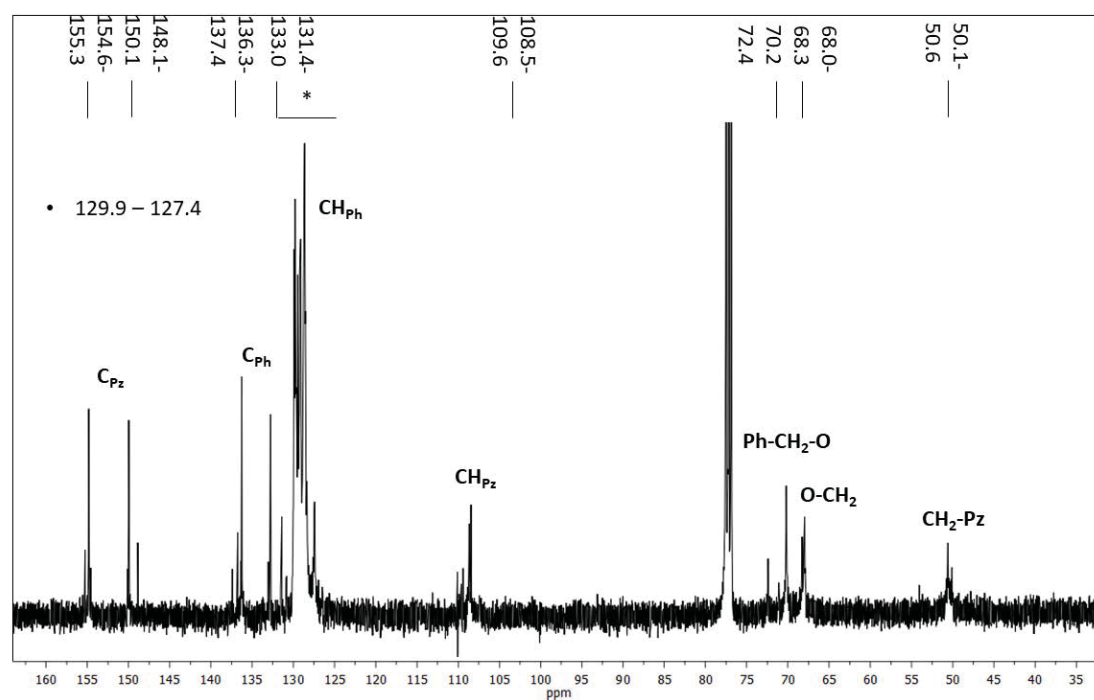


Figure S.3.3.50 $^{13}\text{C}\{^1\text{H}\}$ NMR spectrum of mixture of compounds **22** and **23** (CDCl_3 , 100.6 MHz).

Annex for Section 3.4

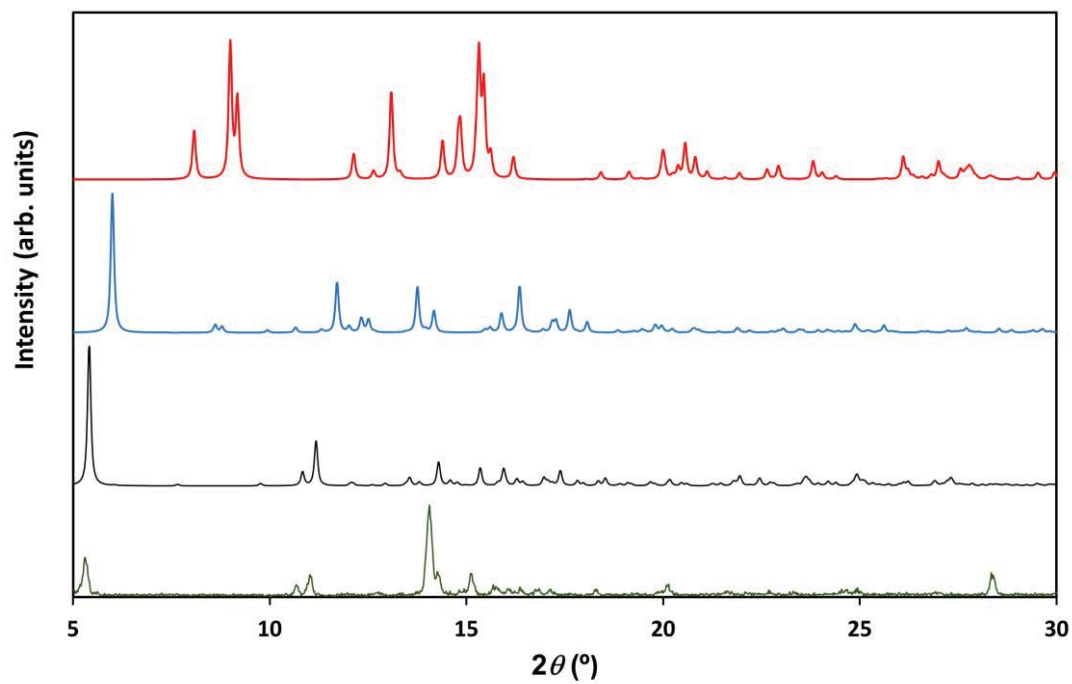


Figure S3.4.1 PXRD pattern of compound **26** (green, bottom). Calculated patterns from resolved crystal structures for **24** (red), **25** (blue) and **27** (black) are included as references

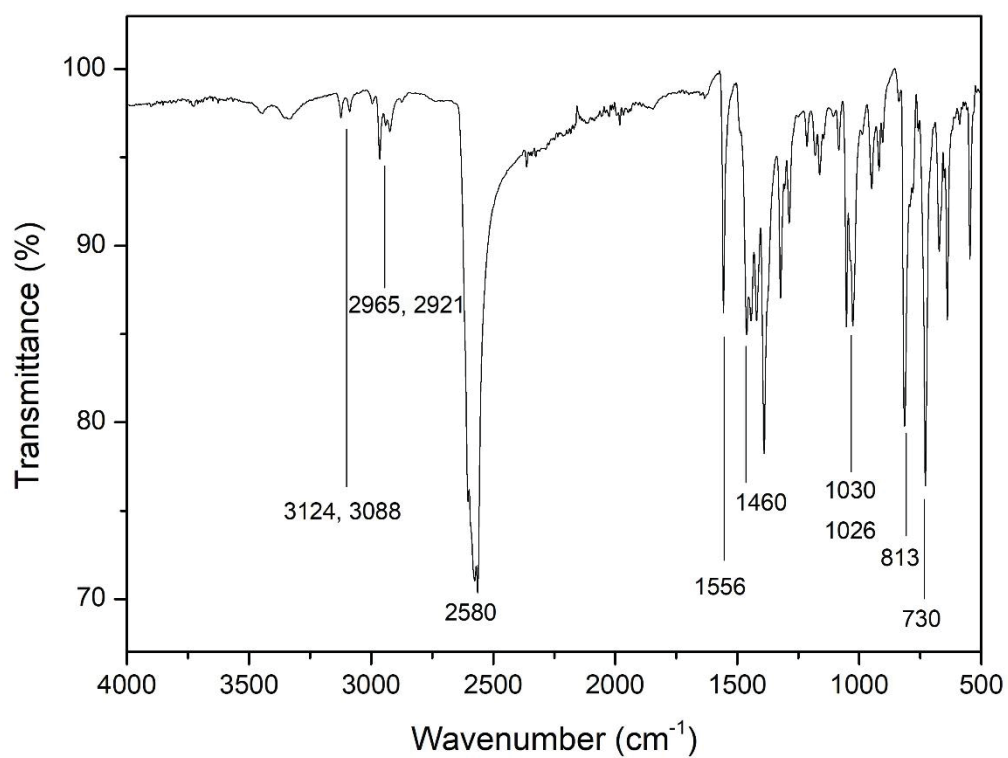


Figure S3.4.2 FTIR-ATR spectrum of compound **24**.

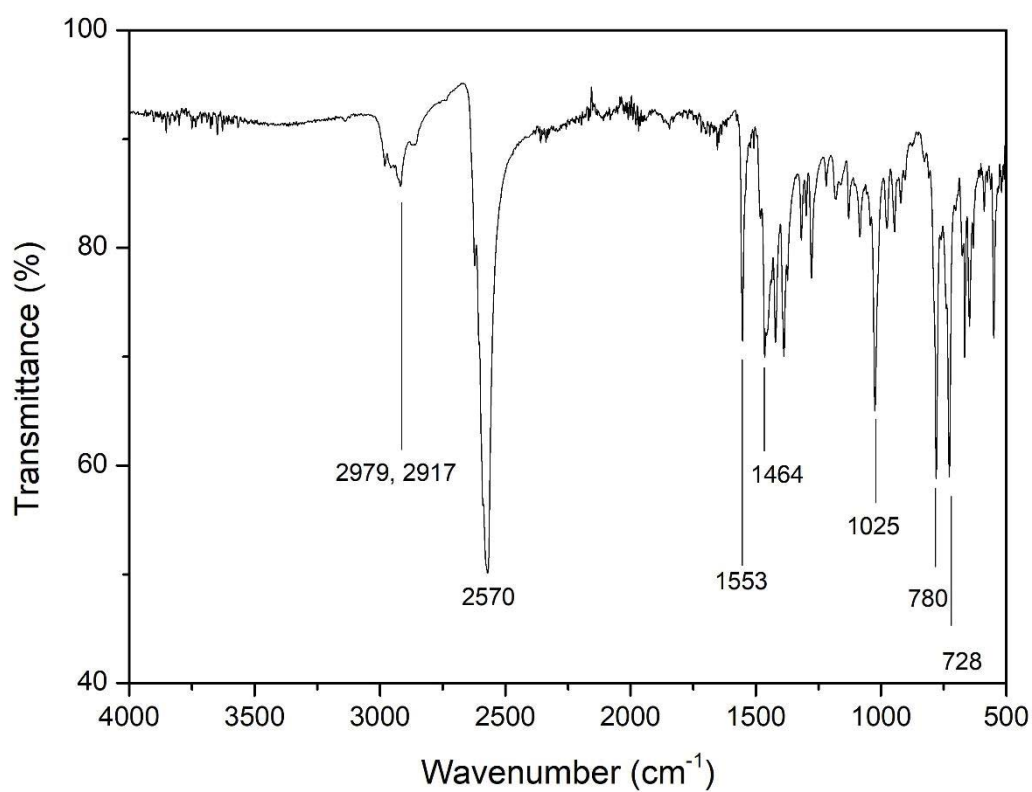


Figure S3.4.3 FTIR-ATR spectrum of compound **25**.

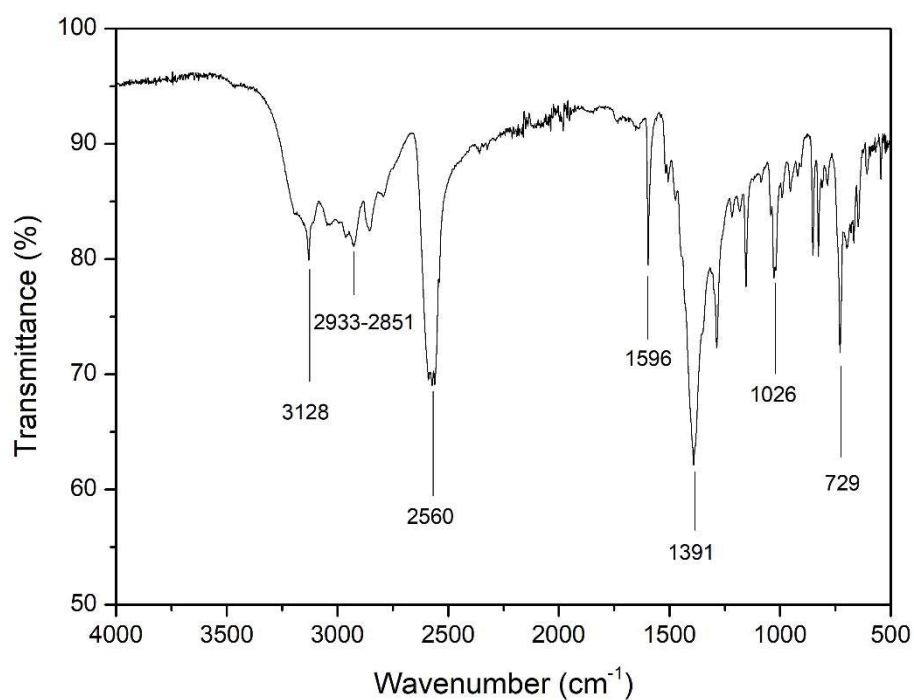


Figure S3.4.4 FTIR-ATR spectrum of compound 26.

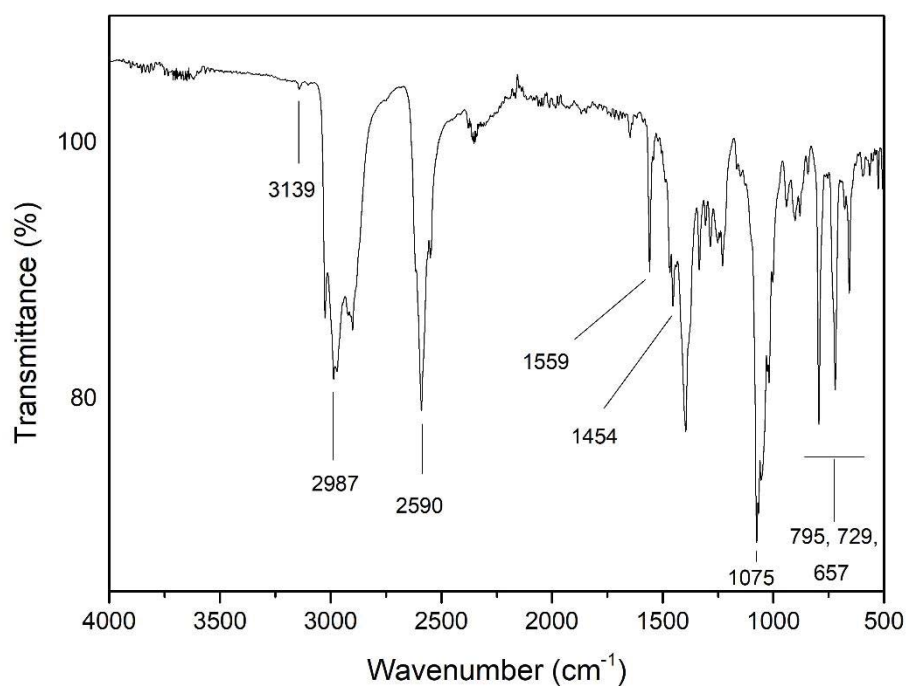


Figure S3.4.5 FTIR-ATR spectrum of compound 28.

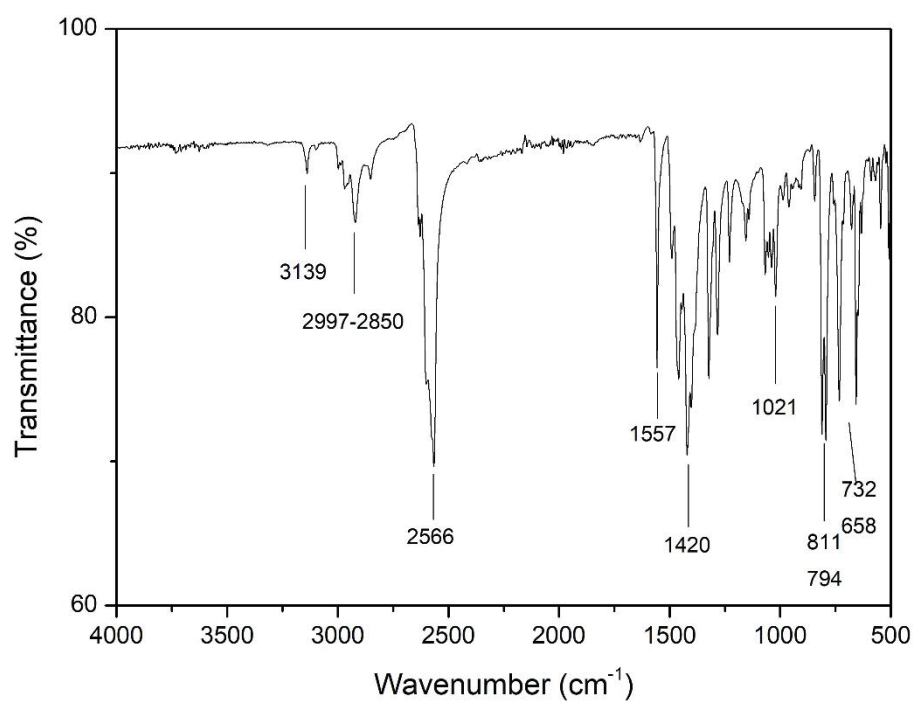


Figure S3.4.6 FTIR-ATR spectrum of compound **29**.

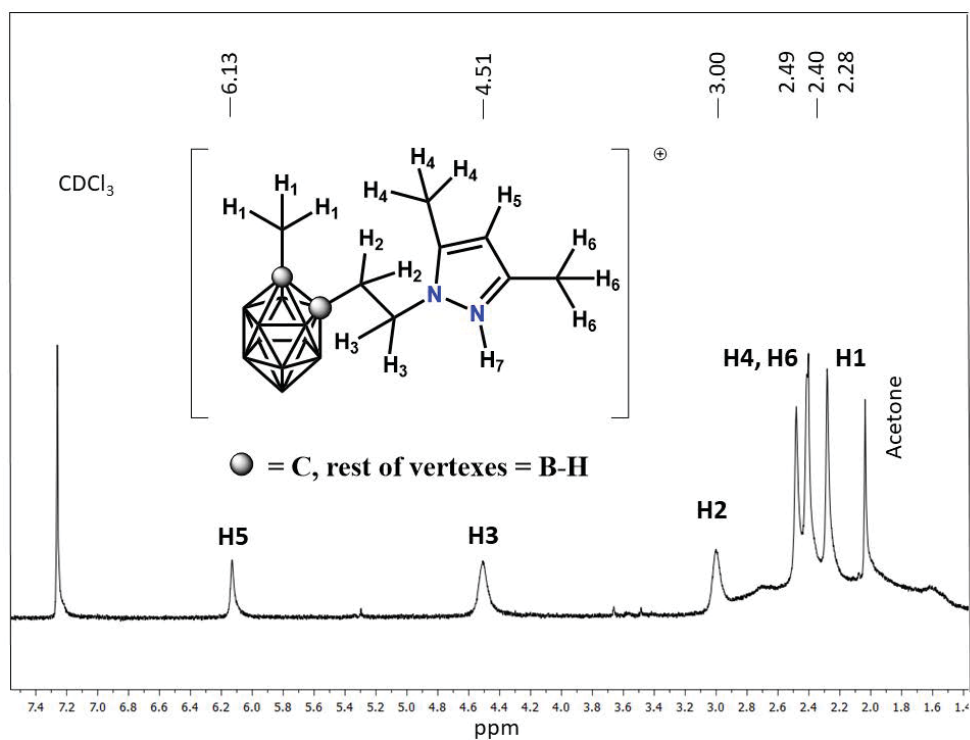


Figure S3.4.7 ^1H NMR spectrum of compound **26** (CDCl_3 , 400.0 MHz).

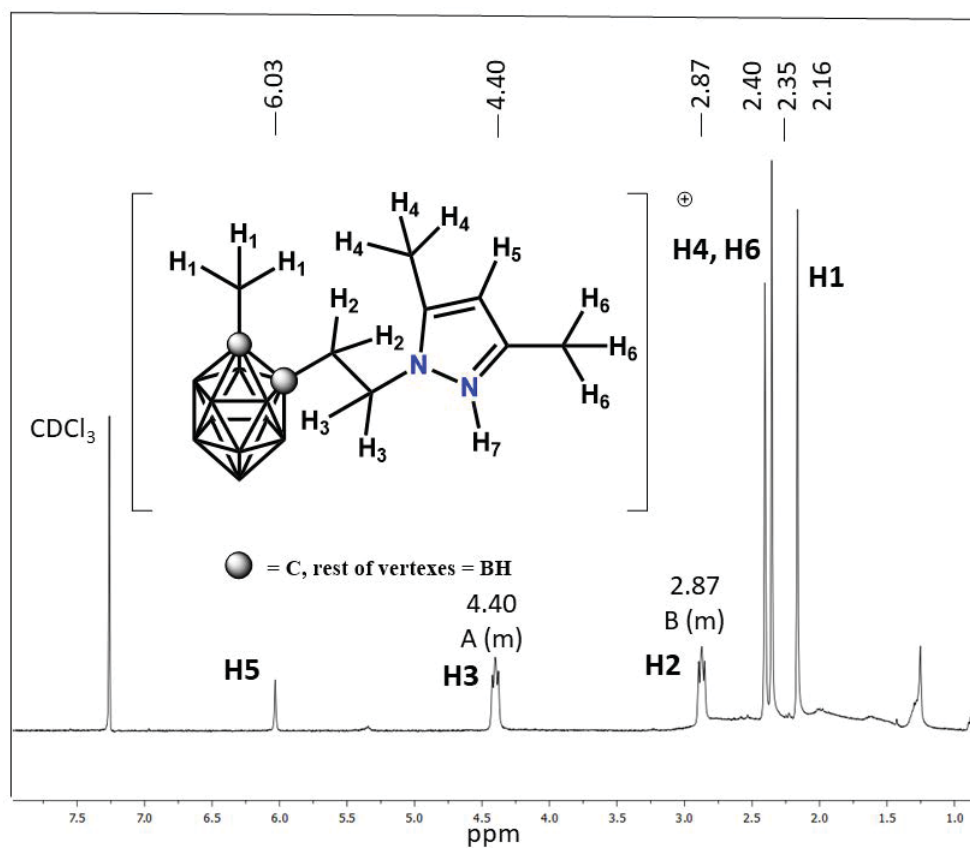


Figure S3.4.8 ^1H NMR spectrum of compound **27** (CDCl_3 , 400.0 MHz).

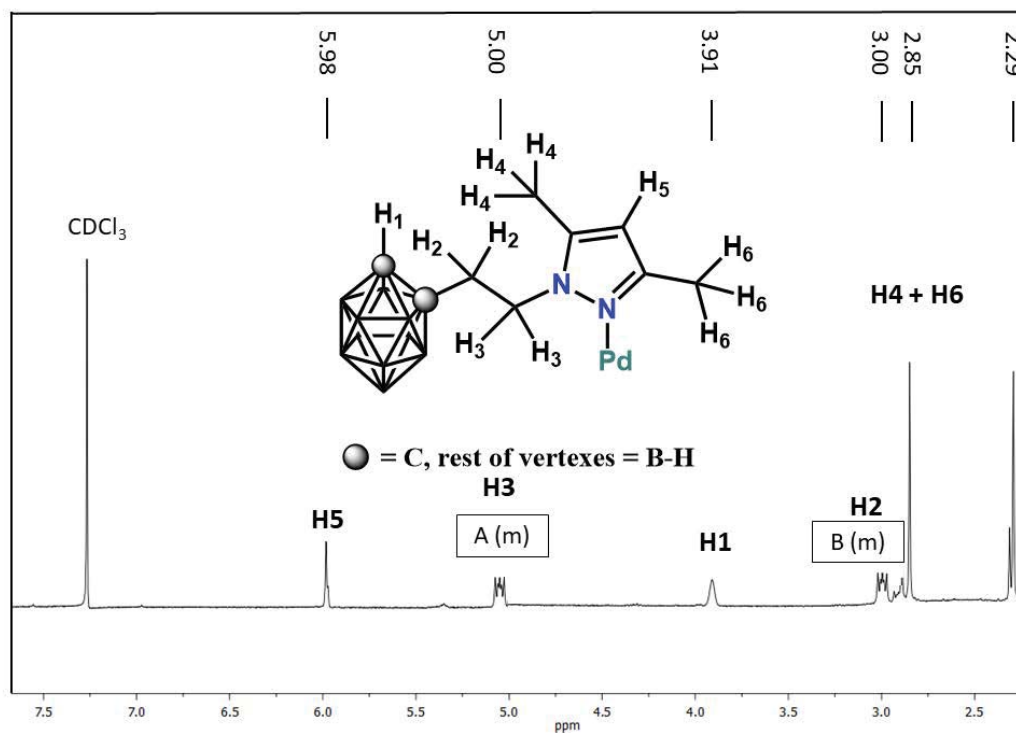


Figure S3.4.9 ^1H NMR spectrum of compound **28** (CDCl_3 , 400.0 MHz).

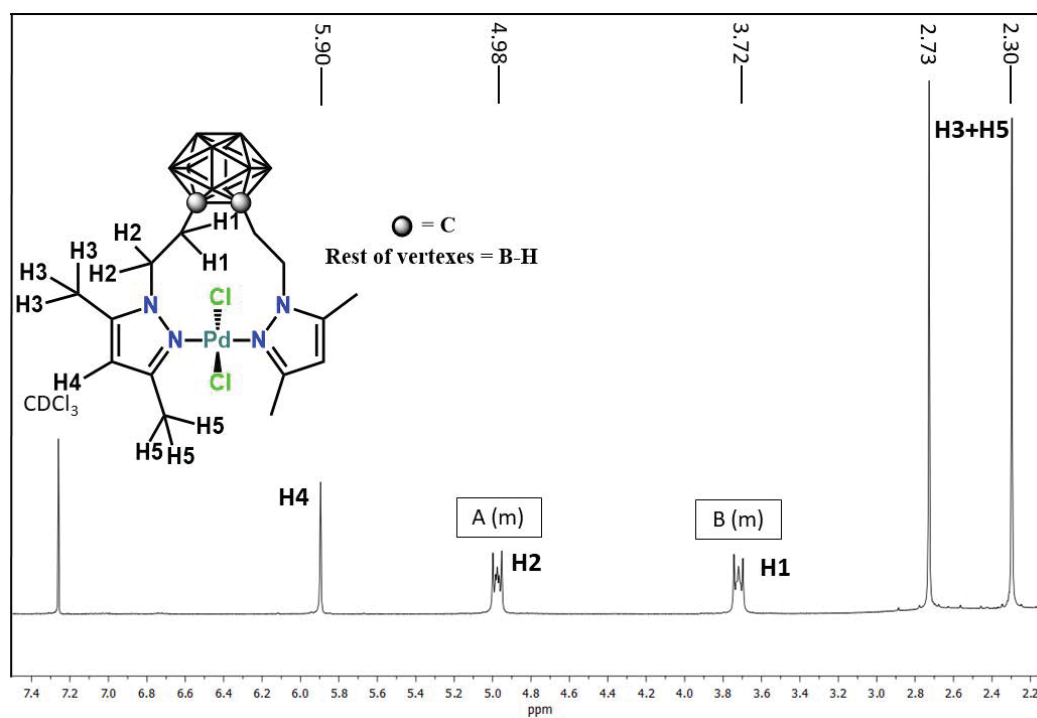


Figure S3.4.10 ^1H NMR spectrum of compound **29** (CDCl_3 , 400.0 MHz).

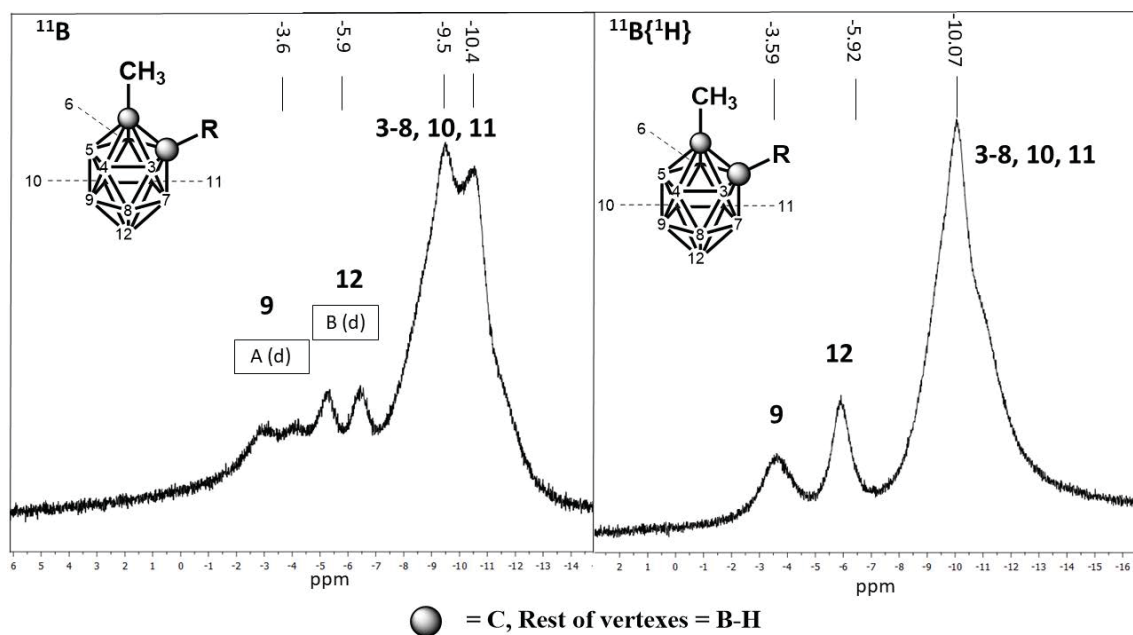


Figure S3.4.11 ^{11}B (left) and $^{11}\text{B}\{^1\text{H}\}$ (right) NMR spectra for **25** (CDCl_3 , 128.6 MHz).

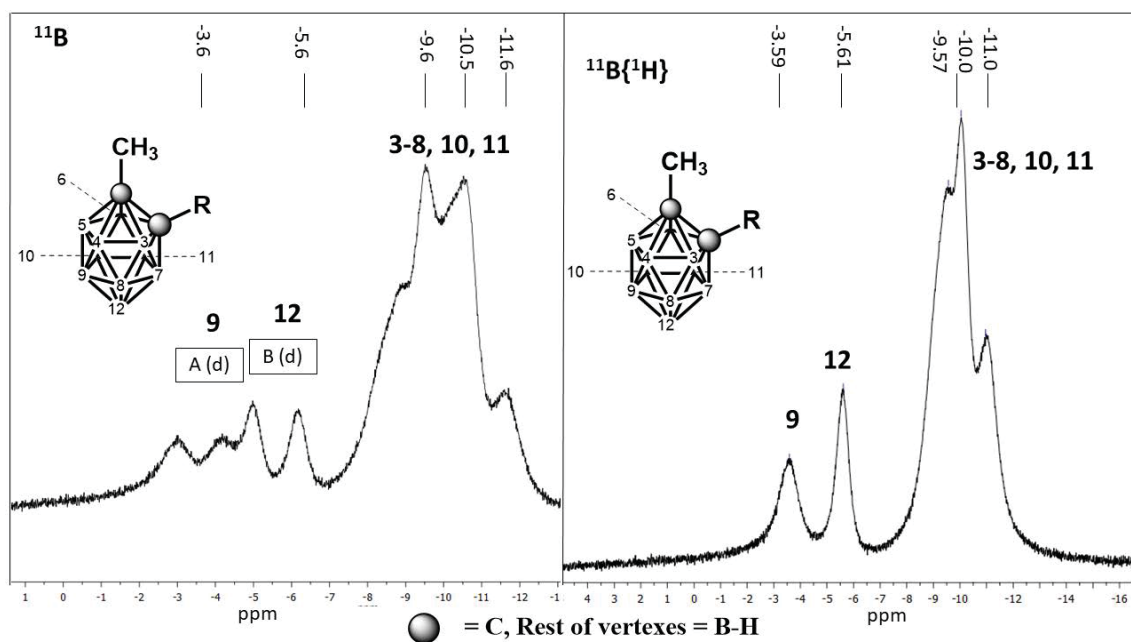


Figure S3.4.12 ^{11}B (left) and $^{11}\text{B}\{^1\text{H}\}$ (right) NMR spectra for **27** (CDCl_3 , 128.6 MHz).

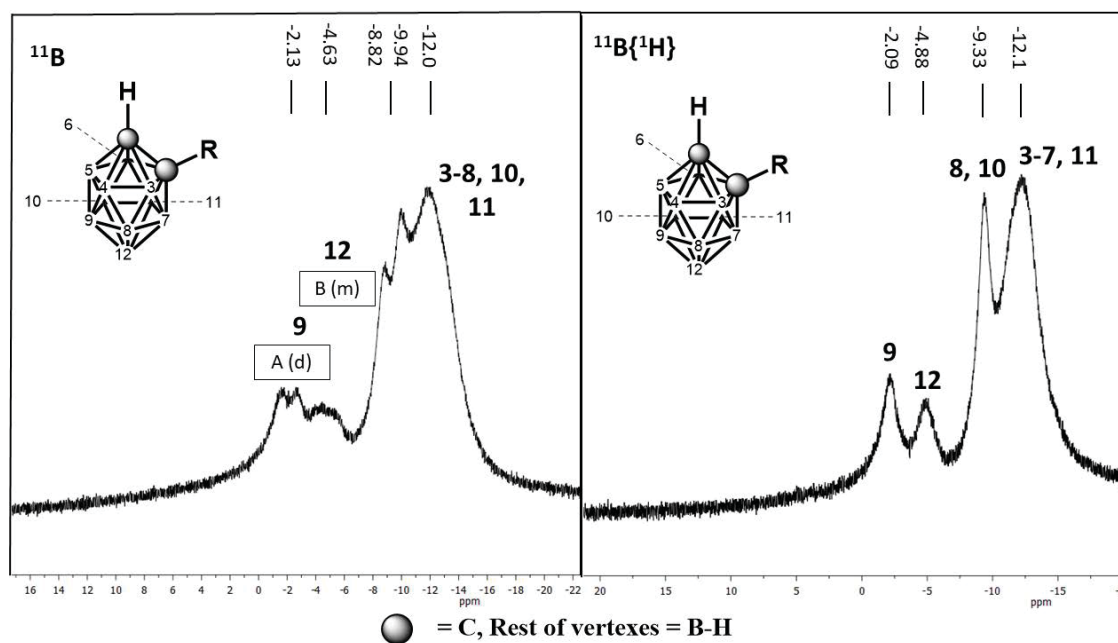


Figure S3.4.13 ^{11}B (left) and $^{11}\text{B}\{^1\text{H}\}$ (right) NMR spectra for **28** (CDCl_3 , 128.6 MHz).

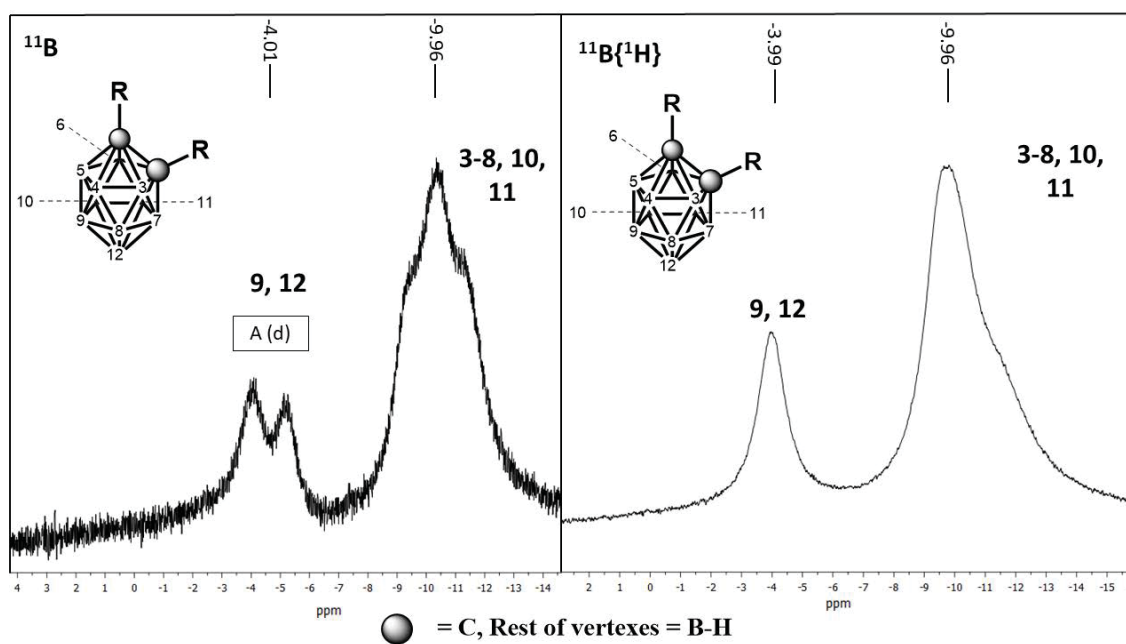


Figure S3.4.14 ^{11}B NMR (left) and $^{11}\text{B}\{^1\text{H}\}$ (right) spectra for **29** (CDCl_3 , 128.6 MHz).

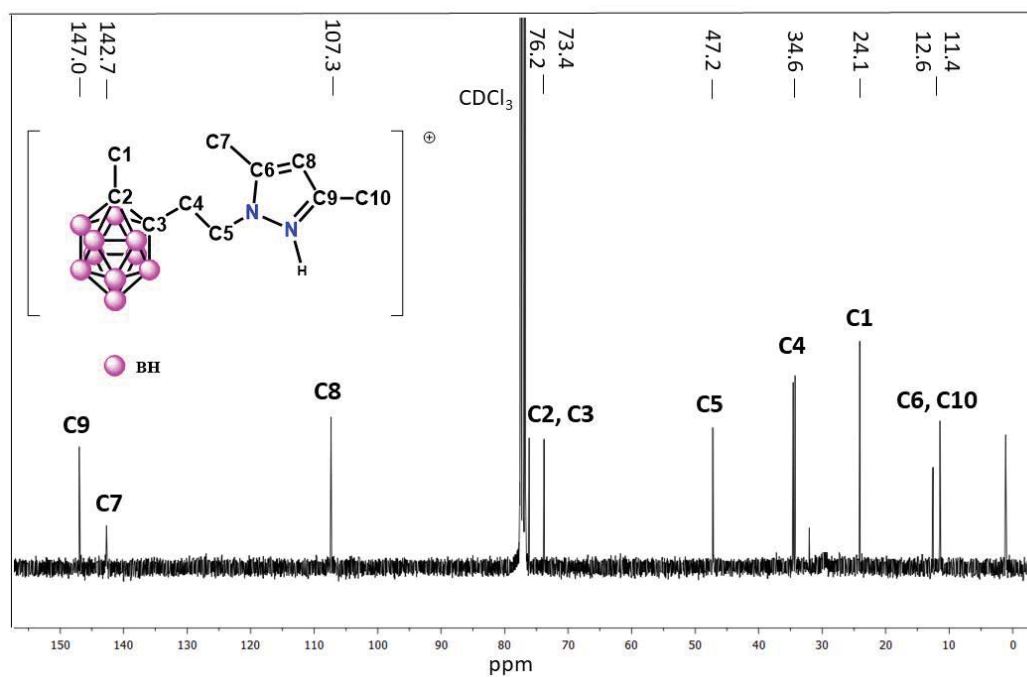


Figure S3.4.15 $^{13}\text{C}\{^1\text{H}\}$ NMR spectrum of compound **26** (CDCl_3 , 100.6 MHz).

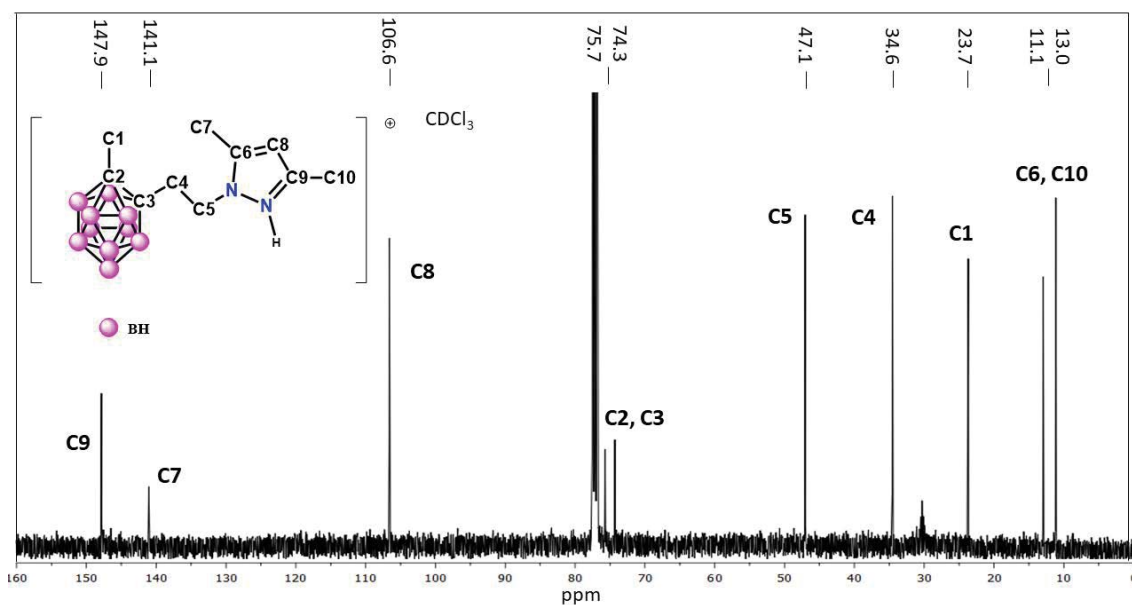


Figure S3.4.16 $^{13}\text{C}\{^1\text{H}\}$ NMR spectrum of compound **27** (CDCl_3 , 100.6 MHz).

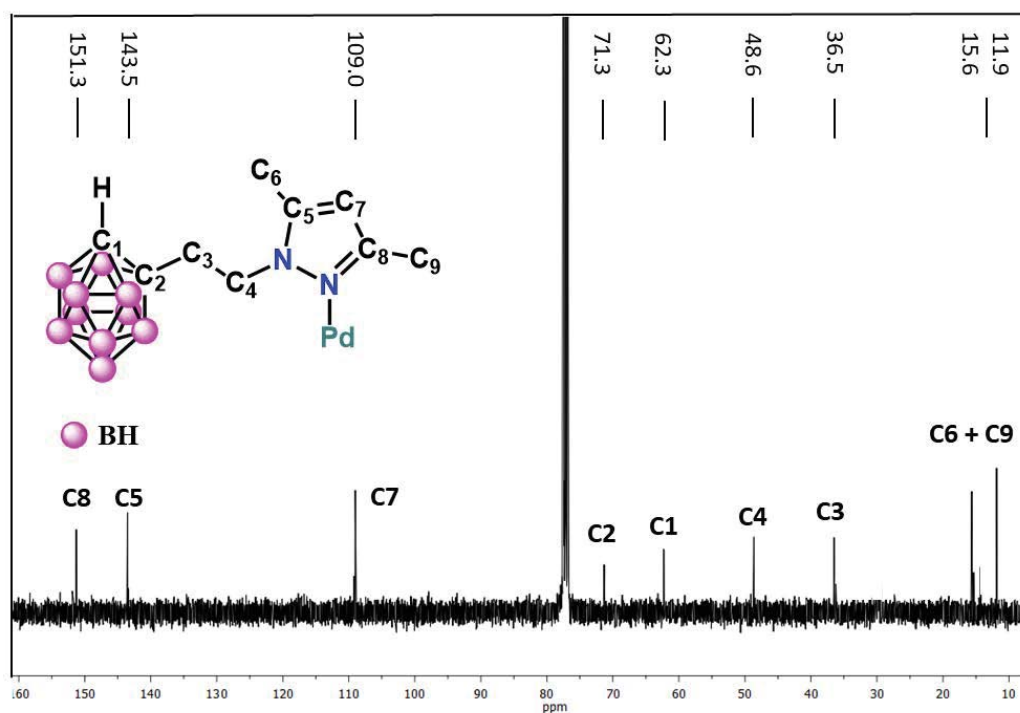


Figure S3.4.17 $^{13}\text{C}\{^1\text{H}\}$ NMR spectrum of compound **28** (CDCl_3 , 100.6 MHz).

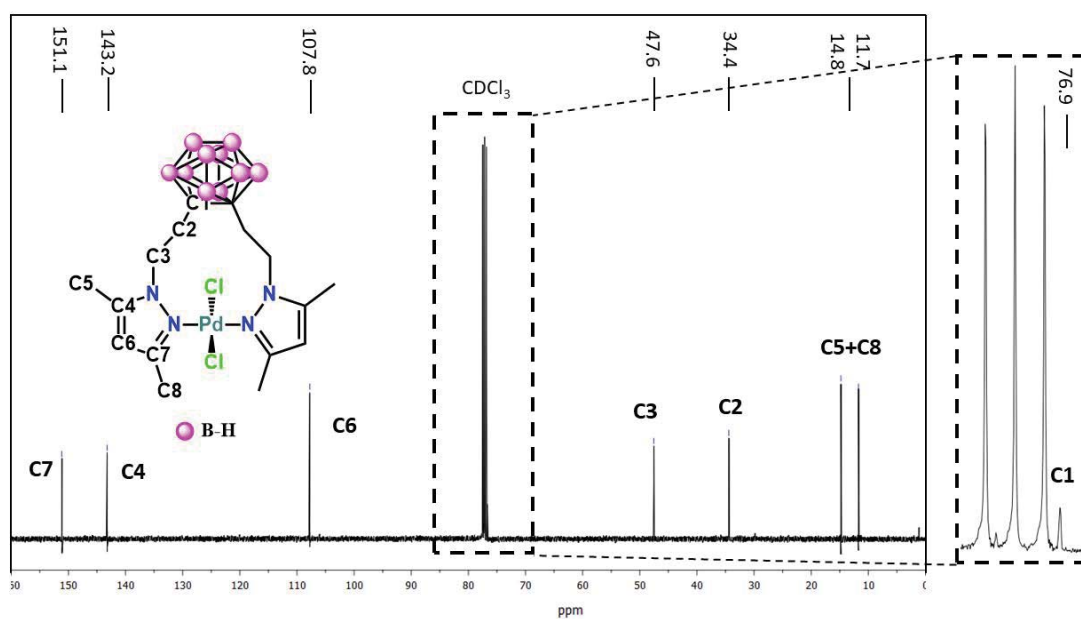


Figure S3.4.18 $^{13}\text{C}\{^1\text{H}\}$ NMR spectrum of compound **29** (CDCl_3 , 100.6 MHz).

Annex for Section 3.5

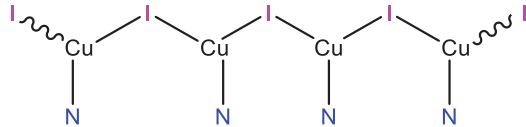
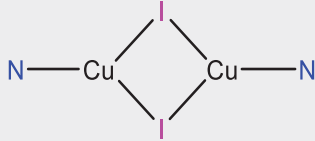
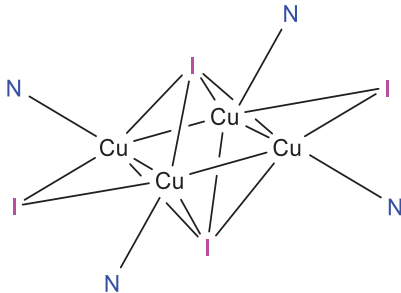
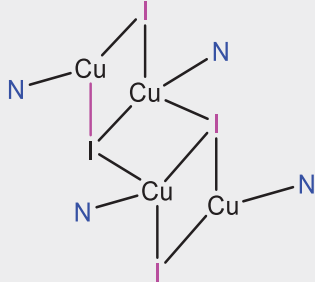
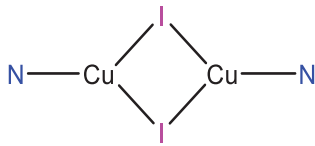
Table S3.5.1 Bond lengths (Å) and angles (°) for 32A

Bond lengths (Å)					
Cu(1)-I(1)	3.1044(8)	Cu(2)-I(1)	2.6985(6)	Cu(2)-N(52)	1.990(4)
Cu(1)-I(1)#1	2.7027(7)	Cu(2)-I(1)#1	2.7437(6)	Cu(1)-Cu(2)	2.5917(8)
Cu(1)-I(2)	2.5662(6)	Cu(2)-I(2)	2.6474(6)	Cu(1)-Cu(2)#1	2.9289(9)
Cu(1)-N(22)	1.984(4)				
Bond angles (°)					
Cu(2)-Cu(1)-Cu(2)#1	81.92(2)	N(22)-Cu(1)-I(1)	121.00(11)	N(52)-Cu(2)-Cu(1)	157.28(11)
Cu(2)-Cu(1)-I(1)	55.680(18)	N(22)-Cu(1)-I(2)	118.79(11)	N(52)-Cu(2)-I(1)	129.93(11)
Cu(2)-Cu(1)-I(1)#1	62.384(19)	Cu(1)-Cu(2)-Cu(1)#1	98.07(2)	N(52)-Cu(2)-I(1)#1	115.49(10)
Cu(2)#1-Cu(1)-I(1)	54.003(17)	Cu(1)-Cu(2)-I(1)	71.83(2)	N(52)-Cu(2)-I(2)	105.24(11)
I(1)#1-Cu(1)-Cu(2)#1	57.089(17)	Cu(1)-Cu(2)-I(1)#1	60.791(18)	Cu(1)#1-I(1)-Cu(1)	91.661(19)
I(1)#1-Cu(1)-I(1)	88.339(19)	Cu(1)-Cu(2)-I(2)	58.645(19)	Cu(1)#1-I(1)-Cu(2)#1	56.823(17)
I(2)-Cu(1)-Cu(2)#1	141.75(3)	I(1)-Cu(2)-Cu(1)#1	57.230(17)	Cu(2)-I(1)-Cu(1)	52.488(17)
I(2)-Cu(1)-Cu(2)	61.762(19)	I(1)#1-Cu(2)-Cu(1)#1	66.265(19)	Cu(2)#1-I(1)-Cu(1)	59.732(17)
I(2)-Cu(1)-I(1)	93.00(2)	I(1)-Cu(2)-I(1)#1	96.383(18)	Cu(2)-I(1)-Cu(1)#1	65.678(19)
I(2)-Cu(1)-I(1)#1	109.71(2)	I(2)-Cu(2)-Cu(1)#1	153.99(2)	Cu(2)-I(1)-Cu(2)#1	83.615(18)
N(22)-Cu(1)-Cu(2)	176.55(11)	I(2)-Cu(2)-I(1)	101.161(19)	Cu(1)-I(2)-Cu(2)	59.593(19)
N(22)-Cu(1)-Cu(2)#1	96.74(11)	I(2)-Cu(2)-I(1)#1	106.11(2)		
N(22)-Cu(1)-I(1)#1	119.52(10)	N(52)-Cu(2)-Cu(1)#1	100.27(11)		

#1: x+1, y, z

#2: x-1, y, z

Table S3.5.2 Relevant bond lengths for compounds **30-33**

	Schematic representation of the <i>core</i> geometrical motif	Cu-N bond lengths (Å) (Mean value)	Cu-I bond lengths (Å) (Mean value)	Cu-Cu bond lengths (Å) (Mean value)
30		1.971(4)	2.5538(6) 2.5499(6) 2.5520(6)	4.275
31		1.9543(3) 1.963(3) 1.958(3)	2.5426(7) 2.6084(7) 2.5439(7) 2.6107(7) 2.5764(7)	2.4726(9) 2.5158(9) 2.4942(9)
32		1.984(4) 1.990(4) 1.987(4)	3.1044(8) 2.7027(7) 2.5662(6) 2.6985(6) 2.7437(6) 2.6474(6) 2.7438(7)	2.5917(8) 2.9289(8) 2.7603(8)
33		1.998(4) 1.987(5) 1.993(5)	2.6351(10) 2.8614(9) 2.7128(9) 2.5547(10) 2.5991(10) 2.6726(10)	2.6373(12)
		1.966(4) 1.979(4) 1.973(4)	2.5523(9) 2.5853(9) 2.5772(9) 2.5421(10) 2.5590(9)	2.5583(10)

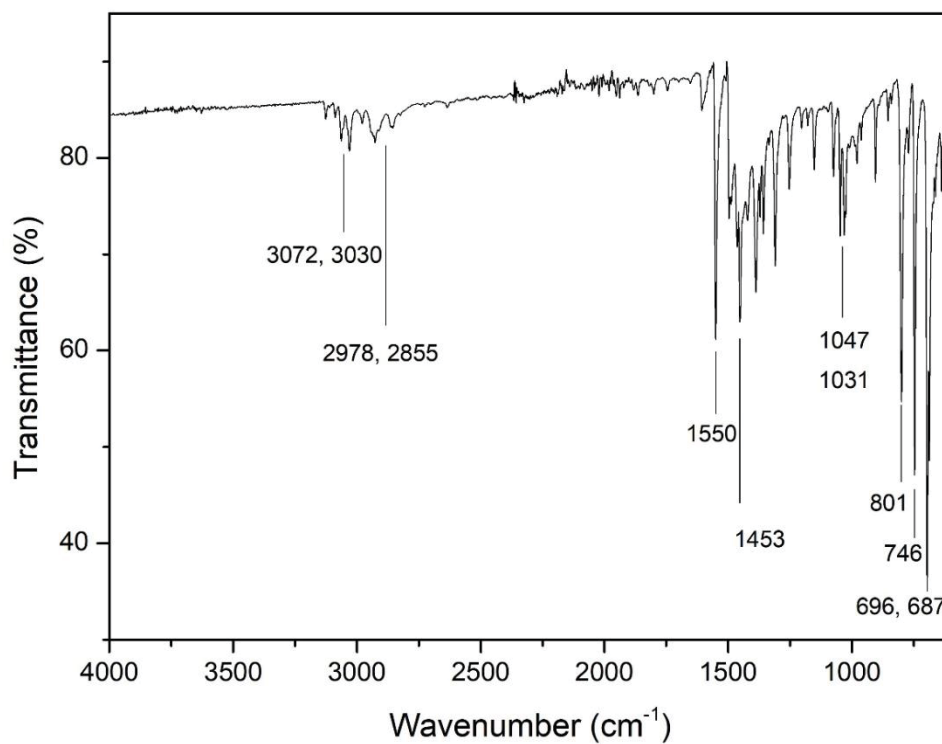


Figure S3.5.1 FTIR-ATR spectrum of compound 30

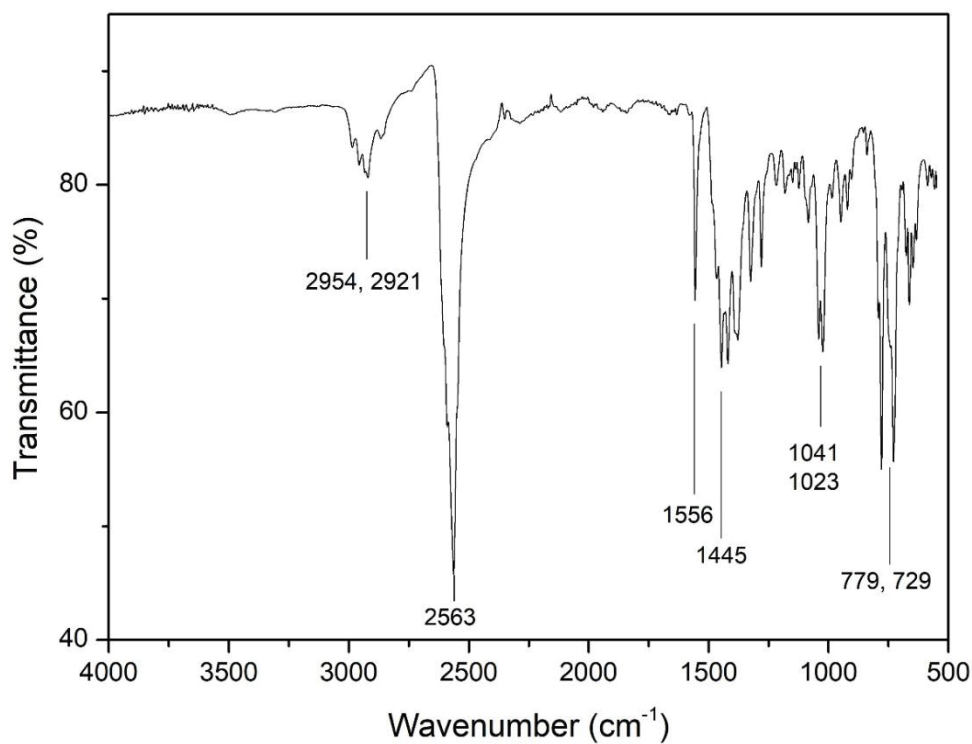


Figure S3.5.2 FTIR-ATR spectrum of compound 32B

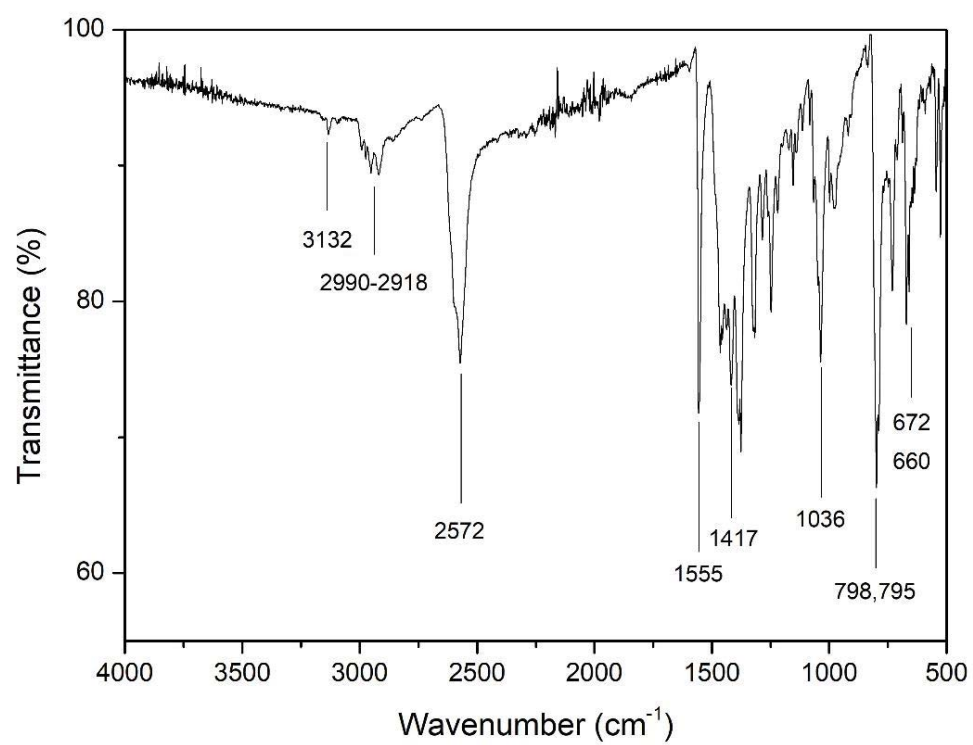


Figure S3.5.3 FTIR-ATR spectrum of compound 33

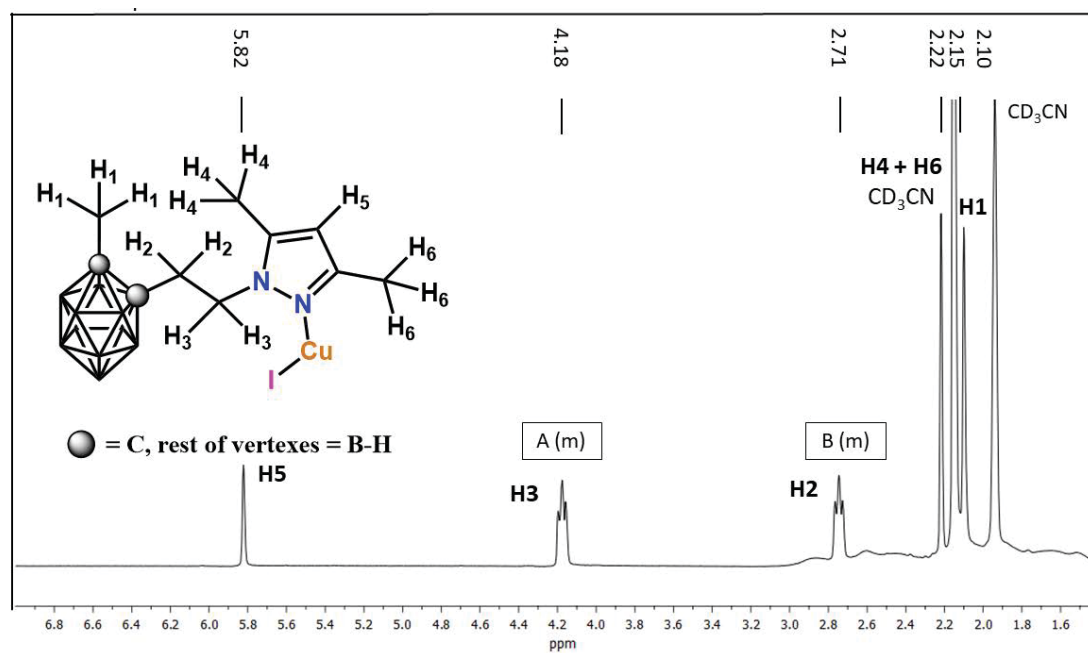


Figure S3.5.4 ^1H NMR spectrum of **32B** (CD_3CN , 400.0 MHz)

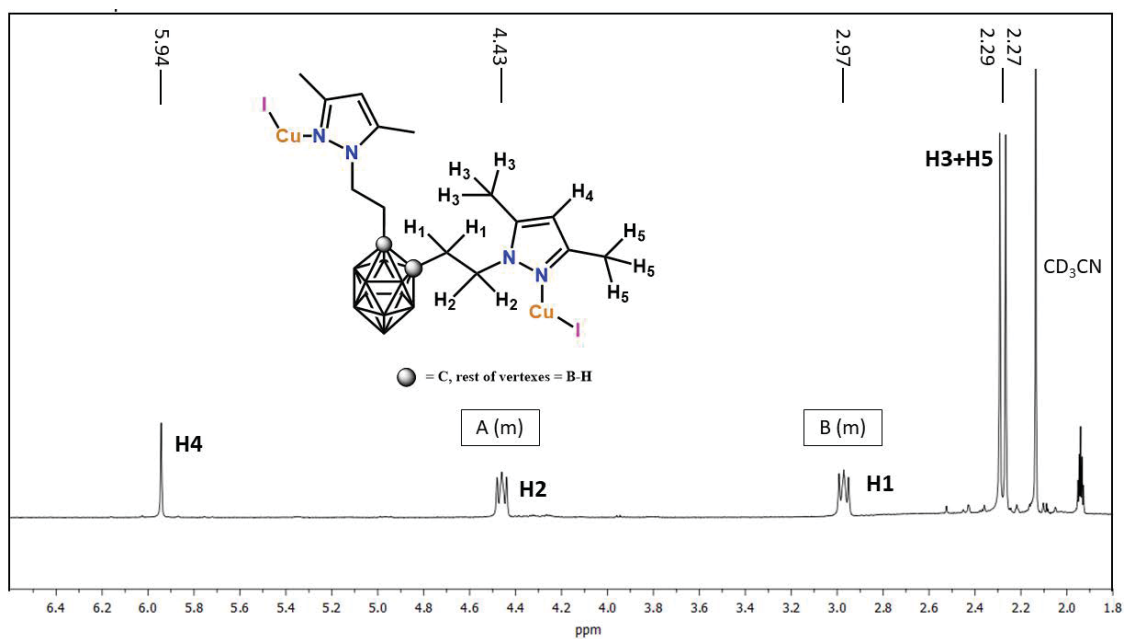


Figure S3.5.5 ^1H NMR spectrum of **33** fragments (CD_3CN , 400.0 MHz)

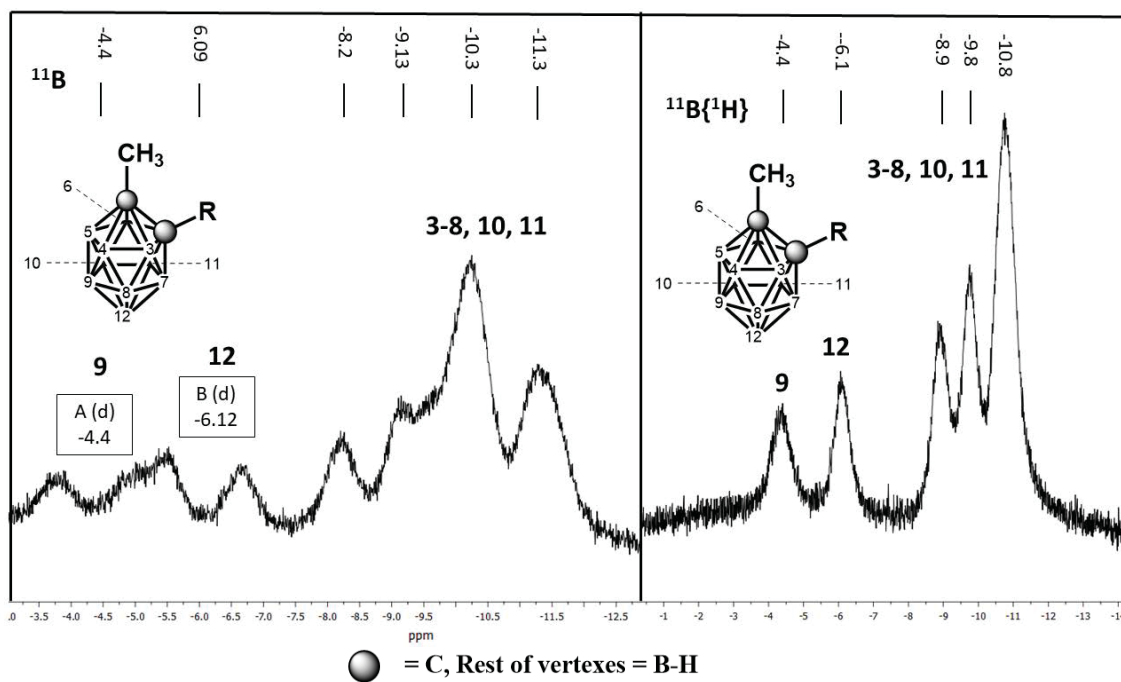


Figure S3.5.6 ^{11}B (left) and $^{11}\text{B}\{^1\text{H}\}$ (right) NMR spectrum of **32B** (CD_3CN , 128.6 MHz)

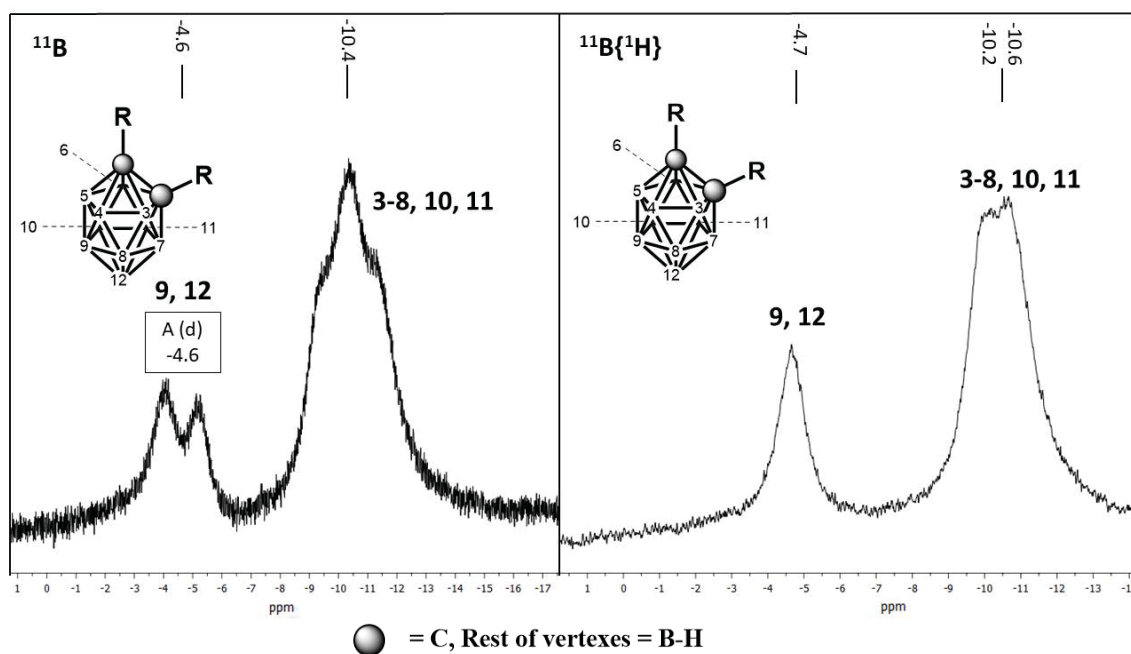


Figure S3.5.7 ^{11}B (left) and $^{11}\text{B}\{^1\text{H}\}$ (right) NMR spectrum of **33** fragments (CD_3CN , 128.6 MHz)

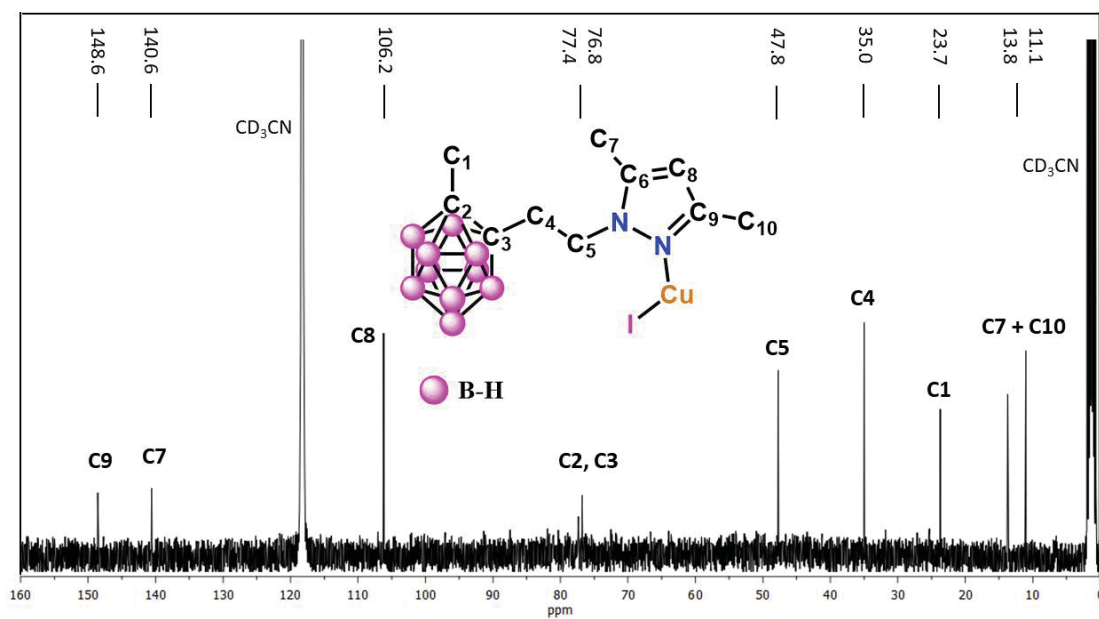


Figure S3.5.8 $^{13}\text{C}\{^1\text{H}\}$ NMR spectrum of **32B** (CD_3CN , 100.6 MHz)

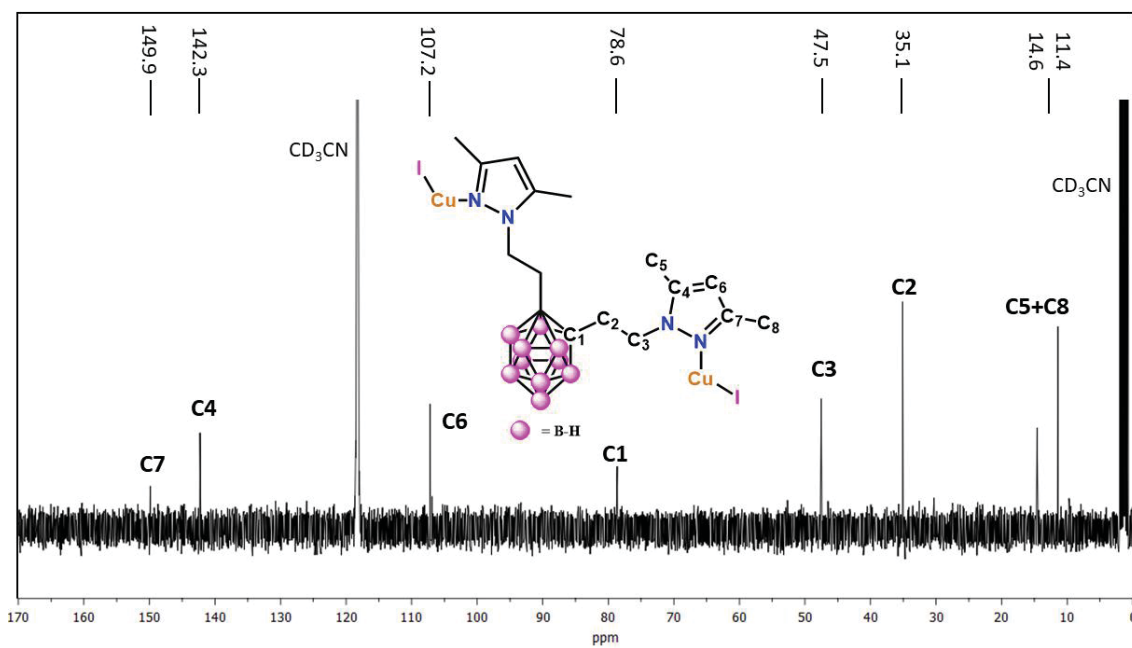


Figure S3.5. $^{13}\text{C}\{^1\text{H}\}$ NMR spectrum of **33** (CD_3CN , 100.6 MHz)

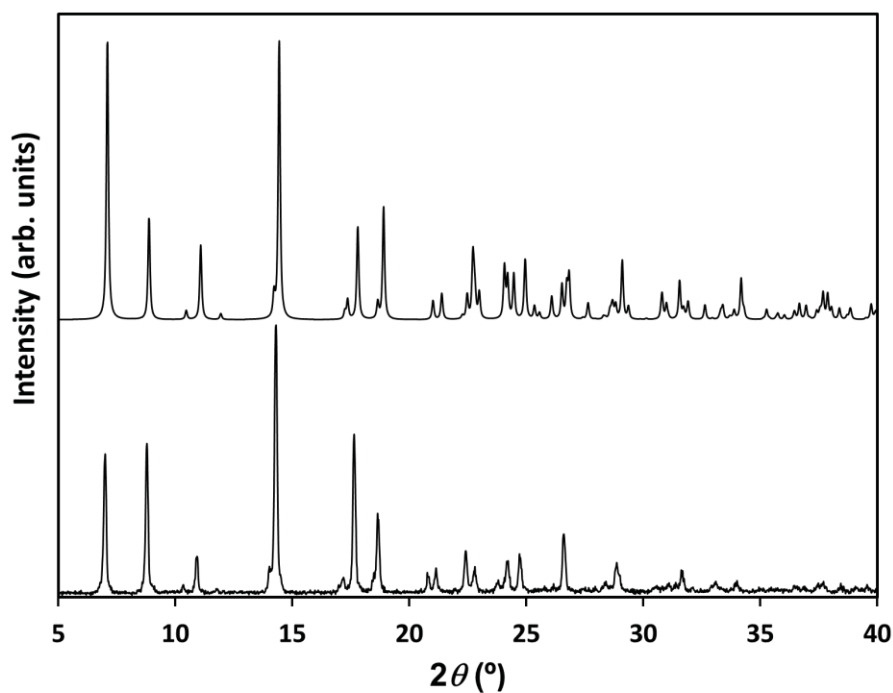


Figure S3.5.10 PXRD pattern of compound **30** (bottom). PXRD pattern from resolved crystal structure at 100(2) K (top) is also included as a reference.

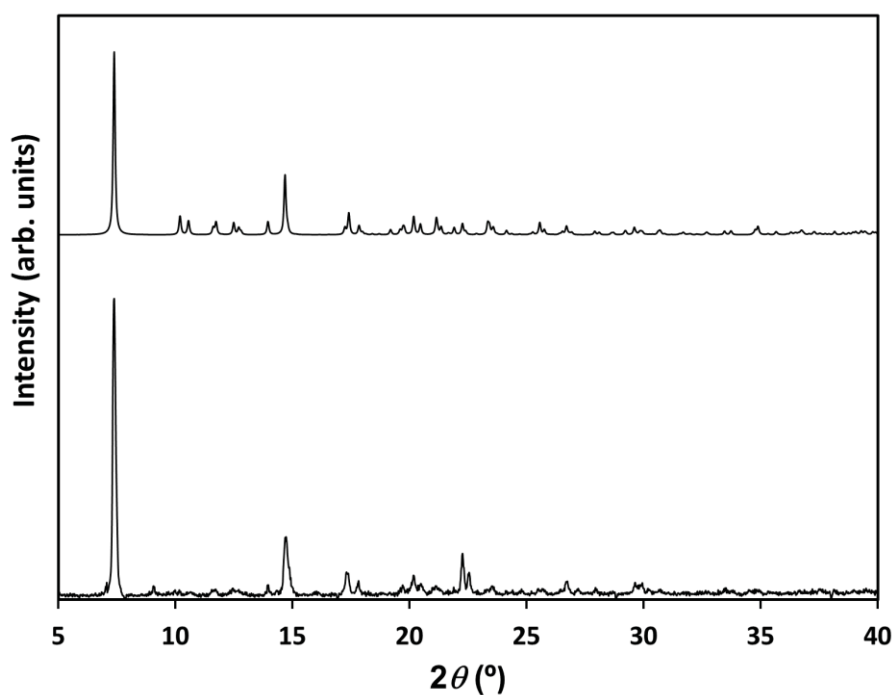


Figure S3.5.11 PXRD pattern of compound **31** (bottom). PXRD pattern from resolved crystal structure at 298(2) K (top) is also included as a reference.

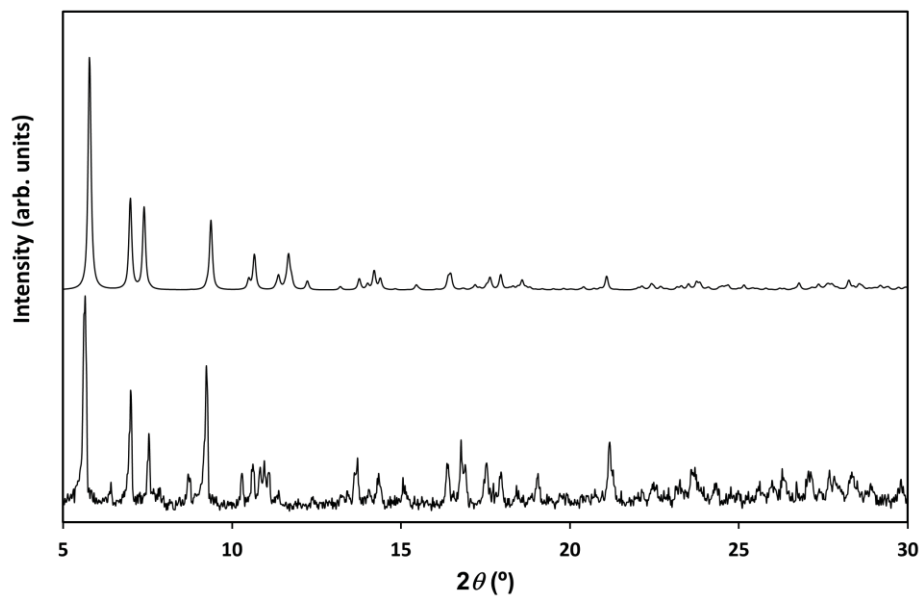


Figure S3.5.12 PXRD pattern of compound **32B** (bottom). PXRD pattern from provisional crystal structure at 298(2) K (top) is also included as a reference.

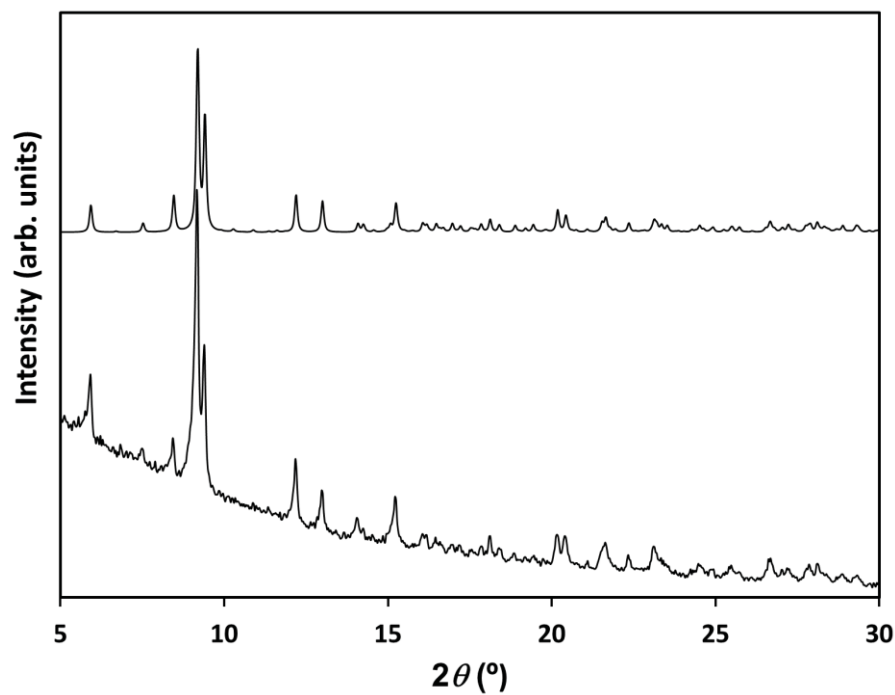


Figure S3.5.13 PXRD pattern of compound **33** (bottom). PXRD pattern from resolved crystal structure at 298(2) K (top) is also included as a reference.

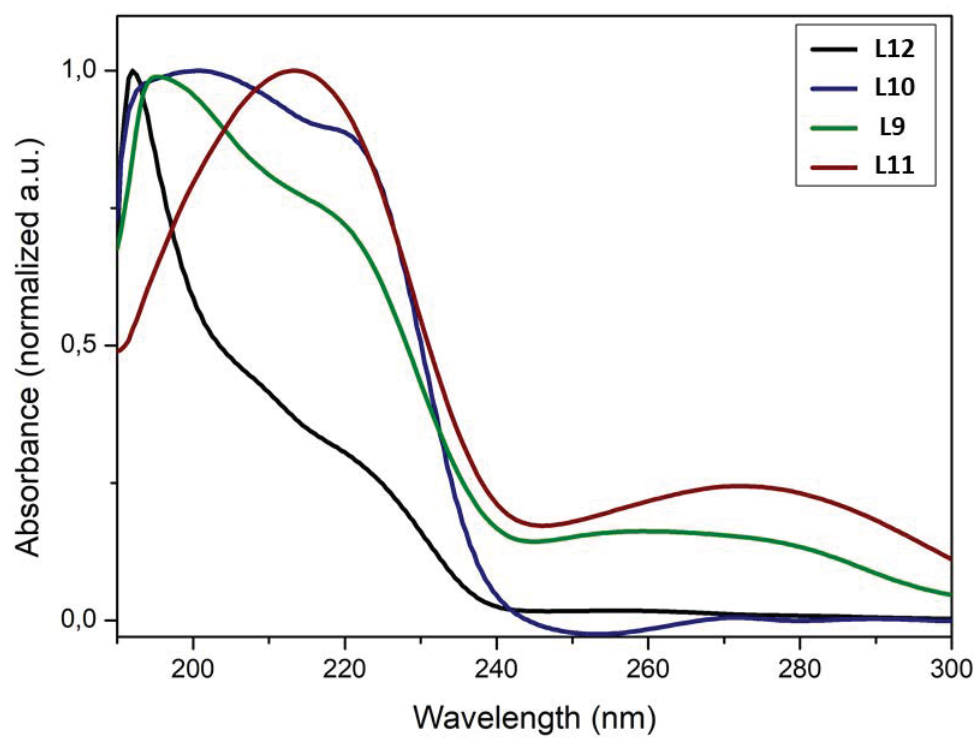


Figure S3.5.2 UV-Vis spectra of ligands **L9-L12** (CH₃CN, $1.45 \cdot 10^{-5}$ M to $6.5 \cdot 10^{-5}$ M, normalized spectra).

ANNEX II: Publications

List of Publications

Article 1: “3,5-disubstituted-N-hydroxyalkylpyrazole Cu(II) compounds: Anion effect on dimensionality, supramolecular structure and magnetic properties”

Joan Soldevila-Sanmartín, Xavier Montaner, Teresa Calvet, Mercè Font-Bardia, Josefina Pons.

Polyhedron 188 (2020) 114686

Article 2: “Dimeric Metallacycles and Coordination Polymers: Zn(II), Cd(II) and Hg(II) complexes of two positional isomers of a flexible N,O-hybrid bispyrazole derived ligand”

Joan Soldevila-Sanmartín, Miguel Guerrero, Duane Choquesillo-Lazarte, José Giner Planas, Josefina Pons.

Inorgánica Chimica Acta 506 (2020) 119549.

Article 3: “Tuning the architectures and luminescence properties of Cu(I) compounds of phenyl and carboranyl pyrazoles: the impact of 2D versus 3D aromatic moieties in the ligand backbone”

Joan Soldevila-Sanmartín, Eliseo Ruiz, Duane Choquesillo-Lazarte, Mark E. Light, Clara Viñas, Francesc Teixidor, Rosario Núñez, Josefina Pons, José Giner Planas.

Journal of Materials Chemistry C 9 (2021) 7643.